



NASA-ISRO SAR (NISAR) Mission Science Users' Handbook

Current Project

Phase: C

Planned Launch Date:

January 2022

Document Date:

August 2019, Version 1

CONTENTS



1	INTRODUCTION	1
<hr/>		
2	SCIENCE FOCUS AREAS	5
2.1	SOLID EARTH PROCESSES: EARTHQUAKES, VOLCANOES, AND LANDSLIDES	6
2.2	ECOSYSTEMS: BIOMASS, DISTURBANCE, AGRICULTURE, AND INUNDATION	8
2.3	DYNAMICS OF ICE: ICE SHEETS, GLACIERS, AND SEA ICE	9
2.4	APPLICATIONS	11
2.5	DISASTER RESPONSE	14
2.6	OCEAN STUDIES AND COASTAL PROCESSES	15
<hr/>		
3	MISSION MEASUREMENTS AND REQUIREMENTS	17
3.1	MEASUREMENTS OF SURFACE DEFORMATION AND CHANGE	17
3.2	LANDCOVER AND FOREST CHARACTERIZATION WITH L-BAND SAR	18
3.3	REQUIREMENTS AND SCIENCE TRACEABILITY	19
3.4	SCIENCE TRACEABILITY TO MISSION REQUIREMENTS	23
<hr/>		
4	MISSION CHARACTERISTICS	27
4.1	OBSERVING STRATEGY	27
4.2	REFERENCE SCIENCE ORBIT	27
4.3	MISSION PHASES AND TIMELINE	33
4.4	GROUND SEGMENT OVERVIEW	34
4.5	TELECOMMUNICATIONS	36
4.6	MISSION PLANNING AND OPERATIONS	38
4.7	INSTRUMENT DESIGN	39
4.8	FLIGHT SYSTEMS/SPACECRAFT	43
4.9	PROJECT STATUS	45

5	MISSION DATA PRODUCTS	47
5.1	L0 DATA PRODUCTS	49
5.2	L1 DATA PRODUCTS	50
5.3	L2 DATA PRODUCTS	52
5.4	DATA PRODUCT DELIVERY/HOW TO ACCESS NISAR DATA	53

6	SCIENCE DATA PRODUCTS AND VALIDATION APPROACHES	55
6.1	SOLID EARTH SCIENCE PRODUCTS	55
6.1.1	Theoretical basis of algorithm	55
6.1.2	Implementation approach for algorithm	57
6.1.3	Planned output products	62
6.2	ECOSYSTEMS PRODUCTS-BIOMASS	62
6.2.1	Theoretical basis of algorithm	63
6.2.2	Implementation approach for algorithm	68
6.2.3	Planned output products	73
6.3	ECOSYSTEMS PRODUCTS-DISTURBANCE	73
6.3.1	Theoretical basis of algorithm	75
6.3.2	Implementation approach for algorithm	77
6.3.3	Planned output products	82
6.4	ECOSYSTEMS PRODUCTS-INUNDATION	82
6.4.1	Implementation approach for algorithm	83
6.4.2	Planned output products	86
6.5	ECOSYSTEMS PRODUCTS-CROP MONITORING	87
6.5.1	Theoretical basis of algorithm	87
6.5.2	Implementation approach for algorithm	89
6.5.3	Planned output products	90

6.6	CRYOSPHERE PRODUCTS-ICE SHEETS	91
6.6.1	Theoretical basis of algorithm	92
6.6.2	Implementation approach for algorithm	94
6.6.3	Planned output products	99
6.7	CRYOSPHERE PRODUCTS-SEA ICE	100
6.7.1	Theoretical basis of algorithm	100
6.7.2	Implementation approach for algorithm	105
6.7.3	Planned output products	107

7	ERROR SOURCES	109
7.1	POLARIMETRIC ERROR SOURCES	109
7.2	INTERFEROMETRIC ERROR SOURCES	110

8	CALIBRATION AND VALIDATION	115
8.1	BACKGROUND	115
8.2	CALIBRATION AND VALIDATION ACTIVITIES	116
8.3	CALIBRATION/VALIDATION ROLES AND RESPONSIBILITIES	122

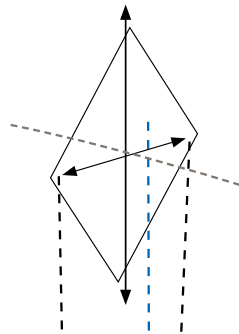
9	CONCLUSIONS	125
----------	--------------------	------------

10	ACKNOWLEDGMENTS	127
-----------	------------------------	------------

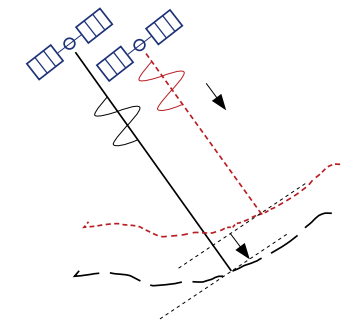
11	REFERENCES	129
-----------	-------------------	------------

12	ACRONYMS	143
-----------	-----------------	------------

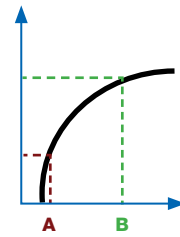
13	APPENDIX A: HISTORICAL BACKGROUND FOR NISAR	145
-----------	--	------------



14	APPENDIX B: NISAR SCIENCE TEAM	147
14.1	NASA SCIENCE DEFINITION TEAM	147
14.2	ISRO SCIENCE TEAM	148
14.3	PROJECT SCIENCE TEAM	149
15	APPENDIX C: KEY CONCEPTS	151
15.1	BASIC RADAR CONCEPTS: RADAR IMAGING, POLARIMETRY, AND INTERFEROMETRY	151
15.1.1	Synthetic Aperture Radar (SAR)	151
15.1.2	Polarimetry	152
15.1.3	Interferometric Synthetic Aperture Radar (InSAR)	153
15.2	DEFORMATION-RELATED TERMINOLOGY	154
15.2.1	Deformation and displacement	156
15.2.2	Strain, gradients, and rotation	157
15.2.3	Stress and rheology	157
15.3	ECOSYSTEMS-RELATED TERMINOLOGY	157
15.3.1	Biomass	157
15.3.2	Disturbance	158
15.3.3	Recovery	158
15.3.4	Classification	158
16	APPENDIX D: BASELINE LEVEL 2 REQUIREMENTS	161
16.1	LEVEL 2 SOLID EARTH	161
16.2	LEVEL 2 CRYOSPHERE	161
16.3	LEVEL 2 ECOSYSTEMS	163
16.4	LEVEL 2 URGENT RESPONSE	165



17	APPENDIX E: NISAR SCIENCE FOCUS AREAS	167
17.1	SOLID EARTH	167
17.1.1	Earthquakes and seismic hazards	168
17.1.2	Volcano hazards	173
17.1.3	Landslide hazards	174
17.1.4	Induced seismicity	176
17.1.5	Aquifer systems	179
17.1.6	Glacial isostatic adjustment	184
17.2	ECOSYSTEMS	184
17.2.1	Biomass	185
17.2.2	Biomass disturbance and recovery	187
17.2.3	Agricultural monitoring	188
17.2.4	Wetlands and inundation	190
17.3	CRYOSPHERE	191
17.3.1	Ice sheets	193
17.3.2	Glaciers and mountain snow	195
17.3.3	Sea ice	197
17.3.4	Permafrost	200
17.4	APPLICATIONS	201
17.4.1	Ecosystems: Food security	204
17.4.2	Ecosystems: Forest resource management	205
17.4.3	Ecosystems: Wildland fires	206
17.4.4	Ecosystems: Forest disturbance	208
17.4.5	Ecosystems: Coastal erosion and shoreline change	209
17.4.6	Geologic Hazards: Earthquakes	210
17.4.7	Geologic Hazards: Volcanic unrest	210
17.4.8	Geologic Hazards: Sinkholes and mine collapse	211



17.4.9	Geologic Hazards: Landslides and debris flows	211
17.4.10	Hazards: Anthropogenic technological disasters	212
17.4.11	Critical Infrastructure: Levees, dams, and aqueducts	212
17.4.12	Critical Infrastructure: Transportation	214
17.4.13	Critical Infrastructure: Facility situational awareness	214
17.4.14	Critical Infrastructure: Arctic domain awareness	214
17.4.15	Maritime: Hurricanes and wind storms	214
17.4.16	Maritime: Sea ice monitoring	215
17.4.17	Maritime: Coastal ocean circulation features	215
17.4.18	Maritime: Ocean surface wind speed	216
17.4.19	Maritime: Iceberg and ship detection	217
17.4.20	Maritime: Oil spills	217
17.4.21	Maritime/Hydrology: Flood hazards	217
17.4.22	Hydrology: Flood forecasting	219
17.4.23	Hydrology: Coastal inundation	220
17.4.24	Hydrology: Soil moisture	221
17.4.25	Underground Reservoirs: Groundwater withdrawal	222
17.4.26	Underground Reservoirs: Oil and gas production	223
17.4.27	Underground Reservoirs: Induced seismicity	223
17.4.28	Rapid damage assessment	225

18

APPENDIX F: IN SITU MEASUREMENTS FOR CAL/VAL 227

18.1	SOLID EARTH IN SITU MEASUREMENTS FOR CAL/VAL	227
18.1.1	Co-seismic, secular, and transient deformation rates	227
18.1.2	Permafrost deformation	229
18.2	CRYOSPHERE IN SITU MEASUREMENTS FOR CAL/VAL	232
18.2.1	Fast/slow deformation of ice sheets and glacier velocity	232
18.2.2	Vertical displacement and fast ice-shelf flow	233
18.2.3	Sea ice velocity	234
18.3	ECOSYSTEMS IN SITU MEASUREMENTS FOR CAL/VAL	236
18.3.1	Above ground biomass (AGB)	237
18.3.2	Forest disturbance	238
18.3.3	Inundation area	242
18.3.4	Cropland area	244

19

APPENDIX G: RADAR INSTRUMENT MODES 249

20

APPENDIX H: SCIENCE TARGET MAPS 253

21

APPENDIX I: DATA PRODUCT LAYERS 255

Updated for Baseline Left-Looking Only Mode —
October, 2018

Suggested Citation: NISAR, 2018. NASA-ISRO SAR (NISAR) Mission Science Users' Handbook. NASA Jet Propulsion Laboratory. 261 pp.

CL# 18-1893

List of Authors

Falk Amelung

University of Miami

Gerald Bawden

NASA Headquarters

Adrian Borsa

Scripps Institution of
Oceanography, UC, San Diego

Sean Buckley

Jet Propulsion Laboratory,
California Institute of Technology

Susan Callery

Jet Propulsion Laboratory,
California Institute of Technology

Manab Chakraborty

Space Applications Centre,
Indian Space Research Organisation

Bruce Chapman

Jet Propulsion Laboratory,
California Institute of Technology

Anup Das

Space Applications Centre,
Indian Space Research Organisation

Andrea Donnellan

Jet Propulsion Laboratory,
California Institute of Technology

Ralph Dubayah

University of Maryland

Kurt Feigl

University of Wisconsin

Eric Fielding

Jet Propulsion Laboratory,
California Institute of Technology

Richard Forster

University of Utah

Margaret Glasscoe

Jet Propulsion Laboratory,
California Institute of Technology

Bradford Hager

Massachusetts Institute of Technology

Scott Hensley

Jet Propulsion Laboratory,
California Institute of Technology

Benjamin Holt

Jet Propulsion Laboratory,
California Institute of Technology

Cathleen Jones

Jet Propulsion Laboratory,
California Institute of Technology

Ian Joughin

Applied Physics Laboratory,
University of Washington

Josef KelIndorfer

Earth Big Data, LLC.

Raj Kumar

Space Applications Centre,
Indian Space Research Organisation

Rowena Lohman

Cornell University

Zhong Lu

Southern Methodist University

Franz Meyer

University of Alaska, Fairbanks

Tapan Misra

Space Applications Centre,
Indian Space Research Organisation

Frank Monaldo

National Oceanic and
Atmospheric Administration

Sandip Oza

Space Applications Centre,
Indian Space Research Organisation

Matthew Pritchard

Cornell University

Eric Rignot

University of California, Irvine

Paul Rosen

Jet Propulsion Laboratory,
California Institute of Technology

Sassan Saatchi

Jet Propulsion Laboratory,
California Institute of Technology

Priyanka Sharma

Jet Propulsion Laboratory,
California Institute of Technology

Marc Simard

Jet Propulsion Laboratory,
California Institute of Technology

Mark Simons

Jet Propulsion Laboratory,
California Institute of Technology

Paul Siqueira

University of Massachusetts,
Amherst

Howard Zebker

Stanford University

1 INTRODUCTION

NISAR PROVIDES
A MEANS OF
DISENTANGLING
AND CLARIFYING
SPATIALLY AND
TEMPORALLY
COMPLEX
PHENOMENA,
RANGING FROM
ECOSYSTEM
DISTURBANCES, TO
ICE SHEET COLLAPSE
AND NATURAL
HAZARDS INCLUDING
EARTHQUAKES,
TSUNAMIS, VOLCANOES,
AND LANDSLIDES.

The NASA-ISRO Synthetic Aperture Radar (SAR), or NISAR mission, (Figure 1-1) is a multidisciplinary radar mission to make integrated measurements to understand the causes and consequences of land surface changes. NISAR will make global measurements of the causes and consequences of land surface changes for integration into Earth system models. NISAR provides a means of disentangling and clarifying spatially and temporally complex phenomena, ranging from ecosystem disturbances, to ice sheet collapse and natural hazards including earthquakes, tsunamis, volcanoes, and landslides. The purpose of this handbook is to prepare scientists and algorithm developers for NISAR by providing a basic description of the mission and its data characteristics that will allow them to take full advantage of this comprehensive data set when it becomes available.

NISAR is a joint partnership between the National Aeronautics and Space Administration (NASA) and the Indian Space Research Organisation (ISRO). Since the 2007 National Academy of Science “Decadal Survey” report, “Earth Science and Applications from Space: National Imperatives for the Next Decade and Beyond,” NASA has been studying concepts for a Synthetic Aperture Radar mission to determine Earth change in three disciplines: ecosystems (vegetation and the carbon cycle), deformation (solid Earth studies), and cryospheric sciences (primarily as related to climatic drivers and effects on sea level). In the course of these studies, a partnership with ISRO developed, which led to a joint spaceborne mission with both L-band and S-band SAR systems onboard. The current 2018 Decadal Survey, “Thriving on Our Changing Planet: A Decadal Strategy for Earth Observation from Space,” confirms the importance of NISAR and encourages the international partnership between NASA and ISRO.

The Earth Science Division (ESD) within the Science Mission Directorate (SMD) at NASA Headquarters has directed the Jet Propulsion Laboratory (JPL) to manage the United States component of the NISAR project. ESD has assigned the Earth Science Mission Program Office (ESMPO), located at Goddard Space Flight Center (GSFC), the responsibility for overall program management.

The NISAR mission is derived from the Deformation, Ecosystem Structure and Dynamics of Ice (DESDynI) radar mission concept, which was one of the four Tier 1 missions recommended in the 2007 Decadal Survey. To satisfy requirements of three distinct scientific communities with global perspectives, as well as address the potentials of the system for new applications, the NISAR system comprises a dual frequency, fully polarimetric radar, with an imaging swath greater than 240 km. This design permits complete global coverage in a 12-day exact repeat to generate interferometric time series and perform systematic global mapping of the changing surface of the Earth. The recommended lidar component of DESDynI will be accomplished with the GEDI mission (Global Ecosystem Dynamics Investigation Lidar). NISAR’s launch is planned for January 2022. After a 90-day commissioning period, the mission will conduct a minimum of three full years of science operations with the L-band SAR in a near-polar, dawn-dusk, frozen, sun-synchronous orbit to satisfy NASA’s requirements; ISRO requires five years of operations with the S-band SAR. If the system does not use its fuel reserved excess capacity during the nominal mission, it is possible to extend mission operations further for either instrument.

NISAR’s science objectives are based on priorities identified in the 2007 Decadal Survey and rearticulated in the 2010 report on NASA’s Climate-Centric Architecture. NISAR will be the first NASA radar mission to systematically and globally study solid Earth, ice masses,

FIGURE 1-1

Artist’s concept of NASA–Indian Space Research Organisation Synthetic Aperture Radar (NISAR) in orbit. The mission will produce L-band (at 25-cm wavelength) polarimetric radar images and interferometric data globally, and comparable S-band (at 12-cm wavelength) data over India and targeted areas around the world. Credit: NASA/JPL-Caltech.



NISAR WILL BE THE FIRST NASA RADAR MISSION TO SYSTEMATICALLY AND GLOBALLY STUDY SOLID EARTH, ICE MASSES, AND ECOSYSTEMS.

and ecosystems. NISAR will measure ice mass and land surface motions and changes, ecosystem disturbances, and biomass, elucidating underlying processes and improving fundamental scientific understanding. The measurements will improve forecasts and assessment of changing ecosystems, response of ice sheets, and natural hazards. NASA also supports use of the NISAR data for a broad range of applications that benefit society, including response to disasters around the world. In addition to the original NASA objectives, ISRO has identified a range of applications of particular relevance to India that the mission will address, including monitoring of agricultural biomass over India, monitoring and assessing disasters to which India responds, studying snow and glaciers in the Himalayas, and studying Indian coastal and near-shore oceans.

All NISAR science data (L- and S-band) will be freely available and open to the public, consistent with the long-standing NASA Earth Science open data policy. With its global acquisition strategy, cloud-penetrating capability, high spatial resolution, and 12-day repeat pattern, NISAR will provide a reliable, spatially dense time series of radar data that will be a unique resource for exploring Earth change (Table 1-1).

Anticipated scientific results over the course of the mission include:

- Comprehensive assessment of motion along plate boundaries that cross land, identifying areas of increasing strain, and capturing signatures of several hundred earthquakes that will contribute to our understanding of fault systems;
- Comprehensive inventories of global volcanoes, their state of activity and associated risks;

- Comprehensive biomass assessment in low biomass areas where dynamics are greatest, and global disturbance assessments, agricultural change, and wetlands dynamics, informing carbon flux models at the most critical spatial and temporal scales;
- In combination with GEDI and other missions, comprehensive global biomass to set the decadal boundary conditions for carbon flux models;
- Complete assessments of the velocity state of Greenland's and Antarctica's ice sheets, each month over the mission life, as a key boundary condition for ice sheet models;
- Regular monitoring of the world's most dynamic mountain glaciers;
- Comprehensive mapping of sea ice motion and deformation, improving our understanding of ocean-atmosphere interaction at the poles;
- A rich data set for exploring a broad range of applications that benefit from fast, reliable, and regular sampling of areas of interest on land or ice. These include infrastructure monitoring, agriculture and forestry, disaster response, aquifer utilization, and ship navigability.

TABLE 1-1. NISAR CHARACTERISTICS

NISAR Characteristic:	Enables:
L-band (24 cm wavelength)	Foliage penetration and interferometric persistence
S-band (12 cm wavelength)	Sensitivity to light vegetation
SweepSAR ¹ technique with imaging swath > 240 km	Global data collection
Polarimetry (single/dual/quad)	Surface characterization and biomass estimation
12-day exact repeat	Rapid sampling
3 – 10 meters mode-dependent SAR resolution	Small-scale observations
3 years science operations (5 years consumables)	Time series analysis
Pointing control < 273 arcseconds	Deformation interferometry
Orbit control < 350 meters	Deformation interferometry
> 30% observation duty cycle	Complete land/ice coverage
Left/right pointing capability	Polar coverage, north and south
Nominal mission pointing: left only	Time series continuity

¹SweepSAR is a technique to achieve wide swath at full resolution. See Section 4.7 for a more detailed description.



FIGURE 1-2

NISAR will image Earth's dynamic surface over time. NISAR will provide information on changes in ice sheets and glaciers, the evolution of natural and managed ecosystems, earthquake and volcano deformation, subsidence from groundwater and oil pumping, and the human impact of these and other phenomena (all images are open source).

2 SCIENCE FOCUS AREAS

IN RESPONSE TO
INTERIOR FORCES,
PLATE TECTONICS
DEFORM THE
SURFACE, CAUSING
EARTHQUAKES,
VOLCANOES,
MOUNTAIN BUILDING,
AND EROSION.

Earth's land and ice surface is constantly changing and interacting with its interior, oceans and atmosphere. In response to interior forces, plate tectonics deform the surface, causing earthquakes, volcanoes, mountain building and erosion. These events shaping the Earth's surface can be violent and damaging. Human and natural forces are rapidly modifying the global distribution and structure of terrestrial ecosystems on which life depends, causing steep reductions in species diversity, endangering sustainability, altering the global carbon cycle and affecting climate. Dramatic changes in ice sheets, sea ice, and glaciers are key indicators of these climate effects. Increasing melt rates of landfast ice contribute to sea level rise.

NISAR addresses the needs of Solid Earth, Ecosystems, and Cryospheric science disciplines, and provides data for many applications. NISAR is an all-weather, global geodetic and polarimetric radar-imaging mission with the following key scientific objectives:

1. Determine the likelihood of earthquakes, volcanic eruptions, landslides and land subsidence;
2. Understand the dynamics of carbon storage and uptake in wooded, agricultural, wetland, and permafrost systems;
3. Understand the response of ice sheets to climate change, the interaction of sea ice and climate, and impacts on sea level rise worldwide.

Applications key objectives are to:

1. Understand dynamics of water, hydrocarbon, and sequestered CO₂ reservoirs, which impact societies;
2. Provide agricultural monitoring capability to support sufficient food security objectives;

3. Apply NISAR's unique data set to hazard identification and mitigation;
4. Provide information to support disaster response and recovery;
5. Provide observations of relative sea level rise from melting land ice and land subsidence.

NISAR will provide systematic global measurements to characterize processes, frequent measurements to understand temporal changes, and a minimum three-year duration to estimate long-term trends and determine subtle rates and rate changes. NISAR will serve the objectives of a number of major science disciplines and will meet the needs of a broad science community with numerous applications, including earthquakes, volcanoes, landslides, ice sheets, sea ice, snow and glaciers, coastal processes, ocean and land parameter retrieval, and ecosystems. In addition, NISAR will play a role in monitoring and assessment of natural disasters such as floods, forest fires and earthquakes.

NISAR will meet the needs of a broad end-user community with numerous applications, including assessing geologic and anthropogenic hazards, monitoring critical infrastructure for risk management, supporting agriculture and forestry agencies, identifying pollution in coastal waters, and evaluating ground surface changes associated with fluid extraction, such as groundwater withdrawal during droughts or elevation changes associated with oil or gas production. In addition, NISAR will play a role in response to and recovery from natural disasters such as floods, wildfires and earthquakes.

NISAR observations will address several science and applications areas that the 2018 Decadal Survey recommends progress in:

- Determining the extent to which the shrinking of glaciers and ice sheets, and their contributions to sea-level rise are accelerating, decelerating or remaining unchanged;
- Quantifying trends in water stored on land (e.g., in aquifers) and the implications for issues such as water availability for human consumption and irrigation;
- Understanding alterations to surface characteristics and landscapes (e.g., snow cover, snow melt, landslides, earthquakes, eruptions, urbanization, land-cover and land use) and the implications for applications, such as risk and resource management;
- Assessing the evolving characteristics and health of terrestrial vegetation and aquatic ecosystems, which is important for understanding key consequences such as crop yields, carbon uptake and biodiversity;
- Examining movement of land and ice surfaces to determine, in the case of ice, the likelihood of

rapid ice loss and significantly accelerated rates of sea-level rise, and in the case of land, changes in strain rates that impact and provide critical insights into earthquakes, volcanic eruptions, landslides and tectonic plate deformation.

2.1 SOLID EARTH PROCESSES: EARTHQUAKES, VOLCANOES, AND LANDSLIDES

Society's exposure to natural hazards is increasing. Earthquakes threaten densely populated regions on the U.S. western coast, home to about 50 million citizens and costly infrastructure. Volcanic eruptions endanger many areas of the Earth and can disrupt air travel. Many natural hazards subtly change and deform the land surface resulting in catastrophic events such as landslides. Properly preparing for, mitigating, and responding to nature's disasters require detecting, measuring, and understanding these slow-moving processes before they trigger a disaster.

NISAR provides an opportunity to monitor, mitigate, and respond to earthquakes, volcanoes and landslides that result in land surface deformation (Figure 2-1). The magnitude and dynamics of these surface expressions

provide information about the underlying processes at work. NISAR will uniquely address several questions posed in NASA's Challenges and Opportunities for Earth Surface and Interior (Davis et al, 2016) Report:

1. What is the nature of deformation associated with plate boundaries, and what are the implications for earthquakes, tsunamis and other related natural hazards?
2. How do tectonic processes and climate variability interact to shape Earth's surface and create natural hazards?
3. How do magmatic systems evolve, under what conditions do volcanoes erupt, and how do eruptions and volcano hazards develop?
4. What are the dynamics of Earth's deep interior, and how does Earth's surface respond?

NISAR will also address to varying degrees several questions posed in the 2018 Decadal Survey by the Earth Surface and Interior Panel:

1. How can large-scale geological hazards be accurately forecast in a socially relevant timeframe?
2. How do geological disasters directly impact the Earth system and society following an event?
3. How will local sea level change along coastlines around the world in the next decade to century?
4. What processes and interactions determine the rates of landscape change?
5. How much water is traveling deep underground, and how does it affect geological processes and water supplies?

Measuring displacements associated with earthquakes is essential for describing which parts of a fault have ruptured and which have not, but may have been brought closer to failure, and for constraining estimates of the distribution of fault slip in the subsurface. Seismic data provides estimates of other rupture characteristics, such as the speed at which the rupture propagates along the fault and the rate at which slip

occurs at a given point on the fault, but the characteristics are also best constrained by combining coseismic displacements, such as from NISAR, with seismic data (e.g., Pritchard et al., 2006; 2007; Duputel et al., 2015). These estimates of fault slip parameters then provide key input into mechanical models of faults and the surrounding crust and upper mantle, estimates of stress change on neighboring faults, and inform our basic understanding of regional seismic hazards.

Measurements of secular velocities within tectonic plate boundary regions place constraints on models of fault physics, contributing to estimates of long-term seismic hazard. NISAR will enable imaging Earth's plate boundary zones at depth, sampling the range of different tectonic styles, capturing plate boundaries at different stages of the earthquake cycle, and informing regional assessments of seismic hazard.

Detecting and quantifying transient deformation play an essential role in improving our understanding of fundamental processes associated with tectonics, subsurface movement of magma and volcanic eruptions, landslides, response to changing surface loads and a wide variety of anthropogenic phenomena. Aseismic and post-seismic fault slip transients, volcanic and landslide deformation, and local subsidence and uplift due to migration of crustal fluids occur globally over temporal and spatial scales ranging from sub-daily to multi-year, and tens of meters to hundreds of kilometers. Many eruptions are preceded by surface deformation induced by moving magma in the subsurface. However, periods of magma movement do not always result in an eruption. Systematic measurement of deformation over volcanoes should help clarify why. Similarly, many landslides move intermittently, and may have periods of increased rates of slow sliding before catastrophic run out. NISAR will enable detection and inventory of slow moving landslides, enabling better understanding of variations in movement and how mass movement is triggered.

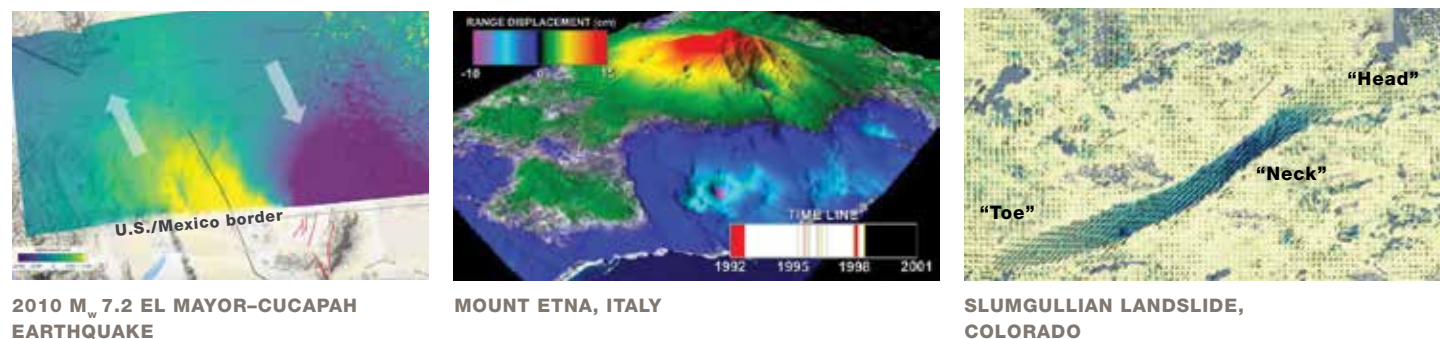


FIGURE 2-1

NISAR will measure surface deformation to determine the likelihood of earthquakes, volcanic eruptions and landslides. (Left) 2010 M_w 7.2 El Mayor – Cucapah earthquake shown in L-band UAVSAR at north end of rupture. Surface fracturing and right-lateral displacement are apparent (after Donnellan et al., 2018 submitted; image NASA/JPL-Caltech/GeoGateway). (Middle) Mount Etna deformation from the C-band ERS-1 satellite (after Lundgren et al; 2004; image ESA/NASA/JPL-Caltech). (Right) Slumgullian landslide inversion of L-band UAVSAR from four images in April 2012 (Delbridge et al., 2016).

2.2 ECOSYSTEMS: BIOMASS, DISTURBANCE, AGRICULTURE, AND INUNDATION

The world's growing population is experiencing unprecedented changes of our climate through intensifying events such as floods, droughts, wildfires, hurricanes, tornadoes and insect infestations and their related health effects. These impacts are putting pressure on our landscapes and ecosystems that generate food, fiber, energy and living spaces for a growing global population. It is imperative to understand the connections between natural resource management and ecosystem responses to create a sustainable future. The 2018 Decadal Survey asks, "What are the structure, function, and biodiversity of Earth's ecosystems, and how and why are they changing in time and space?" It also specifically calls out the need to quantify biomass and characterize ecosystem structure to assess carbon uptake from the atmosphere and changes in land cover, and to support resource management.

NISAR radar data will address the distribution of vegetation and biomass to understand changes and trends in terrestrial ecosystems and their functioning as carbon sources and sinks and characterize and quantify changes resulting from disturbance and recovery.

NISAR will address the following questions:

- How do changing climate and land use in forests, wetlands and agricultural regions affect the carbon cycle and species habitats?
- What are the effects of disturbance on ecosystem functions and services?

The NISAR radar is able to image the landscape using the unique capability of its radio waves that penetrate into the forest canopy and scattering from large woody components (stems and branches) that constitutes the bulk of biomass and carbon pool in forested ecosystems (Figure 2-2). The sensitivity of backscatter measurements at different wavelengths and polarizations to the size and orientation of woody components, and their density, makes radar sensors suitable for measurements of live, above-ground, woody biomass (carbon stock) and structural attributes, such as volume and basal area. NISAR will resolve vegetation biomass over a variety of biomes, including low-biomass and regenerating forests globally, will monitor and identify changes of forest structure and biomass from disturbances such as fire, logging, or deforestation, and will characterize post disturbance recovery.

Changes and degradation of terrestrial ecosystems are leading to steep reductions in biodiversity. Additionally,

quantitative understanding of the role of terrestrial ecosystems in atmospheric CO₂ absorption is limited by large uncertainties in two areas: estimates of current carbon storage in above ground forest biomass, and large uncertainties in changes in biomass. From 1990 to 2000, the global area of temperate forest increased by almost 3 million hectares per year, while deforestation in the tropics occurred at an average rate exceeding 12 million hectares per year. Uncertainty in biomass change is greatest in tropics and more uncertain than changes in forested area (Millennium Ecosystem Assessment Synthesis Report, 2005).

To feed a growing population of more than 8 billion, food production and supply occur on a global basis. In order to better guide policy and decision-making, national and international organizations work to transparently monitor trends and conditions of agriculture on a timely basis. Because of the variable nature of planting and harvesting practices, efforts such as this are work-power intensive and time-consuming.

During natural disasters, first responders often look to NASA to provide timely and valuable information to assist their work to mitigate damage and assess destruction by these common tragic events. Many federal agencies and university researchers that study wetlands have difficulty evaluating the health of our waterways and wetlands due to lack of information regarding the ebb and flow of floodwaters during normal and extreme seasonal inundation.

Among the organizations that respond to flooding disasters are state and local agencies, as well as federal agencies, such as Federal Emergency Management Agency (FEMA), the National Oceanic and Atmospheric Administration (NOAA), and the United States Geological Survey (USGS). International aid in the event of natural disasters caused by flooding often includes data sharing arrangements to help our allies respond to the humanitarian crises that flooding can cause.

The upcoming NISAR mission will provide dependable observations throughout the year and at repeat periods that are on par with the cycles that biomass, disturbance, agriculture and inundation undergo. Hence, the NISAR mission will serve as a new foundation for observing these important ecological environments.

2.3 DYNAMICS OF ICE: ICE SHEETS, GLACIERS, AND SEA ICE

NISAR will address how ice masses interrelate with global climate and sea level (Figure 2-3). Ice sheets and glaciers are the largest contributors to sea level rise with a potential to raise sea level by several tens of centimeters, or more than one meter, in the coming century. Summer sea ice cover is decreasing drastically and may vanish entirely within the next decades. Over the satellite period of observations, Arctic sea ice has thinned, shifted from a predominately perennial to seasonal ice cover, and reduced in extent at the end of summer by nearly 30 percent. Collectively, these effects mean that despite their remote location, changes in ice have global economic and health implications as climate changes. The 2018 Decadal Survey prioritizes observations in "understanding glacier and ice sheet contributions to rates of sea-level rise and how likely they are to impact sea-level rise in the future." It asks, "How much will sea level rise, globally and regionally, over the next decade and beyond, and what will be the role of ice sheets and ocean heat storage?" NISAR will address the following related questions:

- Will there be catastrophic collapse of the major ice sheets, including Greenland and West Antarctic and, if so, how rapidly will this change occur?
- What will be the resulting time patterns of sea-level rise at the global and regional level?
- How are mountain glaciers and ice caps worldwide changing in relation to climate, and what is their impact on sea level now and in the future?
- How rapidly will the Arctic sea ice cover continue to thin and to decrease in summer extent?

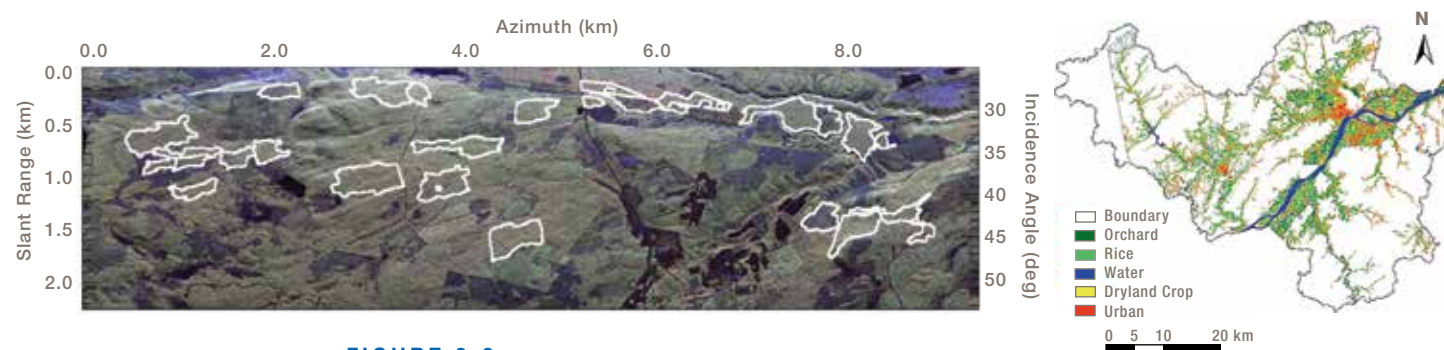


FIGURE 2-2

NISAR will determine the contribution of Earth's biomass to the global carbon budget and characterize ecosystem disturbance and impacts on biodiversity. (Left) Delineated forest stands using L-band ALOS-2 radar using PolInSAR in northern Sweden. Forest stands are delineated in white (Neumann et al., 2012). (Right) Classified crops in southeast China using L-band ALOS data (Zhang et al., 2009).

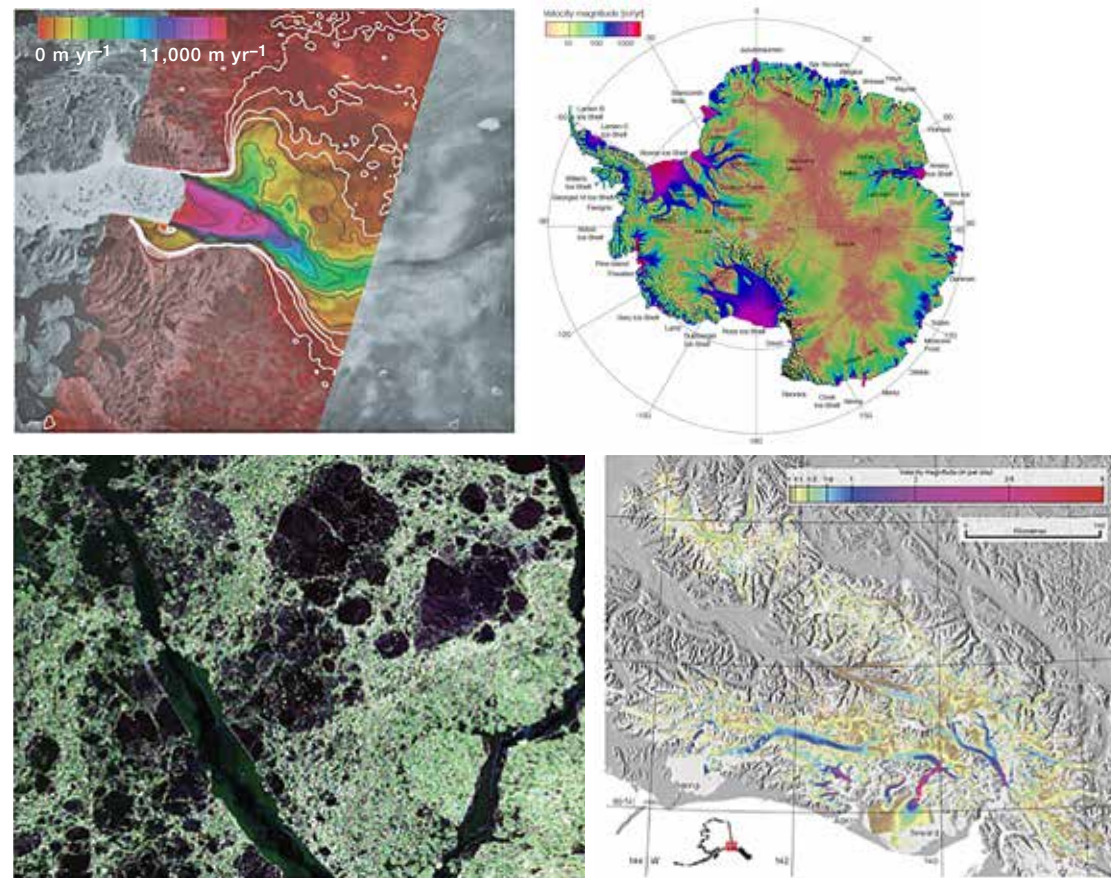


FIGURE 2-3 NISAR will measure changes in glacier and ice sheet motion, sea ice, and mountain glaciers to determine how global climate and ice masses interrelate and how melting of land ice raises sea level. (Top left) Canadian RADARSAT mission shows the rapid speedup of Jakobshavn Isbrae in Greenland between February 1992 and October 2000 (Joughin et al. 2004a). (Top right) Ice flow of the Antarctic ice sheet from ALOS PALSAR, Envisat ASAR, RADARSAT-2, and ERS-1/2 satellite radar interferometry (Rignot et al. 2011a). (Bottom left) UAVSAR L-band sea ice image, which includes old ice, first year ice, and an open lead. (Bottom right) Surface velocity map for the Wrangell-St. Elias Mountains, the Chugach Mountains/Kenai Peninsula, the Alaska Range, and the Tordrillo Range using L-band radar (Burgess et al. 2013).

Flow rates of outlet glaciers around many parts of Greenland and Antarctica have increased significantly, more than doubling in some cases. These accelerations and increased melt rates have caused glacier and ice sheet margins to thin by up to tens of meters per year as ice is lost to the sea. Much of this ice (e.g., floating ice shelves) acts as a buttress holding back interior ice. Loss of this buttressing introduces instability of these ice sheets, which will likely lead to a more rapid rise in sea level. NISAR will provide temporally and geographically comprehensive observations to characterize and understand ice sheet and glacier dynamics. NISAR will

measure velocities of the Greenland and Antarctic ice sheets through time, will determine the time-varying position of the grounding line around Antarctica and will monitor the extent and stability of buttressing ice shelves.

Sea ice is another component of the Earth cryosphere system that is changing rapidly and in ways that can affect climate worldwide. Comprehensive observations of sea-ice extent, motion, concentration and thickness, derived from multiple satellite observations, including NISAR, will improve our understanding of the interac-

tions between the ice, ocean, and atmosphere, and their future behavior. NISAR observations of ice motion over both the Arctic and Antarctic sea ice covers will enable a unique, comprehensive examination of the significantly different responses to climate forcing that are occurring between the two polar regions.

Mountain glaciers and ice caps are among the most important indicators of climate change and furthermore provide fresh water. The Himalayas is the largest and highest mountain range in the world and plays a significant role in the regional hydrological cycle and climate in central and south Asia. The Himalayan region, comprising the highest number of mountain glaciers in the world, has a unique mass-energy exchange regime that may have serious impact on climate change.

Systematic observations of snow-ice extent, density and thickness, glacial inventory and movements, and mass-balance will improve our understanding of underlying processes acting on them and their future behavior under global climate change scenarios. NISAR radar, with its greater penetration depth, large swath, and frequently repeated observations, will enable the study of snow and the global distribution of glaciers at much improved spatio-temporal scales.

Earth is continuously readjusting to redistribution of water and ice masses associated with the retreat of the Pleistocene ice sheets and ongoing melting of remaining glaciers, ice caps and ice sheets. The readjustment, also known as glacial-isostatic adjustment (GIA), includes both an instantaneous elastic response to recent changes in load as well as a delayed visco-elastic response associated with changes in ice loading that occurred thousands of years ago. The resulting surface deformation from glacial-isostatic adjustment has important implications for our ability to predict relative sea level rise, which captures not just sea level rise but also land elevation change from processes like GIA. Accurate sea level rise predictions are also tied to our understanding of the rheological structure of

the mantle, with different structural models predicting different patterns of surface deformation.

2.4 APPLICATIONS

NISAR will add a tremendous data set to create new and greatly improve upon many applications that use earth observation data (see Appendix E, section 17.4). With frequent, repeated observations over hazard-prone areas, NISAR will provide substantial data to guide development of applications and associated scientific studies. All NISAR data products will be freely available through a web portal. This way, the nation's investment in land surveys remotely acquired from space can be widely used by a variety of agencies and individuals.

NISAR will support applications across five main areas, namely critical infrastructure monitoring (Figure 2-4), hazard assessment (e.g., earthquakes, volcanoes, landslides, floods, sinkholes, etc.), maritime and coastal waters situational awareness, ecosystem services, and underground reservoir management (Figure 2-5), the latter of which encompasses water, oil, and gas reservoirs. In addition to urgent response, NISAR can be used to collect pre-event information for mitigation and monitoring, as well as to collect data during and after disasters or other impactful events to support response and recovery. In many cases, operational products can be derived from NISAR data, particularly for ecosystems services where hourly-to-daily updates are not needed. In addition, NISAR's Applications discipline area encompasses science topics not addressed directly by NISAR science requirements, such as soil moisture measurement, snow inventory, and atmospheric sciences. More details about individual applications are given in Appendix E, section 17.4.

NISAR will be a reliable source over the life of the mission for proactive planning for disasters and monitoring the development of conditions that could lead to failure. The stresses induced during a disaster can lead to failure of compromised structures, and a significant part of risk management involves prevention of failure

during disasters, e.g., avoiding overtopping during high water or failure of levees during an earthquake. The impact of disasters, sea level change, land subsidence, and ground movement like landslides or other slope failures is increasing rapidly with growing population and development in high-risk areas. Monitoring regions prone to these disasters before they occur can improve risk management by identifying the tell-tale signs of processes that lead to these disasters, such as regions accumulating elastic strain that will lead to a major earthquake or the signatures of magma migrating in the subsurface near a volcanic edifice. This improved

understanding will be enabled by measurement of surface deformation from NISAR.

NISAR will be a game-changer for many applications by providing time series of changing conditions to disentangle long-term impact from seasonal changes and episodic, event-induced impact. An inventory of changes can be made to assess the rates at which these systems are changing and associated risks through deformation measurements at fine spatial and temporal sampling over the three-year nominal mission lifetime. NISAR will assist in monitoring slow onset disasters like

FIGURE 2-4

NISAR will measure changes in infrastructure. Ground movement along one of the levees that prevents flooding of an island in the Sacramento-San Joaquin Delta (Deverel, 2016). Inset photo shows a view looking east towards the area of rapid deformation (red/orange color). The deformation signal is not obvious to the naked eye on the ground, but ground-based inspection revealed that cracks had formed in the levee.

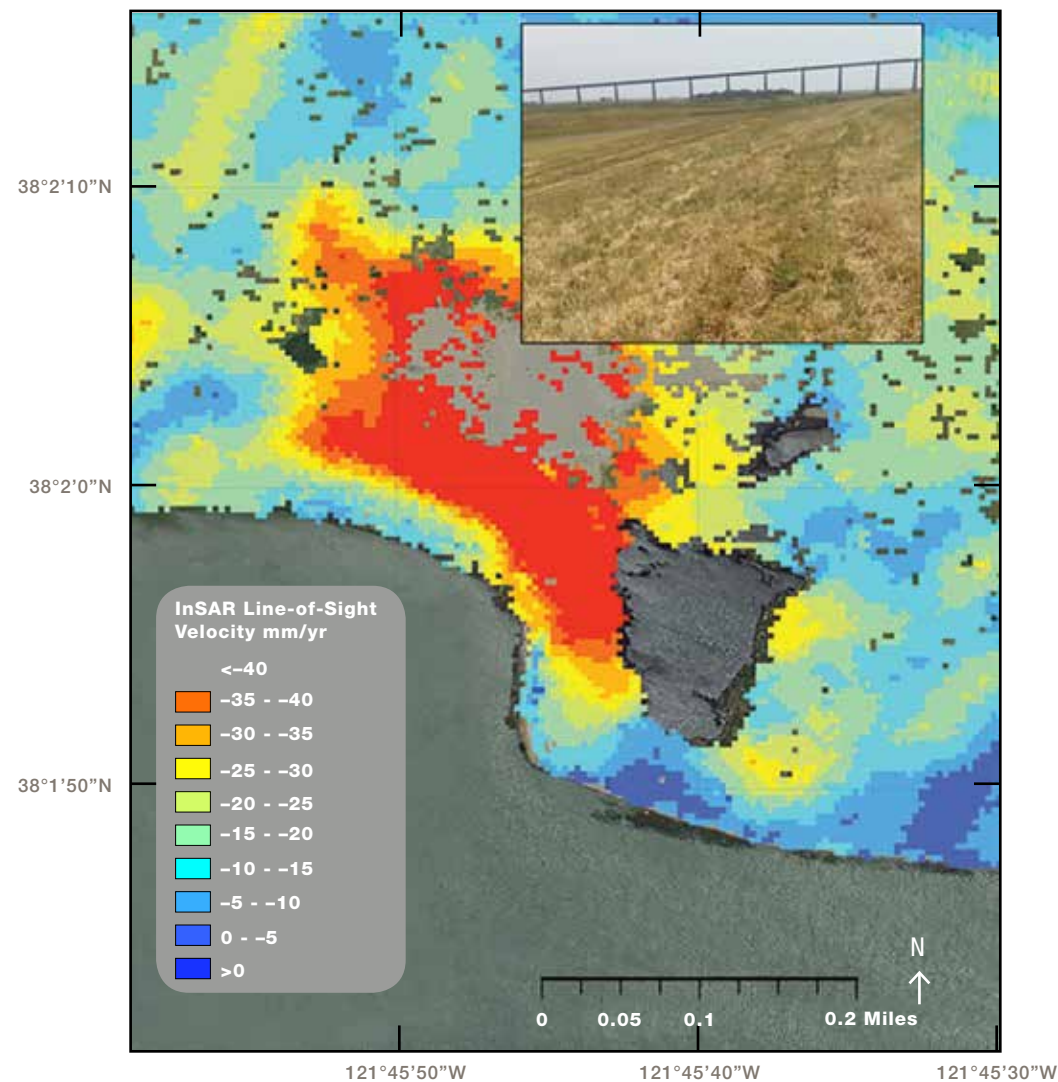
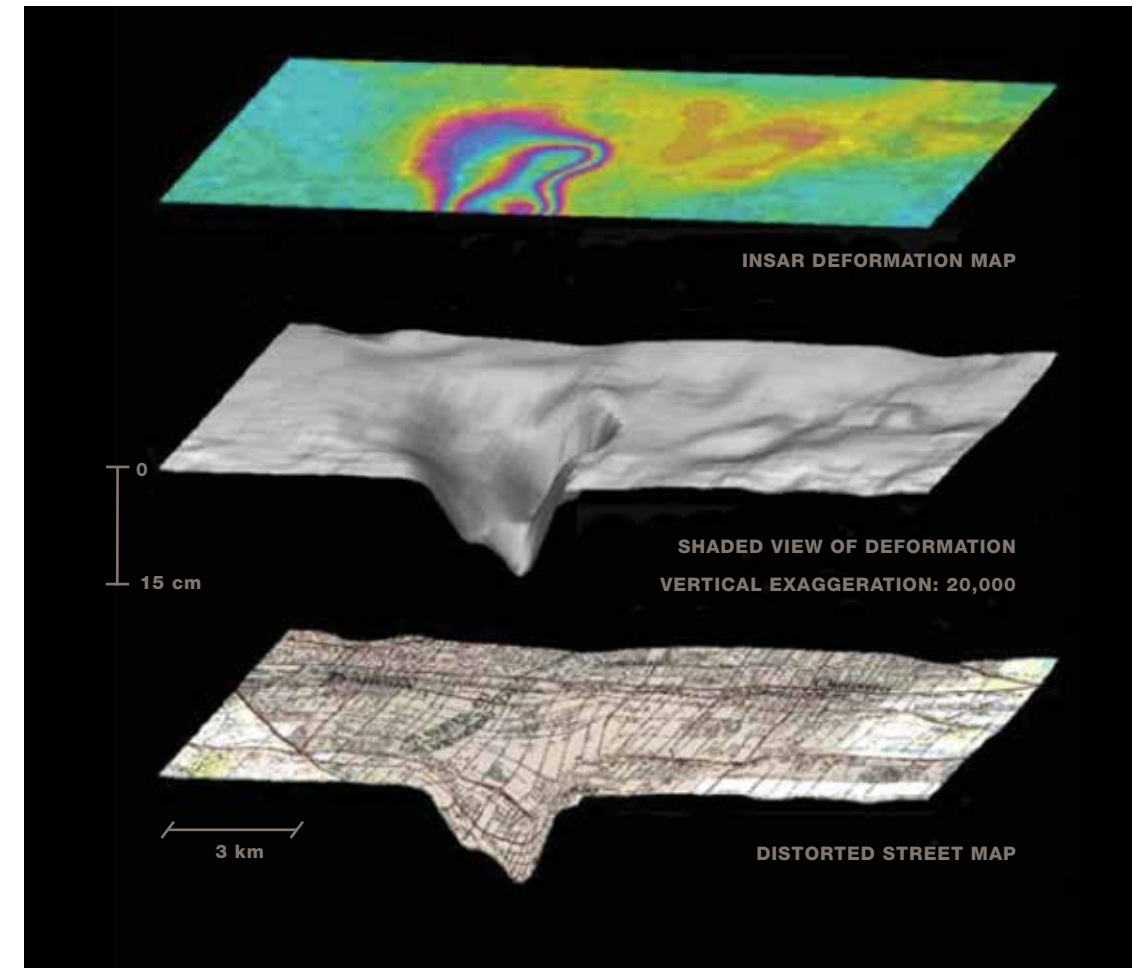


FIGURE 2-5

NISAR will measure changes in reservoirs. Subsidence due to ground water withdrawal measured with C-band ERS-1 northeast of Los Angeles (image created by Gilles Peltzer, JPL/UCLA).



droughts and large-scale crop failures based on tracking changes over a long time period using the frequent, repeated observations. Water resource management and critical infrastructure monitoring will be revolutionized by access to these data to inform short and long term planning (Fig. 2-4). NISAR will be used to monitor levees, dams and aquifers that are under stress from groundwater over-utilization; areas where fluid injection into and withdrawal from the subsurface are causing changes to the surface and potentially affecting water quality; and differentiation of anthropogenic causes of subsidence from that related to the underlying geology of a region.

Small surface deformation signals, such as subsidence, require long time series to accurately determine slow movement. Measurements sensitive to change

from geologic, anthropogenic, or climate-related causes require adequate sampling to resolve temporal variation of displacements with seasonal or finer resolution. Annual cycles result from water withdrawal and recharge in aquifer systems, or from climate-induced patterns, such as the freezing and thawing of the active layer overlying permafrost in the Arctic and sub-Arctic regions. Human-induced deformations, such as those caused by oil and gas mining or degradation of transportation infrastructure, can occur over many different time scales, and their identification and differentiation require resolving processes at much better than the annual time scale. One example of this need is measurement of surface displacement above hydrologic aquifers, for which it is necessary to separate the inelastic subsidence that permanently reduces the storage capacity of an aquifer from the annual

DISASTERS WILL BE DIRECTLY MONITORED AND ASSESSED FOR SUPPORT OF EMERGENCY RESPONSE AS A MISSION GOAL OF NISAR, MOVING BEYOND THE SCIENCE VALUE PROVIDED BY BETTER UNDERSTANDING OF THE PROCESSES INVOLVED, WHICH CAN ALSO LEAD TO BETTER FORECASTING AND RISK ASSESSMENT.

subsidence/inflation due to water use patterns. Since proper management of the aquifer system depends on maintaining the long-term storage of the system, NISAR must be able to distinguish among these components. A similar statement applies to permafrost-induced degradation of roads or other structures, where long-term subsidence trends relating to permafrost decay need to be separated from quasi-seasonal deformation signals caused by the freeze-thaw cycle of the overlying active layer (Liu et al. 2010, 2012). In both examples, the measurements are similar to those needed to determine secular velocities along tectonic boundaries, except that the horizontal component of displacement is small and therefore the emphasis needs to be on accurate determination of the vertical component with sufficiently high resolution to pinpoint critical areas most heavily impacted in order to allocate resources for targeted remediation.

The NISAR program has developed a Utilization Plan outlining how the mission will engage with the end user community to advance the use of its data for practical applications (https://nisar.jpl.nasa.gov/files/nisar/NISAR_Utilization_Plan.pdf). There are also a series of white papers highlighting individual applications (www.nisar.jpl.nasa.gov/applications). Those topics, among others, are included in Appendix E, section 17.4.

2.5 DISASTER RESPONSE

Disasters will be directly monitored and assessed for support of emergency response as a mission goal of NISAR, moving beyond the science value provided by better understanding of the processes involved, which can also lead to better forecasting and risk assessment. Natural disasters, like floods and earthquakes, cause thousands of fatalities and cost billions annually. Nearly ten percent of the world's population lives in low lying coastal areas subject to flooding. Large earthquakes can cause damage hundreds of kilometers from their epicenter, impacting a wide area. Volcanic eruptions destroy cities and towns, eject ash clouds that disrupt

air travel, and impact regional agriculture. Today, the economic and human impacts are growing as population pressure drives development in high-risk areas and as climate change increases the intensity and frequency of severe weather events.

NISAR has a requirement to deliver data for urgent response on a best effort basis. Following a disaster or in anticipation of a forecasted event, NISAR will be programmed for high priority data acquisition, downlink and processing to provide low latency information to support urgent response. There is the unavoidable delay between when a disaster occurs and the next imaging opportunity, so NISAR will add to the set of Earth observing instruments in space that can respond to disasters, shortening overall the time to data delivery. Appendix E, section 17.4, provides information on the many types of disasters to which NISAR can contribute significant response information. Nearly the full range of disasters can be addressed, from floods to fires to earthquakes, volcanos, landslides, and even oil spills and dam collapse.

Disasters like floods, forest fires and coastal and oceanic oil spills can be monitored using radar images that are provided by NISAR. Other disasters result directly in ground movement, such as ground rupture during an earthquake. In these cases, deformation measurements of the disaster area can dramatically improve determination of the scope of the event, leading to better assessment for targeting response assets and more efficient recovery. Furthermore, the same data used to monitor ground deformation in disaster-prone regions can be used to detect large-scale surface disruption, which can be used to develop synoptic high-resolution damage proxy maps. Such damage proxy maps can aid emergency natural disaster response throughout the globe regardless of the level of local infrastructure, so that the response coordinators can determine from afar where to send responders within the disaster zone.

2.6 OCEAN STUDIES AND COASTAL PROCESSES

NISAR will acquire both L-SAR and S-SAR data over areas of interest to India, primarily in and around India and in the Arctic and Antarctic. One of the focus areas for NISAR data will be to study coastal processes over India to address the questions:

- How are Indian coastlines changing?
- What is the shallow bathymetry around India?
- What is the variation of winds in India's coastal waters?

A large percentage of the world's population resides near the coasts and derives their livelihood from the coastal regions, and this is particularly true in India and southeast Asia. Coastal regions, being at the confluence of land, sea and atmosphere, are subjected to various natural forces and processes resulting in erosion of and deposition at the coasts. To understand the nature and magnitude of coastal processes, periodic mapping and monitoring of coastal erosional and depositional landform features, shoreline changes and coastal habitats

are required. SAR has been proven to be a useful tool for mapping and monitoring of coastal areas due to its sensitivity to landform structures, moisture content and high land-water contrast. NISAR will provide a unique opportunity to study coastal features and map shoreline changes through high repeat cycle, synoptic coverage of coastal areas.

NISAR operating in L-band and S-band will be sensitive to the ocean roughness with wide dynamic range, enabling study of oceanic internal waves, current fronts and upwelling zones. NISAR at L-band will image most water at the land-sea coastal interface globally because the radar will be turned on prior to reaching land. In many areas, this will enable mapping of surface wind speed, coastal bathymetry, and near-coast surface features related to currents and eddies. In coastal regions, the repeated and regular measurement of surface wind speed can map wind speed climatology, important for the siting of offshore wind power turbines. In addition, the high target-to-background contrast at L-band will help in identification of oil slicks and ships in the open as well as coastal ocean.

3 MISSION MEASUREMENTS AND REQUIREMENTS

NISAR will utilize the techniques of synthetic aperture radar interferometry and polarimetry to measure surface deformation and change of the solid Earth, cryosphere and ecosystems. For a brief introduction to basic radar concepts, including radar imaging (SAR), polarimetry and interferometry, refer to Appendix C. There are also a wide variety of resources available to learn more about the technology and techniques of NISAR. Here are some examples:

- <https://arset.gsfc.nasa.gov/disasters/webinars/intro-SAR>
- <https://saredu.dlr.de/>
- <https://www.unavco.org/education/professional-development/short-courses/>
- <https://www.asf.alaska.edu/asf-tutorials/>

3.1 MEASUREMENTS OF SURFACE DEFORMATION AND CHANGE

The technique of Interferometric Synthetic Aperture Radar (InSAR) uses coherent processing of radar signals collected over the same scene at two different times to derive surface deformation from the change in the relative phase of the two returns (Figure 3-1; Rosen et al., 2000; Hanssen, 2001). The radar instruments on NISAR will operate as repeat-pass InSAR to measure surface deformation of land and ice-covered surfaces. An InSAR satellite passing over a location before and after an event, such as an earthquake, tectonic deformation, volcanic inflation or ice sheet motion, at exactly the same point in inertial space (zero baseline), measures how the ground shifts between passes,

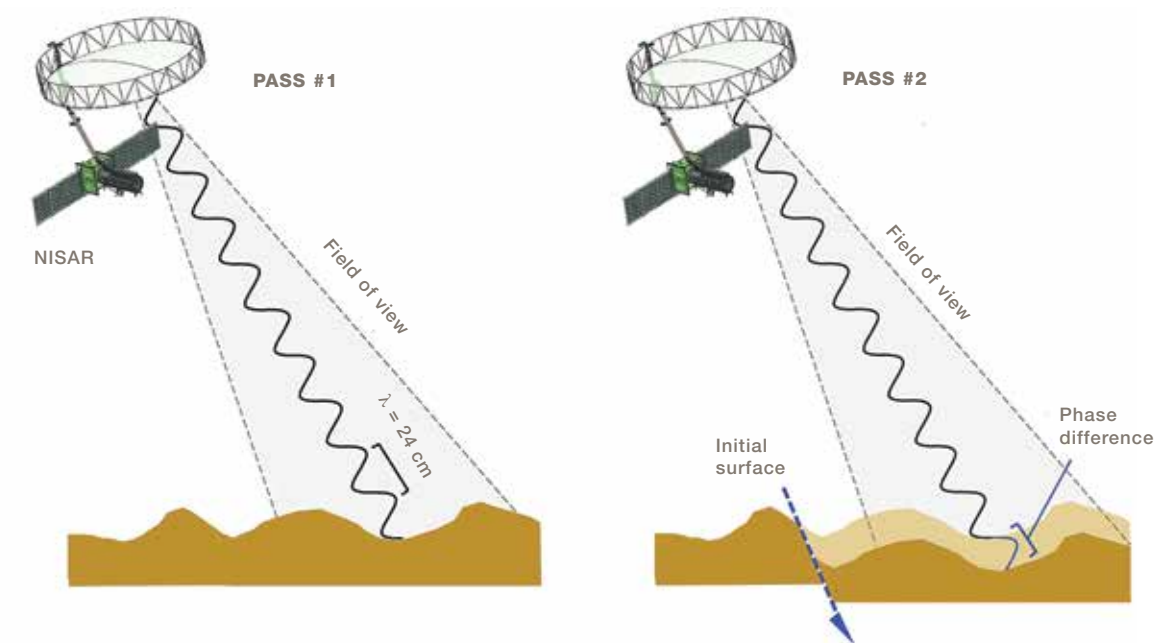


FIGURE 3-1 InSAR measures surface deformation by measuring the difference in the phase of the radar wave between the two passes if a point on the ground moves and the spacecraft is in the same position for both passes (zero baseline). InSAR deformation geometry is demonstrated in these figures at the left and right. On Pass #1, a surface of interest is imaged and the radar satellite measures the phase $\phi_1(x,y)$ between the satellite and the ground along the line-of-sight (LOS) direction. Later at Pass #2, the satellite makes another measurement $\phi_2(x,y)$ between the satellite and the ground. If the ground moves between passes, the phase difference $\Delta\phi(x,y)$ is proportional to the ground deformation between passes along the LOS direction.

via a radar interferogram. This is the product of the first image with the complex conjugate of the second (Donnellan et al., 2008). The interferogram measures the difference in phase of the radar wave between two passes, which is sensitive to ground motion directed along the radar line of sight. An InSAR image of the point-by-point phase difference of the wave on the surface is used to create a map of the movement of the surface over time. In this way, ground deformation along the line-of-sight (LOS) direction on the scale of a fraction of the radar wavelength can be resolved as long as the phase coherence between the signals is maintained (Zebker and Goldstein, 1986; Gabriel et al., 1989). The radar instrument can take observations through cloud cover, without sunlight, and can measure sub-centimeter changes.

3.2 LANDCOVER AND FOREST CHARACTERIZATION WITH L-BAND SAR

NISAR will serve to estimate above ground biomass, identify croplands and inundated extent, and detect forest disturbances. The overall ecosystem science community will greatly benefit from the mission, which is characterized by high frequency revisit time of 12 days and L-band capabilities. By their fundamental nature, ecosystems are driven by the hydrologic and seasonal cycles, and hence undergo dynamic changes throughout the year. When combined with the need for monitoring changes in these systems, through fire, drought, encroachment, deforestation or otherwise, it is important to detect and demarcate these regions in order to provide quantitative measures of inventory and change that affect the many services that ecosystems offer to populations worldwide. NISAR's dynamic observations and compilation of a new historical record will provide an important resource throughout the mission's lifetime and beyond.

Among the important features of the mission characteristics are its wide swath, high resolution, 12-day repeat orbit cycle and dual-frequency (L- and S-band) capability. These features will allow the mission to

provide meaningful observations for a broad diversity of ecosystems with a timely revisit period. With a resource such as NISAR, and distributed under NASA's open data policy, the NISAR mission will support improved management of resources and understanding of ecosystem processes.

Changes in forest structure observed by the NISAR, whether due to natural cycles, or human or natural disturbances, will provide key measurements to assess the role and feedback of forests to the global carbon cycle. Every 12 days, the NISAR mission will resolve severity and time of disturbance with a 1 hectare and 12-day spatial temporal resolution. NISAR's rapid revisit time will provide timely identification of cropland status, estimation of soil moisture, and the monitoring of flooding and inundation extent.

In addition to the basic resource of measuring radar reflectivity, for ecosystems, the NISAR mission has a number of other capabilities that will be useful for the discipline. Among these features is the capability of performing repeat-pass interferometry and in the collection of polarimetric data. While the core capability of the payload is the L-band SAR used to meet all of NASA science requirements, a secondary S-band SAR, built by ISRO, will provide opportunities in collecting dual-frequency observations over key sights in India and others that are distributed globally. The mission itself includes a large diameter (12 m) deployable reflector and a dual frequency antenna feed to implement the SweepSAR wide-swath mapping system, which is the enabling technology to allow for global access, fast revisit, frequent temporal sampling, and full resolution. The polarimetric capability of the NISAR system provides dual-polarized (dual-pol) global observations for every cycle and the potential for quad-pol observations in India and the U.S. The dual-pol system is based on transmitting horizontally or vertically polarized waveforms and receiving signals in both polarizations. Over land surfaces, the transmit polarization will principally be horizontally polarized, and receive will be over both vertical and horizontal polarizations, resulting in polar-

ization combinations known as HH and HV to describe the configuration.

NISAR polarization configurations will enable accurate estimation of vegetation above ground biomass up to 100t/ha. In polarimetric backscatter measurements, forest components (stems, branches, and leaves) are scatterers within the footprint of the radar beam that interact with the incoming waves. The size (volume) and the dielectric constant (moisture or wood density) and orientation and morphology of the scatterers determine the magnitude and polarization of the reflected waves. As a result, the backscatter radar energy at linear polarizations is a function of the forest volume and biomass. The shape of this function depends on the wavelength, polarization, forest type, and moisture conditions. The relationship varies with vegetation type and environmental conditions (e.g., soil moisture and roughness), but with multiple polarizations and repeated measurements, the biomass can be determined with high accuracy.

For a limited set of targets, the NISAR mission will make fully polarimetric measurements (i.e., fully polarimetric, or quad-pol) by alternating between transmitting H-, and V-polarized waveforms and receive both H and V (giving HH, HV, VH, VV imagery). Polarization combinations, such as dual- and quad-pol, allow for a fuller characterization of ground-targets' responses to the SAR. Variations in the polarimetric responses of targets to different combinations of polarization can be related to the physical characteristics of the target reflecting energy back to the radar, and hence can be used for classifying target type and performing quantitative estimates of the target state.

3.3 REQUIREMENTS AND SCIENCE TRACEABILITY

NASA and ISRO have developed a joint set of requirements for NISAR. These agency level requirements

are known as "Level 1" (L1) requirements and control the implementation of the mission: The NISAR Mission must fulfill these requirements to be successful¹. ISRO places additional requirements on the L-band system to acquire data over science areas of interest to India that are above and beyond the NASA requirements, including coastal bathymetry and ocean winds, geology over India, and coastal shoreline studies (Table 3-1). Unlike the NASA requirements, the quantitative values associated with these measurements are characterized as goals; it is the collection of the data toward these goals that drives the ISRO requirements. There are no explicit requirements on science measurements at S-band, just a statement identifying the impact such measurements can make, leaving open a range of options for exploring its potentials.

Table 3-1 shows an overview of the L1 baseline requirements for the mission. Baseline requirements represent the full complement of science requested by NASA of the NISAR Mission. The NISAR project teams at JPL and ISRO use the L1 requirements to develop a detailed set of L2 project requirements, which govern the implementation in such a way that by meeting the L2/L1 requirements, the requirements will be met. The L2 science requirements are described in Appendix D. NASA and ISRO have jointly coordinated all requirements at Level 1 and Level 2. Lower level requirements are generated by the NASA and ISRO project teams independently. The teams coordinate hardware and activities through interface documents.

The requirement on 2-D solid Earth and ice sheet displacement covers a range of lower level requirements on the ability to measure deformation of land. The science described above for deformation relies on time series of data acquired regularly and with fast sampling. This range of science can be specified as individual requirements on velocities or strain rates, but that would lead to a large number of L1 requirements. This requirement is written with the foreknowledge

¹There are also a set of threshold requirements, which define the minimum complement of science considered to be worth the investment. Baseline requirements can be relaxed toward thresholds when implementation issues lead to loss of performance. At this point in Phase C, NISAR continues to work toward the baseline requirements.

TABLE 3-1. LEVEL 1 BASELINE REQUIREMENTS

Attribute	2-D Solid Earth Displacement	2-D Ice Sheet & Glacier Displ.	Sea Ice Velocity	Biomass	Disturbance	Cropland, Inundation Area
Duration	3 years	3 years	3 years	3 years	3 years	3 years
Resolution	100 m	100 m	5 km grid	100 m (1 ha)	100 m (1 ha)	100 m (1 ha)
Accuracy	3.5 (1+L1/2) mm or better, 0.1 km < L <50 km, over 70% of areas interest	100 mm or better over 70% of fundamental sampling intervals	100 m/day or better over 70% of areas	20 Mg/ha for areas of biomass < 100 Mg/ha	80% for areas losing > 50% canopy cover	80% classification accuracy
Sampling	12 days or better, over 80% of all intervals, < 60-day gap over mission	12 days or better	3 days or better	Annual	Annual	12 days or better
Coverage	Land areas predicted to move faster than 1 mm/yr, volcanoes, reservoirs, glacial rebound, landslides	Global ice sheets and glaciers	Arctic and Antarctic sea ice	Global areas of woody biomass cover	Global areas of woody biomass cover	Global areas of crops and wetlands
Urgent Response Latency	24-hour tasking 5-hour data delivery (24/5) Best-effort basis	24/5 Best-effort basis	24/5 Best-effort basis	24/5 Best-effort basis	24/5 Best-effort basis	24/5 Best-effort basis

of flow-down to repeat-pass interferometry and specifies the sampling and accuracy understood to be achievable. The accuracy is controlled largely by the noise introduced by the atmosphere, which the project cannot control. The intent of this requirement is to design a system that reliably delivers regularly sampled, interferometrically viable, data on ascending and descending orbit passes as needed to achieve the science at a particular target. As such, the L2 requirements may improve one aspect of the L1 requirements at the expense of another (e.g., resolution vs. accuracy).

The requirement on 2-D ice sheet and glacier displacement covers a range of lower level requirements on the ability to measure deformation of ice. It is a

similar geodetic measurement as for the solid Earth requirement above, but the environment has a different influence on the ice-covered regions than land, so the L1 requirement is specified with different resolution and accuracy requirements. As with land deformation, the intent of this requirement is to design a system that delivers reliably regularly sampled interferometrically viable data on ascending and descending orbit passes as needed to achieve the science at a particular target. As with solid Earth requirements, the L1 capability as defined allows for a flow-down to a set of L2 requirements that meet the ice-sheet science objectives.

The requirement on sea ice velocity is also a deformation requirement but is called out separately because it relies on different kinds of measurements with different

sampling and accuracy requirements. In this case, the intent of the requirement is to observe the poles regularly and track features in the radar imagery as they move. This is a proven technique, but there is as yet no reliable source of data.

The requirement on biomass and disturbance states that the mission measure global biomass and its disturbance and recovery, but only specifies an accuracy for the low-density woody biomass. The global requirement on biomass and disturbance/recovery allows a specification of the details of disturbance and recovery at L2 but requires global observations at L1. Thus, in regions of high-density woody biomass, where there are no explicit accuracy requirements, measurements must be made to ensure the capture of disturbance and recovery.

The requirement on cropland and inundation area is an overall classification requirement of ecosystems of particular interest to the science community. The classifications are binary (e.g. agriculture/non-agriculture) and are distinct from the biomass disturbance and recovery classifications in the previous requirement.

The urgent response requirement for NISAR is written to ensure that the mission has some capability for disaster response built into it, but one that does not drive the costs for development or operations. NISAR is primarily a science mission, but radar imaging systems are among the most useful space remote sensing assets for understanding disasters because they can deliver reliable imagery day or night, rain or shine, that are not obscured by smoke or fire.

TABLE 3-2. ISRO L-BAND BASELINE GOALS

Attribute	Coastal Wind Velocity	Bathymetry	Coastal Shoreline Position	Geological Features	Sea Ice Characteristics
Duration	3 years	3 years	3 years	3 years	3 years
Resolution	1 km grid	100 m grid	10 m	10 m	10 m
Accuracy	2 m/s over at least 80% of areas of interest	20 cm over at least 80% of areas of interest	5 m over at least 80% of areas of interest	N/A	N/A
Sampling	6 days or better	Every 6 months	12 days or better	90 days or better, with at least two viewing geometries	12 days or better
Coverage	Oceans within 200 km of India's coast	India's coast to an offshore distance where the depth of the ocean is 20 m or less	India's coastal shoreline	Selected regions including paleochannels in Rajasthan, lineaments and structural studies in Himalayas and in Deccan plateau	Seas surrounding India's Arctic and Antarctic polar stations

TABLE 3-3. SCIENCE TRACEABILITY MATRIX

Science Objectives	Science Measurement Requirements		Instrument Requirements		Projected Performance	Mission Requirements (Top Level)
	Physical Parameters (Spatial and Temporal)	Observables				
Determine the contribution of Earth's biomass to the global carbon budget	Annual biomass at 100 m resolution and 20% accuracy for biomass less than 100 Mg/ha	Radar reflectivity radiometrically accurate to 0.5 dB	Frequency	L-band	1215-1300 MHz	Seasonal global coverage per science target mask
			Polarization	Dual-pol	Quad-pol	6 samples per season
			Resolution	5 m range 10 m azimuth	3-m range 8-m azimuth	Ascending/descending
			Geolocation accuracy	1 m	0.5 m	Maximum incidence angle diversity
			Swath-Averaged Co-pol Radiometric Accuracy	0.9dB	0.07 dB	3-year mission
	Annual disturbance/recovery at 100 m resolution		Swath-Averaged Co-pol Radiometric Accuracy	1.2 dB	1.2 dB	
			Range ambiguities	-15 dB	-18 dB	
			Azimuth ambiguities	-15 dB	-20 dB dual-pol	
			ISLR	-15 dB	-20 dB dual-pol	
			Noise equivalent σ^0	-25 dB	-25 dB	
Access	Global	Global				
Determine the causes and consequences of changes of Earth's surface and interior	Surface displacements to 20 mm over 12 days	Radar group and phase delay differences on 12 day centers	Frequency	L-band	1215-1300 MHz	Every cycle sampling
			Polarization	Single-pol	Quad-pol	Ascending/descending
			Resolution	4-m range 10-m azimuth	3 m range 8 m azimuth	Global coverage per science target mask
			Repeat interval (d)	12 days or less	12 days	Non-tidal cycle repeat
			Swath width	238 km	240 km	Reconfigurable
			Incidence angle range	33-46 degrees for d=12	32-47 degrees	Left/viewing for Antarctic/Arctic coverage
			Pointing control	273 arcsec	273 arcsec	Orbit repeatability to <500 m
Determine how climate and ice masses interrelate and raise sea level	Surface displacements to 100 m over 3 days	Radar group delay differences on 3-day centers	Repeat interval (d)	12 days or less	12 days	Every opportunity sampling
			Swath width	240 km	242 km	Complete sea-ice coverage
Respond to hazards	Hazard-dependent imaging	Radar imagery	Any of above			Re-target hazard area to previously acquired mode within 24 hours Deliver data after acquisition within 5 hours

ISRO has identified a number of science goals that do not fall in the joint Baseline requirements as summarized in Table 3-2 and articulated above. The measurement metrics in the table are specified as goals because it is difficult to quantify how well they can be met. NISAR will collect L-band SAR data needed to support these goals.

3.4 SCIENCE TRACEABILITY TO MISSION REQUIREMENTS

The Science Traceability Matrix (STM) connects the science requirements to instrument and mission requirements (Table 3-3). Due to the breadth of the science goals for NISAR, and the interplay between instrument and mission operations scenarios to meet the science goals as just described, it is difficult to capture traceability in a way that the sensitivities of science requirements to mission capabilities and vice versa, is transparent.

All disciplines – solid Earth, cryosphere, and ecosystems – require long wavelengths. For ecosystems, long wavelengths are needed to maximize the sensitivity to biomass variability. For solid Earth and cryospheric deformation, long wavelengths are preferred to minimize the effects of temporal change of the surface; it takes a larger change of the surface to create significant decorrelation when the wavelength is long.

All disciplines benefit from polarimetry – while ecosystems demand polarimetry to meet their objectives, deformation science can take advantage of polarimetry to characterize environmental effects, like soil moisture variations, and potentially optimize correlation in vegetated regions.

All disciplines are interested in mapping dynamic processes – ones that can change from week to week, or instantaneously, such as when a storm front hits, a glacier surges or an earthquake strikes. In that sense, all disciplines are interested in regular sampling with the fastest revisit time achievable given the constraints of the project.

All disciplines also require global reach so that entire systems can be characterized – e.g., all of Amazonia, all of Greenland and Antarctica, or all of the “ring of fire.” For global access and fast revisit, a wide-swath or steerable mapping system is required.

All disciplines also require many samples in time (i.e., every cycle) to reduce noise sources associated with environmental variability – e.g., soil moisture changes – so a solely steerable mapping system generally will not suffice. A wide-swath mapping system such as ScanSAR (Moore et al., 1981) or SweepSAR (Freeman et al., 2009) is required for global access, fast revisit, and frequent temporal sampling.

All disciplines require spatial averaging of intrinsic resolution SAR or InSAR data (looks), to reduce speckle and other local noise effects. To meet the demanding accuracy requirements described below, the system must have fine resolution in both image dimensions to create sufficient looks to average. A ScanSAR system that has reduced resolution in the along-track dimension will not suffice, particularly given the limited

TABLE 3-4. OVERVIEW OF KEY AND DRIVING REQUIREMENTS

Key & Driving Requirement	Why Is It Challenging?	Why Is It Needed?
Interferometry capability between any two repeated acquisitions	Interferometry requires that the spacecraft be (a) controlled in its orbit to better than 350 m positioning throughout the mission and (b) controlled in its pointing to a small fraction of a degree	Interferometry is needed to obtain geodetic measurements at the required spatial sampling
Fast sampling (6 days) and interferometric revisit (12 days) over all Earth's land surfaces	Implies that the accessible field-of-regard of the instrument covers the > 240-km ground track spacing	Fast sampling is required to observe Earth's most dynamic and poorly understood processes without aliasing. The repeat period chosen for NISAR is a balance between covering interesting and practical regions (from an observation planning point of view)
Frequent sampling over most of Earth's surface	Given the multiplicity of disciplines, the only way to acquire sufficient data to meet coverage and accuracy requirements is for the radar to have a field of view equal to its field of regard (> 240 km). This requires specialized hardware to create an extra-wide swath at full resolution (Sweep SAR)	In addition to fast sampling, many samples are needed throughout the mission to defeat the noise sources that limit accuracy. To first order, more data are needed to average errors down to an acceptable level
Polarimetry	Polarimetry requires additional hardware, mass and power resources, adding to complexity and cost	Classification of surfaces and estimation of biomass cannot be done at the required accuracies without a polarimetric capability
Signal-to-noise ratio	The mission must be designed with sufficient power and antenna gain to observe dim targets adequately	Many of Earth's surface types are poor reflectors. When reflection is low, the noise dominates the measurement and leads to less accurate results
Radiometric predictability over time	Knowledge of the signal level enables quantitative associations to be made between radar signals and geophysical parameters. This drives design of structure stiffness and electrical tolerances in the radar	Knowing the signal level is important to the absolute radar cross-section measurements used to derive biomass and classifications

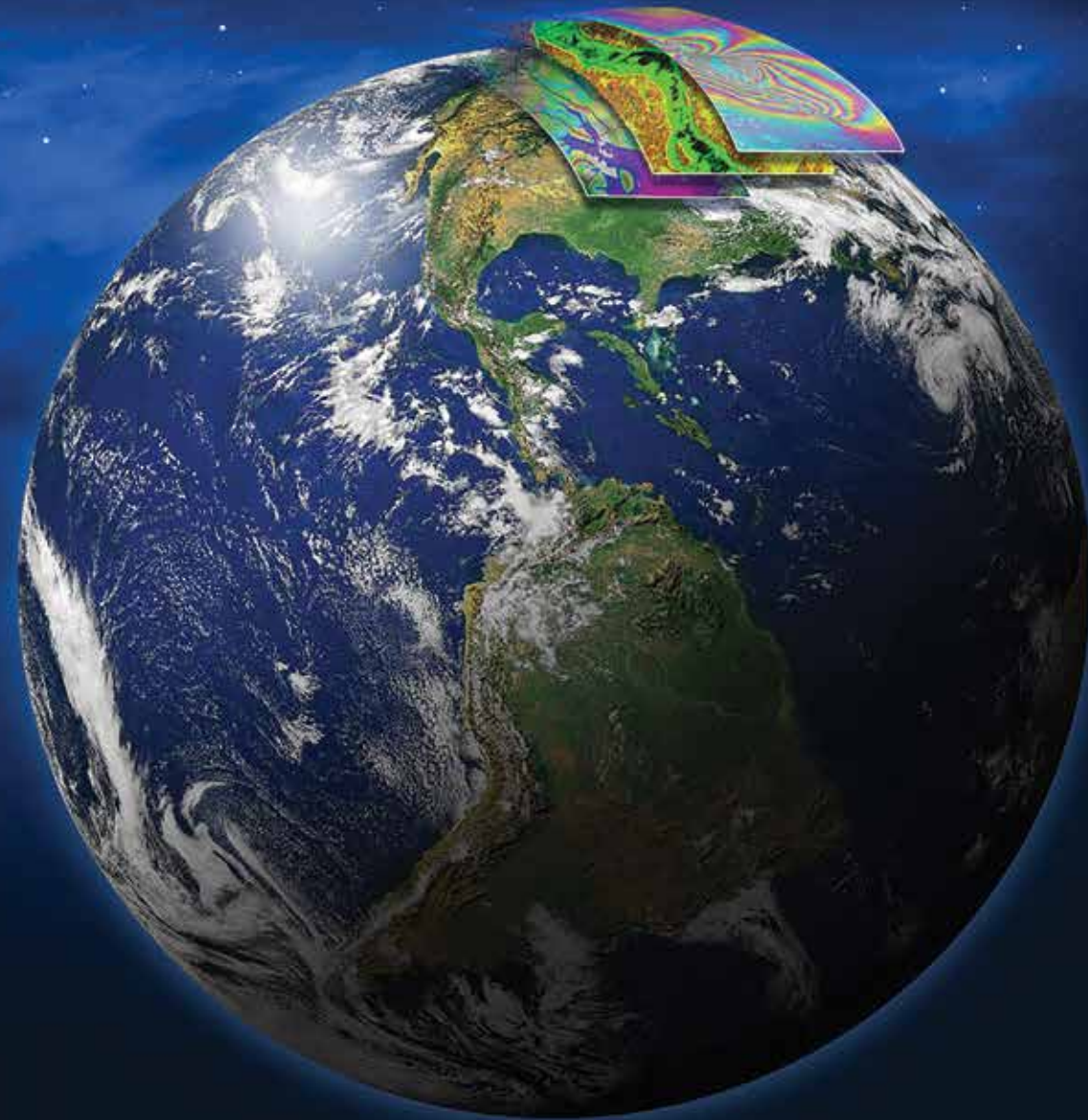
allowable range resolution at L-band. Therefore, a SweepSAR wide-swath mapping system, which allows wide swath while maintaining resolution in the along-track dimension, is required for global access, fast revisit, frequent temporal sampling and full resolution. SweepSAR is explained in greater detail in section 4.7.

At this highest level, the system described in the next section is necessary to meet the objectives of all disciplines.

The general observational characteristics – wide swath, fast repeat, fine resolution and multiple polarizations – represent the most basic flow down from science requirements to mission and instrument requirements. Table 3-4 summarizes the key and driving requirements on the mission system to satisfy the science requirements.

4 MISSION CHARACTERISTICS

THE NISAR
OBSERVATORY
WILL LAUNCH
ON AN ISRO
GEOSYNCHRONOUS
SATELLITE LAUNCH
VEHICLE MARK II
FROM SATISH
DHAWAN SPACE
CENTER IN
SRIHARIKOTA, INDIA.



This section describes NISAR mission attributes that are important to the use and interpretation of the data. The observing strategy attributes include areas of acquisition, mode of operation, frequency of coverage, the orbit, and the radar observational capabilities. The mission operations design and constraints, which can influence science acquisition planning and execution, are also described. This design includes NASA and ISRO's plans to respond to urgent events.

4.1 OBSERVING STRATEGY

The NISAR mission aims to achieve global coverage of land where biomass exists, which is nearly everywhere on land, except the polar areas, full coverage of land and sea ice at both poles and in mountains, frequent coverage of land areas that are deforming rapidly, and regular infrequent global coverage elsewhere to be prepared to respond to events that are unusual, such as mid-plate earthquakes. Global coverage requirements for NISAR science are specified in the L1 requirements (Figure 4-1). Each of the L2 science requirements (listed in Appendix D) specifies a measurement objective, an accuracy of that measurement, and the area of interest or target area over which the measurement must be made.

Science targets are proposed by each of the three NISAR scientific discipline teams (solid Earth, ecosystems and cryosphere), in the form of geographical polygons and nominal radar modes (see Appendix G for NISAR target maps by each discipline). With these targets and the L2 measurement accuracy requirements stated in Appendix D in mind, an observing strategy

can be devised, which takes into account the desired number and frequency of acquisitions needed in any given time interval, radar modes to be used, the season (if relevant), and whether to observe on the ascending or descending pass or both.

All NASA requirements can be met exclusively with the NASA-provided L-band radar system. In addition to the NASA science requirements, ISRO scientists have specified targets of interest in India and its surrounding coastal waters. These areas have similar attributes as those defined by the NASA SDT for global targets. The ISRO requirements combine L-band and S-band observations. Operating the L- and S-band radars simultaneously will provide unique data and also minimize mode conflicts over India. However, the programmatic guideline is to not require simultaneous operation, but to make it an implementation goal.

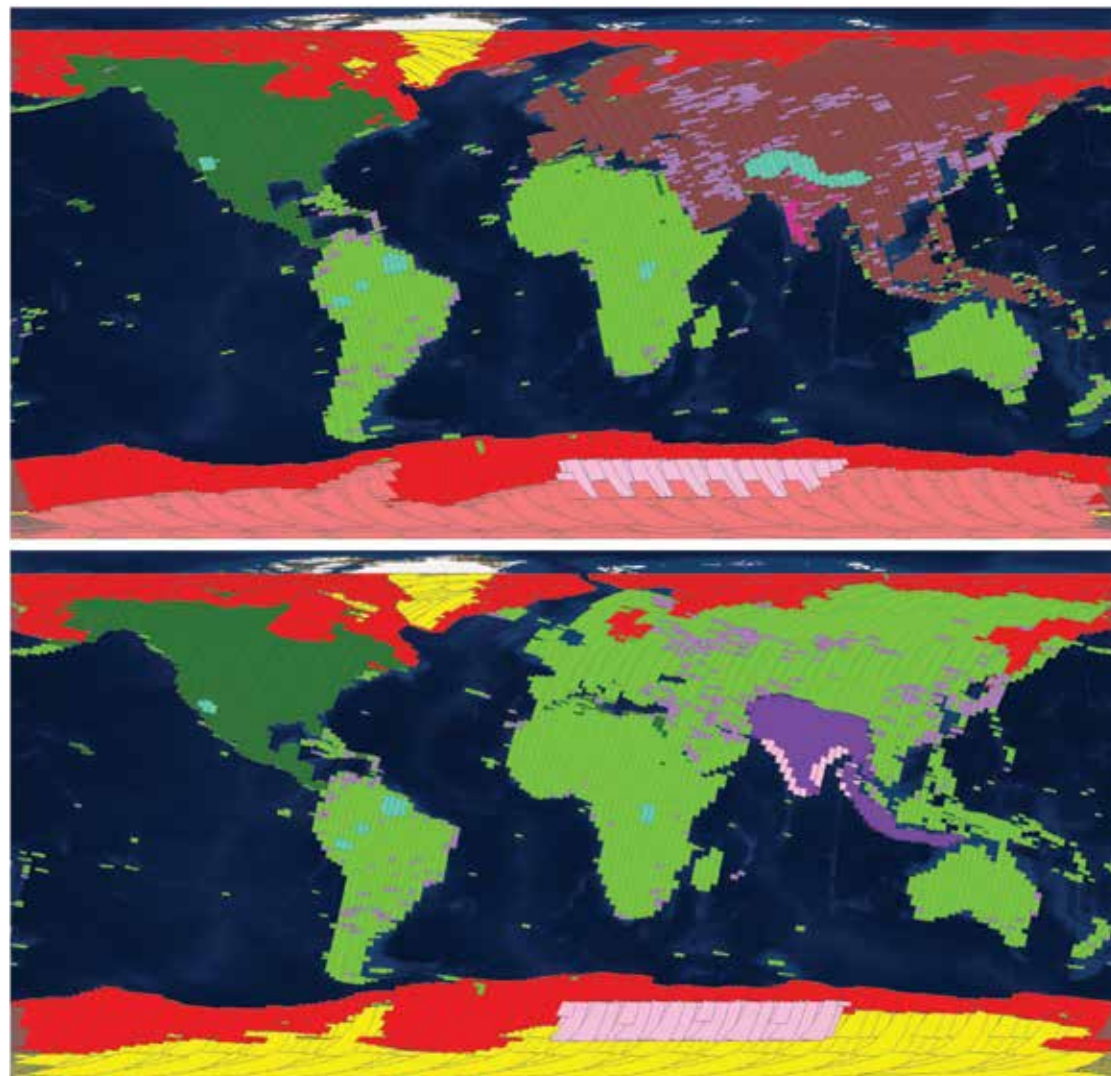
4.2 REFERENCE SCIENCE ORBIT

The NISAR observatory will launch on an ISRO Geosynchronous Satellite Launch Vehicle (GSLV) Mark II from Satish Dhawan Space Center (SDSC) in Sriharikota, India. Launch services will be provided by ISRO, which will manage launch vehicle development and provide all necessary technical documentation. The current target launch date is January 2022. The baseline orbit was selected to satisfy scientific and programmatic requirements. NISAR's 747-km altitude orbit, consisting of 173 orbits/cycle, will allow for global coverage every 12 days, as shown in Figure 4-2 and Table 4-1.

During science operations, NISAR will fly within a diamond-shaped orbital corridor defined for each of the

FIGURE 4-1

Global coverage for ascending (top) and descending (bottom) passes showing instrument modes and target areas. The coverage addresses the three science disciplines of solid Earth deformation, ecosystems, and cryosphere. Many applications objectives will also be satisfied through these observations.



INSTRUMENT MODES

- Background Land (L-SAR only)
- North America SNWG Target (L-SAR only)
- Land Ice (L-SAR only)
- Sea Ice (L-SAR only)
- Low Data Rate Study Mode (L-SAR only)
- Urban Areas (L-SAR only)
- High Res Deformation-Landslide/Urban (Joint mode)
- Antarctic Region (Joint mode)
- ISRO Sea Ice (Joint mode)
- ISRO Agriculture + Instrument Calibration Sites (Joint mode)
- Systematic Coverage (Joint mode)
- Systematic Coverage and Deformation (Joint mode)
- Agriculture/Sea Ice (S-SAR only)

FIGURE 4-2

A snapshot of the Reference Science Orbit orbital elements at the first ascending equator crossing is given in the following table and is specified in an Earth-Centered True Equator and Equinox of Epoch coordinate frame (purple mesh). During every 12-day repeat cycle, NISAR will execute 173 orbits, which will provide global coverage of the Earth.

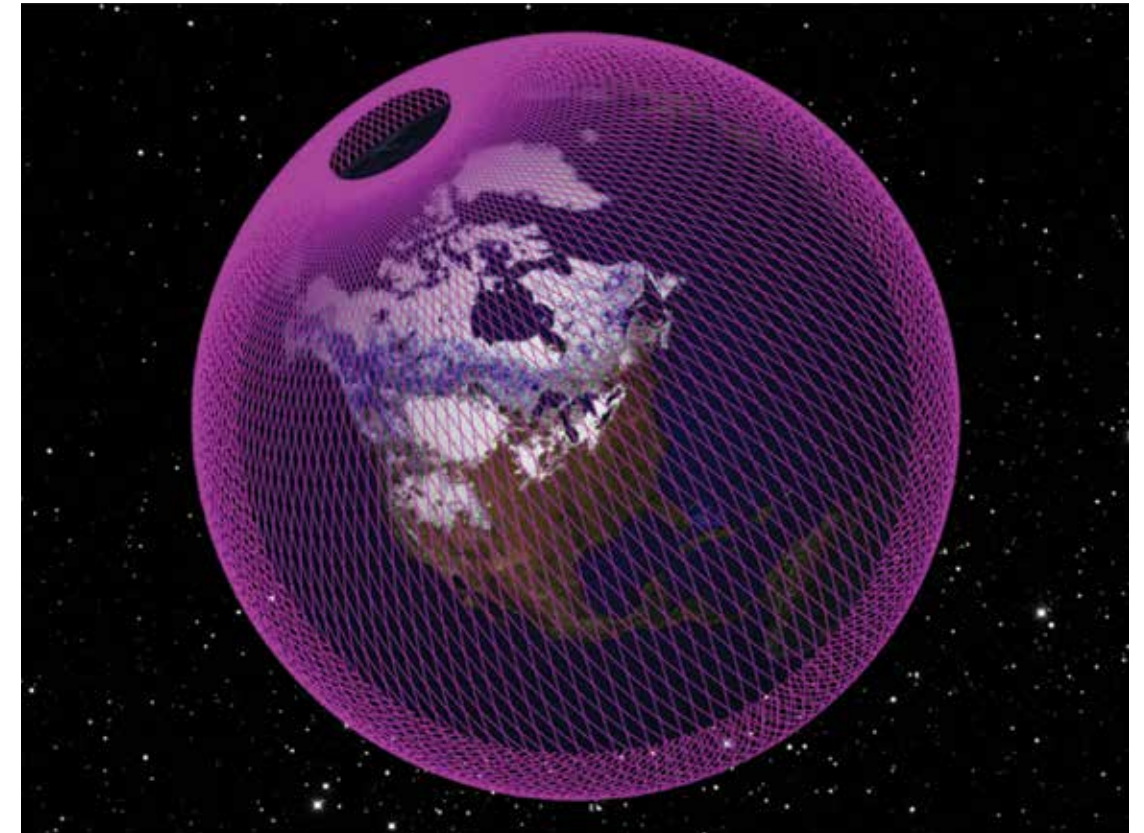


TABLE 4-1. ORBITAL ELEMENTS AT THE FIRST ASCENDING EQUATOR CROSSING FOR THE NISAR REFERENCE SCIENCE ORBIT. NISAR WILL ORBIT THE EARTH IN A NEAR-POLAR, SUN-SYNCHRONOUS ORBIT

ORBITAL ELEMENT	VALUE (osculating)	VALUE (mean)
Semi-Major Axis (SMA), (km)	7134.54476	7125.48662
Eccentricity	0.0012677	0.0011650
Inclination (deg)	98.40508	98.40508
Longitude of Node (deg)	-19.61438	-19.61601
Argument of Periapsis (deg)	68.40031	89.99764
True Anomaly (deg)	-68.40237	-89.99818

repeat cycle's 173 orbits and tied to the rotating Earth (Figure 4-3). This corridor is defined to enable accurate correlation of science observations from pass-to-pass and cycle-to-cycle, supporting assessment of changes in the science targets. The dimensions of the diamond were calculated as an upper bound on acceptable error produced by a non-zero baseline between passes/cycles between three primary factors (Rosen et al., 2000) of phase unwrapping error, geometric decorrelation and topographic leakage, but ultimately dominated by the former (phase unwrapping error, i.e., high fringe rate in regions of large topographic relief).

The center of the Diamond is defined by the 173-orbit reference trajectory (referred to as the reference science orbit), which is fixed to the Earth's surface and is exactly repeated every 12 days. The diamond can be thought of as a fixed altitude, longitude and latitude profile that spans the entire repeat cycle; a conceptual representation of this corridor is shown in Figure 4-4. To maintain the diamond, the JPL Navigation team plans on executing maneuvers over the long ocean

passes (Atlantic and Pacific) as much as possible not to impact science data collection.

The NISAR spacecraft will accommodate two fully capable synthetic aperture radar instruments (24 cm wavelength L-SAR and 10 cm wavelength S-SAR), each designed as array-fed reflectors to work as SweepSAR scan-on-receive wide swath mapping systems. The spacecraft will launch on an ISRO GSLV-II launch vehicle into a polar sun-synchronous dawn dusk orbit. The mapping scenario calls for frequent sampling over broad areas to create time series and allow for noise reduction through stacking methods. Thus, a high-rate instrument and data downlink system are required. The average capacity of the envisioned data downlink is of the order of 26 Tbits per day, supporting the instruments which can produce at L-band from 72 Mbps in its lowest bandwidth mode to over 1500 Mbps in the most demanding high-bandwidth, multi-polarization mode. Tables 4-2 and 4-3 summarize the overall mission characteristics.

FIGURE 4-3
During science operations, NISAR will fly within a diamond-shaped orbital corridor defined for each of the repeat cycle's 173 orbits and tied to the rotating Earth.

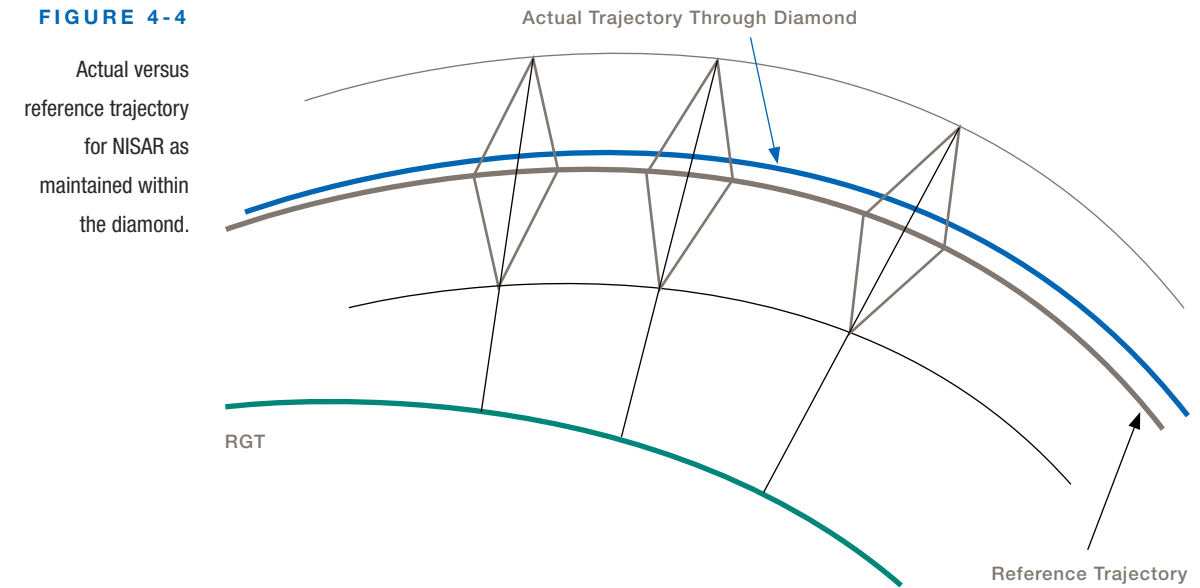
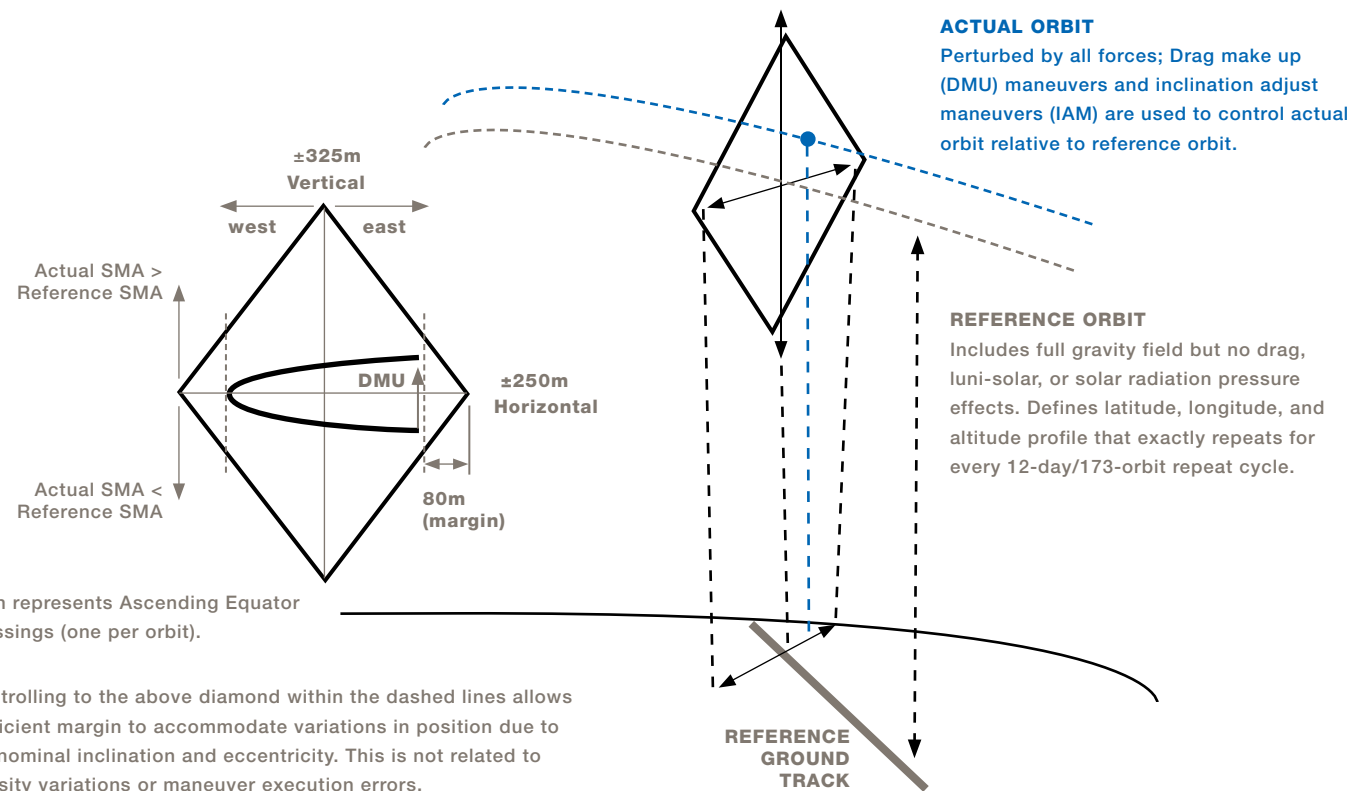


TABLE 4-2. OVERVIEW OF NISAR MISSION CHARACTERISTICS

ELEMENT	DESCRIPTION
Proposed Launch Date	Late 2021
Orbit	12-day exact repeat, sun-synchronous, dawn-dusk, polar, 747 km altitude
Mission Duration	3 years nominal, with extended mission fuel reserve
Science Data Downlink Approach	<ul style="list-style-type: none"> 30-45 minutes of data downlink per orbit at 3.5 Gbps data rate through polar ground stations 1 Gbps direct downlink to India over Indian ground stations
Observation Approach	<ul style="list-style-type: none"> L-band multi-mode global radar imaging S-band multi-mode targeted radar imaging Dual-frequency capable ~240 km swath for all modes Full pol, multiple bandwidths up to 80 MHz Near-zero Doppler pointing, fixed boresight Left-looking for the entire mission, relying on the international SAR constellation to fill in coverage around the Arctic pole
Mapping Approach	Under study – current approach defines a reference mission with fixed modes over broad target areas.

TABLE 4-3. MAJOR MISSION AND INSTRUMENT CHARACTERISTICS FOR NISAR

PARAMETERS	S-BAND	L-BAND
Orbit	747 km with 98° inclination	
Repeat Cycle	12 days	
Time of Nodal Crossing	6 AM/6 PM	
Frequency	3.2 GHz ± 37.5 MHz	1.257 GHz ± 40 MHz
Available Polarimetric Modes	Single Pol (SP): HH or VV Dual Pol (DP): HH/HV or VV/VH Compact Pol (CP): RH/RV Quasi-Quad Pol (QQP): HH/HV and VH/VV	SP: HH or VV DP: HH/HV or VV/VH CP: RH/RV Quad Pol (QP): HH/HV/VH/VV
Available Range Bandwidths	10 MHz, 25 MHz, 37.5 MHz, 75 MHz	5 MHz, 20 MHz, 40 MHz, 80 MHz (Additional 5 MHz iono band for 20 & 40 MHz modes at other end of pass-band)
Swath Width	>240 Km (except for QQP Mode)	>240 Km (except for 80 MHz BW)
Spatial Resolution	7m (Az); 3m–24m (Slant-Ra)	7m (Az); 3m–48m (Slant-Ra)
Incidence Angle Range	37–47 deg	37–47 deg
Noise Equivalent σ°	-25 dB (baseline) -20 dB (threshold)	-25 dB (for required full-swath modes)
Ambiguities	< -20 dB for all modes except QQP	< -23 dB swath average in SP or DP modes < -17 dB swath average in QP modes
Data and Product Access	Free and Open	

NASA contributions include the L-band SAR instrument, including the 12-m diameter deployable mesh reflector and 9-m deployable boom and the entire octagonal instrument structure. In addition, NASA is providing a high capacity solid-state recorder (approximately 9 Tbits at end of life), GPS, 3.5 Gbps Ka-band telecom system, and an engineering payload to coordinate command and data handling with the ISRO spacecraft control systems. ISRO is providing the spacecraft and launch vehicle, as well as the S-band SAR electronics to be mounted on the instrument structure. The coordination of technical interfaces among subsystems is a major focus area in the partnership.

NASA and ISRO will share science and engineering data captured at their respective downlink stations, and each organization will maintain their own ground processing and product distribution system. The science teams and algorithm development teams at NASA and ISRO will work jointly to create a common set of product types and software. The project will deliver NISAR data to NASA and ISRO for archive and distribution. NASA and ISRO have agreed to a free and open data policy for these data.

4.3 MISSION PHASES AND TIMELINE

Figure 4-5 provides a high-level overview of the NISAR mission timeline, and Table 4-4 provides more details on the different phases of the mission.

LAUNCH PHASE

The NISAR Observatory will be launched from ISRO's Satish Dhawan Space Centre (SDSC), also referred to as Sriharikota High Altitude Range (SHAR), located in Sriharikota on the southeast coast of the Indian peninsula, on the GSLV Mark-II expendable launch vehicle contributed by ISRO. The target launch readiness date is December 2021. The launch sequence encompasses the time interval that takes the observatory from the ground, encapsulated in the launch vehicle fairing, to after separation, and ends with the completion of solar array deployment and the observatory in an Earth-pointed attitude and in two-way communication with the ground. The launch sequence is a critical event.

COMMISSIONING PHASE

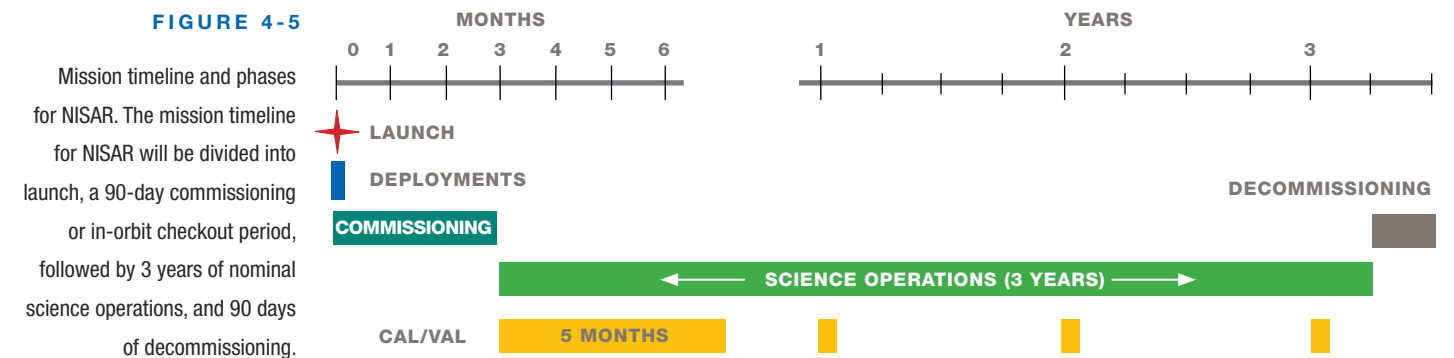
The first 90 days after launch will be dedicated to commissioning, or in-orbit checkout (IOC), the objective of which is to prepare the observatory for science operations. Commissioning is divided into sub-phases of initial checkout (ISRO engineering systems and JPL engineering payload checkout), deployments, space-

craft checkout and instrument checkout. Philosophically, the sub-phases are designed as a step-by-step buildup in capability to full observatory operations, beginning with the physical deployment of all deployable parts (notably the boom and radar antenna, but not including the solar arrays which are deployed during launch phase), checking out the engineering systems, turning on the radars and testing them independently and then conducting joint tests with both radars operating.

SCIENCE OPERATIONS PHASE

The science operations phase begins at the end of commissioning and extends for three years and contains all data collection required to achieve the L1 science objectives. During this phase, the science orbit will be maintained via regular maneuvers, scheduled to avoid or minimize conflicts with science observations. Extensive calibration and validation (CalVal) activities will take place throughout the first 5 months, with yearly updates of 1-month duration.

The observation plan for both L- and S-band instruments, along with engineering activities (e.g., maneuvers, parameter updates, etc.), will be generated pre-launch via frequent coordination between JPL and ISRO. This plan is called the reference mission; the science observations alone within that reference mission are called the reference observation plan (ROP). The schedule of science observations will be driven by a



variety of inputs, including L- and S-band target maps, radar mode tables, and spacecraft and ground-station constraints and capabilities. This schedule will be determined by JPL's mission planning team, and the project will endeavor to fly the reference mission, which includes these science observations exactly as planned pre-launch (accommodating for small timing changes based on the actual orbit). Periodic updates

are possible post-launch which will lead to a new reference mission.

Routine operations of NISAR are dominated by orbit maintenance maneuvers, science observations and data-downlink. Additional activities will include continuous pointing of the solar array to maximize power and continuous zero-doppler steering of the spacecraft.

TABLE 4-4. NISAR MISSION PHASES

MISSION PHASE	START DATE	DURATION	BOUNDARY END STATE
Launch (L)	January 2022 (L - 24 hours)	1 day + ~40 minutes	Spacecraft in target orbit, power positive, in two-way communication
Commissioning	L + ~40 minutes	90 days	All systems ready to begin science data collection
Science Operations	L + 90 days	3 years	Mission objectives are complete
Decommissioning	L + 3.25 years	90 days	Spacecraft in disposal orbit and passivated

DECOMMISSIONING PHASE

The decommissioning phase begins after the three-years of the primary science phase and after any extended operations phases (e.g., NASA Senior Review) have concluded. This phase extends for 90 days. NASA deorbit and debris requirements are not applicable for NISAR, however the project must comply with ISRO's guidelines to safely end the mission. ISRO adheres to the IADC Space Debris Mitigation Guidelines, IADC-02-01, Revision 1, September 2007.

4.4 GROUND SEGMENT OVERVIEW

The NISAR ground segment consists of the Ground Data System (GDS), Science Data System (SDS), and Mission Planning & Operations System. The GDS and SDS manage the end-to-end flow of data from raw data to fully processed science data products.

GROUND DATA SYSTEM

The GDS includes the tracking stations, data capture services, the communications network and end party services (Figure 4-6). The stations, services and communications are NASA multi-mission capabilities managed by the Goddard Space Flight Center (GSFC). The GDS will send the raw science data to the Science Data System (SDS), which converts the downlinked raw data into Level 0a and Level 0b data that are the starting point for the science data processing.

SCIENCE DATA SYSTEM

The SDS converts the Level 0b data into L1/L2 science data products that the NISAR mission provides to the science community for research and applications. The SDS facility is designed to process data efficiently and distribute data products in a timely manner to the community as required to meet mission objectives. The facility includes computer hardware dedicated to oper-

¹ For data product levels see <https://science.nasa.gov/earth-science/earth-science-data/data-processing-levels-for-eosdis-data-products>.

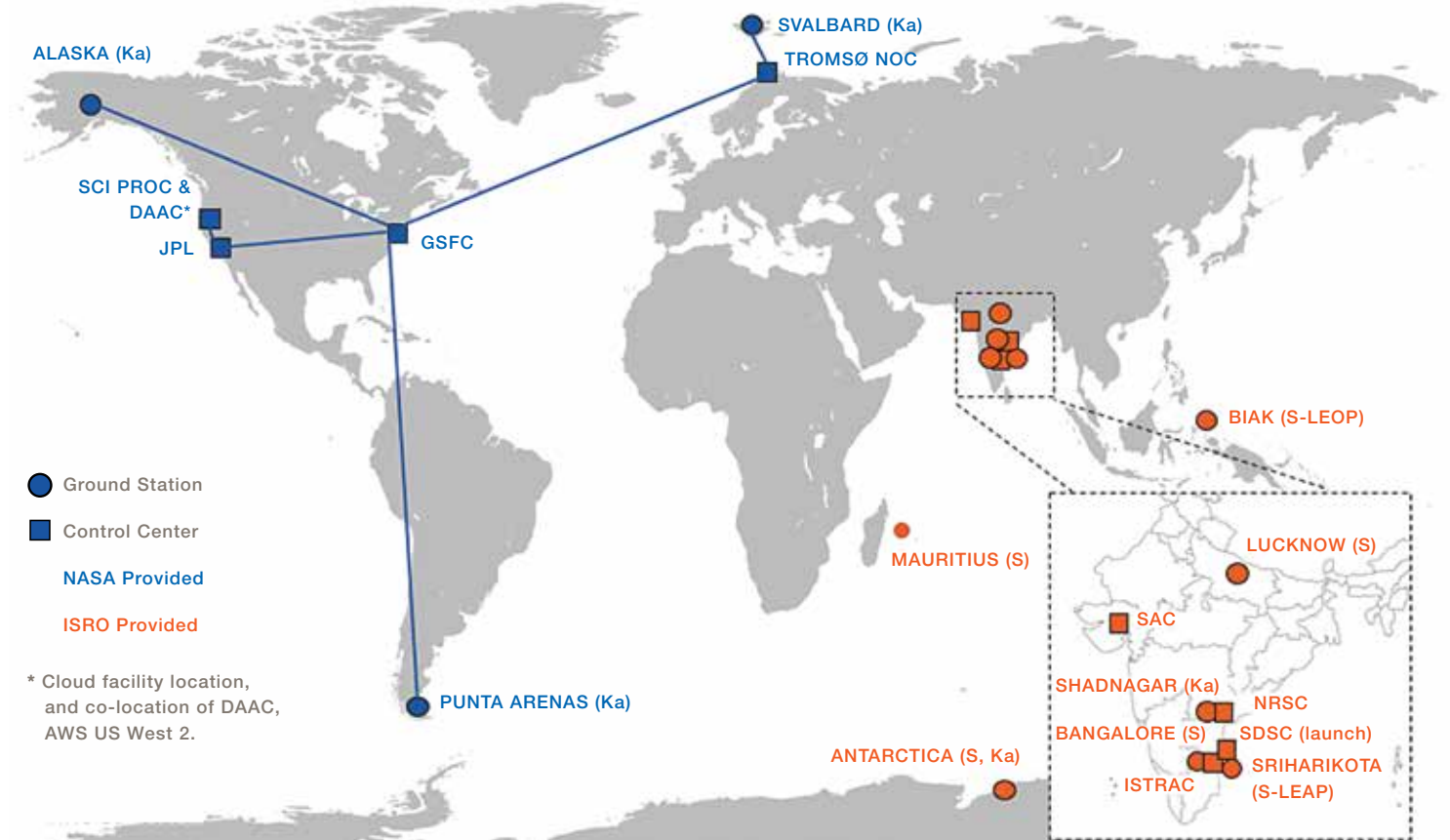


FIGURE 4-6

NISAR ground stations (including the NASA Near-Earth Network stations in Alaska, Svalbard and Punta Arenas; ISRO stations in Antarctica, Shadnagar, Bangalore, Lucknow, Mauritius, Biak), control center and launch location (Sriharikota (SDSC), India).

ational data production. In addition, the SDS facility is planned as a cloud-based hybrid SDS, with all elements cloud-enabled. This allows for some processing to be done at JPL and some to be distributed to the external cloud. The science and algorithm development teams will have access to cloud instances separate from the production instances to enhance algorithmic accuracy and performance.

The SDS is controlled through a cloud-based production management system at the Jet Propulsion Laboratory (JPL) in Pasadena, California. JPL is responsible for implementation of software to generate Level 1 radar instrument data products and Level 2 products. The science team is responsible for generating Level 3 geophysical data products for calibration and validation purposes. As funds permit, software for Level 3 products may be migrated to the production system to generate larger areas of Level 3 products.

To facilitate the software development process, the SDS will establish a mechanism for developmental instances of the SDS to be made available to the algorithm development and science teams. These developmental instances will be logically separate from the production system but will allow development and testing of the software that will be used to automatically generate the science data products once NISAR is in orbit.

NASA NEAR-EARTH NETWORK (NEN)

NISAR will downlink both to ISRO ground stations (see above) and to NASA Near-Earth Network (NEN) stations. For the NASA stations, Ka-band antennas will be used at one or more complexes. The specific antenna complexes currently identified are Alaska, United States; Svalbard, Norway; Punta Arenas, Chile; and Troll, Antarctica.

JPL MISSION OPERATIONS CENTER (MOC)

JPL will perform mission operations from multiple buildings at JPL in Pasadena, California, all of which are considered to make up the Mission Operations Center (MOC). The existing multi-mission Earth Orbiting Missions Operation Center (EOMOC) will provide operations teams with consoles, workstations, and voice and video displays. Navigation and GPS operations will be conducted from other JPL locations.

JPL SCIENCE DATA PROCESSING FACILITY

JPL science data processing will be done using the JPL SDS. SDS software and storage will be hosted by cloud services, likely Amazon Web Services (AWS) in Oregon.

NASA DISTRIBUTED ACTIVE ARCHIVE CENTERS (DAACS)

NASA's Earth Observing System (EOS) operates Distributed Active Archive Centers (DAACs) around the United States and has been interoperating with foreign sites. For NISAR, the Alaska Satellite Facility (ASF) DAAC has been selected. The DAAC will utilize AWS cloud services for processing, storage and distribution.

ISRO TELEMETRY, TRACKING AND COMMAND NETWORK (ISTRAC)

The ISRO ISTRAC facility in Bangalore will be used for spacecraft operations and to schedule and operate a set of S-band Telemetry, Tracking and Commanding (TTC) stations.

NATIONAL REMOTE SENSING CENTRE (NRSC)

The ISRO National Remote Sensing Centre (NRSC) operates an Earth science acquisition, processing and dissemination center in Hyderabad, India. For NISAR, this center operates two Ka-band stations as part of their Integrated Multi-Mission Ground segment for Earth Observation Satellites (IMGEOS), one near NRSC in Shadnagar, India, and another remote station in

Antarctica. The station in Shadnagar is also referred to as the Shadnagar Acquisition Network, or SAN.

SATISH DHAWAN SPACE CENTRE (SDSC), SHRIHARIKOTA RANGE (SHAR)

SDSC SHAR, with two launch pads, is the main launch center of ISRO, located at 100 km north of Chennai. SDSC SHAR has the necessary infrastructure for launching satellites into low Earth orbit, polar orbit and geostationary transfer orbit. The launch complexes provide complete support for vehicle assembly, fueling, checkout and launch operations.

WIDE AREA NETWORKS (WANS)

Wide Area Networks (WANS) will be used for long-distance exchanges among NISAR facilities. All WANS will consist of circuits carrying TCP/IP-based traffic.

4.5 TELECOMMUNICATIONS

The NISAR observatory's telecommunications system provides for one uplink path and three downlink paths. The uplink path is from ISRO's command center at ISTRAC through the observatory's S-band antenna mounted on the ISRO spacecraft bus. The three downlink paths are as follows: tracking and engineering telemetry, from the same S-band antenna back down to ISRO's spacecraft operations center at ISTRAC; instrument data from both L- and S-band systems, through the shared spacecraft Ka-band antenna (provided by ISRO) to ISRO's NRSC facilities near Hyderabad via ISRO's Ka-band ground stations at Shadnagar and Antarctica; and the same instrument data and engineering telemetry through the shared spacecraft Ka-band antenna to NASA NEN stations, (Figure 4-7).

ISRO's 2.88 Gbps Ka-band system provides for science data downlink to Indian ground stations with an effective information rate of 2.0 Gbps. Ka-band downlink to NASA ground stations will be at 4.0 Gbps with

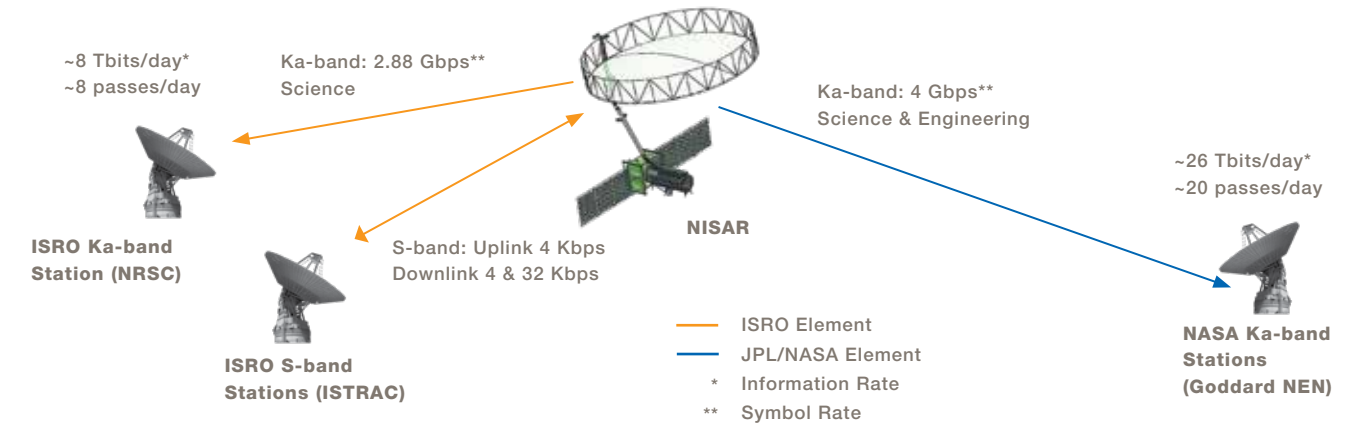


FIGURE 4-7

NISAR telecommunications links include Ka-band downlink to NASA and ISRO stations at 4 Gbps and 2.88 Gbps, respectively, and S-band uplink and downlink from and to ISRO ground stations.

an information rate of 3.45 Gbps via a JPL provided transmitter. ISRO supplies the Ka-band electronics and a 0.7m High Gain Antenna (HGA) mounted on the spacecraft's nadir surface to be used by both ISRO and JPL Ka-band transmitters, through a JPL provided and controlled switch. The antenna gimbal and control of the gimbal will be provided by ISRO. There will be 15 to 20 downlink sessions per day, with average session duration of less than 10 minutes. Note that there are separate Ka-band telecom transmitters, but they share the same Ka-band antenna. This system is fully redundant and cross-strapped except for the antenna and Ka-band gimbal.

KA-BAND COMMUNICATIONS

ISRO's NRSC facility operates an Earth science downlink and processing center in Shadnagar, India, near Hyderabad. This facility is the primary center for ISRO Ka-band communications from the observatory during nominal science operations. NRSC plans to place a Ka-band reception antenna here within the existing Integrated Multi-Mission Ground segment for Earth Observation Satellites (IMGEOS) facility at SAN. ISRO also plans to use another Ka-band ground station (Bharati in Antarctica) for science data downlinks. Primary playback of science data, however, will utilize NASA stations of the NEN at the ASF and Svalbard (Norway). These stations are shown in Table 4-5 and Figure 4-8.

TABLE 4-5. NISAR KA-BAND GROUND STATIONS

NASA/ISRO	STATION	ID	USAGE PLAN	LATITUDE (°)	LONGITUDE (°)	ALTITUDE (M)
NASA	Alaska	AS3	Primary Site: Maximum Utilization	64.859 °N	147.854 °W	431
NASA	Svalbard	SG2	Primary Site: Maximum Utilization	78.230 °N	15.398 °E	499
NASA	Punta Arenas	PA	Backup/Secondary Site – As Needed	52.938 °S	70.857 °W	17
ISRO	Shadnagar	SAN	Primary Site	17.028 °N	78.188 °E	625
ISRO	Antarctica	ANT	Primary Site	69.394 °S	76.173 °E	0

FIGURE 4-8

Locations of NISAR Ka-band ground stations (NASA stations in Alaska, Svalbard and Punta Arenas, and ISRO stations in Shadnagar and Antarctica are shown).



4.6 MISSION PLANNING AND OPERATIONS

Since nearly all objectives are best satisfied with regular repeated observations of any given science target, the NASA-ISRO Joint Science Team will create an overall science observation strategy that establishes a nominal repetitive observing baseline prior to launch. It is anticipated that the Joint Science Team will alter the nominal observation plan during the course of the mission. Applications and other government users may also request plan changes. The project team will strive towards accommodating these within the project constraints. These post-launch updates to the Reference Observation Plan will be applied on a quarterly or semi-annual frequency basis, with accommodation of urgent response requests in response to natural hazards and other emergencies (Figure 4-9). The Joint Science Team will rely on Mission Operations and the Project Science Team to understand the implications of any changes to the observation plan. Changes will be specified through target/mode/attributes as is currently done. The Mission Operations Team will then rerun the mission scenario simulation to examine resource (power, thermal, data downlink, cost) constraint violations. The Project Science Team will apply the updated Candidate Observation Plan through the science performance models to see if there are any

impacts to L1/L2 science requirements. If resource violations or performance impacts are identified, iteration will be required.

JPL will develop the coordinated observation plan that takes into account spacecraft power, maneuvers, data throughput sizing and availability of downlink channels. That plan will be sent to ISRO for uplink to, and execution on, the observatory. JPL manages all L-band SAR instrument operations, with the ISRO uplink station serving as a pass-through for L-band instrument commands. ISRO manages all S-band SAR operations. All instrument operations are guided by the coordinated observation plan, with specific commands/sequences to implement the plan developed by the respective organizations. Navigation is led by JPL, with maneuver design provided from JPL to ISRO to implement the maneuvers. Maneuver implementation is fed back to JPL as input for the next maneuver planning process. In the same vein, JPL provides the telecom sequence for the NASA-provided Ka-band telecom subsystem used for all science data downlink, while ISRO feeds back to JPL the ISRO-provided Ka-band telecom subsystem downlink contacts. JPL is responsible for producing the required science data specified by NASA and delivering them to NASA DAAC(s). The ISRO NRSC will process and distribute the required science data specified by ISRO.

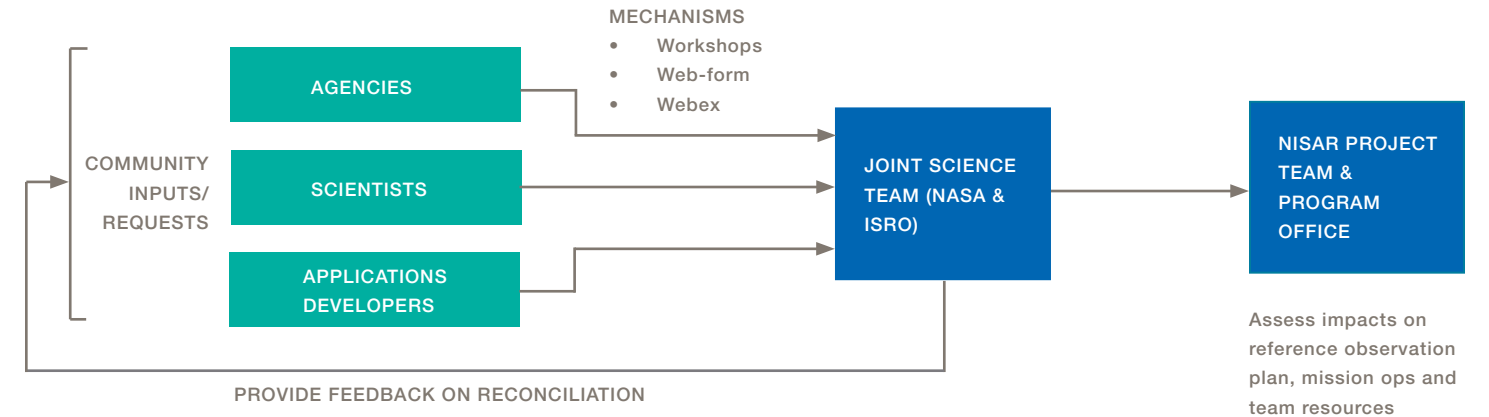


FIGURE 4-9

Flowchart showing steps to be followed for long-term re-planning of Reference Observation Plan. This process will be followed periodically (roughly every 6 months) for updating the plan during operations.

Mission operations will be a joint JPL-ISRO effort. Day-to-day observatory operations will be conducted at the ISRO Telemetry Tracking and Command Network (ISTRAC) center in Bangalore. ISTRAC monitors and controls the spacecraft, downlinking spacecraft telemetry to a local archive from where JPL can pull data as needed. All science data is downlinked via the JPL Ka-band telecom, initially processed, and archived first in the JPL Science Data System, and then in the ASF DAAC, from where ISRO can pull the data as-needed. In addition, a subset of L-band and S-band data (specified by SAC) will be downlinked directly to India (NRSC ground station) via the spacecraft Ka-band telecom.

4.7 INSTRUMENT DESIGN

The L-band Synthetic Aperture Radar (L-SAR) instrument is the focus of the NASA-chartered science goals for NISAR. To meet these goals, it will be heavily utilized during the mission. Current mission scenarios have the instrument on and collecting data for 45-50% per orbit on average, with peaks as high as 70%.

The L-SAR is a side-looking, fully polarimetric, interferometric synthetic aperture radar operating at a wavelength of 24 cm (Rosen et al., 2015). The L-SAR is capable of 242-km swaths, 7-m resolution along track, 2-8 m resolution cross-track (depending on mode) and can operate in various modes including quad-polarimetric modes, i.e., transmitting in both vertical and horizontal polarizations, and receiving in both the same

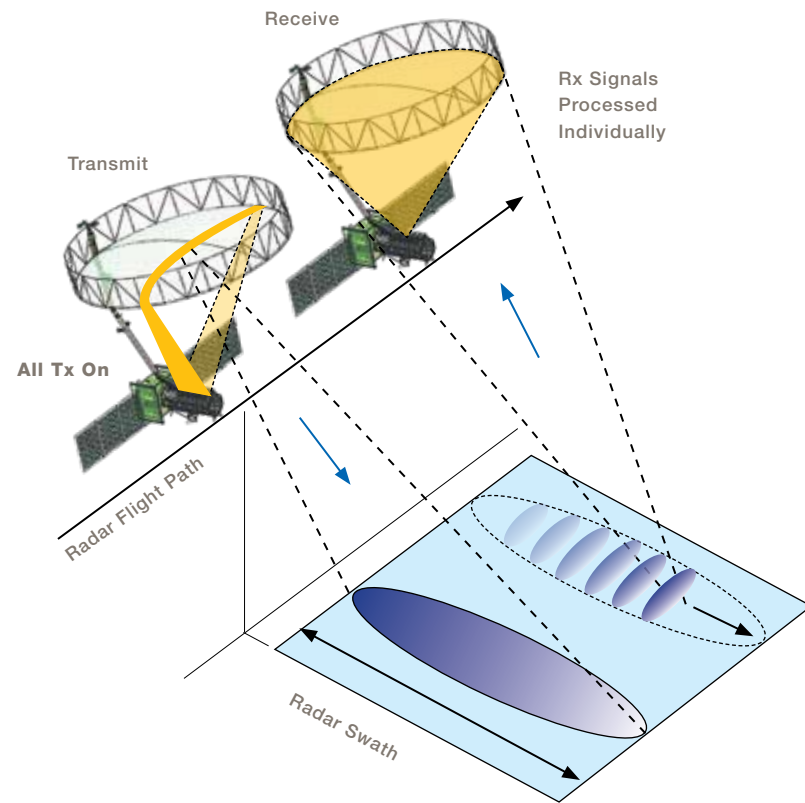
polarizations transmitted, and cross-polarizations. A cross polarization mode, for example, receives the horizontally polarized component of the return signal when vertically polarized pulses were transmitted, and vice versa. From the NISAR science orbit, the instrument's pointing accuracy is such that the L-SAR data can be used to produce repeat-pass interferograms sensitive to large-scale land deformation rates as small as 4 mm/year.

To meet the requirements of all science disciplines, the L-SAR radar instrument is designed to deliver fast sampling, global access and coverage, at full resolution and with polarimetric diversity. The technological innovation that allows this performance is the scan-on-receive "SweepSAR" design, conceived and refined jointly with engineering colleagues at the German Space Agency (DLR) under the DESDynI study phase.

SweepSAR (Figure 4-10) requires the ability to receive the echoed signal on each element independently, such that localized echoes from the ground can be tracked as they propagate at the speed of light across the swath. As an echo moves from receive element to receive element, the signals from neighboring elements must be combined to form a continuous record of the echo. Given the width of the swath (~244 km), returns from two or more echoes must be processed simultaneously. This operation is best performed using digital combining techniques, so the received echo is digitized

FIGURE 4-10

Sweep-SAR technique, which allows full-resolution, multi-polarimetric observations across an extended swath (> 240 km). By transmitting energy across the full feed aperture, a wide swath is illuminated on the ground. Each patch element on the feed can receive independently, allowing localization in time, hence space, of the return echo scattered from the ground. Note: Transmit and scanning receive events overlap in time and space. Along-track offset shown is for clarity of presentation only.



immediately upon reception, filtered, decimated, and then sent to a signal combiner.

On transmit, the entire radar feed aperture is illuminated, which creates a narrow strip of radiated energy on the 12-m reflector that illuminates the full 242 km swath on the ground. On receive, the echo illuminates the entire reflector, and that energy is focused down to a particular location on the radar feed aperture depending on the timing of the return. The narrowness of the receive beam on the ground (due to the wide reflector illumination) minimizes ambiguity noise so that individual pulses can be tracked separately as they sweep across the feed.

The SweepSAR L-band and S-band radars are being designed to work independently or together. The L-band hardware will be built at JPL, and the S-band electronics portion at ISRO. The feed apertures at L- and S-band are also built by JPL and ISRO, respectively, phase-matched to their respective electronics and cabling. In this sense, each radar is a self-contained

instrument up to the radiated energy from the feed aperture. Thereafter, both will share the same reflector, with a nearly identical optical prescription ($F/D=0.75$). Because a distributed feed on a reflector-feed antenna has a single focus, much of the radiated and received energy is not at the focus. Since S-band wavelength is 2.5 times shorter than L-band, yet the feed is the same length to achieve identical swath coverage, the S-band system has greater deviations from the focus. Thus, the design has been iterated to derive the best offset, tilt and phasing of each radar to balance the performance across the two systems. This analysis has been done independently by the JPL and ISRO teams, then cross-compared to validate.

For the radars to operate together as a dual-frequency system, it is necessary to share oscillator and timing information to lock their pulse repetition frequency together, which will be done with simple interfaces. Another concern is the coupling between the feed apertures. In the current design, the two apertures will

be mechanically and electrically separated, to keep the coupling manageable.

Filtering, decimation, calibration estimation and combining are done in a set of FPGAs or ASICs on each radar. This complication exists for both L-band and S-band and leads to a multiplicity of parallel processing efforts in the spaceborne electronics. The SweepSAR technique was demonstrated in an airborne configuration to show its efficacy (Hensley et al., 2010).

With SweepSAR, the entire incidence angle range is imaged at once as a single strip-map swath, at full resolution depending on the mode, and with full polarization capability if required for a given area of the interest. Azimuth resolution is determined by the 12-m reflector diameter and is of order 8 m.

FIGURE 4-11

NISAR system and instrument physical layout.

Because the radar cannot receive echoes during transmit events, there are one or more gaps in the swath if the radar's pulse rate is fixed. NISAR has the ability to

vary the pulse rate in order to move the gaps around over time. The data can then be processed to gapless imagery by interpolating across the gaps.

Over most of the world, the instruments will be operated independently. The requirements for range resolution, polarization and radar modes supported by the instrument are science target dependent. The instrument supports a fixed set of polarizations and bandwidth combinations of those listed in Table 4-6. The physical layout of the payload is depicted in Figure 4-11.

During data collection, the observatory performs near zero Doppler steering to compensate for the Earth's rotation during observations. The mission will be conducted in a left-only mode of operation to better optimize science return, with the expectation that other sensors can achieve science in the high Arctic regions.

The radar is designed to operate in a variety of modes to satisfy the various science objectives; these may

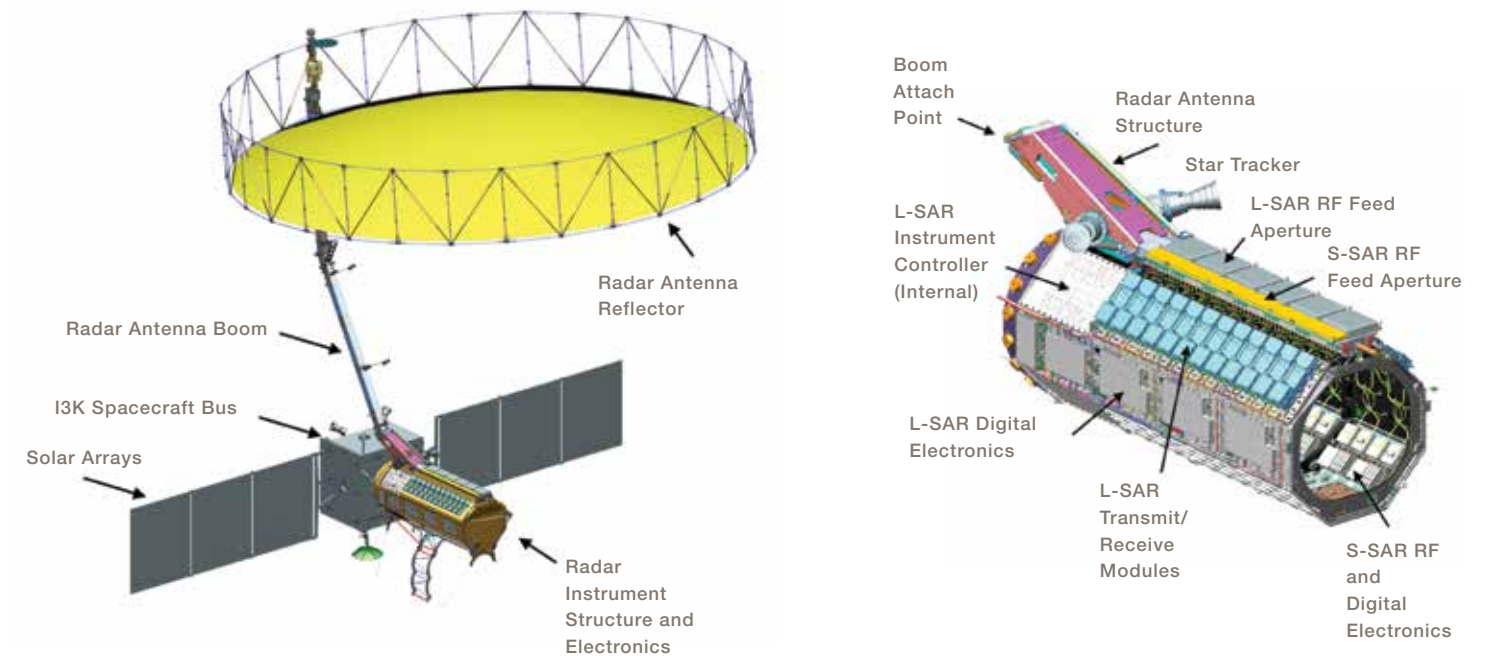


TABLE 4-6. SUPPORTED POLARIZATIONS AND BANDWIDTH COMBINATIONS

ELEMENT	DESCRIPTION
Operational Implementation	SweepSAR scan-on-receive
Configuration	<ul style="list-style-type: none"> 12-m diameter mesh reflector used for both L- and S-band S-band 2 x 24 / L-band 2 x 12 patch array, one TR module per patch-pair subarray per polarization Independent S- and L-band electronics with timing synchronization for possible simultaneous operations Digitization at each receive array element followed by real-time combining
Radar Center Frequency	S-band 3200 MHz; L-band 1260 MHz, simultaneous operations possible
Realizable Bandwidths	<ul style="list-style-type: none"> 5 MHz (L) 10 MHz (S) 25 MHz (S); 40+5 MHz split spectrum (L) 37.5 MHz (S); 40 MHz (L) > 75 MHz (S); 80 MHz (L)
Realizable Polarizations	Single-pol through quad-pol, including compact-pol and split-band dual-pol
Incidence Angle Range	~34-48 degrees
Performance	<ul style="list-style-type: none"> < -20 dB NES0 depending on mode < -15 to -20 dB ambiguities variable across swath 3-10 m range resolution, sub-pixel geolocation; ~ 7 m azimuth resolution

include single polarization (horizontal or vertical only) modes, dual polarization (e.g., transmit in horizontal polarization and receive in both horizontal and vertical polarization) modes, quad polarization (transmit in both and receive in both) modes, special “quasi-quad” modes simulating quad polarization modes with a lower data rate, circular polarization modes, and combinations of any of the above (one for L-band, and a different for S-band). Table 18-1 in Appendix F shows the available modes for the L-SAR and S-SAR instruments. For each of the observation targets, there is a single mode (polarization, bandwidth, radar band combination) that is used over that area. For overlapping targets, such as background land and U.S. agriculture, the more capable mode is a superset of capability of the other mode. Transition between these modes is seamless, which nearly eliminates data loss.

While the global measurements largely will be at L-band, there will also be regular acquisitions at S-band over India. As the mission evolves, insights into the most beneficial uses of S-band in place of L-band or as a dual-frequency system will be gained, with the observation plan modified accordingly.

The Shuttle Imaging Radar-C was the first orbiting multi-frequency, multi-polarization SAR around Earth and demonstrated the value of having multiple wavelengths. Possible benefits include:

- Use of S-band in polar regions can reduce the impact of the ionosphere, since the S-band signal will be five times less sensitive than L-band to ionospheric perturbations.

- Use of L-band and S-band jointly will allow a good estimate of the ionosphere using dual-band mitigation techniques (Rosen et al., 2010).
- Use of L-band and S-band jointly to extend the range of sensitivity for biomass estimation and surface deformation, and aid in estimating soil moisture.
- Use of L-band and S-band jointly to study differential surface roughness and volume scattering effects, improving classification of natural surfaces.
- Use of L-band and S-band jointly or separately to study decorrelation rates of natural surfaces, improving the utility of interferometry for change detection and change classification.

These capabilities will provide researchers with a fundamentally new global (at L-band) and globally distributed (at S-band) data set for research. It is important to note that the system downlink is at present fully tasked, so opportunities for dual-band collection must be balanced against alterations to the nominal observation plan.

4.8 FLIGHT SYSTEMS/SPACECRAFT

The NISAR flight system design, development, integration, testing and operations are a joint venture, with equivalent-scale contributions from both JPL and ISRO. The suite of flight systems consists of the launch vehicle and free-flying observatory. The NISAR observatory is designed around the core payloads of L- and S-band SAR instruments, designed to collect near-global radar data over land and ice to satisfy the L1 science goals. In addition to the two radar instruments, the NISAR payload includes a global positioning system (GPS) receiver for precision orbit determination and onboard timing references, a solid-state recorder, and a high-rate data downlink subsystem to enable transmission of the high-volume science data to the ground. Figure 4-11

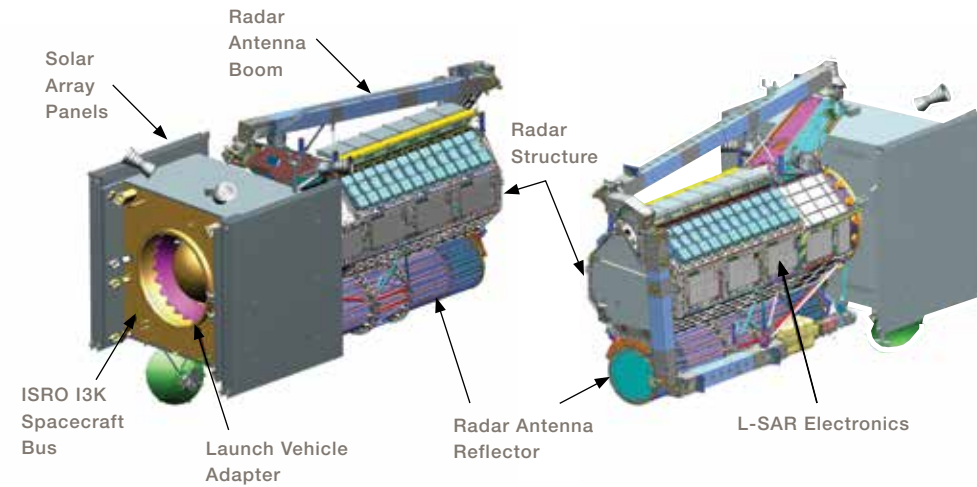
shows the fully integrated and deployed observatory system. The 12-meter Radar Antenna Reflector (RAR) is at top, supported by the Radar Antenna Boom (RAB). The boom is attached to the radar instrument structure (RIS), which is itself attached to the ISRO I3K spacecraft bus. Extending on either side of the bus are two solar arrays each with three panels that together supply approximately 4,000 W of power when illuminated (i.e., at all times when not in eclipse or off Sun-pointing). The radar payload integration (L-band and S-band integration) will occur at JPL, and the overall observatory integration will occur at ISRO Satellite Center (ISAC) in Bangalore, India. The main elements of the system are illustrated in Figures 4-11 and 4-12.

ISRO provides the spacecraft bus, which includes all systems required for central command and data handling, uplink and downlink, propulsion, attitude control, solar arrays, the S-band radar electronics, and a Ka-band telecom system and gimbaled High Gain Antenna (HGA) dish. ISRO also provides the launch vehicle. NASA/JPL provides the L-band radar electronics, the deployed boom and radar reflector, a high-capacity/high-speed Solid State Recorder (SSR), the GPS, high-rate Ka-band Payload Communication Subsystem (PCS), the pyro firing system for boom and antenna deployments, and a Payload Data System (PDS) that monitors and controls the JPL systems and handles communications between all of the JPL systems and the ISRO spacecraft bus.

The NISAR science requirements levy special functional requirements on the heritage ISRO spacecraft and its associated mission operations. Both L-band and S-band radar payloads require substantial average power for operation on-orbit, which leads to a space-

FIGURE 4-12

Spacecraft in stowed configuration.



craft design with large deployable solar arrays. The baseline science observation plan calls for up to 26 Tb (Terabits) per day of radar data collection, downlink and processing. This plan drives the spacecraft design to include a Ka-band telecom system to accommodate the high bandwidth requirements. The spacecraft AOCS (Attitude and Orbit Control Subsystem) is designed to address several critical science-enabling functions: 1) it must fly along the same orbit to within narrow tolerances (500 m) over the life of the mission; 2) it must be able to control the attitude of the observatory as a whole to point at a fixed angular location relative to an ideal orbit track and nadir at any given point on orbit; 3) it must be able to slew and hold attitude to observe Earth from both sides of the orbit plane. For orbit control, there is sufficient fuel to accommodate at least 5 years of operations at the chosen altitude. The propulsion system is agile enough to perform the necessary small orbit control maneuvers every few days that are required to maintain the strict orbital tube requirements. JPL augments the ISRO spacecraft capability with GPS receivers, providing GPS time message and a 1pps (pulse per second) signal to the spacecraft and radar instruments.

To date, the spacecraft design has been optimized to accommodate all key and driving requirements, and refined technical analyses show that predicted performance meets science needs. The solar arrays have the required capability, plus an extra string of cells for contingency. The Ka-telecom system is sized to handle the throughput baseline up to 26 Tb per day, though the margins are tight for many of the elements of the data system, many of which are part of the ground system. For pointing control, rigid-body analysis shows that the system is controllable to the required accuracy. Further flexible body analysis will be performed in the coming years to further characterize requirements compliance. Though the nominal plan calls for left-looking observations only, the spacecraft is being designed to be capable of operating either looking to the left or right. This would support contingency operations, or imaging of the higher latitudes of the Arctic possibly in an extended mission phase.

4.9 PROJECT STATUS

The NISAR project conducted a successful Preliminary Design Review (PDR) on June 21-23, 2016. Key Decision Point-C (KDP-C), the review to confirm the mission for detailed design and development, was held on August 23, 2016. Shortly thereafter the project entered the Design and Build Phase (Phase C), and the

project team passed the Critical Design Review (CDR) in October 2018, where the results of the engineering model and some flight model hardware testing were presented and plans for building the remaining flight hardware were described. The Mission Systems CDR is planned for fall 2019. The planned launch date for the mission is early 2022.

5 MISSION DATA PRODUCTS

THE NISAR DATA
PRODUCT LEVELS
HAVE BEEN DEFINED
IN ACCORDANCE
WITH THE NASA
EOSDIS CRITERIA FOR
SCIENCE PRODUCT
PROCESSING LEVEL
CLASSIFICATION.

NISAR data products will be organized by product level, with Level 0 being a raw form of data and Level 3 being a geocoded derived science product in physical units. The NISAR LOA product is the received raw data with metadata added to support storage at the DAAC. The NISAR LOB product is a refined version of the radar signal data with transmission artifacts removed. NISAR L1 products will include all products in radar (range-doppler) coordinates, including the Single Look Complex (SLC), Multi-Look Detected (MLD), unwrapped (UNW) and wrapped nearest-time interferograms (IFG), and polarimetric images. The NISAR L2 products will be geocoded versions of all the L1 products (except MLD and the wrapped interferogram). The NISAR Science Data System (SDS) team will generate the L-band LO-L2 products (Table 5-1), and the NISAR Project Science and Science Teams will generate the L3 products at selected calibration/validation sites distributed globally.

Level 1 products, including the SLC, IFG, Nearest-Time (UNW), and the L2 geocoded versions of these products (produced for all except IFG) will be relevant for studies of solid Earth deformation and cryospheric sciences. The NISAR ecosystem products include the L2 Geocoded Single Look Complex (GSLC), the L1 polarimetric covariance matrix in range-doppler coordinates (COV), and the L2 polarimetric covariance matrix in geocoded map coordinates (GCOV). The L2 geocoded SLC product, generated from the L1 SLC product, enables users to perform amplitude as well as interferometric analysis directly on a geocoded grid. Depending on the polarimetric acquisition mode (single, dual, or quad), the GSLC product can have 1, 2, or 4 complex-valued layers. Based on the polarimetric acquisition mode (single, dual, or quad) and processing option (symmetrized or non-symmetrized cross-polarimetric channel), the polarimetric covariance matrix can have from 1, 3, or 6 complex-valued layers. These products primarily support the NISAR ecosystem requirements of biomass estimation, disturbance detection, inundation mapping,

and crop area delineation, as well as additional ecosystem and land-cover applications that may be developed during the NISAR mission. Ancillary data needed to create these products, such as orbits and calibration files, are included in the metadata layers of these products. For interferometry, the dense field of range and azimuth offsets, suitable for local resampling to account for substantial motion between scenes, are also included as metadata at L1 and L2. The data layer descriptions are in Tables 21-1 – 21-8 in Appendix I.

The NISAR data product levels have been defined in accordance with the NASA EOSDIS criteria for science product processing level classification (<https://science.nasa.gov/earth-science/earth-science-data/data-processing-levels-for-eosdis-data-products>). The LO-L2 products will consist of two major components: self-describing binary data and quick-look metadata. The binary data component is based on the HDF-EOS5 specification (Klein and Taaheri, 2016), an HDF5-based format that has the following advantages:

- Open, self-describing format
- Supports hierarchical tree data arrangement
- Supported by GIS and database software
- Provides flexibility to support any binary data format making it scalable to support all levels of NISAR products
- Widely used for a range of NASA EOS missions (e.g., MODIS, AIRS, TRMM, CERES, MISR, GSSTF, and Aquarius)

In general, each LO-L2 product will be distributed as a single HDF-EOS5 granule. The NISAR quick-look metadata accompanying the binary data will be in an XML-based format.

Level 3-4 processing will be conducted by the NISAR science team. Measurements will include biomass,



TABLE 5-1. NISAR L-BAND L0-L2 PRODUCTS

PRODUCT LEVEL	PRODUCT NAME	SCOPE	DESCRIPTION
L0	Incoming Data (Raw)	Global	Raw downlinked data delivered to SDS with metadata added for archiving.
	Radar Signal Data (RSD)	Global	Corrected, aligned, and time-ordered radar pulse data derived from RAW products and used for further processing.
L1	Range-Doppler Single Look Complex (SLC)	Global	Standard L1 product that will be used to generate all higher level products.
	Multi-Look Detected (MLD)	Global	Multi-looked amplitude product in ground range coordinates.
	Nearest-Time Interferogram (IFG)	Antarctica and Greenland. Nearest pair in time and co-pol channels only.	Multi-looked flattened (WGS84 ellipsoid) interferogram with topographic fringes in range-Doppler coordinates.
	Nearest-Time Unwrapped Interferogram (UNW)	Global except Antarctica and Greenland. Nearest pair in time and co-pol channels only.	Multi-looked, unwrapped differential Interferogram in range-Doppler coordinates.
	Polarimetric Covariance Matrix (COV)	Global and all channels. Single/dual/quad pol.	Polarimetric covariance matrix (1, 3, or 6 layers) in range-Doppler coordinates.
L2	Geocoded SLC (GSLC)	Global and all channels.	Geocoded L1 SLC product using the MOE state vectors and a DEM.
	Geocoded Nearest-Time Unwrapped Interferogram (GUNW)	Global except Antarctica and Greenland. Nearest pair in time and co-pol channels only.	Geocoded multi-looked unwrapped differential Interferogram. Same as UNW but resampled onto a UTM grid.
	Geocoded Polarimetric Covariance Matrix (GCOV)	Global and all channels. Single/dual/quad pol.	Geocoded polarimetric covariance matrix (1, 3, or 6 layers) using the MOE state vectors and a DEM.

disturbance/recovery maps, ice and land displacements and velocity fields, all in geocoded coordinates. These products will also be delivered to the NASA DAAC; however, they will be generated only over selected regions of the world for calibration and validation purposes.

Figure 5-1 shows the overall data products that will be generated by the project and delivered to the NASA DAAC. The detailed product description, including all the data layers that will be specified in the L0-L2 products, is given in tables in Appendix H.

FIGURE 5-1

Data Product Levels. Products through Level 2 will be produced for the entire mission data set. Products at higher levels will be produced by the science team for calibration and validation purposes.

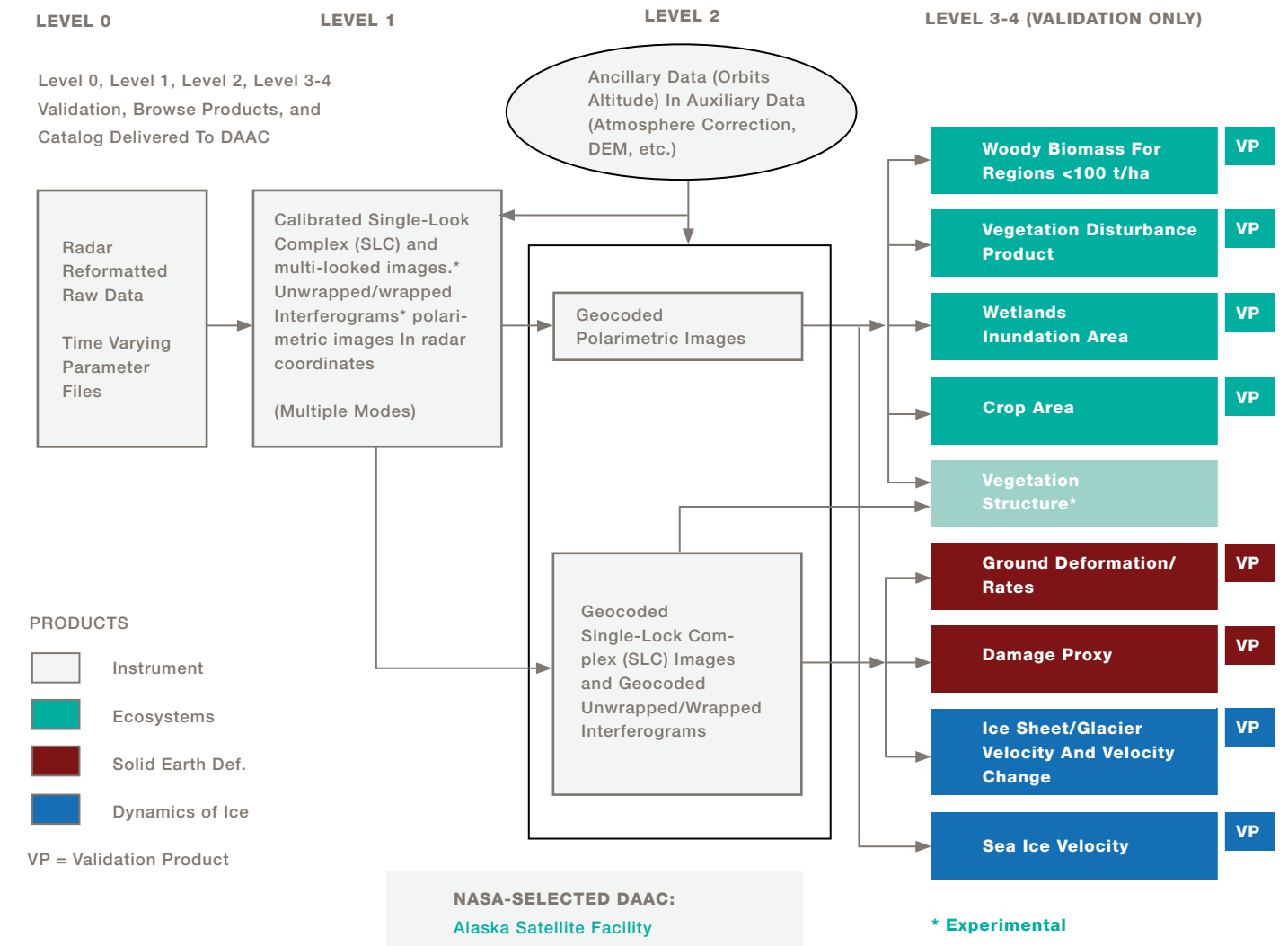
5.1 L0 DATA PRODUCTS

The NISAR SDS will produce two types of Level 0 data. The LOA product is the received raw data with metadata added to support storage at the DAAC. Although the

LOA dataset will be publicly available, this downlinked raw data will not be directly useable by the scientific community. The LOB product is a refined version of the radar signal data with transmission artifacts removed. The project will process all L- and S-band data acquired over the NASA downlink network to LOB, which is a reformatted, organized and regularized version of the instrument science data coming down in the science telemetry. LOB data is a basic input to a SAR image formation processor and is typically the starting point for many SAR scientists.

INCOMING RAW DATA (LOA)

The LOA data product represents a collection of time-tagged raw data packets and telemetry information



downlinked to the GDS, and typically do not have any overlap. The data are ordered in time but not all communication artifacts, missing data and synchronization errors are necessarily corrected. The raw signal data from the primary imaging band and the auxiliary 5 MHz sub-band are interleaved in this product and are not yet decomposed into corresponding I/Q channels. A multi-polarization LOA product will contain layers corresponding to each polarization (for both the primary and auxiliary band). Data are compressed by the radar using a block floating point quantization algorithm, and the LOA product will maintain this compressed state.

Each LOA raw data product will be reduced to a LOB product for use in further processing by the SDS. Each radar pulse will be tagged with its own metadata (e.g., receive time and PRF). The data are arranged on an increasing azimuth time and increasing slant range grid. The downlinked data are packaged into LOA product on reception. LOA data are primarily for archive purposes; it is anticipated that users interested in image processing will start with LOB.

RADAR SIGNAL DATA (LOB)

The LOB product consists of aligned and filled raw radar signal data that are used to derive higher level science products. The block floating point quantized samples from LOA raw data product are decoded and packed into complete range lines in the LOB product. Sampling Window Start Time (SWST) shifts for the radar pulses are aligned and each pulse is annotated with mode and PRF changes as well as missing data information. The following metadata are added at this stage to assist in further processing into L1/L2 products:

- Nominal pulse/chirp characteristics and actual replicas of transmitted chirps
- Doppler centroid estimate
- Orbit and attitude data
- Geographic coordinate boundaries
- I/Q bias estimates

- Calibration antenna patterns and related information
- Calibration noise records
- Channel delay calibration estimates
- Polarimetric compensation matrix

The LOA-to-LOB processor aligns or rearranges the raw radar signal data to ease further processing and does not modify the actual signal data (i.e., operations like RFI removal are not applied at this stage). Raw signal data and metadata corresponding to the main imaging band and the auxiliary 5 MHz sub-band are stored in separate data groups within the HDF-EOS5 product granule. A multi-polarization LOB product will contain layers corresponding to each polarization (for both the primary and auxiliary band). Each radar pulse will be tagged with its own metadata (e.g., receive time and PRF). The data are arranged on an increasing azimuth time and increasing slant range grid. The LOB product is the primary input for L1 product generation.

5.2 L1 DATA PRODUCTS

There are multiple L1 products to support the NISAR science disciplines. The L1 SLC data product is the output of a SAR image formation processor. It is calibrated for time and phase delays in the radar and propagation path (using a standard atmosphere/ionosphere model), and for antenna pattern effects and measured pointing offsets. Each science target may require a different resolution and set of polarizations, hence the product will accommodate multiple modes. This product is created at the fullest resolution possible, given the range bandwidth of the mode and the size of the antenna. Other L1 data products, including interferograms, interferometric correlation maps, and polarimetric backscatter, will be derived from the SLC product. The interferograms and correlation maps will be formed from nearest-in-time pairs of data sets. Given N interferometrically viable data sets, one can produce $N(N-1)/2$ unique interferograms, an impractically large number of interferograms to produce and store given that not all are typically used in scientific analysis. Forming nearest-in-time

pairs yields only $N-1$ interferograms, each of which is typically used in further analysis. Another L1 product, the Multi-Looked Detected imagery, will be derived from the SLC by taking its modulus on a pixel-by-pixel basis and averaging. The SLC and MLD products contain look up tables for radiometric ellipsoid correction. The project plans to use the Medium-fidelity Orbit Ephemeris (MOE) product, available within one day of acquisition for L1 and L2 processing, as it is nearly as accurate as the final orbit product and reduces processing latency.

RANGE-DOPPLER SINGLE LOOK COMPLEX (SLC)

This product refers to the standard range-Doppler geometry SLC imagery that are operationally delivered by SAR sensors around the world (often referred to as Level 1.1 by ESA and JAXA). The L1 SLC product will be distributed in the zero-Doppler radar geometry convention. The LOB-to-L1 processor will handle PRF changes within a data granule and the output imagery will be on a grid characterized by a fixed set of starting slant range, starting azimuth time, azimuth time interval, and slant range spacing values, to allow for easy interpolation of the auxiliary 5 MHz sub-band layers to match the primary image layers. All the primary image layers for a multi-polarization or multi-frequency product will be generated on a common azimuth time-slant range grid.

The L1 SLC is used to derive other L1 and L2 products. This product will contain individual binary raster layers representing complex signal return for each polarization layer. The SLC data corresponding to the auxiliary 5 MHz sub-band is stored in a similar format but in a separate data group within the HDF-EOS5 product granule. The SLC product is also packed with input, instrument and processing facility information; processing, calibration and noise parameters; geolocation grid; and data quality flags. The SLC product complex floating point backscatter is β^0 with secondary layer LUTs provided to convert to σ^0 and γ^0 .

NEAREST-TIME INTERFEROGRAM (IFG)

The L1 IFG product represents the ellipsoid height corrected, wrapped interferogram generated from two L1 range-Doppler SLCs in the range-Doppler geometry of the earlier acquisition. The data is arranged on a uniformly spaced, increasing zero-Doppler azimuth time and increasing slant range grid. The IFG product is primarily meant for detecting grounding lines and is only generated for acquisitions over Antarctica and Greenland. WGS84 ellipsoid is used as the reference surface for flat earth correction and the products are multi-looked to a posting of 25 meters on the ground. The auxiliary 5 MHz sub-band is used to apply an ionospheric phase screen during processing.

The L1 IFG product will contain individual binary raster layers representing complex numbers with the amplitude representing coherence and the phase representing interferometric phase for each co-pol channel. In addition to the metadata of the original L1 SLC granules, lookup tables for the perpendicular and parallel baseline components, range and azimuth offsets are also included. The interferogram will be flattened to the ellipsoid. A DEM will be used for fine registration.

NEAREST-TIME UNWRAPPED INTERFEROGRAM (UNW)

The L1 UNW product represents the unwrapped, multi-looked differential interferogram generated from two L1 range-Doppler SLCs in the range-Doppler geometry of the earlier acquisition. The data is arranged on a uniformly spaced, increasing zero-Doppler azimuth time and increasing slant range grid. For every ingested L1 SLC product, an archived L1 SLC product corresponding to the same imaging geometry and nearest in time is identified and an UNW processing job is launched. The UNW product is generated between co-pol channels and for all regions other than Greenland and Antarctica. Digital Elevation Models (DEMs) will be used for producing these data products which are multi-looked to a posting of 25 meters on the ground.

The L1 UNW product will contain individual binary raster layers representing single precision floating point unwrapped phase for each co-pol channel. In addition, byte layers with quantized coherence, geometry masks and connected component information, and floating-point layers corresponding to the amplitudes of master and slave acquisitions are included in the HDF-EOS5 granule. In addition to the metadata of the original L1 SLC granules, lookup tables for parallel and perpendicular baseline components, range and azimuth offsets are also included. Additional metadata will include lookup tables for various phase corrections (e.g., solid Earth tides, ECMWF tropostatic dry delay and ECMWF tropostatic wet delay, ionospheric phase screen). These phase corrections are not applied to the data but are available to users for application in post-processing workflows.

POLARIMETRIC COVARIANCE MATRIX (COV)

The L1 COV product represents the multi-looked cross-product between all possible polarization channel combinations for one L1 range-Doppler single-, dual- or quad-pol SLC product in the range-Doppler geometry. The polarimetric channels are multiplied in a lexicographic polarimetric basis. The COV product also contains the multilooked backscatter of single pol data. The COV products are radiometrically calibrated for spread loss and antenna pattern in all polarimetric channels. Radiometric ellipsoid correct is also applied. The physical quantity distributed with the COV products is the radar brightness β_0 . The products are multi-looked to a posting of approximately 25 meters on the ground. The data are arranged on a uniformly spaced increasing zero-Doppler azimuth time and increasing slant range grid.

MULTI-LOOK DETECTED IMAGE (MLD)

This product refers to the standard ground range-Doppler geometry multi-looked imagery that is operationally delivered by SAR sensors around the world

(often referred to as Level 1.5 by ESA and JAXA). All L1 MLD products will be distributed in the zero-Doppler geometry convention. MLD products are derived from the L1 SLC products by incoherent averaging of intensity in the azimuth time-slant range grid to provide 25 meter ground resolution data and then projecting the data to an azimuth time-ground range grid, under a constant ellipsoid height assumption. The data are arranged on a uniformly spaced, increasing zero-Doppler azimuth time and increasing ground range grid. The MLD product backscatter amplitude is β^0 with secondary layer LUTs provided to convert to σ^0 and γ^0 .

The L1 MLD product will contain individual binary raster layers representing multi-looked signal amplitude for each polarization layer. The L1 MLD product will not include any layers corresponding to the auxiliary 5 MHz sub-band in the HDF-EOS5 product granule. The lookup tables corresponding to the original L1 SLC are modified to use ground range image coordinates as inputs. In addition to the metadata fields provided in the original L1 SLC, additional lookup tables that allow users to transform ground range coordinates to slant range coordinates are also included in the HDF-EOS5 product granule.

5.3 L2 DATA PRODUCTS

Level 2 products are geocoded versions of all the L1 products (except MLD and the wrapped interferogram IFG) derived from the L1 images. The GSLC product contains look up tables for radiometric ellipsoid correction. The GCOV product has radiometric terrain correction and includes a full resolution projection angle layer.

GEOCODED SINGLE LOOK COMPLEX (GSLC)

The L2 GSLC product is derived from the L1 Range-Doppler SLC product and projected onto a DEM in the UTM system (like Landsat). The data are

arranged on a uniformly spaced, north-south and west-east aligned UTM/WGS84 grid. The spacing of the GSLC product in East and North directions will be comparable to the full resolution original L1 SLC product. The GSLC product can be directly overlaid on a map or combined with other similar GSLC products to derive interferograms and change maps, for example.

The L2 GSLC product will contain individual binary raster layers representing complex signal return for each polarization layer. The GSLC product granule will contain all the same metadata as the source L1 SLC product but with the lookup tables referenced to geographic coordinates instead of image coordinates. The GSLC product includes a byte layer indicating quality, water bodies and shadow-layover. The GSLC product will be produced globally.

GEOCODED NEAREST-TIME UNWRAPPED INTERFEROGRAM (GUNW)

The L2 GUNW product is derived from the L2 UNW product by projecting it onto a DEM in the UTM system (like Landsat) at 25 meter posting. The data are arranged on a uniformly spaced, north-south and west-east aligned UTM/WGS84 grid. All the lookup tables including phase corrections are transformed from image coordinates to geographic coordinates.

GEOCODED POLARIMETRIC COVARIANCE MATRIX (GCOV)

The L2 GCOV product is derived from the L1 COV product by projecting it onto a DEM in the UTM system (like Landsat) at 25 meter posting. The product also contains the multilooked backscatter for single pol data. Product locations are terrain corrected and the radar cross section is corrected for terrain-dependent incident angles. The data are arranged on a uniformly spaced, north-south and west-east aligned UTM/WGS84 grid. The GCOV product is distributed in a lexicographic polarimetric basis. All the lookup tables are transformed

from image coordinates to geographic coordinates. The physical quantity distributed with the GCOV products is γ_0 .

5.4 DATA PRODUCT DELIVERY/HOW TO ACCESS NISAR DATA

One Earth Science Data Center (ESDC) has been designated by NASA's Earth Science Division to archive and distribute NISAR science data: the Alaska Satellite Facility (ASF). ASF will receive validated NISAR science data products from the SDS, along with algorithm source code and ancillary data used in deriving the products and provide long-term archiving and distribution services for the general public. Public release of these data shall conform to the NASA Earth Science Data and Information Policy, U.S. Law, and the NASA/Caltech prime contract (NAS7-03001).

NISAR is required to begin delivering calibrated and validated L1-L2 science products to ASF within eight months after the end of the Commissioning. A beta release of L1-L2 data products will be delivered to ASF within 2 months after Commissioning. Validated L3 science products are required to be available for delivery to ASF within 6 months after Commissioning for displacement related products, and 12 months for ecosystems related products. The beta release of L3 data products will be delivered within 3 months after Commissioning for displacement related products, and 6 months for ecosystems related products. At the end of the L1-L2 and L3 Cal/Val activities, the data products will be reprocessed as needed using enhanced calibrated/validated algorithms, so that they become part of a consistently processed total mission data set. ASF is responsible for permanent archiving and public distribution of the NISAR data products. The specialized data sets used to perform the Cal/Val of the L1-L3 science data products, and Cal/Val reports documenting the data quality and accuracy assessments resulting from the Cal/Val activities, will be delivered to ASF along with the validated L1-L3 science data products.

6 SCIENCE DATA PRODUCTS AND VALIDATION APPROACHES

THE SCIENCE TEAM

USES LEVEL 3/4

SCIENCE DATA

PRODUCTS TO

VALIDATE

LEVEL 2 SCIENCE

REQUIREMENTS.

Section 5 describes the Level 0 to Level 2 data products that will be produced operationally by the NISAR project and made available globally to the science community. This section describes the Level 3 or 4 products that the science team will produce in selected areas to show that the science requirements of the mission will be met in each discipline area: solid Earth, ecosystems, cryosphere. Science requirements have a different "level" scheme than products: The science team uses Level 3/4 science data products to validate Level 2 science requirements, which are enumerated in Appendix D. This section describes the theoretical basis of the algorithms to be used to create science products for each of the Level 2 science requirements by discipline, and the anticipated methods to validate each of these requirements.

6.1 SOLID EARTH SCIENCE PRODUCTS

Solid Earth science products will be produced for co-seismic, transient, and secular displacements. The three primary NISAR Solid Earth L2 requirements on secular, co-seismic and transient deformation rates, that drive the L3 products needed for calibration and validation, are listed in Appendix D.

6.1.1 Theoretical Basis of Algorithm

APPROACH TO VALIDATING SOLID EARTH L2 REQUIREMENTS

Two separate approaches will be used by the NISAR Science Team for validating the Solid Earth L2 requirements, both of which require the generation of a standard set of NISAR L3 data products consisting of surface displacement time series for selected areas that sample a range of vegetation types, topographic relief, and strain rates. Generation of these products, as discussed in Section 6.1.2, requires a set of temporally

contiguous/overlapping SAR interferograms over all time periods of interest.

In the first approach, (approach #1) InSAR-derived surface displacements will be compared with point observations of surface motion from collocated continuous Global Navigation Satellite System (GNSS) stations (GPS and continuous GPS, or cGPS, are components of GNSS). Since all requirements are written in terms of relative displacements (sampling the deformation field at individual points), comparisons are done on the differences of observed surface motion (from both InSAR and GNSS) between GNSS station locations within the scene. For a GNSS station network of N stations, this will yield $N(N-1)/2$ distinct observations for comparison, distributed across a range of length scales. As discussed below, the methodology differs slightly depending on if the comparison is performed directly on interferograms (Requirement 663) versus basis functions derived from sets of interferograms (Requirements 658/660), but the underlying premise is the same: that GNSS provides a sufficiently high-quality time series to validate InSAR observations. This approach is appropriate where measurable displacement is occurring across the cal/val region and the GPS/GNSS network is sufficiently dense to capture most of the expected spatial variability of the signal.

In the second approach (approach #2), which is appropriate for negligibly deforming regions, the autocorrelation of noise in NISAR interferograms will be examined without comparison to GPS/GNSS, under the assumption that surface deformation is essentially zero at all relevant spatial scales. This method involves differencing InSAR displacement observations between a large set of randomly chosen pixel pairs and confirming that the estimates are statistically consistent with there being no deformation within the scene.

L2 REQUIREMENT 658 – SECULAR DEFORMATION RATE

To validate relative secular deformation rates (or velocities) from NISAR, Line-of-Sight (LOS) velocity data will be used for each pixel in a target region. Separate LOS velocities will be generated for ascending and descending passes to meet the requirement for two components of motion over each target location. Although the requirement specifies that the validation span 3 years of data, the NISAR Science Team can perform the validation for periods shorter than 3 years provided annual effects are mitigated by using data that span multiples of 1 year, or by explicitly modeling and removing the seasonal displacements. The relative vector velocity between any two points in the scene will be taken as the difference in the LOS velocity at those points.

In validation approach #1, the LOS velocity product will be used to calculate the relative InSAR velocity between each pair of GNSS stations within the SAR footprint that are less than 50 km apart. For subsequent comparison, the accompanying GNSS velocity differences will be generated by taking the 3-component GNSS position time series, projecting them into the InSAR LOS direction, estimating the GNSS LOS velocities, and differencing the GNSS LOS velocities between all stations pairs. To test NISAR's fulfillment of the 2 mm/y specification, InSAR and GNSS relative velocity estimates for each pair will be differenced, mean and standard deviation of all residuals will be calculated, and a t-test will be performed to check whether the mean error is statistically consistent with a value ≤ 2 mm/y.

Validation approach #2 is identical to approach #1 except that the relative velocities are determined for random pairs of InSAR pixels within a scene, and the statistics are calculated directly from the InSAR estimates. The cal/val regions to be used for both approaches will be defined by the NISAR Science Team and listed in the NISAR cal/val plan.

L2 REQUIREMENT 660 – COSEISMIC DISPLACEMENTS

To validate NISAR's ability to recover relative coseismic displacements of 100 mm and larger within a scene, step functions in surface displacements are estimated at the time of the earthquake from the InSAR and GNSS time series. The simplest version of the InSAR estimate is a coseismic interferogram spanning the earthquake, assuming negligible post-seismic deformation. Greater accuracy can be obtained by modeling the time series using appropriate basis functions (e.g., a secular displacement rate, a Heaviside time function at the time of the earthquake, and an exponential postseismic response) and using the offset thus obtained. A similar analysis can be done for the GPS time series.

In validation approach #1, relative displacements between each pair of GNSS stations within the SAR footprint and less than 50 km apart will be calculated. To do the comparison, GNSS coseismic displacements will be estimated by estimating the amplitude of a Heaviside basis function at the time of the earthquake for the 3-component GNSS positions, and the InSAR displacements in the same way. The GNSS 3-component displacements are then projected into the InSAR line of sight and differenced to obtain the relative GNSS displacements between all station pairs. To test NISAR's fulfillment of the $4(1+L^{1/2})$ mm specification, the InSAR and GNSS relative displacement estimates are differenced for each pair of GNSS station locations, distance L between stations is calculated, mean and standard deviation of all residuals is calculated, and a t-test is performed to check whether the mean error is statistically less than $4(1+L^{1/2})$ mm over length scales $0.1 \text{ km} < L < 50 \text{ km}$ (e.g., ≤ 5 mm at 0.1 km and ≤ 32 mm at 50 km).

Validation approach #2 is similar to approach #1 except that the relative displacements are determined for random pairs of InSAR pixels within a scene that does not include a significant earthquake, and the statistics are calculated directly from the InSAR estimates.

All the solid Earth requirements call for a minimum spatial coverage component. Validation of this component will rely on a combination of assessing the coverage of basic InSAR-quality data and ensuring that the required measurement accuracy is achieved in a suite of selected but comprehensive regions. Many of these regions will be automatically evaluated as part of the targeted sites for the transient deformation requirement.

L2 REQUIREMENT 663 – TRANSIENT DISPLACEMENTS

To validate the L2 requirements on transients, 12-day interferograms will be produced from both descending and ascending tracks over diverse target sites where GNSS observations are available. The two components of vector displacement, ascending and descending, will be validated separately.

For approach #1, unwrapped interferograms will be used at 100-m resolution to produce point-to-point relative LOS measurements (and their associated uncertainties) between GNSS sites. Position observations from the same set of GNSS sites and at the InSAR acquisition times will be projected into the LOS direction and differenced pairwise. These will be compared to the point-to-point InSAR LOS measurements using a methodology similar to that used for validating co-seismic displacements (as described above), except that the accuracy specification is $3(1+L^{1/2})$ mm over $0.1 \text{ km} < L < 50 \text{ km}$. To validate the noise in individual interferograms in approach #2, interferograms over a set of non-deforming sites will be utilized. In practice, characterization of transient deformation will usually be improved by examining longer time series of interferograms – the approach described here validates the requirement that short timescale or temporally complex transients can be characterized with a single interferogram.

Comprehensive validation requires transient sites possessing different deformation characteristics (e.g., volcanoes, landslides, aquifers, hydrocarbons, etc.),

vegetation covers (forest, shrub, bare surface, etc.), seasonality (leaf on/off, snow, etc.), and terrain slopes. The NISAR Science Team will select a set of cal/val regions to be used for this requirement and will list those sites in the NISAR cal/val plan.

GENERALIZED TIME SERIES ANALYSIS

The InSAR and GNSS comparisons described above will be performed in the framework of generalized time series analysis, whereby information in each time series is characterized by one or more underlying basis functions. The problem is cast as an overdetermined least squares (LSQ) estimation problem, from which parameters can be inferred for the simultaneous fit of various components to the time series, on a station-by-station or pixel-by-pixel basis. Implementation of this approach is described in Section 6.1.2.

These components—which include secular velocities, seasonal sinusoids, temporal offsets, and post-seismic exponential decay—represent much of the non-stochastic variance in the time series and are well-suited to the specific validation targets. For instance, for Requirement 658 (secular deformation) the velocity component of these fits will be used, while for Requirement 660 (coseismic deformation) the velocity, Heaviside (instantaneous step), and exponential/logarithmic components will be used. To perform the validations, estimates of the fit parameters for these functions, rather than the raw time series themselves, will be used for the statistical comparisons of InSAR and GNSS.

6.1.2 Implementation Approach for Algorithm

GENERATION OF TIME SERIES FROM SETS OF INTERFEROGRAMS

The time series analysis will be performed using the Generic InSAR Analysis Toolbox (GIAnT) (Hetland et al., 2012; Agram et al., 2013), which is openly downloadable from <http://earthdef.caltech.edu>. This toolbox has been used in many studies including interseismic

deformation along the San Andreas Fault (Jolivet et al., 2015) and will continue to be updated (with separate documentation) and openly released on a regular basis. GIANt is distributed with implementations of SBAS (Berardino et al., 2002, Doin et al., 2011) as well as TimeFun and MInTS (Hetland et al., 2012) techniques. The approach that will be used for the generation of NISAR L3 products is akin to the TimeFun technique (Hetland et al., 2012) implemented in GIANt and allows for an explicit inclusion of key basis functions (e.g., Heaviside functions, secular rate, etc.) into the InSAR inversion. There may be a small number of pixels where the classification is indeterminate. For example, at the given incidence angle, it is not possible to conclusively classify the data. For those cases, the classification would be $C_{x,y}=4$ or $C_k=4$. Figure 6-1 describes the workflow that will be followed for L3 product generation.

The L3 product generation workflow includes the following consecutive steps:

STACK PREPARATION

In this initial processing step, all the necessary L2 unwrapped interferogram products are gathered, organized and reduced to a common grid for analysis with GIANt. For operational NISAR processing, the following information from the L2 products are used in the stack preparation step:

- Unwrapped interferograms (either in radar or ground coordinates) prepared using the software (Rosen et al., 2012).
- Corresponding coherence layers (also generated using ISCE).
- Perpendicular baseline associated with the interferograms.
- A radar simulation file containing the pixels' elevation.
- A file containing radar incidence angles.
- Shadow, layover and land/water mask layers corresponding to the interferograms.

- A processing configuration file that includes processing parameters such as coherence thresholds, flags for applying phase corrections, etc., to allow for region-specific customization.

- Optional: Atmospheric delay metadata layers.

In the current concept, L2 data will be provided as coregistered stacks of unwrapped interferograms. Hence, no separate coregistration is planned during stack preparation. The output of the stack preparation step is a self-contained HDF5 product that is handed off for further processing.

TIMESERIES ESTIMATION AND PARAMETERIZATION

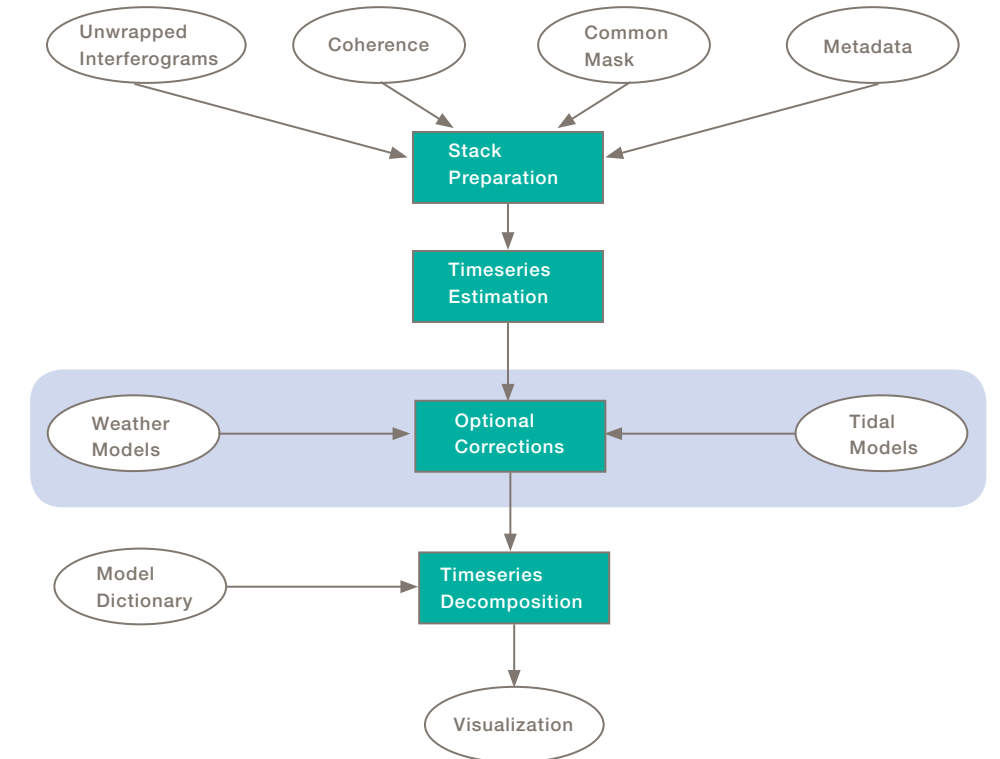
The timeseries (i.e., the unfiltered displacement of each pixel vs. time) is estimated from the processed stack using an SBAS or similar approach, and then parameterized. In practice, GIANt combines the two steps of SBAS and model-based parameterization. As we expect high-quality orbital control for NISAR, we anticipate that the set of interferograms will typically include all nearest-neighbor (i.e., ~12-day pairs) and skip-1 interferograms, so the SBAS step will often be somewhat trivial.

OPTIONAL CORRECTIONS

Phase distortions related to solid Earth and ocean tidal effects as well as those due to temporal variations in the vertical stratification of the atmosphere can be mitigated using the approaches described below. At this point, it is expected that these corrections will not be needed to validate the mission requirements, but they may be used to produce the highest quality data products. Typically, these are applied to the estimated time series product rather than to the individual interferograms since they are a function of the time of each radar acquisition.

Optional atmospheric correction utilizes the PyAPS (Jolivet et al., 2011, Jolivet and Agram, 2012) module within GIANt for implementing weather model-based interferometric phase delay corrections. PyAPS is well

FIGURE 6-1
NISAR L3 product generation workflow for solid Earth



documented, maintained and can be freely downloaded (<http://pyaps.googlecode.com>; PyAPS is included in GIANt distribution). PyAPS currently includes support for ECMWF's ERA-Interim, NOAA's NARR (North American Regional Reanalysis, National Oceanographic and Atmospheric Administration) and NASA's MERRA (Modern-Era Retrospective Analysis, Goddard Space Flight Center, NASA) weather models.

Following Doin et al. (2009) and Jolivet et al. (2011), tropospheric delay maps are produced from atmospheric data provided by Global Atmospheric Models. This method aims to correct differential atmospheric delay correlated with the topography in interferometric phase measurements. Global Atmospheric Models (hereafter GAMs), such as ERA-Interim (European Center for Medium-Range Weather Forecast), MERRA or regional models such as NARR provide estimates

of the air temperature, the atmospheric pressure and the humidity as a function of elevation on a coarse resolution latitude/longitude grid. In PyAPS, this 3D distribution of atmospheric variables is used to determine the atmospheric phase delay on each pixel of each interferogram.

For a given GAM dataset, grid points overlapping with the spatial coverage of the SAR scene are selected. Atmospheric variables are provided at precise pressure levels. These values are vertically interpolated to a regular grid between the surface and a reference altitude, z_{ref} , above which the delay is assumed to be nearly unchanged with time (~30,000 m). Then, the delay function on each of the selected grid points of the GAM is computed as a function of height. The LOS single path delay ($\delta L_{LOS}^s(z)$) at an elevation z is given by (Doin et al., 2009, Jolivet et al., 2011):

$$\delta L_{LOS}^s(z) = \frac{10^{-6}}{\cos(\theta)} \left\{ \frac{k_1 R_d}{g_m} (P(z) - P(z_{ref})) + \int_z^{z_{ref}} \left(\left(k_2 - \frac{R_d}{R_v} k_1 \right) \frac{e}{T} + k_3 \frac{e}{T^2} \right) dz \right\} \quad (6.1-1)$$

where θ is the local incidence angle, $R_d = 287.05$ J kg⁻¹ K⁻¹ and $R_w = 287.05$ J kg⁻¹ K⁻¹ are the dry air and water vapor specific gas constants, g_m is a weighted average of the gravity acceleration between z and z_{ref} , P is the dry air partial pressure in Pa, e is the water vapor partial pressure in Pa, and T is the temperature in K. The constants are $k_1 = 0.776$ K Pa⁻¹, $k_2 = 0.716$ K Pa⁻¹, and $k_3 = 3.75 \cdot 10^3$ K² Pa⁻¹.

The absolute atmospheric delay is computed at each SAR acquisition date. For a pixel a_i at an elevation z at acquisition date i , the four surrounding grid points are selected and the delays for their respective elevations are computed. The resulting delay at the pixel a_i is then the bilinear interpolation between the delays at the four grid points. Finally, the absolute delay maps of the InSAR partner images are combined to produce the differential delay maps used to correct the interferograms. Details and validation of the PyAPS approach are available in Doin et al. (2009) and Jolivet et al. (2012).

Optional corrections for solid Earth and ocean-tide loadings will be done using the SPOTL model (Agnew, 2012). To facilitate an accurate representation of ocean tides, SPOTL provides access to a collection of global and regional ocean models and allows for an easy combination of these models. It also includes methods to convert computed loads into harmonic constants, and to compute the tide in the time domain from these constants.

DECOMPOSITION OF IN SAR TIME SERIES INTO BASIS FUNCTIONS

Given a time series of InSAR LOS displacements, the observations for a given pixel, $U(t)$, can be parameterized as:

$$U(t) = a + vt + c_1 \cos(\omega_1 t - \phi_1) + c_2 \cos(\omega_2 t - \phi_2) + \sum_{j=1}^{N_{eq}} \left(h_j + f_j F_j(t - t_j) \right) H(t - t_j) + \frac{B_{\perp}(t)}{R \sin \theta} \Delta z + residual \quad (6.1-2)$$

which includes a constant offset (a), velocity (v), and amplitudes (c_j) and phases (ϕ_j) of annual (ω_1) and semiannual (ω_2) sinusoidal terms. Where needed we can include additional complexity, such as coseismic and postseismic processes parameterized by heaviside (step) functions H and postseismic functions F (the latter typically exponential and/or logarithmic). $B_{\perp}(t)$, R , θ , and Δz are, respectively, the perpendicular component of the interferometric baseline relative to the first date, slant range distance, incidence angle and topography error correction (e.g., Fattahi and Amelung, 2013) for the given pixel.

This parameterization of ground deformation has a long heritage in geodesy, particularly in analysis of GNSS time series as well as more recently with InSAR data (e.g., Blewitt, 2007, Hetland et al., 2012, Agram et al., 2013). For validation purposes, we will perform the same parameterization on any lowpass-filtered GNSS time series used in the analysis, after projecting the GNSS into the InSAR line of sight.

Thus, given either an ensemble of interferograms or the output of SBAS (displacement vs. time), the LSQ problem can be written as

$$Gm = d \quad (6.1-3)$$

where G is the design matrix (constructed out of the different functional terms in Equation 6.1-2 evaluated either at the SAR image dates for SBAS output, or between the dates spanned by each pair for interferograms), m is the vector of model parameters (the coefficients in Equation 6.1-2) and d is the vector of observations. For GNSS time series, G , d , and m , are constructed using values evaluated at single epochs corresponding to the GNSS solution times, as for SBAS InSAR input. For comparison with InSAR observations, the 3D GNSS time series are projected to the radar LOS

using the appropriate LOS vector. Equation 6.1-3 can be solved as a conventional weighted LSQ problem for the maximum likelihood model, where the L2 norm of the weighted misfit is minimized (e.g., Aster et al., 2018):

$$\min \phi(m) = (d - Gm)^T C_d^{-1} (d - Gm) \quad (6.1-4)$$

Here, the data covariance matrix, C_d , is constructed using the empirical estimate of correlation from each contributing interferogram over the appropriate subset of pixels (i.e., masking out water bodies and regions that are decorrelated, such as agricultural fields) and superscript T denotes matrix transpose. Only pixels that are coherent in most interferograms are used as input to the construction of C_d . The solution for this over-determined minimization problem can be written as

$$m_{est} = G^{-g} d \quad (6.1-5)$$

where

$$G^{-g} = [G^T C_d^{-1} G]^{-1} G^T C_d^{-1} \quad (6.1-6)$$

The full covariance on the estimated parameters, C_m , can be estimated from

$$C_m = G^{-g} C_d G^{-gT} \quad (6.1-7)$$

With this formulation, we can obtain GPS and InSAR velocity estimates and their formal uncertainties (including in areas where the expected answer is zero).

VALIDATION PROCEDURE FOR NISAR SOLID EARTH L2 REQUIREMENTS

Once displacement parameters are derived from GNSS ($m_{est,GNSS}$) and InSAR ($m_{est,InSAR}$) via equations (6.1-2) through (6.1-7), two complementary approaches (here referred to as A and B) can be used to validate the L2 requirements discussed in this document. Both approaches are needed to understand the limits of performance as completely as possible given existing limitations on resources and the distribution of GNSS networks.

A: GNSS-InSAR direct comparison: Here parameterized time series from InSAR and GNSS are compared, across the length scales described in the L2 requirements. Gradients of the relevant time series parameters (i.e., velocity, v) are calculated between all possible pairs of cGPS locations within a validation region, resulting in the vectors $\Delta m_{est,GNSS}$ and $\Delta m_{est,InSAR}$. For all these pairs, unpaired two-sample t-tests (Snedecor and Cochran, 1989) are performed to test the null hypothesis that the two estimates with their respective errors are from the same population. These tests are performed at the 95% confidence level.

B: InSAR residual analysis: Using only InSAR data, the residuals w are analyzed, calculated by subtracting the estimated displacement model $m_{est,InSAR}$ from the observations d ,

$$w = Gm_{est,InSAR} - d \quad (6.1-8)$$

Empirical structure functions, S_w , is calculated from the residuals w for a subsequent analysis of signal noise as a function of spatial scale. We define the semivariogram S as the variance of the difference between two points separated by distance r ,

$$S(r) = E \left[\left(f(x) - f(x-r) \right)^2 \right] \quad (6.1-9)$$

such that the covariance between two points corresponds to:

$$C_n(r) = \sigma^2 - \frac{S(r)}{2} \quad (6.1-10)$$

where σ^2 is the variance of the noise within the data set (Williams et al., 1998).

To calculate $C_n(r)$ for a residual (w), w is first detrended at the scale of the full imaging swath (~240 km) to meet the stationarity assumption inherent to covariance theory. To detrend, a linear plane is fitted and removed

from the data. Subsequently, the structure function S_w is calculated according to (Lohman & Simons, 2005)

$$S_{w,dx,dy} = \frac{1}{n_g} \sum_{k=dx}^{nx} \sum_{l=dy}^{ny} (w_{k,l} - w_{k-dx,l-dy})^2 \quad (6.1-11)$$

where $dx=[1:nx]$, $dy=[1:ny]$ are the sampling intervals of w in the two geographic directions, nx and ny are the maximum distances covered by the matrix w in x and y , and n_g is the number of valid values within the overlapping region at each shift (dx,dy) . n_g is not necessarily equivalent to nx times ny , due to water bodies and other regions that are decorrelated in most interferograms.

While, in general, noise in w is anisotropic, here we neglect this anisotropy and assume that the directional average of S_w versus distance is a good approximation of $C_n(r)$. Given S_w values at scales $L=[5,10,20,30,40,50]$ km are extracted from S_w and compared to the L2 requirements at these scales for validation.

6.1.3 Planned Output Products

NISAR L3 Solid Earth products will include:

- Maps of locations where the InSAR and GNSS data are being compared
- LOS displacement vs. time plots, showing:
 - InSAR time series using a standard SBAS approach (Berardino et al., 2002, Hooper, 2006)
 - The parameterized LSQ solution to the InSAR data
 - The corresponding time series of the LOS component of the GNSS time series
 - The corresponding LSQ solution to the LOS component of the GNSS time series
- Tables and/or figures of comparisons showing LSQ solutions and error estimates of velocities and offsets as a function of baseline length from both InSAR and GNSS observations.

6.2 ECOSYSTEMS PRODUCTS – BIOMASS

The NISAR L2 science requirement for above ground biomass (AGB) is expressed as:

The NISAR project shall measure above ground woody vegetation biomass annually at the hectare scale (1 ha) to an RMS accuracy of 20 Mg/ha for 80% of areas of biomass less than 100 Mg/ha.

Above ground biomass (AGB) is a fundamental parameter for characterizing the spatial distribution of carbon in the biosphere. Biomass is defined as the total mass of living matter within a given unit of environmental area and is of interest for a number of applications. It is the raw material of food, fiber, and fuelwood. It is important for soil, fire and water management. It is also related to the vegetation structure, which, in turn, influences biological diversity of the planet (Bergen et al., 2009; Saatchi et al., 2007; Froking et al., 2009). Biomass density (the quantity of biomass per unit area, or Mg, 10^6 grams of dry weight per ha) is used to determine the amount of carbon released to the atmosphere (as CO_2 , CO, and CH_4 through burning and decay) when ecosystems are disturbed and is a strong indicator of the ecosystem function in terms of carbon sequestration through photosynthesis and primary production. Above ground carbon density of woody vegetation is approximately 50% of the biomass with small variations depending on forest type and composition (IPCC, 2006). The current knowledge of the distribution and magnitude of terrestrial biomass is based almost entirely on ground measurements over an extremely small, and possibly biased sample, with almost no measurements in the southern hemisphere and equatorial regions (Schimel et al., 2015).

The NISAR mission's observing strategy is designed to provide sufficient coverage to estimate above ground woody vegetation biomass at a spatial resolution of 100 m (1 ha), over the lifetime of the mission. This will provide fine-grain products of carbon stocks and changes required for understanding and quantifying the global carbon cycle. An upper threshold of 100 Mg/ha is set to reflect the sensitivity of L-band backscatter measurements to biomass and allowing coverage of more than 50% of the global forests and the entire area of other woody vegetation (FRA, 2010). This sensitivity will allow NISAR to quantify the carbon stocks and changes of the most dynamic and variable component of global vegetation and to provide significant contribution to the global carbon cycle and climate science (Houghton et al., 2009; Saatchi et al., 2011; Harris et al., 2012).

6.2.1 Theoretical Basis of Algorithm

Because of its sensitivity to volume scattering and dielectric contrast Synthetic Aperture Radar (SAR) backscatter measurements are sensitive to vegetation AGB. SAR observations from a spaceborne platform can thus be used for mapping and monitoring AGB on a global scale. However, the SAR backscatter sensitivity to AGB varies depending on the wavelength and geometry of the radar measurements, and is influenced by the surface topography, structure of vegetation, and environmental conditions such as soil moisture and vegetation phenology or moisture. The NISAR algorithm will make use of high-resolution and time series backscatter observations at dual-polarizations (HH and HV) to estimate AGB by compensating for the effects of environmental changes (soil and vegetation moisture and phenology) and structure (vegetation and surface topography).

Radar observations from vegetation have been studied for more than four decades both theoretically and experimentally (Ulaby et al., 1984; Tsang et al., 1985; Ulaby and Dobson, 1989; Cloude, 2012). At L-band frequencies, these studies have shown that the radar

measurements at different polarizations depend strongly on the AGB but the relationship may vary depending on the structure and dielectric properties of vegetation components and underlying soil surface (Saatchi et al., 1994; Saatchi and McDonald, 1997; Ulaby et al., 1990). The soil is most commonly described as a homogeneous medium having a complex dielectric constant, ϵ , that is a function of the volumetric soil moisture, m_v , as well as the soil texture, temperature, and bulk density; several empirical models exist for this relationship (Dobson and Ulaby, 1986; Hallikainen et al., 1985; Mironov et al., 2004; Peplinski et al., 1995). Studies of soil surface scattering and soil moisture remote sensing at L-band have shown that the surface scattering can be expressed in terms of soil dielectric constant at the top 5 cm and the surface roughness characteristics in terms of RMS (Root Mean Square) roughness height and spatial correlation length (Fung et al., 1992). In most SAR-related models for the remote sensing of soil surfaces, it is assumed that the effect of the spatial correlation is reduced significantly during the SAR azimuthal processing and multi-looking, and that the sensitivity of the radar signature to soil surface RMS height variation remains as the dominant surface structure influencing the surface scattering (Oh et al., 1992; Shi et al., 1997; Dubois et al., 1995; Bagdadi et al., 2002; Bryant et al., 2007). Other landscape features such as directional row or tillage may impact radar cross sections at 100-m spatial resolution but are assumed irrelevant in natural vegetation such as forests and shrublands.

A variety of approaches exist for describing vegetation media, including characterization of vegetation structure such as stalks, trunks, and leaves in terms of canonical cylindrical or disk shapes with specified size and orientation distributions in a set of vegetation layers, and with dielectric constants similar to live wood of trees and leaf material (Saatchi et al., 1994; Saatchi and McDonald, 1997; Saatchi and Moghaddam, 2000; Yueh et al., 1992; Lang et al., 1983; Karam et al., 1992;

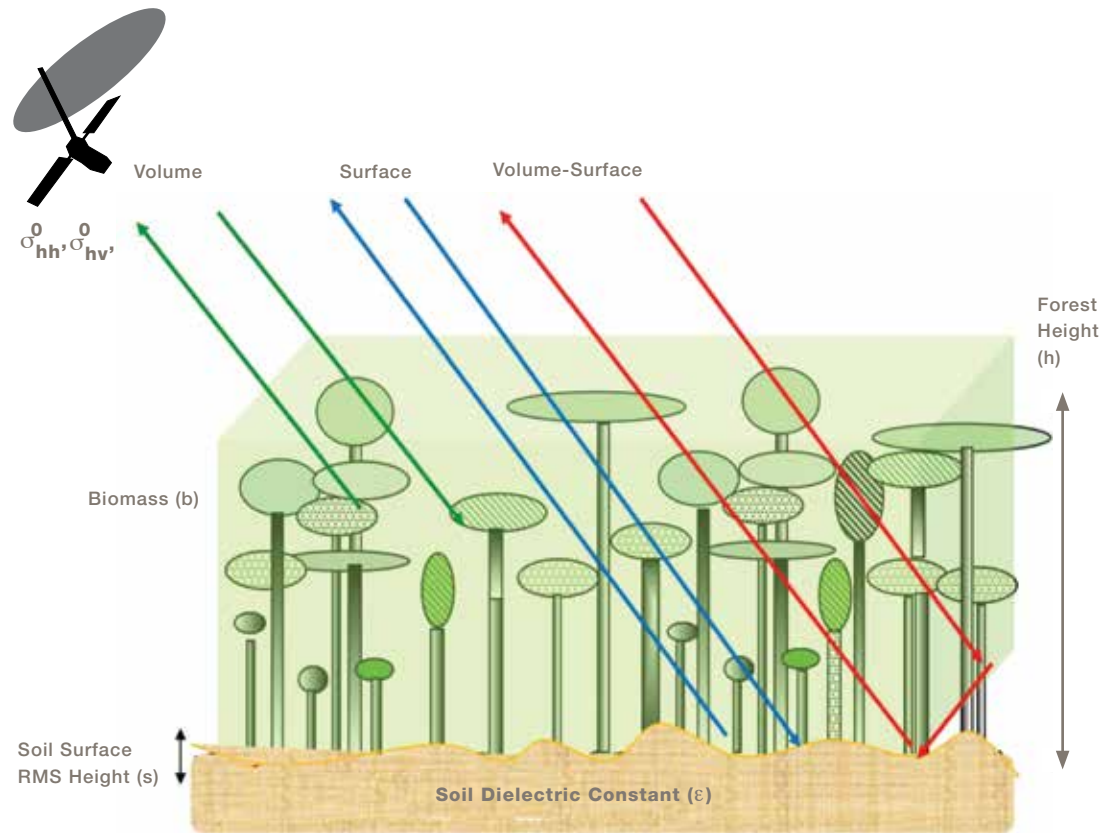


FIGURE 6-2

Dominant scattering mechanisms of L-band SAR measurements of forest ecosystems contributing to NISAR dual-pol backscatter observations.

Ulaby et al., 1990). The total L-band backscatter from vegetation arises from a combination of scattering and attenuation of individual canopy components (trunk, branch, and leaf) that can be represented as a sparse scattering medium (Lang, 1981; Chauhan et al., 1994). This approach requires knowledge of tree structure (size, orientation, and density; or equivalently species and biome), dielectric constant, and ground characteristics (RMS height, correlation length, and dielectric constant).

Simpler approaches only use the vegetation water content (VWC) to provide analytical forms for attenuation and scattering effects. The most common model used in microwave frequencies is the water cloud model that includes two scattering components from the vegetation volume and its underlying ground but ignores the

volume-ground interaction (Attema and Ulaby, 1978). Such models are mainly applicable for higher frequency (C-band and above) characterization of the vegetation backscatter (Matzler, 1994; Ulaby and El-rayes, 1987). In this work, and for the fuller scattering model, the backscattering coefficient is expressed as the combination of three scattering components (Figure 6-2). These are: 1) volume (vol) scattering, 2) volume and surface interaction (vol-surf) and 3) surface scattering (surf):

$$\sigma_{pq}^0 = \sigma_{pq-vol}^0 + \sigma_{pq-vol-surf}^0 + \sigma_{pq-surf}^0 \quad (6.2-1)$$

where p and q denote polarization of transmitted and received radar signals, respectively. These can be either vertical (v) or horizontal (h) in a linear polarization radar system. The three dominant scattering terms are

derived from basic electromagnetic theory by solving Maxwell's equations in a discrete random media (Saatchi and Lang, 1989; Lang, 1981; Tsang et al., 1985; Saatchi and McDonald, 1997; Chauhan et al., 1991).

These terms can be expressed in a closed and semi-empirical form as:

$$\sigma_{pq-vol}^0 = A_{pq} b^{\alpha_{pq}} \cos \theta \left[1 - \exp \left(-\frac{B_{pq} b^{\beta_{pq}}}{\cos \theta} \right) \right] \quad (6.2-2)$$

$$\sigma_{pq-vol-surf}^0 = C_{pq} \Gamma_{pq}(\epsilon, s) b^{\gamma_{pq}} \exp \left(-\frac{B_{pq} b^{\beta_{pq}}}{\cos \theta} \right) \quad (6.2-3)$$

$$\sigma_{pq-surf}^0 = S_{pq}(\epsilon, s) \exp \left(-\frac{B_{pq} b^{\beta_{pq}}}{\cos \theta} \right) \quad (6.2-4)$$

where $S_{pq}(\epsilon, s)$ is the scattering from rough soil surface and can be represented by the semi-empirical model of Oh et al. (1992). The surface reflectivity $\epsilon_{pq}(\epsilon, s)$ in the vol-surf backscatter is given by:

$$\Gamma_{pq} = |R_p(\epsilon) R_q^*(\epsilon)| \exp(-k^2 s^2 \cos^2 \theta) \quad (6.2-5)$$

where $R_p(\epsilon)$ is the Fresnel reflection coefficient of semi-infinite soil medium at polarization p with the dielectric constant of ϵ and $\exp(-k^2 s^2 \cos^2 \theta)$ represents the Kirchhoff's damping factor associated with the RMS height (s) of the surface (Fung et al., 1981), k is the wavenumber, θ is the local incidence angle, and b is the above ground biomass density in the unit of Mg ha^{-1} . The Fresnel reflection coefficients in terms of complex dielectric constant (ϵ) are:

$$\begin{aligned} R_H &= \frac{\cos \theta - \sqrt{\epsilon - \sin^2 \theta}}{\cos \theta + \sqrt{\epsilon - \sin^2 \theta}} \\ R_V &= \frac{\epsilon \cos \theta - \sqrt{\epsilon - \sin^2 \theta}}{\epsilon \cos \theta + \sqrt{\epsilon - \sin^2 \theta}} \end{aligned} \quad (6.2-6)$$

For the scattering from the rough soil surface $S_{pq}(\epsilon, s)$, there are several models that can be adopted at the L-band frequency. The semi-empirical model developed by Oh et al. (1992) is used in the NISAR algorithm. This

model is derived from a set of radar polarimetric measurements at multiple frequencies (L-, C-, and X-bands) and incidence angles (10° – 70°) over rough soil surface with a variety of moisture (dielectric constants) and roughness (RMS height). The model provides good agreements with radar backscatter measurements in the field at L-band frequency and can be summarized as:

$$\begin{aligned} S_{HH} &= g \sqrt{v} \cos^3 \theta \left(|R_H|^2 + |R_V|^2 \right) \\ S_{VV} &= \frac{g}{\sqrt{v}} \cos^3 \theta \left(|R_H|^2 + |R_V|^2 \right) \\ S_{HV} &= u S_{VV} \end{aligned} \quad (6.2-7)$$

where

$$g = 0.7 \left[1 - \exp(-0.65(ks)^{1.8}) \right], \quad u = 0.23 \sqrt{\Gamma_0} \left[1 - \exp(-ks) \right],$$

$$v = 1 - \left(\frac{2\theta}{\pi} \right)^{\frac{1}{3\Gamma_0}} \exp(-ks), \quad \text{and } \Gamma_0 = \frac{1 - \sqrt{\epsilon}}{1 + \sqrt{\epsilon}}$$

is the Fresnel reflectivity of the surface at nadir.

The above model is used because it provides a simple expression as a function of soil dielectric constant and the surface RMS height. Other rough surface scattering models can also be used. Some examples are the Integral Equation Method (IEM) model, small perturbation method and Kirchhoff approximation. These models have been compared and tested over study sites with detailed ground measurements to suggest that 1) the contribution from rough surface scattering is comparatively smaller than the volume and volume-surface contributions, particularly in the forested environments (therefore, the residual effects of the uncertainty of surface scattering characterization is small), 2) the Oh et al. (1992) model is preferred over other models because of its simplicity (based only on two parameters) and its direct link to backscattering coefficients of the soil dielectric constant instead of soil moisture, and 3) other models such as the small perturbation method have no cross polarized (HV) term and underestimate the measurements of radar backscatter over bare soil surfaces.

This model above is characterized by a set of coefficients (A_{pq} , B_{pq} , C_{pq} and α_{pq} , β_{pq} , δ_v) that depend on the polarization of the observation but are independent of the vegetation aboveground biomass (b), and soil dielectric constant (ϵ) and surface roughness (s). These coefficients represent weighting factors for scattering and attenuation of vegetation through its various components (trunks, branches, leaves) that depend on their orientation and configurations (arrangements) within the forest canopy. The semi-empirical model separates the ground and vegetation parameters. The vegetation parameters are all combined into aboveground biomass (b) and ground parameters represented by surface dielectric constant (soil moisture) and roughness.

As discussed earlier, the algorithm model coefficients α_{pq} , β_{pq} , and δ_v are considered the allometric or structure-related parameters and depend on only the orientation or arrangement of scatterers in the vegetation but are independent of biomass. Similarly, A_{pq} , B_{pq} and C_{pq} are considered the radiometric coefficients of the algorithm that depend on the radiometric correction of radar due to the terrain correction and heterogeneity of vegetation structure.

In the volume term, $A_{pq} b^{\alpha_{pq}}$ and $B_{pq} b^{\beta_{pq}}$ control the relationship between biomass and the backscatter power of and the attenuation respectively. These terms are represented in the form of a power-law derived from a series of allometric models combining size, growth rate, and their metabolic characteristics (Sarabandi and Lin, 2000; Enquist et al., 2009; Smith and Heath, 2002). The model parameters α_{pq} and β_{pq} are independent of vegetation biomass and depend on geometry of tree canopies in terms of size and orientation of trunks, branches, and leaves and may vary depending on the vegetation type. The volume surface interaction term $C_{pq} b^{\gamma_{pq}}$ represents the strength of the specular reflection and includes the scattering from both trunk and crown layers reflected from ground surface. Similarly,

the coefficients A_{pq} , B_{pq} , C_{pq} also depend on the forest structure and the SAR backscatter radiometric calibration (e.g., terrain correction) but are independent of aboveground biomass. The model therefore, has three unknown biophysical variables (b , ϵ , s), and six polarization dependent coefficients (A_{pq} , B_{pq} , C_{pq} and α_{pq} , β_{pq} , δ_v) that must be determined for different forest types.

The overall sensitivity of the model at the L-band frequency is shown in terms of the biomass by using data from SAR measurements from the ALOS PALSAR satellite and model simulations (Figure 6-3). The sensitivity of backscatter measurements to AGB depends on the wavelength, with longer wavelengths allowing better penetration of the microwave signal into the canopy and scattering from the tree trunks that contain most of the tree biomass. At shorter wavelengths, the attenuation of the signal limits the penetration and reduces the effect of the scattering from tree components causing a loss of sensitivity to biomass at some threshold AGB. At the NISAR L-band frequency (~24-cm wavelength), the biomass sensitivity threshold also depends on the vegetation structure (configuration and size of scattering elements), the dielectric constant (water content in the vegetation components), soil moisture, topography and surface roughness. It has been established that the upper limit of L-band radar sensitivity to biomass is approximately 100 Mg/ha (Mitchard et al., 2009; Robinson et al., 2013; Saatchi et al., 2007; Saatchi et al., 2011; Mermoz et al., 2015). In regions with forest biomass > 100 Mg/ha, it is considered best to use other sensors such as ESA's P-band SAR mission named BIOMASS (Le Toan et al., 2011), and/or a combination of SAR interferometry and backscatter at L-band, and lidar sensors, such as will be available from NASA's GEDI mission (Saatchi et al., 2011; Shugart et al., 2011; Hall et al., 2011).

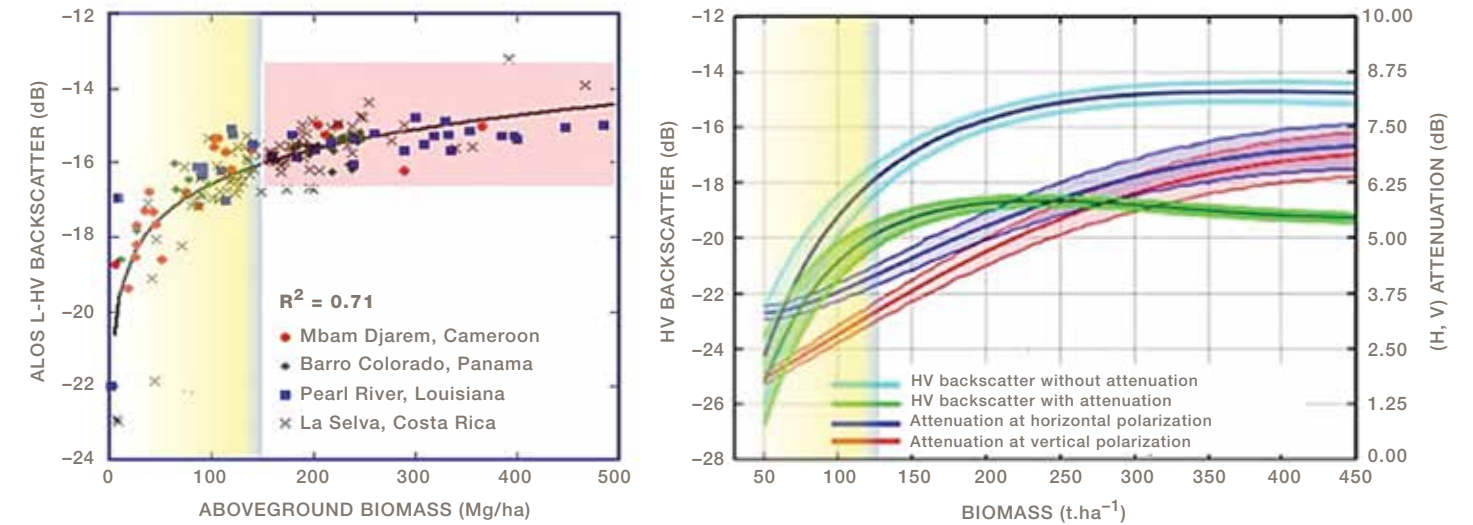


FIGURE 6-3

Sensitivity of L-band HV backscatter to vegetation biomass. Both ALOS PALSAR satellite L-band observations (left) and model simulations (right) show the effect of vegetation attenuation on the radar saturation level.

Based on the empirical/theoretical experience outlined above, NISAR will generate biomass estimates of woody vegetation up to 100 Mg/ha using high-resolution multi-temporal NISAR L-band SAR backscatter imagery, and the above semi-empirical algorithmic model (Saatchi and Moghaddam, 2000; Hensley et al., 2014). The target area of the NISAR biomass product will be all forests and shrublands across different ecoregions, distributed globally (Figure 6-4). Even in regions where forest biomass is larger than 100 Mg/ha, there are significant areas with degraded or naturally heterogeneous vegetation that the biomass may remain below the NISAR sensitivity limit. The low biomass regions are considered among the most dynamic regions due to various management and human land use activities, or frequency of natural disturbance such as drought, fire, and storms.

The semi-empirical algorithm has several advantages over fully empirical regression models. These advantages are:

1. The model is physically based and captures the behavior of radar measurements over complex vegetation structures.
2. The model includes surface moisture variables as the key variable impacting the temporal observations of radar backscatter.

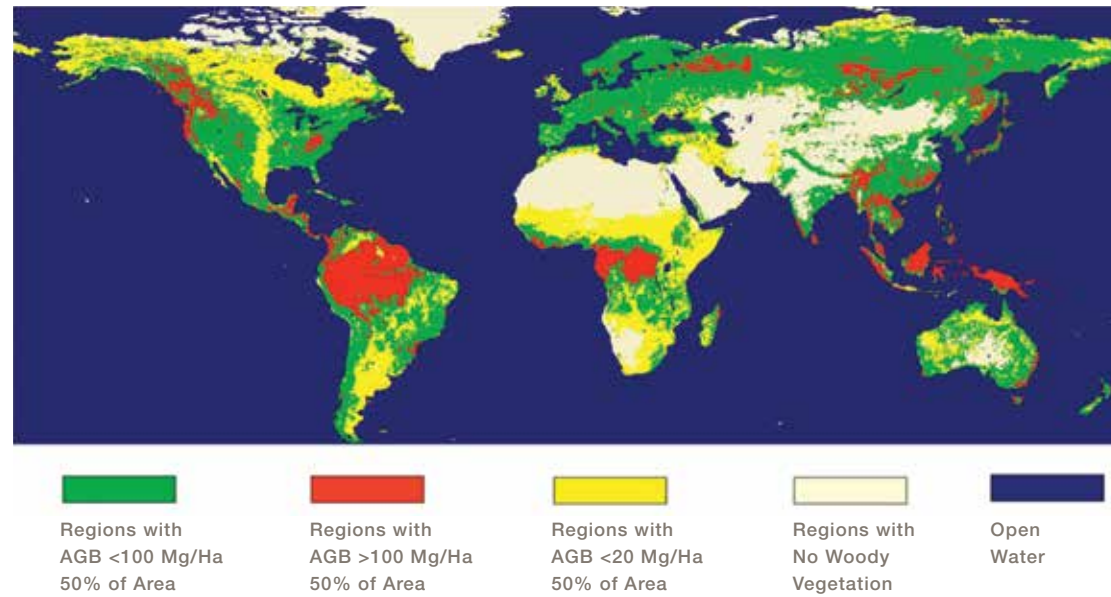
3. The model has a simple analytical formulation allowing sensitivity analysis and error propagation (Hensley et al., 2010).

All vegetation and biome (i.e., coniferous, deciduous, mixed, tropical evergreen, and shrubland savanna as shown in Figure 6-5) specific structural and calibration coefficients of the model will be derived for the NISAR mission.

To use the semi-empirical model as an algorithm to estimate the forest or vegetation AGB requires a priori quantification of the model coefficients for different forest types and the number of observations to account for the soil moisture (ϵ) and surface roughness (s) variations. To meet this challenge, the model must be developed through a process of calibration and validation (CAL/VAL) approach over different forest types or ecoregions before the launch of the NISAR. The model coefficients are quantified over a series of study sites (CAL/VAL sites) that includes ground measurements of vegetation structure, and airborne or satellite L-band observations that can simulate the NISAR observations (see Section 8.0 for ecosystem CAL/VAL plan).

FIGURE 6-4

Global distribution of above ground biomass. Map is stratified in categories to demonstrate areas in green and yellow where NISAR above ground biomass products will be of low uncertainty.



6.2.2 Implementation Approach for Algorithm

During the pre-launch CAL/VAL activities, the science team determines the initialization of the algorithm and evaluates its performance to meet the science requirements. The algorithm depends on a number of model coefficients that are expected to vary as a function of biome and be subjected to a natural variability of observed radar backscatter with changes in soil moisture and season. The following describes the approach that is used for determining these model parameters.

QUANTIFICATION OF MODEL COEFFICIENTS α_{pq} , β_{pq} , AND δ_γ

The model coefficients related to vegetation structure can be determined in two steps:

1. A three-dimensional forward scattering model (Saatchi and McDonald, 1997; Saatchi and Moghaddam, 2000) has been used over the key CAL/VAL study sites with ground measurements of tree structure to fit a power law function to the scattering and attenuation terms of the scattering model to vegetation biomass. The coefficients are

the exponents of the model fits and are used as initial conditions in retrieving these coefficients over CAL/VAL study sites in step 2.

2. It is assumed that the structural parameters of the algorithm will remain fixed and will not change spatially or temporally within each ecoregion and during the NISAR time series observation. To determine α_{pq} , β_{pq} , and δ_γ for different ecoregions and for two polarizations of HH and HV, the CAL/VAL study sites within each ecoregion will be used. At these sites, multi-temporal (3-5 images capturing seasonal variations) radar backscatter measurements, ground vegetation biomass, soil moisture and surface roughness measurements are available or estimated from radar measurements directly over bare surfaces within the study site. The coefficients are determined using the Levenberg-Marquardt Approach (LMA) for non-linear least square estimation (Marquardt, 2009). The method is used in many software applications for solving generic curve-fitting problems and has already been applied in several SAR estimation approaches (Truong-Loi et al., 2015).

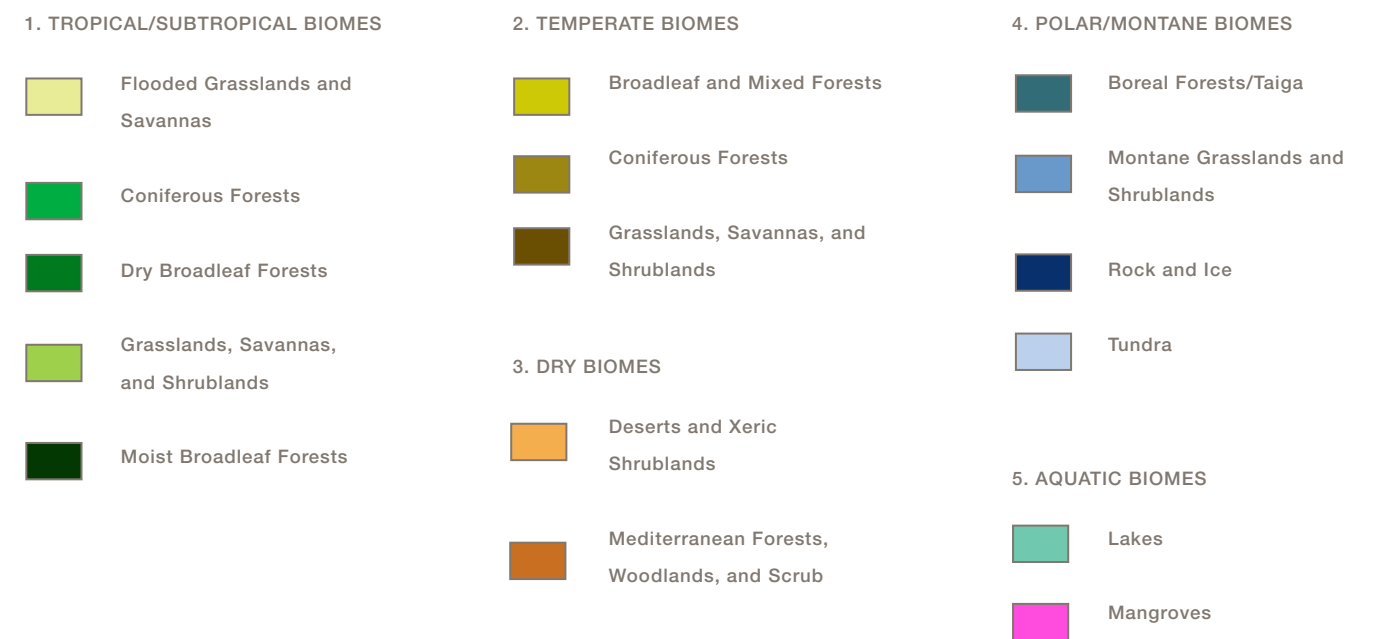
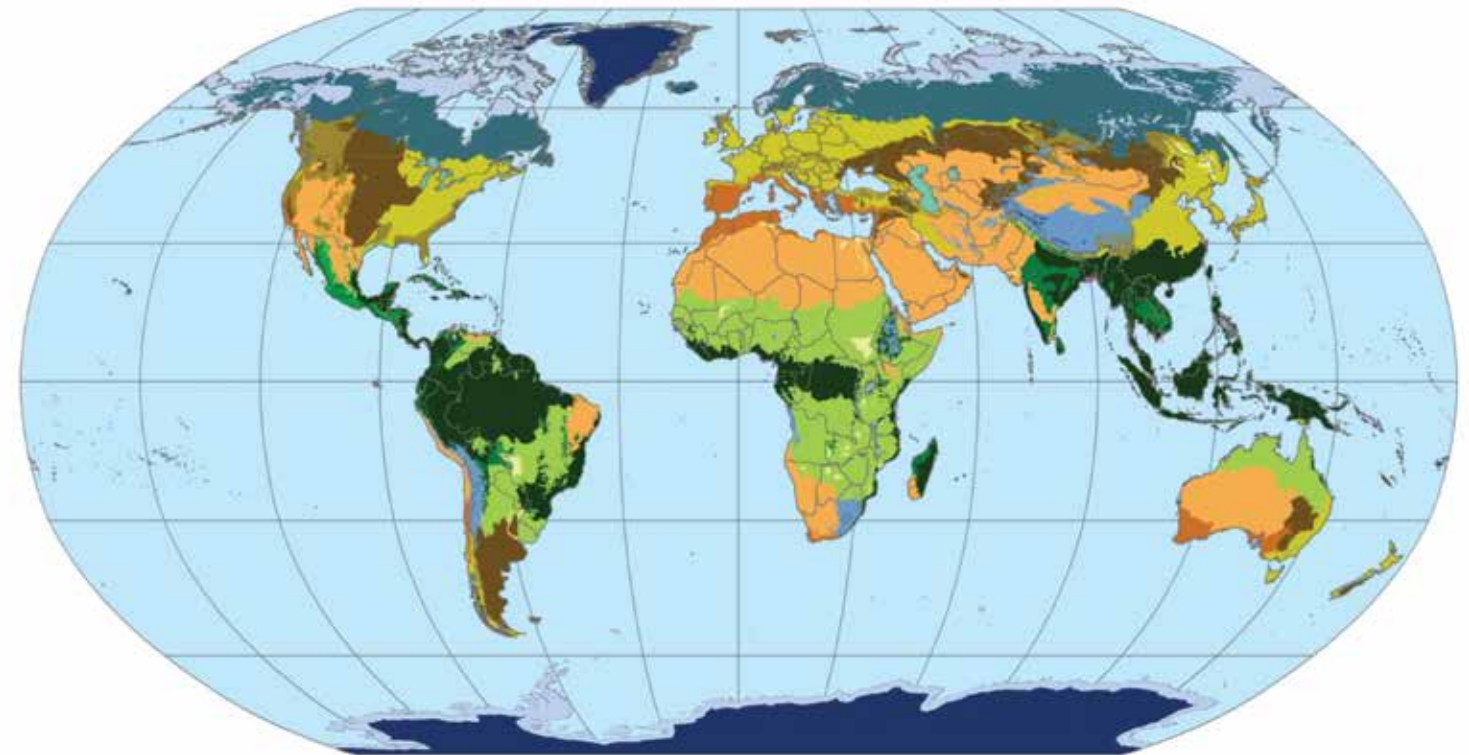


FIGURE 6-5

Distribution of global ecoregions and biomes for the development of the vegetation biomass algorithm. The ecoregions are derived from a combination of climate, topography, soil and vegetation data (Olson et al., 2001). The focus of the CAL/VAL plan and algorithm development would be on biomes that have distinct differences in the model.

- If the soil moisture and roughness data are not available from ground measurements in the CAL/VAL study area, these variables are estimated from areas of low vegetation or bare fields within the study area or the SAR image scene. A crude low vegetation or non-forest mask is generated for the time series data stack. This mask is obtained by thresholding the HV SAR image scene available over the CAL/VAL site. A threshold of -13 dB has been used to generate such a forest mask on ALOS-1 and -2 data sets by JAXA. By assuming $\sigma_{HV}^0 > forest_threshold$, the non-forest or low-vegetation areas are separated. A similar approach is used in the NISAR algorithm for disturbance and will be the same for both algorithms. Once the mask is developed, the soil dielectric constant and RMS height of the surface roughness are determined by inverting the Oh et al., (1992) model described above in equation 6.2-7. These values are used as the initial condition of the estimation of the structural variables for all areas considered forest or vegetation using a nearest neighbor interpolation approach (Truong-Loi et al., 2015).
- For cases where α_{pq} , β_{pq} and γ_{pq} cannot be estimated unambiguously using the LMA curve-fitting or estimation approach, the theoretical values derived from the forward model simulations and power-law model fits will be used. Estimates of coefficients related to vegetation structure will also include uncertainty associated with the LMA least-squared approach. The uncertainty can be used within a Bayesian approach to account for uncertainty in the algorithm and estimation of the biomass.

QUANTIFICATION OF MODEL COEFFICIENTS A_{pq} , B_{pq} , C_{pq}

The radiometric coefficients of the algorithm can be determined simultaneously with those related to vege-

tation structure. The estimation of these coefficients is based on the following assumptions:

- Coefficients A_{pq} , B_{pq} , C_{pq} are assumed to vary temporally due to changes in vegetation water content and phenology. This assumption can be verified over different ecoregions to relax the temporal variations to monthly or seasonal.
- The radiometric coefficients are assumed to remain constant spatially within a local moving window (3x3 or larger) to allow for spatial stability of the algorithm. This assumption depends on the spatial heterogeneity of vegetation structure (e.g., canopy gaps) that influences the magnitude of volume and volume-surface interactions.
- The coefficients can be determined over CAL/VAL study sites where biomass, soil moisture and roughness are available or determined as discussed in 6.2.1 to allow for testing the validity of moving window size for each vegetation type or ecoregion. Using a minimum of 3x3 moving window will allow the algorithm to have different coefficients for each local area. The alternative approach is to use A_{pq} , B_{pq} , C_{pq} derived over the CAL/VAL sites within each ecoregion as the fixed coefficients for the entire ecoregion as shown in Table 6.2 for the five dominant ecoregions globally.

PRE-LAUNCH CALIBRATION OF MODEL COEFFICIENTS

The pre-launch calibration of the algorithm model will apply to the structural coefficients, α_{pq} , β_{pq} and γ_{pq} that remain constant for each ecoregion globally throughout the NISAR mission. Using ALOS PALSAR or UAVSAR data that simulates the NISAR observations can be used to estimate these coefficients. The requirement for pre-launch calibration is the selection of the study sites that represent the variability in structure of the dominant vegetation types.

POST-LAUNCH CALIBRATION OF MODEL COEFFICIENTS

The post-launch calibration is mainly focused on assessing the assumption of spatial heterogeneity as observed by NISAR large incidence angle variations and therefore larger topographical variations.

APPLICATION OF THE BIOMASS ALGORITHM TO THE NISAR TIME SERIES IMAGE STACK

The AGB (b), soil dielectric constant (ϵ) and roughness (s) are estimated from dual-pol (σ_{HH}^0 and σ_{HV}^0) mea-

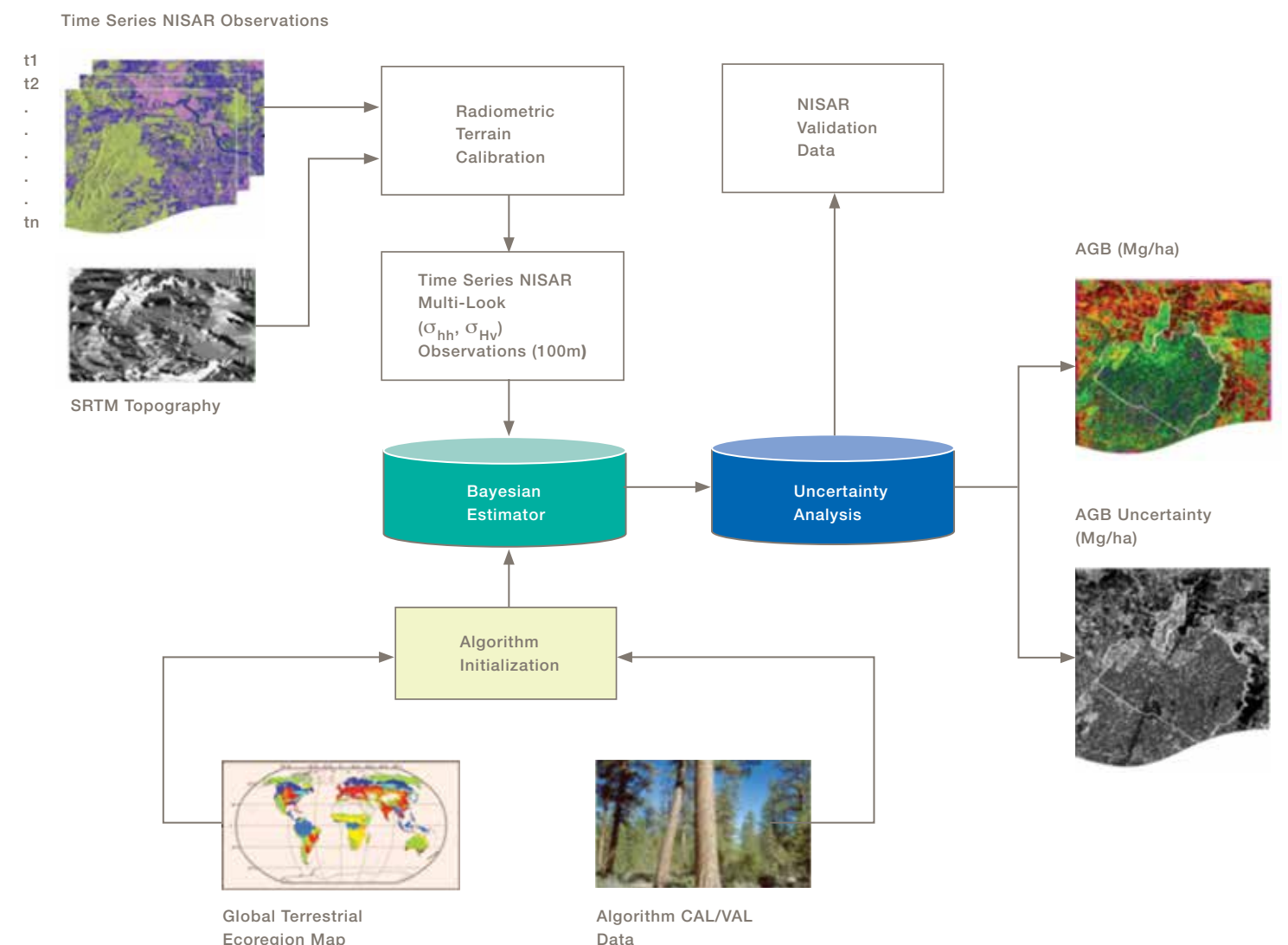
surements. The algorithm, shown in Figure 6-6, uses a Bayesian approach to estimate AGB. The estimation approach enables the use of multi-temporal backscatter measurements to quantify all variables while accounting for measurement uncertainty.

The implementation includes the following steps:

- The time series (t_1, t_2, \dots, t_n) of radiometric terrain corrected (RTC) HH and HV polarized images are fed into the algorithm as they become available from the NISAR processor. NISAR dual-pol observations are collected for NISAR ecosystem science

FIGURE 6-6

Flowchart showing the implementation of the NISAR algorithm for AGB estimation globally.



- in the background land mode every 12 days on descending orbits and every other on ascending orbits. There are approximately 45 observations per year.
2. Use t_1 data at HV polarization and a simple threshold to develop a mask of forest/non-forest over the entire NISAR image scene. This threshold is initially set to -13 dB (as derived from ALOS PALSAR data). It will be adjusted, as necessary, when NISAR data become available.
 3. Use the Oh et al. (1992) model to estimate soil dielectric constant and roughness for all non-forest pixels identified by the mask. Use the estimates of (ϵ_0, s_0) as the initial conditions for all pixels in the NISAR image by using a nearest neighbor interpolation of a simple kriging approach. The interpolation provides initial conditions and bounds for all pixels with forests or vegetation cover that will be used in the NISAR biomass retrieval algorithm.
 4. Use a simple model based on HH and HV polarization, derived from ALOS PALSAR data, and adjusted with local incidence angle (Yu and Saatchi, 2016) to estimate forest biomass (b_0) for all forest and non-forest pixels in the NISAR image scene. Use b_0 and its distribution as the initial condition and the bounds for the biomass for the retrieval algorithm.
 5. Include the NISAR HH, HV as the measurements data and the initial conditions (b_0, ϵ_0, s_0) , and the joint probability distributions as the a priori information in the NISAR Bayesian-based retrieval algorithm.
 6. For ecosystems with a strong phenological signature in the L-band radar cross section, the algorithm uses a global land cover or ecoregion map to set the geographically and temporally appropriate coefficients for the inversion algorithm.
 7. The algorithm will provide the first estimates of the biophysical variables (b_1, ϵ_1, s_1) from the first NISAR image along with the uncertainty of the estimates.
 8. When the NISAR image t_2 becomes available, repeat step 2 to develop a new forest/non-forest mask. Compare the mask derived from t_1 with the mask from t_2 . Develop a new mask to update the forest/non-forest mask by adding the non-forest pixels.
 9. Repeat steps 3 and 4 for all new non-forest pixels.
 10. Update (b_1, ϵ_1, s_1) maps with the all new forest/non-forest pixels.
 11. Repeat steps 5 and 6 by using the updated values for (b_1, ϵ_1, s_1) as the new a priori information in the NISAR retrieval algorithm and produce (b_2, ϵ_2, s_2) and the uncertainty.
 12. If no more NISAR imagery is available, iterate steps 9 and 10 by using the average of b_1 and b_2 as the new *a priori* information for b and the average of s_1 and s_2 as the new a priori information for s . This step is designed to make sure that the biomass and roughness remain constant for the NISAR observations, while soil dielectric constant is updated. The iteration will continue to provide stable values of (b_2, ϵ_2, s_2) and improved estimates of the uncertainty.
 13. If more NISAR imagery is available, repeat steps 7 to 11.
 14. If a disturbance has been detected using the disturbance algorithm during the time series analysis, reset the all three variables for the pixel by repeating steps 2 to 4.
 15. Forest biomass growth can be detected during the algorithm retrieval from the time series NISAR data if a significant trend is observed in biomass estimation after implementing step 10. The time series estimates of the biomass, b , can be used to study or report the trend in biomass from the first NISAR imagery.

16. Annually, the updated biomass values will be reported as a map with 100 m \times 100 m (1 ha) spatial grid cells globally. However, the algorithm will provide estimates of all three variables, and the uncertainty, every time the RTC NISAR images become available throughout the year.
17. The algorithm assumes that during a one-year period of multi-temporal observations, the soil dielectric constant will vary, while AGB and roughness, s , are treated as constant except in cases of land cover change (e.g., deforestation or disturbance; see forest disturbance product description).
18. The algorithm performance using the Bayesian approach is evaluated at 100-m spatial resolution products for all areas with AGB > 0. All areas with AGB > 100 Mg/ha will be identified and aggregated into one class, and areas with AGB = 0 will be another class.

By following this method, the algorithmic model is used to estimate AGB from radar backscatter observations. The effects of other variables associated with soil moisture and surface roughness on the radar backscatter measurements are also taken into account. Currently, the algorithm is calibrated over different ecoregions using the CAL/VAL data. Locations of forests used to derive parameters used by the algorithm, as developed over five key forest and woodland biomes is given in Table 6-1. Parameters are given in Table 6-2. A general flowchart, describing the current algorithm implementation is shown in Figure 6-6. The number of ecoregions that require separate algorithms will be finalized later after performing the algorithm CAL/VAL activities across the global ecoregions.

IDENTIFICATION OF BIOMASS DISTURBANCE

The implementation of the biomass algorithm using the time series stack of dual-pol NISAR imagery requires the detection of disturbance to reset the biomass

values at the pixel level. The detection of disturbance can be the simple band threshold as determined for the forest/non-forest mask or the use of disturbance algorithm. Here, a similar approach as in the disturbance algorithm will be implemented to report the vegetation biomass before the disturbance and detection of the post-disturbance accumulation of the biomass.

6.2.3 Planned Output Products

The L2 above ground biomass product is a raster image at 100-m spatial resolution produced over the CAL/VAL sites. The raster product is in one-byte format with pixel values representing AGB as an integer number from 0 to 100 Mg/ha, and a fixed value for biomass greater than 100 Mg/ha. The product will be generated every year using observations collected during the year. The input product is multi-look L2, 25 m, radiometrically terrain-corrected imagery. Also required for generating the biomass products are ancillary data of a global land ecoregion map to select the algorithm coefficients, surface digital elevation model to improve the inversion model with local incidence angle, a soil moisture map (derived from SMAP or SMOS) and in situ and lidar data for calibration and validation of the model. The Bayesian methodology will also provide uncertainty estimates at the pixel level. Initial values for surface roughness, s , are obtained for the CAL/VAL sites during pre-launch activities and determined post-launch by the closest CAL/VAL site within the same ecoregion.

6.3 ECOSYSTEMS PRODUCTS – DISTURBANCE

The NISAR L2 science requirement for above ground biomass (AGB) is expressed as:

The NISAR project shall measure global areas of vegetation disturbance at 1 hectare resolution annually for areas losing at least 50% canopy cover with a classification accuracy of 80%.

TABLE 6-1. STUDY SITES USED TO DEVELOP REPRESENTATIVE MODELS FOR GLOBAL ESTIMATION OF BIOMASS

FOREST TYPE	RADAR OBSERVATION	LOCATION	DATE	IN SITU DATA	REFERENCE
Needleleaf	AIRSAR	Boreal Forest of Canada	1993–1996	18 Sites, 64 plots	Saatchi and Moghaddam, 2000
Broadleaf Deciduous	UAVSAR	Howland Forest, Maine, USA	2009–2010	32 1-ha plots Lidar data	Robinson et al., 2013
Mixed broad-leaf/Needle Leaf	AIRSAR/ UAVSAR	Maine, Duke, Harvard, etc.	2004/2009	78 plots/Lidar data	Robinson et al., 2013
Broadleaf Evergreen	AIRSAR/ UAVSAR/ ALOS PALSAR	Sites distributed in Costa Rica, Peru, Gabon	2004–2015	Combined plots/Lidar data	Saatchi et al., 2011
Savanna/ Dry Forest	ALOS/ PALSAR	Uganda/ Cameroon/ Mozambique/ Gabon	2007–Present	160 plots 0.4–1.0 ha	Mitchard et al., 2009

TABLE 6-2. MODEL PARAMETERS DERIVED FOR DIFFERENT VEGETATION TYPES DURING THE NISAR PHASE A STUDY OVER EXISTING CAL/VAL SITES

MODEL PARAMETERS	BROADLEAF EVERGREEN	BROADLEAF DECIDUOUS	NEEDLELEAF	MIXED BROADLEAF & NEEDLELEAF	DRY FOREST WOODLAND SAVANNA
A_{HH}	0.229	0.241	0.189	0.211	0.11
A_{HV}	0.0867	0.0683	0.013	0.0365	0.03
B_{HH}	0.0108	0.0944	0.00211	0.0789	0.00908
B_{HV}	0.0148	0.0165	0.00195	0.0855	0.012
C_{HH}	0.005	0.008	0.0076	0.0083	0.009
C_{HV}	0.002	0.0062	0.0047	0.0053	0.007
α_{HH}	1.1	1.1	0.19	0.96	0.20
α_{HV}	0.2	0.3	0.11	0.27	0.18
β_{HH}	1.1	1.1	0.89	0.96	1.0
β_{HV}	1.1	1.0	0.9	0.89	1.0
γ_{HH}	1.1	1.1	0.89	0.96	1.3
γ_{HV}	0.5	0.9	0.23	0.27	1.1

Accurate annual measurements of the global area of forest disturbance from NISAR will be a significant contribution to the global accounting of carbon emissions from land cover change (van der Werf et al., 2009). The NISAR disturbance product complements the NISAR biomass, inundation, and active agricultural area products to jointly improve our understanding of carbon emissions from land cover change and the success of mitigation strategies like avoided deforestation. As such, the disturbance product from NISAR will constitute an invaluable contribution to the accounting needs for the United Nations negotiated policy mechanism for Reducing Emissions from Deforestation and Forest Degradation (REDD) as well as emerging bi- and multi-lateral carbon treaties involving forest carbon accounting (Romijn et al., 2012; Baker et al., 2010). To date, forest carbon accounting with remote sensing methods has made significant progress and international efforts by the Committee on Earth Observing Systems (CEOS) and the GEO Global Forest Observing Initiative (GFOI) strive to improve national efforts on Forest carbon Monitoring, Reporting and Verification (MRV, GFOI, 2013). As cloud-cover is a major impediment to reliably acquiring high-spatial resolution annual data sets with optical sensors over tropical, sub-tropical and boreal regions, SAR observations have emerged as a critical complement (Walker et al., 2010; Kellndorfer et al., 2014; Reiche et al., 2016). Achieving reliable and timely accounting of forest disturbance globally at consistent annual or even sub-annual intervals will improve our scientific understanding of global carbon emission dynamics from forests, both from natural and anthropogenic disturbances.

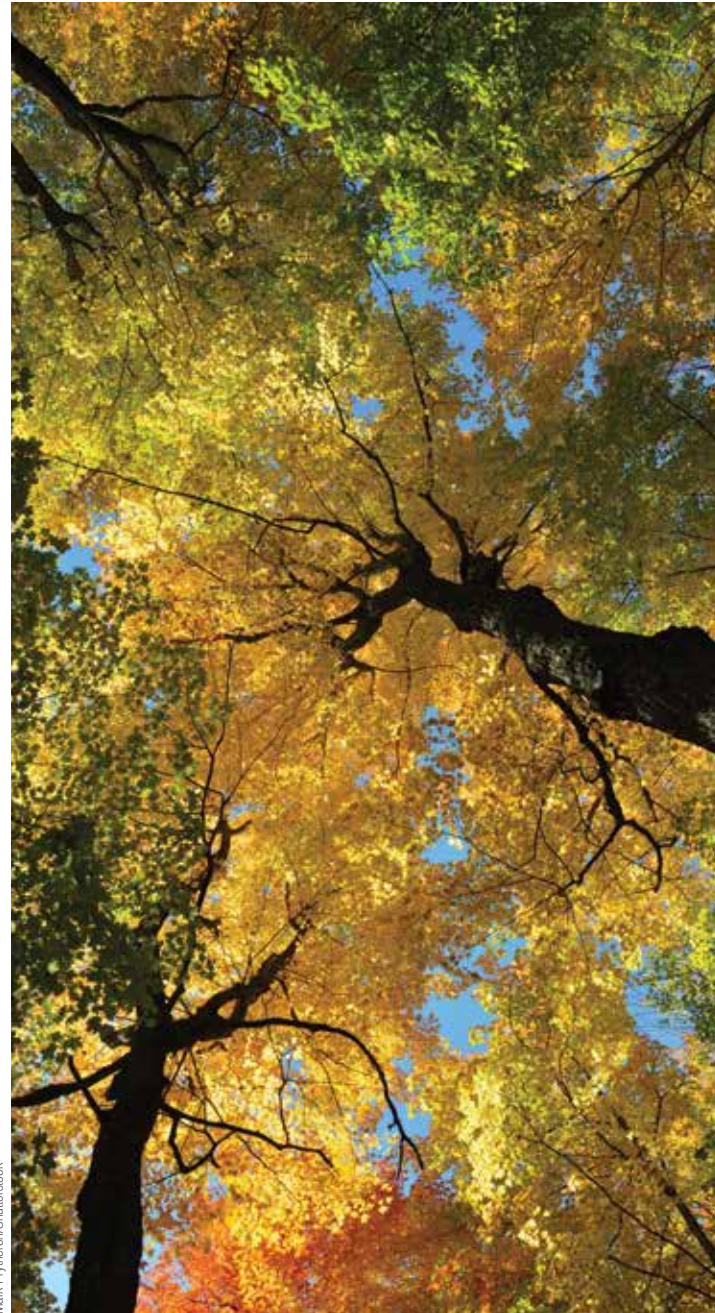
6.3.1 Theoretical Basis of Algorithm

The NISAR L2 science requirement for forest disturbance is expressed as:

The NISAR project shall measure global areas of vegetation disturbance at 1 hectare resolution annually for areas losing at least 50% canopy cover with a classification accuracy of 80%.

The NISAR disturbance detection algorithm is based on time series analysis techniques of observed NISAR L-band calibrated backscatter measurements, foremost using cross-polarized observations (L-HV). At its core, the algorithm is comparing backscatter from a set of two time series of equal observation length from subsequent years. Annual observation time series may be temporally segmented (e.g., freeze/thaw, wet/dry season observations only), determined spatially based on the observational data to account for ecosystem specific seasonality (see Figure 6-5). A simple, yet robust approach for detecting disturbance in these time series of backscatter images is based on change point detection with cumulative sums analysis which have been employed in many sectors such as statistical control, financial trends and meteorological analysis. During the NISAR mission, time series-based cumulative sums are calculated for each 25 m pixel, either from the full year observation period, or from seasonally segmented subsets, which is adequate in complex biomes like the boreal region with strong seasonality.

The corresponding cumulative sum curves from a full year of data initialize the algorithm. Subsequent observations will be classified based on threshold criteria to identify timing of change detected. Backscatter means before and after the detected change points are calculated. Thresholds are established from backscatter-canopy density curves which are established after year one of the mission. Backscatter change for 50% canopy density change can thus be determined. The backscatter-canopy density curves are generated on a per-scene basis based on ancillary canopy density observations from global MODIS or Landsat products and can further be stratified by unsupervised clustering of the NISAR time series data set. With this approach, ecosystem specific variations on backscatter-canopy density relationships are accounted for. If within a 100 × 100 m resolution cell, 8 or more pixels are flagged as disturbed, either from the entire time series or seasonal subsets of the time series, the entire cell is flagged as disturbed.



Mark Ppyfench/Shutterstock

THE NISAR PROJECT SHALL MEASURE GLOBAL AREAS OF VEGETATION DISTURBANCE AT 1 HECTARE RESOLUTION ANNUALLY FOR AREAS LOSING AT LEAST 50% CANOPY COVER WITH A CLASSIFICATION ACCURACY OF 80%.

The NISAR measurement metric for disturbance determination relies on the measurement of cross-polarized L-band backscatter change with forest fractional canopy cover loss of 50% or more as observed and compared over annual timeframes. At its core, L-band cross-polarized backscatter exhibits a significant variation (several dB), depending on initial state of canopy density and forest structure, when forest fractional canopy cover is reduced by 50% or more.

In order to provide a more theoretical foundation for the use of time series analysis of backscatter change based on the target scattering physics, a theoretical scattering model has been developed and described (Cartus et al., 2018). This model includes the scattering model and an observational error model, in order to show the separation between simulated natural and disturbed forest canopies. A summary of this simple observational model tailored for disturbance (i.e., ignoring double bounce) using cross-polarized observations is given here.

In a relationship between radar observation and classification accuracy, an error model is needed for the observations and those components that contribute to the target radar cross section (RCS). The observational error model that relates the observed radar cross-section, for each polarization pq , written here as σ_{obs}° for simplicity, to the observation error sources, $\sigma_{obs-error}^{\circ}$ and the radar cross-section of a forest canopy, σ_{forest}° is

$$\sigma_{obs}^{\circ} = \sigma_{obs-error}^{\circ} + \sigma_{forest}^{\circ} \quad (6.3-1)$$

The observational errors consist of instrumental effects, such as calibration and quantization errors, observational ambiguities, and speckle noise. With these factors taken into account, the radar cross-section of the forest can be written as

$$\sigma_{forest}^{\circ} = (1 - \eta) \sigma_{ground}^{\circ} + \eta \left[\sigma_{ground}^{\circ} e^{-\alpha h} + \sigma_{veg}^{\circ} (1 - e^{-\alpha h}) \right] \quad (6.3-2)$$

which is an “infinite resolution” model borrowed from optical techniques, where the contribution of the ground surface σ_{ground}° is combined with the average return from a layer of vegetation, σ_{veg}° , weighted by the fraction of vegetation canopy cover, η . In the above, the two-way loss of signal energy as it passes through the canopy is accounted for by α , the extinction, and a vegetation height (h) estimate. α is normally given in units of dB/m.

The above equation can be rearranged so as to separate the ground and the vegetation scattering returns, as in

$$\sigma_{forest}^{\circ} = \sigma_{ground}^{\circ} [1 - \eta(1 - e^{-\alpha h})] + \sigma_{veg}^{\circ} [\eta(1 - e^{-\alpha h})] \quad (6.3-3)$$

When multiple observations are made, (6.3-1) through (6.3-3) can be combined to relate the vector of observations to the spatially varying values and the set of constants that describe the mean radar cross section of the ground and vegetation, as in

$$\begin{bmatrix} \sigma_{obs-1}^{\circ} \\ \sigma_{obs-2}^{\circ} \\ \vdots \\ \sigma_{obs-N}^{\circ} \end{bmatrix} = \begin{bmatrix} 1 - \eta_1(1 - e^{-\alpha h}) & \eta_1(1 - e^{-\alpha h}) \\ 1 - \eta_2(1 - e^{-\alpha h}) & \eta_2(1 - e^{-\alpha h}) \\ \vdots & \vdots \\ 1 - \eta_N(1 - e^{-\alpha h}) & \eta_N(1 - e^{-\alpha h}) \end{bmatrix} \begin{bmatrix} \sigma_{ground}^{\circ} \\ \sigma_{veg}^{\circ} \end{bmatrix} \quad (6.3-4)$$

which, for a given number of observations, N , can be inverted to estimate the RCS of the ground and vegetation returns. Through simulations with real ALOS-1 L-band measurements with estimates for h and η from ancillary data sources the validity of backscatter-based change detection of 50% canopy density loss was demonstrated for the project in a memorandum by Siqueira and others in 2014. Time series analysis allows for the minimization of error sources from soil and vegetation moisture as well as speckle noise variations.

6.3.2 Implementation Approach for Algorithm

Pre-requisites for the disturbance detection algorithm are fully calibrated, radiometrically terrain corrected (RTC) backscatter time series where $pq=HV$. Co-polarized data ($pq=HH$) are useful for identifying potential ambiguities and unsupervised clustering and are employed to mask non-forest areas such as wetlands and agricultural areas. The time series RTC products are subjected to multi-temporal speckle noise reduction according to Quegan et al., 2001. A diagram giving the processing flow for the disturbance algorithm is shown in Figure 6-7.

SEASONAL SUB-SETTING OF TIME SERIES DATA STACK

For many biomes, seasonal stratification of time series will improve detection of disturbance events,

e.g., where freeze/thaw or dry/wet season conditions introduce significant backscatter changes. Thus, the first step in the disturbance detection algorithm is the sub-setting of time series data stacks and selection of scenes to minimize gross environmental effects on backscatter levels. Selection of the scenes can be performed with a global scene means comparison and threshold approach as follows:

1. A crude forest/non-forest mask is generated for a time series data stack. This mask is obtained from ancillary existing land cover classifications (e.g., from MODIS, Landsat, ALOS-1), or by thresholding an early HV SAR image from typical seasons of interest (e.g., non-frozen, dry season). A threshold of -13 dB has been used to generate such a forest mask on ALOS-1 and 2 data sets by JAXA.
2. For all pixels t_i under the mask, the mean (on the power scaled data) at each time step $i = 1, n$ is

generated to produce a time series of means as:

$$\tau_{\text{mean}} = \{\bar{\tau}_1, \bar{\tau}_2, \bar{\tau}_3, \dots, \bar{\tau}_p\}$$

3. Here, τ_{mean} is a collection of mean values, where $\bar{\tau}_i$ indicates the mean pixel value for the forested pixels in the image. This is a large-scale assessment of the seasonal effects within the image.
4. τ_{mean} is sorted from low to high values.
5. The gradient for the sorted τ_{mean} is computed as $\nabla\tau_{\text{mean}}$.
6. A threshold for significant major backscatter change is applied to the gradient of the sorted time series means such that $\text{subset}(\nabla\tau_{\text{mean}}) = \nabla\tau_{\text{mean}} > \text{change_threshold}$.
7. NISAR images that correspond to time steps in the subset from step 5 (or the complement of subsets) are selected to form the time series for change detection analysis.

Both the forest mask and change threshold can be estimated per ecosystem from statistical analysis with canopy density masks. During the NISAR mission we will generate a lookup table for biomes and ecoregions for these thresholds.

RELATIVE CALIBRATION OF SUBSETTED DATA STACK

For improved results, the time series stacks are calibrated relative to each other to a higher precision than perhaps required through routine standard calibration of the NISAR imagery. This calibration step examines distributed targets that are expected to be unchanged or minimally changed in brightness over a set time span of images. With NISAR's 240 km swath width, it is reasonably assumed that a statistically large area, A_{ni} , will not be disturbed (or otherwise changing) during any of the observations in the subsetted time series ob-

servations. These areas will be identified partly through use of the threshold-based forest mask from one scene and applied again through all images.

The calibration correction for image n , f_n , for each polarization channel pq , is

$$f_{pq}^n = \frac{\overline{(\sigma_{pq}(A_{ni}))}_t}{\overline{(\sigma_{n,pq}(A_{ni}))}} \quad 6.3-5$$

where $\overline{(\sigma_{pq}(A_{ni}))}_t$ is the average σ over the area A_{ni} for all images over the timespan t corresponding to the selected images according to the procedure above, and $\overline{(\sigma_{n,pq}(A_{ni}))}$ is the average σ over the area A_{ni} for the image n . Image values for the refined calibration of image n for each polarization channel will be given by $\sigma_{n,pq}^c$,

$$\sigma_{n,pq}^c = f_{pq}^n \sigma_{n,pq} \quad 6.3-6$$

CHANGE POINT DETECTION WITH CUMULATIVE SUM ANALYSIS

Disturbance detection for each calibrated pixel x, y (or segment, k) of the image for disturbed forests for image, n , will then be the result of the cumulative sum analysis performed for each pixel.

Cumulative sum analysis of time series is the basis for classical change point detection that investigates the change in mean before and after a change in a time series (Schweder et al., 1976). It is a distribution-free approach, applicable to short, irregular time series for detecting gradual and sudden changes. A graphical example of this process is shown in Figure 6-8.

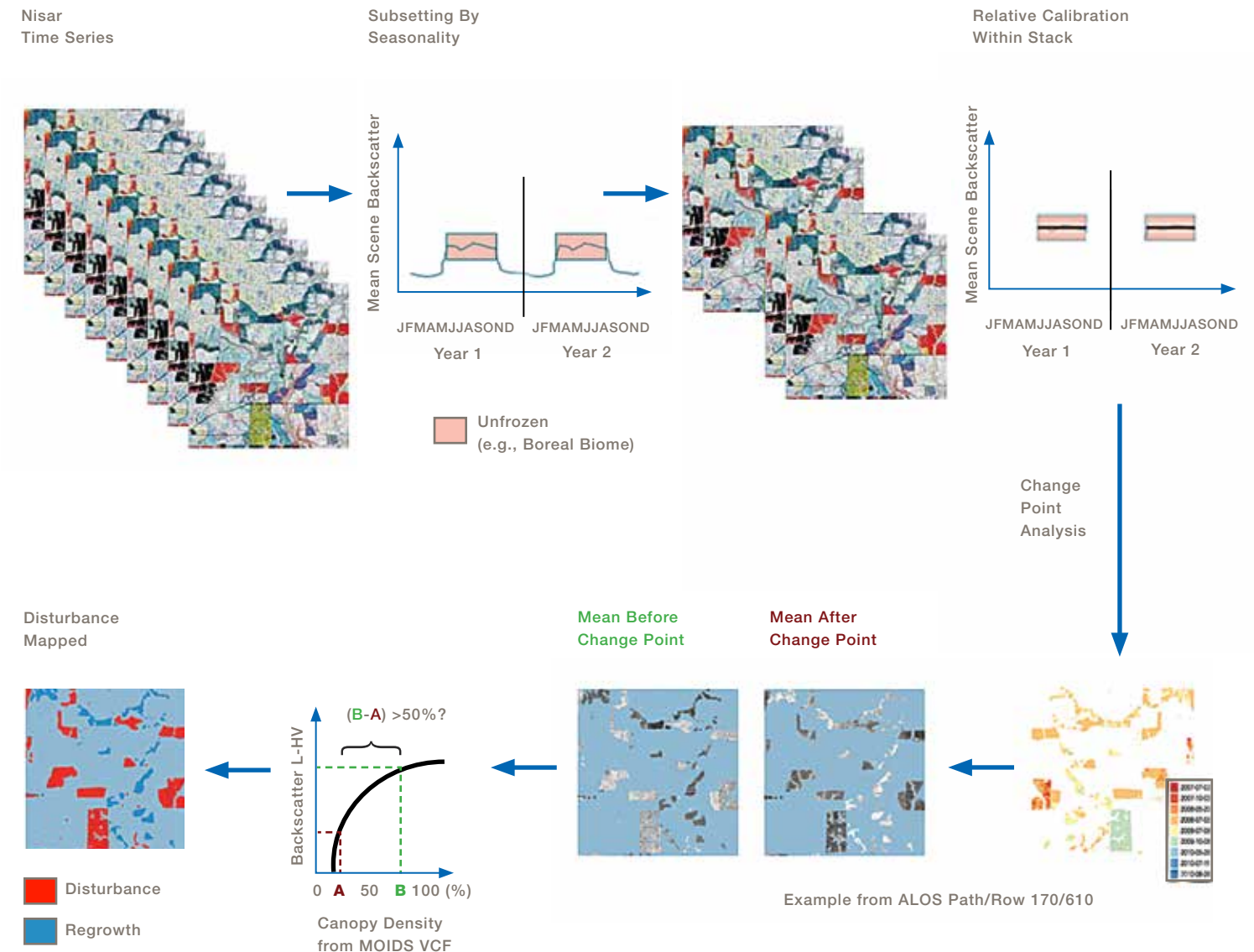


FIGURE 6-7

Algorithmic flow of disturbance detection with NISAR time series data based on change point analysis and canopy density-backscatter curves.

Let X be the time series of the subset of n selected scenes as

$$X = X_1, X_2, \dots, X_n$$

The residuals against the mean of the time series is computed (in power units) as

$$X = X_1, X_2, \dots, X_n$$

The cumulative sums, S_i , are defined as the sum of the residuals, R_i , at each time step such that

$$S_i = S_{i-1} + R_i \quad 6.3-7$$

With $i = 1, \dots, n$ and $S_0 = 0$.

In the cumulative sum, the slope of S is indicative of change in a time series:

- Upward slope: Values are above global mean
- Downward slope: Values are below global mean
- Change in slope direction: Indication of change point location

The magnitude of change is calculated as

$$S_{\text{DIFF}} = \max(S) - \min(S) \quad 6.3-8$$

Larger S_{DIFF} values are indicative of greater change. A change point can be defined with two criteria:

- A clear change in slope is detected in the cumulative sum curve, with upward and downward slopes exceeding a gradient threshold.
- S_{DIFF} exceeds a threshold for change labeling.

Criteria a) and b) are values to be determined empirically from calibration activities as they can be expected to be different for different forest structural types and environments with varying soil moisture conditions.

Also cross-checking will be performed to determine whether all observations shall be part of the cumulative sum calculation, i.e., whether scene subsetting was indeed appropriate or if further pruning might be necessary. Once a threshold value is determined from calibration efforts, change can be flagged based on the cumulative sum values.

A candidate change point is identified from the S curve at the time where S_{MAX} is found: $T_{CPbefore} = T(S_i = S_{MAX})$ with

- $T_{CPbefore}$, timestamp of the last observation before change
- S_p , cumulative sum of R with $i = 1, \dots, n$
- n , number of observations in the time series

The first observation after change occurred ($T_{CPafter}$) is then found as the first observation in the time series following $T_{CPbefore}$.

A possible method to define $threshold_{S_{DIFF}}$ is based on a standard deviation of all S_{DIFF} observations in the image stack. A suitable value found from experimental ALOS-1 data analysis is:

$$threshold_{S_{DIFF}} = MEAN(S_{DIFF}) + 1.5 * STDDEV(S_{DIFF}) \quad 6.3-9$$

This threshold will also vary with ecosystem and forest structural types.

For assessment of the robustness of detected change points, CUMSUM change point detection can be combined with bootstrapping (random reordering of the observation dates in the time series) to measure confidence in marking a change point.

First, a confidence interval is computed from the number of times a bootstrapped S_{DIFF} is less than the original S_{DIFF} . High count corresponds to higher confidence in a change point. Count can be expressed as a percentage confidence level (CL):

$$CL = \text{count}(S_{DIFF-Bootstrapped} < S_{DIFF}) / N \quad 6.3-10$$

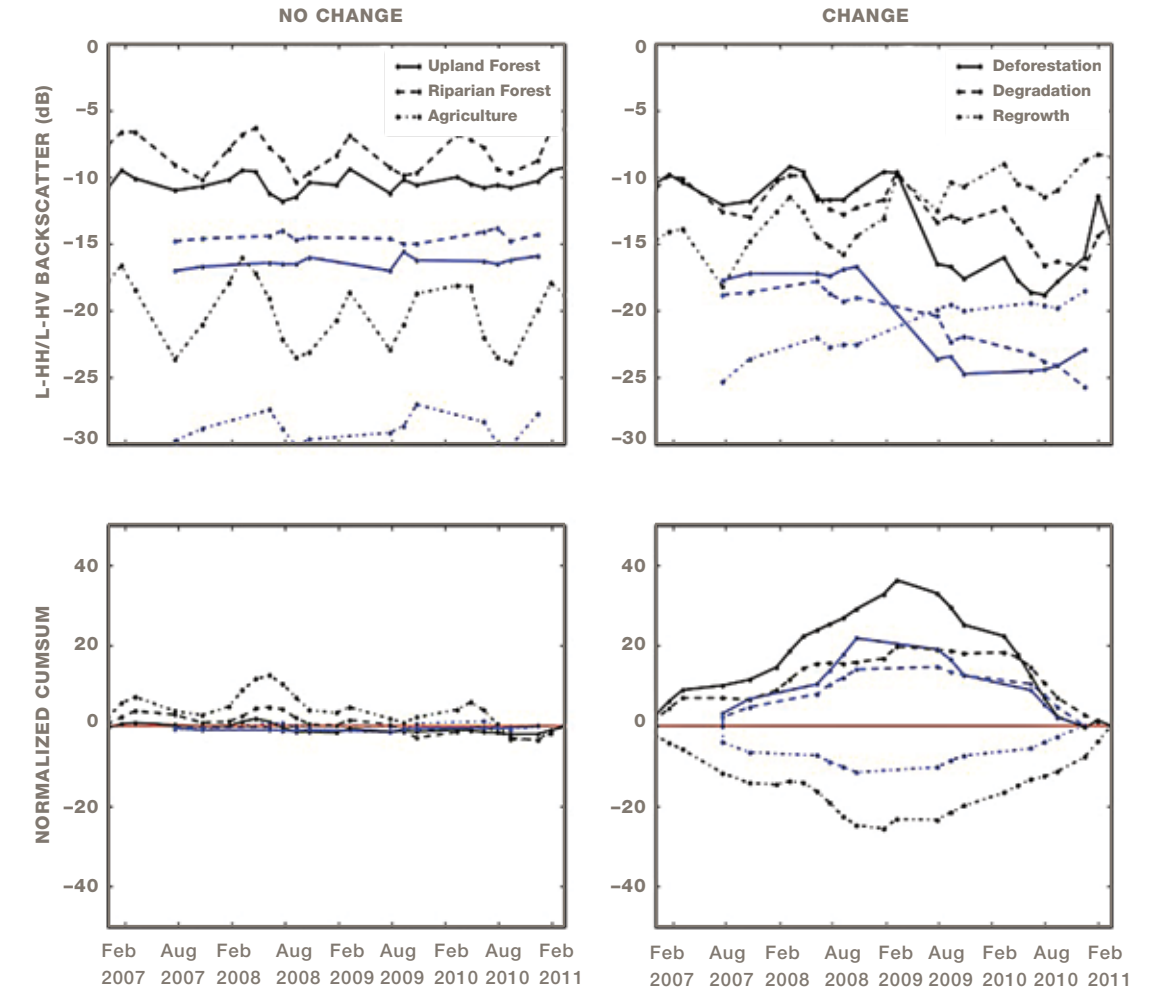
with N = number of bootstrapped samples.

The latter computation also makes change point detection in time series somewhat robust against outliers in a time series as their importance in a bootstrapped analysis decreases.

After applying a confidence level filter to further clean out spurious single 25-m pixels, a 2x2 sieve filter is applied to the raster data set where change points are identified. This is not necessary if the analysis was performed on image segments (to be tested).

FIGURE 6-8

Example of ALOS-1 time series (top) for various unchanged (left) and changed (right) land cover types. Bottom figures show the corresponding cumulative sum curves. Black lines=L-HH, blue lines=L-HV backscatter/cumulative sum curves.



RULE-BASED CLASSIFICATION OF DISTURBANCE

After change point detection a classification rule set is applied based on threshold curves of mean L-HV backscatter values from the time series segments before γ_{before}° and after γ_{after}° the detected change points for each 25-m pixel.

Threshold curves are derived empirically for each time series frame from corresponding MODIS or Land-sat-based canopy density layers and stratified based on

NISAR time series based unsupervised image clustering, e.g. via the Isocluster algorithm. For each cluster, canopy density – backscatter curves are generated based on linear-least squares regression or other appropriate statistical models. From the curves, thresholds for expected L-HV backscatter change in dB for 50% change before and after disturbance observations can thus be established ($Threshold_{50}$). This allows the final labeling of a pixel as disturbed (with greater than 50% loss in fractional forest canopy cover):

$$pixel = \begin{cases} \text{disturbed,} & \overline{\gamma_{before}^{\circ}} - \overline{\gamma_{after}^{\circ}} \rightarrow Threshold_{50} \\ \text{undisturbed,} & \text{other} \end{cases}$$

The resulting image is vectorized to a fixed one-hectare grid, and all polygons containing disturbance flagged pixels are retained for a final output product. If in any one-hectare cell, eight or more 25-m pixels are labeled disturbed, the 1-ha cell is flagged as disturbed.

Retaining only one-hectare cells as vector layers with attributes for number of detected disturbed pixels, error metrics and trends (retaining values of subsequent years), will result in a vast reduction of the image raster layers as only 3%–5% of any given area on average can be expected to be disturbed. In order to monitor disturbance trends, it is suggested that any 1-ha cell is retained where two or more 25-m pixels were flagged as disturbed.

6.3.3 Planned Output Products

The NISAR mission L2 science requirement for disturbance detection defines disturbance as “50% or more fractional forest canopy cover lost in a one-hectare (100×100 m²) resolution cell.” The mission shall measure disturbance annually with an error rate of less than 20% globally. The first NISAR disturbance product will be issued for the second year of the mission. The algorithm specified in this document is designed to produce products meeting this mission requirement by quantifying annually disturbed forested areas. The disturbance product will be issued as a 25-m binary base product with pixels flagged as disturbed (1) or not (0), and a 100-m vector product with numbers from 0 to 16 for the count of marked disturbed pixels. Error metrics for detection will also be made available for the 25-m and 1-ha products.

6.4 ECOSYSTEMS PRODUCTS – INUNDATION

The NISAR L2 science requirement for wetlands inundation is expressed as:

The NISAR project shall measure inundation extent within inland and coastal wetlands areas at a resolution of 1 hectare every 12 days with a classification accuracy of 80%.

A review of publications quantifying the accuracy of mapping wetlands with L-band SAR was completed in October 2014. The review concluded the wetlands accuracy requirement could be achieved by NISAR. Methods to classify radar images ranged from utilizing simple thresholds to machine learning approaches, sometimes in combination with image segmentation. Inundated vegetation can be observed by L-band SAR when woody vegetation vertically emerges from the water surface enhancing the double bounce scattering mechanism which is especially apparent in the HH channel. Wetlands are often adjacent to open water or senesce into open water surfaces that provide significant contrast landscapes, facilitating detection and mapping of inundation regions using the NISAR mission.

The NISAR baseline algorithm uses the most common method to identify inundated vegetation or open water: detection thresholds. A recent example that describes a procedure similar to that which would satisfy the NISAR requirement can be found in Chapman et al, 2015. The algorithm benefits from the double bounce scattering effect that occurs in inundated vegetation, and particularly strong in the HH channel. Meanwhile, the observed HV backscatter changes remains relatively small. To refine wetland classification, a change detection algorithm over a sequence of radar images covering seasonal inundation patterns, allows for partially wetted or temporarily wet pixels to be identified as wetlands.

For classification of open water, the backscatter is generally significantly lower than non-inundated landscapes with three possible exceptions: 1) depending on the noise equivalent σ^0 of NISAR, distinguishing open water from other low backscatter targets such as bare ground or mudflats may be difficult; 2) at steep incidence angles, wind roughening can make open water brighter than typical open water values and; 3) open water with floating vegetation is not categorized separately. In the first case, since open water does not generally change quickly or to a large degree compared to the extent of inundated vegetation, aver-

aging the data over time or over area can be helpful for reducing the noise over bare ground areas, which are generally brighter than the expected noise equivalent σ^0 . In the second case, we will make use of images taken with different viewing geometry and times to identify open water surfaces. Indeed, observing the response of open water and land surfaces viewed from a different perspective differs and could be discovered from comparing ascending and descending passes. Another method to distinguish open water from bare ground is through examination of the interferometric coherence. The observed repeat-pass coherence over bare ground is typically higher than that of open water. For the third case, a subcategory of floating vegetation is not classified, but these areas will often be identified as inundated areas and therefore meet the objectives of the requirement.

As a preliminary step, a baseline classification will be generated from the multi-temporal radar backscatter average of an image sequence to represent the initial inundation state representative of the time period of the images. The wetland classification generated for each orbit cycle is obtained through change detection of the images within this orbit cycle relative to this baseline. The accuracy of the subsequent classifications generated for each orbit cycle could potentially be improved through comparison with an additional but shorter multi-temporal average. This would improve the robustness of the classification by increasing the effective number of looks within 1 ha pixels at the expense of temporal resolution. If multi-temporal averaging were required to meet classification accuracy requirements, the multi-temporal averaging would be accomplished as a separate pre-processing step and implemented as rolling averages to maintain the 12-day interval for the output of classification results. As such, pixels transitioning between different inundation states during the temporal averaging period could still be captured.

6.4.1 Implementation Approach for Algorithm

The detection of inundation in NISAR images follows the processing flow shown in Figure 6-9 and is described here. The images of the multi-temporal sequence are radiometrically calibrated relative to each other to a higher precision than perhaps required through routine standard calibration of the NISAR imagery. This calibration step examines distributed targets that are expected to be unchanged or minimally changed in brightness over a set timespan of the set. With NISAR's 240 km swath width, it is reasonably assumed that a statistically large area, A_{ni} , will not be inundated (or otherwise changing) during any of the 2n observations surrounding the image to be calibrated and classified. These areas will be identified through use of a priori wetlands mask and partly through image segmentation or other methods over the 2n images.

The calibration correction for image n (the middle image of the 2n multi-temporal sequence), f_n , for each polarization channel pq , is

$$f_{pq}^n = \frac{\overline{(\sigma_{pq}(A_{ni}))}_t}{\overline{(\sigma_{n,pq}(A_{ni}))}} \quad 6.4-1$$

where $\overline{(\sigma_{pq}(A_{ni}))}_t$ is the average backscatter, σ , over the area A for all images and all polarizations, pq , over the timespan t corresponding to the 2n images, and $\overline{(\sigma_{n,pq}(A_{ni}))}$ is the average σ over the area A for the image n . Backscatter values for the refined calibration of image n for each polarization channel is given by:

$$\sigma_{n,pq}^c = f_{pq}^n \sigma_{n,pq} \quad 6.4-2$$

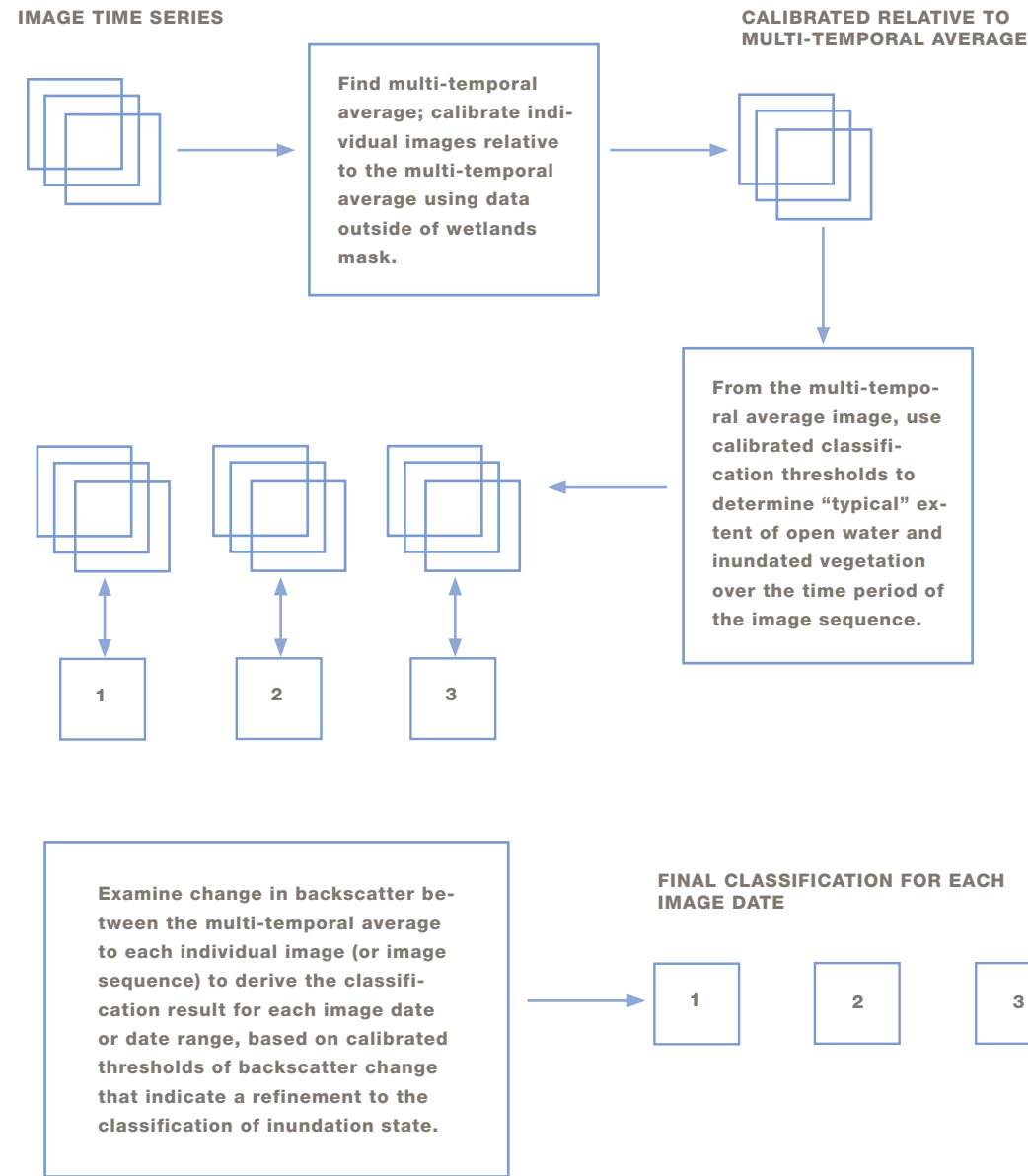


FIGURE 6-9
Algorithm flow for an example multi-temporal sequence of three images for inundation.

The multi-temporal average of the 2n images is given by $\overline{\sigma_{pq}}$. Classification C for each calibrated pixel x, y (or segment k) is:

$$C_{x,y} = 1 \text{ or } C_k = 1 \text{ if } \frac{\overline{\sigma_{HH}}(\theta_{inc})}{\overline{\sigma_{HV}}(\theta_{inc})} > \sigma_T^{r-iv}(\theta_{inc}) \frac{\overline{\sigma_{HH}}(\theta_{inc})}{\overline{\sigma_{HV}}(\theta_{inc})} > \sigma_T^{r-iv}(\theta_{inc}) \text{ and } \overline{\sigma_{HH}}(\theta_{inc}) > \sigma_T^{hh-iv}(\theta_{inc}) \quad 6.4-3$$

where the thresholds $\sigma_T^{r-iv}(\theta_{inc})$ and $\sigma_T^{hh-iv}(\theta_{inc})$ may be a function of the incidence angle, θ_{inc} , and are determined through a pre-launch and post-launch calibration process. $\sigma_T^{r-iv}(\theta_{inc})$ is the threshold value for classification of undated vegetation from the ratio of the polarization channels HH and HV, $\frac{\overline{\sigma_{HH}}(\theta_{inc})}{\overline{\sigma_{HV}}(\theta_{inc})}$ and $\sigma_T^{hh-iv}(\theta_{inc})$ is the threshold value for classification of inundated vegetation from the HH backscatter given by $\overline{\sigma_{HH}}(\theta_{inc})$.

Classification C for each pixel x, y (or segment k) of the image for open water for the multi-temporal average image is:

$$C_{x,y} = 2 \text{ or } C_k = 2 \text{ if } \frac{\overline{\sigma_{HH}}(\theta_{inc})}{\overline{\sigma_{HV}}(\theta_{inc})} > \sigma_T^{r-ow}(\theta_{inc}) \text{ and } \overline{\sigma_{HH}}(\theta_{inc}) > \sigma_T^{hh-ow}(\theta_{inc}) \quad 6.4-4$$

where the thresholds $\sigma_T^{r-ow}(\theta_{inc})$ and $\sigma_T^{hh-ow}(\theta_{inc})$ may be a function of the incidence angle, θ_{inc} , and are determined through a pre-launch and post-launch calibration process. $\sigma_T^{r-ow}(\theta_{inc})$ is the threshold value for classification of open water from the ratio of the polarization channels HH and HV, $\frac{\overline{\sigma_{HH}}(\theta_{inc})}{\overline{\sigma_{HV}}(\theta_{inc})}$, and $\sigma_T^{hh-ow}(\theta_{inc})$ is the threshold value for classification of open water from the HH backscatter given by $\overline{\sigma_{HH}}(\theta_{inc})$.

All other image pixels have $C_{x,y} = 3$ or $C_k = 3$. This generally encompasses areas outside the wetlands mask and may include areas within the wetlands mask, such as those areas determined as not inundated by exclusion from the open water and inundated vegetation classes.

There may be a small number of pixels where the classification is indeterminate. For example, at the given incidence angle, it is not possible to conclusively classify the data. For those cases, the classification would be $C_{x,y} = 4$ or $C_k = 4$.

$$C_{x,y} = 4 \text{ or } C_k = 4 \text{ if } > \sigma_T^{r-in}(\theta_{inc}) > \frac{\overline{\sigma_{HH}}(\theta_{inc})}{\overline{\sigma_{HV}}(\theta_{inc})} > \sigma_T^{r-in}(\theta_{inc}) \text{ and } \sigma_T^{hh-in}(\theta_{inc}) > \overline{\sigma_{HH}}(\theta_{inc}) > \sigma_T^{hh-ind}(\theta_{inc}) \quad 6.4-5$$

$$C'_{x,y} = 31 \text{ or } C'_k = 31 \text{ if } C = 3 \text{ and}$$

$$\sigma_{n,HH}^C(\theta_{inc}) > \sigma_T^{hh-veg}(\theta_{inc}) \text{ and } \frac{\sigma_{n,HH}^C(\theta_{inc})}{\sigma_{HH}^C(\theta_{inc})} > \sigma_T^{rmin-iv}(\theta_{inc}) \text{ and } \frac{\sigma_{n,HV}^C(\theta_{inc})}{\sigma_{HV}^C(\theta_{inc})} > \sigma_T^{rHVmax}(\theta_{inc}) \quad 6.4-6$$

where $\sigma_T^{hh-veg}(\theta_{inc})$ is the minimum HH threshold backscatter value for vegetation covered terrain; $\sigma_T^{rmin-iv}(\theta_{inc})$ is the minimum change threshold ratio relative to the previous observation for HH backscatter indicating a transition from non-inundated to inundated vegetation; and $\sigma_T^{rHVmax}(\theta_{inc})$ is the maximum HV change threshold ratio relative to the previous observation indicating that the vegetation characteristics did not otherwise change.

Looking for areas that may be decreasing in inundation extent from inundated vegetation to not-inundated:

$$\begin{aligned}
 C'_{x,y} &= 13 \text{ or } C'_k = 13 \text{ if} \\
 C &= 1 \text{ and} \\
 \sigma_{n,HH}^C(\theta_{inc}) &> \sigma_T^{hh_{veg}}(\theta_{inc}) \sigma_{n,HH}^C(\theta_{inc}) > \sigma_T^{hh_{veg}}(\theta_{inc}) \text{ and} \\
 \frac{\sigma_{n,HH}^C(\theta_{inc})}{\sigma_{HH}(\theta_{inc})} &< \sigma_T^{r_{max,v}}(\theta_{inc}) \text{ and} \\
 \frac{\sigma_{n,HV}^C(\theta_{inc})}{\sigma_{HV}(\theta_{inc})} &> \sigma_T^{r_{HV_{min}}}(\theta_{inc})
 \end{aligned} \tag{6.4-7}$$

where $\sigma_T^{r_{max,v}}(\theta_{inc})$ is the maximum change threshold ratio relative to the multi-temporal average observation for HH backscatter, indicating a transition from inundated to non-inundated vegetation; and $\sigma_T^{r_{HV_{min}}}(\theta_{inc})$ is the minimum HV change threshold ratio relative to the multi-temporal average, indicating that the vegetation characteristics did not otherwise change.

Similarly, for open water we may examine cases where open water extent is increasing:

$$\begin{aligned}
 C'_{x,y} &= 32 \text{ or } C'_k = 32 \text{ if} \\
 C &= 3 \text{ and} \\
 \sigma_{n,HH}^C(\theta_{inc}) &< \sigma_T^{hh_{veg}}(\theta_{inc}) \text{ and} \\
 \frac{\sigma_{n,HH}^C(\theta_{inc})}{\sigma_{HH}(\theta_{inc})} &< \sigma_T^{r_{max,ov}}(\theta_{inc})
 \end{aligned} \tag{6.4-8}$$

where $\sigma_T^{r_{max,ov}}(\theta_{inc})$ is the maximum change threshold ratio relative to the multi-temporal average for HH backscatter, indicating a transition from non-inundated terrain without vegetation to open water.

Looking for areas that may be decreasing in open water extent:

$$\begin{aligned}
 C'_{x,y} &= 23 \text{ or } C'_k = 23 \text{ if} \\
 C &= 2 \text{ and} \\
 \sigma_{n,HH}^C(\theta_{inc}) &< \sigma_T^{hh_{veg}}(\theta_{inc}) \text{ and} \\
 \frac{\sigma_{n,HH}^C(\theta_{inc})}{\sigma_{HH}(\theta_{inc})} &> \sigma_T^{r_{min,ov}}(\theta_{inc})
 \end{aligned} \tag{6.4-9}$$

where $\sigma_T^{r_{min,ov}}(\theta_{inc})$ is the minimum change threshold ratio relative to the multi-temporal average for HH backscatter indicating a transition from open water to non-inundated terrain without vegetation.

Similar tests for indeterminate areas where C=4 for Equations 6.4-6 and 6.4-8 would be made. For all pixels or regions where C' is nonzero, C is replaced with C'.

An error layer will be generated utilizing the observed probability distribution function of inundated vegetation, open water, and non-inundated backscatter values compared with the calibrated threshold values.

6.4.2 Planned Output Products

The specified product for validation of the L2 requirement to measure inundation extent is a raster classification of inundated extent at a spatial resolution of 1 hectare.

The pixel values have the following values: 1) inundated vegetation; 2) open water; 3) not inundated; 4) indeterminate. Categories 1, 2, 3 and 4 may have subcategories for pixels in transition. The resolution of the product will be 1 ha. The product will be generated every 12 days after the first 6 (approximate) months of observations are completed, and assumes that 20 MHz dual polarization HH, HV data are acquired every 12 days for both ascending and descending orbit directions. The input product is the L2, 25 m, radiometric and terrain corrected, multi-look imagery. The incidence angle for each image pixel should also be provided.

Also required for generating the classification product is an a priori wetlands mask where inundation could occur and excluding confounding landscape types such as urban areas and agricultural areas, as well as terrain slopes, volcanic terrains and deserts. The output resolution of the product will be 1 ha. The value of the 1-ha cell will be either through direct classification of the average of the input 25-m SAR data product or by majority vote among the classes of the 16 input pixels and the direct classification of the 1 ha SAR.

An error probability layer for the classification will be provided, based on a statistical analysis of the observed backscatter distributions versus the backscatter thresholds used in the classification.

6.5 ECOSYSTEMS PRODUCTS – CROP MONITORING

The NISAR L2 science requirement for agricultural crop area is expressed as:

The NISAR project shall measure crop area at 1 hectare resolution every 3 months with a classification accuracy of 80%.

To feed a growing population of more than 8 billion, food production and supply occur on a global basis. In order to better guide policy and decision making, national and international organizations work to transparently monitor trends and conditions of agriculture on a timely basis. Because of the variable nature of planting and harvesting practices, efforts such as this are manpower intensive and time-consuming tasks. Organizations such as the USDA, World Bank, and FAO publish statistics on crop area, type and yield on a regular basis. Much of these data are derived from in-country surveys, augmented by what are, to date, limited remote sensing components.

Recent efforts to increase the use and accuracy of remote sensing data for agriculture applications have been led by the Group on Earth Observations (GEO) under the GEOGLAM initiative (GEO Global Agriculture Monitoring). This initiative consists of governmental education and non-governmental organizations that use such data for allocating resources, projecting agricultural outlook, publishing market projections, allocating resources and assessing food security often on a month-to-month basis. While current remote sensing inputs for crop-area identification methods rely primarily on reflectance spectra from optical data, radar has the potential for making a great impact because of its sensitivity to the structure of ground-cover and its insensitivity to cloud cover and lighting conditions.

Through its global observing strategy and 12-day revisit period, the NISAR mission has the capacity for collecting data that is relevant to the societally important applications of monitoring and measuring global food production. This is reflected in the mission's crop area requirement.

6.5.1 Theoretical Basis of Algorithm

The NISAR L2 science requirement for wetlands inundation is expressed as:

The NISAR project shall measure crop area at 1 hectare resolution every 3 months with a classification accuracy of 80%.

The crop area algorithm is based on the coefficient of variation (CV), which is the ratio of the standard deviation over the mean for a time series of orthorectified radar cross-section data (Whelen and Siqueira, 2018). Here, the coefficient of variation is computed for both the co- and cross-polarized data (HH and VH) averaged to a hectare-scale, and where the time series are collected quarterly. These time periods cover typical growing seasons of crops and make best use of the background (i.e., HH ± HV) land observations planned by NISAR.

There are two principal advantages that are offered by NISAR over existing technical approaches for crop area estimation. These are: 1) an effectively all-weather observing strategy that will provide observations of a given area every 12 days (every 6 days if we include ascending and descending passes), and 2) the measure of radar cross section, which is dependent on contributions of volume and surface scattering which are likely to change dramatically for actively managed agricultural landscapes. Measures of radar cross section are more robust than interferometric measures of change, such as through the decorrelation signature, which may be an appealing alternative or augmentation to the base-algorithm that will be used for estimating active crop-area.

There are two types of error that can affect the active crop area estimates mentioned here: those associated with the instrument and those related to the region being observed.

For sources of error related to the instrument, measurement stability and cross-track variability in the signal to noise ratio (SNR) will be the dominant factors. Simulations and ALOS-1 observations for India have shown that the coefficient of variation will be robust for relative calibration errors up to 1 dB (ALOS-1 is quoted to have a calibration accuracy of some 10ths of a dB). Variation in the SNR will occur as a function of the target brightness and the incidence angle. Normalization of the RCS standard deviation by the RCS mean will remove much of this variability. Regions with very low SNR, close to the noise floor of NISAR, will be removed through a simple threshold classifier based on the brightness of the mean RCS.

Sources of error in active crop area that are associated to the target can be principally assigned to three sources. These are: 1) weather induced changes to the radar cross section, 2) disturbance events mistaken for crop regions, and 3) misclassification of regions as potentially belonging to agricultural landscapes (e.g., urban areas and open water).

Errors that are related to weather induced changes in the RCS will manifest themselves as short-term variations in the trajectory of the RCS as the agricultural region changes from barren land, emergent plants, full grown crops to harvested land. As the plants above the soil grow and mature, changes in the soil moisture will have less of an effect on the overall signature, even for regions which are left fallow, and hence classified as non-active crop regions. The changes in the radar cross-section for barren ground is only on the order of a few dB or less, much smaller when compared to the many dB that the RCS undergoes throughout the growing season.

Errors induced by a disturbance event as opposed to actively managed land may result in a degree of misclassification for agricultural area. This effect is expected to be small however, especially when comparing regions from one year to the next. For this reason, estimates of active agricultural crop area are not planned to meet the full requirement accuracy of 80% until after the first year of NISAR observations.

Lastly, misclassified regions such as open water and urban regions included in the mask for NISAR assessment of agricultural area are a potential source of error. Use of a simple threshold classifier on the RCS mean however has shown to be an effective method for removing open water regions and those with low SNR; while urban regions with a bright RCS and proportionally small variation in the RCS as a function of time, have been shown thus far to be correctly identified by the CV-based classifier of crop area used here, and appear to be more successful and detailed than those classifiers that depend on optical data alone.

The NISAR measurement metric for crop area determination relies on the CV, which is a measure of the degree of change (normalized with respect to the mean backscatter) as a function of time. This metric makes use of the fact that agricultural landscapes are heavily managed, and hence, the scattering physics of agricultural crops change more than other landcover types. A full treatment and analysis using the CV for crop area determination using ALOS-1 observations can be found in Whelen and Siqueira (2018).

In order to provide a more theoretical foundation for the use of the CV based on the target scattering physics, a theoretical scattering model was developed and described in the above-mentioned NISAR memorandum; one that includes the scattering model and an observational error model, in order to show the separation between simulated natural and actively managed landscapes. A summary of this model is given here.

A relationship between radar observation and classification accuracy is needed for the observations and those components that contribute to the target RCS. The observational error model is the same model as used by the forest disturbance algorithm (Cartus et al., 2018). It relates the observed radar cross-section for each polarization pq , written here as σ_{obs}^o for simplicity, to the observation error sources, $\sigma_{obs-error}^o$ and the radar cross-section of an agricultural field, σ_{field}^o is

$$\sigma_{obs}^o = \sigma_{obs-error}^o + \sigma_{field}^o \quad 6.5-1$$

It can be shown that the radar cross-section of the field can be broken down into components of the return from the ground, σ_{ground}^o , volume, σ_{vol}^o , and double-bounce, σ_{db}^o , returns from the vegetation components. Additional parameters that govern the model are the fractional canopy cover, η , the attenuation of the signal as it passes through the vegetation layer, α , and the height of the vegetation layer, h . The net model, which is based on (Dobson and Ulaby, 1986; Askne et al., 1997) is given as

$$\sigma_{field}^o = \sigma_{ground}^o \left[1 - \eta \left(1 - e^{-\alpha h} \right) \right] + \sigma_{vol}^o \left[\eta \left(1 - e^{-\alpha h} \right) \right] + \sigma_{db}^o \eta h e^{-\alpha h} \quad 6.5-2$$

By creating a time series model for the inputs of equation 6.5-2 (e.g., in terms of how η , h , are changing over the growing season) it is possible to create a time series for the radar cross-section observed for a field. A similar time series is created for a landcover type that is not changing over time (e.g., given values for the RCS of ground, volume and double-bounce). With these two simulated time series, the observing period of NISAR is included to determine the season during which the two target types are being observed, and a time series of NISAR observations simulated and the CV computed. Once done, a threshold classifier is employed based on the CV and a hypothesis test applied to the resulting classification. Given that the CV pdfs have thus been determined for the two different landcover types (managed versus

unmanaged) the hypothesis test and probabilities of correct and incorrect classification are determined as a function of the choice of threshold.

6.5.2 Implementation Approach for Algorithm

The algorithm flow is presented in Figure 6-10. Time series are assembled every 3 months after the first year of data collection, and from that, the CV is computed for each available polarization. Minimally, this would be HH and HV polarized fields; however, in the U.S. and in India, it is expected that fully polarimetric data will be available. For each of the computed coefficients of variation, a determination will be made via a pre-determined threshold, on a per hectare basis, if the CV indicates that the area is actively being managed or not. Results for each polarization will be compared with the other polarization results, as well as combined with ancillary data that may be available from ESA's CCI (esa-landcover-cci.org) and the SRTM (or better) topographic map. Based on the limited set of inputs, and comparison to the previous quarter's results, a determination will be made for which of the four classes that each 1-ha region should be classified: 1) active crop area, 2) newly active crop area, 3) inactive crop area, and 4) not crop.

The observing strategy for the determination of crop area is broken down into two time periods: 1) during the first year of observations, there is no planned delivery of crop area determination from NISAR, and 2) during successive years, a 1 ha-resolution raster image of the crop area classification will be generated every three months.

The first year of NISAR observations are used for the determination of baseline thresholds for crop area classification based on the CV metric determined for both HH and HV polarizations (CV_{HH} and CV_{HV}), computed separately for the ascending and descending passes of NISAR. These thresholds are determined through the

NISAR post-launch calibration period, where histograms of CV_{HH} and CV_{HV} for the ascending and descending passes are created for crop and non-crop regions using pre-determined validation resources from ESA's CCI and USDA's CropScape data layers.

Values of CV_{HH} and CV_{HV} are determined for each 3-month period, post launch, bracketed by the dates: January 1 – March 31, April 1 – June 30, July 1 – September 30, and October 1 – December 31, as well as for the entire one-year period.

The CV for each polarization is determined by the standard deviation of the radar cross-section divided by the mean of the radar cross-section, collected as a function of time (e.g., the 3-month period), at the 25-m resolution of the input data product. Units of the input radar cross-sections should be in m^2/m^2 and not dB. That is:

$$CV_{pq} = \frac{\text{stddev}(\sigma_{pq}^{\circ}(t))}{\text{mean}(\sigma_{pq}^{\circ}(t))} \quad 6.5-3$$

where

$$\text{mean}(\sigma_{pq}^{\circ}(t)) = \overline{\sigma_{pq}^{\circ}} = \frac{1}{N} \sum_{n=1}^N \sigma_{pq}^{\circ}(n\Delta t) \quad 6.5-4$$

and

$$\text{stddev}(\sigma_{pq}^{\circ}(t)) = \sqrt{\frac{1}{N-1} \sum_{n=1}^N (\sigma_{pq}^{\circ}(n\Delta t) - \overline{\sigma_{pq}^{\circ}})^2} \quad 6.5-5$$

In the above, N is the total number of observations in the observing period, and Δt is the time period between NISAR passes (expected to be 12 days). Calculations of the CV are made on a per-pixel (25 m) basis and aggregated after computation into 1 hectare pixels where both the mean and standard deviation of the CV determination are kept at the 1 ha-resolution for each polarization and orbital direction of the satellite. Hence, each 1 ha-resolution element will consist of eight

values, four for the mean of the CV, and four for the standard deviations, as in:

$$\begin{aligned} & CV_{HH-asc}, CV_{HV-asc}, CV_{HH-desc}, CV_{HV-desc}, \\ & \text{stddev}(CV_{HH-asc}), \text{stddev}(CV_{HV-asc}), \text{stddev}(CV_{HH-desc}), \\ & \text{stddev}(CV_{HV-desc}) \end{aligned}$$

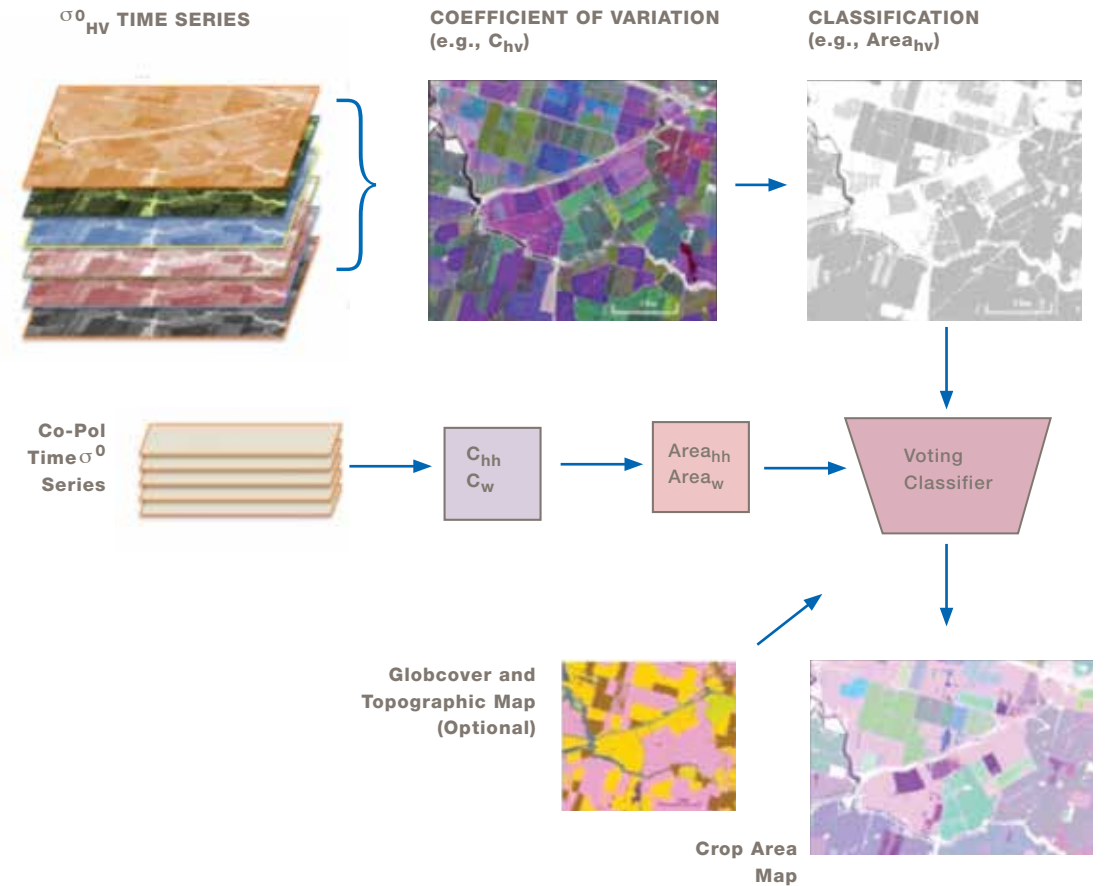
Of the group of four estimates of CV, the estimate with the highest standard deviation will be eliminated and the remaining three will be used in a threshold classification whose value of threshold is determined through the NISAR calibration phase. An additional threshold will be used for detecting water bodies, which, because of their small values for radar cross-section, will also display large values for CV. In the last step, a voting classifier is used to determine if the region is an active crop region or not.

Determination of which pixels change classes over time can be determined by comparing one time period classification versus a previous, thus providing useful information about planting and harvesting periods. More accurate determination of the start of the planting and harvesting seasons can be determined on a per-pixel basis by going back to the original radar cross-section data and using a running window to determine when the CV statistics changed.

6.5.3 Planned Output Products

The specified product for validation of the L2 requirement to measure crop area is a raster classification. The pixel values based on prior and current determination of active crop area are given in Table 6-3: 1) not a crop; 2) newly active crop area; 3) inactive crop area (fallow); 4) active crop area; and 5) not evaluated (class 0). The resolution of the product will be 1 ha. The product is intended to be generated every 3 months after the first year of observations are completed, and assumes that 20-MHz dual polarization HH, HV data are acquired every 12 days for both ascending and descending orbit directions.

FIGURE 6-10 Data and algorithm flow diagram.



The input product is the L2, 25-m, radiometric and terrain corrected, calibrated multi-look imagery for each of the polarizations, for each period of data collection. Mosaics of the data are not desired. In order to make the co-registration and geolocation of images a trivial process, pixel locations should be quantized onto a pre-determined geographic grid.

Also required for generating the classification product is a landcover mask that indicates those regions where agricultural monitoring is intended to be performed. Additional layers would prove useful in increasing the accuracy of the agricultural area classification and are being investigated as part of the NISAR phase C efforts. These are as follows:

1. An up-to-date version of ESA's CCI landcover map (esa-landcover-cci.org). These data are useful

for defining limits of urban areas, inside of which formal agricultural practices are excluded from the analysis.

2. Topographic and look angle maps that are co-registered to the NISAR data grid. Such maps need only be supplied once using the expected viewing geometry of the sensor.

6.6 CRYOSPHERE PRODUCTS – ICE SHEETS

A major objective for NISAR is to collect data to measure velocity over the Greenland and Antarctic ice sheets through time. These same data will be used to determine the time-varying position of the grounding line around Antarctica and on floating ice tongues in Greenland. The ice sheet related science requirements call for measurements of ice sheet velocity derived

using a combination of interferometric phase data and offsets from speckle tracking. Near ice sheet grounding lines, time series of interferometric phase will be differenced to estimate relative tidal displacement, which helps grounding line position. This section describes the algorithms needed to generate these products.

6.6.1 Theoretical Basis of Algorithm

For slow-moving areas (<50 m/yr) and some fast moving areas where the data are conducive to such measurement, horizontal velocity will be measured using radar-line-of sight determined from the interferometric phase from at least two crossing orbit tracks (i.e., ascending/descending) under the assumption that flow is parallel to the known surface (Joughin et al., 1998). An advantage of this technique is that the data are relatively high-resolution (<100 m) and the phase noise is low (<~2 cm). A major disadvantage is that for fast moving areas it is difficult or impossible to unwrap the phase. Another issue is regions where there is significant ionospheric activity such that the spatially variable path delay introduces large interferometric phase errors (several m/yr errors). For NISAR, these errors will largely be removed using split-spectrum processing applied to the 80-MHz-bandwidth data.

In areas where the motion is too fast for interferometric phase measurements, velocity will be determined using the azimuth and range offsets derived by cross-correlating patches from pairs of images to determine

displacements between image acquisitions (Gray et al., 1998; Michel and Rignot, 1999). Although image features can improve correlation, this technique works best when the speckle patterns are well correlated; hence this technique is often called speckle tracking. Advantages to this method are that velocity estimates can be derived from a pair of images collected along a single orbit track (i.e., ascending or descending only orbits) and it can be used to measure extreme motion (>10 km/yr). Because the technique uses image chips several 10s of pixels in dimension, the spatial resolution is much poorer (>~200 m) than phase estimates. Since displacement is resolved to within a fraction (i.e., ~1/20 of a several-meter pixel) of a range or azimuth pixel, accuracy also is much less than phase estimates, which resolve motion to a fraction of a wavelength.

In polar regions, ionospheric distortion can be severe, particularly for the azimuth offsets. This distortion can produce errors of more than 100 m/yr in some locations. This problem can be mitigated by using range-only offsets from crossing orbits as described below.

The requirements for fast and slow motion reflect the fact that lower resolution speckle tracking is best suited to measuring fast-flowing outlet glaciers, while interferometric phase is ideal for the slow-flowing interior. Although the 50 m/yr distinction between slow and fast flow in the requirements is aimed at separating the areas where each technique should work the best, in many cases interferometric phase will still work in considerably faster-flowing areas (up to about 500 m/yr for NISAR). Thus, no single velocity threshold can cleanly separate the regions where phase fails and speckle-tracking must be used. For example, with RADARSAT phase can sometimes be unwrapped on smooth flowing ice shelves at speeds approaching 1000 m/yr. By contrast, for some regions on the ice sheets where the speeds are less than 100 m/yr, there

are strong phase gradients where ice flows over bumps that make phase unwrapping difficult or impossible. As a result, for all of the velocity related requirements, at each point on the ice sheet, the corresponding requirement will be met using the best available combination of interferometric phase and speckle-tracked offsets. The different temporal and spatial resolutions specified in the requirements reflect the amount of spatial and temporal averaging necessary to meet each requirement.

The basic algorithmic approach will follow earlier approaches (Joughin, 2002). Specifically, at each point in the output grid, the algorithm will cycle through the various options:

1. Range-azimuth offsets from a single orbit track,
2. Unwrapped phase (for range) with azimuth offsets from a single orbit track,
3. Range-range offsets from crossing orbit tracks, and
4. Unwrapped phase-phase data from crossing orbits.

At each point in the output, all of the viable combinations will be calculated. Estimated errors for each type of velocity estimate will be used to weight the results to produce an optimal inverse-error weighted average for the horizontal components of velocity. All of these combinations have been widely used (Joughin et al., 2010a; Rignot et al., 2011a; Mougnot et al., 2017), with recent work demonstrating the range-range offsets combination (Joughin et al., 2018). This latter combination is more attractive for NISAR because a) the 80-MHz mode provides considerably finer range (~2.5 m) than azimuth (~7 m) resolution, b) there will be ample ascending/descending coverage, and c) relative to azimuth offsets, the range offsets are less affected by ionospheric distortion. Hence, the range-range offsets combination likely will be the dominant

contributor to velocity estimates in regions of fast flow. All of the above methods will be implemented, but any of them can be selectively turned off (e.g., methods 1 and 2 where azimuth offsets add no improvement to the derived estimates).

All ice-sheet velocity maps will be produced on polar stereographic grids at a posting of 100 m (actual resolution in faster-moving regions will be 250 m or better). Consistent with the existing products, the Greenland map-projection will use a standard latitude of 70°N and a central meridian of 45°E and the Antarctica projection will use a standard latitude of 71°S and a central meridian of 0°. Glacier products outside of Greenland and Antarctica will use region-dependent projection (e.g., UTM).

TIDAL DISPLACEMENT

Differential tidal displacement products will be produced by differencing pairs of interferograms over the ice shelves and grounding lines. This differencing approach cancels the horizontal motion (assumed constant) common to both interferograms, leaving only the double-differenced, time-varying, vertical tidal displacement, which indicates the location of the grounding line/zone, i.e., the place where ice detaches from the bed and starts becoming afloat in the ocean waters (Rignot et al., 2011b; Scheuchl et al., 2016). Although this technique is generally applied to phase-only data, in the presence of very high strain rates it is possible to apply the technique on range offsets with a reduced level of precision in determining the grounding line position and in detecting vertical displacements (Joughin et al., 2016).

GLACIER ESTIMATES

The mission will collect an unprecedented volume of data to measure glacier velocities in regions outside of Greenland and Antarctica. The steep terrain where many of these glaciers exist, however, present chal-

TABLE 6-3. PIXEL CLASSES FOR ACTIVE CROP AREA BASED ON PRIOR AND CURRENT DETERMINATION

		PRIOR DETERMINATION	
		0	1
Current determination	0	Not a crop (class 1)	Fallow (class 2)
	1	Newly active (class 3)	Active (class 4)

lenges (e.g., glaciers lying in radar-shadowed regions) that make it difficult to quantify what fraction of glaciers can be successfully mapped; prior measurements indicate a relatively high likelihood of success for many regions (Burgess et al., 2013). As a result, glaciers are a mission goal rather than a requirement, requiring no formal validation. Thus, the focus of this document is on producing ice-sheet velocity measurements. These algorithms, however, are directly applicable to mapping glaciers. Actual implementations of production processors might require some modification for specific projections and other region dependent data. Hence, throughout the remainder of the document where ice-sheet velocity mapping is referred to it is with the understanding that the text is equally applicable to glaciers; any place where this might not be the case will be so noted.)

6.6.2 Implementation Approach for Algorithm

The implementation approach for estimating ice velocities uses speckle tracking and interferometric phase to compute the velocities.

QUANTITIES USED IN VELOCITY ESTIMATION

Velocity estimates are derived using either interferometric phase or speckle-tracked matches as described below. Here we define the notation used for the quantities that go into the velocity estimation equations.

RAW SPECKLE TRACKED OFFSETS

At a given set of range-azimuth coordinates, (ρ_1, s_1) , in the reference SLC (first image acquired), cross correlation is used to locate same point, (ρ_2, s_2) in the second SLC, which is in non-integer values. The raw range and azimuth offsets, (δ_ρ, δ_s) , are given by

$$\delta_\rho = \rho_2 - \rho_1 \text{ and } \delta_s = s_2 - s_1 \quad 6.6-1$$

RAW INTERFEROMETRIC PHASE

Given to co-registered SLCs, I_{1-1} and I_{1-2} , the phase of the interferogram is given by

$$\phi_w = \text{Arg}(I_1 I_2^*) \quad 6.6-2$$

which is only known modulo 2π . Thus, a phase unwrapping algorithm is applied to determine the unwrapped phase, ϕ .

CALIBRATED OFFSETS AND PHASE

The interferograms and range offsets also contain information about the topography, with sensitivity determined by the baseline. The imaging geometry will introduce additional displacements unrelated to surface motion. These differences can be corrected using the orbit and timing information. Here we encapsulate this information (i.e., state vectors, range delays, and any other ancillary information) into vectors, \mathbf{o}_1 and \mathbf{o}_2 , for the first and second images, respectively. With this information, then signals other than those related to surface motion can be removed to produce the surface-displacement only component of the range offset as

$$\tilde{\delta}_\rho = \delta_\rho - f_\rho(\mathbf{o}_1, \mathbf{o}_2, z) \quad 6.6-3$$

Note here we assume the offsets have been scaled from pixels to meters. As our purpose here is to define terms rather than to provide the details of the corrections, which are provided elsewhere, here we have bundled the geometry, baseline, and elevation dependent corrections in a scalar function f_ρ . Similarly, we can correct the azimuth displacements as

$$\tilde{\delta}_s = \delta_s - f_s(\mathbf{o}_1, \mathbf{o}_2) \quad 6.6-4$$

The unwrapped interferometric phase, ϕ , requires similar correction such that

$$\tilde{\phi} = \phi - f_\phi(\mathbf{o}_1, \mathbf{o}_2, z) \quad 6.6-5$$

Note this correction for phase assumes that at least one point of known speed is used as control point to determine the unknown $2-\pi$ ambiguity associated with phase unwrapping. Such control points are routinely used in ice-sheet velocity mapping (Joughin et al., 2010b; Rignot et al., 2011a).

VELOCITY ESTIMATES AT A POINT

The following subsection describes how velocity is estimated at each point. Note all equations are computed assuming the look vector lies in a plane orthogonal to the satellite track (e.g., small squint). These equations have been widely used with data from a variety of sensors, with no issues thus far. The imaging geometry for NISAR has low squint, so these equations should be similarly valid. As synthetic products become available, we will examine the validity of this assumption given the more rigorous NISAR error requirements (< 1 m/yr). Should this assumption not hold, then a transformation to a squinted coordinate system will be applied to the equations below. Such a transformation, however, does not change any of the underlying principles described below, nor have an impact on the viability of the algorithms, which are all well tested.

ICE VELOCITY DERIVED FROM SPECKLE TRACKING ALONG A SINGLE ORBIT TRACK

Speckle tracking provides two components of the three-component velocity vector: the along-track horizontal component and the line-of-sight component, which mixes vertical and horizontal motion (Figure 6-11). Although there is a component of the vertical velocity directed toward or away from the ice-sheet surface, this motion generally is small enough (< 1 m/yr) that it can be ignored or estimated independently. Instead, much of the vertical motion is assumed to be due to surface-parallel flow (i.e., a particle on the surface flowing along the surface gradient; Joughin et al., 1996). If the slope is known and surface-parallel flow can be assumed, the line-of-sight component can be resolved into horizontal and vertical components.

The line of sight displacement is given by

$$\tilde{\delta}_\rho = \Delta g \sin(\psi) - \Delta z \cos(\psi) \quad 6.6-6$$

where ψ is the local incidence angle (with respect to an ellipsoidal Earth), and Δz and Δg are the vertical and ground-range displacements, respectively. Solving for the horizontal displacement yields

$$\Delta g = \frac{\tilde{\delta}_\rho}{\sin(\psi)} + \Delta z \cot(\psi) \quad 6.6-7$$

Assuming surface parallel flow, the vertical displacement is given by

$$\Delta z = \tilde{\delta}_s \frac{\partial z}{\partial s} + \Delta g \frac{\partial z}{\partial g} \quad 6.6-8$$

Combining these two equations yields

$$\Delta g = \frac{\frac{\tilde{\delta}_\rho}{\sin(\psi)} + \tilde{\delta}_s \cot(\psi) \frac{\partial z}{\partial s}}{1 - \cot(\psi) \frac{\partial z}{\partial g}} \quad 6.6-9$$

Using this equation and the azimuth-offset estimate the velocities in the radar-determined horizontal coordinates are given by

$$v_g = \frac{\Delta g}{\Delta T} \text{ and } v_s = \frac{\tilde{\delta}_s}{\Delta T} \quad 6.6-10$$

Equation 6-6.13 gives the horizontal ice velocity in the radar-determined coordinates, but the final estimate is produced in the projection-determined xy-coordinate system (Figure 6-11). The rotation angle of the radar coordinates with respect to north is given by

$$\alpha_r = \text{atan2} \left(\frac{ds}{dlat}, \frac{dg}{dlat} \right) \quad 6.6-11$$

The rotation angle relative to north for a point (x_{PS}, y_{PS}) in polar stereographic coordinates is given by

$$\alpha_{PS} = \text{atan2}(y_{PS}, x_{PS}) \quad 6.6-12$$

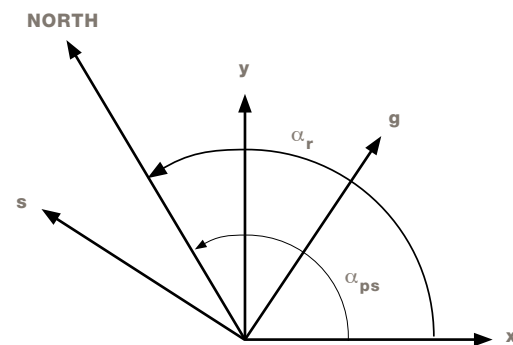


FIGURE 6-11 Radar- and projection-determined coordinate systems and their rotation angles relative to north.

Horizontal velocities are then determined by rotating to the polar stereographic system as

$$\begin{bmatrix} v_x \\ v_y \end{bmatrix} = \begin{bmatrix} \cos(\alpha_{ps} - \alpha_r) & \sin(\alpha_{ps} - \alpha_r) \\ -\sin(\alpha_{ps} - \alpha_r) & \cos(\alpha_{ps} - \alpha_r) \end{bmatrix} \begin{bmatrix} v_g \\ v_s \end{bmatrix} \quad 6.6-13$$

Note the polar-stereographic coordinate system preserves angles but has a latitude-dependent scale distortion. While locations are posted in polar-stereographic coordinates, which are subject to this distortion, velocity vectors are posted in meters/year with no scale distortion.

ICE VELOCITY DERIVED FROM SPECKLE TRACKING AND INTERFEROMETRY ALONG SINGLE ORBIT TRACK

In areas where interferometric fringes are noisy or aliased so they cannot be unwrapped, speckle tracking provides a reasonable estimate. If data are available only along a single orbit track and the phase can be unwrapped, then a hybrid estimate can be derived (Figure 6-12). In this case, substituting the range displacement given by the offsets ($\tilde{\delta}_p * \Delta_p$) for the equivalent displacement in phase ($\lambda\tilde{\phi}/4\pi$) in Equation 6.6-9 yields the surface-parallel-flow approximated ground range displacement as

$$\Delta g = \frac{\frac{\lambda\tilde{\phi}}{4\pi\sin(\psi)} + \delta_s\Delta_s\cot(\psi)\frac{\partial z}{\partial s}}{1 - \cot(\psi)\frac{\partial z}{\partial g}} \quad 6.6-14$$

Substituting this quantity into Equations 6.6-10 and 6.6-13 yields the horizontal velocity vector in polar-stereographic coordinates.

ICE VELOCITY DERIVED FROM INTERFEROMETRY FROM CROSSING ORBITS WITH SURFACE-PARALLEL FLOW

When data from crossing ascending/descending orbits are available the surface-parallel flow assumption can be used to estimate horizontal components of velocity (Joughin et al., 1998; Mohr et al., 1998). Geometrically, this makes this 3-D problem a 2-D problem by assuming the velocity vector lies in tangent-plane to the ice surface. In this case, using phase from ascending and descending passes, the horizontal components of the velocity vector are given by

$$\begin{bmatrix} v_x \\ v_y \end{bmatrix} = (\mathbf{I} - \mathbf{ABC})^{-1} \begin{bmatrix} \frac{\lambda_a\tilde{\phi}_a}{4\pi\Delta T_a\sin(\psi_a)} \\ \frac{\lambda_d\tilde{\phi}_d}{4\pi\Delta T_d\sin(\psi_d)} \end{bmatrix} \quad 6.6-15$$

Where

$$\mathbf{A} = \begin{bmatrix} \cos\beta & \cos(\alpha + \beta) \\ \sin\beta & \sin(\alpha + \beta) \end{bmatrix}, \quad 6.6-16$$

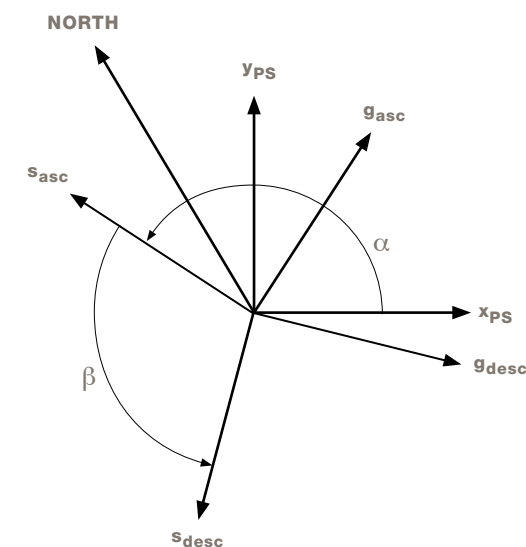
$$\mathbf{B} = \left(\frac{1}{\sin\alpha}\right)^2 \begin{bmatrix} 1 & -\cos\alpha \\ -\cos\alpha & 1 \end{bmatrix}, \text{ and } \quad 6.6-17$$

$$\mathbf{C} = \begin{bmatrix} \frac{\partial z}{\partial x}\cot(\psi_a) & \frac{\partial z}{\partial y}\cot(\psi_a) \\ \frac{\partial z}{\partial x}\cot(\psi_d) & \frac{\partial z}{\partial y}\cot(\psi_d) \end{bmatrix}. \quad 6.6-18$$

In the equations, quantities are as defined above with subscripts *a* and *d* to indicate whether they are from an ascending or descending pass, respectively. The angles α and β are defined in Figure 6-12. The incidence angles ψ_a are ψ_d are defined relative to an ellipsoidal Earth. A detailed derivation of these equations is given by Joughin et al. (1998).

FIGURE 6-12

Definition of angles used in the computation of horizontal velocities from ascending and descending orbits. The angle between the polar stereographic x-axis and the local along-track direction is denoted by α and the angle between the ascending and descending along-track directions by β .



ICE VELOCITY DERIVED FROM SPECKLE TRACKING FROM CROSSING ORBITS WITH SURFACE-PARALLEL FLOW

As described above, the ionosphere may introduce unacceptably large errors in some azimuth offset estimates. Range offsets are much less sensitive to ionospheric errors, so when range offsets are combined from crossing orbits, they can produce far less noisy velocity estimates. Such horizontal velocity estimates can be determined from range-offsets with the same methods as for interferometric phase. This measurement is made by replacing $(\lambda_a\tilde{\phi}_a)/4\pi$ and $(\lambda_d\tilde{\phi}_d)/4\pi$ in Equation 6.6-15 with $\tilde{\delta}_{p,a}$ and $\tilde{\delta}_{p,d}$, where the *a* and *d* subscripts indicate the offsets for the ascending and descending orbits, respectively.

ICE VELOCITY MOSAICKING

The sections above describe how to measure velocity at a point given the relevant phase or offset data. Rather than point measurements, continental-scale mosaics stitched together from data derived from hundreds to thousands of SAR image pairs are required for ice sheets. Such algorithms are relatively mature and ice-sheet wide mosaics have already been produced from earlier sensors (e.g., Figure 6-13; Joughin et al., 2010a; Rignot et al., 2011a). While providing a

major leap forward in our understanding of ice sheet behavior, products from existing sensors are limited in accuracy by insufficient data collection from instruments not optimized for this type of mapping. Temporal resolution of these products is also limited by a dearth of data (i.e., it took 20 years of the data from several SARs to produce a gap-free Greenland mosaic). Thus, by routinely imaging the ice sheets NISAR will greatly improve the coverage, accuracy, and spatio-temporal resolution of ice velocity estimates to help improve our understanding of how the ice sheets will contribute to sea level change.

COMBINED ESTIMATE

As described above, there are multiple methods for determining velocity at each point using phase or offsets from single or crossing orbit tracks. To apply these methods, a mosaicking algorithm is needed to produce a large-scale mosaic, using the best data available at each point. Here we describe an approach to mosaicking the data based on a specific implementation of a processor, which implements all of the algorithms described above to produce a mosaic (Joughin, 2002). Variations on this approach exist (Mouginot et al., 2017).

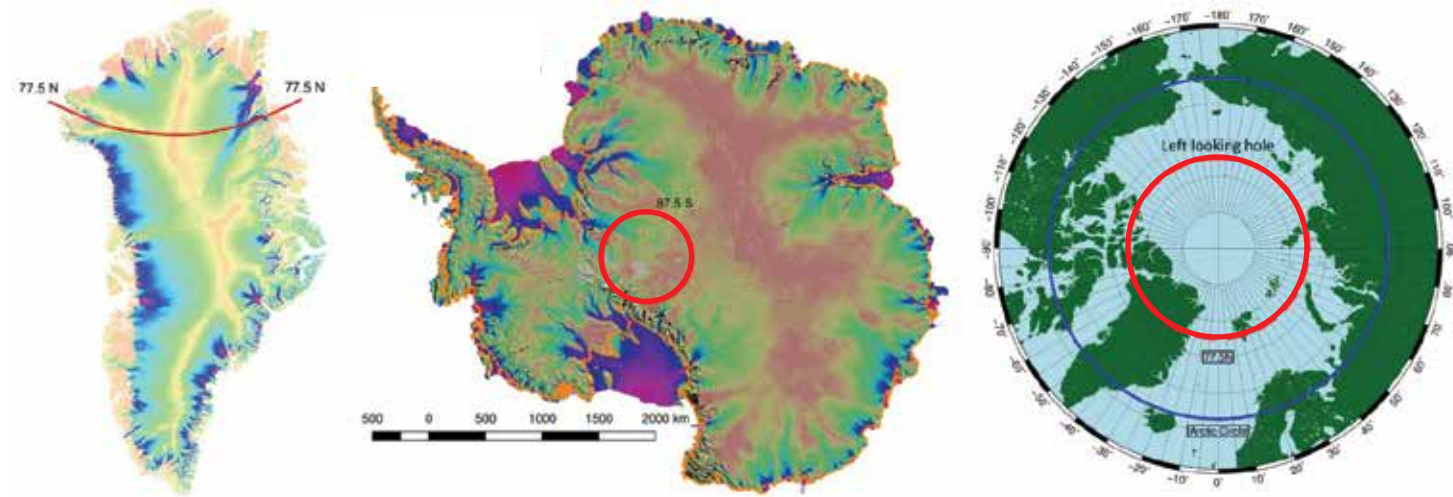


FIGURE 6-13

Example of the types of Level 3 products that will be produced for the cryosphere using the algorithms described in this document. (Left) Greenland example with slow moving interior velocity and fast moving glaciers derived from ALOS PALSAR and RADARSAT-1 tracks. (Middle) Antarctic with ice sheet interior and fast ice streams example from RADARSAT-2, ALOS PALSAR, Envisat ASAR and ERS-1/2 tracks using speckle tracking. Latitudes from the pole to red line in each image will not be observed with the left-looking mission. Errors in these maps do not meet NISAR requirements. With 30+ acquisitions a year along each track and phase data, NISAR will meet its stated requirements. (Right) Coverage at the north pole. Because NISAR will be left-looking the northernmost part of Greenland will not be imaged. Sea ice outside the red circle will be imaged, but not inside.

In producing such a mosaic, the algorithm proceeds by looping over the images to be mosaicked. If an estimate is being derived using data from along a single track (i.e., azimuth offsets are used), the algorithm next identifies where the corresponding region in the output grid lies, and loops over the corresponding points in the output grid. It then interpolates the relevant offset or phase data from the source image, which is in radar coordinates. Where this interpolation is successful and there are valid data, the velocity components, v_x and v_y , are determined using Equations 6.6-10, 6.6-13, and 6.6-14. At each point, the algorithm uses phase data if available for the range component, and if not, then range-offset data. After looping through all points in the sub-region of output grid, the algorithm proceeds to the next image.

Where crossing orbits are used, the algorithm cycles through all of the descending (arbitrarily decided; ascending first will work just as well) images. For each of these descending images, the program then loops over all of the ascending images to determine if there is overlap. If there is overlap, then the code identifies where the region of overlap falls in the output grid. Next, the algorithm loops over these output points and computes the surface-parallel-flow approximated velocities using Equation 6.6-15, using either phase or range-offset data. Above we have assumed that where phase data are available, they are available for both

ascending and descending passes and, if not, then range-offset data are available for both passes. There can be cases, however, where range-offset data only are available from one track direction and phase data from the other. In this case, there is nothing to preclude using Equation 6.6-15 with range-offset from one track direction and phase data from the other.

As just described, for each pair or crossing pair the algorithm estimates, v_x and v_y , at each point in the output grid. For coastal velocities, there may only be a single estimate for most points in the output grid. By contrast, for annual velocities, thirty or more independent estimates may be averaged for each point in the final output. Thus, as each point estimate is derived using image pairs, the individual estimates are weighted by w_x and w_y , summed in an output buffer. The final velocity estimate in the x-direction is derived from N individual estimates given by

$$v_x = \sum_{i=1}^N f_i w_{x,i} v_{x,i} \quad 6.6-19$$

and a similar expression applies for v_y . Note f_i is an additional feathering weight as described below. If we assume the errors are unbiased (zero mean), then the weights must sum to one. In this case and assuming the individual estimates are independent, the minimum error (σ_x^2) is given by $f_i=1$ and weights

$$w_{x,i} = \frac{1}{\sigma_{x,i}^2} \left(\sum_{i=1}^N \frac{1}{\sigma_{x,i}^2} \right)^{-1} \quad 6.6-20$$

If feathering (see below) is applied ($f_i \neq 1$) then

$$f_i w_{x,i} = \frac{f_i}{\sigma_{x,i}^2} \left(\sum_{i=1}^N \frac{f_i}{\sigma_{x,i}^2} \right)^{-1} \quad 6.6-21$$

In practice, the mosaicking algorithm doesn't know how many estimates are available at any given point in the output grid. As a result, it weights each estimate $v_{x,i}$ by $f_i/\sigma_{x,i}^2$ and sums the result in the output buffer. At the same time, a separate buffer is maintained and the weights are summed $\left(\sum_{i=1}^N \frac{f_i}{\sigma_{x,i}^2} \right)$. When all data are included in the mosaic, the weighted average is completed by normalizing the final result by the summed weights.

The error estimate for the weighted average is given by

$$\sigma_x^2 = \sum_{i=1}^N f_i w_{x,i} \sigma_{x,i}^2 = \left(\sum_{i=1}^N \frac{f_i}{\sigma_{x,i}^2} \right)^{-2} \sum_{i=1}^N \frac{f_i}{\sigma_{x,i}^2}. \quad 6.6-22$$

As a result, error estimates are cumulated by summing $f_i/\sigma_{x,i}^2$ in error buffer, and the results are normalized as indicated in Equation 6.6-22.

FEATHERING

While the weighting method described above is designed to achieve a minimum variance estimate, it may be sub-optimal with respect to other factors. In particular, a discontinuity at a data-take boundary is a non-physical result and can lead to problems when attempting model inversions. As a result, additional weighting is employed to "feather" the data and redistribute local errors over a wider range. This additional weighting function is used to apply a linear taper from the edge of the data to some distance from the edge. This is accomplished by applying a distance transform that gives the distance, d , at any point in the interior to the nearest point on the image edge. The feathering function is then given by

$$f(d) = \begin{cases} \frac{d}{f_i} & 0 \leq f_i \leq 1 \\ 1 & f_i \geq 1 \end{cases}. \quad 6.6-23$$

This is similar to the feathering scheme used for the SRTM mosaicking. Note the distance transform is applied to the source data, so the feather length, f_i , is in radar coordinates. This function is applied as indicated by Equation 6.6-19.

As an example, if the feather length is 20, then pixels on the edge are weighted by 0, pixels within 20 pixels of the edge are weighted linearly with distance from the edge over a range from 0 to 1, and interior pixels by 1. The feathering weights are used to update the initial weights in the temporary buffers, and the results are added to the weight buffers as indicated in Equation 6.6-19.

6.6.3 Planned Output Products

The Science Team shall produce the following ice-sheet demonstration/validation products:

- Ice sheet velocity products at time scales of 12 days to a year for validation purposes. Examples of such products are velocity maps covering the GPS validation sites, areas that overlap with coverage provided by other sensors, and regions of ice-free stationary areas (e.g., bedrock outcrops).
- Differential tidal displacement maps to validate grounding line requirements.
- Velocity estimates to validate the mountain glacier measurement goals.
- A limited set of demonstration products within budgetary limitations.

These products are designed to validate the L2 requirements, but not to completely fulfill them. While data will be collected to meet the requirements throughout the mission, the bulk of the processing to fully meet the requirements will be carried out by the scientific community at large, with funding external to the project.

6.7 CRYOSPHERE PRODUCTS – SEA ICE

The basic concepts of sea ice motion are position, displacement, and velocity. Displacement is the difference in position over time of an ice feature. Velocity is derived from displacement during the measured time interval. Sea ice moves with the general ocean circulation forced by winds and currents but also at the smaller scales of individual floes, aggregates of floes, and the formation of leads (or open water). Ice motion controls the abundance of thin ice and surface exchange processes including heat flux between the ocean and atmosphere and ice production. Sea ice is materially considered to be a brittle solid with some plasticity and its motion is spatially discontinuous forced by winds and currents, which results in both lead formation where new ice is formed and deformation that produces ridges and complex motions including rotation, shear, and vorticity.

6.7.1 Theoretical Basis of Algorithm

In this section, we describe a fundamental concept of sea ice parameters that explains the role of sea ice motion and deformation from SAR.

SEA ICE THICKNESS DISTRIBUTION

The sea ice thickness distribution is probably the single most important parameter of sea ice and its role in the global climate system. The thickness distribution includes both dynamic and thermodynamic sea ice processes. Over both small and large scales, several types of sea ice may be present as an aggregate containing a range of thickness due to varying stages of growth and mechanical deformation. Thorndike et al. (1975) conceived of the temporal development of ice thickness distribution, $\delta g / \delta t$, which can be written as:

$$\delta g / \delta t = -\delta (fg) / \delta h + \text{div} (vg) + \Phi$$

As summarized by Haas (2010), the three terms that contribute to the thickness distribution are as follows: $f(h, x, t) = dh/dt$ is the thermodynamic growth or melt rate of ice of thickness h at a location x and time t , v is the ice drift velocity vector, and Φ is the so-called redistribution function. In general, the thinner and thicker components of the thickness distribution arise from dynamics and the median values from thermodynamics (Figure 6-14, upper panel). Thermodynamic growth is faster for thin ice than thick due to steeper temperature gradients between the ocean and atmosphere (Figure 6-14 (lower left)). The presence of snow reduces ice growth and pressure ridges (keels) may exceed a depth that will lead to melt if the depth extends down into the warmer ocean layers.

The second term in the equation above represents divergence and advection due to ice motion, as forced by winds and currents. Away from the coast or at the margins of the central ice pack itself, ice will drift freely, and drift direction and speed are closely related to geostrophic wind (outlined below). Divergence generates cracks, leads, or polynyas, all areas of open water where new ice will form. Divergence changes the sea ice fraction of an area or grid cell, removing ice of finite thickness and causing a delta signal at zero thickness in the thickness distribution (Figure 6-14).

The last term in the above equation is the redistribution function describing how thin ice is deformed and transformed into thicker ice classes from both convergence and deformation. It is the most critical term to understand the temporal development of the thickness distribution and also most unknown, since it depends on fracture mechanics and other factors including small-scale ice properties, friction between ice blocks, snow and ice interfaces and deformation energy and length scales. Thinner ice will deform more readily than thicker ice (Figure 6-14 (lower right)). Within the redistribution term, ice strength and rheology are of great importance. Models were derived that consider ice rhe-

ology as a plastic or viscous-plastic (Hibler, 1979; Coon, 1980). The rheology describes a viscous flow of an ice field, with plastic deformation once ice concentration and internal ice forces exceed a certain threshold, driven by winds and currents. Contemporary models include coupled atmosphere-ice-ocean conditions (e.g., Zhang et al., 2000; Holland et al., 2006).

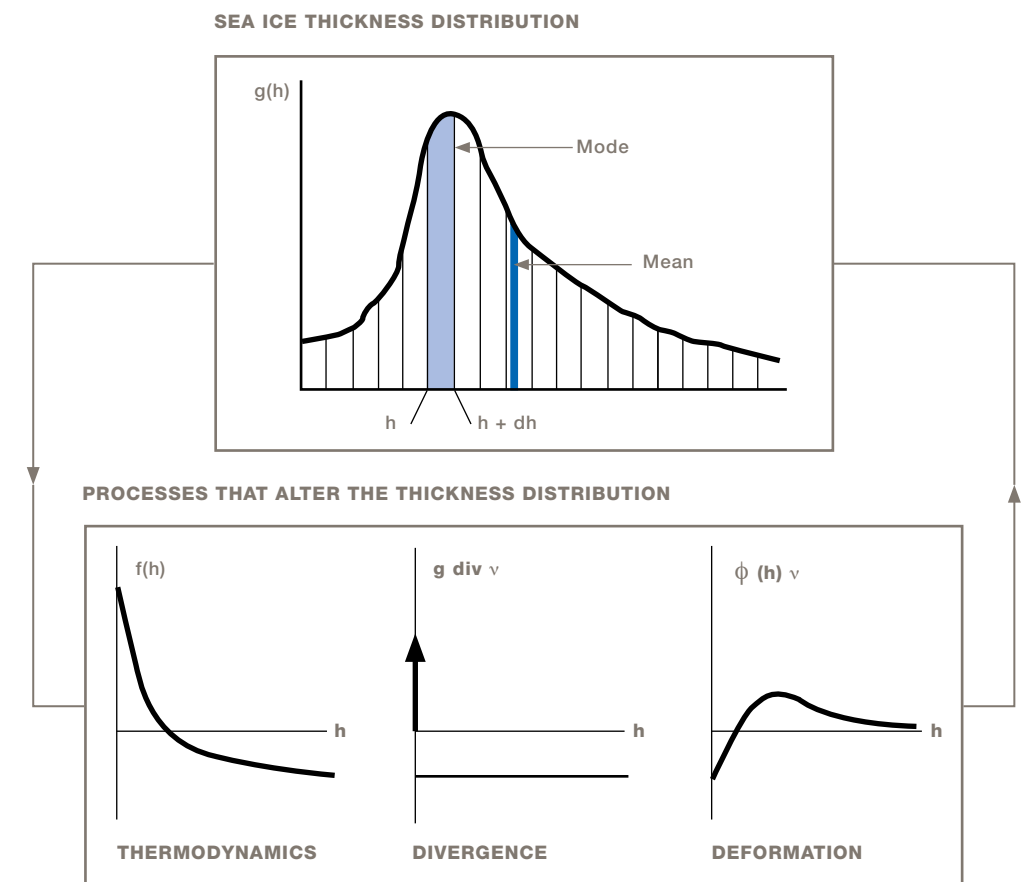
ICE MOTION AND OBSERVATIONAL BASIS

Sea ice moves in response to wind and ocean currents. Large-scale circulation of sea ice (Figure 6-15) determines the advective part of the ice balance (i.e., the regional exchange of sea ice and export to lower-latitude oceans). This knowledge provides a velocity boundary condition on the ocean surface, while the small-scale motion describes the interaction of indi-

vidual floes, aggregation of floes, and the formation of leads (areas of open water) and ridges.

The mechanical response of the ice cover to large-scale atmospheric and oceanic forcing is concentrated along fractures up to kilometers in widths, and lengths that can span thousands of kilometers. Rather than deforming continuously throughout the ice cover, sea ice moves and deforms due to fractures/cracks created by brittle failure (see Figure 6-15). When openings along these cracks expose the warm underlying ocean to the frigid winter atmosphere, heat exchanges are large and local brine production increases as new ice grows and seawater freezes. Convergence or closing of pack ice forces the ice to raft or pile up into pressure ridges and to be forced down into keels, increasing the ice-ocean and ice-atmosphere drag. Typically, a distribution of

FIGURE 6-14 Illustration of the contribution of the different terms and processes in the equation above to the ice thickness distribution. After Haas (2010) and Thorndike et al. (1975).



openings and closings is formed when collections of ice floes with irregular boundaries are sheared relative to one another. Over time, the redistribution of ice associated with deformation alters the volume of sea ice and heat that can be stored within a given area of an ice-covered ocean. Together with thermodynamic growth, these dynamic processes shape the unique character of the ice cover's thickness distribution and profoundly impact the strength of the ice and its thermal properties over a wide range of temporal and spatial scales. Accurate quantification and simulation of the relative contributions of thermodynamics and dynamics to ice thickness distribution are thus crucial for understanding the behavior and the vulnerability of the Arctic ice cover in a warming climate.

SEA ICE DEFORMATION

Summarizing from Kwok (2001) and Holt et al. (1992), multiple forces act on sea ice, which include the Corio-

lis force, water drag, air drag, gradients due to the tilt of the sea surface, and the ice stress gradients resulting from floe-to-floe interactions and stress variations within individual floes. In the Arctic Ocean, where sea ice motion is constrained by continental boundaries, strong interactions between ice floes take place and influence the basin-wide circulation and deformation/convergence of the ice cover. In contrast, ice motion around Antarctica is mostly divergent (Kottmeier et al., 1992), with a northerly drift component toward the surrounding open ocean.

Mechanical deformation results in divergence, convergence, and shear of the ice pack. The relative motion of floes creates areas of open water and significantly affects air-ice-ocean interaction. In winter, newly opened leads are the source of new ice growth, brine rejection to the ocean, and rapid heat transfer from the ocean to the atmosphere. Areas of open water and thin ice dominate the net heat flux into the atmosphere and brine flux into the ocean. The stresses by which

ice floes resist motion are related to the strain rate, the spatial variation in ice velocity. Closings of the ice cover cause ice to raft and to pile up into pressure ridges and forced down into keels, increasing the ice-atmosphere and ice-ocean drag.

These spatial differences in relative motion exist on small floe-floe scales but also may extend over considerable distances, at both linear and nonlinear scales. This complex interplay of thermodynamics and dynamics maintains the character of the thickness distribution of the Arctic Ocean ice cover. These processes are typically included in aggregate form in sea ice dynamics models. An accurate ice dynamics model must reflect the appropriate portions of these processes as well as their beginning and end states. Each of these processes alters the sea ice thickness distribution in a unique manner. SAR-derived ice motion and deformation have been fundamental in providing measurements of spatial distribution and temporal development of these processes.

After Kwok (2001), the basic forms of sea ice deformation are divergence, vorticity, and shear, as below:

$$\nabla \cdot u = \frac{1}{2}(u_x + v_y),$$

$$\zeta = \frac{1}{2}(u_x - v_y),$$

$$e = \left[(u_x - v_y)^2 + (u_x + v_y)^2 \right]^{\frac{1}{2}}$$

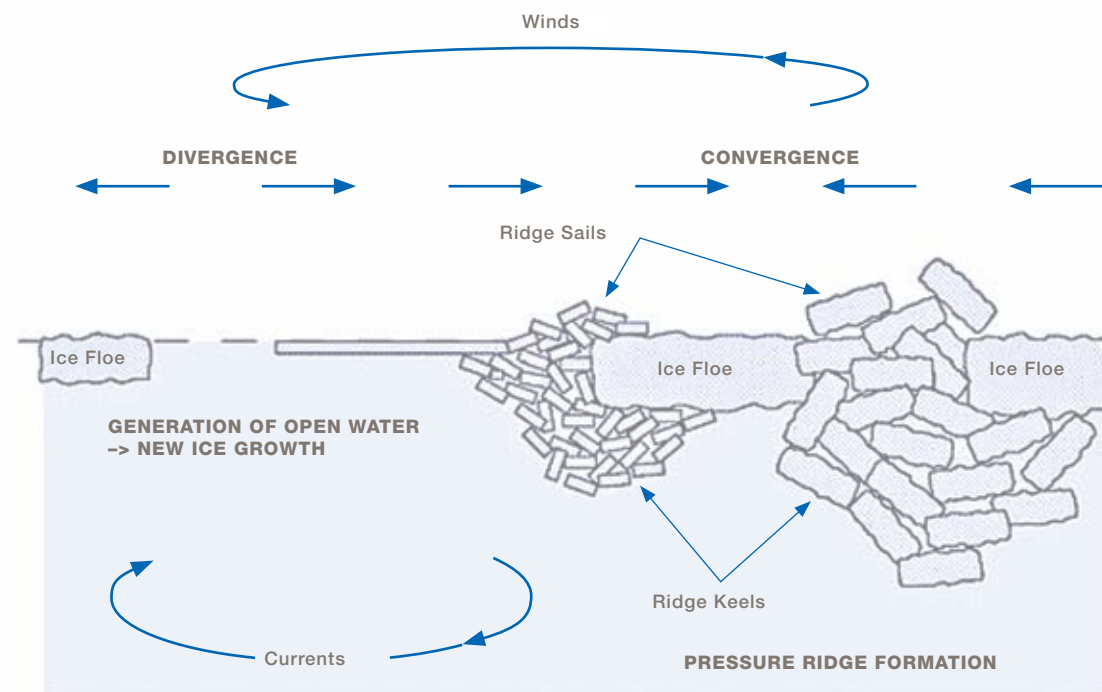
u_x, u_y, v_x, v_y are the spatial gradients in ice motion computed using a contour integral around the boundary of an area of ice, or in terms of SAR, a grid cell (~10 km on a side). The boundaries are defined by the line segments connecting the four vertices of a cell.

Divergence, $\nabla \cdot u$, is a measure of area change. Vorticity, ζ , is the principle measure of rotation. Shear, e , is the scalar magnitude of shear. Figure 6-16 is a schematic of motion and deformation concepts from a sequential image pair.

When combined with thermodynamics, i.e., ice growth and melt, how do measurements of dynamics contribute to the sea ice thickness distribution? That ice exists as an aggregate composed of multiple forms of sea ice in terms of thickness and age. Motion or velocity, distance traveled over time, simply indicates that ice is forced by wind and currents and is not stationary in space. When two pieces of ice move apart from each other, an opening or lead is formed, exposing the ocean directly to the atmosphere. In winter, ice grows rapidly within the lead as heat is lost from the relatively warmer ocean to the colder atmosphere. In summer, the open water will be warmed preferentially to the ice by solar radiation, enhancing ice melt. This can occur within a defined area or cell or between adjacent cells and is defined as a fractional increase in area. When two pieces of ice are forced together, this represents a loss in area within a cell or between adjacent cells. This generally represents a ridging process, where the thinnest components of sea ice will preferentially break-up and be piled up into pieces which stack up both on

FIGURE 6-15

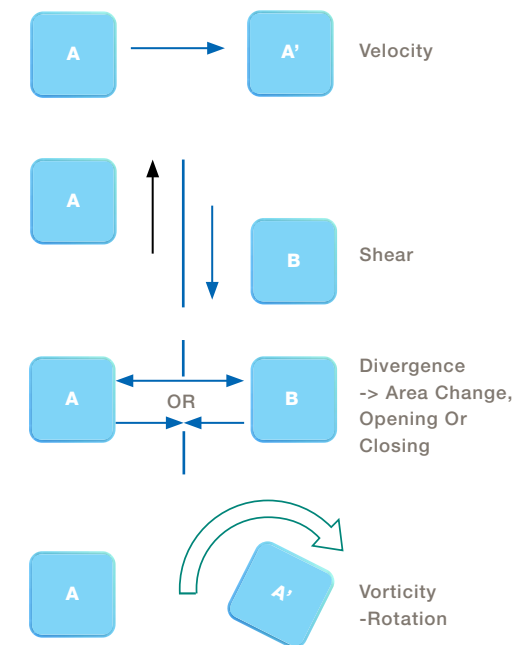
Illustration of the processes that dynamically (by divergent or convergent ice motion and deformation) modify the ice thickness distribution. (After Haas, 2010.)



ICE MOTION, DEFORMATION

FIGURE 6-16

Illustration of basic forms of ice motion over time of a single ice floe (velocity, vorticity) and deformation of a floe or adjoining floes that undergo shear or divergence (results in opening or closing).



top and also below the remaining ice floe. Shear and vorticity represent other components of deformation and have less effect on the overall sea ice thickness distribution but may be closely related to adjacent divergence.

Measurement of small-scale sea ice motion is challenging because of the spatial and temporal scales spanned by the processes responsible for producing its variability. The relative motion between ice floes along narrow (meters to kilometers) fractures requires imaging sensors with not only high spatial resolution but also short sampling intervals. Ice deformation at sub-daily time scales associated with tidal forcing or inertial effects are becoming more prominent as the ice cover thins. Presently, basin-scale fields of sea ice motion at different spatial resolutions can be derived from tracking common ice features in a variety of satellite imagery. Of particular interest are those from satellite SAR imagery. SARs are uniquely suited for small-scale observations of sea ice cover because of their spatial resolution (tens of meters), their day/night coverage, and their ability to see through clouds. Temporal resolution, however, remains an issue because orbiting satellite SARs are limited in their ability to cover the same area repeatedly. Thus, though sub-daily sampling is currently not achievable, it remains a sampling issue due to limitations of repeat coverage from orbiting satellites.

EULERIAN AND LAGRANGIAN ICE MOTION

There are two general ways of sampling a sea ice motion field: Eulerian and Lagrangian. In the Eulerian specification, the motion field is sampled using specific grids or individual ice particles in the space through which the ice moves as time passes between pairs of observations and then is repeated by resetting the grid or individual ice particles in the next pair of observations. The Eulerian approach provides velocity and deformation over a single pair of observations. With the Lagrangian specification, in contrast, the motion field is

sampled and followed over time starting with an initial grid or individual ice particles through multiple observation pairs, producing an array of trajectories as the particles move through space and time. This particle array has the advantage of being able to provide sampling of the motion field as well as a time record of the deformation of material elements within the ice cover (Kwok and others, 1995; Stern and others, 1995). Since sea ice is a brittle solid, it does not deform continuously throughout the ice cover; rather, sea ice moves and deforms due to fractures and cracks created by brittle failure. As local ice strength is determined by weaknesses in the fracture patterns that advect with the ice cover, the Lagrangian approach is more appropriate where details of ice kinematics and the openings and closings of the ice cover, for understanding ice mechanics and surface heat balance, are of interest. However, this observational requirement adds complexity to the ice-motion tracking process and quality checking. In addition to recording the location history of the array at each time-step, the connectivity of the particles that define the material elements has to be maintained. Both Eulerian and Lagrangian type products have been generated previously using Radarsat-1 and Envisat ASAR for the Arctic and limited portions and times of the Southern Ocean sea ice cover. For NISAR, the focus for development and post-mission validation will be on the use of Eulerian tracking.

For a given winter, grid cells with initial dimensions of 5 of 10 km on a side are used to sample the motion and deformation of the ice cover. Past results show that basin-scale deformation of the divergence, vorticity, and shear of the ice cover may extend across a significant distance of the sea ice cover. The deformation fields indicate linear kinematic features (LKFs) that characterize the opening, closing, and shear of the ice cover. The high-resolution ice motion vectors derived from this approach have a data quality comparable to that from buoy drifts (~0.1 cm/s) and have provided an unprecedented level of spatial and temporal detail

of deformational features. On a routine basis, the location, coverage, and seasonal development of leads and ridges can be provided. Narrow fracture zones (up to kilometers wide) are long linear features that can extend for thousands of kilometers and these fracture patterns appear as oriented rather than random patterns from the kilometer scale to the scale of the Arctic basin. Lastly, we point out that most of the effort to date has focused on the western Arctic Ocean. Deriving complete maps of the Arctic Ocean as well as new motion/deformation mapping of the dynamic sea ice cover surrounding Antarctica will provide complete information on the motion and deformation of the detectable sea ice cover of both major sea-ice covered oceans for the first time.

6.7.2 Implementation Approach for Algorithm

The derivation of sea ice motion and deformation employs the use of feature tracking using cross correlation. Basin-wide seasonal sea ice motion fields are obtained using repeating image pairs obtained over a few day time separation.

BASIC SEA ICE MOTION CONCEPT

Following Holt et al. (1992), the fundamental concepts of ice motion are position, displacement, and velocity. Consider ice at a position x at time $t = 0$, at some later time the ice has moved to a new position $x(t+1)$. A displacement is the difference in the positions of an ice particle at two different times

$$u = [x(t_1 + 1) - x(t_1)] \quad 6.7-1$$

The average velocity over the intervening time interval $T = t_{t+1} - t_1$, is

$$v = \frac{u}{T} \quad 6.7-2$$

As described in Kwok et al., (1990) and Holt et al. (1992), the linear model of ice motion relates the mean ice velocity v of an ice field to the geostrophic wind

(Thorndike and Colony, 1992; Colony and Thorndike, 1986),

$$v = AG \quad 6.7-3$$

where v , the ice velocity, and G , the geostrophic wind, are vectors and consequently treated as complex numbers. The term A is a complex multiplier, giving the ratio of ice speed to wind speed and an ageostrophic drift angle θ (positive counterclockwise) from the wind vector to the ice vector. Typical values for the Arctic of (A , θ) range from (0.011, -18°) in summer to (0.008, -5°) in winter in relation to the mean wind speed (Thorndike and Colony, 1992). For the Weddell Sea, these numbers are 0.016 and $10-15^\circ$, respectively (Kottmeier et al., 1992). While the physical processes are many, on the time scales of days, more than 70% of the variance of the ice motion is explained by the geostrophic wind alone. As will be described in a later section, this relationship of ice motion and geostrophic wind is used in the ice motion algorithm to do the initial identification of the second of the image pair to be used for tracking, guided by weather data.

GEOLOCATION ERRORS

Following Holt et al., (1992) and Kwok and Cunningham (2002), the two primary sources of error in measuring ice motion with satellite imagery are absolute geographic position (e_g) of each image pixel and a tracking error (e_t), which is the uncertainty in identifying common features from one image to the next. The position error applies independently to each position in each image, i.e., a position is the true position plus an error of $x + e_g$. The tracking error e_t applies to a displacement observed between two images. If it is assumed that eg and et are each normally distributed with zero bias, have standard deviations σ_g and σ_t and are uncorrelated between two time-separated images A and B , the two errors can be treated separately. Including errors, an estimate of the displacement of an ice feature is given by

$$u = (x_b + e_{gB}) - (x_a + e_{gA}) + e_f \quad 6.7-4$$

The standard error in u has a zero mean and a variance of

$$\sigma_u^2 = 2\sigma_g^2 + \sigma_f^2 \quad 6.7-5$$

where σ_g and σ_f are uncertainties in the geolocation of the image data and the tracking of sea ice features from one image to the next. The error in velocity is σ_u divided by the time interval of displacement. Errors in the time interval are usually negligible.

Given two images, if the locations of an ice feature found in each image are close together, the geolocation errors between the two images are assumed to be correlated. The spatial differences between the two points are not dependent on geolocation error, so the error in displacement tends to $2\sigma_f^2$. When SAR displacement is compared to that of a drift buoy, buoy location errors must be also considered. In previous efforts, displacement errors between SAR and ice drift buoys were found to be on the order of 0.2 – 0.3 km, derived from sensor geolocation errors of 0.1 km, tracking errors from 0.1 – 0.3 km, and pixel resolutions from 0.05 – 0.1 km, not including error offsets in drift buoy locations. Currently, most sea ice drift buoys include the use of GPS, which significantly reduces location errors. The NISAR geolocation errors are also significantly improved from the previous sensors, so it is anticipated the errors in SAR-derived sea ice motion and deformation will be significantly improved compared to previous results.

NISAR SEA ICE MOTION RETRIEVAL ALGORITHM

The NISAR science team requirement is to produce Eulerian sea ice motion products due to their expediency in production, which requires a minimum of operator quality assurance and correction. It is expected at some point that Lagrangian products will also be produced

supported by additional funding, such as from NASA MEaSURES opportunities. The Lagrangian products are fundamentally equivalent in terms of the ice displacements but because these are generated based on observing and maintaining the original grid area over time even when the ice undergoes deformation, additional valuable products are generated.

There are several fundamentally key components of the NISAR mission that make it particularly valuable for deriving sea ice motion and deformation, that will lead to the derivation of uniquely valuable sea ice products. First, the longer frequency of L-band has been shown to highlight deformed ice preferentially compared to the long and extensive C-band SAR record. This is expected to provide improved and more accurate sea ice feature tracking in the winter and spring and importantly for a longer and more continuous period into the summer months, where ice surface features on C-band become less distinct due to surface melt. Next, the synoptic coverage of the Arctic and Southern Ocean sea ice covers during the entire duration of the mission will provide unprecedented SAR coverage of both polar regions that can be used for ice motion. Radarsat-1 provided annual ice motion mappings of much of the western Arctic but never complete and continuous coverage for multiple years over the entire Arctic. Ice motion of Antarctic sea ice from SAR was also previously limited to only 1-2 mappings for periods of a few months from the Ross or Weddell Seas. The sea ice motion mapping of the Southern Ocean from NISAR will be unprecedented and will enable a thorough derivation of the different ice dynamics from both polar oceans.

The algorithm to be used has been described in multiple publications based on the use of ERS-1 and primarily Radarsat-1 SAR imagery (Kwok et al., 1990; Holt et al., 1992; Kwok et al., 1995; Kwok and Baltzer, 1995;

Kwok and Cunningham, 2002) and will be modified to incorporate the NISAR image format and metadata. To summarize, the design includes comprehensive steps to locate image pairs using an ice motion estimator, for tracking ice in both the central pack and marginal ice zones using areal correlation and feature matching and displaying ice motion fields based on a grid system mapping to a polar stereographic projection. The ice motion estimator uses a linear ice drift model for image selection with potential overlap using geostrophic wind as input. The algorithm uses a combination of different filters at several stages of the tracking process to remove spurious or low quality vectors, based on correlation statistics. Clustering of the motion vectors is used to identify dominant modes of motion in the sampled field, whereupon the filtering process discards erroneous vectors by examining cluster centroids that are inconsistent with the dominant modes. Also, a smoothness constraint is applied to ensure the spatial consistency of the displacement field. A quality factor is assigned to each vector to give a quantitative indication of the quality of the derived vector. The filtering process in the algorithm attempts to optimize the ratio of good to bad vectors so that 95% of the motion vectors are accurate to the determined displacement error.

6.7.3 Planned Output Products

NISAR will produce ice motion products for the Arctic and Southern Oceans. It will also produce demonstra-

tion products of seasonal maps of sea-ice motion for the Arctic Ocean and Weddell Sea and export for the Arctic Ocean.

EULERIAN ICE MOTION PRODUCTS

- a. Displacement (x, y, km)
- b. Ice motion vector (direction, deg)
- c. Deformation (spatial variation of velocity): shear, divergence, vorticity

A seasonal examination of the Arctic region where there is a large density of sea ice drift buoys will be done each year for validation. This will be performed over a region of Antarctic sea ice cover if a sufficient number of sea ice drift buoys are present.

DEMONSTRATION PRODUCTS

- a. First product (Year1-Year2). Map of one full season of sea ice motion for the Weddell and Arctic sea ice covers.
- b. Second product (Year2-Year3): Map of one full season of sea-ice motion for the Southern Ocean and map of one full season of sea ice motion and export from the Arctic Ocean.

7 ERROR SOURCES

This section describes errors in the measurements that impact science performance. Understanding these sources of errors will help users interpret NISAR data. These errors can be related to instrument noise, geometric considerations, scattering behavior, or propagation effects, to name a few.

7.1 POLARIMETRIC ERROR SOURCES

The radiometric properties of a surface, represented by the observed backscatter amplitude and phase, are characterized through the radar backscattering cross section. The amount of energy scattered back to the radar depends on the detailed arrangements of scatterers within a resolution element and their electrical properties; so in general the cross section is dependent on the observation angle and environmental conditions. Since radar images are coherent, they exhibit “speckle” properties: even in a region with multiple distributed scatterers with uniformly constant radar cross section, each resolution element will exhibit amplitude and phase variations that differ wildly, such that the images appear to be spatially random from element to element. This natural variance, coupled with random noise sources in the radar system, requires describing radar cross section as a statistical process, using the covariances of the observed quantities.

The element-to-element random error from the radar system includes additive thermal noise in the radar system, and multiplicative noise from quantization, like- and cross-channel signal leakage, and ambiguities, which are ghosts of pulse echoes taken at a different place and time but show up in the data. Multiplicative

noise is by definition target-dependent, and therefore can be correlated with the signal of interest.

In polarimetry, we observe the covariances of like- and cross-polarization images and use these to infer properties of the surface. To reduce the natural variance of the covariance estimates, we typically must average data over a local region. Thus, to achieve good estimation performance at a desired resolution, the observations must be acquired at finer resolution to allow for such averaging. The number of independent resolution elements averaged is generally referred to as the number of looks.

Besides errors related to element-by-element random noise, the other major sources of error in polarimetry are systematic amplitude and phase fluctuations that vary over the image and potentially over time. These arise from uncertainties in the knowledge of the radar's system delays and losses, its antenna pattern or the pointing of the antenna pattern. To derive the radar cross section, the total “link budget” from signal transmission to backscatter to its reception must be quantified according to the radar equation, which involves these quantities. Thus, the radiometric accuracy requirements arising from the science requirements imply knowledge and stability requirements throughout the radar system.

Overall, the error in the radar backscatter measurements, $\Delta\sigma_{pq}$ ($pq=hh,hv,vv$), is a function of speckle, thermal noise, temporal variability of the backscatter, calibration errors (which in turn depend on pointing DEM errors) and area projection correction terms. An

expression for this error (in terms of the measurement parameters) is given by Hensley et al., 2013:

$$\Delta\sigma_{pq} = \left[\underbrace{\left(\frac{1}{\sqrt{N}} \frac{1}{\sqrt{N_{os}}} + \frac{1}{\sqrt{N}} \frac{1}{\sqrt{N_{oi}}} \frac{1}{SNR} \right)}_{\text{SPECKLE NOISE}} \sigma_{pq} + \underbrace{\frac{1}{\sqrt{N_{ot}}}}_{\text{THERMAL NOISE}} \Delta\sigma_{pq}(b) + \underbrace{\frac{1}{\sqrt{N_{ot}}}}_{\text{BACKSCATTER TEMPORAL VARIABILITY}} \Delta\sigma_c + \underbrace{\frac{1}{\sqrt{N_{ot}}}}_{\text{CALIBRATION ERRORS}} \Delta\sigma_c + \underbrace{\sqrt{\frac{A_{dem}}{A_{pix}} \frac{1}{\sqrt{N}} \frac{1}{\sqrt{N_{os}}}}}_{\text{AREA PROJECTION ERRORS}} \Delta\sigma_a \right]$$

where Table 7-1 defines the symbols:

TABLE 7-1. BACKSCATTER ERROR MODEL DEFINITIONS

Symbol	Definition
N	Number of spatial looks per observation
Not	Total number of observations
Nos	Observations with non-correlated speckle
Noi	Observations with correlated speckle
SNR	Signal-to-noise ratio
$\Delta\sigma_{pqt}$	Backscatter temporal variability
$\Delta\sigma_c$	Backscatter calibration error
$\Delta\sigma_a$	Backscatter area projection error
A_{dem}	Area of a pixel in DEM used for slope computations
A_{pix}	Area in a radar pixel

7.2 INTERFEROMETRIC ERROR SOURCES

As with polarimetry, random resolution element-to-element noise is introduced from speckle, thermal effects, and multiplicative noise sources. These are quantified by the interferometric correlation, which is the amplitude-normalized cross covariance of the interferometric observations. As with polarimetry, local averaging reduces this noise component.

The broader systematic effects on the phase difference are important in interferometry. Since it is a differential measurement, if the system is stable and the pointing is perfect over time, phase due to system delays or

antenna pattern will cancel in the phase difference. In practice the system will not be perfectly pointed, or the antenna patterns and system phases will vary over time. These differential phase effects typically have a different nature from those due to ground motions and are tied to the geometry to the spacecraft orbit, so they can often be mitigated in scientific data reduction.

Another effect of importance is the phase delay experienced by the electromagnetic wave propagating through the ionosphere and the neutral atmosphere. The state of these media changes rapidly over time, so every time an observation is made (i.e., every 12 days from a given vantage point), the phase delay across the image will be different. These introduce a spatially cor-

related but random component to the differential signal that is one of the chief limiting noise sources. The wide bandwidth of the radar data can be exploited to estimate signal dispersion due to the ionosphere such that this dispersion can be mitigated (Meyer et al., 2011). We can mitigate the effects of atmosphere propagation noise through a combination of modeling using an independent estimate of the state of the atmosphere and through an averaging or filtering process that assumes a spatially correlated but temporally uncorrelated random process, as distinct from the ground motion which is generally both spatially and temporally correlated.

$$\Delta\phi = \Delta\phi_{def} + \Delta\phi_{err} = \Delta\phi_{def} + \Delta\phi_{atmos} + \Delta\phi_{orb} + \Delta\phi_{topo} + \Delta\phi_n$$

where $\Delta\phi_{def}$ is the phase due to the true ground deformation in the LOS direction, $\Delta\phi_{atmos}$ is the phase due to the tropospheric and ionospheric delays, $\Delta\phi_{orb}$ is the phase due to satellite orbit errors, $\Delta\phi_{topo}$ is the phase due to error in the surface topography, and $\Delta\phi_n$ is a re-

sidual noise term that includes scattering variability and thermal noise. All of the noise terms contribute to the signal quality, as quantified by correlation, at various spatial scales. The correlation can be expressed as:

$$\gamma_e = \gamma_{SNR} \gamma_B \gamma_V \gamma_\phi \gamma_T$$

where the correlation terms are defined in Table 7-2. The table provides formulas illustrating the dependency of the various correlation terms in terms of system parameters.

The displacement noise corresponding to this correlation is given by

$$\sigma_d = \frac{\lambda}{4\pi} \frac{1}{\sqrt{2N}} \sqrt{\frac{1-\gamma_e^2}{\gamma_e^2}}$$

When the correlation is low, the displacement noise is high and vice versa. N is the number of pixels that can be averaged to reduce the noise level.

Interferometric performance depends critically on how well the total interferometric phase difference φ_{int} can

TABLE 7-2. ELEMENTS OF THE INTERFEROMETRIC CORRELATION

Correlation Term	Expression	System Dependence
Total SNR	$\gamma_e = \gamma_{SNR} \gamma_B \gamma_V \gamma_\phi \gamma_T$	Signal-to-noise-ratio
Geometric Baseline	from $\gamma_{SNR} = \frac{SNR}{SNR + 1}$ $\gamma_B = 1 - \frac{2B \cos \theta_i^2 \delta_g}{\lambda \rho}$	Short baseline B , fine resolution δ_g , and long wavelength λ maximize correlation. Look angle θ_i and range ρ are relatively fixed in useful orbits with low drag (above ~ 600 km)
Geometric Volume	from $\gamma_V = \sin c \left(\frac{k_z h_c}{2} \right)$ $k_z = 4\pi \left(\frac{B}{\lambda \rho \sin \theta_i} \right)$	Short baseline B , and long wavelength λ maximize correlation. Look angle θ_i and range ρ are relatively fixed in useful orbits with low drag (above ~ 600 km)
Geometric Rotation	from $\gamma_B = 1 - \frac{2 \sin \theta_i \phi_{rot} \delta_{az}}{\lambda}$	Small pointing rotation ϕ_{rot} , fine along-track resolution δ_{az} , and long wavelength λ maximize correlation. Look angle θ_i and range ρ are relatively fixed in useful orbits with low drag (above ~ 600 km)
Temporal	$\gamma_T = e^{-\left(\frac{4\pi}{\lambda}\right)^2 \sigma_{los}^2}$	Depends on natural targets. Longer wavelengths decorrelate less for a given surface change, proportional to wavelength squared in general

be measured, which in turn depends on the SNR. We can relate SNR to the phase-difference measurement uncertainty $\sigma_{\phi_{int}}$. The variance of the measured phase difference, $\sigma_{\phi_{int}}^2$ is due to the random phase component introduced by the noise accompanying the signal, and it is approximately proportional to the inverse of the SNR,

$$\sigma_{\phi_{int}}^2 \approx \frac{1}{\text{SNR}}$$

So, for example, to secure the single-look value $\sigma_{\phi_{int}} = 0.1$ rad, it is necessary that $\text{SNR} = 100$, or, equivalently, 20 dB.

Phase artifacts in InSAR images are often attributed to neutral tropospheric delays (Zebker et al., 1997; Hanssen et al., 1998). Because the Earth's troposphere is non-dispersive at appropriate frequencies, radar signals that operate at different frequencies are subject to the same tropospheric delays. For a typical X-band interferogram (such as TerraSAR-X), a phase cycle of 2π in the interferogram corresponds to $\lambda/2 = 1.55$ cm deformation, where λ is the radar signal wavelength. In a typical radar scene, tropospheric noise occurs with variation on the order of centimeters or even greater across the interferogram. As a result, any expected centimeter-level crustal deformation signature is obscured by tropospheric noise.

In order to obtain accurate InSAR deformation measurements, some effort is needed to handle or suppress the atmospheric noise signature. Onn and Zebker (2006) introduced a method to correct for atmospheric phase artifacts in a radar interferogram using spatially interpolated zenith wet delay data obtained from a network of GNSS receivers in the region imaged by the radar. Li et al. (2006a, 2006b) used Medium Resolution Imaging Spectrometer (MERIS), Moderate Resolution Imaging Spectroradiometer (MODIS) and GPS data to estimate the water vapor field in order to correct inter-

ferograms that are corrupted by atmospheric artifacts. Foster et al. (2006) employed a high-resolution weather model to predict tropospheric delays for the acquisition times of SAR images. However, estimating tropospheric delays using auxiliary data such as GNSS, MERIS/MODIS or weather model usually produces a tropospheric noise model with resolution much coarser than InSAR image resolution, and the model uncertainty can be relatively large for studying centimeter-level crustal deformations.

Many have proposed algorithms to estimate tropospheric delays during SAR data acquisition times directly from InSAR data. Emardson et al. (2003) mitigated tropospheric effects by averaging N independent interferograms because the wet component of the neutral atmosphere is uncorrelated at time scales longer than 1 day. This stacking approach is limited by the number of interferograms that are available over the time of interest. Lin et al. (2010), Lauknes (2011), and Hooper et al. (2012) assumed that tropospheric delays in InSAR data are topographically correlated and can be partially removed by knowledge of the local elevation changes. However, the assumption that tropospheric delay is proportional to surface elevation may not be valid for turbulent tropospheric processes. Use of globally available weather reanalysis models (e.g., ECMWF and NARR) has also shown considerable ability to mitigate topographically correlated phase errors – with the advantage of not absorbing potential geophysical signals into empirical corrections (e.g., Jolivet et al., 2014a).

Since many of the problems proposed by the science team for this mission require correction at the mm to cm level, a more complex approach will be required. A variety of InSAR time series algorithms now exist including SBAS, NSBAS, MInTS and various permutations of these approaches. These algorithms can filter out

tropospheric delays in InSAR data assuming that errors in InSAR deformation estimates are primarily due to tropospheric noise that are uncorrelated in time. These methods require many observations at frequencies much greater than the expected time scale of deformation. Such algorithms to mitigate tropospheric noise

have been shown to be very effective, even in reducing the very short wavelength TerraSAR-X data. Thus, with long and dense time series, we can address many state of the art problems and applications.

8 CALIBRATION AND VALIDATION

Calibration and Validation for NISAR comprises instrument calibration, image calibration, calibration of algorithms used to derive higher level science products such as biomass or glacier velocities, as well as demonstration (validation) that the data acquired, when flowed through the science processing algorithms, create products that meet the mission's science requirements. Instrument calibration is generally addressed in the pre-launch period through measurements made in a relevant simulated space-like environment. This section addresses the other elements of Cal/Val mentioned above.

8.1 BACKGROUND

In developing the Calibration/Validation plan for NISAR, there are precedents and experiences that can be utilized. The Committee on Earth Observation Satellites (CEOS) Working Group on Calibration and Validation (WGCV; <http://calvalportal.ceos.org/CalValPortal/welcome.do>) has established standards that may be used as a starting point for NISAR. The Land Products Sub-Group (<http://lpvs.gsfc.nasa.gov/>) has expressed the perspective that “A common approach to validation would encourage widespread use of validation data, and thus help toward standardized approaches to global product validation. With the high cost of in-situ data collection, the potential benefits from international cooperation are considerable and obvious.”

Cal/Val has become synonymous in the context of remote sensing with verifying the suite of processing algorithms that convert raw data into accurate and useful geophysical or biophysical quantities. This can include vicarious calibration, which refers to techniques that make use of natural or artificial sites on the surface of the Earth for the post-launch calibration of sensors, which is typically called “image calibration” for SAR systems.

A useful reference in developing a validation plan is the CEOS Hierarchy of Validation:

- Stage 1: Product accuracy has been estimated using a small number of independent measurements obtained from selected locations and time periods and ground-truth/field program effort.
- Stage 2: Product accuracy has been assessed over a widely distributed set of locations and time periods via several ground-truth and validation efforts.
- Stage 3: Product accuracy has been assessed, and the uncertainties in the product well-established via independent measurements made in a systematic and statistically robust way that represents global conditions.

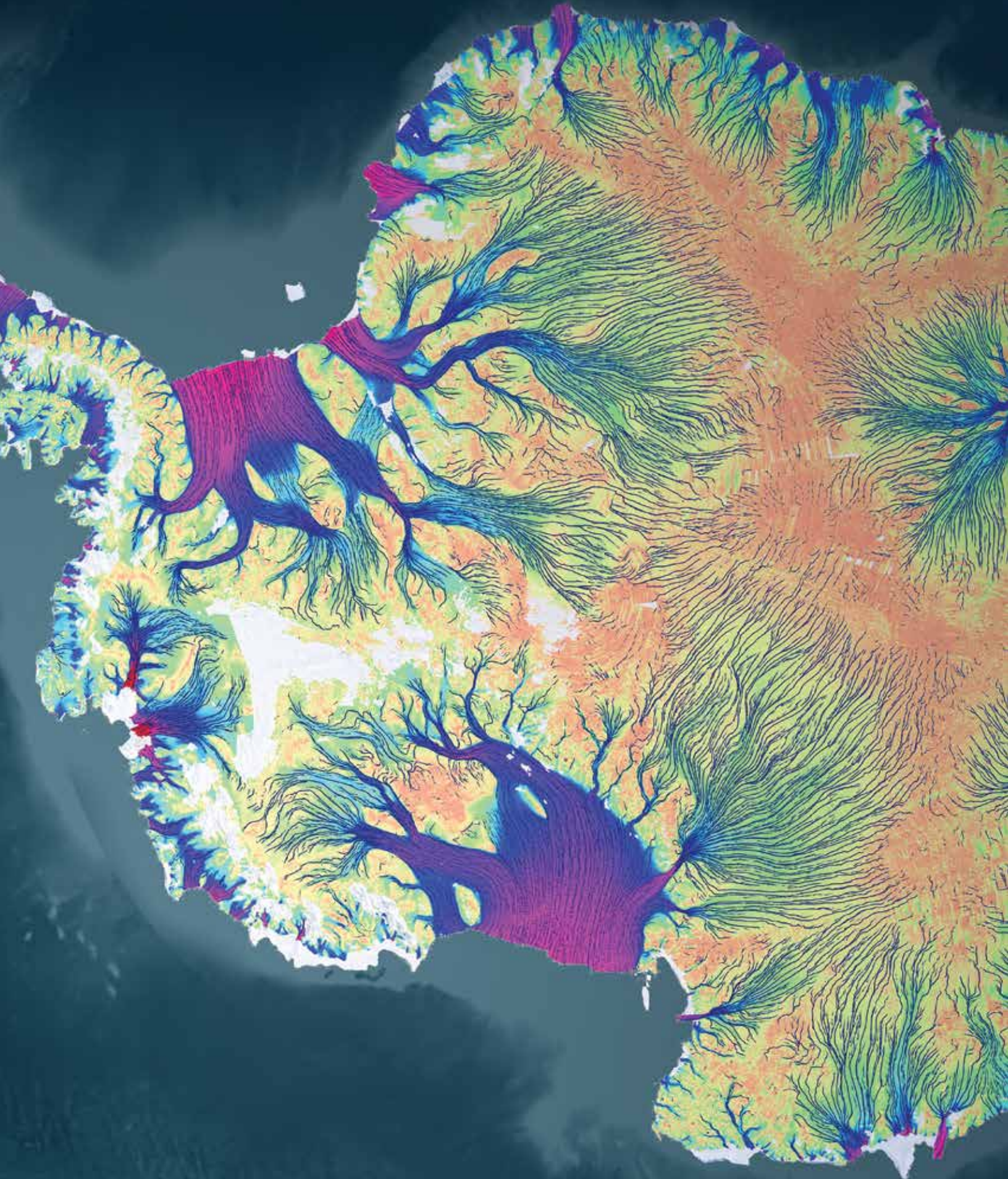
A validation program would be expected to transition through these stages over the mission life span. The NISAR mission collaborates with the NASA Global Ecosystem Dynamics Investigation Lidar (GEDI) mission and the ESA BIOMASS mission due to complementary science requirements for measuring above ground biomass. It is likely that science operations for all three missions will partly overlap in time. Therefore, joint validation of biomass requirements may be possible and desirable.

DEFINITIONS

In order for the Calibration/Validation Plan to effectively address the achievement of mission requirements, a unified definition base has to be developed. The NISAR Cal/Val Plan uses the same source of terms and definitions as the NISAR Level 1 and Level 2 requirements.

NISAR Calibration and Validation are defined as follows:

- Calibration: The set of operations that establish, under specified conditions, the relationship



between sets of values of quantities indicated by a measuring instrument or measuring system and the corresponding values realized by standards.

- Validation: The process of assessing by independent means the quality of the data products derived from the system outputs.

8.2 CALIBRATION AND VALIDATION ACTIVITIES

Calibration and validation is divided into pre- and post-launch activities. Pre-launch activities focus on instrument calibration. Post launch calibration and validation activities focus on the data products.

PRE-LAUNCH

During the pre-launch period, there are a variety of activities that fall under calibration and validation. These mainly involve on-ground instrument calibration, algorithm development and evaluation, and establishing the infrastructure and methodologies for post-launch validation. Requirements for Cal/Val related to specific NISAR data products will be identified by the respective science algorithm teams in their Algorithm Theoretical Basis Documents (ATBDs). The production processing algorithms in the ATBDs will be coded and tested in later phases of the project (prior to launch). Pre-launch activities will include development of the calibration procedures and algorithms for the NISAR radar (L1 products), higher level image products (L2) (incorporating such characteristics as geocoding and/or multilooking), and the L3 products (which will be used to validate the NISAR science requirements).

Pre-launch instrument calibration will include modeling, analysis, simulations, and laboratory and test-facility measurements. Algorithm development for all products will include testbed simulations, laboratory and test-facility data, field campaigns, exploitation of existing in-situ and satellite data, and utilization of instrument and geophysical models.

The science team will identify calibration and validation sites and resources needed for post-launch calibration. For calibration of radar specific-parameters, the Project will either deploy or employ existing corner reflector arrays, for example the array at Rosamond dry lake on Edwards Air Force Base, currently used for calibration of NASA's airborne L-band radar instrument UAVSAR (Uninhabited Aerial Vehicle Synthetic Aperture Radar). For some science requirements, ground instrumentation will be deployed prior to launch to Cal/Val sites and verified with contemporary data sources. Contemporary and historical data sets, especially L-band SAR and time series data from Sentinel-1, will be compiled for Cal/Val sites; demonstration products will be developed for algorithm testing and verification.

POST-LAUNCH

In the post-launch period, the calibration and validation activities will address directly the measurement requirements for the L1-L3 data products. Each data product has quantifiable performance specifications to be met over the mission lifetime, with calibration and validation requirements addressed in their respective ATBDs.

Post-launch calibration and validation activities are divided into three main parts after launch:

1. Three-month instrument checkout phase, after which delivery of validated L1 products to the public archive will begin.
2. Five-month geophysical product Cal/Val phase, after which delivery of validated L3 products to the public archive will begin.
3. Periodic Cal/Val performed annually. During this period, additional algorithm upgrades and reprocessing of data products can be implemented if found necessary (e.g., as a result of drifts or anomalies discovered during analysis of the science products), as well as validation of those science requirements that require a year's worth of data or more.

The main objectives of post-launch calibration/validation activities are two-fold: 1) Monitoring the stability of instrument calibration and, 2) Validation of higher-level data products (L3) with ground truth at selected validation sites. Instrument calibration stability is verified by continuing to collect calibration data over sites used during instrument checkout, using the same radar modes as in nominal science operations (this is different from instrument checkout, when multiple modes are used for various calibrations). Table 8-1 lists the instrument parameters that will be calibrated post-launch by the instrument and science team.

The objective of science data product validation is to validate that global data yielded by NISAR will meet the project's L2 science requirements. L3 products will be generated by the science team at the selected validation sites. Validation of the L3 science products will be carried out by a combination of fieldwork and analysis.

For solid Earth deformation, there are a number of natural validation sites in the world that can be used: GNSS networked arrays exist throughout western North America and in other parts of the world, and these serve as natural validation sites. GNSS sites and arrays have been used for a number of years for this purpose. The density of GNSS stations is on the order of one per 10-20 km, which will allow validation of the upper end of the accuracy length scale. The shorter scales will be validated by analysis – examining areas known to be stable over a period of time and comparing the expected noise performance to that measured. Since the errors tend to be dominated by environmental effects like water vapor and surface decorrelation, what is most important is to validate that the contributions of instrument noise are within acceptable values allowing the overall accuracies to be met.

TABLE 8-1. POST-LAUNCH CALIBRATION PARAMETERS AND METHODS

Parameters	Methods
Antenna Pattern and Beamforming	Use undisturbed Amazon rainforest to compare residual brightness variations relative to ideal
Impulse Response	Measure 3-dB resolution, ISLR, PLSR of corner reflector arrays
Multiplicative Noise Characterization	Use a radar-opaque fence to measure total MNR plus thermal noise
Thermal Noise Characterization	Use sniffer pulses to measure thermal noise levels
Common Time Delay	Compare range measurement on surveyed corner reflectors
Differential Time Delay	Cross-correlate data between polarimetric channels to measure channel misregistration
Time Tag	Compare along-track position measurement on surveyed corner reflectors
Pointing Angle Biases	Use bright homogeneous backscatter region to compare measured Doppler centroid to expected Doppler centroid and measure angle biases
Polarimetric Balance	Use combination of polarization targets and distributed targets to estimate polarimetric calibration

For ice sheets and glaciers, the higher level products will be validated in the relevant environment of Greenland and Antarctica. The plan calls for the deployment of arrays of GNSS ground stations on a divide-to-coast flow line, through a variety of ice types to which the ice velocity products will be compared.

For sea-ice, the project will exploit buoy data in the Arctic, comparing buoy velocities to measured ice velocity vectors from the data.

For biomass and disturbance, there is a worldwide network of managed and measured forests and fields that provide a natural in situ data set against which to validate the biomass and disturbance products. The Project will support fieldwork at these and any supplemental sites needed to acquire enough forest types to validate the product over the range of biomass validity.

For permafrost deformation, wetlands inundation, and crop area requirements, the science team will compare NISAR products to those derived from a combination of proven remote sensing techniques using other data sets, such as optical imagery, and through the collection of field measurements.

Table 8-2 shows the nominal list of global sites at which L3 data products for all science disciplines will be generated and validated.

A number of teams will be performing various functions during the calibration/validation sub-phase.

- The joint science team, which will be composed of the NISAR science team and the Project science team at JPL, will plan and organize field campaign support (e.g., corner reflectors, GNSS stations, in situ campaigns).
- The necessary NISAR observations for Cal/Val activities will be planned by the MOS team.
- The instrument health and performance will be evaluated with auxiliary measurements on the spacecraft and instrument by the Radar instrument team.

- The SAR image data will be processed by the SDS team.
- All image calibration parameters will be evaluated and validated by the algorithm development team.
- Algorithm parameters needed for generating L3 data products (e.g., biomass algorithm parameters, inundation threshold values, etc.) are to be calibrated and updated by the joint science team as validation data becomes available or at TBD intervals. Frequency of updates is TBD and may depend on the sensitivity of the algorithm and the timing of the field campaigns.
- The L2 science requirements will be validated by the joint science team.

A variety of field experiments/campaigns to validate the L3 science products that will be used to validate the L2 science requirements will be organized by the joint science team during this sub-phase. Possible campaigns include, but are not limited to:

- Deployment, inspection and maintenance of trihedral corner reflectors at selected PBO stations and/or the Surat Basin site in Australia.
 - Used for instrument calibration and performance
 - Reflectors are to be deployed prior to launch, and inspected and maintained during the Cal/Val phase and once every year of science operations thereafter
- Biomass estimated from airborne and/or field measurements for globally representative forest areas
 - Used for calibration of biomass algorithm parameters, and validation of science requirement
- Field validation of inundation extent for boreal, temperate, and tropical wetlands
 - Used for calibration of inundation threshold values and validation of inundation science requirement

TABLE 8-2. SUMMARY OF NISAR Cal/Val VALIDATION SITES

Measurement	Validation Site	Comment
Instrument calibration	Corner reflector arrays such as the Rosamond Corner Reflector Array, California; Delta Junction, Alaska; Surat Basin, Australia	Absolute radiometric calibration, relative calibration, instrument performance, geolocation, beam formation
Instrument calibration	Distributed targets in non-flooded, non-deforested tropical forest locations in South America and Africa	Cross-talk calibration, antenna pattern, channel imbalance, relative calibration
2-D and 3-D velocity time series of ice sheet	10 GNSS receivers along a divide-to-coast flow line in Greenland. 4 GNSS devices on Antarctic Ice Shelf. ISRO and independently funded investigators may have GNSS devices at additional locations	Also, could use wider area data such as Ice Bridge contemporaneous data sets, should they exist
Sea-ice velocities	West Arctic, Southern Ocean	Using available buoy data from the International Arctic Buoy Program (IABP) and International Programme for Antarctic Buoys (IPAB)
2-D deformation time series of solid Earth	U.S. Network of the Americas (NOTA), Hawaii Volcano Observatory (HVO), GEONET-Japan, GEONET-New Zealand, AGOS, ISRO network, CALM network	Other similar size and scale geodetic ground networks may be available as well
Biomass	Five canonical biomes with field measurements of biomass: Needleleaf, Broadleaf Deciduous, Mixed Broadleaf/Needleleaf, Broadleaf Evergreen, Savanna/Dry Forest	Use existing and heritage Cal/Val locations (roughly 30 sites distributed globally). Collaboration with BIOMASS and GEDI validation campaigns
Disturbance	Known areas of forest management (e.g. southeastern U.S.); fire databases; and targets of opportunity (determined after disturbance events)	Forest management plans for clearcutting and selective logging. Use of high resolution optical data to determine canopy fraction change. Use of active fire databases
Crop area	U.S. and India agricultural areas imaged with quad pol mode, and selected JECAM sites	Local assessment surveys and cropscape, JECAM data
Inundation area	Wetland sites with NASA funded studies in Alaska (ABoVe); South America (Pacaya-Samiria, or Pantanal); AfriSAR (Gabon) site; Florida everglades; Louisiana Delta; coastal lagoon sites in India; Sudd, South Sudan	Other international sites as well if field data are available. Five types of validation data may be used depending on location

- Field validation of active crop area
 - Used for calibration of crop area threshold values and validation of the active crop area science requirement
- Field validation of surface deformation in permafrost areas
 - Used for validation of the permafrost deformation science requirement
- Installation of 10 GNSS receivers along a divide-to-coast flow line in Greenland and 4 GNSS receivers on an ice shelf in Antarctica
 - GNSS receivers will be deployed after launch
 - Used for validating observations for all snow types and melt states of glacier velocities

Members of the joint science team will also utilize data from various resource networks for validating the L3 data products, e.g., NASA ABoVe (Arctic-Boreal Vulnerability Experiment), NEON (NSF National Ecological Observatory Network), NOTA (Network of the Americas), Corner reflector arrays and GNSS station networks that are distributed globally.

The exit criteria/final conditions to be satisfied for ending the calibration/validation sub-phase are:

TABLE 8-3. EXISTING OR NEAR-TERM AIRCRAFT-BASED SENSORS

Airborne Systems	Sensor
NASA UAVSAR	L-band quad-pol repeat pass InSAR, P-band quad-pol SAR, Ka-band single pass InSAR
DLR FSAR	X-band through P-band quad pol repeat pass InSAR
JAXA Pi-SAR	L-band quad-pol SAR
LVIS	Scanning laser altimeter
G-LiHt	Scanning lidar, profiling lidar, VNIR imaging spectrometer, thermal imager
ISRO L/S airborne radar	S-band and L-band SAR
UAS	Lidar, thermal IR, and/or multispectral instruments

- L-SAR and S-SAR instrument calibration stability has been demonstrated and verified. Appropriate adjustments have been proposed, verified and processed (revisions resultant from Cal/Val could affect mission timeline, radar modes, Cal/Val process, SDS processing and data analysis, ground systems, mission operations, ground field campaigns and supporting infrastructure including corner reflectors, GNSS stations, etc.).
- L3 data products over Cal/Val sites have been validated via a mix of ground truth and remote sensing data (this only refers to the initial validation; these products will be validated periodically over the course of the mission).
- The flight systems (spacecraft, engineering payload, RBA), payloads (L-SAR and S-SAR instruments) and ground systems (GDS, SDS, MOS) biases are well characterized, so that calibrations can be routinely applied and incorporated to adjust or remove biases to generate calibrated L1/L2 data products.
- The algorithms and retrieval of geophysical parameters (L3 data products) from L1/L2 products are validated, and any biases can be sufficiently characterized and removed.

TABLE 8-4. POSSIBLE FIELD EXPERIMENTS FOR NISAR Cal/Val

Field Experiments/ Airborne Data/ Satellite Observations	Objectives	Number of Planned Experiments					
		Pre-Launch	Observ. Checkout	Cal/Val Phase	Science Operations Year 1	Science Operations Year 2	Science Operations Year 3
Deployment of 50 corner reflectors (CR)	Instrument calibration	1					
Inspection and maintenance of 50 CRs	Instrument calibration				1	1	1
Deployment of one passive receiver	Validation of antenna pattern and digital beamforming parameters		1- 3				
Biomass from field measurements/airborne lidar	Calibration of biomass algorithm parameters, and validation of science requirement	TBD		6	6	6	
Field validation of inundation extent for boreal, temperate, and tropical wetlands	Calibration of inundation threshold values and validation of inundation science requirement	1		2	2	2	2
Field validation of crop area	Calibration of crop area threshold values and validation of inundation science requirement	2		2	2	2	2
Field validation of permafrost deformation	Validate surface deformation in permafrost areas	2		2	2	2	2
10 GNSS receivers Greenland	Velocity measurements for all snow facies and melt states	1	1				
Maintain 10 GNSS receivers Greenland	Validate observations for all snow facies and melt states				1	1	1
4 GNSS receivers on ice shelf in Antarctica	Validate velocity measurements	1	1				
Maintain 4 GNSS receivers on ice shelf in Antarctica	Validate velocity measurements	1	1		1	1	1

Some validation campaigns will involve comparisons with datasets from airborne sensors (e.g., NASA UAVSAR, DLR F-SAR, LVIS; see Table 8-3) and other contemporary spaceborne sensors (e.g., NASA GEDI, ICESat-2, ESA Biomass, World View-3, Landsat 8, Sentinel-1 A/B, Sentinel 2). Possible field campaigns are noted in Table 8-4.

8.3 CALIBRATION/VALIDATION ROLES AND RESPONSIBILITIES

The NISAR joint science team (consisting of scientists selected by NASA and ISRO), along with the supporting Project Science Team (PST), will plan and organize field campaign support (e.g. corner reflectors, GNSS stations, in situ campaigns). The SDS will nominally collect and process the radar data. The NISAR SDS and radar instrument team will work together to regularly update instrument calibration parameters for generating L1 and L2 products. The instrument team will work with the mission planning team to ensure appropriate calibration data are acquired. The joint science team will analyze and evaluate imagery data processed by the SDS, interpret results and generate L3 data products over selected science validation sites. They will calibrate and update algorithm parameters (e.g., biomass algorithm parameters, inundation threshold values,

etc.) regularly in their calculations of L3 products. They will also verify the end to end acquisition, calibration, and processing of the imagery. Lastly, the joint science team will validate that the science requirements have been achieved by the mission.

The NISAR Cal/Val Plan is developed and implemented by the NISAR Cal/Val team, which includes members of the joint science team, the ISRO Cal/Val team, and members of the project science and science data system staff at JPL. The NISAR Cal/Val Plan will be developed taking into consideration a broad range of inputs and contributions from the U.S. and international communities, including Cal/Val plans of other Synthetic Aperture Radar (SAR) missions related to the NISAR science disciplines. Detailed roles and responsibilities for specific tasks are shown in Table 8-5.

COMMUNITY INVOLVEMENT

The NISAR project welcomes high-quality in situ data that can be used for calibrating or validating NISAR images, algorithms, and products. A formal mechanism organized through the NISAR Project Cal/Val lead will be established and described on the NISAR web site.

TABLE 8-5. Cal/Val ROLES AND RESPONSIBILITIES

	Project Science Team	Joint Science Team	Science Data Systems Team	Radar Instrument Team
Validation Algorithms				
L0a-L0b			X	X
L0-L1			X	X
L1-L2	X	X	X	
L2-L3	X	X		
Calibration Algorithms				
Point target analysis			X	X
Doppler analysis			X	X
GNSS network comparisons	X	X		
Tropospheric phase calibration	X	X		
Ionosphere (absolute delay/relative split spectrum delay)	X	X		
Soil moisture	X	X		
Others				
Calibration Activities				
Work associated with calibration algorithms	X	X	X	X
Coding of algorithms (Phase C/D)	X	X	X	
Acquisition of test data - scoped by each discipline	X	X		
Testing of calibration tools			X	
Field Work - scoped by each discipline	X	X		
Validation Activities				
Validation field work	X	X		
Processing test data	X	X	X	
Processing of mission data		X	X	
Comparison of results to requirements	X	X	X	

9 CONCLUSIONS

TRAINING PROGRAMS
FOCUSED ON RADAR
DATA ANALYSIS AND
PROCESSING WILL BE
PROVIDED TO FOSTER
INTEGRATION OF
NISAR DATA INTO
EARTH SCIENCE
STUDIES BY FUTURE
GENERATIONS
OF SCIENTISTS,
GEOLOGISTS, AND
ENGINEERS.

Earth's surface and vegetation cover are constantly changing on a wide range of scales. Measuring these changes globally from NISAR will enable breakthrough science with important applications to society. NISAR will significantly expand the value of NASA's missions from being purely science-driven to also encompassing informed decision support across a wide range of applications.

The baseline requirements for the NISAR mission express challenging and exciting goals, to measure the deforming land and ice surfaces to accuracies and spatial extents that go well beyond what past and current international missions have accomplished and what future missions plan. These requirements are met by the system described in this document: first-of-a-kind technology for wide-area mapping, with a regular and uniform observation strategy.

The NISAR mission will be the first NASA radar mission to systematically and globally study the solid Earth, the ice masses, and ecosystems by regularly sampling Earth's land and ice covered surfaces from ascending and descending orbit vantage points every 12 days. As an all-weather, day/night imaging system with an exceedingly rich and far-reaching set of science objectives, NISAR is arguably the most likely Decadal Survey mission to fulfill the call from the committee to expand the value of NASA's missions from purely scientifically driven to encompass applications for societal benefit. Many of the examples shown in this document demonstrate the potential of SAR missions for applications. NISAR will add a tremendous new data set to create new, and greatly improve upon existing, applications. As the mission progresses to launch in the next few years, one of the goals of the project will be broader community engagement involving the scientific as well

as the applications communities. Training programs focused on radar data analysis and processing will be provided to foster integration of NISAR data into Earth science studies by future generations of scientists, geologists, and engineers. Workshops and conferences will be organized to develop detailed plans for calibration and validation, as well as other science activities.

The potential for synergistic satellite observations, complementary to the NISAR science objectives, is also quite exciting. The ESA Sentinel-1 satellites are already providing regular global sampling at C-band. The CSA RADARSAT constellation mission will provide similar C-band measurements in and around Canada systematically, and elsewhere around the world with more limited sampling. NASA's Global Ecosystem Dynamics Investigation (GEDI) Lidar is expected to launch to the International Space Station in the year 2019. This lidar mission has a biomass measurement goal which is relevant to NISAR, in addition to measuring forest structure. The European Space Agency's BIOMASS mission is also expected to launch prior to NISAR. BIOMASS is a fully polarimetric P-band SAR whose main goal is to measure above ground biomass. In a complementary fashion, the primary biomass objectives of the BIOMASS mission (biomass measured in areas over 100 Mg/ha) is complementary to the NISAR biomass science requirement (biomass measured in areas under 100 Mg/ha). The Argentine Space Agency's (CONAE) SAOCOM satellite constellation, which will use L-band SAR for disaster monitoring, is also expected to launch in the years preceding NISAR's launch. Studies based on combining datasets from these complementary sources will not only assist in verification and validation but will also yield new insights for investigations of Earth surface processes (which were previously impossible due to the lack of such overlapping datasets).

Over 20 years in the making, NISAR represents the hopes and aspirations of a generation of scientists awaiting the data they need to perform broad-area Earth system studies in their disciplines, using the uniquely sampled data from this mission. The NISAR science team comprises many scientists who have exploited SAR data from many sources, some from as early as SEASAT in 1978. These scientists have tremendous depth of experience in what SAR can and cannot do. They are of like mind in both frustration with the lack of available science-grade SAR data available

to the research community, and excitement about the opportunities NISAR will provide to scientists over the world. Many of the techniques developed with SEASAT and SIR-C, both short-lived missions flown two decades ago, are as relevant today as they were then. The international SAR sensors that blossomed after these U.S. missions flew have indeed led to new and exciting discoveries. The examples shown in this document can only hint at the orders of magnitude improvement in our understanding of Earth that the NISAR mission will contribute.

10 ACKNOWLEDGMENTS

This document was produced at Jet Propulsion Laboratory, California Institute of Technology, under a contract with the National Aeronautics and Space Administration. It was initially generated with the assistance of the 2012-2016 NISAR Science Definition Team and Project Science Team as a means to report on science progress through the formulation and early development phases of the NISAR project.

Andrea Donnellan has served as chief editor of this NISAR handbook since January 2018, shepherding it to its current published form. Priyanka Sharma served as chief editor and custodian of an earlier version after

NISAR entered Phase C in August 2016. Paul Rosen and Margaret Glasscoe also contributed to organization and editing of the handbook. The current science team has supplied continuing updated science results, prose, and feedback on the document. The project engineering team has dedicated countless hours to developing a first-of-a-kind radar system with unprecedented capabilities and has provided content to demonstrate that in this document. In particular, Josh Doubleday as mission planner, Scott Shaffer as instrument system engineer, Sara Hatch as mission design and navigation engineer, and Peter Xaypraseuth as flight system engineer, have provided key content.

Cost estimates stated herein are as of publication and do not necessarily represent cost at final mission.

CONTRIBUTORS

2012-2016 NISAR Science
Definition Team

Susan Callery, JPL

Paul Rosen, JPL

2016-2019 NISAR
Science Team

Andrea Donnellan, JPL

Priyanka Sharma, JPL

Margaret Glasscoe, JPL

Sean Buckley, JPL

Scott Hensley, JPL

11 REFERENCES

DOCUMENTS

ACIA, 2004. Impacts of a Warming Arctic: Arctic Climate Impact Assessment. ACIA Overview report. Cambridge University Press. 140 pp.

CEOS, C., 2014. Strategy for Carbon Observations from Space. The Committee on Earth Observation Satellites (CEOS) Response to the Group on Earth Observations (GEO) Carbon Strategy., April 2014 (issued date: September 30, 2014).

DESDynI Applications Workshop report (2008). Available at: http://appliedsciences.nasa.gov/pdf/09DESDynI_Applications_Report_V1.0.pdf

FRA, 2010, The Global Forest Resources Assessment 2010, Wilkie, M.L., Cumani, R., Martucci, A. and Latham, J., 2007. The Global Forest Resources Assessment 2010. Forest. Tsang et al., 1985: Tsang, L., Kong, J.A. and Shin, R.T., 1985. Theory of microwave remote sensing.

GCOS. 2010. Implementation Plan for the Global Observing System for Climate in Support of the UNFCCC (2010 Update), GCOS-138. Secretariat of the World Meteorological Organization: Geneva, Switzerland, p 180.

"GEOSS 10-year Implementation Plan," Group on Earth Observations (GEO) Implementation Plan Task Team (IPTT), 2005.

GFOI, 2013, Integrating remote-sensing and ground-based observations for estimation of emissions and removals of greenhouse gases in forests: Methods and Guidance from the Global Forest Observations Initiative: Pub: Group on Earth Observations, Geneva, Switzerland, 2014.

Global Carbon Project, <http://www.globalcarbonproject.org/carbonbudget/>

IPCC 2006, 2006 IPCC Guidelines for National Greenhouse Gas Inventories, Prepared by the National Greenhouse Gas Inventories Programme, Eggleston H.S., Buendia L., Miwa K., Ngara T. and Tanabe K. (eds). Published: IGES, Japan.

IPCC, 2007: Climate Change 2007: Synthesis Report. Contribution of Working Groups I, II and III to the Fourth Assessment Report of the Intergovernmental Panel on Climate Change [Core Writing Team, Pachauri, R.K and Reisinger, A. (eds.)]. IPCC, Geneva, Switzerland, 104 pp.

IPCC, 2007: Climate Change 2007: The Physical Science Basis. Contribution of Working Group I to the Fourth Assessment. Report of the Intergovernmental Panel on Climate Change, 996 pp., Cambridge University Press, Cambridge and New York.

JECAM, 2014, JECAM Guidelines for Cropland and Crop Type Definition and Field Data Collection, Group on Earth Observations, 7 pp. downloaded from <http://jecam.org/documents/> December 3, 2018.

Millennium Ecosystem Assessment, 2005. Ecosystems and Human Well-being: Synthesis. Island Press, Washington, D.C.

National Research Council, 1991. Mitigating Losses from Land Subsidence in the United States. National Academies Press.

National Research Council and Board, O.S., 2007. Mitigating Shore Erosion along Sheltered Coasts. National Academies Press.

National Research Council, 2013. Induced Seismicity Potential in Energy Technologies. National Academies Press.

Responding to the Challenge of Climate and Environmental Change: NASA's Plan for a Climate-Centric Architecture for Earth Observations and Applications from Space (2010). Available at: https://smd-prod.s3.amazonaws.com/science-green/s3fs-public/atoms/files/Climate_Architecture_Final.pdf.

UNFCC, 2006. Climate Change: Impacts, Vulnerabilities, and Adaptation in Developing Countries, United Nations Framework Convention on Climate Change.

A

Agnew, D.C., 2012. SPOTL: Some Programs for Ocean-Tide Loading. SIO Technical Report, Scripps Institution of Oceanography, <https://escholarship.org/uc/item/954322pg>.

Agram, P.S., Jolivet, R., Riel, B., Lin, Y.N., Simons, M., Hetland, E., Doin, M.P. and Lasserre, C., 2013. New radar interferometric time series analysis toolbox released. Eos, Transactions American Geophysical Union, 94(7), pp. 69-70.

Ahlström, A., Andersen, S.B., Nick, F.M., Reijmer, C.H., van de Wal, R.S.W. and Hubbard, A., 2013. Seasonal velocities of eight major marine-terminating outlet glaciers of the Greenland ice sheet from continuous in situ GPS instruments. Earth system science data discussions, 6(1), pp. 27-57.

Alley, W.M., Healy, R.W., LaBaugh, J.W. and Reilly, T.E., 2002. Flow and storage in groundwater systems. Science, 296(5575), pp. 1985-1990.

Alley, R.B., Clark, P.U., Huybrechts, P. and Joughin, I., 2005. Ice-sheet and sea-level changes. Science, 310(5747), pp. 456-460.

Ali, S.T. and Feigl, K.L., 2012. A new strategy for estimating geophysical parameters from InSAR data: application to the Krafla central volcano in Iceland. Geochemistry, Geophysics, Geosystems, 13(6).

Alpers, W., 1992, May. SAR imaging of ocean waves-A review. In Geoscience and Remote Sensing Symposium, 1992. IGARSS'92. International (Vol. 1, pp. 451-454). IEEE.

Alsdorf, D.E., Melack, J.M., Dunne, T., Mertes, L.A., Hess, L.L. and Smith, L.C., 2000. Interferometric radar measurements of water level changes on the Amazon flood plain. Nature, 404(6774), p. 174.

Amelung, F., Galloway, D.L., Bell, J.W., Zebker, H.A. and Lacznik, R.J., 1999. Sensing the ups and downs of Las Vegas: InSAR reveals structural control of land subsidence and aquifer-system deformation. Geology, 27(6), pp. 483-486.

Arendt, A.A., Echelmeyer, K.A., Harrison, W.D., Lingle, C.S. and Valentine, V.B., 2002. Rapid wastage of Alaskan glaciers and their contribution to rising sea level. *Science*, 297(5580), pp. 382-386.

Askne, J.I., Dammert, P.B., Ulander, L.M. and Smith, G., 1997. C-band repeat-pass interferometric SAR observations of the forest. *IEEE Transactions on Geoscience and Remote Sensing*, 35(1), pp. 25-35.

Aster, R.C., Borchers, B. and Thurber, C.H., 2018. *Parameter Estimation and Inverse Problems*. Elsevier.

Attema, E.P.W. and Ulaby, F.T., 1978. Vegetation modeled as a water cloud. *Radio Science*, 13(2), pp. 357-364.

B

Baccini, A.G.S.J., Goetz, S.J., Walker, W.S., Laporte, N.T., Sun, M., Sulla-Menashe, D., Hackler, J., Beck, P.S.A., Dubayah, R., Friedl, M.A. and Samanta, S., 2012. Estimated carbon dioxide emissions from tropical deforestation improved by carbon-density maps. *Nature Climate Change*, 2(3), p. 182.

Baker, D.J., Richards, G., Grainger, A., Gonzalez, P., Brown, S., DeFries, R., Held, A., Kellendorfer, J., Ndunda, P., Ojima, D. and Skrovseth, P.E., 2010. Achieving forest carbon information with higher certainty: A five-part plan. *Environmental Science & Policy*, 13(3), pp. 249-260.

Baghdadi, N., King, C., Chanzy, A. and Wigneron, J.P., 2002. An empirical calibration of the integral equation model based on SAR data, soil moisture and surface roughness measurement over bare soils. *International Journal of Remote Sensing*, 23(20), pp. 4325-4340.

Baghdadi, N., Gauthier, Y. and Bernier, M., 1997. Capability of multitemporal ERS-1 SAR data for wet-snow mapping. *Remote Sensing of Environment*, 60(2), pp. 174-186.

Bally, P., 2012. Scientific and Technical Memorandum of the international Forum on Satellite EO and Geohazards, 21–23 May 2012. Santorini, Greece. doi, 10, p. 5270.

Bamber, J.L., Alley, R.B. and Joughin, I., 2007. Rapid response of modern day ice sheets to external forcing. *Earth and Planetary Science Letters*, 257(1-2), pp. 1-13.

Bartsch, A., Wiesmann, A., Strozzi, T., Schmillius, C., Hese, S., Duguay, C., Heim, B. and Seifert, F.M., 2010, June. Implementation of a satellite data based permafrost information system—The DUE Permafrost Project. In *Proceedings of the ESA Living Planet Symposium*, Bergen, Norway, 28 June–2 July 2010, ESA Spec. Publ., SP (Vol. 686).

Bawden, G.W., Thatcher, W., Stein, R.S., Hudnut, K.W., and Pletzer, G., 2001: Tectonic contraction across Los Angeles after removal of groundwater pumping effects, *Nature*, 412, pp. 812-815.

Berardino, P., Fornaro, G., Lanari, R. and Sansosti, E., 2002. A new algorithm for surface deformation monitoring based on small baseline differential SAR interferograms. *IEEE Transactions on Geoscience and Remote Sensing*, 40(11), pp. 2375-2383.

Bergen, K.M., Goetz, S.J., Dubayah, R.O., Henebry, G.M., Hunsaker, C.T., Imhoff, M.L., Nelson, R.F., Parker, G.G. and Radeloff, V.C., 2009. Remote sensing of vegetation 3-D structure for biodiversity and habitat: Review and implications for lidar and radar spaceborne missions. *Journal of Geophysical Research: Biogeosciences*, 114(G2).

Bindschadler, R.A., King, M.A., Alley, R.B., Anandakrishnan, S. and Padman, L., 2003. Tidally controlled stick-slip discharge of a West Antarctic ice. *Science*, 301(5636), pp. 1087-1089.

Blewitt, G., GPS and space based geodetic methods, in *Treatise on Geophysics*, vol. 3, edited by T. Herring, pp. 351–390, Academic, Oxford, U.K., 2007.

Bonan, G.B., 2008. Forests and climate change: forcings, feedbacks, and the climate benefits of forests. *Science*, 320(5882), pp. 1444-1449.

Bourne, S., Maron, K., Oates, S., and Mueller, G., 2006. Monitoring deformation of a carbonate field in Oman: Evidence for large scale fault re-activation from microseismic, InSAR, and GPS. *Proceedings of 68th EAGE Annual Conference and Exhibition/SPE Europec*, June 12–15, 2006. EAGE Publications BV, Vienna, Austria.

Bryant, R., Moran, M.S., Thoma, D.P., Collins, C.H., Skirvin, S., Rahman, M., Slocum, K., Starks, P., Bosch, D. and Dugo, M.G., 2007. Measuring surface roughness height to parameterize radar backscatter models for retrieval of surface soil moisture. *IEEE Geoscience and Remote Sensing Letters*, 4(1), pp. 137-141.

Burgess, E.W., Forster, R.R. and Larsen, C.F., 2013. Flow velocities of Alaskan glaciers. *Nature Communications*, 4, p. 2146.

Bürgmann, R., Rosen, P.A. and Fielding, E.J., 2000. Synthetic aperture radar interferometry to measure Earth's surface topography and its deformation. *Annual review of Earth and Planetary Sciences*, 28(1), pp. 169-209.

C

Cairns, M.A., Brown, S., Helmer, E.H. and Baumgardner, G.A., 1997. Root biomass allocation in the world's upland forests. *Oecologia*, 111(1), pp. 1-11.

Canadell, J.G., Le Quéré, C., Raupach, M.R., Field, C.B., Buitenhuis, E.T., Ciais, P., Conway, T.J., Gillett, N.P., Houghton, R.A. and Marland, G., 2007. Contributions to accelerating atmospheric CO₂ growth from economic activity, carbon intensity, and efficiency of natural sinks. *Proceedings of the National Academy of Sciences*, 104(47), pp. 18866-18870.

Capps, D.M., Rabus, B., Clague, J.J. and Shugar, D.H., 2010. Identification and characterization of alpine subglacial lakes using interferometric synthetic aperture radar (InSAR): Brady Glacier, Alaska, USA. *Journal of Glaciology*, 56(199), pp. 861-870.

Cartus, O., Siqueira, P. and Kellendorfer, J., 2018. An Error Model for Mapping Forest Cover and Forest Cover Change Using L-Band SAR. *IEEE Geoscience and Remote Sensing Letters*, 15(1), pp. 107-111.

Castañeda, C., Gutiérrez, F., Manunta, M. and Galve, J.P., 2009. DInSAR measurements of ground deformation by sinkholes, mining subsidence, and landslides, Ebro River, Spain. *Earth Surface Processes and Landforms*, 34(11), pp. 1562-1574.

Casu, F., Buckley, S.M., Manzo, M., Pepe, A. and Lanari, R., 2005, July. Large scale InSAR deformation time series: Phoenix and Houston case studies. In *Geoscience and Remote Sensing Symposium*, 2005. IGARSS'05. *Proceedings. 2005 IEEE International (Vol. 7, pp. 5240-5243)*. IEEE.

Chambers, J.Q., Negron-Juarez, R.I., Marra, D.M., Di Vittorio, A., Tews, J., Roberts, D., Ribeiro, G.H., Trumbore, S.E. and Higuchi, N., 2013. The steady-state mosaic of disturbance and succession across an old-growth Central Amazon forest landscape. *Proceedings of the National Academy of Sciences*, 110(10), pp. 3949-3954.

Chapman, B.D., Celi, J.E., Hamilton, S.K. and McDonald, K.C., 2014, December. Detection and Monitoring of Inundation with Polarimetric L-Band SAR. In *AGU Fall Meeting Abstracts*.

Chatterjee, R.S., Fruneau, B., Rudant, J.P., Roy, P.S., Frison, P.L., Lakhera, R.C., Dadhwal, V.K. and Saha, R., 2006. Subsidence of Kolkata (Calcutta) City, India during the 1990s as observed from space by differential synthetic aperture radar interferometry (D-InSAR) technique. *Remote Sensing of Environment*, 102(1-2), pp. 176-185.

Chatterjee, R.S., Roy, P.S., Dadhwal, V.K., Lakhera, R.C., Quang, T.X. and Saha, R., 2007a. Assessment of land subsidence phenomenon in Kolkata city, India using satellite-based D-InSAR technique. *Current Science*, pp. 85-90.

Chatterjee, R.S., Sinha, A., Mahato, A.B., Champati-ray, P.K., Lakhera, R.C., Singh, K.B., Varuna Kumar, G., Sengupta, S., Raju, E.V.R., Sharma, P.D., 2007b. Geoenvironmental Mapping of Jharia Coalfield from Multi-polarization and Interferometric Synthetic Aperture Radar Data, Conference of JEP-Microwave held at Space Application Centre, Ahmedabad during May 15-16, 2007, SAC/RSMET/JEPMW/ CP/03/2007, pp. 5-58 – 5-83.

Chauhan, N.S., Lang, R.H. and Ranson, K.J., 1991. Radar modeling of a boreal forest. *IEEE Transactions on Geoscience and Remote Sensing*, 29(4), pp. 627-638.

Chauhan, N.S., Le Vine, D.M. and Lang, R.H., 1994. Discrete scatter model for microwave radar and radiometer response to corn: comparison of theory and data. *IEEE Transactions on Geoscience and Remote Sensing*, 32(2), pp. 416-426.

Chazdon, R.L., Chao, A., Colwell, R.K., Lin, S.Y., Norden, N., Letcher, S.G., Clark, D.B., Finegan, B. and Arroyo, J.P., 2011. A novel statistical method for classifying habitat generalists and specialists. *Ecology*, 92(6), pp.1332-1343.

Chen, C.W. and Zebker, H.A., 2002. Phase unwrapping for large SAR interferograms: Statistical segmentation and generalized network models. *IEEE Transactions on Geoscience and Remote Sensing*, 40(8), pp. 1709-1719.

Chen, J., 2014a. InSAR Time Series Analysis of Subtle Transient Crustal Deformation Signals Associated with the 2010 Slow Slip Event at Kilauea, Hawaii (Doctoral dissertation, Stanford University).

Chen, J., Zebker, H.A., Segall, P. and Miklius, A., 2014b. The 2010 slow slip event and secular motion at Kilauea, Hawai-i, inferred from TerraSAR-X InSAR data. *Journal of Geophysical Research: Solid Earth*, 119(8), pp. 6667-6683.

Cho, M.A., Debba, P., Mutanga, O., Dudeni-Tihone, N., Magadla, T. and Khuluse, S.A., 2012. Potential utility of the spectral red-edge region of SumbandilaSat imagery for assessing indigenous forest structure and health. *International Journal of Applied Earth Observation and Geoinformation*, 16, pp. 85-93

Chubey, M.S., Franklin, S.E. and Wulder, M.A., 2006. Object-based analysis of Ikonos-2 imagery for extraction of forest inventory parameters. *Photogrammetric Engineering & Remote Sensing*, 72(4), pp. 383-394.

Clark, D.B., Read, J.M., Clark, M.L., Cruz, A.M., Dotti, M.F. and Clark, D.A., 2004. Application of 1-M and 4-M resolution satellite data to ecological studies of tropical rain forests. *Ecological Applications*, 14(1), pp. 61-74.

Cloude, S.R., Goodenough, D.G. and Chen, H., 2012. Compact decomposition theory. *IEEE Geoscience and Remote Sensing Letters*, 9(1), pp.28-32.

Coe, J.A., 2016. Landslide hazards and climate change: A perspective from the United States. *Slope Safety Preparedness for Impact of Climate Change*, pp. 479-523.

Cohen, W.B., Fiorella, M., Gray, J., Helmer, E. and Anderson, K., 1998. An efficient and accurate method for mapping forest clearcuts in the Pacific Northwest using Landsat imagery. *Photogrammetric Engineering and Remote Sensing*, 64(4), pp. 293-299.

Colony, R. and Thorndike, A.S., 1984. An estimate of the mean field of Arctic sea ice motion. *Journal of Geophysical Research: Oceans*, 89(C6), pp. 10623-10629.

Coon, M.D., 1980. A review of AIDJEX modeling. *Sea Ice Processes and Models*, pp. 12-27.

D

Dale, V.H., Joyce, L.A., McNulty, S., Neilson, R.P., Ayres, M.P., Flannigan, M.D., Hanson, P.J., Irland, L.C., Lugo, A.E., Peterson, C.J. and Simberloff, D., 2001. Climate change and forest disturbances: climate change can affect forests by altering the frequency, intensity, duration, and timing of fire, drought, introduced species, insect and pathogen outbreaks, hurricanes, windstorms, ice storms, or landslides. *AIBS Bulletin*, 51(9), pp. 723-734.

Darras, S., Michou, M., Sarrat, C. 1998. IGBP-DIS Wetland Data Initiative: A First Step Towards Identifying a Global Delineation of Wetlands. IGBP-DIS Office, Toulouse.

Davis, J.L., Kellogg, L.H., Arrowsmith, J.R., Buffett, B.A., Constable, C.G., Donnellan, A., Ivins, E.R., Mattioli, G.S., Owen, S.E., Pritchard, M.E. and Purucker, M.E., 2016. Challenges and Opportunities for Research in ESI (CORE): Report from the NASA Earth Surface and Interior (ESI) Focus Area Workshop, November 2-3, 2015, Arlington, VA., 88 pp.

Delbridge, B.G., Bürgmann, R., Fielding, E., Hensley, S. and Schulz, W.H., 2016. Three-dimensional surface deformation derived from airborne interferometric UAVSAR: Application to the Slumgullion Landslide. *Journal of Geophysical Research: Solid Earth*, 121(5), pp. 3951-3977.

Deverel, S.J., Bachand, S., Brandenberg, S.J., Jones, C.E., Stewart, J.P. and Zimmaro, P., 2016. Factors and processes affecting delta levee system vulnerability. *San Francisco Estuary and Watershed Science*, 14(4).

Dixon, T.H., Amelung, F., Ferretti, A., Novali, F., Rocca, F., Dokka, R., Sella, G., Kim, S.W., Wdowinski, S. and Whitman, D., 2006. Space geodesy: Subsidence and flooding in New Orleans. *Nature*, 441(7093), p. 587.

Dobson, M.C. and Ulaby, F.T., 1986. Active microwave soil moisture research. *IEEE Transactions on Geoscience and Remote Sensing*, (1), pp. 23-36.

Doin, M.P., Lasserre, C., Peltzer, G., Cavalié, O. and Doubre, C., 2009. Corrections of stratified tropospheric delays in SAR interferometry: Validation with global atmospheric models. *Journal of Applied Geophysics*, 69(1), pp. 35-50.

Doin, M.P., Guillaso, S., Jolivet, R., Lasserre, C., Lodge, F., Ducret, G. and Grandin, R., 2011, September. Presentation of the small baseline NSBAS processing chain on a case example: The Etna deformation monitoring from 2003 to 2010 using Envisat data. In *Proceedings of the Fringe Symposium* (pp. 3434-3437). ES.

Donnellan, A., Rosen, P., Graf, J., Loverro, A., Freeman, A., Treuhaf, R., Oberto, R., Simard, M., Rignot, E., Kwok, R. and Pi, X., 2008, March. Deformation, ecosystem structure, and dynamics of ice (DESDynI). In *2008 IEEE Aerospace Conference* (pp. 1-13). IEEE.

Donnellan, A., Parker, J., Heflin, M., Lyzenga, G., Moore, A., Ludwig, L.G., Rundle, J., Wang, J. and Pierce, M., 2018. Fracture Advancing Step Tectonics Observed in the Yuha Desert and Ocotillo, CA, Following the 2010 Mw7. 2 El Mayor-Cucapah Earthquake. *Earth and Space Science*.

Dubois, P.C., Van Zyl, J. and Engman, T., 1995. Measuring soil moisture with imaging radars. *IEEE Transactions on Geoscience and Remote Sensing*, 33(4), pp. 915-926.

Duputel, Z., Jiang, J., Jolivet, R., Simons, M., Rivera, L., Ampuero, J.P., Riel, B., Owen, S.E., Moore, A.W., Samsonov, S.V. and Ortega Culaciati, F., 2015. The Iquique earthquake sequence of April 2014: Bayesian modeling accounting for prediction uncertainty. *Geophysical Research Letters*, 42(19), pp. 7949-7957.

Dzurisin, D., 2007, *Volcano Deformation—Geodetic Monitoring Techniques: Springer-Praxis Books in Geophysical Sciences*, Springer, Berlin, 441 p.

Eiken, O., Ringrose, P., Hermanrud, C., Nazarian, B. and Torp, T., 2011. Lessons learned from 14 years of CCS Operations: Sleipner, In Salah and Snøhvit. *Energy Procedia*, Volume 4, 5541-5548.

Emardson, T.R., Simons, M. and Webb, F.H., 2003. Neutral atmospheric delay in interferometric synthetic aperture radar applications: Statistical description and mitigation. *Journal of Geophysical Research: Solid Earth*, 108(B5).

Emery, W.J., Fowler, C.W. and Maslanik, J.A., 1997. Satellite-derived maps of Arctic and Antarctic sea ice motion: 1988 to 1994. *Geophysical Research Letters*, 24(8), pp. 897-900.

Enquist, B.J., West, G.B. and Brown, J.H., 2009. Extensions and evaluations of a general quantitative theory of forest structure and dynamics. *Proceedings of the National Academy of Sciences*, 106(17), pp. 7046-7051.

Falkowski, M.J., Evans, J.S., Martinuzzi, S., Gessler, P.E. and Hudak, A.T., 2009. Characterizing forest succession with lidar data: An evaluation for the Inland Northwest, USA. *Remote Sensing of Environment*, 113(5), pp. 946-956.

Fattahi, H. and Amelung, F., 2013. DEM error correction in InSAR time series. *IEEE Transactions on Geoscience and Remote Sensing*, 51(7), pp.4249-4259.

Ferretti, A., Prati, C. and Rocca, F., 2001. Permanent Scatterers in SAR Interferometry, *IEEE Transactions on Geoscience and Remote Sensing*, (39), pp. 8–20.

Finlayson, C.M., Davidson, N.C., Spiers, A.G. and Stevenson, N.J., 1999. Global wetland inventory—current status and future priorities. *Marine and Freshwater Research*, 50(8), pp. 717-727.

Foley, J.A., DeFries, R., Asner, G.P., Barford, C., Bonan, G., Carpenter, S.R., Chapin, F.S., Coe, M.T., Daily, G.C., Gibbs, H.K. and Helkowski, J.H., 2005. Global consequences of land use. *Science*, 309(5734), pp. 570-574.

Foster, J., Brooks, B., Cherubini, T., Shacat, C., Businger, S. and Werner, C.L., 2006. Mitigating atmospheric noise for InSAR using a high resolution weather model. *Geophysical Research Letters*, 33(16).

Fournier, T.J., Pritchard, M.E. and Riddick, S.N., 2010. Duration, magnitude, and frequency of subaerial volcano deformation events: New results from Latin America using InSAR and a global synthesis. *Geochemistry, Geophysics, Geosystems*, 11(1).

Freeman, A., Krieger, G., Rosen, P., Younis, M., Johnson, W.T., Huber, S., Jordan, R. and Moreira, A., 2009, May. SweepSAR: Beam-forming on receive using a reflector-phased array feed combination for spaceborne SAR. In *Radar Conference, 2009 IEEE* (pp. 1-9). IEEE.

Frolking, S., Palace, M.W., Clark, D.B., Chambers, J.Q., Shugart, H.H. and Hurtt, G.C., 2009. Forest disturbance and recovery: A general review in the context of spaceborne remote sensing of impacts on aboveground biomass and canopy structure. *Journal of Geophysical Research: Biogeosciences*, 114(G2).

Fung, A. and Eom, H., 1981. Multiple scattering and depolarization by a randomly rough Kirchhoff surface. *IEEE Transactions on Antennas and Propagation*, 29(3), pp. 463-471.

Fung, A.K., Li, Z. and Chen, K.S., 1992. Backscattering from a randomly rough dielectric surface. *IEEE Transactions on Geoscience and Remote Sensing*, 30(2), pp. 356-369.

G

Gabriel, A.K., Goldstein, R.M. and Zebker, H.A., 1989. Mapping small elevation changes over large areas: differential radar interferometry. *Journal of Geophysical Research: Solid Earth*, 94(B7), pp. 9183-9191.

Galloway, D.L., Hudnut, K.W., Ingebritsen, S.E., Phillips, S.P., Peltzer, G., Rogez, F. and Rosen, P.A., 1998. Detection of aquifer system compaction and land subsidence using interferometric synthetic aperture radar, Antelope Valley, Mojave Desert, California. *Water Resources Research*, 34(10), pp. 2573-2585.

Galloway, D.L., Jones, D.R. and Ingebritsen, S.E., 1999. Land Subsidence in the United States (Vol. 1182). US Geological Survey.

Gardner, A.S., Moholdt, G., Cogley, J.G., Wouters, B., Arendt, A.A., Wahr, J., Berthier, E., Hock, R., Pfeffer, W.T., Kaser, G. and Ligtenberg, S.R., 2013. A reconciled estimate of glacier contributions to sea level rise: 2003 to 2009. *Science*, 340(6134), pp. 852-857.

Girard-Arduin, F., Mercier, G., Collard, F. and Garello, R., 2005. Operational oil-slick characterization by SAR imagery and synergistic data. *IEEE Journal of Oceanic Engineering*, 30(3), pp. 487-495.

González, P.J., Tiampo, K.F., Palano, M., Cannavó, F. and Fernández, J., 2012. The 2011 Lorca earthquake slip distribution controlled by groundwater crustal unloading. *Nature Geoscience*, 5(11), p. 821.

Goodison, B.E., Waterman, S.E. and Langham, E.J., 1981. Application of synthetic aperture radar data to snow cover monitoring. In *Canadian Symposium on Remote Sensing*, 6th, Halifax, Canada (pp. 263-271).

Gray, A. L., Mattar, K.E., and Vachon, P.W. 1998. InSAR results from the RADARSAT Antarctic mapping mission data: estimation of data using a simple registration procedure. In Stein, T., ed. *IGARSS '98. 18th International Geoscience and Remote Sensing Symposium*, 6, 10 July 1998, Seattle, Washington. Proceedings. Piscataway, NJ, Institute of Electrical and Electronics Engineers, pp. 1638-1640.

Grenerczy, G. and Wegmüller, U., 2011. Persistent scatterer interferometry analysis of the embankment failure of a red mud reservoir using ENVISAT ASAR data. *Natural Hazards*, 59(2), p. 1047.

Grosse, G., Harden, J., Turetsky, M., McGuire, A.D., Camill, P., Tarnocai, C., Frolking, S., Schuur, E.A., Jorgenson, T., Marchenko, S. and Romanovsky, V., 2011. Vulnerability of high-latitude soil organic carbon in North America to disturbance. *Journal of Geophysical Research: Biogeosciences*, 116(G4).

Gupta, M., Kamini Kanta Mohanty and Tapan Jyoti Majumdar, 2007. Land Subsidence Mapping in Jharia Coalfield using InSAR and DGPS Measurements, In proceedings of Conference of JEP towards Microwave Remote Sensing Data Utilization (JEP-MW), SAC, Ahmedabad, pp. 7-21-7-30.

Haas, C., 2010. Dynamics versus thermodynamics: The sea ice thickness distribution. *Sea Ice*, 82, pp. 113-152.

Hall, F.G., Bergen, K., Blair, J.B., Dubayah, R., Houghton, R., Hurtt, G., Kellendorfer, J., Lefsky, M., Ranson, J., Saatchi, S. and Shugart, H.H., 2011. Characterizing 3D vegetation structure from space: Mission requirements. *Remote Sensing of Environment*, 115(11), pp. 2753-2775.

Hallikainen, M.T., Ulaby, F.T., Dobson, M.C., El-Rayes, M.A. and Wu, L.K., 1985. Microwave dielectric behavior of wet soil-Part 1: Empirical models and experimental observations. *IEEE Transactions on Geoscience and Remote Sensing*, (1), pp. 25-34.

Hansen, J., Sato, M., Ruedy, R., Lacis, A. and Oinas, V., 2000. Global warming in the twenty-first century: An alternative scenario. *Proceedings of the National Academy of Sciences*, 97(18), pp. 9875-9880.

Hanson, R.T., 1988. Aquifer-system compaction, Tucson Basin and Avra Valley, Arizona. U.S. Geological Survey Water-Resources Investigations Report 88–4172, 69 p.

Hanssen, R.F., 2001. *Radar interferometry: Data Interpretation and Error Analysis* (Vol. 2). Springer Science & Business Media.

Hansen, M.C., Potapov, P.V., Moore, R., Hancher, M., Turubanova, S.A.A., Tyukavina, A., Thau, D., Stehman, S.V., Goetz, S.J., Loveland, T.R. and Kommareddy, A., 2013. High-resolution global maps of 21st-century forest cover change. *Science*, 342(6160), pp. 850-853.

Harris, N.L., Brown, S., Hagen, S.C., Saatchi, S.S., Petrova, S., Salas, W., Hansen, M.C., Potapov, P.V. and Lotsch, A., 2012. Baseline map of carbon emissions from deforestation in tropical regions. *Science*, 336(6088), pp. 1573-1576.

Hasager, C.B., Vincent, P., Badger, J., Badger, M., Di Bella, A., Peña, A., Husson, R. and Volker, P.J., 2015. Using satellite SAR to characterize the wind flow around offshore wind farms. *Energies*, 8(6), pp. 413-5439.

Hensley, S., Chen, C., Erkmen, B., Haddad, Z., Harcke, L., Rosen, P., Saatchi, S., Oveisgharan, S., Shaffer, S., Simard, M. and Papathanassiou, K., 2010, June. A Performance Estimation Methodology for DESDynI. In *Synthetic Aperture Radar (EUSAR)*, 2010 8th European Conference on (pp. 1-4). VDE.

Hensley, S., Agram, P., Buckley, S., Ghaemi, H., Gurrrola, E., Harcke, L., Veeramachaneni, C., Yun, S., 2014. NISAR Performance Model and Error Budget, NISAR Project Document.

Hess, L.L., Novo, E.M., Slaymaker, D.M., Holt, J., Steffen, C., Valeriano, D.M., Mertes, L.A., Krug, T., Melack, J.M., Gastil, M. and Holmes, C., 2002. Geocoded digital videography for validation of land cover mapping in the Amazon basin. *International Journal of Remote Sensing*, 23(7), pp. 1527-1555.

Hetland, E.A., Musé, P., Simons, M., Lin, Y.N., Agram, P.S. and DiCaprio, C.J., 2012. Multiscale InSAR time series (MInTS) analysis of surface deformation. *Journal of Geophysical Research: Solid Earth*, 117(B2).

Hibler III, W.D., 1979. A dynamic thermodynamic sea ice model. *Journal of Physical Oceanography*, 9(4), pp. 815-846.

Hilley, G. E., Bürgmann, R., Ferretti, A., Novali, F., and Rocca, F., 2004, Dynamics of Slow-Moving Landslides from Permanent Scatterer Analysis. *Science*, v. 304, pp. 1952-1955. Doi: 10.1126/science.1098821.

Hinzman, L.D., Bettez, N.D., Bolton, W.R., Chapin, F.S., Dyurgerov, M.B., Fastie, C.L., Griffith, B., Hollister, R.D., Hope, A., Huntington, H.P. and Jensen, A.M., 2005. Evidence and implications of recent climate change in northern Alaska and other arctic regions. *Climatic Change*, 72(3), pp. 251-298.

Hock, R., 2005. Glacier melt: a review of processes and their modelling. *Progress in Physical Geography*, 29(3), pp. 362-391.

Hock, R. and Jansson, P., 2006. Modeling glacier hydrology. In: Anderson, M.G. and J. McDonnell (Eds.). *Encyclopedia of Hydrological Sciences*. John Wiley & Sons, Ltd, Chichester, 4, 2647-2655, 2005.

Hoffmann, J., Zebker, H.A., Galloway, D.L. and Amelung, F., 2001. Seasonal subsidence and rebound in Las Vegas Valley, Nevada, observed by synthetic aperture radar interferometry. *Water Resources Research*, 37(6), pp. 1551-1566.

Holland, M.M., Bitz, C.M. and Tremblay, B., 2006. Future abrupt reductions in the summer Arctic sea ice. *Geophysical Research Letters*, 33(23).

Holt, B., Rothrock, D.A. and Kwok, R., 1992. Determination of sea ice motion from satellite images. *Microwave Remote Sensing of Sea Ice*, pp. 343-354.

Hooper, A., Zebker, H., Segall, P. and Kampes, B., 2004. A new method for measuring deformation on volcanoes and other natural terrains using InSAR persistent scatterers. *Geophysical research letters*, 31(23).

Hooper, A.J., 2006. Persistent scatter radar interferometry for crustal deformation studies and modeling of volcanic deformation.

Hooper, A., Bekaert, D., Spaans, K. and Ankan, M., 2012. Recent advances in SAR interferometry time series analysis for measuring crustal deformation. *Tectonophysics*, 514, pp. 1-13.

Hooper, A. and Zebker, H.A., 2007. Phase unwrapping in three dimensions with application to InSAR time series. *JOSA A*, 24(9), pp. 2737-2747.

Houghton, R.A., Lawrence, K.T., Hackler, J.L. and Brown, S., 2001. The spatial distribution of forest biomass in the Brazilian Amazon: a comparison of estimates. *Global Change Biology*, 7(7), pp. 731-746.

Houghton, R.A., 2005a. Aboveground forest biomass and the global carbon balance. *Global Change Biology*, 11(6), pp. 945-958.

Houghton, R.A., 2005b. Tropical deforestation as a source of greenhouse gas emissions. *Tropical Deforestation and Climate Change*, 13.

Houghton, R.A., Hall, F. and Goetz, S.J., 2009. Importance of biomass in the global carbon cycle. *Journal of Geophysical Research: Biogeosciences*, 114(G2).

Howat, I.M., Joughin, I. and Scambos, T.A., 2007. Rapid changes in ice discharge from Greenland outlet glaciers. *Science*, 315(5818), pp. 1559-1561.

Howat, I.M., Smith, B.E., Joughin, I. and Scambos, T.A., 2008. Rates of southeast Greenland ice volume loss from combined ICESat and ASTER observations. *Geophysical Research Letters*, 35(17).

Hsu, Y.J., Simons, M., Avouac, J.P., Galetzka, J., Sieh, K., Chlieh, M., Natawidjaja, D., Prawirodirdjo, L. and Bock, Y., 2006. Frictional afterslip following the 2005 Nias-Simeulue earthquake, Sumatra. *Science*, 312(5782), pp. 1921-1926.

Hurtt, G.C., Fisk, J., Thomas, R.Q., Dubayah, R., Moorcroft, P.R. and Shugart, H.H., 2010. Linking models and data on vegetation structure. *Journal of Geophysical Research: Biogeosciences*, 115(G2).

.....

Immitzer, M., Atzberger, C. and Koukal, T., 2012. Tree species classification with random forest using very high spatial resolution 8-band WorldView-2 satellite data. *Remote Sensing*, 4(9), pp. 2661-2693.

Inoue, Y., Kurosui, T., Maeno, H., Uratsuka, S., Kozu, T., Dabrowska-Zielinska, K. and Qi, J., 2002. Season-long daily measurements of multifrequency (Ka, Ku, X, C, and L) and full-polarization backscatter signatures over paddy rice fields and their relationship with biological variables. *Remote Sensing of Environment*, 81(2-3), pp. 194-204.

Ireland, R. L., Poland, J. F. and Riley, F. S., 1984. Land Subsidence in the San Joaquin Valley, California, as of 1980, U.S. Geol. Surv. Prof. Pap., 437-I, 93 pp.

Ismaya, F. and Donovan, J., 2012. Applications of DInSAR for measuring mine-induced subsidence and constraining ground deformation model. In *GeoCongress 2012: State of the Art and Practice in Geotechnical Engineering* (pp. 3001-3010).

Iwahana, G., Uchida, M., Liu, L., Gong, W., Meyer, F.J., Guritz, R., Yamanokuchi, T. and Hinzman, L., 2016. InSAR detection and field evidence for thermokarst after a tundra wildfire, Using ALOS-PALSAR. *Remote Sensing*, 8(3), p. 218.

.....

Jenkins, A. and Doake, C.S.M., 1991. Ice-ocean interaction on Ronne Ice Shelf, Antarctica. *Journal of Geophysical Research: Oceans*, 96(C1), pp. 791-813.

Jolivet, R., Grandin, R., Lasserre, C., Doin, M.P. and Peltzer, G., 2011. Systematic InSAR tropospheric phase delay corrections from global meteorological reanalysis data. *Geophysical Research Letters*, 38(17).

Jolivet, R. and Agram, P. S., 2012. Python-based atmospheric phase screen mitigation using atmospheric re-analysis, URL: <http://pyaps.googlecode.com>.

Jolivet, R., Duputel, Z., Riel, B., Simons, M., Rivera, L., Minson, S. E., Zhang, H., Aivazis, M. A. G., Ayoub, F., Leprince, S., Samsonov, S., Motagh, M., and Fielding, E. J., 2014b, The 2013 Mw 7.7 Balochistan Earthquake: Seismic Potential of an Accretionary Wedge: *Bulletin of the Seismological Society of America*, v. 104, no. 2, pp. 1020-1030.

Jolivet, R., P. S. Agram, N. Y. Lin, M. Simons, M.-P. Doin, G. Peltzer, and Z. Li, 2014a, Improving InSAR geodesy using Global Atmospheric Models, *Journal of Geophysical Research: Solid Earth*, 119(3), 2324-2341, doi:10.1002/2013JB010588.

Jolivet, R., Simons, M., Agram, P.S., Duputel, Z. and Shen, Z.K., 2015. Aseismic slip and seismogenic coupling along the central San Andreas Fault. *Geophysical Research Letters*, 42(2), pp. 297-306.

Jones, C.E. and Blom, R.G., 2014. Bayou Corne, Louisiana, sinkhole: Precursory deformation measured by radar interferometry. *Geology*, 42(2), pp. 111-114.

Joughin, I., Kwok, R. and Fahnestock, M., 1996. Estimation of ice-sheet motion using satellite radar interferometry: method and error analysis with application to Humboldt Glacier, Greenland. *Journal of Glaciology*, 42(142), pp. 64-575.

Joughin, I.R., Kwok, R. and Fahnestock, M.A., 1998. Interferometric estimation of three-dimensional ice-flow using ascending and descending passes. *IEEE Transactions on Geoscience and Remote Sensing*, 36(1), pp. 25-37.

Joughin, I., 2002. Ice-sheet velocity mapping: a combined interferometric and speckle-tracking approach. *Annals of Glaciology*, 34, pp. 195-201.

Joughin, I. and Padman, L., 2003. Melting and freezing beneath Filchner-Ronne Ice Shelf, Antarctica. *Geophysical Research Letters*, 30(9).

Joughin, I., Abdalati, W. and Fahnestock, M., 2004a. Large fluctuations in speed on Greenland's Jakobshavn Isbrae glacier. *Nature*, 432(7017), p. 608.

Joughin, I., MacAyeal, D.R. and Tulaczyk, S., 2004b. Basal shear stress of the Ross ice streams from control method inversions. *Journal of Geophysical Research: Solid Earth*, 109(B9).

Joughin, I., Smith, B.E., Howat, I.M., Scambos, T. and Moon, T., 2010a. Greenland flow variability from ice-sheet-wide velocity mapping. *Journal of Glaciology*, 56(197), pp. 415-430.

Joughin, I., Smith, B.E. and Holland, D.M., 2010b. Sensitivity of 21st century sea level to ocean-induced thinning of Pine Island Glacier, Antarctica. *Geophysical Research Letters*, 37(20).

Joughin, I., Smith, B.E. and Abdalati, W., 2010b. Glaciological advances made with interferometric synthetic aperture radar. *Journal of Glaciology*, 56(200), pp. 1026-1042.

Joughin, I. and Alley, R.B., 2011. Stability of the West Antarctic ice sheet in a warming world. *Nature Geoscience*, 4(8), p. 506.

Joughin, I., Alley, R.B. and Holland, D.M., 2012. "Ice-Sheet Response to Oceanic Forcing." *Science* 338(6111): pp. 1172-76.

Joughin, I., Shean, D.E., Smith, B.E. and Dutrieux, P., 2016. Grounding line variability and subglacial lake drainage on Pine Island Glacier, Antarctica. *Geophysical Research Letters*, 43(17), pp. 9093-9102.

Joughin, I., Smith, B.E. and Howat, I., 2018. Greenland Ice Mapping Project: ice flow velocity variation at sub-monthly to decadal timescales. *Cryosphere*, 12(7).

.....

K

Kääb, A., Huggel, C., Fischer, L., Guex, S., Paul, F., Roer, I., Salzmann, N., Schlaefli, S., Schmutz, K., Schneider, D. and Strozz, T., 2005. Remote sensing of glacier-and permafrost-related hazards in high mountains: an overview. *Natural Hazards and Earth System Science*, 5(4), pp. 527-554.

Kääb, A., 2008. Remote sensing of permafrost related problems and hazards: Permafrost and Periglacial Processes, v. 19, pp. 107-136.

Karam, M.A., Chen, K.S. and Fung, A.K., 1992. Statistics of backscatter radar return from vegetation.

Kaser, G., Cogley, J.G., Dyurgerov, M.B., Meier, M.F. and Ohmura, A., 2006. Mass balance of glaciers and ice caps: consensus estimates for 1961-2004. *Geophysical Research Letters*, 33(19).

Ke, Y. and Quackenbush, L. J., 2011, A review of methods for automatic individual tree-crown detection and delineation from passive remote sensing. *International Journal of Remote Sensing*. <https://doi.org/10.1080/01431161.2010.494184>.

Kellendorfer, J., Cartus, O., Bishop, J., Walker, W. and Holecz, F., 2014. Large scale mapping of forests and land cover with synthetic aperture radar data. In *Land Applications of Radar Remote Sensing*. InTech.

Kheshgi, H.S., Jain, A.K., Kotamathi, V.R. and Wuebbles, D.J., 1999. Future atmospheric methane concentrations in the context of the stabilization of greenhouse gas concentrations. *Journal of Geophysical Research: Atmospheres*, 104(D16), pp. 19183-19190.

Kienholz, C., 2010. Shrinkage of Selected South-Central Alaskan Glaciers AD 1900-2010: A Spatio-temporal Analysis Applying Photogrammetric, GIS-based and Historical Methods (Doctoral dissertation, Verlag nicht ermittelbar).

Kindermann, G., McCallum, I., Fritz, S. and Obersteiner, M., 2008. A global forest growing stock, biomass and carbon map based on FAO statistics. *Silva Fennica*, 42(3), pp. 387-396.

King, N.E., Argus, D., Langbein, J., Agnew, D.C., Bawden, G., Dollar, R.S., Liu, Z., Galloway, D., Reichard, E., Yong, A. and Webb, F.H., 2007. Space geodetic observation of expansion of the San Gabriel Valley, California, aquifer system, during heavy rainfall in winter 2004-2005. *Journal of Geophysical Research: Solid Earth*, 112(B3).

Klein L. and Taaheri A., 2016, Data Model, File Format and Library. HDF-EOS, NASA ESDS-RFC-008. v1. 1.

Kottmeier, C., Olf, J., Frieden, W. and Roth, R., 1992. Wind forcing and ice motion in the Weddell Sea region. *Journal of Geophysical Research: Atmospheres*, 97(D18), pp. 20373-20383.

Kwok, R., Curlander, J.C., McConnell, R. and Pang, S.S., 1990. An ice-motion tracking system at the Alaska SAR facility. *IEEE Journal of Oceanic Engineering*, 15(1), pp. 44-54.

Kwok, R. and Baltzer, T., 1995. The geophysical processor system at the Alaska SAR Facility. *Photogrammetric Engineering and Remote Sensing*, 61(12), pp. 1445-1453.

Kwok, R., Nghiem, S.V., Yueh, S.H. and Huynh, D.D., 1995. Retrieval of thin ice thickness from multifrequency polarimetric SAR data. *Remote Sensing of Environment*, 51(3), pp. 361-374.

Kwok, R., 2001. Deformation of the Arctic Ocean sea ice cover between November 1996 and April 1997: a qualitative survey. In *IUTAM Symposium on Scaling Laws in Ice Mechanics and Ice Dynamics* (pp. 315-322). Springer, Dordrecht.

Kwok, R. and Cunningham, G.F., 2002. Seasonal ice area and volume production of the Arctic Ocean: November 1996 through April 1997. *Journal of Geophysical Research: Oceans*, 107(C10).

Kwok, R., Cunningham, G.F. and Hibler, W.D., 2003. Sub-daily ice motion and deformation from Radarsat observations, *Geophysical Research Letters*, 30 (23), doi:10.1029/2003GL018723.

Kwok, R., 2010. Satellite remote sensing of sea-ice thickness and kinematics: a review. *Journal of Glaciology*, 56(200), pp. 1129-1140.

L

Lanari, R., Lundgren, P., Manzo, M. and Casu, F., 2004. Satellite radar interferometry time series analysis of surface deformation for Los Angeles, California. *Geophysical Research Letters*, 31(23).

Lang, R.H., 1981. Electromagnetic backscattering from a sparse distribution of lossy dielectric scatterers. *Radiation Science*, 16(1), pp. 15-30.

Lang, R.H. and Sighu, J.S., 1983. Electromagnetic backscattering from a layer of vegetation: A discrete approach. *IEEE Transactions on Geoscience and Remote Sensing*, (1), pp. 62-71.

Larour, E., Rignot, E., Joughin, I. and Aubry, D., 2005. Rheology of the Ronne Ice Shelf, Antarctica, inferred from satellite radar interferometry data using an inverse control method. *Geophysical Research Letters*, 32(5).

Lauknes, T.R., Zebker, H.A. and Larsen, Y., 2011. InSAR deformation time series using an L1-norm small-baseline approach. *IEEE Transactions on Geoscience and Remote Sensing*, 49(1), pp.536-546.

Le Quéré, C., Andrew, R.M., Friedlingstein, P., Sitch, S., Pongratz, J., Manning, A.C., Korsbakken, J.I., Peters, G.P., Canadell, J.G., Jackson, R.B. and Boden, T.A., 2017. Global carbon budget 2017. *Earth System Science Data Discussions*, pp.1-79.

Le Toan, T., Quegan, S., Davidson, M.W.J., Balzter, H., Paillou, P., Papathanassiou, K., Plummer, S., Rocca, F., Saatchi, S., Shugart, H. and Ulander, L., 2011. The BIOMASS mission: Mapping global forest biomass to better understand the terrestrial carbon cycle. *Remote Sensing of Environment*, 115(11), pp.2850-2860.

Li, Z. H., Fielding, E. J., Cross, P., and Muller, J. P. 2006a. Interferometric synthetic aperture radar atmospheric correction: GPS topography-dependent turbulence model, 111, B02404.

Li, Z., Muller, J. P., Cross, P., Albert, P., Fischer, J., and Bennartz, R. 2006b. Assessment of the potential of MERIS near-infrared water vapour products to correct ASAR interferometric measurements. *Int. J. Rem. Sens.*, 27, pp. 349–365.

Lin, Y.N.N., Simons, M., Hetland, E.A., Muse, P. and DiCaprio, C., 2010. A multiscale approach to estimating topographically correlated propagation delays in radar interferograms. *Geochemistry, Geophysics, Geosystems*, 11(9).

Lindsay, R.W. and Stern, H.L., 2003. The RADARSAT geophysical processor system: Quality of sea ice trajectory and deformation estimates. *Journal of Atmospheric and Oceanic Technology*, 20(9), pp.1333-1347.

Liu, L., Zhang, T., and Wahr, J., 2010, InSAR measurements of surface deformation over permafrost on the North Slope of Alaska: *Journal of Geophysical Research*, v. 115, p. F03023.

Liu, L., Schaefer, K., Zhang, T. and Wahr, J., 2012. Estimating 1992–2000 average active layer thickness on the Alaskan North Slope from remotely sensed surface subsidence. *Journal of Geophysical Research: Earth Surface*, 117(F1).

Liu, M., Tian, H., Yang, Q., Yang, J., Song, X., Lohrenz, S.E. and Cai, W.J., 2013. Long-term trends in evapotranspiration and runoff over the drainage basins of the Gulf of Mexico during 1901–2008. *Water Resources Research*, 49(4), pp.1988-2012.

Liu, L., Jafarov, E.E., Schaefer, K.M., Jones, B.M., Zebker, H.A., Williams, C.A., Rogan, J. and Zhang, T., 2014. InSAR detects increase in surface subsidence caused by an Arctic tundra fire. *Geophysical Research Letters*, 41(11), pp.3906-3913.

Lohman, R.B., Simons, M. and Savage, B., 2002. Location and mechanism of the Little Skull Mountain earthquake as constrained by satellite radar interferometry and seismic waveform modeling. *Journal of Geophysical Research: Solid Earth*, 107(B6), pp.ETG-7.

Lohman, R.B. and Simons, M., 2005. Locations of selected small earthquakes in the Zagros mountains. *Geochemistry, Geophysics, Geosystems*, 6(3).

Lu, Z., and Wicks, C., 2010, Study of the 6 August 2007 Crandall Canyon mine (Utah, USA) collapse from ALOS PALSAR InSAR: *Geomatics, Natural Hazards and Risk*, 1, pp. 85-93.

Lu, Z., and Dzurisin, D., 2014. InSAR Imaging of Aleutian Volcanoes: Monitoring a Volcanic Arc from Space, Springer Praxis Books, Geophysical Sciences, ISBN 978-3-642-00347-9, 388 pp.

Lu, Z., Dzurisin, D., Biggs, J., Wicks, C., Jr, and McNutt, S., 2010, Ground surface deformation patterns, magma supply, and magma storage at Okmok volcano, Alaska, from InSAR analysis: 1. Intereruption deformation, 1997–2008: *Journal of Geophysical Research*, 115, B00B02, doi:10.1029/2009JB006969.

Lucas, R., Bunting, P., Paterson, M., and Chisholm, L., 2008, Classification of Australian forest communities using aerial photography, CASI and HyMap data. *Remote Sensing of Environment*, 112(5), pp. 2088–2103.

Lundgren, P., F. Casu, M. Manzo, A. Pepe, P. Berardino, E. Sansosti, and R. Lanari, 2004, Gravity and magma spreading of Mount Etna volcano revealed by radar interferometry, *Geophysical Research Letters*, L04602, doi:10.1029/2003GL018736.

M

MacAyeal, D.R., 1993. A tutorial on the use of control methods in ice-sheet modeling. *Journal of Glaciology*, 39(131), pp. 91-98.

Malinowski, R., Groom, G., Schwanghart, W. and Heckrath, G., 2015. Detection and delineation of localized flooding from WorldView-2 multispectral data. *Remote Sensing*, 7(11), pp. 14853-14875.

Malvern, L. E., 1969. *Introduction to Mechanics of a Continuous Medium*, Prentice-Hall, 713 pp.

Marquardt, F., 2009. F. Marquardt and SM Girvin, *Physics* 2, 40 (2009). *Physics*, 2, p. 40.

Massonnet, D., Rossi, M., Carmona, C., Adragna, F., Peltzer, G., Feigl, K. and Rabaute, T., 1993. The displacement field of the Landers earthquake mapped by radar interferometry. *Nature*, 364(6433), p. 138.

Matthews, E., 2000: 12. Wetlands. In *Atmospheric Methane: Its Role in the Global Environment*. and M.A.K. Khalil, Ed. Springer Verlag, pp. 202-233.

Matzler, C., 1994. Microwave (1-100 GHz) dielectric model of leaves. *IEEE Transactions on Geoscience and Remote Sensing*, 32(4), pp. 947-949.

Meier, M.F., Dyurgerov, M.B., Rick, U.K., O'neel, S., Pfeffer, W.T., Anderson, R.S., Anderson, S.P. and Glazovsky, A.F., 2007. Glaciers dominate eustatic sea-level rise in the 21st century. *Science*, 317(5841), pp. 1064-1067.

Meinzer, O.E., 1928. Compressibility and elasticity of artesian aquifers. *Economic Geology*, 23(3), pp. 263-291.

Mermoz, S., Réjou-Méchain, M., Villard, L., Le Toan, T., Rossi, V. and Gourlet-Fleury, S., 2015. Decrease of L-band SAR backscatter with biomass of dense forests. *Remote Sensing of Environment*, 159, pp. 307-317.

Meyer, F.J., 2011. Performance requirements for ionospheric correction of low-frequency SAR data. *IEEE transactions on geoscience and remote sensing*, 49(10), pp. 3694-3702.

Meyer, F.J., 2014, June. Quantifying ionosphere-induced image distortions in L-band SAR data using the ionospheric scintillation model WBMOD. In *EUSAR 2014; 10th European Conference on Synthetic Aperture Radar*; Proceedings of (pp. 1-4). VDE.

Michel, R. and Rignot, E., 1999. Flow of Glaciar Moreno, Argentina, from repeat-pass Shuttle Imaging Radar images: comparison of the phase correlation method with radar interferometry. *Journal of Glaciology*, 45(149), 93-100.

Mironov, V.L., Dobson, M.C., Kaupp, V.H., Komarov, S.A. and Kleshchenko, V.N., 2004. Generalized refractive mixing dielectric model for moist soils. *IEEE Transactions on Geoscience and Remote Sensing*, 42(4), pp. 773-785.

Mitchard, E.T., Saatchi, S.S., Woodhouse, I.H., Nangendo, G., Ribeiro, N.S., Williams, M., Ryan, C.M., Lewis, S.L., Feldpausch, T.R. and Meir, P., 2009. Using satellite radar backscatter to predict above-ground woody biomass: A consistent relationship across four different African landscapes. *Geophysical Research Letters*, 36(23).

Mohr, J.J., Reeh, N. and Madsen, S.N., 1998. Three-dimensional glacial flow and surface elevation measured with radar interferometry. *Nature*, 391(6664), p. 273.

Monaldo, F. and Kerbaol, V., 2004, June. The SAR measurement of ocean surface winds: an overview for the 2nd workshop on coastal and marine applications of SAR. In *Proc. of the 2nd Workshop on SAR Coastal and Marine Applications* (pp. 8-12).

Monaldo, F., Jackson, C., Li, X. and Pichel, W.G., 2016. Preliminary evaluation of Sentinel-1A wind speed retrievals. *IEEE Journal of Selected Topics in Applied Earth Observations and Remote Sensing*, 9(6), pp. 2638-2642.

Moon, T., Joughin, I., Smith, B. and Howat, I., 2012. 21st-century evolution of Greenland outlet glacier velocities. *Science*, 336(6081), pp. 576-578.

Moore, R.K., Claassen, J.P. and Lin, Y.H., 1981. Scanning spaceborne synthetic aperture radar with integrated radiometer. *IEEE Transactions on Aerospace and Electronic Systems*, (3), pp. 410-421.

Morlighem, M., Seroussi, H., Larour, E. and Rignot, E., 2013. Inversion of basal friction in Antarctica using exact and incomplete adjoints of a higher-order model. *Journal of Geophysical Research: Earth Surface*, 118(3), pp. 1746-1753.

Mouginot, J., Rignot, E., Scheuchl, B. and Millan, R., 2017. Comprehensive annual ice sheet velocity mapping using Landsat-8, Sentinel-1, and RADARSAT-2 data. *Remote Sensing*, 9(4), p. 364.

Myneni, R.B., Dong, J., Tucker, C.J., Kaufmann, R.K., Kauppi, P.E., Liski, J., Zhou, L., Alexeyev, V. and Hughes, M.K., 2001. A large carbon sink in the woody biomass of northern forests. *Proceedings of the National Academy of Sciences*, 98(26), pp. 14784-14789.

N

Neumann, M., Saatchi, S.S., Ulander, L.M. and Fransson, J.E., 2012. Assessing performance of L- and P-band polarimetric interferometric SAR data in estimating boreal forest above-ground biomass. *IEEE Transactions on Geoscience and Remote Sensing*, 50(3), pp. 714-726.

O

Oh, Y., Sarabandi, K. and Ulaby, F.T., 1992. An empirical model and an inversion technique for radar scattering from bare soil surfaces. *IEEE Transactions on Geoscience and Remote Sensing*, 30(2), pp. 370-381.

Olofsson, P., Foody, G.M., Herold, M., Stehman, S.V., Woodcock, C.E. and Wulder, M.A., 2014. Good practices for estimating area and assessing accuracy of land change. *Remote Sensing of Environment*, 148, pp. 42-57.

Olson, D.M., Dinerstein, E., Wikramanayake, E.D., Burgess, N.D., Powell, G.V., Underwood, E.C., D'amico, J.A., Itoua, I., Strand, H.E., Morrison, J.C. and Loucks, C.J., 2001. *Terrestrial Ecoregions of the World: A New Map of Life on Earth: A new global map of terrestrial ecoregions provides an innovative tool for conserving biodiversity*. *BioScience*, 51(11), pp. 933-938.

Onn, F. and Zebker, H.A., 2006. Correction for interferometric synthetic aperture radar atmospheric phase artifacts using time series of zenith wet delay observations from a GPS network. *Journal of Geophysical Research: Solid Earth*, 111(B9).

Onuma, T. and Ohkawa, S., 2009. Detection of surface deformation related with CO₂ injection by DInSAR at In Salah, Algeria. *Energy Procedia*, 1(1), pp. 2177-2184.

P

Paine, J.G., Buckley, S.M., Collins, E.W. and Wilson, C.R., 2012. Assessing collapse risk in evaporite sinkhole-prone areas using microgravimetry and radar interferometry. *Journal of Environmental and Engineering Geophysics*, 17(2), pp. 75-87.

Pan, Y., Birdsey, R.A., Fang, J., Houghton, R., Kauppi, P.E., Kurz, W.A., Phillips, O.L., Shvidenko, A., Lewis, S.L., Canadell, J.G. and Ciais, P., 2011. A large and persistent carbon sink in the world's forests. *Science*, p. 1201609.

Paterson, W. S. B., 1994. *The Physics of Glaciers*, 3rd ed., 480 pp., Pergamon, Oxford.

Paulson, A., Zhong, S. and Wahr, J., 2007. Inference of mantle viscosity from GRACE and relative sea level data. *Geophysical Journal International*, 171(2), pp. 497-508.

Payne, A.J., Vieli, A., Shepherd, A.P., Wingham, D.J. and Rignot, E., 2004. Recent dramatic thinning of largest West Antarctic ice stream triggered by oceans. *Geophysical Research Letters*, 31(23).

Peltzer, G., Hudnut, K.W. and Feigl, K.L., 1994. Analysis of coseismic surface displacement gradients using radar interferometry: New insights into the Landers earthquake. *Journal of Geophysical Research: Solid Earth*, 99(B11), pp. 21971-21981.

Penman, J., Gytarsky, M., Hiraishi, T., Krug, T., Kruger, D., Pipatti, R., Buendia, L., Miwa, K., Ngara, T., Tanabe, K. and Wagner, F., 2003. Good practice guidance for land use, land-use change and forestry.

Peplinski, N.R., Ulaby, F.T. and Dobson, M.C., 1995. Dielectric properties of soils in the 0.3-1.3-GHz range. *IEEE Transactions on Geoscience and Remote Sensing*, 33(3), pp. 803-807.

Peters, G.P., Marland, G., Le Quéré, C., Boden, T., Canadell, J.G. and Raupach, M.R., 2012. Rapid growth in CO₂ emissions after the 2008–2009 global financial crisis. *Nature Climate Change*, 2(1), p.2.

Phillips, O.M., 2003. Groundwater flow patterns in extensive shallow aquifers with gentle relief: Theory and application to the Galena/Locust Grove region of eastern Maryland. *Water Resources Research*, 39(6).

Poland, J.F., 1984. *Guidebook to Studies of Land Subsidence Due to Ground-Water Withdrawal*.

Pritchard, M.E. and Simons, M., 2002. A satellite geodetic survey of large-scale deformation of volcanic centres in the central Andes. *Nature*, 418(6894), p. 167.

Pritchard, M.E. and Simons, M., 2004. An InSAR-based survey of volcanic deformation in the central Andes. *Geochemistry, Geophysics, Geosystems*, 5(2).

Pritchard, M.E., Ji, C. and Simons, M., 2006. Distribution of slip from 11 Mw > 6 earthquakes in the northern Chile subduction zone. *Journal of Geophysical Research: Solid Earth*, 111(B10).

Pritchard, M.E., Norabuena, E.O., Ji, C., Boroschek, R., Comte, D., Simons, M., Dixon, T.H. and Rosen, P.A., 2007. Geodetic, teleseismic, and strong motion constraints on slip from recent southern Peru subduction zone earthquakes. *Journal of Geophysical Research: Solid Earth*, 112(B3).

Pullman, E.R., Torre Jorgenson, M. and Shur, Y., 2007. Thaw settlement in soils of the Arctic Coastal Plain, Alaska. *Arctic, Antarctic, and Alpine Research*, 39(3), pp. 468-476.

Q

Qu-lin, T., Qing-chao, W., and Song-lin, Y., 2010. Discussion on Monitoring the Subsidence of Subgrade in Permafrost Region With Satellite D-InSAR Technology: *Journal of Railway Engineering Society*.

R

Ramaswamy, V., Boucher, O., Haigh, J., Hauglustine, D., Haywood, J., Myhre, G., Nakajima, T., Shi, G.Y. and Solomon, S., 2001. Radiative forcing of climate. *Climate Change*, 349.

Reiche, J., Lucas, R., Mitchell, A.L., Verbesselt, J., Hoekman, D.H., Haarpaintner, J., Kellendorfer, J.M., Rosenqvist, A., Lehmann, E.A., Woodcock, C.E. and Seifert, F.M., 2016. Combining satellite data for better tropical forest monitoring. *Nature Climate Change*, 6(2), p. 120.

Richards, J. A., 2009. *Remote Sensing with Imaging Radar*, Springer Publishers. ISBN 978-3-642-02020-9.

Rignot, E. and Kanagaratnam, P., 2006. Changes in the velocity structure of the Greenland Ice Sheet. *Science*, 311(5763), pp. 986-990.

Rignot, E. and Jacobs, S.S., 2002. Rapid bottom melting widespread near Antarctic ice sheet grounding lines. *Science*, 296(5575), pp. 2020-2023.

Rignot, E., Casassa, G., Gogineni, P., Krabill, W., Rivera, A.U. and Thomas, R., 2004. Accelerated ice discharge from the Antarctic Peninsula following the collapse of Larsen B ice shelf. *Geophysical Research Letters*, 31(18).

Rignot, E., Mouginot, J. and Scheuchl, B., 2011a. Ice Flow of the Antarctic Ice Sheet, *Science*, 333(6048), pp. 1427–1430, doi:10.1126/science.1208336.

Rignot, E., Mouginot, J. and Scheuchl, B., 2011b. Antarctic grounding line mapping from differential satellite radar interferometry. *Geophysical Research Letters*, 38: L10504, doi:10.1029/2011GL047109.

Rignot, E., Velicogna, I., van den Broeke, M.R., Monaghan, A. and Lenaerts, J.T., 2011c. Acceleration of the contribution of the Greenland and Antarctic ice sheets to sea level rise. *Geophysical Research Letters*, 38(5).

Rignot, E., Jacobs, S., Mouginot, J. and Scheuchl, B., 2013. Ice-shelf melting around Antarctica. *Science*, 341(6143), pp. 266-270.

Rigor, I.G., Wallace, J.M. and Colony, R.L., 2002. Response of sea ice to the Arctic Oscillation. *Journal of Climate*, 15(18), pp. 2648-2663.

Riley, F.S., 1969. Analysis of borehole extensometer data from central California. *Land Subsidence*, 2, pp. 423-431.

Ringrose, P., et al., 2009, Plume development around well KB-502 at the In Salah CO₂ storage site, *First Break*, v. 27, pp. 85-89. www.firstbreak.org.

Robinson, C., Saatchi, S., Neumann, M. and Gillespie, T., 2013. Impacts of spatial variability on aboveground biomass estimation from L-band radar in a temperate forest. *Remote Sensing*, 5(3), pp. 1001-1023.

Romanovsky, V.E., Smith, S.L., and Christiansen, H.H., 2010, Permafrost thermal state in the polar Northern Hemisphere during the International Polar Year 2007–2009: a synthesis: Permafrost and Periglacial Processes, v. 21, pp. 106-116.

Romeiser, R., 2013. The Future of SAR-Based Oceanography: High-Resolution Current Measurements by Along-Track Interferometry. *Oceanography*, 26(2), pp. 92-99.

Romijn, E., Herold, M., Kooistra, L., Murdiyarto, D. and Verchot, L., 2012. Assessing capacities of non-Annex I countries for national forest monitoring in the context of REDD+. *Environmental Science & Policy*, 19, pp. 33-48.

Rosen, P.A., Hensley, S., Joughin, I.R., Li, F.K., Madsen, S.N., Rodriguez, E. and Goldstein, R.M., 2000. Synthetic aperture radar interferometry. *Proceedings of the IEEE*, 88(3), pp. 333-382.

Rosen, P.A., Hensley, S. and Chen, C., 2010. Measurement and mitigation of the ionosphere in L-band Interferometric SAR data. *Proc. IEEE Radar Conference 2010*, Washington DC.

Rosen, P.A., Gurrola, E., Sacco, G.F. and Zebker, H., 2012, April. The InSAR scientific computing environment. In *Synthetic Aperture Radar, 2012. EUSAR. 9th European Conference on* (pp. 730-733). VDE.

Rosen, P.A., Hensley, S., Shaffer, S., Veilleux, L., Chakraborty, M., Misra, T., Bhan, R., Sagi, V.R. and Satish, R., 2015, May. The NASA-ISRO SAR mission—an international space partnership for science and societal benefit. In *Radar Conference (RadarCon), 2015 IEEE* (pp. 1610-1613). IEEE.

Rosenqvist, Å., Milne, A., Lucas, R., Imhoff, M. and Dobson, C., 2003. A review of remote sensing technology in support of the Kyoto Protocol. *Environmental Science & Policy*, 6(5), pp. 441-455.

Rosenqvist, A., Shimada, M., Ito, N. and Watanabe, M., 2007. ALOS PALSAR: A pathfinder mission for global-scale monitoring of the environment. *IEEE Transactions on Geoscience and Remote Sensing*, 45(11), pp. 3307-3316.

Rott, H. and Davis, R.E., 1993. Multifrequency and polarimetric SAR observations on alpine glaciers. *Annals of Glaciology*, 17, pp. 98-104.

Rykhus, R., and Lu, Z., 2011, Monitoring a 2003, Yukon Flats, Alaska wildfire using multi-temporal Radarsat-1 intensity and interferometric coherence images: *Geomatics, Natural Hazards and Risk*, Vol. 2, No. 1, pp. 15–32.

S

Saatchi, S.S. and Lang, R.H., 1989. Self Consistent Approach to Average Waves in a One Dimensional Discrete Random Medium. In *PIERS: Progress in Electromagnetics Research Symposium* (p. 277).

Saatchi, S.S., Le Vine, D.M. and Lang, R.H., 1994. Microwave backscattering and emission model for grass canopies. *IEEE Transactions on Geoscience and Remote Sensing*, 32(1), pp. 177-186.

Saatchi, S.S. and McDonald, K.C., 1997. Coherent effects in microwave backscattering models for forest canopies. *IEEE Transactions on Geoscience and Remote Sensing*, 35(4), pp. 1032-1044.

Saatchi, S.S. and Moghaddam, M., 2000. Estimation of crown and stem water content and biomass of boreal forest using polarimetric SAR imagery. *IEEE Transactions on Geoscience and Remote Sensing*.

Saatchi, S.S., Houghton, R.A., Dos Santos Alvala, R.C., Soares, J.V. and Yu, Y., 2007. Distribution of aboveground live biomass in the Amazon basin. *Global Change Biology*, 13(4), pp. 816-837.

Saatchi, S.S., Harris, N.L., Brown, S., Lefsky, M., Mitchard, E.T., Salas, W., Zutta, B.R., Buermann, W., Lewis, S.L., Hagen, S. and Petrova, S., 2011. Benchmark map of forest carbon stocks in tropical regions across three continents. *Proceedings of the National Academy of Sciences*, 108(24), pp. 9899-9904.

Saatchi, S., Halligan, K., Despain, D.G. and Crabtree, R.L., 2007. Estimation of forest fuel load from radar remote sensing. *IEEE Transactions on Geoscience and Remote Sensing*, 45(6), pp. 1726-1740.

Saatchi, S., Marlier, M., Chazdon, R.L., Clark, D.B. and Russell, A.E., 2011. Impact of spatial variability of tropical forest structure on radar estimation of aboveground biomass. *Remote Sensing of Environment*, 115(11), pp. 2836-2849.

Saatchi, S., Asefi-Najafabady, S., Malhi, Y., Aragão, L.E., Anderson, L.O., Myneni, R.B. and Nemani, R., 2013. Persistent effects of a severe drought on Amazonian forest canopy. *Proceedings of the National Academy of Sciences*, 110(2), pp. 565-570.

Sahagian, D., Melack, J., Birkett, C., Chanton, J., Dunne, T., Estes, J., Finlayson, M., Fresco, L., Gopal, B., Hess, L. and Hollis, T., 1997. Global wetland distribution and functional characterization: Trace gases and the hydrologic cycle. In *Joint IGBP GAIM-DIS-BAHC-IGAC-LUCC workshop, IGBP GAIM/IGBP Global Change*, Santa Barbara CA, USA, 1996 (pp. 45-45).

Sandwell, D.T., and Price, E.J., 1996. Multiple pass INSAR processing for geophysical applications: stack phase gradient then unwrap, in *Eos Trans. Amer. Geophys. Un. Meeting Suppl.*, p. F52.

Sarabandi, K. and Lin, Y.C., 2000. Simulation of interferometric SAR response for characterizing the scattering phase center statistics of forest canopies. *IEEE Transactions on Geoscience and Remote Sensing*, 38(1), pp. 115-125.

Scambos, T.A., Bohlander, J.A., Shuman, C.U. and Skvarca, P., 2004. Glacier acceleration and thinning after ice shelf collapse in the Larsen B embayment, Antarctica. *Geophysical Research Letters*, 31(18).

Schaefer, K., Liu, L., Parsekian, A., Jafarov, E., Chen, A., Zhang, T., Gusmeroli, A., Panda, S., Zebker, H.A. and Schaefer, T., 2015. Remotely sensed active layer thickness (ReSALT) at Barrow, Alaska using interferometric synthetic aperture radar. *Remote Sensing*, 7(4), pp. 3735-3759.

Scheuchl, B., Mouginit, J., Rignot, E., Morlighem, M. and Khazendar, A., 2016. Grounding line retreat of Pope, Smith, and Kohler Glaciers, West Antarctica, measured with Sentinel-1a radar interferometry data. *Geophysical Research Letters*, 43(16), pp. 8572-8579.

Schimel, D., Pavlick, R., Fisher, J.B., Asner, G.P., Saatchi, S., Townsend, P., Miller, C., Frankenberg, C., Hibbard, K. and Cox, P., 2015. Observing terrestrial ecosystems and the carbon cycle from space. *Global change biology*, 21(5), pp. 1762-1776.

Schweder, T., 1976. Some "optimal" methods to detect structural shift or outliers in regression. *Journal of the American Statistical Association*, 71(354), pp. 491-501.

Segall, P., 2013. Volcano deformation and eruption forecasting, Geological Society, London, Special Publications, V. 380, doi:10.1144/SP380.4, 2013.

Shi, J., Wang, J., Hsu, A.Y., O'Neill, P.E. and Engman, E.T., 1997. Estimation of bare surface soil moisture and surface roughness parameter using L-band SAR image data. *IEEE Transactions on Geoscience and Remote Sensing*, 35(5), pp. 1254-1266.

Shimada, T., Kawamura, H. and Shimada, M., 2003. An L-band geophysical model function for SAR wind retrieval using JERS-1 SAR. *IEEE Transactions on Geoscience and Remote Sensing*, 41(3), pp. 518-531.

Short, N., LeBlanc, A.M., Sladen, W., Oldenborger, G., Mathon-Dufour, V. and Brisco, B., 2014. RADARSAT-2 D-InSAR for ground displacement in permafrost terrain, validation from Iqaluit Airport, Baffin Island, Canada. *Remote Sensing of Environment*, 141, pp. 40-51.

Shugart, H.H. and Woodward, F.I., 2011. Global change and the terrestrial biosphere: achievements and challenges. John Wiley & Sons.

Simons, M. and Rosen, P.A., 2007. Interferometric synthetic aperture radar geodesy. In: *Treatise on Geophysics - Geodesy*. Vol.3. Elsevier, Amsterdam, pp. 391-446. ISBN 9780444527486

Smith, J.E. and Heath, L.S., 2002. A model of forest floor carbon mass for United States forest types. Res. Pap. NE-722. Newtown Square, PA: US Department of Agriculture, Forest Service, Northeastern Research Station. 37 p. 722.

Smith, S.L., Burgess, M.M., Riseborough, D. and Mark Nixon, F., 2005. Recent trends from Canadian permafrost thermal monitoring network sites. *Permafrost and Periglacial Processes*, 16(1), pp. 19-30.

Snedecor, G.W. and Cochran, W.G., 1989. *Statistical Methods*, 8th Edn. Ames: Iowa State Univ. Press Iowa.

Sneed, M. and Galloway, D.L., 2000. Aquifer-system compaction and land subsidence: measurements, analyses, and simulations—the Holly Site, Edwards Air Force Base, Antelope Valley, California (No. 2000-4015). Geological Survey (US).

Sneed, M., Brandt, J., Solt, M., 2013. Land Subsidence along the Delta-Mendota Canal in the Northern Part of the San Joaquin Valley, California, 2003-10: U.S. Geological Survey Scientific Investigations Report 2013-5142, 87 p.

Spreen, G., Kern, S., Stammer, D. and Hansen, E., 2009. Fram Strait sea ice volume export estimated between 2003 and 2008 from satellite data. *Geophysical Research Letters*, 36, L19502, doi:10.1029/2009GL039591.

Stehman, S.V., 2005. Comparing estimators of gross change derived from complete coverage mapping versus statistical sampling of remotely sensed data. *Remote Sensing of Environment*, 96(3-4), pp. 466-474.

Stern, H.L., Rothrock, D.A. and Kwok, R., 1995. Open water production in Arctic sea ice: Satellite measurements and model parameterizations. *Journal of Geophysical Research: Oceans*, 100(C10), pp. 20601-20612.

Strozzi, T., Kouraev, A., Wiesmann, A., Wegmüller, U., Sharov, A. and Werner, C., 2008. Estimation of Arctic glacier motion with satellite L-band SAR data. *Remote Sensing of Environment*, 112(3), pp. 636-645.

T

Tello, M., López-Martínez, C. and Mallorqui, J.J., 2005. A novel algorithm for ship detection in SAR imagery based on the wavelet transform. *IEEE Geoscience and Remote Sensing Letters*, 2(2), pp. 201-205.

Terzaghi, K., 1925. Principles of soil mechanics, IV—Settlement and consolidation of clay. *Engineering News-Record*, 95(3), pp. 874-878.

Thorndike, A.S., and Colony, R., 1982, Sea ice motion in response to geostrophic winds, *Journal of Geophysical Research*, 80(33), pp. 4501-4513.

Thorndike, A.S., Rothrock, D.A., Maykut, G.A. and Colony, R., 1975. The thickness distribution of sea ice. *Journal of Geophysical Research*, 80(33), pp. 4501-4513.

Toda, S., Lin, J. and Stein, R.S., 2011. Using the 2011 M w 9.0 off the Pacific coast of Tohoku Earthquake to test the Coulomb stress triggering hypothesis and to calculate faults brought closer to failure. *Earth, Planets and Space*, 63(7), p. 39.

Truong-Loi, M.L., Saatchi, S. and Jaruwatanadilok, S., 2015. Soil moisture estimation under tropical forests using UHF radar polarimetry. *IEEE Transactions on Geoscience and Remote Sensing*, 53(4), pp. 1718-1727.

Tsang, L., Kong, J.A. and Shin, R.T., 1985. Theory of microwave remote sensing.

U

Ulaby, F.T., Stiles, W.H. and Abdelrazik, M., 1984. Snowcover influence on backscattering from terrain. *IEEE Transactions on Geoscience and Remote Sensing*, (2), pp. 126-133.

Ulaby, F.T. and El-Rayes, M.A., 1987. Microwave dielectric spectrum of vegetation-Part II: Dual-dispersion model. *IEEE Transactions on Geoscience and Remote Sensing*, (5), pp. 550-557.

Ulaby, F.T. and Dobson, M.C., 1989. *Handbook of Radar Scattering Statistics for Terrain* (Artech House Remote Sensing Library). Norwood, MA, USA: Artech House.

Ulaby, F.T., Sarabandi, K., McDonald, K.Y.L.E., Whitt, M. and Dobson, M.C., 1990. Michigan microwave canopy scattering model. *International Journal of Remote Sensing*, 11(7), pp. 1223-1253.

V

van der Werf, G. R., Morton, D. C., DeFries, R. S., Olivier, J. G. J., Kasibhatla, P. S., Jackson, R. B., ... Randerson, J. T., 2009, CO₂ emissions from forest loss. *Nature Geoscience*, 2, 737.

van Oort, P.A., 2006. *Spatial Data Quality: from Description to Application*. Wageningen Universiteit.

van Zyl, J. and Kim, Y., 2011. Synthetic Aperture Radar Polarimetry, John Wiley and Sons, DOI:10.1002/9781118116104.

Vasco, D. W., Rucci, A., Ferretti, A., Novali, F., Bissell, R. C., Ringrose, P. S. Mathieson, A. S. and Wright, I. W., 2010. Satellite-based measurements of surface deformation reveal fluid flow associated with the geological storage of carbon dioxide. *Geophysical Research Letters*, Vol. 37, L03303.

Vesecky, J.F., Samadani, R., Smith, M.P., Daida, J.M. and Bracewell, R.N., 1988. Observation of sea-ice dynamics using synthetic aperture radar images: Automated analysis. *IEEE Transactions on Geoscience and Remote Sensing*, 26(1), pp. 38-48.

W

Wadhams, P., 2000. *Ice in the Ocean*, Gordon and Breach Publishers, 351 pp.

Walker, W. S., Stickler, C. M., Kellendorfer, J. M., Kirsch, K. M. and Nepstad, D. C., 2010, Large-area classification and mapping of forest and land cover in the Brazilian Amazon: a comparative analysis of ALOS/PALSAR and Landsat TM data sources. *Journal of Selected Topics in Applied Earth Observations and Remote Sensing*, 3(4), 594-604.

Walter, K.M., Zimov, S.A., Chanton, J.P., Verbyla, D. and Chapin III, F.S., 2006. Methane bubbling from Siberian thaw lakes as a positive feedback to climate warming. *Nature*, 443(7107), p. 71.

Whelen, T. and Siqueira, P., 2018. Coefficient of variation for use in crop area classification across multiple climates. *International Journal of Applied Earth Observation and Geoinformation*, 67, pp. 114-122.

Williams, S., Bock, Y. and Fang, P., 1998. Integrated satellite interferometry: Tropospheric noise, GPS estimates and implications for interferometric synthetic aperture radar products. *Journal of Geophysical Research: Solid Earth*, 103(B11), pp. 27051-27067.

Woodall, C.W., 2010. Carbon flux of down woody materials in forests of the North Central United States. *International Journal of Forestry Research*, 2010.

Woodcock, C.E., Macomber, S.A., Pax-Lenney, M. and Cohen, W.B., 2001. Monitoring large areas for forest change using Landsat: Generalization across space, time and Landsat sensors. *Remote Sensing of Environment*, 78(1-2), pp. 194-203.

Y

Yu, Y. and Saatchi, S., 2016. Sensitivity of L-band SAR backscatter to aboveground biomass of global forests. *Remote Sensing*, 8(6), p. 522.

Yueh, S.H., Kong, J.A. and Shin, R.T., 1992. External calibration of polarimetric radars using point and distributed targets. *Journal of Electromagnetic Waves and Applications*, 6(7), pp. 921-941.

Z

Zebker, H.A. and Goldstein, R.M., 1986. Topographic mapping from interferometric synthetic aperture radar observations. *Journal of Geophysical Research: Solid Earth*, 91(B5), pp. 4993-4999.

Zebker, H.A., Rosen, P.A. and Hensley, S., 1997. Atmospheric effects in interferometric synthetic aperture radar surface deformation and topographic maps. *Journal of Geophysical Research: Solid Earth*, 102(B4), pp. 7547-7563.

Zhang, J., Rothrock, D. and Steele, M., 2000. Recent changes in Arctic sea ice: The interplay between ice dynamics and thermodynamics. *Journal of Climate*, 13(17), pp. 3099-3114.

Zhang, S., Sadras, V., Chen, X. and Zhang, F., 2014. Water use efficiency of dryland maize in the Loess Plateau of China in response to crop management. *Field Crops Research*, 163, pp. 55-63.

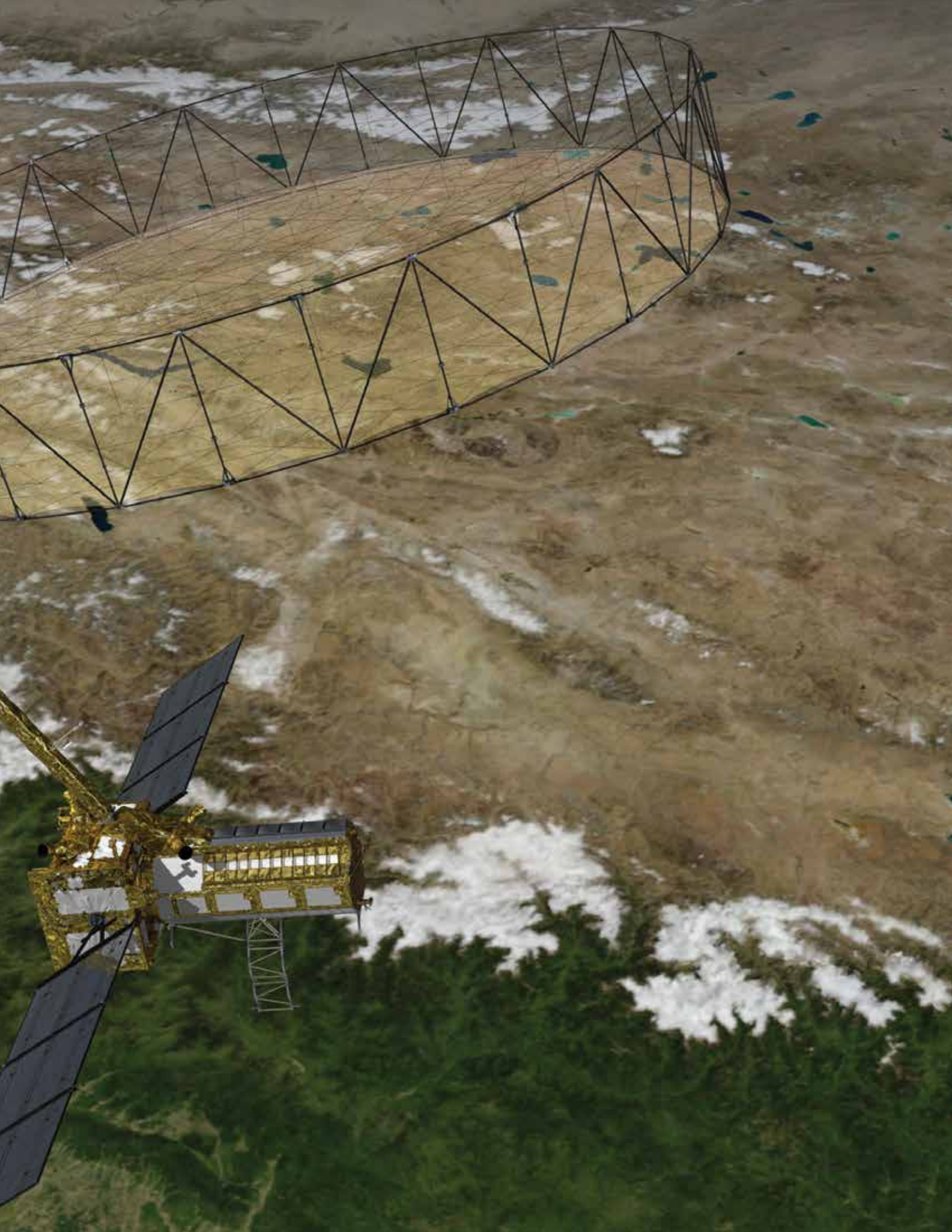
Zhang, Y., Wang, C., Wu, J., Qi, J. and Salas, W.A., 2009. Mapping paddy rice with multitemporal ALOS/PALSAR imagery in southeast China. *International Journal of Remote Sensing*, 30(23), pp. 6301-6315.

Zhao, W., Amelung, F., Dixon, T.H., Wdowinski, S. and Malservisi, R., 2014. A method for estimating ice mass loss from relative InSAR observations: Application to the Vatnajökull ice cap, Iceland. *Geochemistry, Geophysics, Geosystems*, 15(1), pp. 108-120.

Zhen, L., and Huadong, G., 2000, Permafrost mapping in the Tibet plateau using polarimetric SAR, *Geoscience and Remote Sensing Symposium*, 2000. Proceedings. IGARSS 2000. IEEE 2000 International, Volume 5, pp. 2024-2026.

12 ACRONYMS

Acronym	Definition	Acronym	Definition
ABG	Above Ground Biomass	LUT	Lookup Table
AOCS	Attitude and Orbit Control System	MCR	Mission Concept Review
CEOS	Committee on Earth Observing Systems	MEaSURES	Making Earth System Data Records for Use in Research Environments
DAAC	Distributed Active Archive Center	MERRA	Modern-Era Retrospective analysis for Research and Applications
DESDynI	Deformation, Ecosystem Structure and Dynamics of Ice	MLD	Multilook Detected
DESDynI-R	DESDynI Radar	MNR	Multiplicative Noise Ratio
DSSG	DESDynI Science Study Group	MODIS	Moderate Resolution Imaging Spectroradiometer
ECMWF	European Centre for Medium-Range Weather Forecasts	NARR	North American Regional Reanalysis
ERA	ECMWF Re-Analysis	NAIS	North American Ice Service
FAO	Food and Agriculture Organization of the United Nations	NASA	National Aeronautics and Space Administration
FFCC	Forest Fractional Canopy Cover	NIC	National Ice Center
FIRMS	Fire Information for Resource Management System	NISAR	NASA-ISRO SAR
GAM	Global Atmospheric Model	PRF	Pulse Repetition Frequency
GEDI	Global Ecosystem Dynamics Investigation Lidar	PSI	Persistent Scatterer Interferometry
GEO	Group on Earth Observations	PSInSAR	Persistent Scatterer Interferometric SAR
GEOGLAM	GEO Global Agricultural Monitoring	PSLR	Peak Side Lobe Ratio
GFOI	Global Forest Observing Initiative	RCS	Radar Cross Section
GIAnT	Generic InSAR Analysis Toolbox	SAC	Space Applications Centre (ISRO)
GLOF	Glacial Lake Outburst Flood	SAR	Synthetic Aperture Radar
ICC	Indicative Crop Classification	SBAS	Small BAseline Subset
ISAC	ISRO Satellite Centre	SDD	Science Definition Document
ISLR	Integrated Side Lobe Ratio	SDT	Science Definition Team
ISRO	Indian Space Research Organisation	SLC	SingleLook Complex
JECAM	Joint Experiment for Crop Assessment and Monitoring	SMA	Semi-Major Axis
LIDAR	Light Detection and Ranging	SPOTL	Some Programs for Ocean-Tide Loading
LMA	Levenberg-Marquardt Approach	SNR	Signal to Noise Ratio
		USDA	United States Department of Agriculture
		VIIRS	Visible Infrared Imaging Radiometer Suite
		WWF	World Wildlife Federation



13 APPENDIX A HISTORICAL BACKGROUND FOR NISAR

SEASAT LED TO A SERIES OF NASA SPACE SHUTTLE-BASED RADAR MISSIONS AND INSPIRED THE DEVELOPMENT OF SPACEBORNE SAR SYSTEMS WORLDWIDE.



The first civilian SAR satellite in history, called SEASAT, was launched by NASA in 1978. SEASAT's L-band (24 cm wavelength) SAR operated for three months before the failure of the spacecraft's power system. SEASAT led to a series of NASA space shuttle-based radar missions and inspired the development of spaceborne SAR systems worldwide. Launching another free-flying scientific SAR in the U.S. has proven elusive, despite strong demand from the science and applications community.

In 2007, the National Research Council Committee on Earth Science and Applications from Space recommended a mission to measure changes in land, ice, and vegetation structure, called DESDynI (Deformation, Ecosystem Structure, and Dynamics of Ice) as one of the first in a series of Decadal Survey missions to carry forward the nation's spaceborne observation program. The objective for DESDynI was to address the critical needs of three major science disciplines – Solid Earth, Ecosystems, and Cryospheric sciences – plus provide data important for many applications. The primary mission objectives for DESDynI were to: 1) determine the likelihood of earthquakes, volcanic eruptions, and landslides through surface deformation monitoring; 2) characterize the global distribution and changes of vegetation aboveground biomass and ecosystem structure related to the global carbon cycle, climate and biodiversity; and 3) project the response of ice masses to climate change and impact on sea level. In addition, NISAR will provide observations that will greatly improve our monitoring of groundwater, hydrocarbon, and sequestered CO₂ reservoirs. The Decadal Survey noted that these surface processes can be characterized and monitored from space using SAR and Light Detection

and Ranging (lidar). Initial designs of DESDynI consisted of an L-band polarimetric SAR designed to operate as a repeat-pass interferometric SAR (InSAR) and a multi-beam lidar.

In 2008, NASA appointed a DESDynI Science Study Group (DSSG) to articulate specific science requirements for the DESDynI mission and established a pre-formulation project team at Jet Propulsion Laboratory (JPL) and Goddard Space Flight Center (GSFC) to flow these requirements down to a specific mission implementation. JPL was overall project lead and responsible for the SAR project element; GSFC was responsible for the lidar project element. The DSSG wrote a Science Definition Document (SDD) describing in great detail the science behind the mission and developed a set of Level 1 and Level 2 requirements and preliminary science targets, including observing attributes such as radar mode, sampling strategy, pointing diversity, etc., which guided the project work.

A complete mission concept was developed for DESDynI. The pre-formulation team successfully conducted a Mission Concept Review (MCR) in January 2011. After the MCR, NASA received direction from the US Administration (Office of Management and Budget) to reformulate the concept to reduce its scope. The lidar was to be removed as a component of the DESDynI program, and the cost of the radar project element was to be reduced significantly.

In May 2012, NASA competed and selected a DESDynI radar (DESDynI-R) Science Definition Team (SDT) to redefine DESDynI science to flow to an affordable,

radar-only NASA mission. Past and current SDT members are listed in Tables 14-1 and 14-2 in Appendix B. At the same time, the JPL project team studied a number of options to reduce cost and/or scope including partnerships with other space agencies.

Through discussions between NASA and ISRO on the possibility of a joint radar mission, it became clear that the goals originally identified for DESDynI-R were of great interest to the ISRO science community. In January 2012, ISRO identified targeted science and applications that were complementary to the primary mission objectives, agricultural monitoring and characterization, landslide studies, Himalayan glacier studies, soil moisture, coastal processes, coastal winds and monitoring hazards. For many of these objectives, the addition of an S-band polarimetric capability will add consider-

ably to the measurement, extending the measurement sensitivity at L-band to lower values while decreasing sensitivity to ionospheric and soil moisture effects.

Since January 2012 when the initial L- and S-band SAR mission concept was put forward as a partnership, JPL and ISRO teams have been attempting to refine the science plan and its implications for the mission. In September 2013, ISRO received initial approval from the Government of India for jointly developing with NASA the L- and S-band SAR mission. A Technical Assistance Agreement (TAA) between ISRO and California Institute of Technology/JPL was enacted on September 30, 2013. NASA Administrator Charles Bolden and K. Radhakrishnan, Chairman of ISRO, signed the NISAR Implementing Arrangement (IA) on September 30, 2014.

14 APPENDIX B NISAR SCIENCE TEAM

The NISAR science team members are drawn from the science disciplines related to the mission. The science team is renewed at three-year intervals and the makeup of the team evolves to fit the NISAR science and mission needs. An ISRO science team addresses the ISRO objectives. JPL also has an internal project science team to coordinate technical activities.

14.1 NASA SCIENCE DEFINITION TEAM

NASA selected a science definition team (SDT) known as the “DESDynI-R SDT” in May 2012. The expertise of the members spans the science disciplines identified in the 2007 NRC Decadal Survey of Earth Science and Applications for the DESDynI mission concept.

TABLE 14-1. NASA SAR MISSION SCIENCE DEFINITION TEAM (2012-2015)

SDT Member	Institutional Affiliation	Areas of Interest
Bradford Hager Deformation Lead	Massachusetts Institute of Technology	Solid Earth
Ralph Dubayah Ecosystems Lead	University of Maryland	Ecosystems
Ian Joughin Cryosphere Lead	University of Washington Applied Physics Lab	Cryosphere
Gerald Bawden*	US Geological Survey/ NASA HQ	Hazards, hydrology, applications
Kurt Feigl	University of Wisconsin	Solid Earth
Benjamin Holt	Jet Propulsion Laboratory	Sea ice
Josef Kellendorfer	Woods Hole Research Center	Ecosystems, carbon policy
Zhong Lu	Southern Methodist University	Volcanoes
Franz Meyer	University of Alaska, Fairbanks	Applications, techniques, deformation
Matthew Pritchard	Cornell University	Solid Earth, cryosphere
Eric Rignot	University of California, Irvine	Cryosphere
Sassan Saatchi	Jet Propulsion Laboratory	Ecosystems
Paul Siqueira	University of Massachusetts, Amherst	Ecosystems, techniques
Mark Simons	California Institute of Technology	Solid Earth, hazards, cryosphere
Howard Zebker	Stanford University	Solid Earth, applications, techniques

*Transitioned from SDT member to NASA HQ after selection

“DESDynl-R” refers to the radar component of the DESDynl concept. In addition to discipline scientists, the team comprises applications and radar phenomenology experts. Table 14-1 lists the 2012-2015 SDT members, their affiliations and areas of interest. A solicitation was issued in 2015 to recompile the SDT. Selections were made in April 2016, and the new team has been in place since May 2016. The new team has 11 returning members and 9 new team members. Table 14-2 lists the new science definition team.

TABLE 14-2. NASA SAR MISSION SCIENCE DEFINITION TEAM (2016-2019)

SDT Member	Institutional Affiliation	Areas of Interest
Mark Simons Deformation Lead	California Institute of Technology	Solid Earth
Paul Siqueira Ecosystems Lead	University of Maryland	Ecosystems
Ian Joughin Cryosphere Lead	University of Washington Applied Physics Lab	Cryosphere
Cathleen Jones Applications Lead	Jet Propulsion Laboratory	Applications
Falk Amelung	University of Miami	Solid Earth, atmospheres
Adrian Borsa	Scripps Institution of Oceanography	Solid Earth
Bruce Chapman	Jet Propulsion Laboratory	Wetlands
Eric Fielding	Jet Propulsion Laboratory	Solid Earth
Richard Forster	University of Utah	Cryosphere
Bradford Hager	Massachusetts Institute of Technology	Solid Earth
Benjamin Holt	Jet Propulsion Laboratory	Sea ice
Josef Kelldorfer	Earth Big Data, LLC.	Ecosystems, carbon policy
Rowena Lohman	Cornell University	Solid Earth, cryosphere
Zhong Lu	Southern Methodist University	Volcanoes
Franz Meyer	University of Alaska, Fairbanks	Applications, techniques, deformation
Frank Monaldo	National Oceanic and Atmospheric Administration	Oceans, sea ice
Eric Rignot	University of California, Irvine	Cryosphere

14.2 ISRO SCIENCE TEAM

ISRO forms a science team once a project is approved, which is the equivalent of entering formulation. Though the project has been approved, a science team has not yet been formed. To date, ISRO science formulation has been conducted by an ad hoc team of ISRO staff scientists. The ISRO scientists involved in defining the ISRO specific science requirements through KDB-B are given in Table 14-3.

TABLE 14-2. NASA SAR MISSION SCIENCE DEFINITION TEAM (2016-2019) contd

SDT Member	Institutional Affiliation	Areas of Interest
Sassan Saatchi	Jet Propulsion Laboratory	Ecosystems
Marc Simard	Jet Propulsion Laboratory	Ecosystems, techniques
Howard Zebker	Stanford University	Solid Earth, applications, techniques

In April 2015, Dr. Chakraborty retired and Tapan Misra became the director of the Space Applications Centre. For most of Phase B, the science element at ISRO was led by Dr. Raj Kumar.

14.3 PROJECT SCIENCE TEAM

JPL maintains a project science team distinct from the SDT, headed by a project scientist, currently Paul Rosen. The project scientist works side-by-side with

the project manager to coordinate the science and technical developments and calls on JPL staff scientists to perform analysis in support of the SDT activities.

The project scientist conducts weekly coordination teleconferences with the SDT leads, and alternate fortnightly teleconferences with the full SDT to maintain information flow and coordinate analysis, requirements definition, and documentation.

TABLE 14-3. ISRO PRE-FORMULATION SCIENCE TEAM (PRIOR TO KDP-B)

SDT Member	Institutional Affiliation	Areas of Interest
Tapan Misra*	Space Applications Centre, Ahmedabad	Radar phenomenology, lead prior to KDP-B
Manab Chakraborty** Raj Kumar (after KDP-B)	Space Applications Centre, Ahmedabad	Agriculture oceans, lead after KDP-B
Anup Das	Space Applications Centre, Ahmedabad	Ecosystems
Sandip Oza	Space Applications Centre, Ahmedabad	Cryosphere

*Became SAC director in April 2016

** Retired in April 2016

15 APPENDIX C KEY CONCEPTS

This appendix covers the key concepts for the NISAR radar mission. The key concepts include an overview of the radar imaging and the basic related science products that the mission will produce.

15.1 BASIC RADAR CONCEPTS: RADAR IMAGING, POLARIMETRY, AND INTERFEROMETRY

For those unfamiliar with the NISAR mission, this section gives a brief introduction to key concepts and terms that are central to NISAR science and measurements. These include radar imaging, polarimetry, and interferometry concepts. There are a number of excellent introductory books (Richards, 2009; van Zyl and Kim, 2011; Hanssen, 2001) and book chapters (Simons and Rosen, 2007; Burgmann et al., 2000) on these subjects.

15.1.1 Synthetic Aperture Radar (SAR)

Synthetic Aperture Radar (SAR) refers to a technique for producing fine resolution images from an intrinsically resolution-limited radar system. The wavelengths, λ , that are used for radar remote sensing of Earth's surface are typically in the range of a few to tens of centimeters. At these wavelengths, the energy radiated from a radar antenna of dimension D fans out over an angular range that is equivalent to the beam width λ/D of the antenna. For a typical spaceborne SAR configuration with wavelengths of ~ 10 cm and an antenna of 10 m size, this beam width is $1/100$ radians, or about 0.6 degrees. For a radar in space observing Earth 1000 km below, the beam size on the ground is then $1000 \lambda/D = 10$ km. This intrinsic resolution of the radar system is insufficient for many applications, and practical solutions for improving the resolution needed to be found.

SAR techniques exploit the motion of the radar in orbit to synthesize an aperture (antenna), which typically will be about 10-km long in the flight direction. This principle is illustrated in Figure 15-1. While the radar is traveling along its path, it is sweeping the antenna's footprint across the ground while it is continuously transmitting and receiving radar pulses. In this scenario, every given point in the radar swath is imaged many times by the moving radar platform under constantly changing yet predictable observation geometries. In SAR systems, this change in observation geometry, resulting in a constant change of the distance from the radar to the point on the ground, is precisely encoded in the phase of the observed radar response. The phase history for any point on the ground located at a constant distance parallel to the flight track is unique to that point. By compensating the phase history of each pulse that is affecting a particular point on the ground, it is possible to focus the energy across the 10 km synthetic aperture and create an image of vastly improved resolution. The theoretically achievable synthetic aperture resolution can be calculated from $D/2$, is independent of the range or wavelength, and corresponds to $D/2=5$ m for the previously outlined spaceborne scenario.

Through the outlined principles, SAR defeats the intrinsic resolution limits of radar antennas in the along-track direction. In the cross-track or range direction, orthogonal to the satellite path, the resolution is not defined by the antenna beam width, but rather the width of the transmitted pulse. Referring to Figure 15-1, this is because the transmitted pulse intersects the imaged surface as it propagates in the beam. After a two-way trip of a transmitted pulse from sensor to the ground and back, two objects can be distinguished if they are spatially separated by more than half the pulse width. Hence, range resolution is controlled by the transmit-

THIS APPENDIX
COVERS AN
OVERVIEW OF THE
RADAR IMAGING
AND THE BASIC
RELATED SCIENCE
PRODUCTS THAT
THE MISSION WILL
PRODUCE.

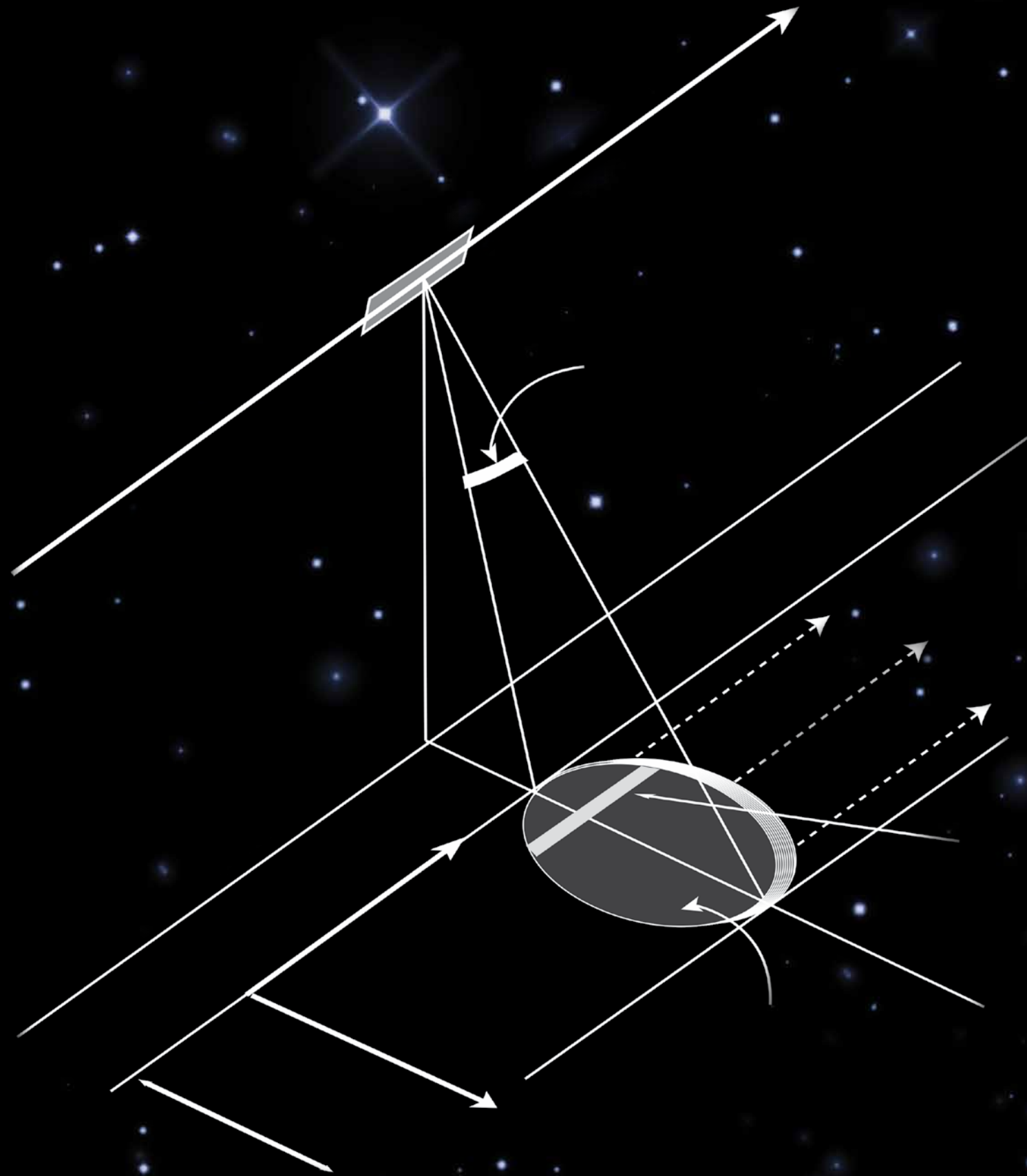
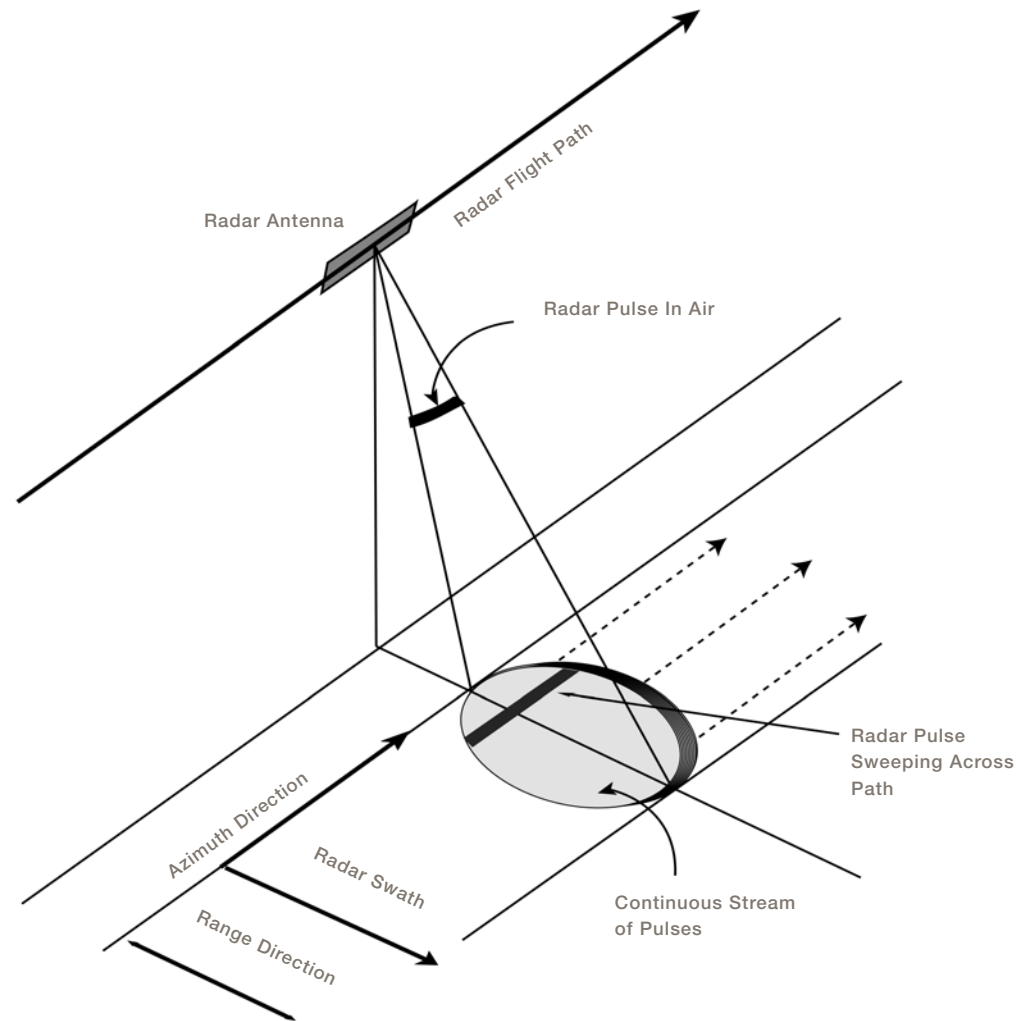


FIGURE 15-1

Configuration of a radar in motion to enable synthetic aperture radar imaging. Radar antenna illuminates an area on the ground determined by its wavelength and antenna dimension. Pulses are sent and received continuously such that any point on the ground is sampled often. The range/phase history of each point is compensated to focus energy acquired over the synthetic aperture time to fine resolution. In range, resolution is achieved by coding the pulse with a wide bandwidth signal waveform.



ted waveform that is generated by the radar and not the size of the antenna footprint on the ground. Wider bandwidth signals generate finer resolution images in range.

For most purposes, the transmitted signal can be thought of as a single frequency sinusoid with a well-defined amplitude and phase. Thus, the image constructed from the SAR processing is a complex image – each resolution element, or pixel, has an amplitude and phase associated with it. Once calibrated, the amplitude is proportional to the reflectance of the surface. The phase is proportional to the distance the wave traveled between the radar and the ground, any propagation phase delays due to the atmosphere or ionosphere, and any phase contribution imparted by the reflectance from the surface.

15.1.2 Polarimetry

A radar antenna can be designed to transmit and receive electromagnetic waves with a well-defined polarization, which is defined as the orientation of the electric field vector in the plane orthogonal to the wave propagation direction. By varying the polarization of the transmitted signal, SAR systems can provide information on the polarimetric properties of the observed surface. These polarimetric properties are indicative of the structure of the surface elements within a resolution element. Oriented structures such as buildings or naturally aligned features (e.g., sand ripples) respond preferentially to similarly oriented polarizations and tend to preserve polarimetric coherence, whereas randomly oriented structures lead to depolarization of the scattered signals.

A polarimetric radar can be designed to operate as a single-pol system, where there is a single polarization transmitted and a single polarization received. A typical single-pol system will transmit horizontally or vertically polarized waveforms and receive the same (giving HH or VV imagery). A dual-pol system might transmit a horizontally or vertically polarized waveform and measure signals in both polarizations in receive (resulting in HH and HV imagery). A quad-pol or full-pol system will alternate between transmitting H- and V-polarized waveforms and receive both H and V (giving HH, HV, VH, VV imagery). To operate in quad-pol mode requires a pulsing of the radar at twice the rate of a single- or dual-pol system since the transmit polarization has to be alternated between H and V in a pulse-by-pulse manner to enable coherent full-polarized data acquisitions. Since this type of operation can cause interference between the received echoes, a variant of quad-pol known as quasi-quad-pol can be used, whereby two dual-pol modes are operated simultaneously: an HH/HV mode is placed in the lower portion of the allowable transmit frequency band and a VH/VV mode is operated in the upper portion. Being disjoint in frequency, the modes do not interfere with each other. However, the observed HH/HV and VH/VV data are mutually incoherent.

While most spaceborne systems are linearly polarized, it is also possible to create a circularly polarized signal on transmit, whereby the tip of the electric field vector is rotating in a circle as it propagates. This is typically implemented by simultaneously transmitting equal amplitude H and V signals that are phase shifted by 90 degrees. Various combinations of right-circular and left-circular polarization configurations on transmit and receive allow synthesizing single-, dual-, and quad-pol mode data from circular-polarized observations. Circular polarization is relevant to NISAR as recent work has emphasized the benefits of hybrid polarization, where a circularly polarized wave is transmitted and H and V signals are received. The dual-pol instance of this mode is known as compact-pol. Compact-pol captures many of the desirable scattering properties of a

dual-pol system, e.g., discriminating between oriented and random surfaces, while better balancing the power between the receive channels.

Classical radar polarimetry focuses on relating the complex backscatter observed in various polarimetric combinations to the electrical and geometric properties of the observed surfaces in order to extract meaningful information. Observation-based empirical work, as well as theoretical modeling, helps establish these relationships. For example, over soils, surface roughness and moisture both contribute to the backscattered amplitude, but it can be shown that HH and VV images have similar responses to roughness, such that the ratio HH/VV is primarily an indicator of moisture content. As another example, bare surfaces have a weak depolarizing effect, while vegetation canopies generally are highly depolarizing. So, a joint examination of the dual-pol channels HH and HV can distinguish these surface types.

For this mission, quantifying biomass is an important measurement objective. Empirical relationships have been developed that allow mapping of radar backscatter amplitude to the amount of biomass present in an image resolution cell. The relationship varies with vegetation type and environmental conditions (e.g., soil moisture and roughness), but with multiple polarizations and repeated measurements, the biomass can be determined with sufficient accuracy.

15.1.3 Interferometric Synthetic Aperture Radar (InSAR)

As noted above, each resolution element encodes the phase related to the propagation distance from the radar to the ground as well as the intrinsic phase of the backscattering process. The resolution element comprises an arrangement of scatterers – trees, buildings, people, etc. – that is spatially random from element to element and leads to a spatially random pattern of backscatter phase in an image. As such, since we can only measure the phase in an image within one

cycle (i.e., we do not measure the absolute phase), it is not possible to observe the deterministic propagation component directly.

Interferometric synthetic aperture radar (InSAR) (Rosen et al., 2000; Hanssen, 2001) techniques use two or more SAR images over the same region to obtain surface topography or surface motion. In this section, we explain how an InSAR phase measurement relates to actual ground deformation (see Massonnet et al. 1993; a tutorial summary is found in Chen 2014a).

Figure 15-2 illustrates InSAR imaging geometry. At time t_1 , a radar satellite emits a pulse at S_1 , then receives an echo reflected from a ground pixel, A, and measures the phase ϕ_1 of the received echo. All scatterers within the associated ground resolution element contribute to ϕ_1 . As a result, the phase ϕ_1 is a statistical quantity that is uniformly distributed over interval $(0, 2\pi)$ so that we cannot directly use ϕ_1 to infer the distance r_1 between S_1 and A. Later at time t_2 , the satellite emits another pulse at S_2 and makes a phase measurement ϕ_2 . If the scattering property of the ground resolution element has not changed since t_1 , all scatterers within the resolution element contribute to ϕ_2 the same way as they contribute to ϕ_1 . Under the assumption that $|r_1 - r_2| \ll |r_1|$ (the parallel-ray approximation), the phase difference between ϕ_1 and ϕ_2 can be used to infer the topographic height z of the pixel A (Hanssen, 2001, Section 3.2).

If we know the topographic height z , we can further measure any small ground deformation occurring at pixel A between t_1 and t_2 . Figure 15-3 illustrates the InSAR imaging geometry in this case. At time t_1 , a radar satellite measures the phase ϕ_1 between the satellite and a ground pixel A along the LOS direction. Later at time t_2 , the ground pixel A moves to A' and the satellite makes another phase measurement ϕ_2 between the satellite and the ground pixel. The phase difference $\Delta\phi$ is proportional to the ground deformation between t_1 and t_2 along the LOS direction.

topography, the unwrapped (module 2π) InSAR phase $\Delta\phi = \phi_2 - \phi_1 - \phi'$ is proportional to the ground deformation Δd between t_1 and t_2 along the satellite LOS ground direction as:

$$\Delta\phi = \phi_2 - \phi_1 - \phi' = \frac{4\pi\Delta d}{\lambda}$$

where λ is the radar wavelength. In this equation, we assume that there is no error in the InSAR phase measurement. Below we discuss in depth various error sources in InSAR deformation measurements and their impact on InSAR image quality.

Note that InSAR techniques only measure one-dimensional LOS motion. However, deformation is better characterized in three dimensions: east, north and up. Given an LOS direction unit vector $e = [e_1, e_2, e_3]$, we can project the deformation in east, north and up coordinates along the LOS direction as:

$$\Delta d = e_1\Delta d_{\text{east}} + e_2\Delta d_{\text{north}} + e_3\Delta d_{\text{up}}$$

Because radar satellites are usually polar orbiting, the north component of the LOS unit vector e_2 is often negligible relative to the east and vertical components. When InSAR measurements along two or more LOS directions are available, we can combine multiple LOS deformation measurements over the same region to separate the east and vertical ground motions, given that the term $e_2\Delta d_{\text{north}}$ is negligible.

For this mission, interferometric observations of any given point on the ground are acquired every 12 days. Ground motion can be measured for a gradually changing surface that is not disrupted between images.

15.2 DEFORMATION-RELATED TERMINOLOGY

The Earth's crust and cryosphere deform due to difference forces acting on them. Deformation may be linear, episodic, or transient.

FIGURE 15-2

Illustration of InSAR imaging geometry. The distance between the satellite at S_1 and a ground pixel A is r_1 and the distance between the satellite at S_2 and the ground pixel A is r_2 . The topographic height of the pixel A is z . Here we assume $|r_1 - r_2| \ll |r_1|$ (the parallel-ray approximation) and no ground deformation occurs at pixel A between the two SAR data acquisition times.

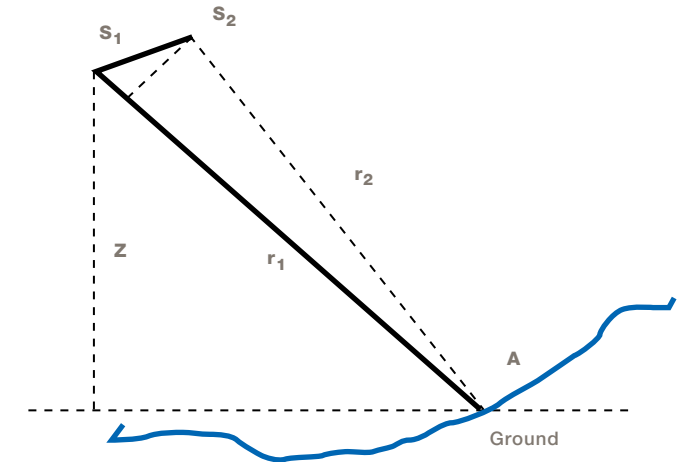
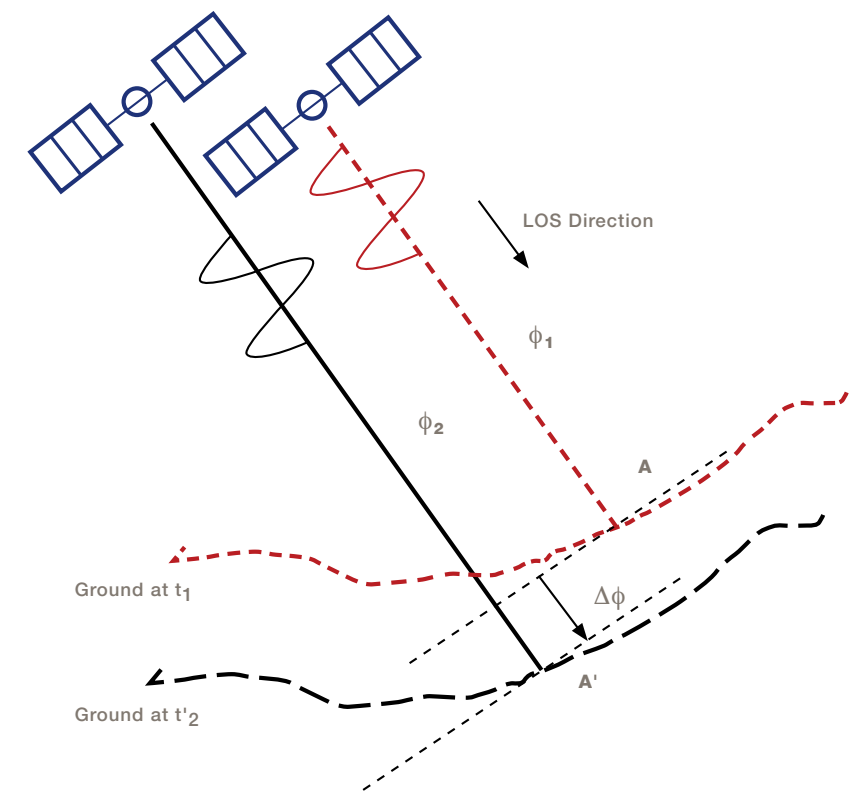


FIGURE 15-3

InSAR deformation geometry. At time t_1 , a ground pixel of interest is at point A and a radar satellite measures the phase ϕ_1 between the satellite and the ground pixel along the LOS direction. Later at time t_2 , the ground pixel moves to A' and the satellite makes another measurement ϕ_2 between the satellite and the ground pixel. The phase difference $\Delta\phi$ is proportional to the ground deformation between t_1 and t_2 along the LOS direction.



15.2.1 Deformation and Displacement

In general, the term deformation refers to the change in shape of a solid or quasi-solid object. In the context of this mission, surface deformation refers to the change in shape as observed on the Earth's free surface, i.e., the interface separating the atmosphere from the uppermost layer of solid Earth, whether rock, soil, ice or a combination thereof.

Displacement \mathbf{u} is a vector quantity defined as the change in a particle's position \mathbf{X} between one instant in time (epoch) t_1 and a later epoch t_2 , such that $\mathbf{u} = \mathbf{X}(t_2) - \mathbf{X}(t_1)$. Typically, displacement is calculated with respect to the particle's initial, fixed position $\mathbf{X}(t_0)$ at some reference time t_0 .

The *change in range* $\Delta\rho$ is a scalar quantity equal to the change in the (1-way) distance from the radar sensor to the target pixel on the ground. Range change is a particular component of the displacement vector. To calculate the range change, we project the displacement vector \mathbf{u} onto the line of sight using the scalar ("dot") product such that $\Delta\rho = -\mathbf{u} \cdot \mathbf{s}$, where \mathbf{s} is a unit vector pointing from the target on the ground toward the radar sensor in orbit. If the target moves toward the sensor, then the distance between them decreases and the range decreases such that $\Delta\rho < 0$.

Line-of-sight (LOS) displacement u_{LOS} is a scalar quantity that is equal in absolute value to the range change $\Delta\rho$. Most, but not all, authors reckon upward motion of the target (toward the sensor) to be a positive value of LOS displacement, such that $u_{\text{LOS}} > 0$.

Velocity \mathbf{v} is a vector quantity defined as the derivative of displacement with respect to time t such that $\mathbf{v} = d\mathbf{u}/dt$. In discussing velocity fields, it is important to define the reference frame. The relative velocity of a particle j with respect to particle i is $\mathbf{v}_{j,i} = \mathbf{v}_j - \mathbf{v}_i$. A so-called absolute velocity is taken with respect to a fixed origin located at position \mathbf{X}_0 that is assumed to be stationary, such that $\mathbf{v}_0 = \mathbf{0}$.

To quantify deformation using radar, the mission offers at least two approaches:

1. Degrees or cycles. One fringe in an interferogram corresponds to one cycle (2π radians) of phase change or half a wavelength in range change. Phase is ambiguous because it is defined as an angle on the unit circle such that $\pi \leq \Delta\phi \leq \pi$. Since the phase change is known only to within an integer number of cycles (i.e., modulo 2π), it is called "wrapped". Converting ambiguous, wrapped phase change $\Delta\phi$ in radians to range change $\Delta\rho$ in millimeters requires unwrapping algorithms (e.g., Chen and Zebker, 2002; Hooper and Zebker, 2007).
2. The techniques called speckle tracking and feature tracking estimate the shift of an image patch relative to its neighbors by cross-correlating the amplitudes or complex values of two images covering the same location at two different times (e.g., Vesecky et al., 1988). To do so, the technique generates "normalized cross-correlation" of image patches of complex or detected real-valued SAR images. The location of the peak of the two-dimensional cross-correlation function yields the image offset (displacement).

The successful estimation of the local image offsets depends on having correlated speckle patterns (speckle tracking) and/or the presence of nearly identical features (feature tracking) in the two SAR images at the scale of the employed patches. If speckle correlation is retained and/or there are well-defined features, the tracking with image patches of tens to hundreds of meters in size can be performed to a tenth-of-a-pixel or better accuracy with improved accuracy at the expense of resolution by averaging adjacent estimates (Gray et al., 1998; Michel and Rignot, 1999; Strozzi et al., 2008). The result yields two horizontal components of the displacement vector. Of these, the component that is parallel to the ground track of the satellite is also called an azimuth offset. The other effectively measures the same range displacement as the interferometric phase, albeit with more noise and poorer resolution. Where available, the less noisy phase data can be combined with the azimuth offsets to produce a less noisy vector estimate of displacement (Joughin, 2002).

15.2.2 Strain, Gradients, and Rotation

For a one-dimensional element, the strain ϵ is expressed as the dimensionless ratio of its change length ΔL to its original length L , such that $\epsilon = \Delta L/L$. If one end of the element is held fixed, then the change in length is equal to the displacement of the other end, such that $\Delta L = u$. For small strains, we can think of the strain as the gradient of the displacement, i.e., the partial derivative of displacement u with respect to the position coordinate x . Generalizing to three dimensions yields a second-order tensor called the deformation gradient tensor $F_{ij} = \partial_{u_i} / \partial_{x_j}$ (Malvern, 1969). The deformation tensor can be decomposed into a symmetric part, called the strain tensor, and an anti-symmetric part called a rotation or spin. The temporal derivatives of these quantities are called the velocity gradient tensor L_{ij} , the strain rate tensor E_{ij} , and the spin rate tensor Ω_{ij} respectively (Malvern, 1969).

SAR interferometry is especially sensitive to gradients of the displacement field. For example, if a rock outcrop 10 meters in width stretches by 10 mm, then the strain will be $\epsilon = 0.001$. Similarly, if the same outcrop tilts by 10 mm (about a horizontal axis) or spins (about a vertical axis), then the angle of rotation will be approximately 1 milliradian. Such behavior was observed in interferograms of the deformation field produced by the Landers earthquake in California (Peltzer et al., 1994).

To quantify the deformation gradient tensor F_{ij} , we can differentiate the wrapped phase in an interferogram to find the range gradient ψ . Following Sandwell and Price (1996), Ali and Feigl (2012) take the discrete derivative of range change $\Delta\rho$ with respect to a horizontal coordinate in position X to define the observable quantity for the k^{th} pixel as:

$$\psi^k = \frac{\Delta\rho^{(k+1)} - \Delta\rho^{(k-1)}}{X^{(k+1)} - X^{(k-1)}}$$

For example, a difference of 0.1 cycles in phase or 2.8 mm in range change over the 100 m distance between adjacent pixels in a C-band interferogram corresponds to a range gradient of $\psi \sim 2.8 \times 10^{-5}$. While range change is one component of the displacement vector (measured in millimeters), its (dimensionless) gradient is one component of the "deformation gradient" tensor F_{ij} (Malvern, 1969). Unlike wrapped phase change, the range change gradient is continuous and differentiable (Sandwell and Price, 1996), offering a number of advantages for streamlining data analysis.

15.2.3 Stress and Rheology

Stress is the force applied to a body per unit area. It also can imply the resistance a solid body offers to an applied force. In mechanics, constitutive relationships describe how stress and strain depend on each other. The study of constitutive relationships and the relevant material properties is called rheology. For example, during an earthquake, Earth's crust deforms with an elastic rheology according to Hooke's Law. Understanding Earth's rheology is one of the primary goals of the mission.

15.3 ECOSYSTEMS-RELATED TERMINOLOGY

NISAR addresses the amount of living material in ecosystems as well as the disturbance and recovery of ecosystems.

15.3.1 Biomass

Biomass is defined as the total mass of living matter within a given unit of environmental area, usually measured as mass or mass per unit area of dry weight. Biomass is a fundamental parameter characterizing the spatial distribution of carbon in the biosphere. The NISAR mission will focus on the above-ground biomass

of woody plants and forests, comprising about 80% of terrestrial total biomass in vegetation (Houghton, 2005a; Cairns et al., 1997). Half of all biomass in woody vegetation is carbon equivalent to approximately 3.67 units of CO₂ that directly links biomass to the terrestrial carbon cycle and climate change (Penman et al 2003).

15.3.2 Disturbance

Disturbance is defined as a discrete event that involves the removal of biomass, mortality, or change in the structure and is considered the major agent in determining the heterogeneity of forest ecosystems across a broad range of scales in space and time. Forest disturbance can be abrupt (e.g., hurricanes) or chronic (e.g., acid rain); stand-replacing (e.g., clear-cut logging) or not (e.g., selective logging); complete (e.g., landslides) or incomplete (e.g., insect defoliation); natural (e.g., tornados) or anthropogenic (e.g., land conversion); widespread (e.g., fire) or geographically restricted (e.g., avalanches); temporary (e.g., blow downs) or permanent (deforestation and land use conversion) (Frolking et al., 2009; Chambers et al., 2013). We focus on disturbances as abrupt events that cause changes in forest biomass and are at the scale detectable by spaceborne remote sensing (> 100 m). Disturbance is measured as the area and/or the intensity of biomass changes in units of area/year or mass/area/year.

15.3.3 Recovery

Recovery of forests and woody vegetation refers to the reestablishment or redevelopment of above ground biomass and structure characteristics after the impact of a particular disturbance. The nature and rate of recovery depend on the size and severity of disturbance and the pre-disturbance state of the ecosystem (Frolking et al., 2009; Chazdon et al., 2001). Recovery can follow a prescribed trajectory to meet certain production goals in managed ecosystems and or a natural trajectory depending on environmental conditions in the case of unmanaged ecosystems. We focus on recovery as a process or trajectory defined by the area of the post-disturbance growth of biomass at scales of disturbance (> 100 m) and measured in the units of area/year or mass/area/year.

15.3.4 Classification

Classification is the problem of identifying to which set of categories a set of objects or new observations belongs on the basis of their relationships or characteristics. This includes the classification of observations into events, processes, or thematic categories that impact the vegetation structure, biomass, cover, and characteristics. Classification involves definition of class boundaries based on objective criteria including type, scale, and source used in a diagnostic system as a classifier. We focus on classification of SAR imagery as the new observations, at landscape scale (> 100 m) into disturbance (e.g., deforestation, degradation), recovery (e.g., biomass regrowth) or change of vegetation status (e.g., inundation).

16 APPENDIX D

BASELINE LEVEL 2 REQUIREMENTS

The Level 1 requirements (Table 16-1) capture the essential elements of the measurements by discipline and expand to greater detail at Level 2. The baseline L2 requirements capture the specific measurements that will be validated by research area and product type. Table 16-2 shows the high-level mapping from L1 to L2. The colors codify the relationships at Levels 1 and 2. The tabs on the corners of the requirements boxes indicate the radar technique used to make the measurements. It should be clear that there are a limited number of techniques used to support a multiplicity of requirements, which should help reduce the amount of validation required.

16.1 LEVEL 2 SOLID EARTH

Table 16-2 itemizes the solid Earth L2 requirements, which comprise interseismic, coseismic, and post-seismic deformation, and a set of additional deforming sites on land that include volcanoes, landslide-prone areas, aquifers, and areas of increasing relevance such as hydrocarbon reservoirs and sequestration sites.

The requirements for deformation are specified in terms of accuracy over relevant relative length scale, and at a particular resolution, and vary depending on the style of deformation and its expected temporal variability. Interseismic deformation is specified in terms of a relative velocity over a given length scale. Interseismic deformation is slow, on the order of cm/yr. To adequately model this deformation, accuracies far better, on the order of mm/yr, are required. To achieve good accuracy, often many measurements are needed over time to reduce noise via averaging. Coseismic deformation is extremely rapid, on the order of seconds, with postseismic deformation occurring thereafter, and generally larger in magnitude, so frequent, less

accurate measurements preceding and soon after the event are needed.

Resolutions vary depending on science focus. Interseismic deformation is generally broad except at aseismically creeping faults, so low resolution is adequate. For deformation associated with earthquakes, volcanoes, subsidence and landslides, the spatial patterns of deformation are finer, so finer resolution is required. The coseismic deformation requirement for large earthquakes specifies the entire land surface. Unlike the interseismic and targeted requirements, this requirement ensures that there will be observations sufficient to capture events outside of the areas that are known to be deforming rapidly.

The validation requirement is included to specify that the validation program is limited in scope to fixed areas, employing analysis to extrapolate performance to the globe.

16.2 LEVEL 2 CRYOSPHERE

Table 16-3 identifies the cryosphere L2 requirements. These requirements have a very similar form to the solid earth requirements, as they too map to geodetic imaging methods. Ice sheets and glaciers move quickly, so the faster the sampling rate for measurements, the greater the coverage of dynamic processes and the more interesting the science. Sea-ice moves even faster. Thus, the cryosphere L2 requirements are explicit in terms of the required sampling as well as regionally differentiated velocity accuracy and resolution requirements.

The permafrost requirement is explicitly a deformation requirement similar to the solid Earth requirement. It will be considered one of the targeted sites in the solid

TABLE 16-1. LEVEL 2 REQUIREMENTS FOR SOLID EARTH

Attribute	Secular Deformation (658)	Co-seismic Deformation (660)	Transient Deformation (663)
Measurement	Spatially averaged relative velocities in two dimensions	Point-to-point relative displacements in two dimensions	Point-to-point relative displacements in two dimensions
Method	Interferometry, speckle tracking	Interferometry, speckle tracking	Interferometry, speckle tracking
Duration	3 years	3 years	Episodic over mission, depending on science target
Product Resolution	100 m; smoothed according to distance scale L	100 m	100 m
Accuracy	2 mm/yr or better, 0.1 km < L < 50 km, over > 70% of coverage areas	4 (1+L ^{1/2}) mm or better, 0.1 km < L < 50 km, over > 70% of coverage areas	3 (1+L ^{1/2}) mm or better, 0.1 km < L < 50 km, over > 70% of ~ 2,000 targeted sites
Sampling	One estimate over 3 years, two directions	4 times per year to guarantee capture of any earthquake on land before surface changes too greatly	Every 12 days, two directions
Coverage	Land areas predicated to move faster than 1 mm/yr	All land, as earthquake locations are known a priori	Post-seismic events, volcanoes, ground-water, gas, hydrocarbon reservoirs, land-slide-prone
Response Latency	N/A	24-hour tasking, 5-hour data delivery. Best effort basis on event	24/5 Best effort basis on event

TABLE 16-2. SOLID EARTH LEVEL 1 AND 2 REQUIREMENTS SUMMARY



Earth L2 requirements but is included here to call out the explicit cryosphere focus. The validation requirement is included to specify that the validation program is limited in scope to fixed areas, employing analysis to extrapolate performance to the globe.

16.3 LEVEL 2 ECOSYSTEMS

Table 16-4 identifies the ecosystems L2 requirements. These are parallel but give greater specificity to the L1 requirements. The woody biomass accuracy requirement is the same at Levels 1 and 2. In addition, the details of the requirement for classification are spelled out. While biomass is required to meet its accuracy requirements only where biomass is below 100 Mg/

ha, the classification accuracy must be met for all biomass. The key implication of this is that the observing strategy must include sufficient global observations of biomass to enable this classification.

The requirements related to wetlands, areas of inundation and agriculture are “globally distributed”, implying regional measurements, as specified in the science implementation plan target suite.

In addition to the requirements, the ecosystems subgroup has identified a goal to determine the ability of NISAR to estimate vertical canopy structure. Current research in polarimetric interferometry shows that

TABLE 16 3. LEVEL 2 BASELINE REQUIREMENTS FOR CRYOSPHERE

Attribute	Ice Sheets & Glaciers Velocity Slow Deformation (667)	Ice Sheets & Glaciers Velocity Fast Deformation (668)	Ice Sheet Time-Varying Velocity (738)
Measurement	Point-to-point displacements in two dimensions	Point-to-point displacements in two dimensions	Point-to-point displacements in two dimensions
Method	Interferometry, speckle tracking	Interferometry, speckle tracking	Interferometry, speckle tracking
Duration	3 years	3 years	3 years
Product Resolution	100 m	250 m	500 m
Accuracy	3% of the horizontal velocity magnitude plus 1m/yr or better, over > 90% of coverage areas	3% of the horizontal velocity magnitude plus 5 m/yr or better, over > 90% of coverage areas	3% of the horizontal velocity magnitude plus 10 m/yr or better, over > 80% of coverage areas
Sampling	Each cold season, two directions	Each cold season, two directions	Each 12 days, two directions
Coverage	Areas moving slower than 50 m/yr of both poles and glaciers and ice caps	Areas moving slower than 50 m/yr of both poles	Outlet glaciers, or other areas of seasonal change
Response Latency	N/A	N/A	24/5 Best effort basis on event

Attribute	Permafrost Displacement (671)	Grounding Line Vertical Displacement (445)	Sea Ice Velocity (670)
Measurement	Spatially averaged in two dimensions	Point-to-point displacements in two dimensions	Point-to-point relative horizontal displacements
Method	Interferometry	Interferometry, speckle tracking	Backscatter image feature tracking
Duration	3 years	3 years	3 years
Product Resolution	100 m	100 m	Gridded at 5 km
Accuracy	4*(1+L ^{1/2}) mm or better, over length scales 0.1 km < L < 50 km, > 80% of coverage areas	100 mm or better, over 95% of coverage areas annually, over 50% of coverage areas monthly	100 m/day, over 70% of coverage area
Sampling	In snow-free months sufficient to meet accuracy (semi-monthly)	Monthly	Every 3 days
Coverage	Targeted priority regions in Alaska and Canada	Greenland and Antarctic coastal zones	Seasonally-adjusted Artic and Antarctic sea ice cover
Response Latency	N/A	24 hour tasking, 5 hour data delivery. Best effort on event	24/5 Best effort basis on event

TABLE 16-4. LEVEL 2 BASELINE REQUIREMENTS FOR ECOSYSTEMS

Attribute	Biomass (673)	Disturbance (675)	Inundation (677)	Crop Area (679)
Measurement	Biomass	Areal extent	Areal extent	Areal extent
Method	Polarimetric backscatter to biomass	Polarimetric backscatter temporal change	Polarimetric backscatter contrast	Polarimetric backscatter contrast and temporal change
Duration	3 years	3 years	3 years	3 years
Product Resolution	100 m	100 m	100 m	100 m
Accuracy	20 Mg/ha or better where biomass is < 100 Mg/ha, over 80% of coverage areas	80% or better classification accuracy where canopy cover changes by >50%	80% or better classification accuracy	80% or better classification accuracy
Sampling	Annual	Annual	Seasonal, sampled every 12 days to track beginning and end of flooding events	Quarterly; sampled every 12 days to track beginning and end of growing season
Coverage	Global areas of woody biomass	Global areas of woody biomass	Global inland and coastal wetlands	Global agricultural areas
Response Latency	N/A	24/5 Best effort basis on event	24/5 Best effort basis on event	N/A

when temporal decorrelation is small and the interferometric baselines are large (but not too large), it is possible to retrieve canopy structure from the data. As a repeat-pass interferometer designed for two disciplines to have small baselines, NISAR is not ideally suited to this technique. However, the dense interferometric time series may lead to new innovations that allow structure estimates of value, and the team expects to explore these possibilities.

The validation requirement is included to specify that the validation program is limited in scope to fixed areas, employing analysis to extrapolate performance to the globe.

16.4 LEVEL 2 URGENT RESPONSE

There is no urgent response L2 science requirement. While the mission envisioned by the community – one with relatively fast revisit and a capacity for acquiring data over the globe – can serve an operational need for reliable, all-weather, day/night imaging in the event of a disaster, the project has been sensitive to the costs associated with operational systems that must deliver such data. However, demonstrating the utility of such data for urgent response for the benefit of society is important and in keeping with the recommendations of the 2007 Decadal Survey. To that end, the NISAR L1 urgent response requirement has been written with a focus on targeting and delivery latency, as previously described. The L1 urgent response requirement flows to other L2 mission requirements, but not to science directly.

17 APPENDIX E

NISAR SCIENCE FOCUS AREAS

This appendix provides additional background and rationale for the science objectives to be addressed by NISAR. Each section describes the 2007 Decadal Survey objectives that guided the development of the requirements for NISAR in each major science focus area, amplifying their importance through examples in the literature that were generated from existing data – something that can only loosely approximate the richness of the results that will be derived from NISAR's dense spatial and temporal data set.

17.1 SOLID EARTH

The 2007 Decadal Survey identified the following overarching science goals and related questions for solid Earth:

- Determine the likelihood of earthquakes, volcanic eruptions, landslides and land subsidence. How can observations of surface deformation phenomena lead to more complete process models for earthquakes, volcanoes, landslides and land subsidence and better hazard mitigation strategies?
- Understand the behavior of subsurface reservoirs.
- Observe secular and local surface deformation on active faults to model earthquakes and earthquake potential.
- Catalog and model aseismic deformation in regions of high hazard risk.
- Observe volcanic deformation to model the volcano interior and forecast eruptions.
- Map pyroclastic and lahar flows on erupting volcanoes to estimate damage and model potential future risk.
- Map fine-scale potential and extant landslides to assess and model hazard risk.

- Characterize aquifer physical and mechanical properties affecting groundwater flow, storage, and management.
- Map and model subsurface reservoirs for efficient hydrocarbon extraction and CO₂ sequestration.
- Determine the changes in the near surface stress field and geometry of active fault systems over major seismically active regions in India.
- Determine land subsidence rates of major reported land subsidence areas (due to mining and/or groundwater induced) in India.
- Map major landslide prone areas in the hilly regions of India.

These objectives require dense spatial coverage of Earth, and dense temporal sampling to measure, characterize and understand these often unpredictable and dynamic phenomena.

In situ GNSS arrays constrain the large-scale motions of Earth's surface where the arrays exist. In particular, these GNSS data can provide temporally continuous point observations that are best exploited when combined with the spatially continuous coverage provided by the InSAR imaging that NISAR will provide.

With NISAR, scientists will be able to comprehensively generate time series of Earth's deforming regions. When combined with other sources of geodetic imaging – optical satellite imagery when daytime, cloud-free observations are available and when expected ground displacements are large; international SAR imagery when data are available and of suitable quality – an even more complete picture of Earth's 3-D motions can be constructed.

U.S. Geological Survey scientists Randy Jibson and Jon Godt investigate the Seaside landslide that was triggered by the 2016 magnitude 7.8 Kaikoura, New Zealand, earthquake, along a fault that experienced significant surface offsets.

17.1.1 Earthquakes and Seismic Hazards

NISAR data will address several aspects of earthquake physics and seismic hazards including:

1. Determine crustal strains across the different phases of the seismic cycle. Because Earth's upper crust is elastic, inter-seismic deformation rates can be mapped to stressing rates, which in turn are used to guide assessments of future earthquake occurrence.
2. Derive physics-based models of faulting and crustal rheology consistent with multi-component displacement maps across all phases of the seismic cycle, complementing conventional land-based seismological and geodetic measurements. Estimates of rheological parameters are essential to understand transfer of stress within fault systems.
3. Assimilate vector maps of surface deformations through various stages of the earthquake cycle in large-scale simulations of interacting fault systems, currently a "data starved" discipline.

THE EARTHQUAKE CYCLE

Deformation of Earth's crust in tectonically active regions occurs on a rich variety of spatial and temporal scales. To date, the best temporal sampling is obtained from continuously operating GNSS sites. Figure 17-1 shows the evolution of displacements at the GNSS site Carr Hill (CARH), near Parkfield, CA. The Mw 6.0 Parkfield earthquake of September 27, 2004, corresponds to the discrete jump midway through the time series. The average secular motion (i.e., linear trend) has been subtracted from each component. These time series can be divided conceptually into three parts: (1) the "interseismic" part that occurs in the interval several years after the previous earthquake until just before the most recent earthquake; (2) the coseismic step at the time of the earthquake; and (3) the "postseismic" period, occurring in the days to years immediately following the earthquake, after which it merges continuously into the interseismic phase. Regions where

elastic strain (i.e., the spatial gradient in displacements) is accumulating most rapidly (not shown in the figure) are those where earthquakes are most likely. Temporal changes in the elastic stressing rate such as occurred at CARH in March 2004, are associated with temporal changes in the probability of earthquake occurrence.

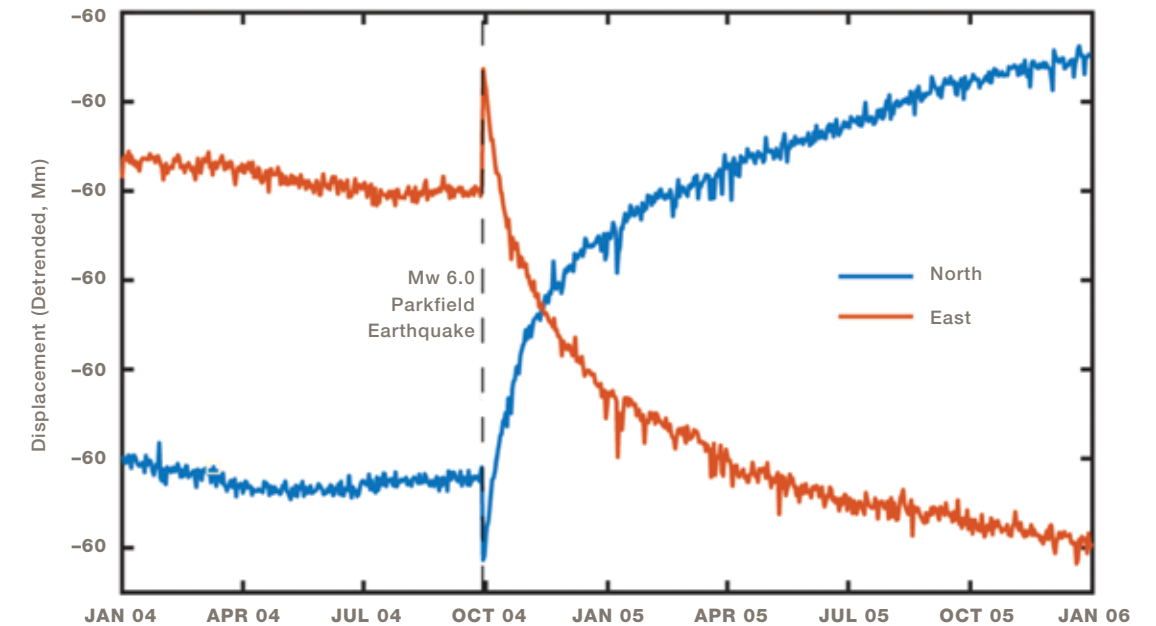
Understanding coseismic fault slip magnitude and geometry, as well as regional local deformation signals such as triggered slip can lead to understanding of changes in surface deformation on nearby (and distant) faults. For example, CARH lurched about 15 mm to both the north and west at the time of the Mw 6.0 Parkfield earthquake. These detailed displacement measurements allow inference of the magnitude and sense of slip on the fault plane during the earthquake. Changes in deformation rates on distant faults are then monitored for evaluating any "linkages". Because of the sharp discontinuity in surface displacement and immediate postseismic deformation, a rapid repeat sampling strategy permits accurate determination of coseismic displacements, which can otherwise be obfuscated by postseismic deformation occurring between the time of the earthquake and the time of the first observation. The post-seismic deformation field immediately following an earthquake can be significant, with decelerating surface displacements in the following week to months and possibly years for larger earthquakes. Such postseismic displacements as a function of time are frequently characterized by a logarithmic dependence on time consistent with a frictionally controlled fault slip process (as opposed to viscous processes). Within the time interval shown in the figure, rates have not yet returned to those observed preceding the earthquake.

COSEISMIC DEFORMATION

Small earthquakes: NISAR will provide unique observations of ground displacement that will improve location accuracy of such events by an order of magnitude (e.g., Lohman et al., 2002; Lohman and Simons, 2005). Such improved locations can be used to improve

FIGURE 17-1

Daily position time series at GNSS site CARH for north (blue) and east (red) components, illustrating the coseismic offset and postseismic deformation associated with the Mw 6.0 Parkfield earthquake (September 27, 2004, dashed line). A linear trend has been subtracted from each component using the time period January 2008-January 2018.



seismic tomographic models of Earth's interior structure by reducing the tradeoff between seismic wave velocities and source locations. Detailed understanding of the location and mechanism of small earthquakes is also essential to illuminate important faults. These earthquake parameters provide important ingredients when estimating the state of stress and changes in the state of stress in the crust, as well as indicators of the boundaries between creeping and non-creeping fault segments of a given fault.

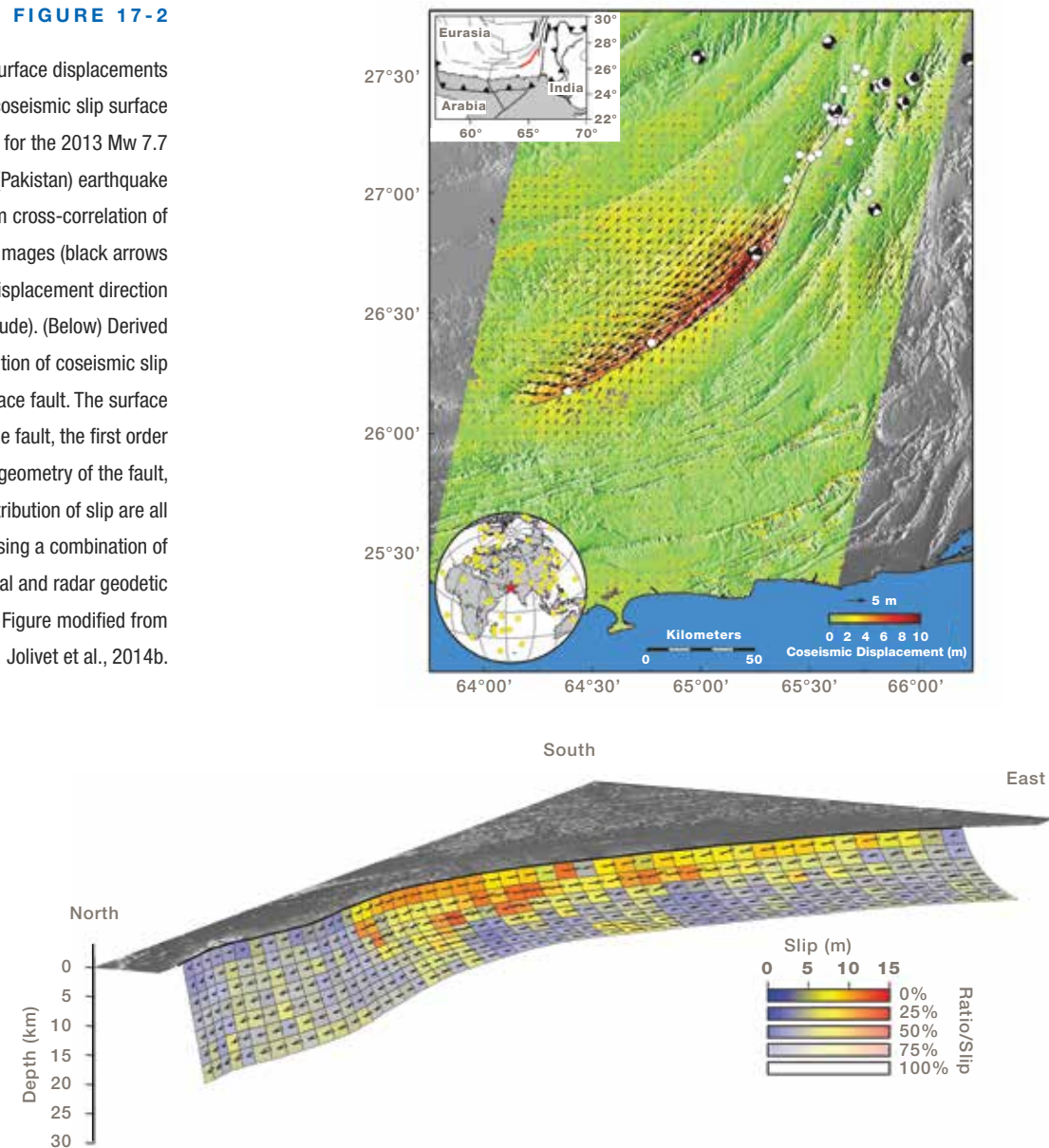
Larger earthquakes: NISAR will provide maps of surface faulting complexity and will constrain first order geometric variability of the coseismic rupture at depth. Spatially continuous maps (combined with GNSS data when available) of surface displacements provide critical constraints on models of coseismic fault rupture for both small and large earthquakes. The geodetic imaging data of the kind that will be routinely provided by NISAR has already been shown to be crucial in estimating the distribution of coseismic slip on the subsurface fault and earthquake-induced changes in crustal stress. Elastic models of the lithosphere and geodetic data, combined with seismic data, reveal temporal evolution (i.e., kinematic models) of slip during an earthquake,

which are in turn used to understand strong ground motions that impact the built environment. These kinematic models are among the few constraints we have on the underlying physics that shape our understanding of earthquake rupture mechanics. Such well-constrained coseismic earthquake source models are also routinely compared with inferences of earthquake magnitudes from geological field observations, providing a needed calibration of paleo-seismological inferences of historic earthquakes.

The fusion of multiple imagery sources illustrates the power of geodetic imaging (here a combination of radar and optical geodetic imaging) to constrain the complex curved surface trace of the 2013 Mw 7.7 Pakistan earthquake (Figure 17-2). The geodetic data also require the dip of the fault to approximately 45 degrees from vertical, thereby documenting this event as the first example of a large strike slip event on a non-vertical fault – well outside the expectations from conventional faulting theory. Such "surprise" events that challenge conventional wisdom frequently occur outside the scope of existing ground-based geodetic networks and thus underscore the need for the global access provided by NISAR.

FIGURE 17-2

(Top) Surface displacements and coseismic slip surface displacements for the 2013 Mw 7.7 Balochistan (Pakistan) earthquake derived from cross-correlation of Landsat 8 images (black arrows indicate the displacement direction and amplitude). (Below) Derived distribution of coseismic slip on the subsurface fault. The surface rupture of the fault, the first order subsurface geometry of the fault, and the distribution of slip are all derived using a combination of available optical and radar geodetic imaging data. Figure modified from Jolivet et al., 2014b.



POSTSEISMIC DEFORMATION

Important constraints on fault behavior are also gleaned from comparisons of the distribution of coseismic fault slip with estimates of interseismic and postseismic fault slip. For instance, in Figure 17-3, we see the spatially complementary distribution of coseismic and postseismic fault slip associated with the 2005 Mw 8.8 Nias earthquake, with little overlap between the two phases of fault slip. Future geodetic study will need to deter-

mine the extent to which such behavior is ubiquitous for large earthquakes and if so, raises the question of what controls seismogenic behavior. Only with data from many additional events will we be able to address this fundamental question.

Beyond seismic and postseismic fault slip, recent results document an exciting range of aseismic fault slip events (fault slip not associated with a preceding large earthquake) in both strike slip and thrust faulting environments. Such events have been documented in

Mexico, Japan, Chile, the Pacific Northwest, Alaska, New Zealand and Southern California. These events are sometimes quasi-periodic, they are frequently associated with increased seismic tremor, and remain enigmatic as to their origin. Of great interest is the extent to which such aseismic fault slip transients occur at different time scales (days, weeks, years) and the degree to which large seismic earthquakes are more or less likely in periods of these aseismic transient events. Thus far, the existence of these events has been limited to regions with pre-existing ground-based networks and we have no knowledge of the occurrence, or lack thereof, on most of the world's major faults. The global coverage, frequent repeats, and high correlation geodetic imaging provided by NISAR will enable a complete inventory of shallow aseismic fault slip and thereby allow us to begin to understand the underlying causes of these events.

Fault slip events result in a redistribution of stress in the crust and thus may be important in triggering seismic activity. Current research is elucidating the nature of earthquake-to-earthquake interactions, quantifying the statistical likelihood of linkages, and elucidating time-dependent processes (e.g., postseismic relaxation, state and rate of fault friction) that influence triggered activity. For instance, Figure 17-3 compares the cumulative rate of aftershock production after the 2005 Mw 8.8 Nias earthquake with the rate of postseismic displacement observed at one of a few sparse GNSS sites. Note that seismicity represents only a few percent of the total slip required to explain the GNSS data. The observed behavior suggests that the temporal behavior of displacement and seismicity is nearly identical and that postseismic fault slip processes control the rate of earthquake production.

Existing observations of seismicity and fault slip also suggest longer-range interactions that are not fully understood. Such interactions should have detectable deformation signatures (Toda et al., 2011). Synoptic space-based imaging offers a new and promising means to identify deformation causes and effects linking regional earthquake events. Thus, NISAR will allow

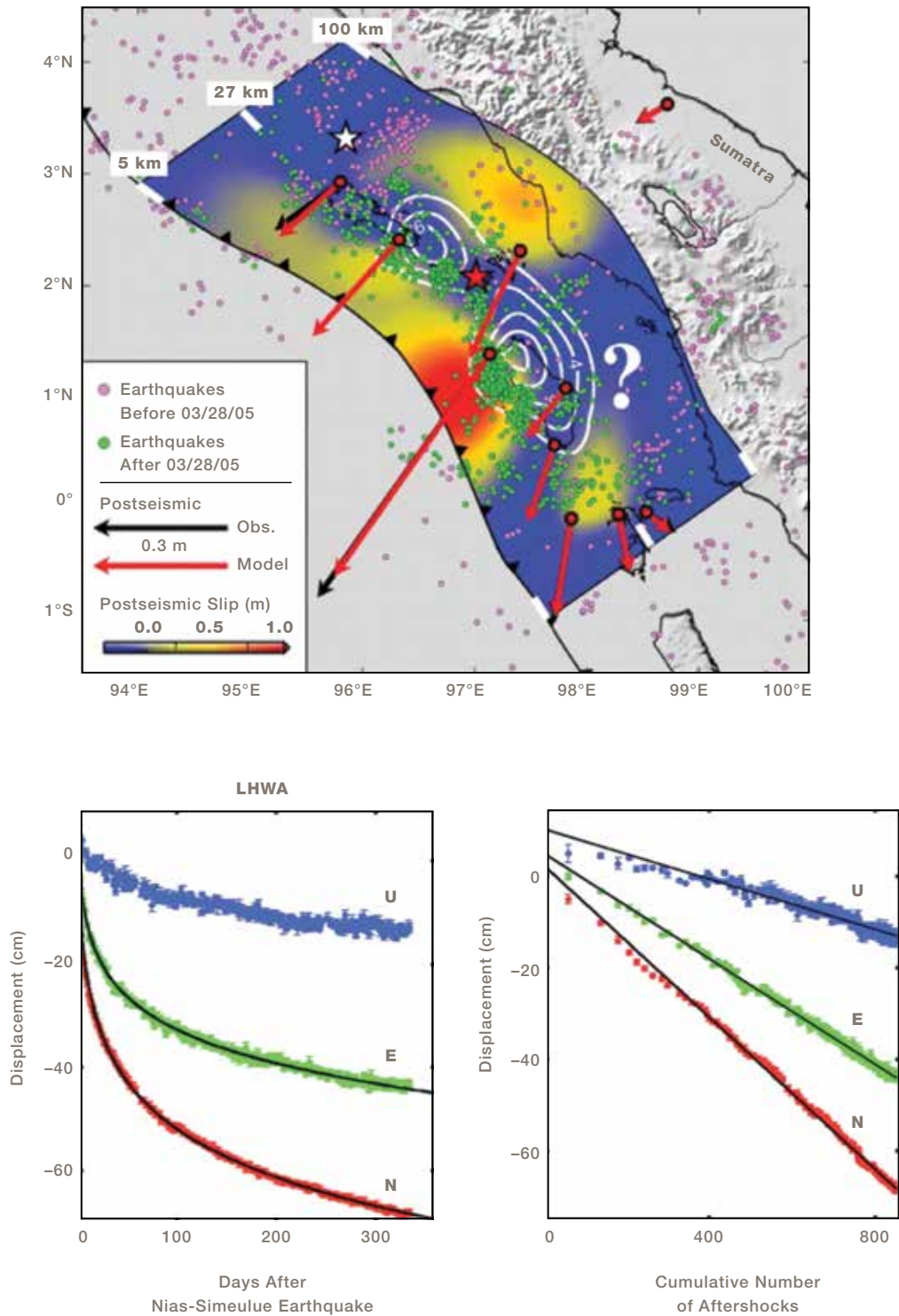
a systematic assessment of the relationship between seismicity and fault slip across the different phases of the seismic cycle.

Viewed from above, Earth's outer rock layers are divided into multiple tectonic plates. The slow movement of each plate results in concentrated zones of deformation in Earth's crust – zones that are frequently found at the boundaries between the plates and are the locus of large destructive seismic events on interacting systems of faults. The next leap in our understanding of earthquakes and our ability to minimize their associated hazards requires us to (1) detect regions that are undergoing slow elastic loading of seismogenic faults, (2) understand what controls the distribution of subsurface fault slip during individual large events, (3) quantify Earth's response to large earthquakes (essentially using these events as probes of the mechanical nature of faults and the surrounding crust), and (4) understand the role played by major earthquakes on changing the likelihood of future seismic events in neighboring regions.

Earthquakes are part of a cycle commonly divided into periods associated with elastic stress accumulation, release of elastic stress during an earthquake, and a period associated with rapid readjustment of the fault system and surrounding crust following a large tremor. In some faults, there are periods of very slow transient fault slip events that are so slow they do not cause significant ground shaking. Models currently used to understand the earthquake system explore the frictional properties of faults (which fault segments creep aseismically versus which segments fail in a stick-slip fashion) across all phases of the seismic cycle. These models also incorporate both elastic and inelastic behavior of the crust in which earthquake faults are embedded. The aim of these models is to rigorously simulate observations over short time scales (e.g., a single earthquake or a short period of time before and after an earthquake) in a way that is consistent with observations of longer time scale deformation as inferred from geology. There are many proposed models

FIGURE 17-3

Nias-Simeulue earthquake data. (Top) Coseismic (2-m interval white contours) and postseismic slip (color), from the 2005 Mw 8.8 aftershock of the 2004 Mw 9.1 Sumatra earthquake. Arrows indicate observed (black) and predicted (red) GNSS observations, stars show epicenters of 2004 (white) and 2005 (red) earthquakes. Dots denote earthquakes before (pink) and after (green) the 2005 event. (Bottom left) Observed and modeled postseismic displacements at one continuous GNSS site. Black solid lines are estimated from a 1D spring-slider model in which afterslip obeys a velocity-strengthening friction law. Data shown for vertical (U), east (E), and north (N) displacements. (Bottom right) The relationship between post-seismic ground displacement and the cumulative number of regional aftershocks. Figure from Hsu et al (2006).



designed to explain existing observations of deformation in different phases of the earthquake cycle but we lack sufficient observations to test these reliably. The dedicated observing schedule of NISAR will increase the number, spatial coverage, temporal resolution, and accuracy of observations sufficiently to allow us to systematically test, reject and/or constrain the competing models of earthquake forcing.

17.1.2 Volcano Hazards

Improving volcano hazard prediction requires determining the location, size and composition of magma reservoirs via geodetic, seismic, geochemical, and other observations. We must also identify the type of magmatic unrest associated with eruptions, characterize deformation prior to volcanic eruptions, and predict the type and size of impending eruptive events. High-quality geodetic observations are necessary in order to constrain timescales and mechanisms of these processes.

Volcanic hazard science flows from the same crustal deformation data used to study the seismic cycle. Deformation data allow us to:

1. Identify and monitor surface deformation at quiescent and active volcanoes: Only InSAR has the capability for monitoring virtually all of the world's potentially active volcanoes on land (approximately 1400 volcanoes).
2. Derive models of magma migration consistent with surface deformation preceding, accompanying, and following eruptions to constrain the nature of deformation sources (e.g., subsurface magma accumulation, hydrothermal-system depressurization resulting from cooling or volatile escape).
3. Monitor and characterize volcanic processes such as lava-dome growth and map the extent of eruptive products (lava and pyroclastic flows and ash deposits) from SAR backscattering and coherence imagery during an eruption, an important diagnostic of the eruption process. Similar methods can

be used during or after an eruption to determine the locations of lahars or landslides.

4. Map localized deformation associated with volcanic flows that can persist for decades to understand physical property of volcanic flows, guide ground-based geodetic benchmarks, and help avoid misinterpretations caused by unrecognized deformation sources.

Deformation data are the primary observables in understanding the movement of magma within volcanoes. Although uplift from the ascent of magma into the shallow crust has been observed prior to some eruptions, particularly on basaltic shield volcanoes, the spatio-temporal character of such transient deformation is poorly known, especially at the locations of the largest explosive eruptions. Little is known about deformation on most of the world's volcanoes because only a small fraction of them are monitored. Even the incomplete surveys to date from previous satellites have discovered many newly active volcanoes (Pritchard and Simons, 2004; Fournier et al., 2010).

Detection and modeling of deformation can provide warning of impending eruptions, reducing loss of life, and mitigating impact on property. Even remote volcanoes are important to monitor as large eruptions can have a global impact through ash ejected into the stratosphere that can affect air travel (e.g., the billion-dollar impact of the 2010 Eyjafjallajokull, Iceland eruption) and climate (like the 1991 Mt. Pinatubo, Philippines eruption). In addition, InSAR data provide detailed spatial information not available from GNSS and other available geodetic data, allowing us to explore models to reveal complex geometries of intrusions and their interactions with regional crustal stress regimes. Furthermore, higher temporal resolution deformation imagery combined with other geophysical and geochemical observations will make it possible to advance volcano forecasting from empirical pattern recognition to one based on deterministic physical-chemical models of the underlying dynamics (Segall, 2013).

An example of the potential of frequent InSAR observations to monitor the temporal evolution of a volcano through an eruption cycle is illustrated (Figure 17-4) by the work of Lu et al. (2010). Mt. Okmok in the Aleutian arc erupted during February–April 1997 and again during July–August 2008. The inter-eruption deformation interferograms suggest that Okmok began to re-inflate soon after its 1997 eruption, but the inflation rate generally varied with time during 1997–2008. Modeling these interferograms suggests that a magma storage zone centered about 3.5 km beneath the center of the 10-km-diameter caldera floor was responsible for the observed deformation at Okmok. Multi-temporal InSAR deformation images can be used to track the accumulation of magma beneath Okmok as a function of time: the total volume of magma added to the shallow storage zone from the end of the 1997 eruption to a few days before the 2008 eruption was 85–100% of the amount that was extruded during the 1997 eruption. While the eruptive cycle from Okmok shows a pattern of deformation that may be diagnostic of impending eruption, only a fraction of the potentially active volcanoes have frequent enough observations from available GNSS or existing SAR satellites to detect such patterns. Furthermore, even from limited observations, it seems that other volcanoes show different and sometimes more complex patterns of deformation before eruption – in some cases, no deformation is observed before eruptions (Pritchard and Simons, 2004). The observations from NISAR will allow us to make dense time series observations at nearly all the world's subaerial volcanoes to better understand the relation between deformation and eruption.

Among the most important parameters needed to assess short-term volcanic hazards and better understand volcanic processes are the location, volume, and composition of potentially eruptible magma (Figure 17-5). Together with seismology, continuous ground deformation measurements (like GNSS), and gas geochemistry observations, the spatially dense, InSAR-derived deformation field can play a pivotal role in constraining these unknowns (Pritchard and Simons, 2002; Dzurisin, 2007; Lu and Dzurisin, 2014). InSAR data

from past satellite missions has been characterized by comparatively poor coherence and temporal resolution, restricting the application of those data to simple kinematic models of magma storage and transport—especially location, geometry, and volume change. A better understanding of volcanic activity requires models that are based on the underlying physics of magma ascent and eruption. As input, such models require a variety of geochemical and geophysical data, including, critically, deformation measurements with improved spatial and temporal resolution. NISAR will provide 2-D vector deformation measurements at higher temporal resolution and better coherence than any past or present satellite InSAR sensor, making it possible to explore volcano models with complex source geometries in heterogeneous media. When combined with GNSS, seismic, gas emissions, and other measurements of volcanic activity, NISAR will facilitate the development of more realistic models that estimate, for example, absolute magma storage volume, reservoir overpressure, volatile concentrations, and other parameters. These results are critical for deterministic eruption forecasting that can be updated as new data are acquired, which represents a fundamental advance over empirical forecasting that is based primarily on past experience—a common practice presently at most volcanoes worldwide (Segall, 2013).

17.1.3 Landslide Hazards

Landslides threaten property and life in many parts of the world. Steep slopes, rock types and soil conditions are key underlying causes of landslides, which are typically (but not always) triggered by rainfall events, earthquakes, or by thawing in arctic regions. Improved knowledge of surface composition and topography are important for characterizing landslide risk. Prediction of landslide movement is aided significantly by spatially and temporally detailed observations of down-slope motion at the millimeter to centimeter level. Such observations, possible with InSAR measurements such as NISAR, can identify unstable areas. Similar to the Mt Okmok volcano, studies in areas that can be monitored with current InSAR capable satellites have shown the

FIGURE 17-4

Volcano monitoring. (Top) Average deformation of Mt. Okmok volcano in the Aleutian volcanic arc is related to magma movement from 1997. Each fringe (full color cycle) represents 2.83-cm range change between the ground and satellite along the satellite line-of-sight direction. Areas that lack interferometric coherence are uncolored. (Bottom) Estimated volume of magma accumulation beneath Mt. Okmok as a function of time based on multi-temporal InSAR (Lu et al., 2010) error bars represent uncertainties. The shaded zone represents the source volume decrease associated with the 1997 eruption, as inferred from a co-eruption interferogram.

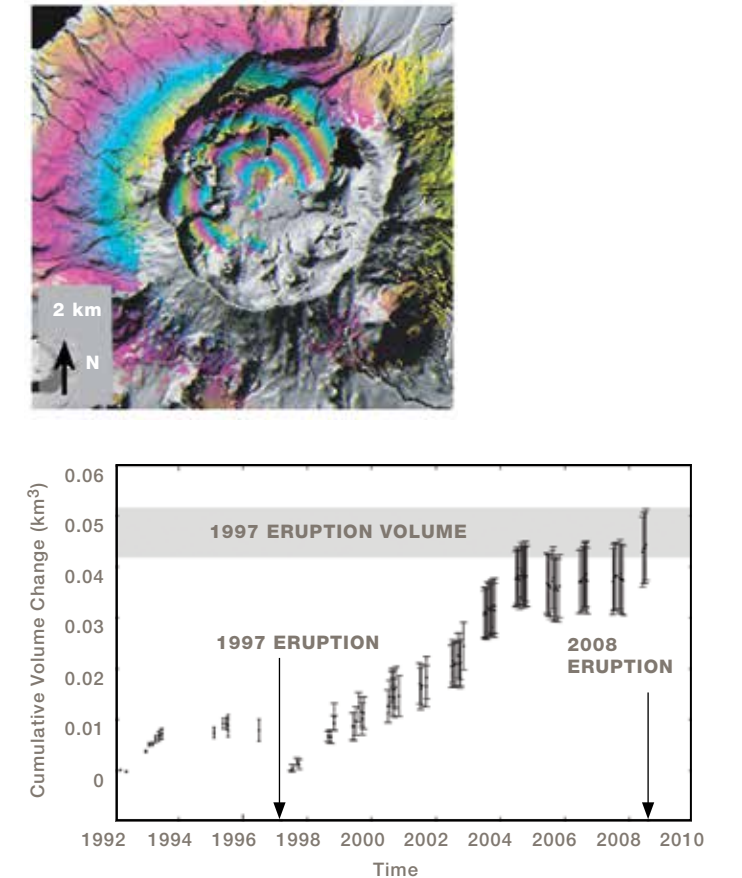


FIGURE 17-5 AGUNG VOLCANO

High-resolution Cosmo-SkyMed interferogram (top right) and backscatter SAR images (bottom) of Agung volcano, Bali, Indonesia of the 2017-2018 unrest and eruption.

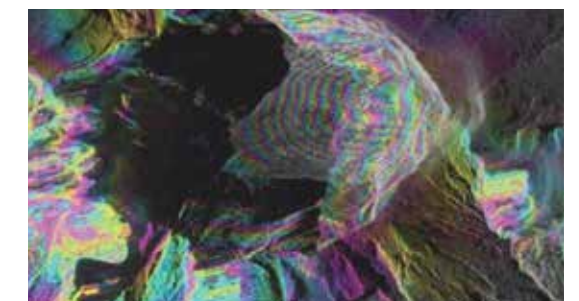
The interferogram shows about 15 cm of inflation within the summit crater that occurred prior to the eruptions of November 2017. The backscatter image of November 28 clearly shows the accumulation of new lava within the crater. Imagery from the Italian Space Agency (ASI) through the CEOS volcano pilot.



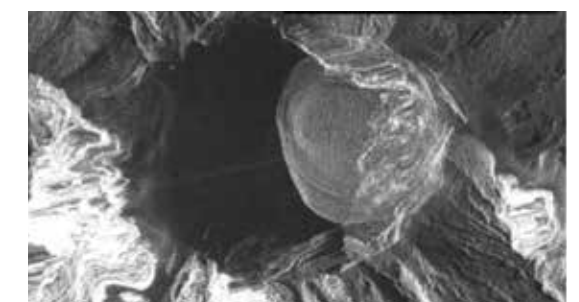
NOVEMBER 20, 2017



MAY 4 –NOVEMBER 16, 2017



NOVEMBER 28, 2017



IN ADDITION TO
EARTHQUAKE ACTIVITY
ASSOCIATED WITH THE
PRODUCTION OF
HYDROCARBONS, THERE
IS NOW EVIDENCE THAT
PRODUCTION OF WATER
FROM AQUIFERS CAN
TRIGGER EARTHQUAKES.

potential for observations at critical times. One example is in the Berkeley Hills region in Northern California, where interferometric analysis reveals the timing, spatial distribution, and downslope motion on several landslides that had damaged homes and infrastructure (Hilley et al., 2004). A more active example, shown in Figure 17-6, is the Slumgullion landslide in southwestern Colorado, which is moving at 1-3 cm/day, as determined using L-band UAVSAR observations.

17.1.4 Induced Seismicity

Management of subsurface fluid reservoirs is an economically and environmentally important task. Obtaining observations to better manage subsurface reservoirs can have substantial benefits. In addition, the past decade has seen a substantial increase in the number of earthquakes triggered by both injection and production of subsurface fluids (Figure 17-7), leading to a review by the National Research Council (2013). InSAR provides an important tool for understanding and managing the risks.

An early investigation into understanding the geomechanical response to hydrocarbon production and induced seismicity at a hydrocarbon field in Oman (Bourne et al., 2006) utilized InSAR. An oil field is overlain by a gas reservoir. InSAR, and microseismic data were acquired to monitor the reservoirs' responses to changes in fluid pressure. The changes in stress associated with differential compaction resulted in fault reactivation. As hypothesized for tectonic earthquakes, there is a strong relationship between stressing rates and seismicity, with the rate of seismic activity proportional to both the rate of pressure change and the rate of surface deformation. Based on these observations, geomechanical models can be built to enable accurate prediction of the risk for well-bore failure due to fault reactivation.

Understanding the relationship between production of hydrocarbons and induced seismicity is a problem of tremendous economic importance. For example, the

vast gas reservoir in Groningen province of the Netherlands provides almost 60 percent of the gas production in the Netherlands. A recent increase in earthquake activity associated with production at Groningen has caused great public concern and in response, the Dutch government decided to cut the production cap for this reservoir in half in January 2014 (van Daalen, Wall Street Journal, 01/17/2014). The financial cost to the Dutch government in 2014 is 700 million euros (\$1.14 billion). Observations such as those to be provided by NISAR will provide a comprehensive geodetic dataset that will inform such billion-dollar decisions.

In addition to earthquake activity associated with the production of hydrocarbons, there is now evidence that production of water from aquifers can trigger earthquakes. On May 11, 2012, an Mw 5.1 earthquake struck the town of Lorca, Spain, resulting in 9 fatalities. Despite its relatively small magnitude, the quake was shallow enough that InSAR observations of surface deformation allowed inversion for the distribution of slip at depth (González et al., 2012). Most slip occurred at a depth of 2–4 km, with a second slip patch shallower than 1 km depth – both very shallow hypocentral depths for this region. Over 250 m of water had been pumped from a shallow aquifer, with subsidence of up to 160 mm/yr observed by InSAR (Figure 17-8). González et al. (2012) hypothesize that stress changes from depletion of the aquifer triggered this unusually shallow event.

InSAR measurements of surface deformation can also provide a powerful tool for short-term risk assessment associated with production of unconventional reservoirs. For example, a recent major bitumen leak from cyclic steam injection in Alberta, Canada, in June 2013, associated with substantial precursory surface deformation would have placed valuable constraints on the physics of this unusual sequence. Unfortunately, there appears to be no existing InSAR coverage.

Finally, injection of CO₂ into the crust is expected to become an increasingly important means for sequestering this greenhouse gas from the atmosphere. Monitoring

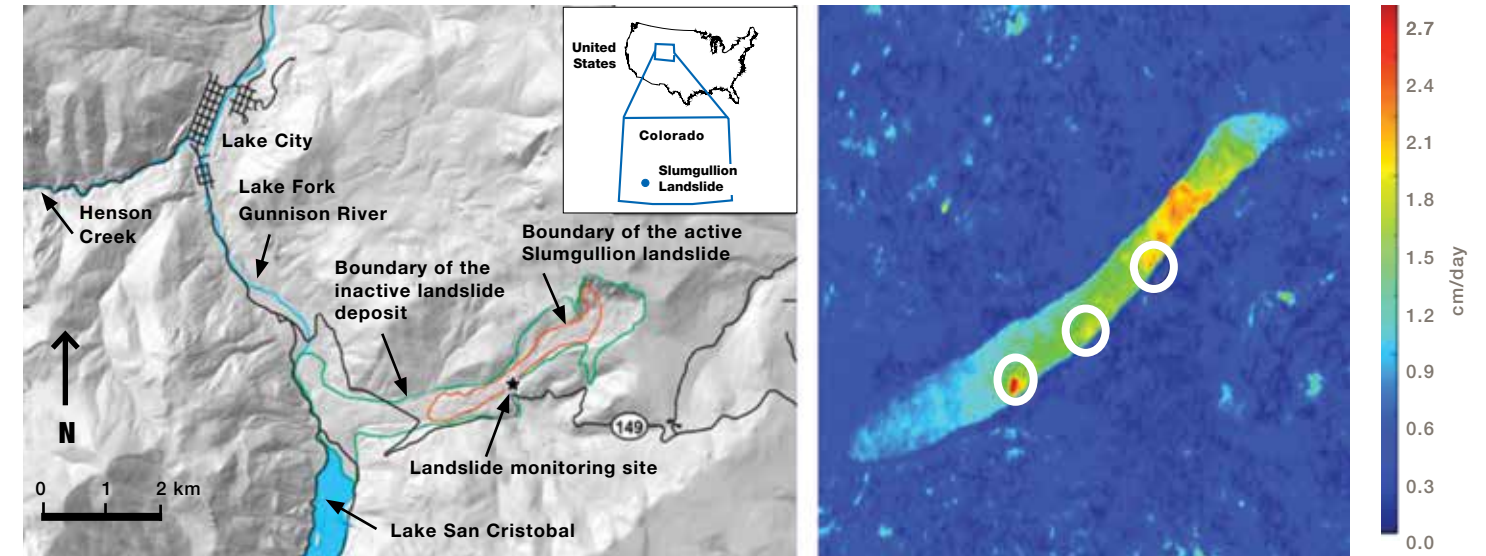


FIGURE 17-6 Creeping Slumgullion landslide in southwestern Colorado (Left, at the Slumgullion Natural Laboratory). Figure on the right shows a velocity map derived from UAVSAR repeat pass observations separated by 7 days in April 2012.

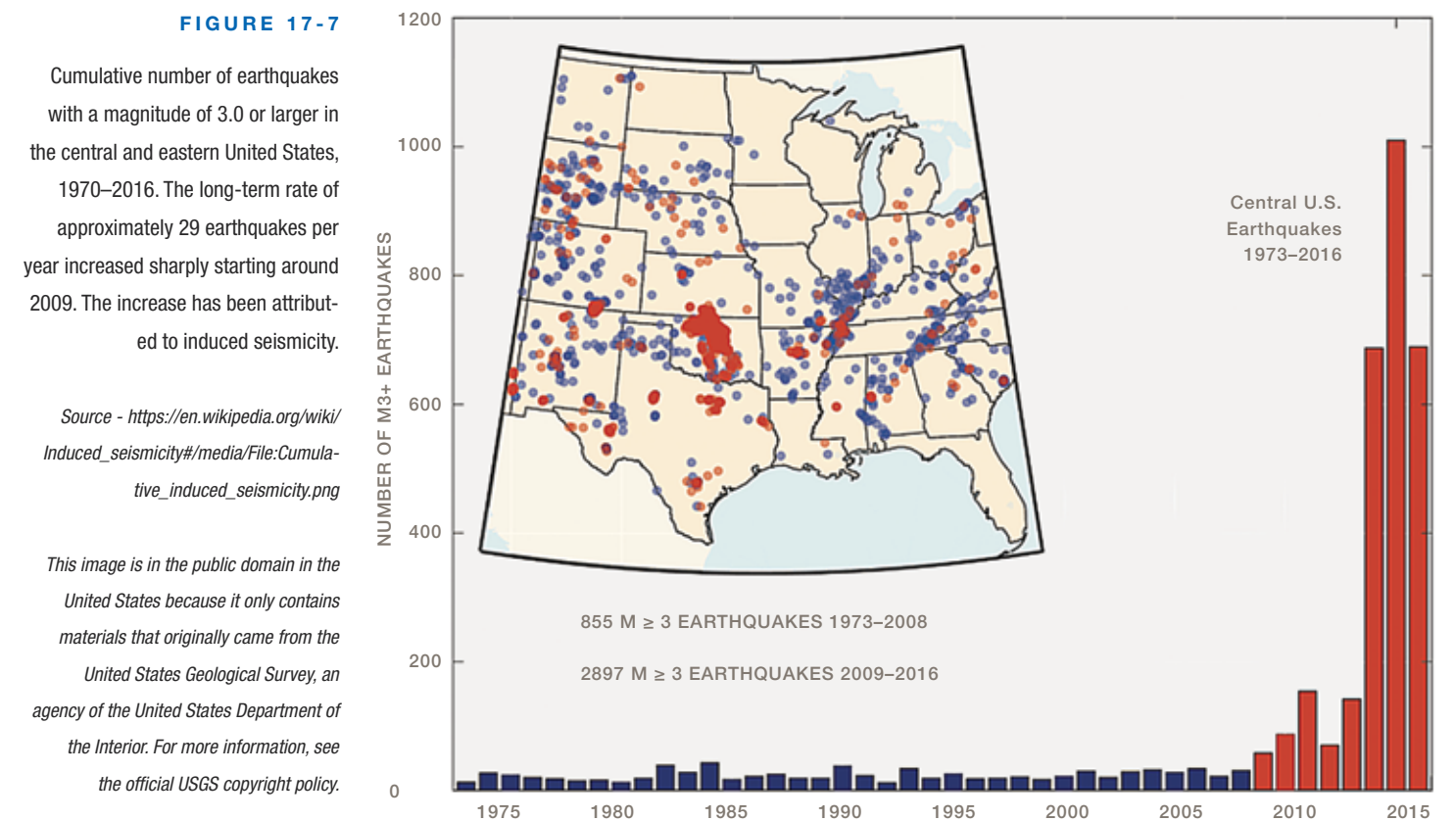


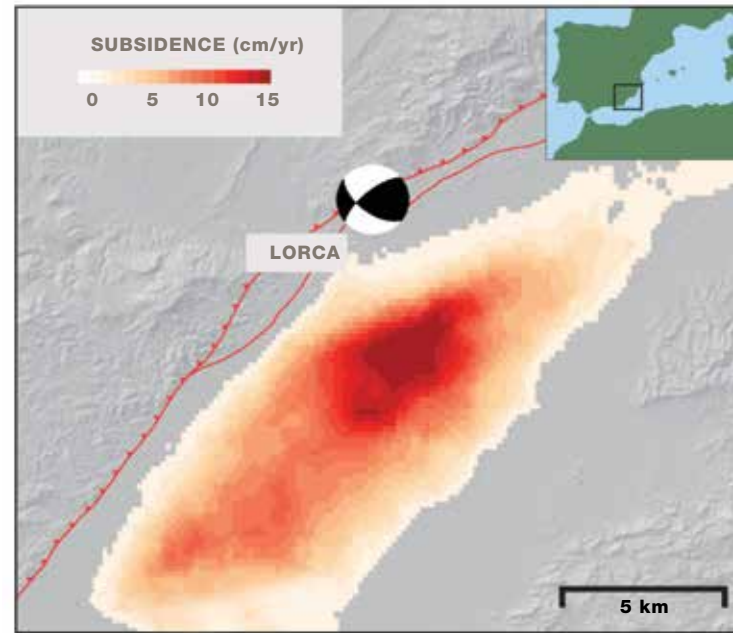
FIGURE 17-7 Cumulative number of earthquakes with a magnitude of 3.0 or larger in the central and eastern United States, 1970–2016. The long-term rate of approximately 29 earthquakes per year increased sharply starting around 2009. The increase has been attributed to induced seismicity.

Source - https://en.wikipedia.org/wiki/Induced_seismicity#/media/File:Cumulative_induced_seismicity.png

This image is in the public domain in the United States because it only contains materials that originally came from the United States Geological Survey, an agency of the United States Department of the Interior. For more information, see the official USGS copyright policy.

FIGURE 17-8

Relationship between subsidence associated with groundwater withdrawal (red shading) and the May 11, 2012, Mw 5.1 earthquake near the city of Lorca, Spain (after González et al., 2012).



the surface deformation caused by fluid injection will likely become an important technique for understanding reservoir behavior and monitoring its integrity. The In Salah field in Algeria is in a favorable environment for monitoring by InSAR. ENVISAT C-band InSAR studies of deformation associated with CO₂ injection show that the field response can indeed be monitored in this way (Ringrose et al., 2009). In particular, as shown in Figure 17-9, the surface deformation observed by InSAR shows a two-lobed pattern near well KB-502, a horizontal well injecting CO₂ into a 20-m thick saline aquifer at 1.8 km depth. Such a two-lobed pattern indicates that, in addition to a component of isotropic volume expansion, a vertical fracture has opened, apparently extending into the caprock above the aquifer (Vasco et al., 2010). This fracture explains the early breakthrough of CO₂ into observing well KB-5 along strike to the northwest. In response to the confirmation

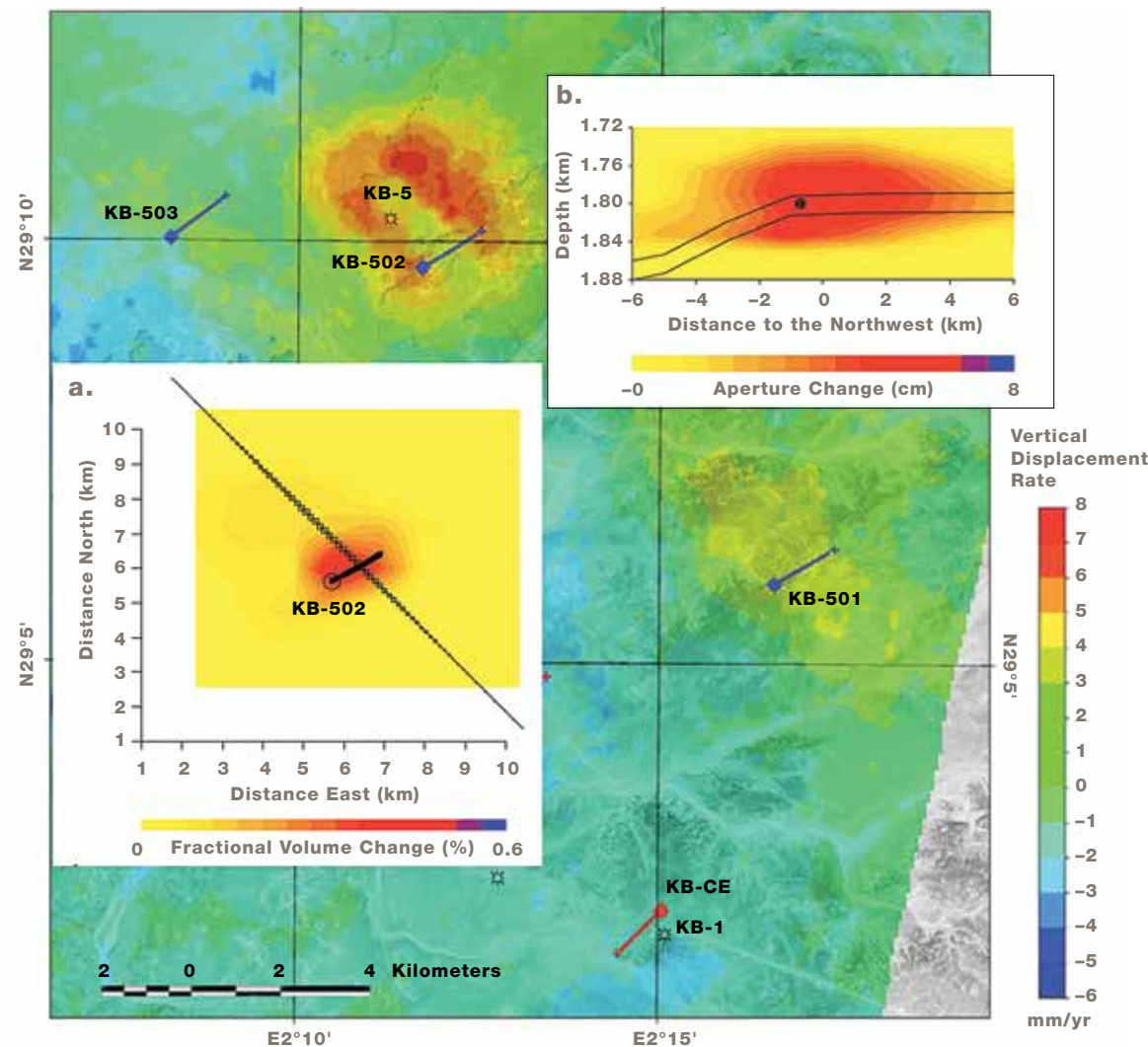
of the fracturing of the caprock, the injection of CO₂ at this site has been suspended.

17.1.5 Aquifer Systems

Natural and human-induced land-surface subsidence across the United States has affected more than 44,000 square kilometers in 45 states and is estimated to cost \$168 million annually in flooding and structural damage, with the actual cost significantly higher due to unquantifiable 'hidden costs' (National Research Council, 1991). More than 80 percent of the identified subsidence in the United States is a consequence of the exploitation of underground water. The increasing development of land and water resources threaten to exacerbate existing land subsidence problems and initiate new ones (Figure 17-10) (Galloway et al., 1999). Temporal and spatial changes in the surface elevation

FIGURE 17-9

In Salah oil field deformation. Interferogram of the In Salah oil field in Algeria, showing deformation associated with CO₂ injection over the period from March 2003 to December 2007 (Onuma & Ohkawa, 2009).



CALIFORNIA

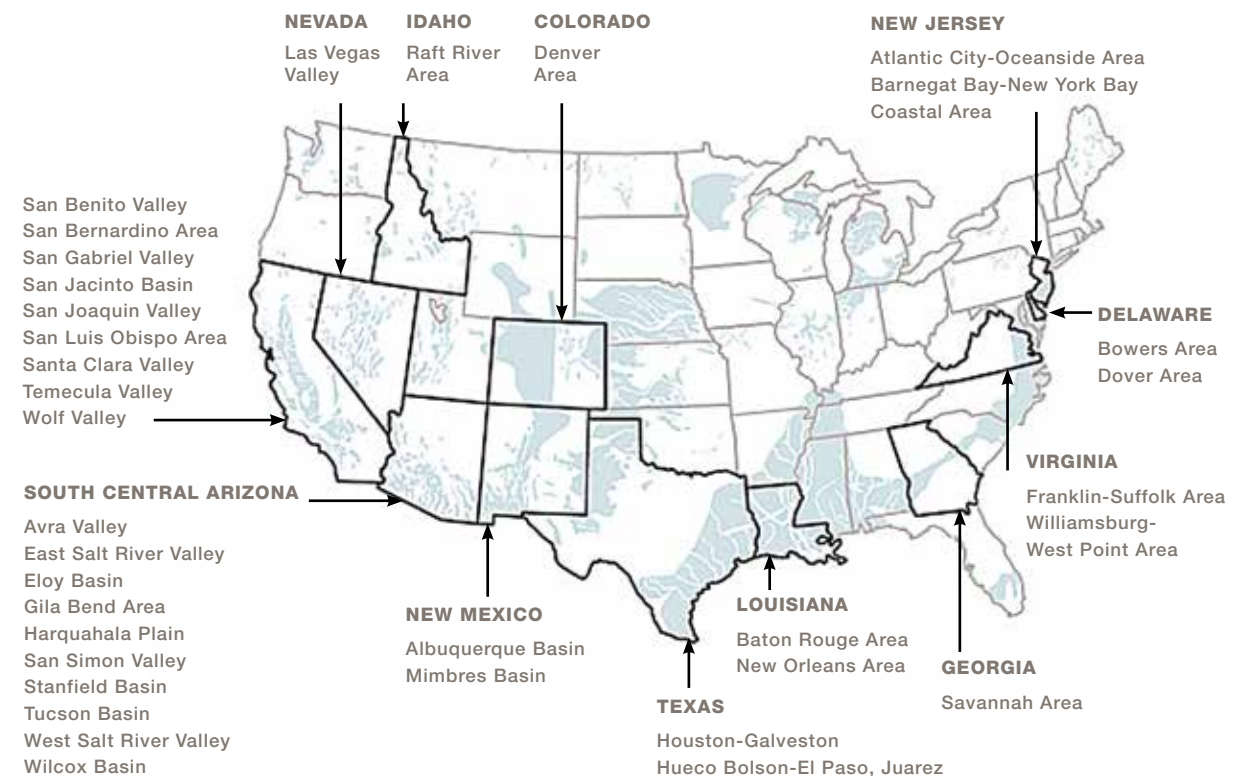
- Antelope Valley
- Coachella Valley
- Elsinore Valley
- La Verne Area
- Lucerne Valley
- Mojave River Basin
- Oxnard Plain
- Pomona Basin
- Sacramento Valley
- Salinas Valley

SOUTH CENTRAL ARIZONA

- Avra Valley
- East Salt River Valley
- Eloy Basin
- Gila Bend Area
- Harquahala Plain
- San Simon Valley
- Stanfield Basin
- Tucson Basin
- West Salt River Valley
- Wilcox Basin

FIGURE 17-10

U.S. Subsidence areas. Areas where subsidence has been attributed to groundwater pumping (Galloway et al, 1999)



above aquifers measured with geodetic techniques provide important insights about the hydrodynamic properties of the underground reservoirs, the hydro-geologic structure of the aquifer, the potential infrastructure hazards associated with pumping, and effective ways to manage limited groundwater resources.

Groundwater extraction from aquifers with unconsolidated fine-grained sediments like clay can lead to irreversible land subsidence (Poland, 1984). A sedimentary aquifer system consists of a granular skeleton with interstices (pores) that can hold groundwater. The pore fluid pressure is maintained by the groundwater that fills the intergranular spaces (Meinzer, 1928). Under conditions of constant total stress, the pore fluid pressure decreases as groundwater is withdrawn, leading to an increase in the intergranular stress, or effective stress, on the granular skeleton. The principle of effective stress (Terzaghi, 1925) relates changes in pore fluid pressure and compression of the aquifer system as

$$\sigma_e = \sigma_T - \rho$$

where effective or intergranular stress (σ_e) is the difference between total stress or geostatic load (σ_T) and the pore-fluid pressure (ρ). Changes in effective stress cause deformation of the aquifer granular skeleton. Aquifer systems consisting primarily of fine-grained sediments, e.g., silt and clay, are significantly more compressible than those primarily composed of coarse-grained sediments, e.g., sand and gravel, and hence experience negligible inelastic compaction (Ireland et al., 1984; Hanson, 1998; Sneed and Galloway, 2000). Groundwater pumping can cause short- or long-term recoverable (elastic) or non-recoverable (inelastic) compaction that reduces aquifer storage capacity (Sneed et al., 2013).

Permanent (irrecoverable) compaction can occur if an aquifer is pumped below its pre-consolidation head (lowest prior pressure; Phillips et al., 2003), resulting in collapse of the skeleton, decreased pore space, and permanent loss of storage capacity. Over-development of aquifers can induce long-term elastic subsidence

that lasts for decades to centuries. Depending on the thickness and the vertical hydraulic diffusivity of the fine-grained strata (aquitards) within an aquifer, the fluid-pressure change within those layers will lag behind the pressure/hydraulic head change from pumping. The pressure gradient between the pumped (usually coarse-grained) strata and the center of the fine-grained strata takes time to re-equalize. In practice, land subsidence can continue for decades or centuries after cessation of groundwater pumping, whatever time is required for balance to be restored between the pore pressure within and outside the fine-grained units (Sneed et al., 2013). The time constant of an aquitard is defined as the time following an instantaneous decrease in stress that is required for 93% of the excess pore pressure to dissipate, i.e., the time at which 93% of the maximum compaction has occurred. The time constant is directly proportional to the inverse of the vertical hydraulic diffusivity and, for a confined aquitard (draining both above and below), to the square of the half-thickness of the layer:

$$\tau = \frac{S'_s \left(\frac{b'}{2}\right)^2}{K'_v}$$

where S'_s is the specific storage of the aquitard, b' is the aquitard thickness, K'_v is the vertical hydraulic conductivity of the aquitard, and S'_s / K'_v is the inverse of the vertical hydraulic diffusivity (Riley, 1969). Ireland et al. (1984) estimated time constants of 5–1350 years for aquifer systems at fifteen sites in the San Joaquin Valley. The scale of groundwater pumping currently underway in many areas makes this a global issue (Alley et al., 2002).

Repeat-pass interferometric SAR has become an invaluable tool for hydrologists to resolve spatially and temporal-varying aquifer properties and model parameters that are impractical to obtain with any other technology. Numerous studies have exploited InSAR imagery to assess land subsidence globally (Figure 17-11). Early research in the United States focused on the deserts and major cities in the Western

U.S. including the Mojave Desert (Galloway et al., 1998; Hoffman et al., 2001), Los Angeles (Bawden, et al., 2001), Las Vegas (Amelung et al.; 1999), and Phoenix (Casu et al., 2005). PSInSAR and related processing approaches allow InSAR to measure subsidence in agriculture and heavily vegetated regions such as New Orleans (Dixon et al., 2006) and the California Central

Valley (Sneed et al., 2013). More than 200 occurrences of land subsidence have been documented throughout the world during the past few years. Globally, InSAR has measured and tracked subsidence in areas across Europe, the Middle East, China, Japan, and Thailand. The extent of the InSAR imagery allows hydrologists to model spatially varied skeletal storage aquifer param-

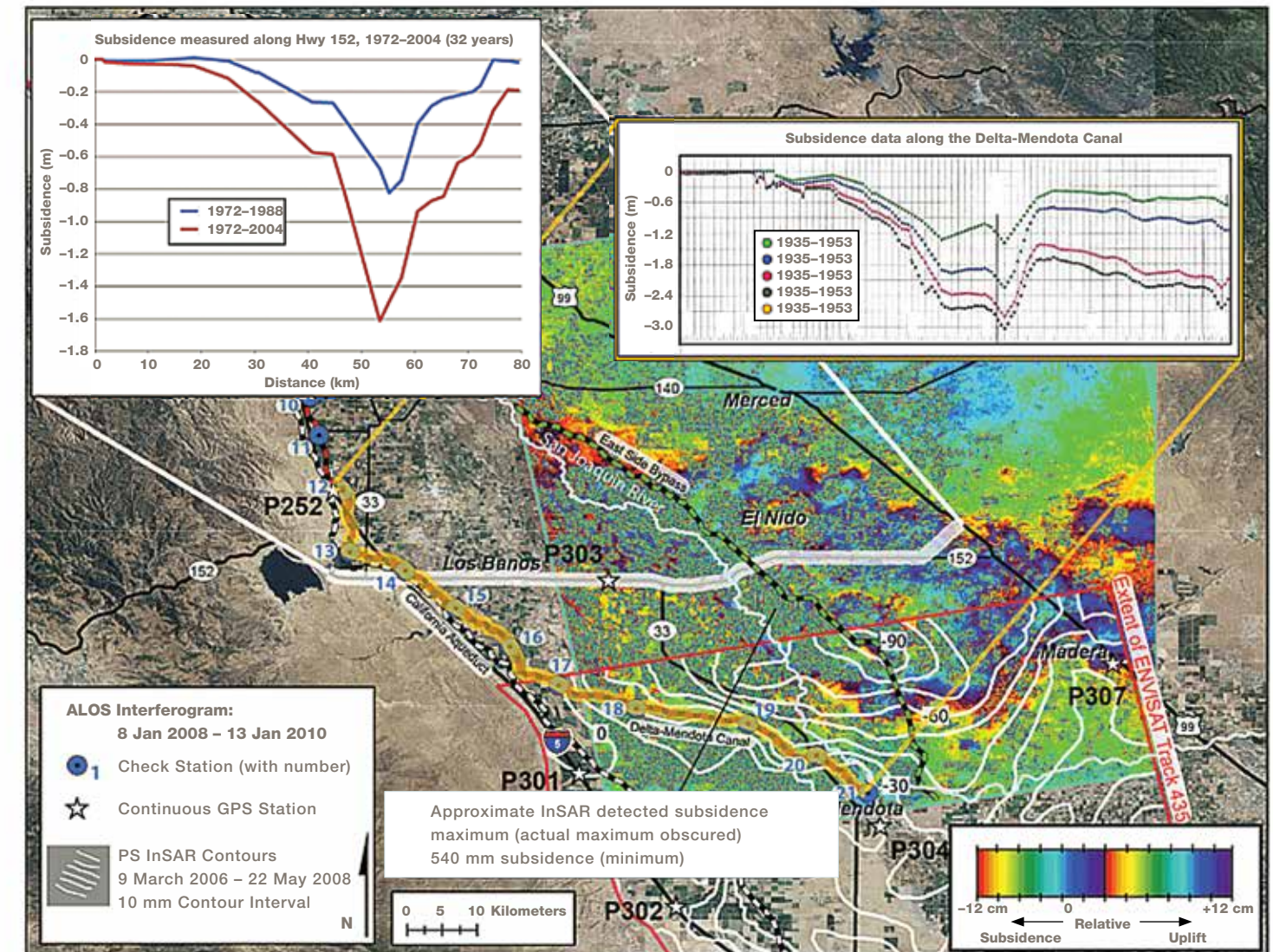


FIGURE 17-11

Subsidence measured with C-Band PSI and L-band InSAR. Ascending and descending ENVISAT PSI subsidence in the San Joaquin Valley, California measured between March 9, 2006 and May 22, 2008 shows a maximum subsidence rate of 30 mm/yr (white contours). ALOS interferogram (color image) shows a large subsidence feature in the region north of where the C-band ENVISAT data acquisition ended (red boundary) (January 2008-January 2010). Insets show subsidence computed from repeat leveling surveys along Highway 152 for 1972-2004 and along the Delta-Mendota Canal for 1935-1996, subsidence computed from GNSS surveys at selected check stations for 1997-2001. Contours show subsidence measured using PS InSAR during March 9, 2006-May 22, 2008 (Sneed et al., 2013).

eters as they change seasonally and annually. Before the advent of InSAR, it was not possible to know the boundary conditions of a pumped aquifer; subsidence gradients are used to understand the margin locations and aquifer interactions.

InSAR's ability to measure the spatial and temporal changes associated with aquifer system compaction/land subsidence provides a direct methodology for determining the hydrologic properties that are unique to each aquifer system, thereby providing fundamental geophysical constraints needed to understand and model the extent, magnitude, and timing of subsidence. Furthermore, water agencies can take advantage of these geophysical and hydrodynamic parameters to optimize water production while minimizing subsidence and mitigating the permanent loss of aquifer storage.

One of the greatest challenges for measuring land subsidence is the loss of interferometric correlation in heavily vegetated regions and in areas with extensive agricultural production. Persistent Scatterer Interferometry (PSI) based DInSAR techniques (e.g., Ferretti et al., 2001; Hooper et al., 2004) have greatly expanded the efficacy of C-band SAR investigations in challenging agricultural areas but are limited to the temporal sampling density of the SAR archive. Sneed et al. (2013) combined PSI C-band and differential L-band InSAR to capture the full extent of the subsidence (Figure 17-11). The PSI approach, shown as contours in the figure, involved a long time series of C-band images, and resolved a maximum subsidence rate of 30 mm/yr. Only 2 ALOS L-band images spanning 2 years were available, from which a subsidence rate of 54 cm in 2 years was derived.

The improved temporal coherence achieved by L-band imagery in agriculture and heavy vegetation regions (see, e.g., Figure 17-12) is one of the key motivations for India's interest in a long-wavelength radar mission, particularly coupled with more densely sampled data to reduce tropospheric noise and other effects. The C-band subsidence map in and around the city of Kolkata in Figure 17-12 shows coherence only in the urbanized areas (Chatterjee et al., 2006; 2007a; 2007b; Gupta et al., 2007). With longer wavelength radar to improve coherence everywhere, however, subsidence measurements can be extended to much broader areas in places like India.

It can be difficult to resolve small-scale surface deformation associated with slip at depth on faults and the migration of magmatic fluids from the large ground-surface deformations caused by anthropogenic fluid withdrawal and injection. However, on their own, the large signals provide information to better understand managed groundwater, hydrocarbon, and geothermal resources, aiding in the characterization and modeling of reservoir dynamics. Pumping of unconfined aquifers can lead to elastic deformation (e.g., seasonal uplift/subsidence) if fluid extraction/recharge is well balanced; but when net fluid production is unbalanced, it can induce long-term surface deformation or permanent (inelastic) deformation. Surface change specific to fluid management is observed as horizontal and vertical deformation signals in GNSS and InSAR time series data that correlate with the production activities. The timing, location and spatial extent of the InSAR signals is key to isolating individual processes particularly in situations where quasi-steady state fluid pumping/injection mimics or masks tectonic/magmatic signal in GPS time series (Figure 17-13).

FIGURE 17-12

Kolkata city land subsidence. Deformation maps showing average rate of land subsidence in Kolkata city obtained from differential interferogram of ERS-1 data. The rate of land subsidence was found to be 6.55 mm/year (Chatterjee et al., 2006).

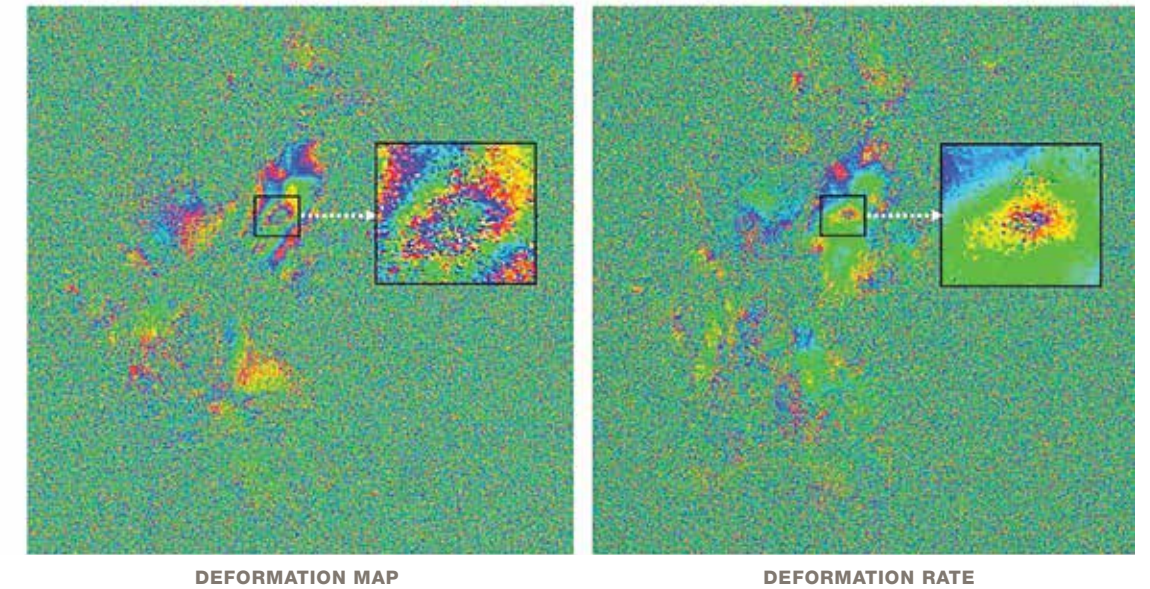
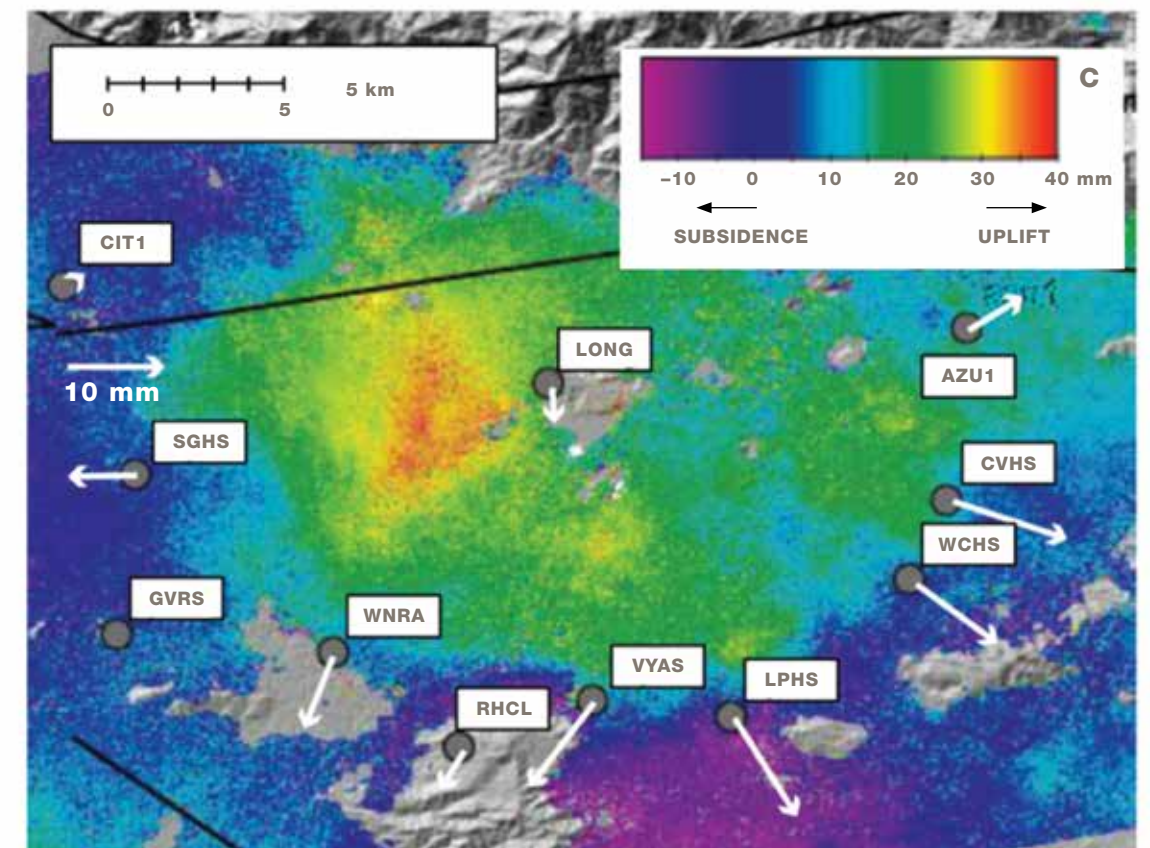


FIGURE 17-13

Example of non-tectonic deformation. Unwrapped ENVISAT interferogram (January 2005 to July 2005) of the San Gabriel Valley (CA) showing surface deformation over an area 40 x 40 km associated with natural aquifer recharge during a record rainfall during the winter of 2005. The land surface uplifted 40 mm pushing GNSS sites on the margins of the basin radially outward in excess of 10 mm (labeled vectors). This groundwater hydrology transient was initially interpreted as an aseismic earthquake in an active tectonic environment; combined InSAR imagery and GNSS time-series along with water levels were needed to resolve its genesis (King et al., 2007)



NISAR imagery can be used to help isolate, model, and remove the effects of fluid extraction on tectonic/volcanic GNSS time series data. Future GNSS networks can be optimized to avoid anthropogenic and natural surface deformation associated with the pumping of fluids and natural groundwater recharge processes. GNSS sites placed on the margins of active aquifer/reservoir will have horizontal motion that can mask and at times mimic the tectonic signal (Bawden et al., 2001). GNSS sites placed near the center of the subsidence will have high vertical signal with nominal horizontal displacements therefore improving the ability to resolve tectonic deformation in an active groundwater basin.

17.1.6 Glacial Isostatic Adjustment

In areas of present or past glaciation, surface deformation can be caused by a solid earth response to current glacier advance or retreat as well as a delayed response to changes centuries or millennia ago. The magnitude and spatial patterns of ground deformation can be used to infer changes in the ice load and the rheology of Earth's crust and upper mantle. InSAR has been used to measure the elastic response of ice mass loss in Iceland in recent decades (Zhao et al., 2014) and NISAR has the potential to make similar measurements around most of the current ice-covered areas. Furthermore, frequent L-band (high coherence) measurements with good orbital baseline control provided by NISAR will open new possibilities to measure deformation caused by ice load changes since the Little Ice Age and the Last Glacial Maximum (called Glacial Isostatic Adjustment, GIA) that can better constrain both the ice load history and the viscosity beneath areas like Canada, Alaska, Patagonia and Scandinavia. Deformation measurements in some of these areas have been made by GNSS, but NISAR will add important spatial resolution. For example, NISAR observations can test some of the predictions of GIA made by GRACE satellite gravity observations, such as large uplift rates in northern Canada (e.g., Paulson et al., 2007) that should be detectable with NISAR.

17.2 ECOSYSTEMS

The 2007 Decadal Survey identified that a key goal for ecosystems sciences is to characterize the effects of changing climate and land use on the terrestrial carbon cycle, atmospheric CO₂ levels, and ecosystem services. Human induced disturbances have dramatically altered the terrestrial ecosystems directly by widespread land use changes, converting old-growth and carbon-rich forests into permanent croplands and urban landscapes. Disturbances have also led to extensive losses of wetlands of up to 50 percent and increased the probability of natural disturbances such as fire, droughts, hurricanes, and storms due to fundamental shifts in the climate and atmospheric CO₂ concentrations (Foley et al., 2005; Dale et al., 2001; IPCC, 2007). In recent years, the critical ecosystem services provided by mangroves have been particularly hard hit by warming ocean temperatures, rising sea levels, and population pressures. Shifts in vegetation are occurring, especially in high altitude regions where alpine tree lines are advancing.

While these changes have important implications for the global carbon cycle and its climate feedback, there remains large uncertainty in the global extent and magnitude of these changes in the terrestrial component. The Decadal Survey highlights this shortcoming by stating that, "there are no adequate spatially resolved estimates of the planet's biomass and primary production, and it is not known how they are changing and interacting with climate variability and change."

Dynamics of global vegetation with strong impacts on global carbon cycle are identified as changes of woody biomass from deforestation, degradation, and regrowth; changes in the extent and biomass production of global crops; and the extent and inundation cycling of global wetlands (NRC, 2007). Quantifying these changes is critical for understanding, predicting, and ultimately managing the consequences of global climate change. It is the consensus of the scientific community that systematic observations from space with the aim of monitoring ecosystem structure and dynamics are a

priority to significantly reduce large remaining uncertainties in global carbon cycle and climate prediction and ecosystem models (CEOS, 2014). Therefore, a spaceborne mission meant to address the needs of the link between ecosystems and the climate will have the following scientific objectives ranked amongst the highest priority:

- Quantify and evaluate changes in Earth's carbon cycle and ecosystems and consequences for ecosystem sustainability and services.
- Determine effects of changes in climate and land use on the carbon cycle, agricultural systems and biodiversity.
- Investigate management opportunities for minimizing disruption in the carbon cycle (ISRO).
- Determine the changes in carbon storage and uptake resulting from disturbance and subsequent regrowth of woody vegetation.
- Determine the area and crop aboveground biomass of rapidly changing agricultural systems.
- Determine the extent of wetlands and characterize the dynamics of flooded areas.
- Characterize freeze/thaw state, surface deformation, and permafrost degradation.
- Explore the effects of ecosystem structure and its dynamics on biodiversity and habitat.

17.2.1 Biomass

In May 2013, atmospheric CO₂ concentrations passed 400 ppm, indicating an alarming rise of more than 30% over the past 50 years, caused by fossil fuel emissions (~75%) and land use change (~25%). There is strong evidence that during this period the terrestrial biosphere has acted as a net carbon sink, removing from the atmosphere approximately one third of CO₂ emitted from fossil fuel combustions (Canadell et al., 2007). However, the status, dynamics, and evolution of the terrestrial biosphere are the least understood and most uncertain element of the carbon cycle (IPCC, 2007). This uncertainty spans a wide range of temporal and

spatial scales. The IPCC has identified interannual variability of atmospheric CO₂ being strongly controlled by the terrestrial biosphere, while the coupling between the terrestrial biosphere and climate was identified as one of the major areas of uncertainty in predicting climate change over decadal to century time scales. Spatially, large uncertainties exist in the distribution of carbon stocks and exchanges-in estimates of carbon emissions from forest disturbance and the uptake through forest growth.

A fundamental parameter characterizing the spatial distribution of carbon in the biosphere is biomass, which is the amount of living organic matter in a given space, usually measured as mass or mass per unit area, with half of all dry biomass being carbon (Figure 17-14). Therefore, biomass represents a basic accounting unit for terrestrial carbon stock, and its temporal changes from disturbance and recovery play a major role in controlling the biosphere interaction with climate. Estimates of the amount of biomass in the world's terrestrial ecosystems range from 385 to 650 PgC (Houghton et al., 2009). Forests contain more than 80 percent of the aboveground carbon stock and are thus a dominant component of the global carbon cycle (Houghton, 2005b). Because of its importance for climate, forest biomass is identified by the United Nations Framework Convention on Climate Change (UNFCCC) as an essential climate variable needed to reduce the uncertainties in our knowledge of the climate system (Global Climate Observing System GCOS, 2010).

Our current knowledge of the distribution and amount of terrestrial biomass is based almost entirely on ground measurements over an extremely small, and possibly biased sample, with many regions still unmeasured. A global-detailed map of aboveground woody biomass density will halve the uncertainty of estimated carbon emissions from land use change (Houghton et al., 2009; Saatchi et al., 2013) and will increase our understanding of the carbon cycle, including better information on the magnitude, location, and mechanisms responsible for terrestrial sources and sinks of carbon. Biomass density

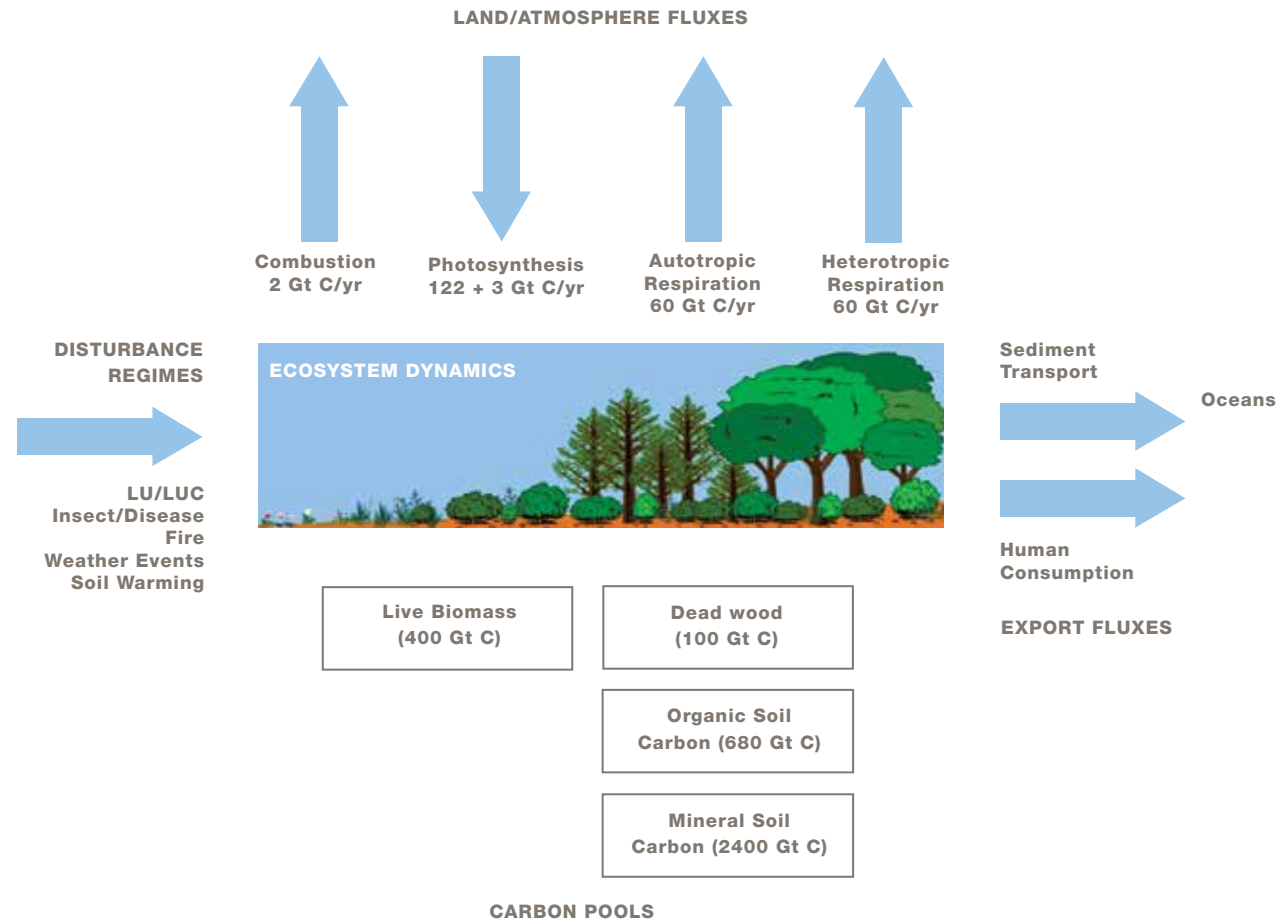


FIGURE 17-14 Major elements of the terrestrial carbon cycle: (1) Disturbance regimes; (2) Land/Atmosphere fluxes; (3) Ecosystem dynamics; (4) Terrestrial carbon pools, and; (5) Export fluxes. NISAR makes key observations in each element. (CEOS, 2014).

varies spatially and temporally. Living biomass ranges over two to three orders of magnitude, from less than 5 MgC/ha in treeless grasslands, croplands, and deserts to more than 300 MgC/ha in some tropical forests and forests in the Pacific Northwest of North America.

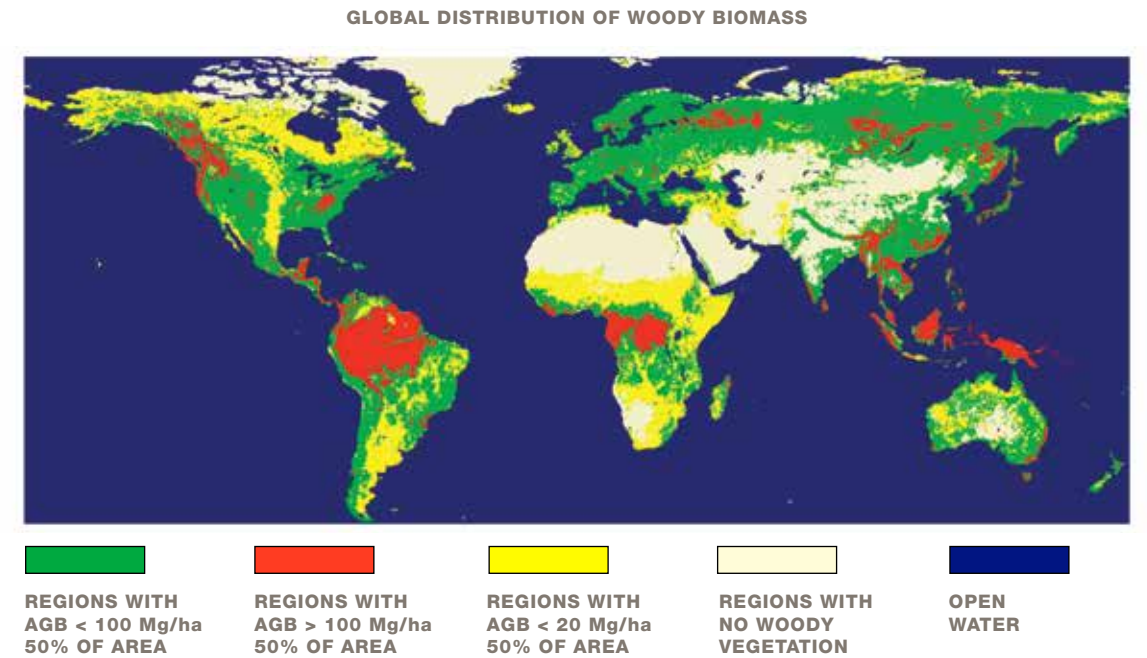
Biomass density also varies considerably within ecosystem types. This variability results, in part, from limitations of the environment (for example, soil nutrients or the seasonal distribution of precipitation and temperature), and in part from disturbance and recovery. The aboveground living biomass density of a recently burned forest may be nearly zero, but it

increases as the forest recovers (Figure 17-15). Forests do not accumulate biomass indefinitely, however, because stand-replacing disturbances keep turning old forests into young ones. However, most forest stands are in the process of recovering from natural or human-induced disturbances and, thus, are accumulating carbon, albeit generally at lower rates as they age.

Forests in temperate and boreal regions have low biomass density (< 100 Mg/ha) but are extensive in area and are subject to climate change and variability causing widespread disturbance (e.g., fire, hurricanes, droughts), and human land use change (Bonan, 2008).

FIGURE 17-15

Global distribution of woody biomass. Forest biomass density predicted from a combination of inventory data and available statistics (Kinderman, et al., 2008). Percentages refer to the percent of area for that class of biomass in each grid cell.



These forests are also considered a major carbon sink from long periods of management (Woodall et al, 2010) and increasing length of growing season from climate change (Myneni et al., 2001). Other low biomass density regions are savanna woodlands and dry forests, distributed globally in temperate and tropical regions. These regions cover more than 50 percent of the area of forest cover globally and are considered highly heterogeneous spatially and dynamic temporally.

17.2.2 Biomass Disturbance and Recovery

Perhaps more important than biomass distribution to the global carbon cycle, is the quantification of biomass change and its associated carbon flux (Houghton et al., 2009). The magnitude of the uncertainty in the global carbon flux is particularly large in the tropics. Recent calculations estimate a net positive flux from the tropics of between 0.84 and 2.15 PgC per year (Harris et al., 2012; Baccini et al., 2012; Pan et al., 2011; Le Quéré et al., 2017). In the context of global climate mitigation approaches (UNFCC, 2006) and the relevant calculations of national carbon emissions, the difference between these two estimates (1.3 PgC per year) lies between the total carbon emissions of the

United States (1.5 PgC per year) and China (2.5 PgC per year), the top two carbon-emitting nations (Peters et al., 2012; Global Carbon Project, 2012).

The location of the land carbon sinks and sources are unknown, as well as the reasons for their annual swings in strength that on occasion are as much as 100% (Canadell et al. 2007). To what degree are these large shifts a result of climate variability, or disturbance? Even where estimates of mean forest biomass are known with confidence, as in most developed countries, the spatial distribution of biomass is not, and the possibility that deforestation occurs in forests with biomass systematically different from the mean, suggests that this potential bias may also contribute to errors in flux estimates (Houghton et al., 2001; Houghton, 2005). To address the uncertainty in carbon fluxes and the terrestrial carbon sinks and sources, a series of accurate, annual global maps of disturbance and recovery will significantly improve estimates of emissions to the atmosphere and quantification of the large proportion of the residual terrestrial sink attributable to biomass recovery from such disturbances. The spatial and temporal distribution of disturbance

events, many of which occur at one hectare or below, must be observed at fine spatial resolution. Examples of such events include clear cutting, selective logging, fire, hurricanes, floods, disease and insect infestation. Figure 17-16 shows a typical landscape mosaic of disturbance and recovery following disturbance in the Amazon basin and the emissions calculated from the use of forest biomass maps (Saatchi et al., 2007; Harris et al., 2012). By developing an annual disturbance and recovery map at the same spatial resolution of the biomass map, we can radically improve the estimates of emissions and removals (Houghton et al., 2009).

Because of various environmental and climate variables, forest ecosystems are heterogeneous in their cover, structure, and biomass distribution. The heterogeneity of ecosystems occurs at different scales and has been studied extensively in ecological theory and landscape dynamics. These studies recommend detection and classification of disturbance and recovery events at one-hectare spatial scales to reduce the uncertainty of carbon fluxes (Hurt et al., 2010). NISAR will provide a means to reliably generate annual disturbance and recovery estimates at hectare-scale resolution for the duration of the mission and thus help reduce the uncertainties in carbon emissions and sequestration estimates.

17.2.3 Agricultural Monitoring

Since the beginning of the agricultural revolution and followed by the industrial revolution, agriculture has been a driver and early adopter of technology for the efficient production of crops. As populations have grown and moved into urban centers, governmental organization have had an interest in food security and in assessing their availability and impact on world markets.

Crop assessment depends on multiple sources of data that are used for determining crop condition and area, often relying on inputs from the previous year's production. The various sources of inputs include

satellite-based observations, weather data, ground information and economic reporting. All of these are used to inform government and commodities markets that direct the allocation of resources and predict nutrient availability.

Identified in the 2010 GEO Carbon Strategy is the monitoring and measurement of agriculture biomass and areal extent, which are important components of the global carbon budget and in the understanding of the effects of policy and climate on land management and crop yields. In the two-decade period from 1990-2010, large-scale clearing and conversion of forests to agriculture has resulted in an average flux of 1.3 to 1.6 GtC/y since the 1990's (Pan et al., 2011). While the gross distribution of growing regions worldwide is generally well known (Figure 17-17), it is not at resolutions required for carbon assessment and for generating reliable, accurate, timely and sustained crop monitoring information and yield forecasts. The role of agriculture in the GEO System of Systems (GEOSS) has given rise to the Joint Experiment for Crop Assessment and Monitoring initiative (JECAM), created by GEO Agricultural Monitoring community, which has identified high-resolution SAR and optical remote sensing capabilities as the necessary sensor platforms for crop monitoring and agricultural risk management (GEOSS Tasks AG0703a, b; 2005).

With biomass levels in agriculture crops typically less than 50 t/ha, SAR backscatter observations provide an observational approach for the estimation of crop biomass (Figure 17-18). By making short-revisit observations throughout the growing season, additional information is obtained that will help refine these biomass estimates as well as provide timely and sustained crop monitoring information that will inform yield forecasts and help evaluate agriculture management practices in response to weather and governmental policy initiatives.

Because crop yield and resource planning are dependent, in part, on soil moisture, an L-band SAR can play

FIGURE 17-16

Spatially explicit information on forest cover change and disturbance and aboveground biomass map from NISAR will significantly improve the estimates of carbon emissions from land use change to the atmosphere. Top panel shows annual deforestation of tropical forests at 1 ha grid cell simulated from Landsat based forest cover change data (Hansen et al., 2013). Bottom panel shows how by having annual biomass map of tropical forests of the Amazon basin (left image: resampled to 100 m from Saatchi et al., 2007) at the same resolution as the deforestation map can provide improved estimates of gross emissions from deforestation compared to the use of a regional mean biomass value (Harris et al., 2012).

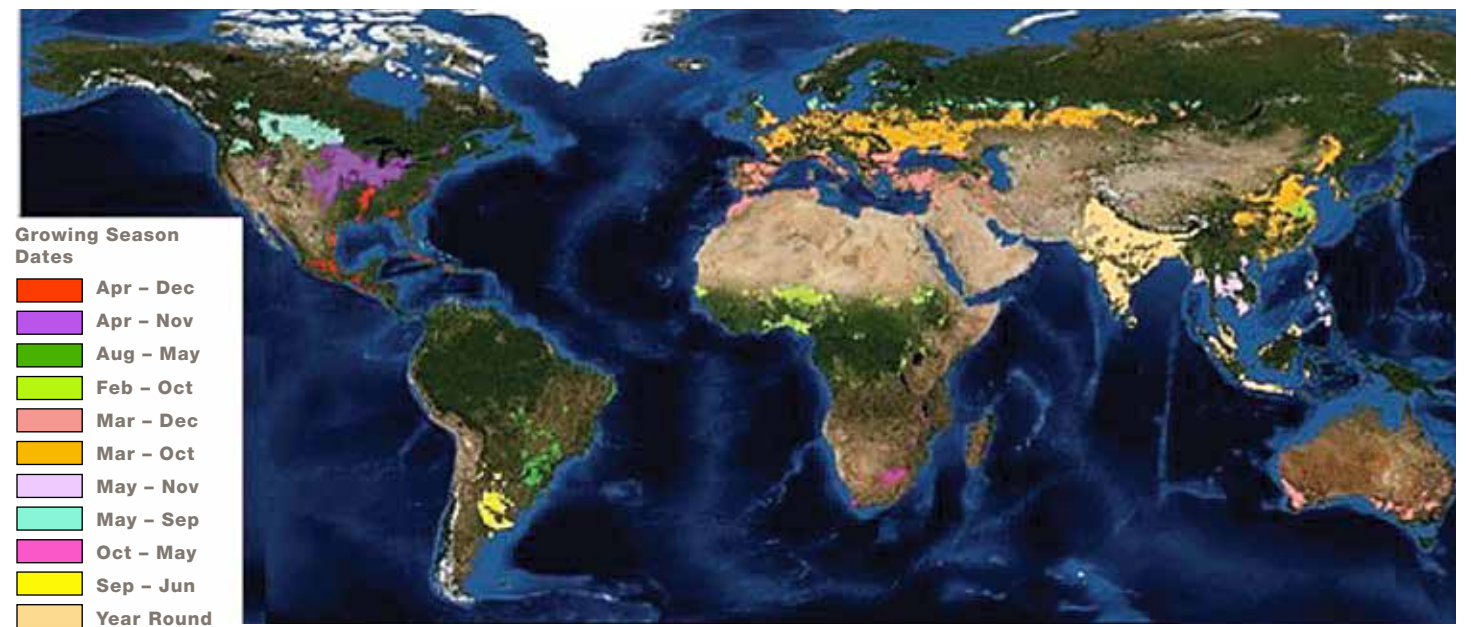
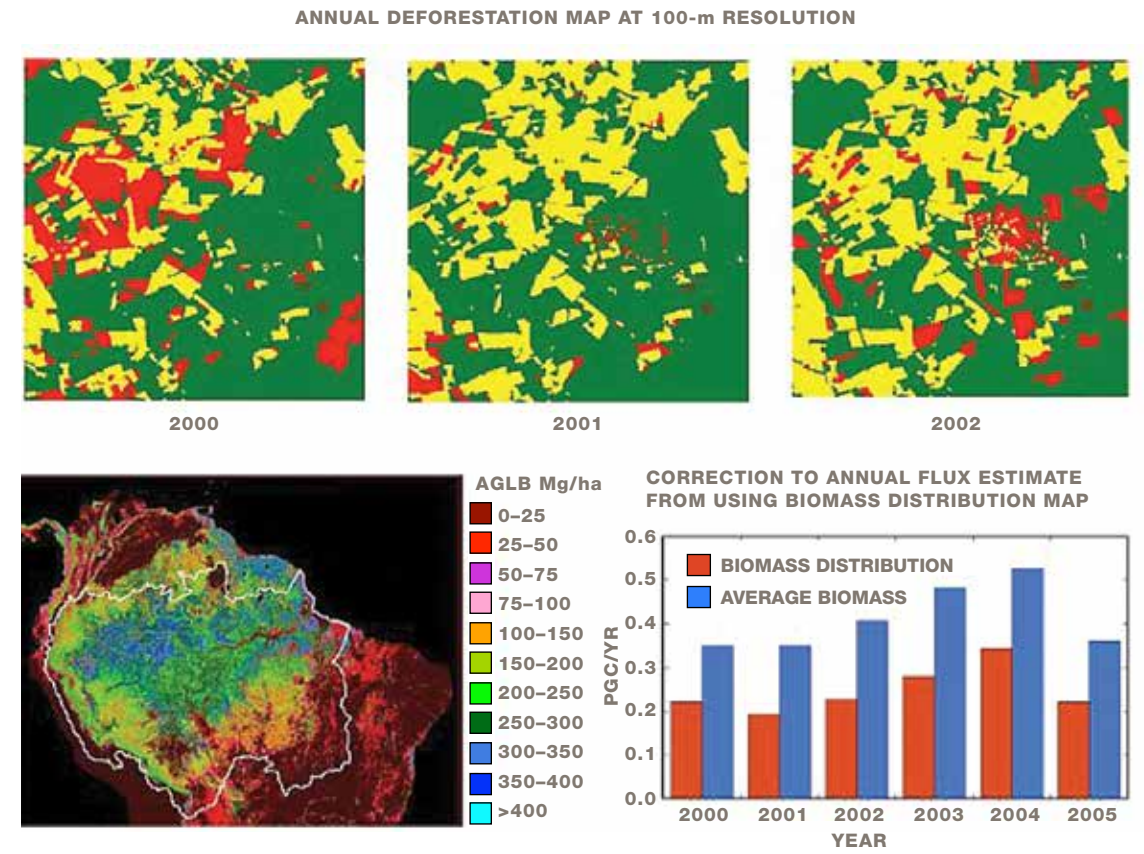
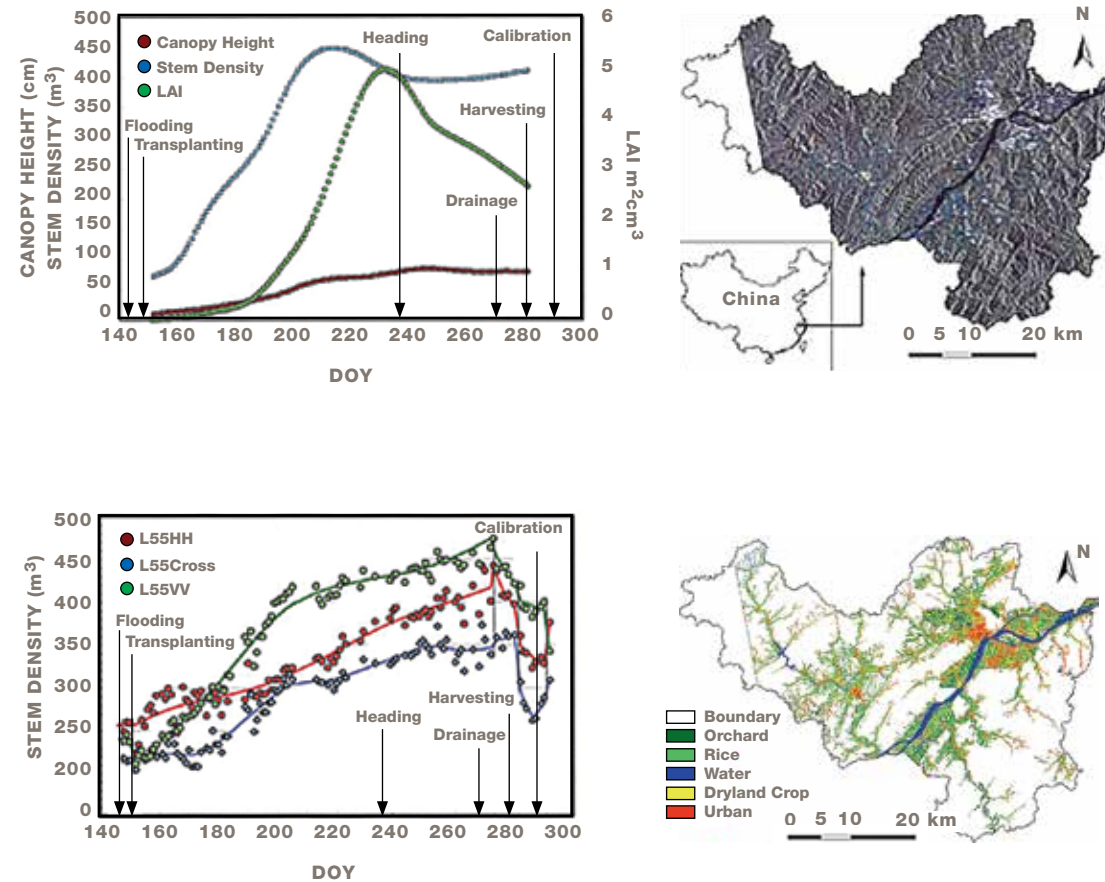


FIGURE 17-17

Global image of agriculture crop areas and growing seasons. Crop types used for the assessment are based on basic grains and economically significant crops of world agriculture (e.g., rice, wheat, soybean, maize, etc.). Data source: earthstat.org.

FIGURE 17-18

Examples of agricultural change. Seasonal change of plant variables determined by destructive sampling on the weekly time-cycle and interpolated on a daily time series (left). Time course change of microwave backscattering coefficients at all combinations of polarization and incident angle for the L-band over capturing the crop yield and biomass change. (bottom left; Inoue et al., 2002) to after China. The L-band ALOS PALSAR composite of three dates over Zhejiang Province in southeast China (top) and the crop classification from multi-temporal PALSAR imagery separating dry and wet crops from forests and urban areas (bottom right; Zhang et al., 2014).



an important role in the planning and projecting of agricultural output. The longer wavelengths of NISAR's L- and S-band systems compared to that of C- and X-band systems (e.g., Radarsat 2, Sentinel-1 and TerraSAR-X) make it uniquely capable of assessing this component of plant growth.

The timeliness of observation for agriculture applications is also an important component. Because agricultural applications are a fundamental part of NISAR's observing strategy, and NISAR's polarimetric capability, observations collected by the sensor in a consistent configuration will be collected throughout the growing season and hence provide a resource that will be of immediate use to global agricultural monitoring efforts (e.g., GEOGLAM). Furthermore, NISAR will provide a

base set of observations that will be combined with yield measures, weather records, and other remote sensing resources to create predictive models that can be used from one season to the next.

17.2.4 Wetlands and Inundation

Global wetlands and their hydrologic dynamics are of major concern with respect to their impact on climate change. Wetlands are characterized by waterlogged soils and distinctive communities of plant and animal species that have evolved and adapted to the constant presence of water. Due to this high level of water saturation as well as warming weather in low and mid-latitudes and accelerated freeze/thaw cycles in high latitudes, wetlands are one of the most significant natural sources of increased atmospheric methane.

Emissions from wetlands contribute about 100–230 Tg/yr (Matthews, 2000) of methane to the atmosphere and represent 20–45% of total emissions (~500 Tg/yr). Thus, changes in wetland emissions can significantly impact future methane levels. Methane increases have contributed about 0.7 W/m² to global radiative forcing since preindustrial times (0.5 W/m² directly, plus an additional roughly one half the forcing from CO₂). This makes methane emissions the second most important greenhouse gas forcing (Hansen et al., 2000; Ramaswamy et al., 2001). Therefore, controlling methane emissions could mitigate global warming as much as controlling CO₂ over the next century (Kheshgi et al., 1999), and might be a more practical way to reduce near-term climate forcing, owing to methane's shorter lifetime and the collateral economic benefits of increased methane capture (Hansen et al., 2000). Projections of future emissions are typically based only on potential changes in anthropogenic emissions. It is possible, however, that natural emissions could also change substantially.

Globally, wetlands are also a critical habitat of numerous plants and animal species and play a major role in maintaining the biodiversity of the planet. Furthermore, natural wetlands and managed rice paddies are a major source of food and fiber. These regions cover 5.7 x 10⁶ km² and 1.3 x 10⁶ km² with an estimated net primary production of 4–9 x 10¹⁵ and 1.4 x 10¹⁵ g dry matter per year, respectively. The RAMSAR convention on wetlands has emphasized the role of remote sensing technology in obtaining inventory information and monitoring the status and activity of wetlands globally (Rosenqvist et al., 2007). A key challenge facing wetland researchers and managers is in the development of techniques for assessing and monitoring the condition of wetlands (Sahagian and Melack, 1996; Darras et al., 1998). Parameters that have been used for these purposes include the composition, location, areal extent, water status and productivity of wetlands over time (see reviews in Finlayson et al., (1999)). For wetland inventory, techniques are sought that can

reliably distinguish between wet and dry land areas (regardless of vegetation cover) and the degree of soil saturation (Sahagian et al, 1997). In addition, attributes for which data can be collected through an inventory and later used to determine when change has occurred are particularly valuable as wetlands are subject both to natural change and, increasingly, to destruction and degradation associated with human activities.

Many wetlands are subject to seasonal or periodic flooding, i.e., inundation, and knowledge of the spatial and temporal characteristics of flooding patterns is crucial to understand wetland biochemical processes, including methane production. Furthermore, river inundation represents a dominant mechanism in the lateral transport of sediments to the ocean basins, and thus is a critical factor controlling the export flux of carbon from terrestrial ecosystems (Figure 17-19).

17.3 CRYOSPHERE

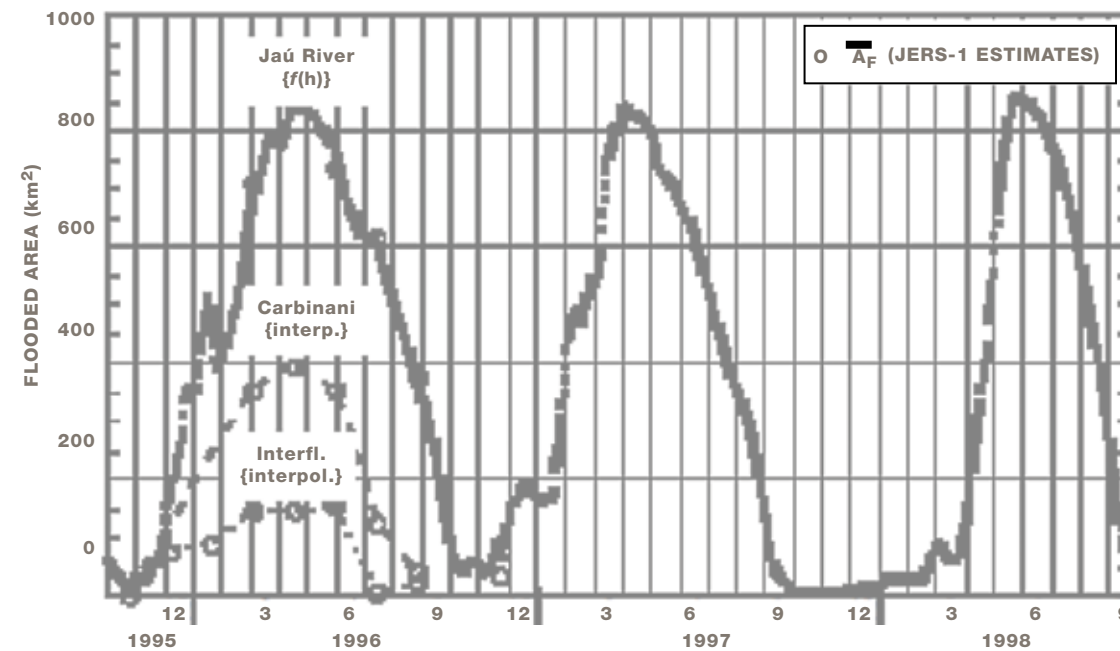
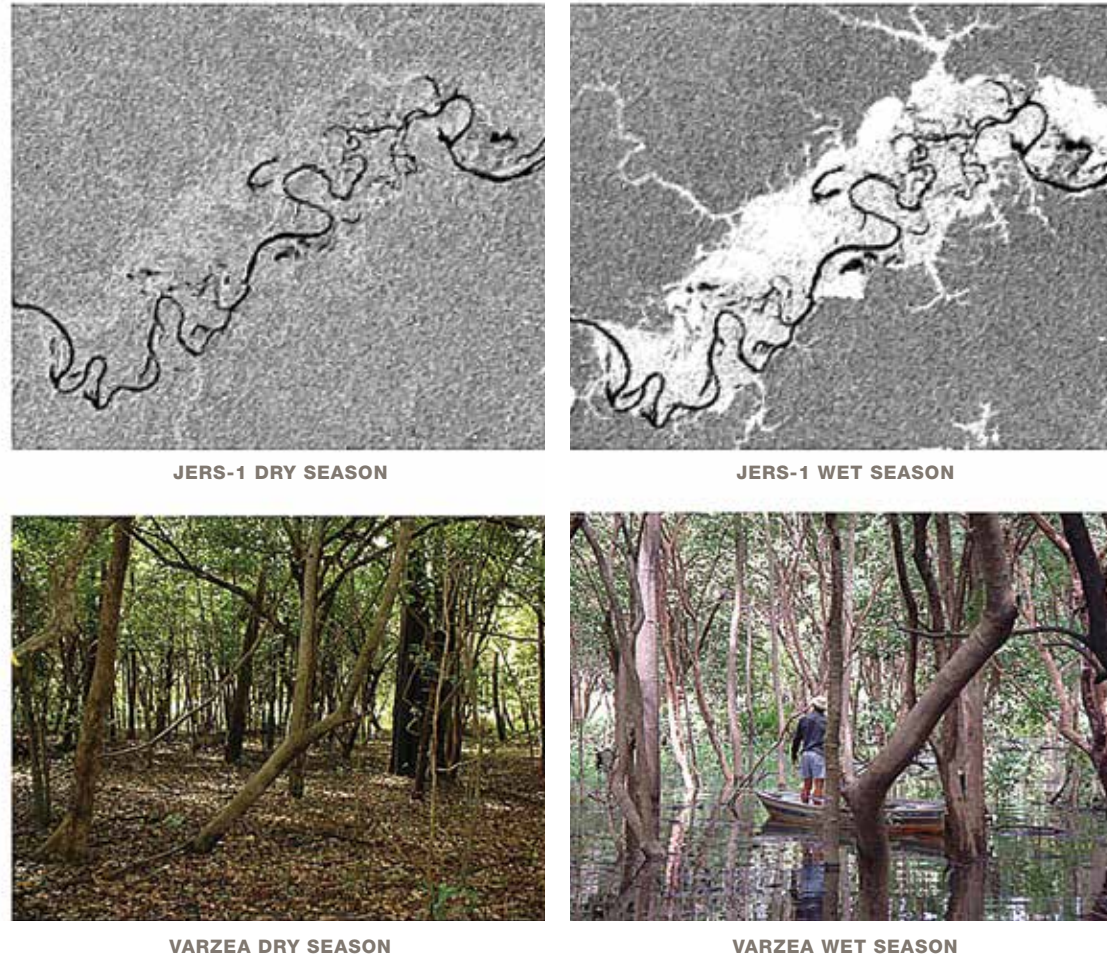
The cryosphere represents Earth's ice and snow-covered areas. In particular, NISAR science objectives will primarily focus on the ice sheets, glaciers, sea ice, and permafrost. Although these are the primary focus, the mission will ultimately enhance science and application studies aimed at many other elements of cryosphere such as snow cover and lake and river ice.

The Decadal Survey articulated several overarching cryosphere-related objectives. Of these, NISAR will contribute to addressing the following scientific objectives:

- Characterize and understand the processes that determine ice sheet and glacier sensitivity to climate change.
- Incorporate ice sheet and glacier displacement information into coupled ice-sheet/climate models to understand the contribution of ice sheets to sea level change.
- Understand the interaction between sea ice and climate.

FIGURE 17-19

L-band HH sensitivity in wetlands. Sensitivity of L-band radar backscatter at HH polarization for mapping the area and the cycle of inundation of the wetlands of the Amazon basin. (Rosenqvist et al., 2003).



- Characterize the short-term interactions between the changing polar atmosphere and changes in sea ice, snow extent, and surface melting.
- Characterize freeze/thaw state, surface deformation, and permafrost degradation.

17.3.1 Ice Sheets

Spaceborne InSAR and altimetry observations have already made major changes to our perception of how ice sheets evolve over time (Alley et al., 2005; Bamber et al., 2007; Joughin and Alley, 2011), overturning the conventional wisdom that ice sheets respond sluggishly to climate change at centennial to millennial time scales (e.g., Paterson, 1994). Numerous observations have shown that large Greenlandic and Antarctic glaciers and ice streams can vary their flow speed dramatically over periods of seconds to years (e.g., Bindshadler et al., 2003; Joughin et al., 2004a; Rignot and Kanagaratnam, 2006; Rignot, 2011c). It was this unanticipated variability that prompted the Intergovernmental Panel on Climate Change (IPCC, 2007) to conclude:

Dynamical processes related to ice flow not included in current models but suggested by recent observations could increase the vulnerability of the ice sheets to warming, increasing future sea level rise. Understanding of these processes is limited and there is no consensus on their magnitude.

Thus, NISAR's major ice sheet goals are to provide data critically needed to remove this gap in our understanding of the fundamental processes that control ice-sheet flow. This knowledge is required to reliably model ice-sheet response to climate change and to project the resulting contribution to sea level change over the coming decades to centuries.

Because of the highly variable dynamics of outlet glaciers and ice streams, recent observations provide only isolated snapshots of ice-sheet velocity (Figure 17-20; Howat et al., 2007; Joughin et al., 2004a; Rignot and Kanagaratnam, 2006; Rignot et al., 2011a). Space-

borne altimeters designed for mapping large-scale ice changes (e.g., ICESAT-II), under-sample many of the narrow fast-moving glaciers with large thinning rates—up to 100 m/yr-(Howat et al., 2008). Therefore, special care must be taken in how such observations are evaluated, particularly when extrapolating to the future, since short-term spikes could yield erroneous long-term trends. In addition to indicating a trend of sustained speedup, recent results are significant in that they show flow speed and mass balance can fluctuate rapidly and unpredictably (Moon et al., 2012). While existing sensors have revealed major changes, these observations, cobbled together from a variety of sensors, are far from systematic. Prior to 2015, there were no systematic observations by existing or future sensors with which to characterize ice-sheet flow variability and with which to develop the required modeling capability to accurately project sea level trends. While such observations have begun with the launch of the Copernicus Sentinel 1A/B SARs and the USGS/NASA Landsat 8 optical instrument, existing coverage does not meet community needs in terms of resolution, coverage, and accuracy. Therefore, to accurately determine ice discharge variability, to gain a firm understanding of the dynamics that drive mass balance, and to avoid aliasing these rapidly changing variables, NISAR will acquire annual-to-sub-annual observations of outlet-glacier and ice-stream variability.

Ice-sheet velocity and surface elevation are two of the most important observables for studying ice dynamics. While observations from space are largely limited to the ice sheet's surface, when used in conjunction with ice flow models, such data can be inverted to determine basal and englacial properties (Joughin et al., 2004b; Larour et al., 2005; MacAyeal, 1993; Morlighem et al., 2013). In particular, ice-flow velocity and accurate ice topography (ICESAT-II) can constrain model inversions for basal shear stress. Observations of changes in ice-sheet geometry and the associated response also provide important information. For example, inversions such as shown in Figure 17-21 provide the magnitude of the shear stress, but not the form of the sliding law.

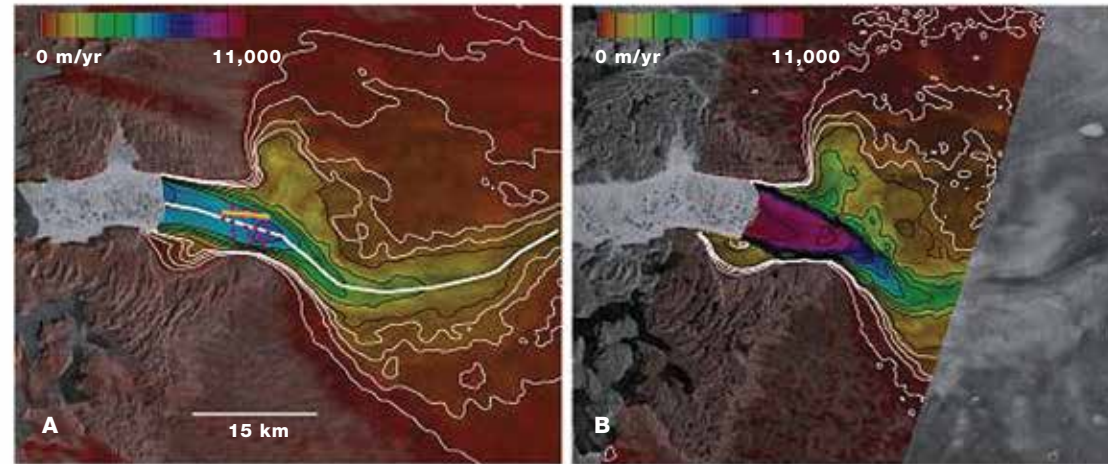


FIGURE 17-20 Ice flow velocity at Jakobshavn Isbrae. Ice flow velocity determined from speckle-tracking as color over SAR amplitude imagery showing the rapid speed up of Jakobshavn Isbrae from a) February 1992 (ERS-1) to b) October 2000 (RADARSAT). In addition to color, speed is contoured with thin black lines at 1000-m/yr intervals and with thin white lines at 200, 400, 600, and 800 m/yr (Joughin et al., 2004a). Over the last decade, glaciers in Greenland have sped up on average by more than 30% (Rignot and Kanagaratnam, 2006; Moon et al., 2012). NISAR will provide continuous observations of such speedup to provide a better understanding of the processes governing such change.

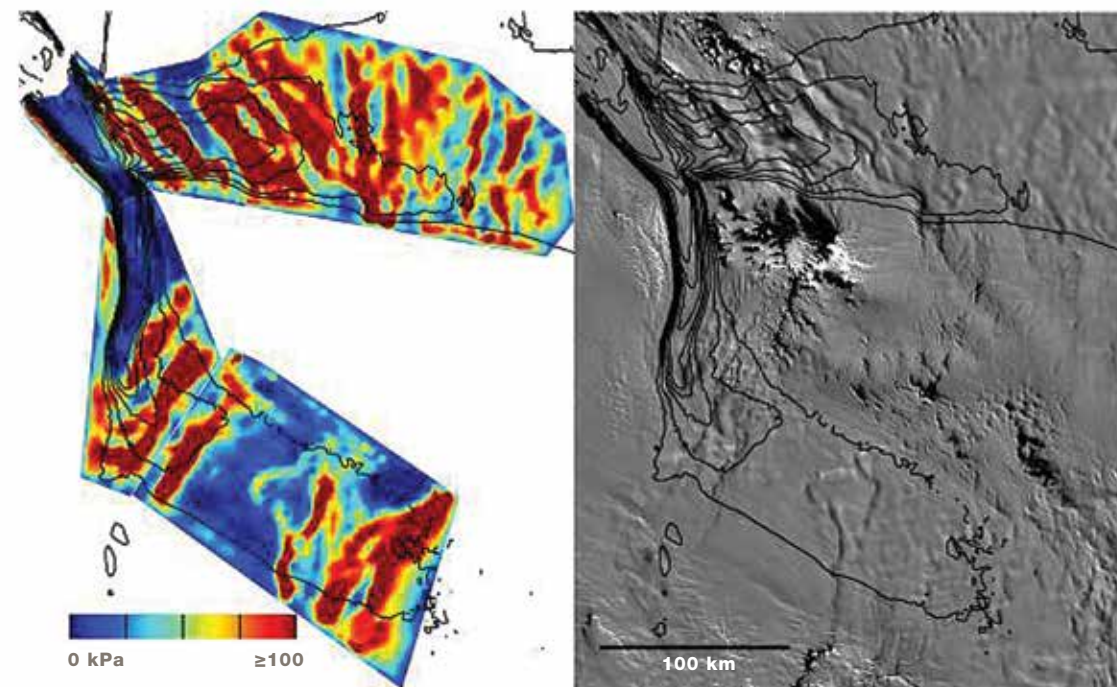


FIGURE 17-21 Basal shear stress estimate for Foundation Ice Stream (left) and corresponding MOA image (right). Flow speed is shown with 100-m/yr contours (black lines).

Observations of the spatio-temporal response to an event such as the loss of ice-shelf buttressing can be used to derive parameters such as the exponent of a power-sliding law or may indicate another type of sliding law is needed (e.g., plastic) (Joughin et al., 2010b). Sustained and frequent sampling of rapidly changing areas by NISAR will provide the velocity observations necessary for such studies in place of the scattershot observations current systems provide, with ICESAT-II providing complementary elevation data.

Antarctica has several large floating ice shelves that extend over the ocean from the grounded ice sheet. In contact with the ocean and at low elevation, these elements of the coupled ice-sheet/ice-shelf system are the most at risk in a warming climate (Rignot et al., 2013). While the loss of floating ice has no direct impact on sea level, ice shelves buttress the flow of inland ice and a reduction of this buttressing as ice shelves have thinned or disintegrated is believed to be responsible for the majority current mass loss in Antarctica (Payne et al., 2004; Rignot et al., 2004; Scambos et al., 2004; Joughin et al., 2012). Critical to studying ice shelves is accurate knowledge of velocity and thickness, which determine the mass flux distribution, the horizontal divergence of which can be used to infer basal melt rates (Jenkins and Doake, 1991; Joughin and Padman, 2003; Rignot and Jacobs, 2002). Unlike sparse spatial and temporal sampling from other missions, for the first time NISAR will provide comprehensive ice-shelf velocity data. Similarly, ICESAT-II will provide comprehensive measurements of ice shelf elevation, which can be used to determine thickness by assuming hydrostatic equilibrium. Together, these data will provide the required observations to derive time series of ice-shelf melting around Antarctica and areas of Greenland where ice shelves still exist. These observations of ice flow on floating ice will serve multiple purposes. First, along with observations of velocity for the grounded ice-sheet periphery at high temporal resolution, NISAR will provide an advanced warning system for rapid shifts in ice flow and the resulting contributions to sea level rise. Second, these observations will provide critical constraints to

ocean models at the ice-ocean boundary, which are needed to evaluate the skill of these models, to improve the models through massive data assimilation, and to reduce uncertainties of sea level rise projections.

17.3.2 Glaciers and Mountain Snow

Glaciers and snow-covered regions are important for many applications such as melt runoff, hydropower stations and long-term climatic change studies. Because they are often cloud-covered, microwave remote sensing is particularly useful for studying these areas due to its all-weather capability and ability to image through darkness. Radar backscatter is influenced by material properties like surface roughness and dielectric constant and can therefore offer considerable information in relatively featureless snow-covered terrain. The potential of Synthetic Aperture Radar (SAR) imagery for monitoring of snow cover was discussed as early as in 1980 (Goodison et al., 1981). The attenuation length of microwave radiation in cold dry snow is large and this kind of snow is transparent and therefore invisible to radar (Rott and Davis, 1993) unless the snow pack is very deep or at radar frequencies above about 10 GHz (i.e., a factor of 5-10 higher than NISAR). However, when the liquid water content of snow exceeds about 1 percent, the attenuation length is reduced to a few centimeters, and the radar backscatter is usually dominated by surface scattering (Ulaby et al., 1984). The question of whether such snow can be discriminated from snow-free terrain depends on the geometric and electromagnetic characteristics of snow cover and snow-free terrain. Various studies have shown that wet snow cover can be generally distinguished from snow-free terrain using SAR data (Baghdadi et al., 1997). Many studies have demonstrated that use of multi-polarization SAR and InSAR techniques have substantially improved snow cover mapping and detection of dry and wet snow. Periodic mapping of snow cover is important to estimate the runoff and understand the effect of climate change on mountain ecosystems.

Himalayan glaciers feed into three major river systems of India, and glaciers in many other parts of the world are an important source of fresh water. Thus, runoff from changes in snow cover and glacier volume plays an essential role in long-term water resource management and hydropower planning activities. Glaciers have generally been in retreat during the last century, with a marked acceleration in global mass-losses in recent years (Kaser et al., 2006; Meier et al., 2007). For instance, glaciers in Alaska (see e.g., Figure 17-22) are currently retreating at some of the highest rates on Earth (Arendt et al., 2002; Hock, 2005). Such rapid changes in glacier extent and volume will modify the quantity and timing of stream flow, even in basins with only minimal glacier cover (Hock and Jansson, 2006). In highly glaciated regions, at times the increases in runoff can exceed the runoff changes from other components of the water budget. Thus, in glacierized drainage basins, accurate simulation of glacier response to climate change cannot be achieved without high-resolution observations, such as those NISAR will acquire, of glacier dynamics, wastage, and retreat (Hock, 2005).

In addition to influencing water resources, snow and glaciers pose hazards to nearby populations (e.g., Kääb et al., 2005). For example, glacier advance can threaten infrastructure while glacier-controlled dams (usually below the surface) can fail catastrophically causing glacial lake outburst floods (GLOFs). While NISAR observations are unlikely to be frequent enough to provide immediate warning for GLOFs, subglacial lakes can be detected and monitored by InSAR to provide some indication of the hazards they create (e.g., Capps et al., 2010).

The global distribution of glaciers, including those in Greenland and Antarctica but not connected to the ice sheets, contribute significantly to global sea-level rise and are sensitive indicators of climate change. A consensus estimate (Gardner et al., 2013) indicated that glaciers contributed 259 ± 28 Gt/yr (0.71 ± 0.08 mm Sea Level Equivalent (SLE)/yr) during the period October 2003 to October 2009, even though they make up less than 1 percent of the Earth's global ice volume (roughly 0.5–0.6 m, SLE). Thus, glaciers contribute to present sea level rise at a rate similar to the combined

rate from the Greenland and Antarctic ice sheets (289 ± 49 Gt/yr, Shepherd et al., 2012). Hence, any attempt to close the sea-level budget of the past and coming decades/centuries needs to include the contribution from glaciers as well as ice sheets. Therefore, just as for ice sheets, frequent observations of glaciers by NISAR are needed to understand glacier contributions to sea level rise.

17.3.3 Sea Ice

Within the global climate system, sea ice is a primary indicator of climate change, primarily due to the powerful 'ice albedo' feedback mechanism that enhances climate response at high latitudes. The Arctic Ocean's sea ice cover is rapidly evolving in response to climate change. Over the satellite period of observations, Arctic sea ice has thinned, shifted from predominately perennial ice to seasonal ice, and reduced in extent at the end of summer by nearly 30 percent. The resulting increase in open water, subsequent reduction in surface albedo, and increased absorption of incoming radiation appears to be enhancing the strong ice-albedo feedback mechanism. The expanded open water extent has also led to an increase in ocean surface temperatures, marine productivity and shifts in the marine ecosystem composition, and an increase in wave height that further impacts the margins of the sea ice cover. By contrast, sea ice in the Southern Ocean, largely composed of thinner seasonal ice, may in fact be increasing in extent, albeit slightly, largely due to regional advances in ice advection from recent changes in wind forcing.

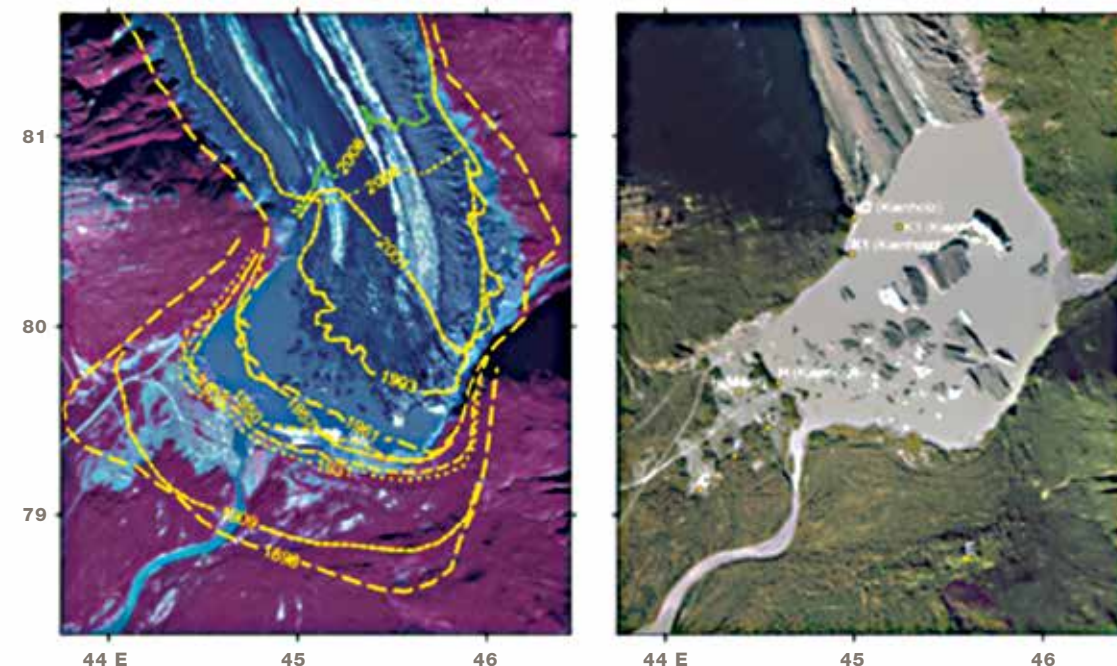
Sea ice thickness, a primary indicator of climate change in the polar oceans, is a time-integrated result of both thermodynamic and dynamic processes. As sea-ice is a solid, large-scale atmospheric and oceanic forcings concentrate stress along quasi-linear fractures in the ice with widths that are typically less than several hundred meters. The dynamic process leads to ice motion and deformation and a resulting change in ice volume, heat exchange, and thickness distribution.

As the Arctic sea ice has thinned, there has been a subsequent increase in ice motion and deformation. In comparison, there is a paucity of information on sea ice thickness, motion and deformation for the Southern Ocean and whether any changes to these parameters are occurring. With the recent and expected continuing increases in global ocean temperatures, wind speed, and wave height, what will be the response and rate of impact on the contrasting polar sea ice regimes? Will the response influence the ice albedo-temperature feedback, for example, with enhanced changes in the ice thickness distribution and motion/deformation? Such changes in thickness and deformation are not well captured in climate models, hence extending the observational record with NISAR in both polar regions will lead to improvements in understanding of atmosphere-ice-ocean interactions and fluxes as well as in the short-term forecasting of changes in the sea ice cover.

Away from the margins of the sea ice cover, the response of the ice cover to large-scale gradients in atmospheric and oceanic forcing is concentrated along narrow zones of failure (up to tens of kilometers in width) resulting in openings, closings or shears. In winter, openings dominate the local brine production and heat exchange between the underlying ocean and the atmosphere. Convergence of the pack ice forces the ice to raft or pile up into pressure ridges and to be forced down into keels, increasing the ice-ocean and ice atmosphere drag. A combination of openings and closings is typical when irregular boundaries are sheared relative to one another. These processes shape the unique character of the thickness distribution of the ice cover and have profound impacts on the strength of the ice and its deformation properties over a wide range of temporal and spatial scales. A key observation for understanding the basin-scale mechanical character of the sea ice cover is how the ice moves at different length scales. These observations are of importance in quantifying and modeling sea ice behavior in a changing climate and in facilitating operational applications.

FIGURE 17-22

Glacier change over time. From Kienholz (2010). Aerial imagery showing the terminus of Valdez Glacier. (left) AHAP 1978 false color orthophoto. Historical termini positions are indicated by yellow lines. The green line indicates the terminus position measured in summer 2008 using GPS. (right) True color Aero-Metric orthoimage of 2007. The rock covered terminus of the glacier can be seen at the approximate position of the green line marking the 2008 position on the left image.



Systematic mapping of the sea ice with spaceborne SAR has proven to be the ideal method to measure small-scale detailed sea ice motion at the scales required to quantify sea ice deformation, based on the fine resolution, increased temporal sampling in the polar regions due to converging orbits, and operations independent of cloud cover and daylight. Mapping is required at regular intervals (3-6 days) with sufficient resolution (50-100 m) to be able to identify morphological features of the sea ice cover such as ridges and the edges of floes. In the late 1980s and most of the 1990s, the availability of small volumes of ice motion data from the European SAR satellites (ERS-1, 2) allowed examination of sea ice strain rates at 5-10 km length scales and demonstrated the utility of these measurements for sea ice studies. The most significant results to date were obtained with the systematic mapping of the western Arctic Ocean obtained by RADARSAT-1, where the collaborative mission between the Canadian Space Agency and NASA enabled systematic data collections during the winter months for nearly all of the mission's lifetime, from 1996 through 2008 (Figure 17-23). Using both Eulerian and Lagrangian tracking, which enables the continuous tracking of grid elements over time, ice trajectory and detailed deformation of a grid element were observed. In addition, these data were used to derive the age of newly formed ice and the loss of ice area due to ridging.

The decade-long ice-motion dataset from RADARSAT-1 has been used to quantify the various measures of opening, closing and shear, and to estimate ice production and thickness. The data reveal extent of the activity, persistence, orientation, and length scale of the fracture patterns that are quite remarkable. The abundance of these quasi-linear fractures is correlated to motion gradients and material strength, and they are organized into coherent patterns that persist for days. Contrast in the deformation shows that there are distinct differences in the deformation-induced ice production, and the density of these features in the seasonal and perennial ice zones. The long-time series of SAR ice motion were also used to determine the flux of ice out of the Arctic Ocean on an annual basis. These were combined with SAR-derived deformation and ice production estimates

as well as independently derived sea ice thickness measurements to estimate annual changes in sea ice volume. RADARSAT observations show that deformation-induced ice production in the seasonal ice zone is greater than 1.5 times that of the perennial ice zone. The younger seasonal ice is mechanically weaker; this points to a negative feedback mechanism where higher deformation and ice production is expected as the ice cover thins. Such important information is not available in the Southern Ocean, where only limited SAR-derived ice motion maps have been generated of the Ross Sea.

In the coastal margins of the Arctic, InSAR observations are useful for observation of land fast ice, which is sea ice that remains attached and grounded to the coastal land margin, i.e., ice that is held fast to the land. Within the moving pack ice, the ice cover is changing too rapidly to derive coherence with InSAR. However, land fast ice by definition remains unchanged for long periods of time. Thus, InSAR observations are useful for the automated detection of the extent of land fast ice and information on the mechanisms by which such ice attaches or detaches from the coast (Figure 17-24). There is an increasing presence of human activities in the Arctic coastal margins due to ice retreat, related to oil exploration, increasing ship traffic, and the heightened need for a military presence previously not required. Along with the increasing potential of a hazardous event such as an oil spill, the need to improve the environmental understanding and monitoring of the dynamic coastal margins is clear.

The NISAR mission enables the unprecedented capability to derive ice motion and deformation for systematic mapping of both polar regions, to the extent previously not possible with international SAR missions. While RADARSAT-1 provided excellent motion products for the western Arctic, the dynamic eastern portion of the Arctic was not mapped nor essentially was the Southern Ocean, so no detailed observations of those regions have ever been obtained. The Southern Ocean provides a challenging mapping scenario compared to

FIGURE 17-23

Sea ice motion and deformation in the Arctic. Sea ice deformation (left column) and motion (right column) of the Arctic Ocean ice cover at a length scale of ~10 km derived from SAR data. (Deformation units: day⁻¹; motion units: km/day). (Kwok, 2010).

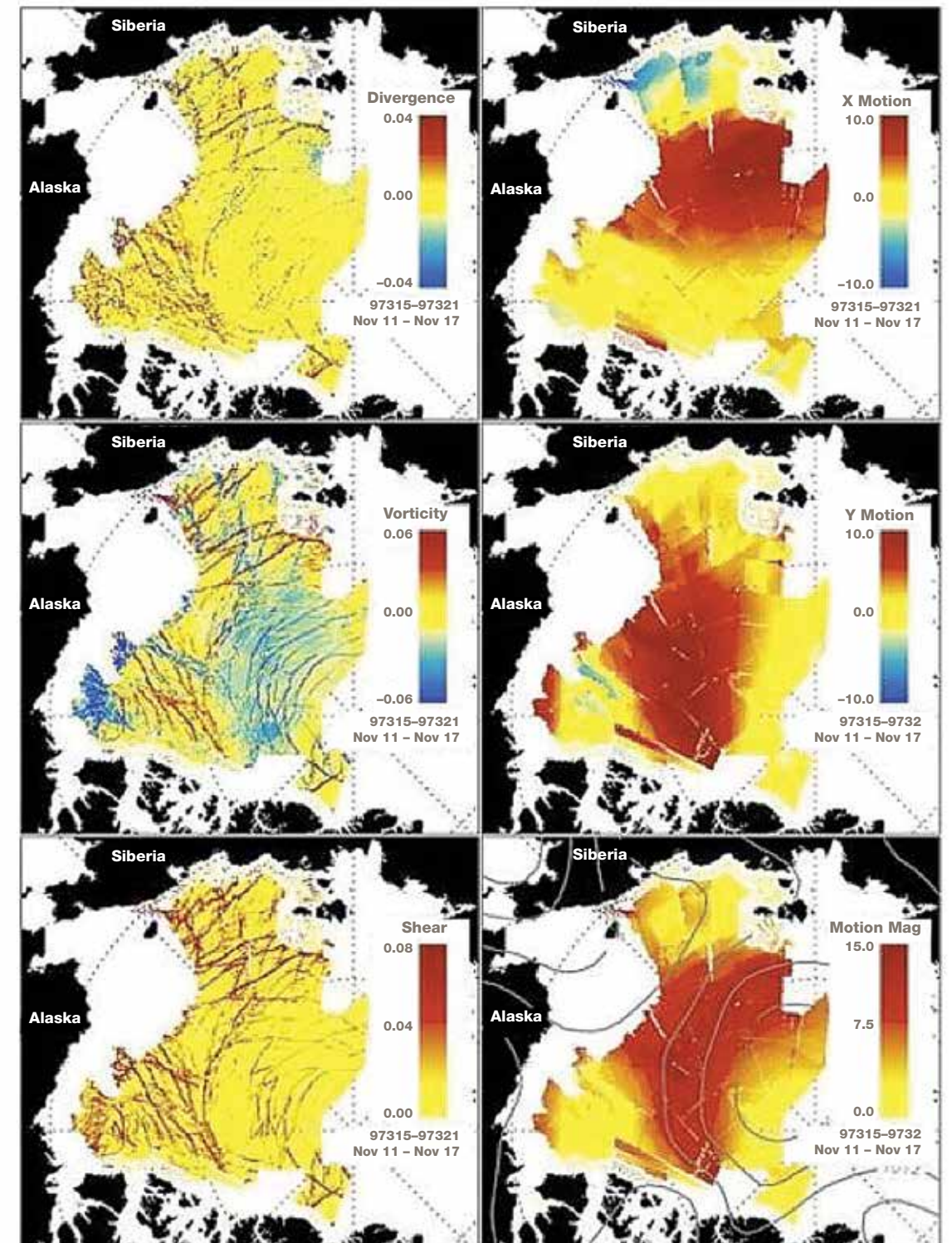
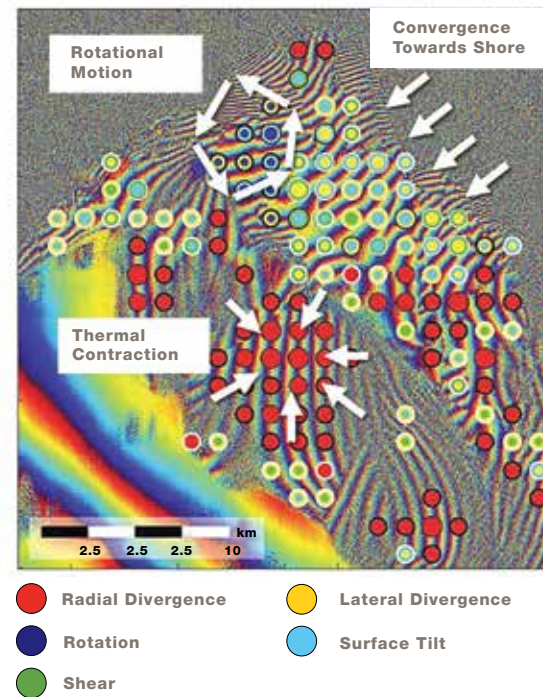


FIGURE 17-24

Small-scale motion of land fast ice. Physical interpretation of small-scale motion within otherwise stationary land fast ice based on simple physical models. Hypotheses for motion regimes are indicated by white arrows and associated text boxes.



the Arctic, due to its relatively lower latitude range and that the ice motion is not constrained by land as in the Arctic. For a thinner ice cover than in the Arctic ice motion has reduced, but, essentially unknown deformation rates and faster velocities. NISAR will achieve systematic and detailed mapping of the Southern Ocean sea ice cover for the first time. Mapping of the Arctic Ocean will enable continuing deformation observations of the rapidly changing and likely still thinning sea ice cover.

NISAR will enable precise motion and deformation measurements of the sea ice cover in view of the satellite, at an unprecedented detail and scope. These will be used to improve models of the sea ice circulation and energy fluxes within the global climate system. When combined with thickness observations, such as are planned to be obtained from ICESAT-2, critical time series of sea ice thickness distribution and mass balance parameterization can be utilized within coupled climate models to improve the prediction of sea-ice changes and their role in Earth's climate system, based on both polar oceans (Kwok, 2010).

17.3.4 Permafrost

Many permafrost regions contain large amounts of ground ice that cause significant surface disturbance upon thaw. As a result, in many Arctic and sub-Arctic environments, changing permafrost conditions are a major hazard to industrial installations, transportation corridors, and human settlements. Thawing permafrost also affects other environmental conditions, including hydrological cycles, biochemical processes, and habitat (Grosse et al., 2011; Hinzman et al., 2005; Smith et al., 2005; Walter et al., 2006). Spatially distributed permafrost models, driven by global climate model data, project strong degradation of permafrost by the end of the century due to the Arctic warming at a rate more rapid than the global average (ACIA, 2004). These results are consistent with a trend over the last several decades of persistent rise in permafrost temperatures measured throughout a pan-Arctic network of boreholes (Romanovsky et al., 2010).

Permafrost changes manifest themselves mainly as land surface elevation changes, which are well suited to measurement by NISAR. The main drivers of elevation changes in permafrost regions are seasonal freeze-thaw cycles, short-term and long-term natural disturbances caused by climate change, or anthropogenic disturbances. In addition to surface displacement, NISAR data will help detect changes in soil moisture, hydrology, and vegetation on various time scales. Observing permafrost and its change using NISAR will help tie together sparse field measurements to help provide a comprehensive view of a problem that has been a major challenge. In particular, recent research indicates that L-band SAR provides valuable large-scale information on changes in land surface conditions that can be used to directly infer permafrost and active layer dynamics and their response to environmental change. Previous research has verified that permafrost-related surface deformation on Alaska's North Slope can be derived from time series of L-band InSAR data (Kääb, 2008; Liu et al., 2010; Qu-lin et al., 2010).

Polarimetric data can also provide a means to identify regions with permafrost in Tibet (Zhen & Huadong, 2000).

Data from the NISAR instrument will provide simultaneous observations of several key parameters for seasonal active layer (freeze-thaw, subsidence, heave) and long-term permafrost dynamics (subsidence, lateral movements) in sufficient spatial and temporal resolution as well as accuracy, to substantially transform our understanding of pan arctic active layer dynamics and permafrost thaw. Hence, NISAR will allow us to begin to perform a spatially explicit assessment of regional to global impacts of permafrost dynamics on hydrology, carbon cycling, and northern ecosystem character and functioning.

17.4 APPLICATIONS

The same data that are used by the science disciplines to improve understanding of physical and ecological processes can be used by the applications community to inform decision making, improve risk management, assess resource status, and respond to and recover from disasters. The involvement of the applications community in the development of NASA's Decadal Survey mission requirements greatly expands the societal benefit and functionality of the NISAR mission to include cross-disciplinary and applied science research; opens new collaborative opportunities between scientists, engineers, and policy makers; and significantly augments science unrelated to the primary mission goals. NISAR will contribute to the following activities relevant to applications, among others:

- Improve hazard resilience by providing the observational foundation guiding future tasking, modeling, and forecasting strategies.
- Detect early transients associated with natural, anthropogenic, and environmental and extreme hazards.
- Characterize evolving disasters in support of response and recovery efforts and better understanding of fundamental science.

- Support ecosystems applications in forestry and agriculture.
- Determine environmental factors that influence the coastal processes such as erosion/deposition and coastal land use/land cover change.
- Contribute to India's science, applications, and disaster response.

The NISAR mission, through the mission science requirements, has placed an emphasis on Disaster/Hazard Response because of the unique value of frequent and regular observations of nearly all land across the globe. This focus acknowledges the value of the mission to both the U.S. and India (Figure 17-25). In most cases, the driving requirements for response are met by the science and applications communities' needs, with the exception of rapid processing for response, which is incorporated into the mission system design.

Every year, natural and technological hazards in the United States cost an estimated \$1 billion per week in the form of lives lost and public and private properties destroyed. In 2004 alone, more than 60 major disasters, including floods, hurricanes, earthquakes, tornadoes, and wildfires, struck the United States.
 Subcommittee on Disaster Reduction (<http://www.sdr.gov>).

Between 2004 and 2013, there have been an average of 147 disaster declarations per year in the United States (<http://www.fema.gov/disasters/grid/year>). In 2011, both India and the United States had more than 10 major natural disasters with an economic cost >\$5 billion in the U.S. alone (Figure 17-25).

Historically, satellite imagery has been utilized on an ad-hoc basis for disaster response and hazard science. In 1999, the establishment of the International Charter (<http://www.disasterscharter.org>), an agreement that now includes 14 of the world's space agencies and satellite management organizations, significant-

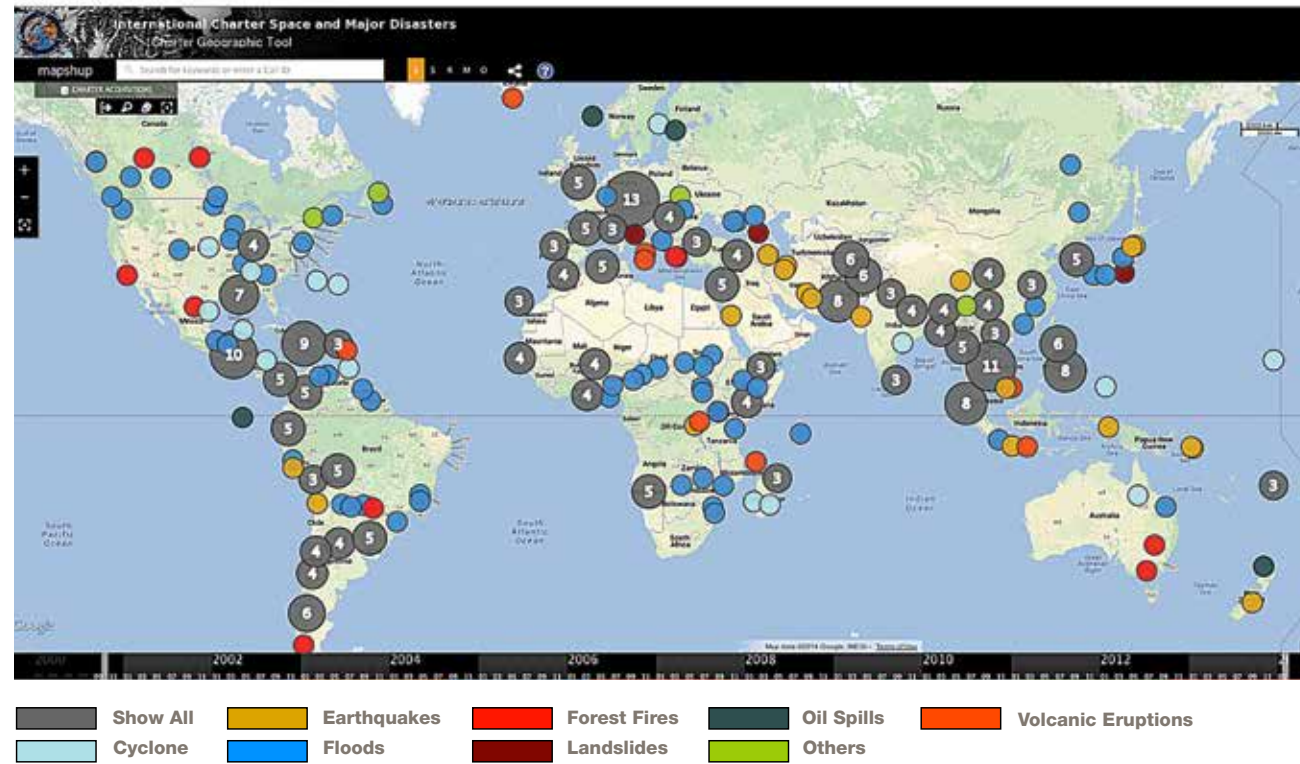


FIGURE 17-25 International charter activations. Map of 474 international charter activations since the formation of the Charter in 1999 to February 2014. The color of the circle indicates the activation disaster type. Regions with multiple activations are shown as gray circles, with the number of activations in white text, and the circle sized to represent the number of activations (<http://www.disasterscharter.org/>)

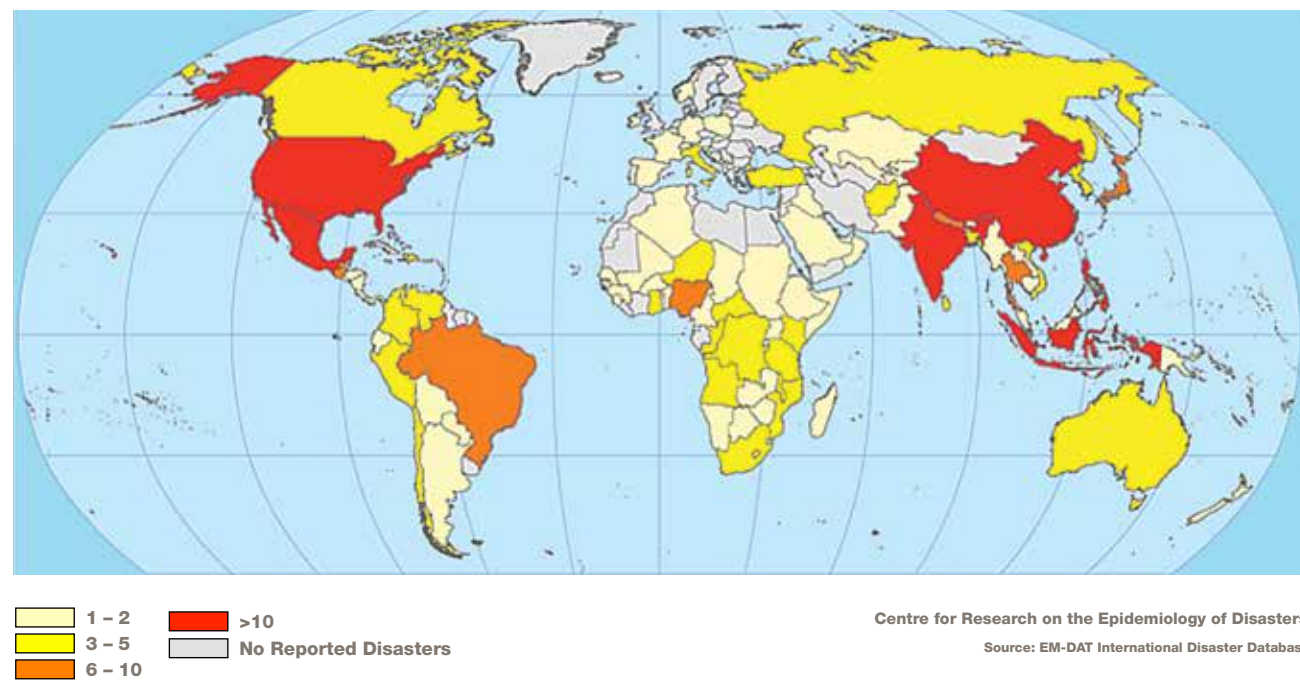


FIGURE 17-26 Natural disaster occurrence statistics for 2011. The US and India have among the highest rates of natural disasters.

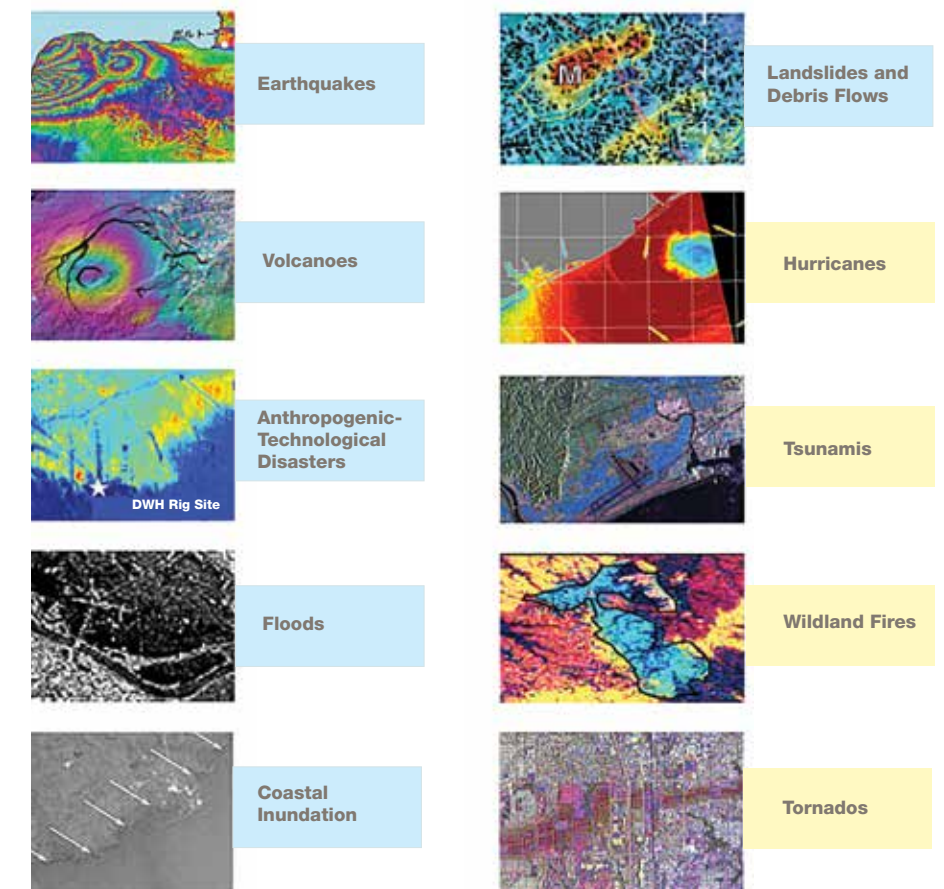
ly advanced hazard science by providing a global mechanism to collect and distribute satellite imagery in support of emergency response efforts during significant disasters with the objective to minimize the loss of life and property. As of January 2014, the International Charter has been activated 474 times since its inception, providing satellite imagery for global disasters regardless of geopolitical boundaries for a wide range of disasters, including earthquakes, floods, volcanic unrest, cyclones, fires, landslides/debris flows, and anthropogenic disasters (Figure 17-26).

The Subcommittee on Disaster Reduction (SDR) identified four key factors for successful hazard mitigation and developed six 'Grand Challenges' to provide a framework for sustained federal investment in science and technology related to disaster reduction; the SDR vision has been incorporated into the science and applications objectives of NISAR for 10 of the 15 hazards

(Figure 17-27) recognized by the SDR. Specifically, NISAR hazard response applications objectives are part of the traceability matrix for the mission and cover distinct areas of the hazard cycle: hazard detection, disaster characterization, societal impact, and societal integration. Hazard detection requires systematic collection of geodetic observations to detect, characterize and model potential hazards and disasters. Disaster characterization requires rapid disaster assessment to develop the situational awareness of the primary hazard and the ability to recognize and characterize secondary hazards associated with the primary event. Societal impact, requires rapid damage assessment for emergency rescue efforts, system integrity assessment of lifelines, infrastructure (i.e., pipelines, levees, dams, urban corridors, factories), and environmentally sensitive regions, as well as long-term facilitation of societal/environment recovery efforts. Finally, societal integration combines the hazard response and hazard

FIGURE 17-27

SAR utility for disaster response. NISAR will provide response products for ten of the fifteen disasters identified by the Subcommittee on Disaster Reduction. NISAR data will directly contribute to disasters labeled in blue and will partially support disasters labeled in yellow.



science with societal needs to improve hazard mitigation efforts by enhancing hazard resilience science, providing the observational foundation guiding future tasking, modeling, and forecasting strategies.

The following sections present the range of NISAR applications, generally split between:

- Ecosystem applications
- Geologic and land hazard monitoring
- Critical infrastructure monitoring
- Maritime and coastal ocean applications
- Hydrology and underground reservoirs

The NISAR applications topics include disaster/hazard response, which cuts across all of the above categories. In many cases, the difference between science and applications is one of information usage, with applications end users interested in regularly available observations or operationalizing product generation for situational awareness, resource management, decision support, and event response.

FIGURE 17-28

Two-frequency radar image of the Dnieper River growing region collected in 1994 by NASA's Shuttle Imaging Radar program. In this false color image, developing wheat fields show up as bright magenta and forests as the bright white patches that follow the river's border.



17.4.1 Ecosystems: Food Security

To feed a growing population of more than 8 billion, food production and supply occur on a global basis. In order to better guide policy and decision making, national and international organizations work to transparently monitor trends and conditions of agriculture in a timely basis. Because of the variable nature of planting and harvesting practices, efforts such as this are workpower intensive and time-consuming. Among the organizations that track the trends in agricultural production on a global basis is the United Nations Food and Agriculture Organization (FAO). According to FAO's 2015 statistics, over eleven percent of Earth's land surface (1.5 billion hectares) is used for farming. With an increasing population, after taking into account expected improvements in land use efficiency, the amount of land dedicated to food production is expected to grow 7 percent by 2030 to keep up with demand. This increase is equivalent to an additional 90 million hectares, roughly the size of Texas and Oklahoma combined. With the world's population critically dependent on the timely production of food and fresh water resources, the need is greater now than ever before for the application of technology to assure that population needs are met. Among the technical tools that are used to address these issues are the satellites that provide synoptic views of the globe from space. Satellite sensors are routinely used to guide decision-makers and commercial interests alike in scheduling future plantings and monitoring the effects of policy changes and a dynamic global marketplace.

The NISAR mission will provide dependable observations throughout the growing season. Radar imagery will provide near weekly observations of almost all land areas that complement the optical data and provide independent information that is sensitive to the changing structure and moisture conditions of the crops being imaged. NISAR's data products will be available open access.

The structures of different crop and land cover types provide a rich variety of responses to the radar illumination in terms of varying polarization and frequency signatures. Because of the rapid, time-varying nature of crop rotation, growth, and harvest, frequently repeated radar observations can be used to determine both the type of crop and its stage of growth. Information like this is used to predict the health of the region's crops and the planned agricultural output. Figure 17-28 shows data collected by SIR-C, a NASA mission launched on board the space shuttle in 1994. Data from areas such as the Dnieper River region of Ukraine were collected at study sites distributed throughout the globe and have been used by NISAR mission planners and other space agencies worldwide to understand how radar data can be used to improve our knowledge of the world around us. Modern day SAR, such as the Canadian Space Agency's RADARSAT and the European Commission's Sentinel satellite series, have benefited from the SIR-C mission and are being actively used today.

17.4.2 Ecosystems: Forest Resource Management

Forest ecosystems provide timber, fuel, and bioproducts and a variety of services by sequestering carbon from the atmosphere into the forest, purifying water and air, and maintaining wildlife habitats. One of the greatest challenges facing forest managers in the U.S. and elsewhere in the world is to maintain the health and resilience of the forest ecosystems. This requires a coordinated effort for systematic monitoring of forest cover, volume, and productivity, to develop techniques and policies for improving the stock and sustainable use of woody biomass. Optical satellite observations as from Landsat have played a major role in monitoring the forest cover and changes globally. But, with the advent of modern radar techniques as for NISAR, frequent and uninterrupted observations of forest volume can become a reliable data and tool for forest managers to assess forest status.

Forest managers and the agroforestry industry are in need of accurate and timely data over large areas to assess forest development and prescribe actions necessary to achieve regeneration objectives. Increasing emphasis on ecosystem management, escalating silvicultural (e.g., reforestation) treatment costs, evolving computer-based decision support tools, and demands for greater accountability have produced significant demands for spatial data on forest structure and productivity at national and subnational scales globally.

In the U.S., the Forest and Rangeland Renewable Resources Planning Act of 1974 directed the Secretary of Agriculture to make and keep current a comprehensive inventory for a prospective Renewable Resources Assessment of the forests and rangelands of the US. These assessments were focused on analysis of present and anticipated uses, demand for, and supply of the renewable resources, with consideration of the international resource situation and with a strong emphasis of pertinent supply, demand and price trends. With increasing threats to forest resources from droughts, fire, and fragmentations, tracking the forest health, biomass stock, and tangible products such as timber has become a part of national security both at home and globally.

Moving toward an inclusive monitoring system, which can augment and enhance the national inventory data, requires a departure from the past remote sensing of only the forest cover. New active remote sensing techniques using both lidar and radar have the capability to measure both forest height and biomass. This high spatial resolution data on forest structure and biomass density can be readily integrated into existing forest inventory systems. The NISAR mission will observe forests weekly and collect the information needed to map global forests and shrub lands multiple times per year. Data products will be made available at intervals that are commensurate with the need of forestry organizations and industry in the U.S. and around the

world. NISAR images will provide near global information sensitive to aboveground forest structure and biomass. The measurements can help monitor forest disturbance and recovery from both natural and human sources allowing managers to improve forest health and products.

With increased urbanization in proximity to forests, along with a growing variety of vegetation (fuel types) from changes in the landscape and management strategies, there is a pressing need for accurate, cost-efficient, large scale maps of forest biomass, fuel loads, disturbance and recovery. Emerging remote sensing technologies can provide exactly the kind of large scale maps needed to more accurately predict forest biomass, fuel loads, fire risk, and fire behavior.

“The technology is now there to use radar to estimate forest fire fuel load (e.g., branch and stem biomass). And the team recognized that a much more efficient, accurate, and cost-effective approach to sensing forest structure and fuels—and then mapping them—might lie at the heart of radar remote sensing technology.”

said biologist Don Despain, now retired from the U.S. Geological Survey in Montana, who was instrumental in generating the fire management plans for Yellowstone National Park. Figure 17-29 shows the derived forest volume from airborne radar data (AIRSAR) data over Yellowstone National Park. NISAR will provide similar measurements from a spaceborne platform to enable monitoring changes of forest volume and fuel loads across the park weekly.

17.4.3 Ecosystems: Wildland Fires

Unplanned wildland fires impact tens of millions of acres annually around the world and cost billions of dollars per year to manage and control. Although fires are crucial to many ecosystems, uncontrolled wildfires can burn homes, damage infrastructure and natural resources, kill and injure emergency responders, firefighters and the public, impact local/regional econ-

omies, and adversely affect the global environment (<http://www.sdr.gov>). Categorizing fire danger, detecting fires, identifying area burned and quantifying the severity of fires is critical for mitigating the impacts of fire.

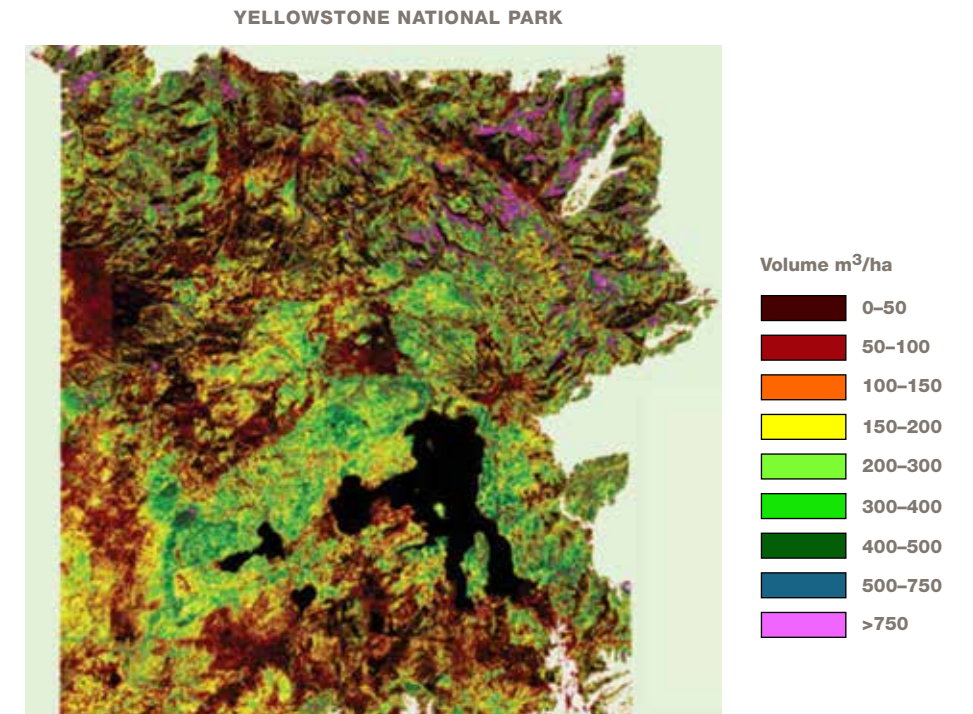
NISAR will provide a dependable observing strategy that will collect high-resolution SAR images over 90 percent of Earth's land surfaces throughout the year. NISAR imagery can provide observations that complement optical data and independent information that is sensitive to the changing structure and moisture conditions of terrestrial (land) ecosystems. Because of the dangerous nature of fires and their sometimes remote locations, remote sensing is a widely used and accepted tool used by national and international organizations to detect active fires, monitor impacts from fire and assess fire danger. For example, the National Interagency Coordination Center (NICC), the U.S. Forest Service Wildland Fire Assessment System (WFAS), the U.S. Forest Service Remote Sensing Application Center and the National Aeronautics and Space Agency (NASA) are among the key organizations in the U.S. providing information to land and fire managers of daily and seasonal projected fire danger, active fire detections, area burnt, and fire severity. Fire danger is determined by current moisture conditions, duration of those conditions, and vegetation water content, while fire severity refers to the total environmental change caused by fire. Managers customize this information based on local expert knowledge of the total fuels available to burn to provide public service announcements and develop management strategies to mitigate potential impacts.

NISAR observations can be used for detecting vegetation and soil water content for assessing fire danger, and biomass that is used to quantify total available fuel to burn and emissions lost to the atmosphere. Biomass, estimated from polarimetry data, is useful as input in fire management models for quantifying total available fuel to burn and emissions lost to the atmosphere.

The structures of different land cover types provide a rich variety of responses to radar illumination through

FIGURE 17-29

L-band airborne radar data collected over Yellowstone National Park in 2003 was used to develop maps of forest volume and fire fuel load to help with park management and fire suppression for improving the recreational resources and revenues. (Saatchi et al. 2007).



time-varying polarization signatures. Because of rapid changes in structure and composition after disturbance like wildfire, information like this can be used to determine area burnt, even when traditional methods do not work well. NISAR polarimetry data can be used to estimate the fuel load of unburned regions that can be used in fire management models during a wildfire, to map burn area perimeters, and to assess burn severity post facto (Rykhus and Lu, 2011). Maps of InSAR coherence change can be used to detect changes in the land surface associated with wildland fires, thereby mapping fire perimeter.

Time series data following a major fire can be used to track the ecosystem response and recovery and characterize secondary hazards such as debris flows and landslides. NISAR alone cannot be used to track fires: since fires can travel tens of kilometers per day, the imaging frequency (twice in 12 days) is not sufficient to guide the hazard response community as the disaster unfolds, for which low-latency daily to sub-daily products are required.

Figure 17-30 shows the fire burn scar of the 2015 Lake Fire in San Bernardino National Forest, California. The radar is able to identify the more severely burned areas. Although it was possible in this particular fire to use both Landsat and InSAR data, there are many areas (e.g., Alaska) where it is frequently too dark or overcast to produce maps from optical data on a regular basis. NISAR data can improve mapping capabilities across many areas, times of year, and weather conditions.

17.4.4 Ecosystems: Forest Disturbance

Optimal forest management requires knowledge of how forests change over time in response to natural disturbances and management activities, including invasive species; diseases; plant and animal pests; fire; changes in climate and serious weather events such as tornadoes, hurricanes and ice storms; pollution of the air, water, and soil; real estate development of forest lands; and timber harvest. With the world's population critically dependent on sustainably managed and utilized forest resources, the need is greater now than ever before for the application of modern technology

to provide detailed and timely informational map data to the timber industry, resource managers and forest policy makers. Satellite sensors provide synoptic views of the globe from space. This information is routinely used to guide policy for both decision-makers and commercial interests. Examples include planning forest management activities, supporting preparation of information for forest real estate transactions domestically and in foreign countries, and monitoring the effects of forest policy changes, such as logging concessions or illegal logging activities.

NISAR will provide bi-weekly observations that complement optical data and provide independent information that is sensitive to the mapping of forest disturbance, including below-canopy inundation from natural and catastrophic flooding events. Observations of Earth's land surfaces from space using active microwave sensors allows for reliable and repeated measurements to be made even under dense cloud cover. When forest canopies are disturbed, such that standing trees are

partially or wholly felled or removed, or significant fractions of the upper canopy are lost, e.g., in a forest fire, the changes are reflected in a rich variety of radar signals that can be measured. The time history of changes shows when, where, and by how much the woods were altered. Figure 17-31 shows data collected by the JAXA ALOS L-band SAR mission operating from 2006 to 2011. The image is a three-date color composite, where radar signatures result in color combinations that are directly related to various types of forest disturbance and regrowth.

The NISAR mission will provide data of similar quality, yet at greater observation frequency and with easy data access by the U.S. timber industry, natural resource managers, natural disaster prevention and response teams, researchers, and decision makers. The data will be a critical complement to the U.S. global land observing system by providing routine, global, cloud-free forest monitoring capacity.

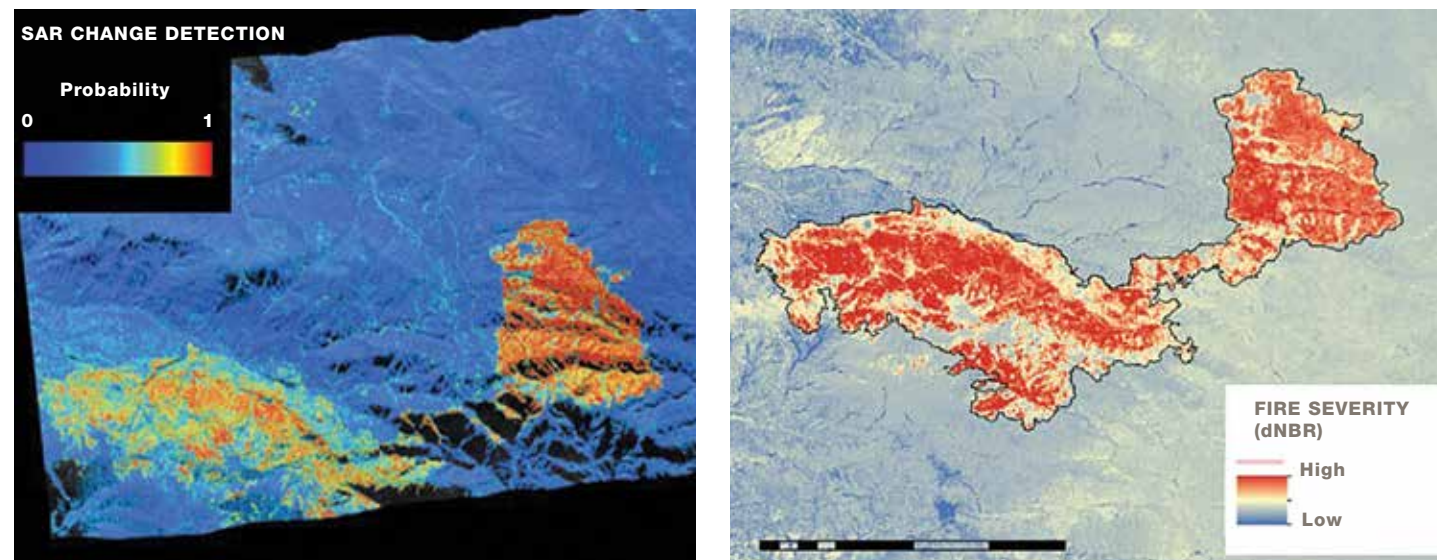
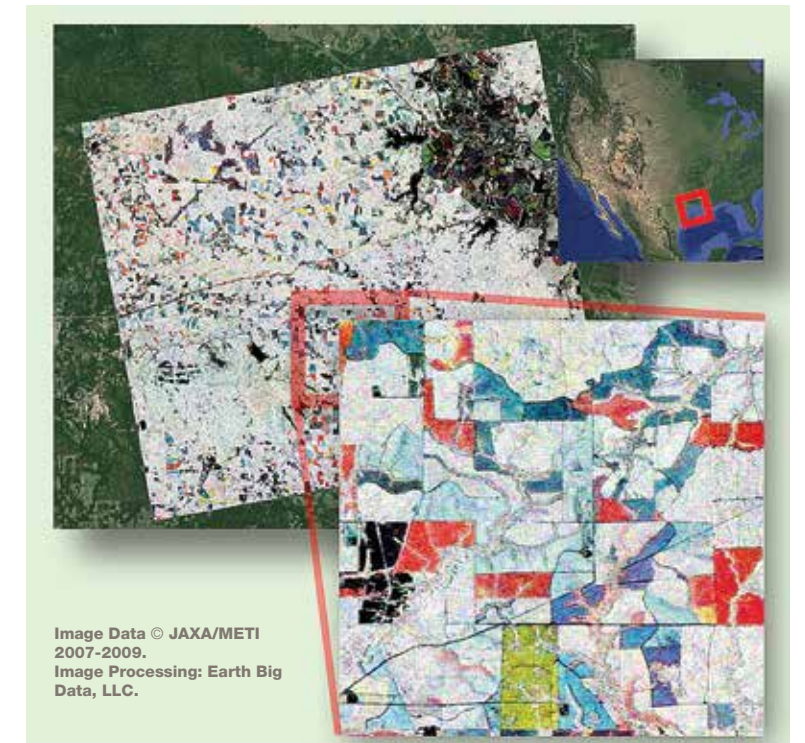


FIGURE 17-30 Fire burn scar of the 2015 Lake Fire in San Bernardino National Forest, California. The left image shows probability of change derived from interferometric radar (InSAR) using 14 pre-event images and one post-fire image from an overflight on June 29, 2015, using the airborne Jet Propulsion Laboratory (JPL) Uninhabited Aerial Vehicle (UAVSAR) radar instrument. Right image is the differenced Normalized Burn Ratio (dNBR) fire severity map obtained from Landsat.

FIGURE 17-31

Three-date (2007, 2008, 2009) L-Band radar image (JAXA ALOS) of timber production land in southern Louisiana, one of the most intensive timber production areas of the United States. Red and yellow colors readily show various dates and intensities of forest management activities (clear-cut and selective logging). Blue and purple colors show areas and stage of re-growing forest plantations.



17.4.5 Ecosystems: Coastal Erosion and Shoreline Change

Coastlines are continuously being reshaped by the interaction of strong wave action, storm surges, flooding, currents, sea-level rise, river discharge, and human activities with the local geology and mitigation efforts designed to minimize the effects of shoreline recession on coastal communities. Coastal erosion in the U.S. has increased over the past few decades, and therefore represents a major coastline hazard to low-lying communities, infrastructure, and lifelines located near the coast which are areas often with high population densities. In the contiguous United States, 45 percent of the coastline is along the Atlantic or Gulf coast. The average erosion rate along the Gulf coast is nearly 2-meters a year and along the Atlantic is approaching 1-meter a year. Coastal erosion is also significant in Alaska where degradation of permafrost and reductions in coastal sea ice contribute to increased erosion rates (e.g., Eicken et al., 2011). Extreme storms, sea-level rise, land subsidence, landslides, and flooding all

accelerate costal erosion. Periodic observations of the coastline are necessary to characterize the dynamics of coastal erosion and coastal accretion processes on coastal communities and infrastructure and begin to develop models and coastal erosion/accretion scenarios for societal resiliency.

NISAR will collect systematic polarimetric SAR imagery to directly measure positional changes to the global coastline. The combined analysis of cross-polarized SAR and like-polarized images will be used to uniquely demarcate coastlines. Changes in the coastline pattern on a half-yearly interval will address the coastal dynamics scenario. Like and cross-polarized images will be useful for monitoring the changes in the geomorphological features and land use/land cover patterns. Time series SAR data may also be used to monitor shoreline changes. SAR data can be used to demarcate high tide lines (highest of high tides) along the coast based on manifestation of the effect of seawater on coastal landforms and landward moisture content.

17.4.6 Geologic Hazards: Earthquakes

Earthquakes are amongst the deadliest natural hazards. There have been 35 earthquakes since 1900 that have killed more than 10,000 people, with seven since the year 2000 (Bally, 2012). The 2004 Mw 9.1 Indonesian earthquake and tsunami, the 2010 Mw 7.0 Haiti earthquake, and the 2011 Mw9.0 Japan earthquake and tsunami combined killed more than 450,000 people. The International Charter has been activated 70 times since 2000 to help the emergency response community directly following a major earthquake by providing rapid imagery to help develop the situational awareness necessary to respond to disaster. Furthermore, through the globalization and interconnectedness of the world's economy, earthquakes can have a negative worldwide impact, e.g., the 2011 Mw 9.0 Tohoku earthquake in Japan resulted in suspension of auto manufacturing in Detroit due to parts shortage (Wall Street Journal, 2011) and elevated insurance rates globally.

The NISAR imagery collection requirements for pure research science and earthquake applications are effectively the same – collect SAR data on every possible orbit. The key difference is that the applications community needs low-latency data to develop the situational awareness for the hazard response community. They seek to quickly understand the scope of the disaster and how to best allocate limited resources. Key questions include: What is the area affected? Where have buildings been damaged? How many? Are there secondary hazards like landslides, dam collapse, fires, etc.? Where are the safe places to evacuate people?

What infrastructure and lifelines were damaged? Where was the greatest shaking or liquefaction? NISAR imagery will be used in a variety of ways (e.g., backscatter or coherence change), along with integrated infrastructure and population density information and optical imagery where available to address these questions.

17.4.7 Geologic Hazards: Volcanic Unrest

Earth is home to about 1,500 volcanoes that have erupted in the past 10,000 years, and today volcanic activity affects the lives and livelihoods of a rapidly growing number of people around the globe. In the United States, more than 50 volcanoes have erupted one or more times in the past 200 years. Volcanic eruptions destroy cities and towns, eject ash clouds that disrupt air travel, and impact regional agriculture. Explosive eruptions eject ballistic rock fragments that can impact the surface up to several kilometers away from the vent. Smaller fragments are carried upward in eruption columns that sometimes reach the stratosphere, forming eruption clouds that pose a serious hazard to aircraft. Volcanic ash fall can collapse buildings, and even minor amounts can impact electrical systems and disrupt everyday life. Volcanic gases contribute to health problems, and also to acid rain that causes corrosion and harms vegetation and livestock. Lava flows inundate property and destroy infrastructure. Volcanic mudflows have the potential to devastate entire cities even far from the source volcano. Pyroclastic flows—high-speed avalanches of hot pumice, ash, rock fragments, and gas—can move at speeds in excess of 100 km/hr and destroy everything in their path.

Worldwide, it is estimated that less than 10% of active volcanoes are monitored on an on-going basis, meaning that about 90% of potential volcanic hazards do not have a dedicated observatory and are either monitored only occasionally, or not monitored at all (Bally, 2012). As for earthquakes, the NISAR imagery collection requirements for pure research science and volcanic applications are effectively the same – collect SAR data on every possible orbit, but the applications community also needs low latency data.

Many volcanic eruptions are preceded by surface deformation induced by moving magma beneath the ground. Measuring this deformation is key to understanding the potential for future eruptions. Radar

observations from NISAR and other satellite missions can play a direct role in helping to monitor volcanoes and assess associated hazards, both during periods of unrest and during ensuing eruptions. Data from NISAR and other radar missions allow us to identify and monitor surface deformation at quiescent and active volcanoes through the use of radar interferometry (InSAR). Only InSAR has the capability for monitoring deformation at virtually all of the world's potentially active volcanoes on land. InSAR observations allow us to build models of subsurface magma movement preceding, accompanying, and following eruptions—information that is critically important to understand the state of activity and anticipated hazards. Radar images that allow us to monitor and characterize volcanic processes are also used to map the extent of eruptive products, like lava and ash, during an eruption. When combined with other measurements of volcanic activity, data from NISAR will facilitate the development of more realistic depictions of active volcanoes, which are critical for eruption forecasting.

17.4.8 Geologic Hazards: Sinkholes and Mine Collapse

Sinkholes are formed either naturally in Karst regions where carbonate rock is dissolved into groundwater or grow due to human activities such as oil extraction. Many sinkholes occur rapidly over a small spatial scale, so it is difficult to capture precursory deformation using remote sensing techniques. In some cases, however, there may be slow deformation, before sinkholes collapse catastrophically, indicating where a future collapse is possible (e.g., Castañeda et al., 2009; Paine et al., 2012; Jones and Blom, 2014). In addition, subsidence from mining activities and catastrophic mine collapse can be measured by NISAR (e.g., Lu and Wicks, 2010; Ismaya and Donovan, 2012).

17.4.9 Geologic Hazards: Landslides and Debris Flows

Landslides, debris flows, and other forms of ground failure affect communities in every state of the United

States and result in the loss of life and cost billions of dollars in property losses and environmental degradation every year (<http://www.sdr.gov>). During a two-year period between 2014 and 2016, 61 people were killed by landslides in the U.S., including 43 in the Oso landslide in Washington State (Coe, 2016). Approximately two-thirds of the United States population lives in counties where landslide susceptibility is moderate to high. Landslides are triggered by a number of mechanisms, including intense or long duration rainstorms, earthquakes, volcanic activity, wildland fire, coastal erosion, excavation for infrastructure, and the loss of permafrost in arctic regions. Some landslides can remain active for years or even decades, and some of these slowly moving landslides may transition to catastrophic collapse. In areas of steep slopes, the debris flows are a dangerous relative of landslides where slope material becomes saturated with water forming a slurry of rock and mud that moves rapidly down slope and along channels picking up trees, houses, and cars, thus, at times, blocking bridges and tributaries, causing flooding along its path. Landslide danger may continue to be high even as emergency personnel are providing rescue and recovery services.

Both L and S band NISAR images have the potential to significantly advance research for landslide science and provide invaluable information to the broader landslide science application communities. First, NISAR's cloud penetrating imagery, coherence mapping, and rapid tasking capabilities will allow emergency responders to identify triggered landslides and assess their societal impact. For example, the 2008 Mw 7.9 Great Wenchuan earthquake in China triggered more than 60,000 landslides, blocking roads, impeding emergency response efforts, isolating and destroying villages, and damming rivers thereby creating additional life threatening conditions. The 1997-1998 El Niño rainstorms in the San Francisco Bay Area produced thousands of landslides and caused over \$150 million in direct public and private losses (<http://www.sdr.gov>). Secondly, given that two-thirds of the counties in the United States

have moderate to high landslide risk, NISAR will be able to identify and track motion on landslides greater than 20 m in scale that pose a significant societal risk over wide areas. Time series analysis of these slides will detect transient changes in deformation patterns that may represent an elevated societal risk and provide early warning of imminent catastrophic failure. Finally, time series analysis of coherence images in recent burn areas can be used to map the area of vegetation removal and then help identify and map subsequent debris flows and their spatial distribution with respect to lifelines, infrastructure and residences. When combined with computer modeling, new debris flow hazard assessments can be made with the aim of improving societal resiliency.

17.4.10 Hazards: Anthropogenic Technological Disasters

Anthropogenic hazards, e.g., intentional attacks, industrial explosion, dam failure, etc., are broadly distributed across the globe and events that warrant monitoring can occur with little to no a priori information on the location and timing. The anthropogenic disasters can also form as a result of a cascading natural disaster (e.g. Fukushima, Japan), highlighting the importance of timely generation and delivery of disaster response data after the primary event. Anthropogenic-technological disasters that impact human populations often are related to critical infrastructure, such as bridges, dams, power plants, and industrial facilities, or involve the release of material that can be distributed widely in the environment by air or water. NISAR can be tasked in response to such events after an unforewarned disaster occurs or in advance if it is known to be likely to occur.

17.4.11 Critical Infrastructure: Levees, Dams, and Aqueducts

Water storage, conveyance, and defense structures are critical elements of a country's infrastructure that provide water and protection to businesses and

communities. Levees and dams not only protect the low-lying areas but also channel the water to communities and businesses where it is needed. Dams irrigate at least 10 percent of U.S. cropland and help protect more than 43% of the U.S. population from flooding, while satisfying 60 percent of the electricity demand in the Pacific Northwest (2017 NISAR Critical Infrastructure Workshop). Monitoring of levees and dams in the traditional manner through visual inspection and in situ instruments is time-consuming and personnel intensive, leading to infrequent monitoring of most areas. NISAR will increase inspections as it can image the entire U.S. several times a month regardless of cloud-cover. NISAR's resolution of 6-to-12 m is a significant improvement over the Sentinel 1a/b resolution of 20 m, particularly for monitoring mid-size structures like levees and aqueducts.

When levees (or other water defense structures) subside, there is a high risk of catastrophic flooding. Such subsidence was observed by InSAR phase change before the Hurricane Katrina floods in New Orleans (e.g., Dixon et al., 2006). InSAR also detected motion of embankments before they failed catastrophically in Hungary, creating the worst environmental disaster in that country's history (e.g., Grenerczy and Wegmüller, 2011). Both the New Orleans and Hungary studies utilized high-resolution InSAR time series analysis methods, which will benefit from the frequent and repeated high-resolution NISAR observations. It is important to note that while these studies came after the disasters took place, with the processing of higher level products over hazard-prone areas, NISAR will allow the local, state and federal agencies to switch from disaster response to disaster preparation and resilience.

An example of this is persistent monitoring of the California Aqueduct. Figure 17-32 shows subsidence associated with groundwater withdrawal that occurred during the drought and was derived from a time series of images acquired from 2013 to 2017.

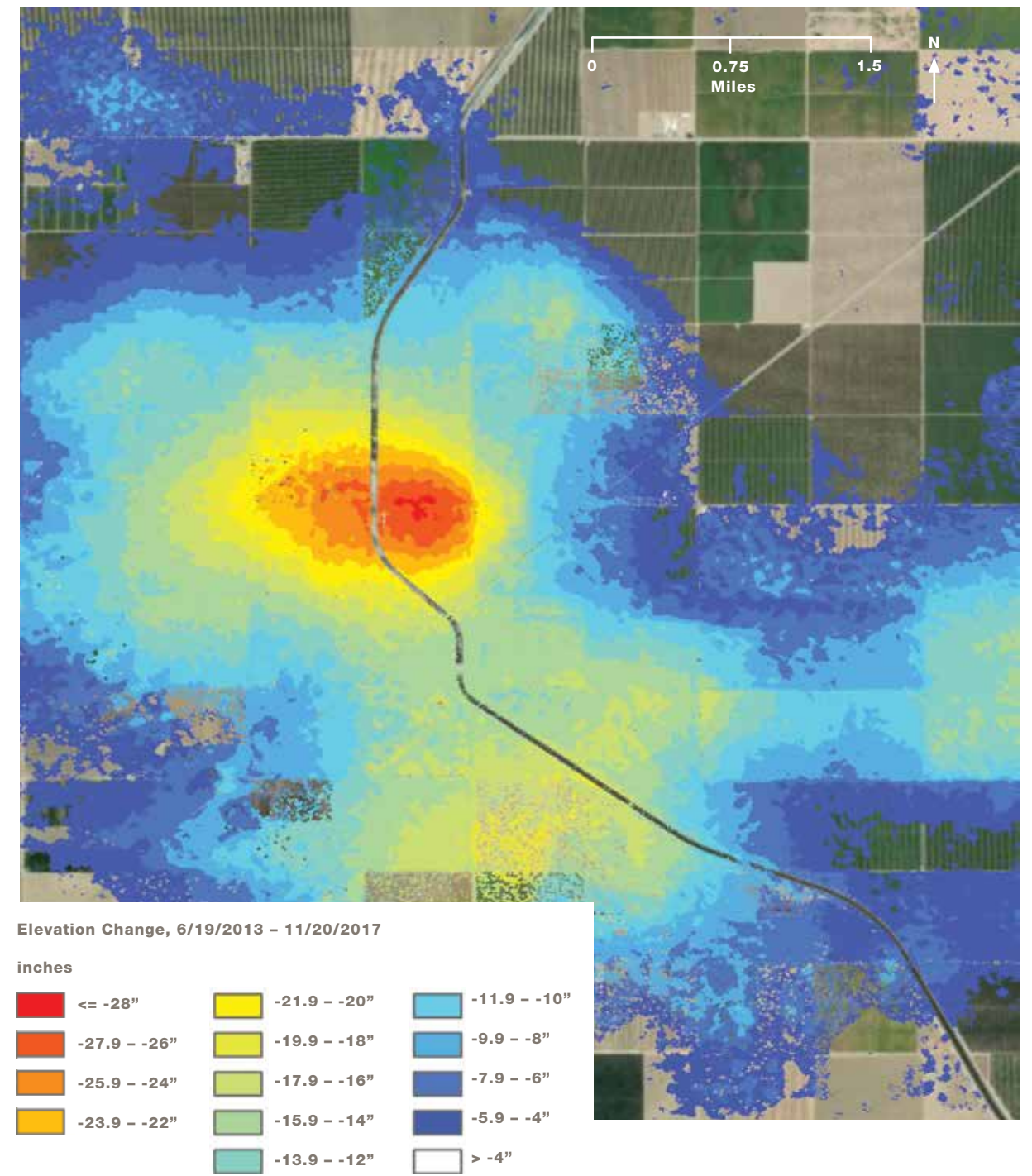


FIGURE 17-32 Subsidence bowl that formed from groundwater pumping during the 2012-2016 drought in the Central Valley, California. Measurements with the L-band UAVSAR instrument were used to detect and track changes in the depth and extent of the feature during the drought.

17.4.12 Critical Infrastructure: Transportation

Roads, bridges, railway tracks, and other transportation infrastructure or facilities require careful and continuous monitoring to maintain integrity. The regular time series of images from NISAR, analyzed to produce InSAR products, can be used to monitor the structures and the ground nearby at scales greater than 20 m for movement that could presage damage or failure.

17.4.13 Critical Infrastructure: Facility Situational Awareness

In many cases critical infrastructure operators have a good understanding of their facility through instruments deployed within its confines. NISAR can augment point measurements with extended spatial coverage, and NISAR can provide information about changes happening outside the facility that could potentially impact operation or safety. NISAR can augment their knowledge by providing information in the neighborhood and regional environment in the vicinity of the facility. For example, impending or actual water intrusion into the facility could be identified during overbank flow on nearby rivers, or changes in land use identified downwind from a facility. Slow creep landslides or fault slip could be identified that causes slow degradation of performance or stress on structures.

17.4.14 Critical Infrastructure: Arctic Domain Awareness

The high latitude regions of Earth are facing increased challenges related to dynamic changes of the arctic environment and modified land use patterns by polar communities and industry. SAR can provide important information to improve situational awareness and crisis response capabilities related to a range of these emerging issues including maritime security, infrastructure health, natural disaster resilience, and transportation.

The U.S. Arctic region is characterized by vast areas with limited infrastructure. Furthermore, its land and ocean areas are increasingly affected by extreme environmental conditions, threatening human lives and damaging existing infrastructure installations. On land, the annual freeze-and-thaw cycles of thick soil layers lift surfaces several tens of centimeters every winter, damaging roads and affecting the integrity of buildings and oil pipelines. An abundance of unstable slopes threatens some of the most sensitive transportation corridors in Alaska, while regular earthquakes and volcanic eruptions interfere with human life and endanger international air traffic. A recent increase in commercial activities on the opening U.S. Arctic oceans have led to rising risks of anthropogenic disasters such as oil spills and shipwrecks that require regular large-scale remote sensing data to enable sufficient situational awareness.

NISAR will provide frequent, regular, and comprehensive coverage of arctic land to identify and monitor surface deformation related to landslides, permafrost change, and natural hazards such as active volcanoes and earthquake zones through the use of InSAR. These deformations are important for the assessment of hazards affecting infrastructure and people living in the Arctic. Only InSAR has the capability of monitoring deformation across the entire Arctic region to provide a synoptic picture of ongoing risks. Radar images have the additional capability to detect changes in the northern coastlines, map flood extent and identify ice jams, monitor ship traffic (cooperative and non-cooperative) in Arctic waters, track the progression of oil spills and identify sea ice features that may threaten infrastructure installations and ship traffic. In concert with other data, radar has shown to be an important tool in emergency response, which is important for remote areas where physical access is limited.

17.4.15 Maritime: Hurricanes and Wind Storms

According to FEMA, hurricanes account for seven of the top ten most costly disasters in United States history.

The state of Florida was struck by four major hurricanes in 2004 with losses totaling \$42 billion (<http://www.sdr.gov>). NISAR imagery can be used to estimate wind speeds within the hurricane, show the shape and structure of the hurricane eye, map the spatial extent of the storm surge and flooding, detect coastal erosion, and assess damage to buildings, infrastructure, and the ecosystem. Combining NISAR's ascending and descending repeat orbits provides two satellite images every 12-days which will provide the science and operations communities detailed SAR imagery and geodetic measurements. Although this temporal frequency is not sufficient to provide systematic coverage, NISAR will augment the global Earth observation instrument network, and because of the global observations in some circumstances it may acquire the only pre-event images.

17.4.16 Maritime: Sea Ice Monitoring

The U.S. National Ice Center (NIC) is a joint effort of the US Navy, NOAA, and the U.S. Coast Guard. The NIC is also a part of the Northern American Ice Service (NAIS) which is joint with the Canadian Ice Service. Their primary goal is to monitor sea-ice extent and type, especially in the Arctic, for safety of navigation. In addition to the important cryospheric science goals of NISAR, the routine imaging of the polar regions will potentially yield important benefits for operational monitoring. One of the primary observational products are available SAR data. Since SARs provide all-weather, day-night high-resolution, they represent the preferred means of observation. The primary limitation of SARs is coverage. At this point, C-band SAR imagery from Sentinel-1A and-1B are the NICs primary SAR data source. The Canadian C-band Radar Satellite Constellation to be launched in 2019 will provide additional imagery.

NISAR will not only represent an opportunity for additional polar coverage to support operational monitoring, but L-band will augment the information available from C-band. Both frequencies are useful in delineating

areas of sea-ice coverage. However, the longer wavelength of L-band permits deeper ice penetration and makes L-band more capable in discriminating sea-ice type.

For operational sea ice uses, the priorities for NISAR data acquisition in order are:

1. Polar coverage, particularly in the Arctic where there are more frequent marine operations.
2. The preferred data latency is 6 to 12 hours. After 24 hours, the data are less useful for operations.
3. The preferred polarization is dual VV and HH.
4. The next preferred polarization configuration is any like-polarization plus cross polarization.
5. The least preferred polarization configuration, but still very valuable, is any like-polarization.
6. Providing sufficiently low latency is the primary challenge to operational usage of NISAR data for sea-ice monitoring.

17.4.17 Maritime: Coastal Ocean Circulation Features

NISAR will dominantly acquire data over land and the cryosphere. To the extent that coastal regions are also imaged, NISAR data can be applied to a variety of marine applications. Radar backscatter from the ocean surface is directly dependent upon the roughness of the ocean surface on scale of the radar. The rougher the surface the larger the return from the surface. SAR marine applications are tied to how different ocean phenomena affect surface roughness. NISAR will image long ocean surface waves (>50 m wavelength). Although the exact mechanisms for imaging of waves is more complicated, to first order the slope variations of the ocean surface and the fact that surface roughness and hence radar cross section at the crests of waves is higher than in the wave troughs renders waves visible in SAR imagery. From this imagery, the two-dimen-

sional ocean wave spectrum can be computed (Alpers, 1992). There are other, more advanced, marine applications of SAR that depend on taking advantage of direct velocity measurements by SAR to map ocean currents (Romeiser, 2013).

L-band or S-band radar may be more attractive for imaging of current boundaries, fronts, eddies and internal waves, since the longer (compared to C-band) wavelength is less sensitive to rapid variations in the boundary layer wind speed and will therefore be more modulated by varying surface currents. Dual-frequency measurement capabilities will allow tailoring of observations to different wind speed regimes.

Coastal upwelling processes and the formation of coastal jets and fronts result in temperature gradients, which may be detected by SAR due to reduced surface roughness over the colder water regions. Reduced sensible and latent fluxes over the colder water because of lowered air-sea temperature differences is accompanied by reduced atmospheric turbulence levels, and thus less roughness in the regions of the cooler ocean contacting the atmosphere. At VV polarization, such a pattern would appear similar to an HH-polarization image under stable air/sea conditions; however, under unstable conditions, simultaneous imagery at the two polarizations will differ significantly.

17.4.18 Maritime: Ocean Surface Wind Speed

The most direct SAR marine application is SAR wind speed retrieval. Radar backscatter at off-nadir incidence is proportional to surface roughness near the scale of the radar wavelength. The higher the wind speed, the rougher the ocean surface, and the higher the backscattered cross section. This principle is relied upon by conventional wind speed scatterometry. Radar cross section is maximum looking in the wind direction and a minimum is the cross-wind direction. SAR wind speed measurements generally have over an order of magnitude finer resolution than conventional scatterometers.

Figure 17-33 shows a radar cross section image off the east coast of Mexico acquired by Sentinel-1 at 2018-01-25 00:32 UTC and the corresponding wind speed at resolution of 500 m. Sentinel operates at C-band (5-cm wavelength). NISAR wind speed images will be roughly similar though may be less sensitive at low wind speeds (5 m/s), but more accurate at higher wind speeds (>15 m/s; Monaldo et al., 2016; Monaldo and Kerbaol, 2004; Shimada and Shimada, 2003). Not only can SAR wind speeds be used for weather forecasting, but high-resolution wind speed climatologies can be used to help select sites for offshore wind power tur-

bines (Hasager et al., 2015). Wide swath observations, similar to those for currents in the open ocean, are preferred for the winds, with resolutions being finer than the scales of frontal systems and storm gradients at sea. These will produce even sub-kilometer scale wind estimates, which are important for coastal areas with respect to, for example, building wind-turbines, coastal structures, shipping, and biological interactions.

17.4.19 Maritime: Iceberg and Ship Detection

One important marine application not directly related to ocean surface roughness is to monitor ship traffic and icebergs. At the high resolution of SARs, ships and icebergs are often visible (Tello et al, 2005). Imaging the Atlantic shipping routes during seasons when icebergs often move into the lanes will support the NIC's mandate to provide situational awareness data on that hazard. Identifying ships near coasts can also help locate and identify illegal dumping of material in coastal water.

17.4.20 Maritime: Oil Spills

Ocean surface roughness is suppressed by surfactants and oil slicks. In coastal regions, NISAR has the potential to be used to monitor oil spills from ships or oil-drilling platforms (Girard-Arduin, 2005). Oil spills in oceans and coastal waters have widespread impact to the environment, marine life, human health/safety, society, and regional economy. The 2010 Deepwater

Horizon oil spill caused a major economic disaster, spreading oil from ~50 miles off the Louisiana coast throughout much of the Gulf of Mexico and to coastal areas in all U.S. states bordering the Gulf (Figure 17-34). Smaller, yet significant, spills occur regularly, mainly in coastal areas around the globe. The hazard response community and the International Charter have extensively used SAR imagery to track oil spills and help guide the mitigation efforts. A region of increasing concern regarding the potential of hazardous oil spills is the Arctic coastal zone, where the retreating and thinning sea ice cover has increased interest in transportation and petroleum exploration. A hazardous spill in the Arctic presents an extremely challenging containment and cleanup response, where NISAR may play a critical role, enhanced by the converging nature of polar observations and the ability to image throughout the extensive periods of darkness and cloud cover. Tasking of NISAR in response to such disasters may be critical and will commence after the disaster occurs.

17.4.21 Maritime/Hydrology: Flood Hazards

Floods and other water related hazards are among the most common and destructive natural hazards, causing extensive damage to infrastructure, public and private services, the environment, the economy and devastation to human settlements. Recurring hydrological disaster-related losses from floods caused by tsunamis, storm surge, and precipitation have handicapped the economic advancement of both developed

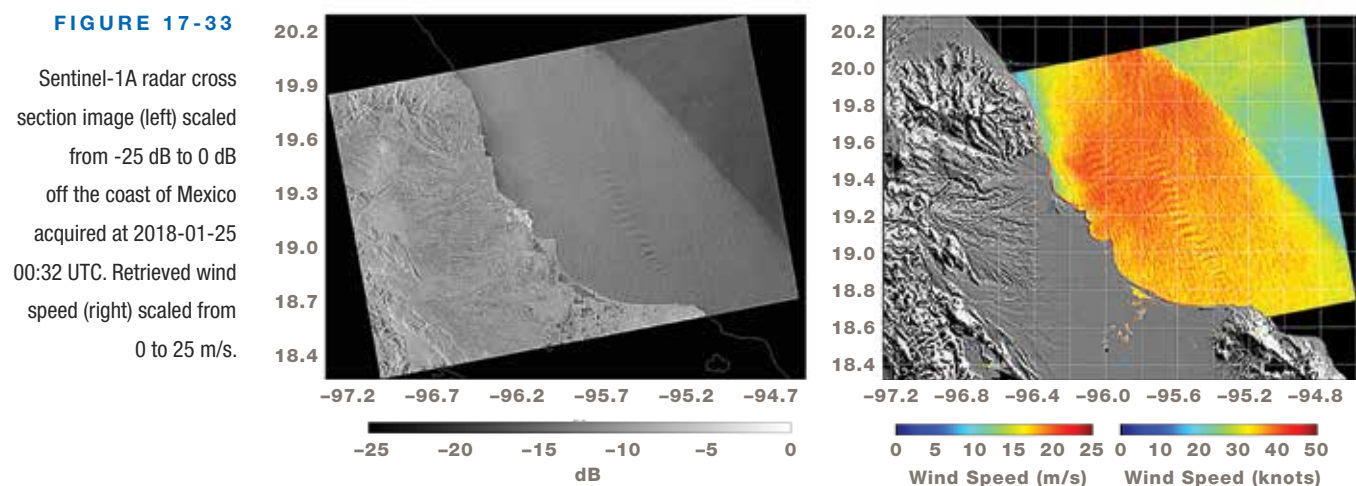
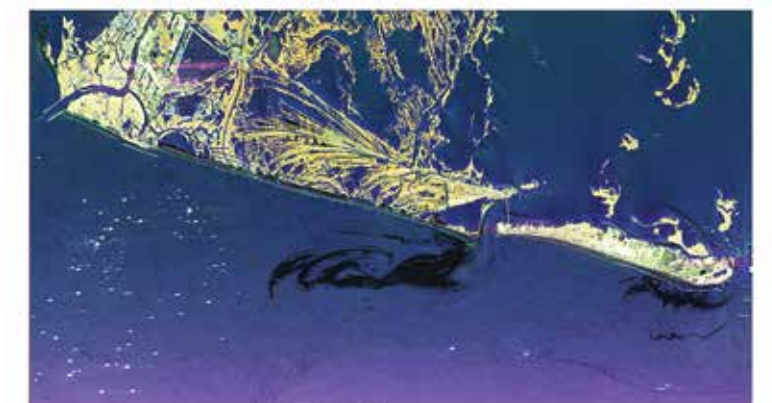


FIGURE 17-34

UAVSAR image of oil from the Deepwater Horizon spill acquired over southeastern Louisiana. The oil slick shows up as a dark area in this false color image, as it dampens the capillary waves smoothing the surface, resulting in reduced backscatter energy.



and developing countries (e.g., https://www.gov.uk/government/uploads/system/uploads/attachment_data/file/286966/12-1295-measuring-human-economic-impact-disasters.pdf). Most hazardous hydrologic events are local and short-lived and can happen suddenly and sometimes with little or no warning. Millions of people can be impacted by major floods. U.S. insurance claims from floods total in the billions of dollars per year. In 2015 and 2016, for example, 18 major flood events hit Texas, Louisiana, Oklahoma, and Arkansas causing extensive damage (Figure 17-35). Timely evaluation of flooding conditions is crucial for effective disaster response. Saving lives and property are the initial priorities, while later assessments are needed to evaluate the extent and severity of the disaster zone.

Because satellite radar is a cloud penetrating technology, NISAR can acquire snapshots of the disaster extent regardless of atmospheric conditions, help delineate flood hazard zones; measure water level changes, primarily in wetland environments; and measure flood depth in areas where an accurate digital elevation model (DEM) is available. NISAR can be used to map flooding events on a global basis twice every 12 days. Observations will be uninterrupted by clouds and will provide timely information for flood responders. Even flooding hidden beneath forest canopies will be visible in many areas. Multiple types of NISAR measurements will be useful for flood assessment: InSAR phase, coherence and backscatter change, including polarim-

etry, can be used to discern water flow direction, map inundation extent and duration, estimate changes in water level, and determine measurements. NISAR will be capable of monitoring water level change in marsh areas, allowing for prediction of downstream flooding. Permanent stream gauges are installed and monitored specifically for that purpose, but they are sparsely distributed. NISAR data will augment these data and provide increased spatial coverage, filling in the gaps between gauges.

Among the organizations that respond to flooding disasters are state and local agencies, as well as federal agencies, such as Federal Emergency Management Agency (FEMA), the National Oceanic and Atmospheric Administration (NOAA), and the United States Geological Survey (USGS). International aid in the event of natural disasters caused by flooding often includes data sharing arrangements to help our nations respond to the humanitarian crises that flooding can cause.

Surface water hydrology hazards have similar mission requirements as the solid earth hazard applications, where they need to have an up-to-date baseline data archive, rapid tasking to ensure that the satellite is collecting data on every possible orbit in case of an event, adequate spatial coverage of the target, and data quickly delivered in a georeferenced format that is easily disseminated to the emergency responders. The addition of polarimetric SAR capabilities provides im-

proved subcanopy imaging and characterization of the flood extent and will likely provide better estimates of the vegetative frictional contribution in the storm surge modeling (DESDynI Applications Workshop, 2008). Data frequency needs for the emergency responders are daily with sub-daily optimum for hazard response, and thus NISAR will not fully meet these needs on its own. Flooding, coastal inundation, and tsunami applications will greatly benefit from the high frequency data collection to assess flood duration, inundation zones, draining and habitat response.

17.4.22 Hydrology: Flood Forecasting

Flood forecasting informs downstream communities if a flood is coming and how much flooding to expect. Like a virtual stream gauge, synthetic aperture radar is able to measure changing water levels in standing vegetation as flood waters from heavy upriver rains head downstream.

Change in upstream water levels can be very useful for predicting downstream flooding. Permanent stream gauges are installed and monitored specifically for that purpose, but they are sparsely distributed. Not only

will NISAR be capable of augmenting this network of stream gauges with continuous maps of change in water level in some areas, but NISAR will also be capable of monitoring the change in the level of floods far from the main river channel, where water can increase in level and subside at different rates. The same technology can provide information about soil moisture, another parameter needed for flood forecast models.

During natural disasters, first responders often look to NASA to provide timely and valuable information to assist their work to mitigate damage and assess destruction by these common tragic events. Many federal agencies and university researchers have difficulty evaluating the health of our waterways and wetlands due to lack of information regarding the ebb and flow of food waters during normal and extreme seasonal flooding. The data from NISAR over wetland areas will be invaluable to management authorities, scientists, and local planning agencies. NISAR can meet these diverse needs through its dependable observing strategy that will collect high resolution data over 90 percent of Earth's land surface. NISAR will provide crucial information regarding flooding events, even in remote areas

FIGURE 17-35

Left: Radar false color image product near Farmerville LA (March 13, 2016, by NASA's UAVSAR) during a devastating flood. Orange and yellow areas are flooded forests, and black areas are lakes and open floods.

This type of information is invaluable for local, state, and federal agencies that provide assistance. Right: Example of the immense and costly flooding that occurred in the Farmerville region during this flood. (James Fountain, USGS)

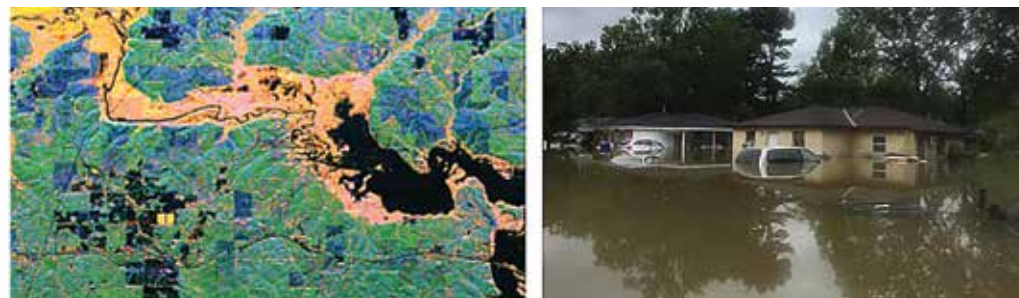
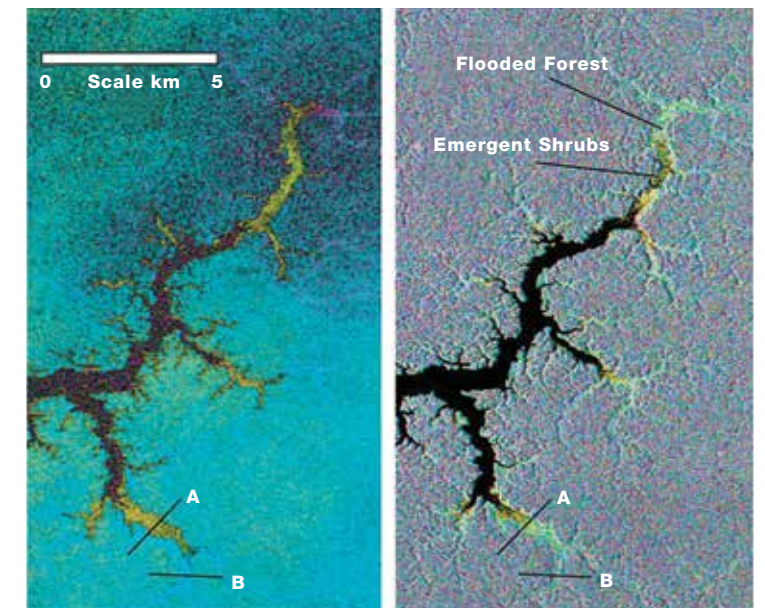


FIGURE 17-36

“Change in water level” products in flooded, vegetated areas were first demonstrated by the NASA SIR-C Synthetic Aperture Radar (SAR). In this image, centimeter-level changes in water level were measured over the Purus River in Brazil from two observations acquired just 24 hours apart. (Alsdorf et al., Nature, 2000). Colors indicate how much the water level changed between the two observations. Between transects A & B was a 1-5 cm change in water level.



without stream gauges or other sources of ground data measuring flood conditions.

InSAR can be used to precisely measure very small changes in water level in areas with standing vegetation if repeated observations by radars like NISAR, are made from the same vantage point, i.e., from the same orbit. This was first demonstrated with the NASA SIR-C mission that flew on the NASA Space Shuttle in 1994. SIR-C twice imaged the Purus River, a tributary of the Amazon–Solimões River, during flooded conditions. From these images, it was possible to measure centimeter-level changes in water level during the 24 hours that had elapsed between the observations. SIR-C demonstrated that radar could be used to make these types of measurements (Figure 17-36).

NISAR will function like a virtual stream gauge for flooded conditions that occur along most of the world's major rivers, capable of precisely measuring change in water level with every observation.

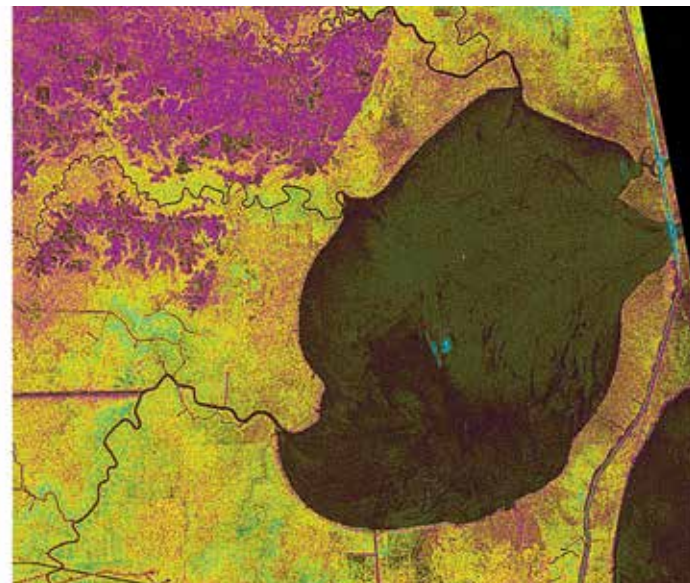
17.4.23 Hydrology: Coastal Inundation

Monitoring inundation of marshes, swamps or other flooded areas is difficult: on the ground, inundated areas can be treacherously difficult to navigate, while from above, vegetation, clouds, and weather can make the water difficult to observe. Beyond the human impact, the extent and duration of inundation has a heavy influence on fish and other wildlife habitats, vegetation health, and other parameters of ecosystem health. NISAR will allow uniquely detailed monitoring of the seasonal ebb and flow of flood waters in Earth's wetland areas, not just storm-related flooding. The NISAR all-weather and forest-penetrating radar can detect open water areas, and also the flooded areas below trees (Figure 17-37).

Many federal agencies and researchers that study wetlands have difficulty evaluating their health status due to lack of information regarding the ebb and flow of flood waters during normal and extreme seasonal inundation. NISAR imagery will provide near weekly observations that complement optical data, imaging through clouds and below the canopy. This capability makes NISAR's imaging of wetland areas valuable to

FIGURE 17-37

Dual polarization radar image of the Maurepas Lake and surrounding swamp in Louisiana. This image was acquired from space by the Japanese ALOS-2 L-band radar. In this false color image, yellow areas are the flooded Cypress Tupelo swamp, pink are unflooded areas, orange areas are degraded swamp marshes, and dark areas are open water. Image © JAXA 2016.



management authorities, scientists, and local planning agencies. NISAR will provide invaluable new and independent information regarding flooding events in disaster scenarios, as well as data to develop unique seasonal evaluations of wetland dynamics.

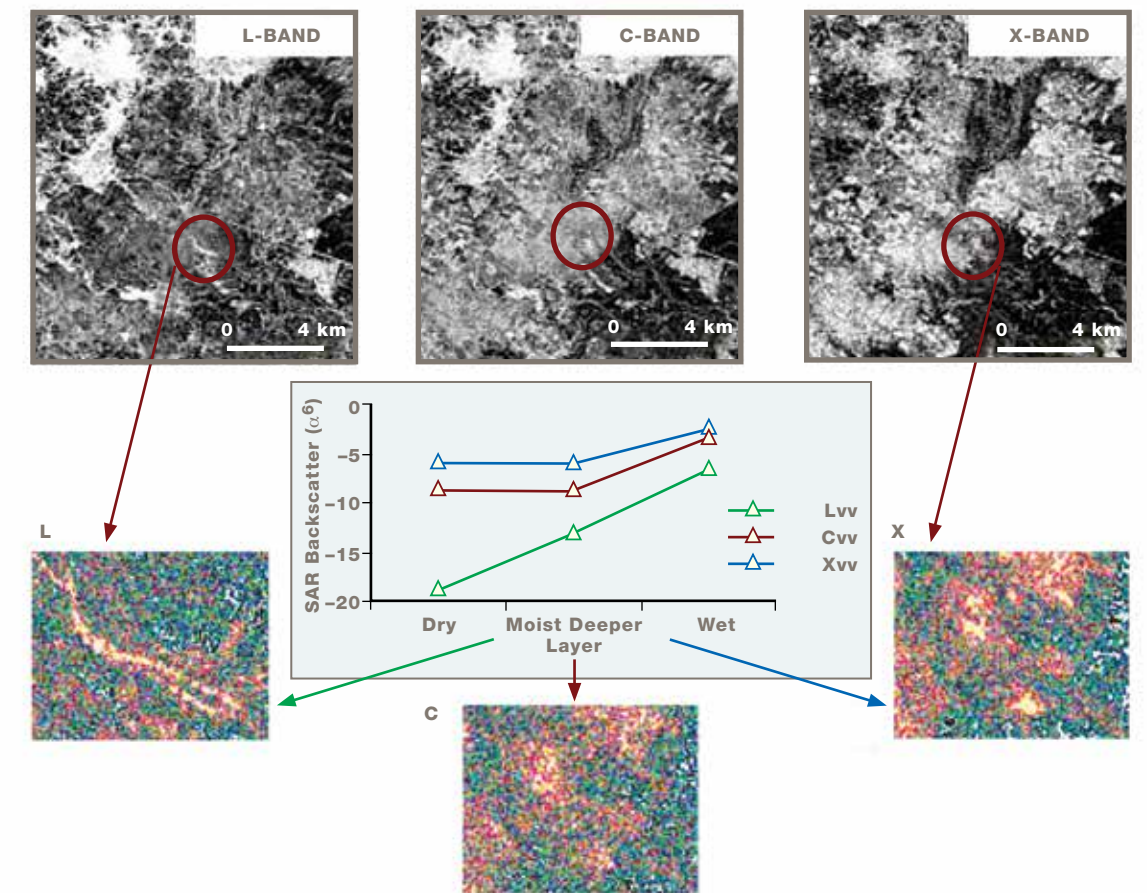
17.4.24 Hydrology: Soil Moisture

Estimating spatial and temporal variability of soil moisture globally at sufficient resolution to help manage agriculture production, assess wildfire risks, track regional drought conditions, detect spills, and contribute to surface water routing models that estimate rainfall runoff for reservoirs, water conveyance systems, and floods will benefit a wide societal cross-section. SAR backscatter is directly related to near-surface moisture content (volumetric) that changes the reflective target properties. At microwave frequencies, the dielectric constant of dry soil is around 3, while that of water is around 80 and depends on salinity. The dielectric

constant for a moist soil ranges between 3 and 30. As the dielectric constant of a material increases, the Fresnel reflectivity also increases, resulting in an increased backscatter. Radar wavelength determines the penetration depth. As longer wavelengths have higher penetration depth within the soil medium, they sense soil moisture from deeper layers as compared to shorter wavelengths. The soil surface roughness is also a function of the wavelength. For longer wavelengths the soil surface appears smoother, i.e., at L-band soil surface appears smoother as compared to C-band. Thus, the impact of soil moisture is more prominent in the L-band signal as compared to C-band.

Potential applications of multi-frequency SAR data in the field of soil moisture estimation were explored with the SIR-C/X-SAR mission over Bhavnagar, Gujarat. SIR-C/X-SAR operated in the L-, and C- and X-bands. This mission clearly showed (Figure 17-38) that L-band, and

FIGURE 17-38
Multi-frequency SIR-C response to deeper layer soil moisture



presumably that S-band, is able to sense deeper layer soil moisture, whereas, C-band and X-band are not able to sense deeper layer soil moisture due to their low penetrability within the soil medium.

A similar study conducted to understand the usefulness of L-band in soil moisture estimation over agricultural terrain used DLR-ESAR data over an agricultural area having varying surface roughness, crop cover and varying soil moisture content. This study also showed that L-band is able to capture the signature of soil moisture better than C-band.

An advantage of co-collecting L- and S-band radar imagery will be characterizing soil moisture as a function of penetration depth and differentiating phase signatures from soil penetration variations from deformation in repeat pass interferometry. While surface deformation is non-dispersive, one would expect the phase signature from soil moisture variations to be wavelength-dependent, so differences in S-band and L-band interferometric phase can be used to discriminate deformation from moisture changes.

NISAR has the potential to provide high-resolution soil moisture variability products that will contribute to each of the science components of the mission by characterizing and removing soil-moisture-induced noise within SAR imagery. The co-collection of L- and S-band imagery will provide depth dependent soil moisture variability and will help isolate and remove soil moisture phase noise in targeted deformation interferograms. This combination will lower the detection threshold for resolving subtle and transient deformation in NISAR imagery. The resolution of the NISAR imagery will be at a level that can be used to manage crops, help estimate wildfire probability, constrain snowpack water content (see Section 17.3.2), develop water routing and flooding numerical models, and detect spills.

17.4.25 Underground Reservoirs: Groundwater Withdrawal

Extraction of groundwater often causes the aquifers to contract at depth that in turn causes the overlying ground surface to subside. The water in the aquifers, called groundwater, is an extremely valuable resource, like a water savings account that can be drawn on when times are hard. The water in the aquifers originally was precipitation that made its way down through the soil and rock via cracks and pores. All aquifers are not created equal: aquifers can hold small or vast amounts of water and recharge quickly or slowly depending upon the type of rock both in and above the aquifer. The rate of groundwater extraction often increases rapidly during droughts when surface water is not available to supply demand for water. Groundwater is extracted from aquifers in every U.S. state and nearly every country around the world, so this is a widespread issue.

Ground subsidence due to groundwater withdrawal can have many effects on infrastructure and buildings. These can extend from cracks in roads and bridges to reduction in freeboard on levees, canal walls, and dams to large-scale changes in runoff, river flow, or coastal flooding. Large amounts of contraction in aquifers can also damage the water extraction wells themselves and require costly redrilling. The contraction of the aquifers when water is extracted usually includes both temporary elastic contraction that can be recovered when the water is replaced and permanent deformation that cannot be recovered. When aquifers are permanently deformed, they lose capacity to store future water.

Sustainable, low impact groundwater extraction is possible, though, given information about the aquifer and the surface changes associated with pumping. This is where imaging by satellite radars capable of measuring changes in surface elevation, like NISAR, has

immediate and practical value. NISAR will image global land areas every 12 days, providing a time series of the surface uplift and subsidence. This information shows both the long-term decline in surface elevation, which corresponds to unrecoverable loss or slow recharge of groundwater, and a seasonal cycle of uplift and subsidence that correlates to a sustainable balance between precipitation and withdrawals. Armed with this information, users can protect this valuable renewable water asset over the long term, avoiding the terrible consequences of permanent loss of water supply.

17.4.26 Underground Reservoirs: Oil and Gas Production

Efforts to utilize subsurface resources, including water, oil, gas, and geothermal power, necessarily involve the extraction and injection of large volumes of fluid from the ground – often in areas that also host valuable infrastructure and large population centers. Groundwater effects were described in the previous section. Oil, gas, and geothermal extraction operations affect a subset of the United States and other countries around the world, but new technologies, including hydraulic fracturing, have expanded the areas. Oil and gas are extracted from a wide variety of rock reservoir types and depths, using a large range of methods. Geothermal power is often extracted from the ground by pumping water out of hot rocks.

Withdrawing fluid from rocks at shallow depths without replacement will cause compaction within the reservoirs and subsidence of the overlying land surface similar to the compaction of groundwater aquifers and its associated surface subsidence. Extracting heat from geothermal reservoirs can also cause the rocks to contract and subsidence of the surface. Some advanced methods of oil and gas extraction involve the injection of water or steam into the reservoirs to stimulate extraction. If injection volumes exceed extraction, then the ground surface above may move upward. Geothermal operations may also involve greater injection than extraction, leading to uplift of the surface. In some cas-

es, the oil and gas extracted includes a large amount of wastewater that requires disposal. In most places wastewater is reinjected into rocks at depth, which can cause induced seismicity, which is described in another section.

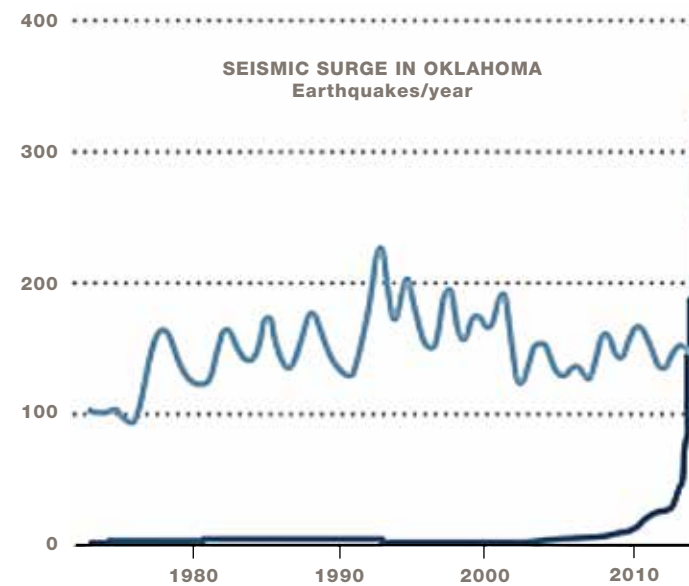
The NISAR satellite mission will provide high-resolution ground movement maps on a global basis with weekly sampling. Observations will be uninterrupted by weather and facilitate safe resource development by improving understanding of processes that impact regions undergoing active extraction or injection of subsurface fluids, including oil, gas, and geothermal power. The observations made over the lifetime of NISAR will be a giant step forward in our understanding of subsurface fluid flow and associated seismicity and will inform the next generation of methods for characterizing and managing these resources.

17.4.27 Underground Reservoirs: Induced Seismicity

Earth scientists have been investigating earthquakes of tectonic origin for more than a century, developing significant insights and understanding about where they occur, how frequently they occur, their links to geologic structures and processes, their magnitude distribution, and how frequently main shocks trigger aftershocks. For the past 40 years, and particularly over the past decade, a new class of earthquakes has become increasingly important – earthquakes induced or triggered by human activities. Human activities hypothesized to have caused earthquakes, in decreasing order of numbers of suggested instances (e.g., www.inducedearthquakes.org) include mining, water reservoir impoundment, conventional hydrocarbon production, fluid injection including disposal of wastewater associated with hydrocarbon production, geothermal energy production, hydraulic fracturing, groundwater extraction, and carbon sequestration. The recognition that human activity can trigger earthquakes has led to great concern among government, industry, and the public.

FIGURE 17-39

Increasing rates of earthquakes in the central United States. Recent advances in the technology used in hydrocarbon production, including enhanced oil recovery and increases in the volume of wastewater injected into the subsurface, are associated with a dramatic increase in earthquakes felt in the central United States since the mid-2000's. Damaging earthquakes only appear to be related to a small fraction of wells, but there is not yet enough data to definitively determine in advance the safety of operations at a particular site. Seismology can tell us the response of Earth's crust to forcing by fluid injection and production. However, seismic data is blind to the slow, longer term deformation of the ground surface associated with pumping, injection and even incipient creep on faults that will eventually rupture in a more damaging earthquake. NISAR can provide the missing link to this puzzle, complementing the available seismic data and helping to track how patterns of fluid flow beneath the surface relate to patterns of observed earthquakes.



Number of earthquake sequences each year that contain at least one magnitude 3 or larger earthquake, since 1973, for California (light blue) and Oklahoma (dark blue). From McGarr et al., 2015, in the journal *Science*.

Some instances of earthquakes that may be triggered by human activity occur in regions that naturally experience frequent earthquakes (e. g., California, Italy, Spain, Tibet). Others, such as those in the 21st century in the central United States and the Netherlands, represent a significant change: Oklahoma now experiences more earthquakes each year than California (Figure 17-39). Efforts to reduce our society's reliance on fossil fuels also compound the problem, with increases in earthquake frequency associated with energy production at geothermal power plants and at dams that contribute hydrothermal power to the grid.

The increased frequency of triggered and induced earthquakes creates new challenges, particularly since the energy and resource needs of our population are likely to continue to grow. Even forecasting the expected damage from these new types of earthquakes is not just "business as usual." Analyses of shaking reports from the central United States and the Netherlands sug-

gest that the distribution of damage from these earthquakes, which tend to be shallower, are different from the damage expected from "traditional" earthquakes, which often occur deep underground.

Satellite-based radar imagery, when available, can be an extraordinary tool for characterizing how Earth's surface warps and deforms before, during, and after induced earthquakes. The examples of induced earthquakes in the central United States (Figure 17-40) are cases where we were fortunate to have data both before and after the earthquake. Many other earthquakes in these regions have been impossible to study because of the complete lack of data before the event. This situation should change in the future: NISAR data would be acquired regularly over the entire United States, allowing imaging of areas like Oklahoma, Texas and Kansas that have both active agriculture and hydrocarbon/water resource development.

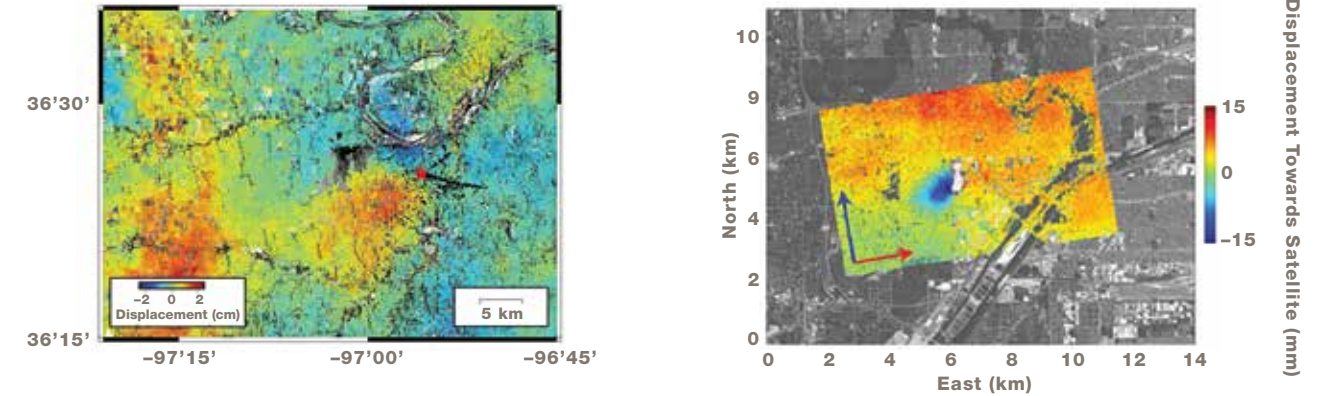


FIGURE 17-40

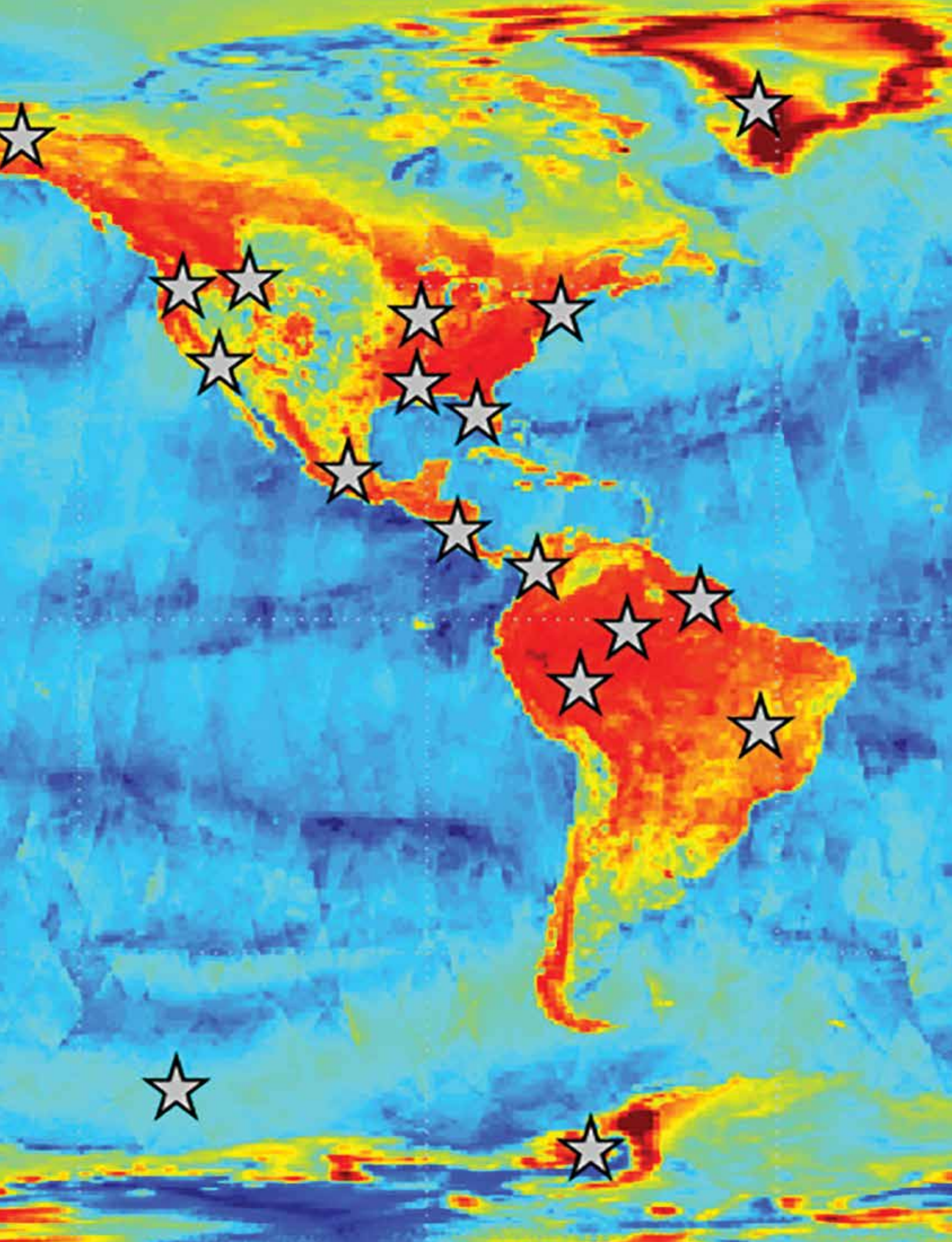
Left: NISAR data will permit systematic mapping and monitoring of earthquakes, even in agriculturally active areas. In this example, using data from the European Space Agency's Sentinel-1a and -1b platforms, we can see several centimeters of displacement over a 10 km x 10 km region associated with the 2016 magnitude 5.8 Pawnee, Oklahoma, earthquake. The main earthquake location (red star) and aftershocks (black dots) outline a complicated pattern that provides insight into the patterns of weakness in the subsurface. The red band on left is the signature of a large storm that was present during one of the image acquisitions. When many images are available, such as would be provided by NISAR, such atmospheric effects can be averaged out more

effectively to determine the true ground movement. Right: Even tiny earthquakes can be imaged when enough data is available. This image uses data from the European Space Agency's TerraSAR-X platform to constrain subsidence of the ground during a 2013 magnitude 3.2 earthquake within the Chicago metropolitan area, triggered by a blast at a limestone quarry. Color indicates displacement of the ground surface towards or away from the satellite, which was traveling to the northwest in the direction of the blue arrow and aimed down towards the Earth in the direction of the red arrow. The observed displacement shown here tightly constrains the depth of this earthquake to 700 meters, much shallower than the zone where "natural" earthquakes occur.

17.4.28 Rapid Damage Assessment

A key need after disasters, with both natural and human-induced causes, is a rapid assessment of damage to buildings and other infrastructure. Frequent coverage of the land areas by imaging radar satellites, including NISAR, enables all-weather assessment of damage with measurements of coherency changes. Processing of a damage proxy map, or change detection map, can show areas of potential damage very quickly after the radar data is received. This method has been demonstrated for a wide variety of disasters, including earthquakes, tsunamis, volcanic eruptions, hurricanes, tornadoes, and landslides.

One example of rapid damage proxy mapping was after a magnitude 7.8 earthquake hit central Nepal on April 25, 2015. The quake killed nearly 9,000 people and induced more than 4,000 landslides in the precipitous valleys of the Himalayan Mountains. Widespread building damage was rapidly mapped using radar data acquired by Italian COSMO-SkyMed and Japanese ALOS-2 satellites. The maps were quickly released to national and international responding agencies. Field crews were dispatched to damaged sites and made ground observations guided by the maps, and a satellite operating company used these maps to target areas for imaging with ultra-high resolution spaceborne optical sensors.



18 APPENDIX F IN SITU MEASUREMENTS FOR CAL/VAL

18.1 SOLID EARTH IN SITU MEASUREMENTS FOR CAL/VAL

Solid earth measurements for Cal/Val requires determining time dependent rates of crustal deformation from tectonics. Active and passive sites are needed for Cal/Val of permafrost deformation.

18.1.1 Coseismic, Secular, and Transient Deformation Rates

The most direct validation of NISAR solid earth deformation measurements is with continuous GNSS measurements of ground displacements. For individual point locations, GNSS provides continuous time series of 3-component vector ground displacements that can be projected onto the SAR line-of-sight imaging direction to allow direct comparison with InSAR-derived displacement/velocity observations. Validation will be repeated annually in order to assess improvements with increased numbers of image acquisitions and to detect any potential degradation of the system.

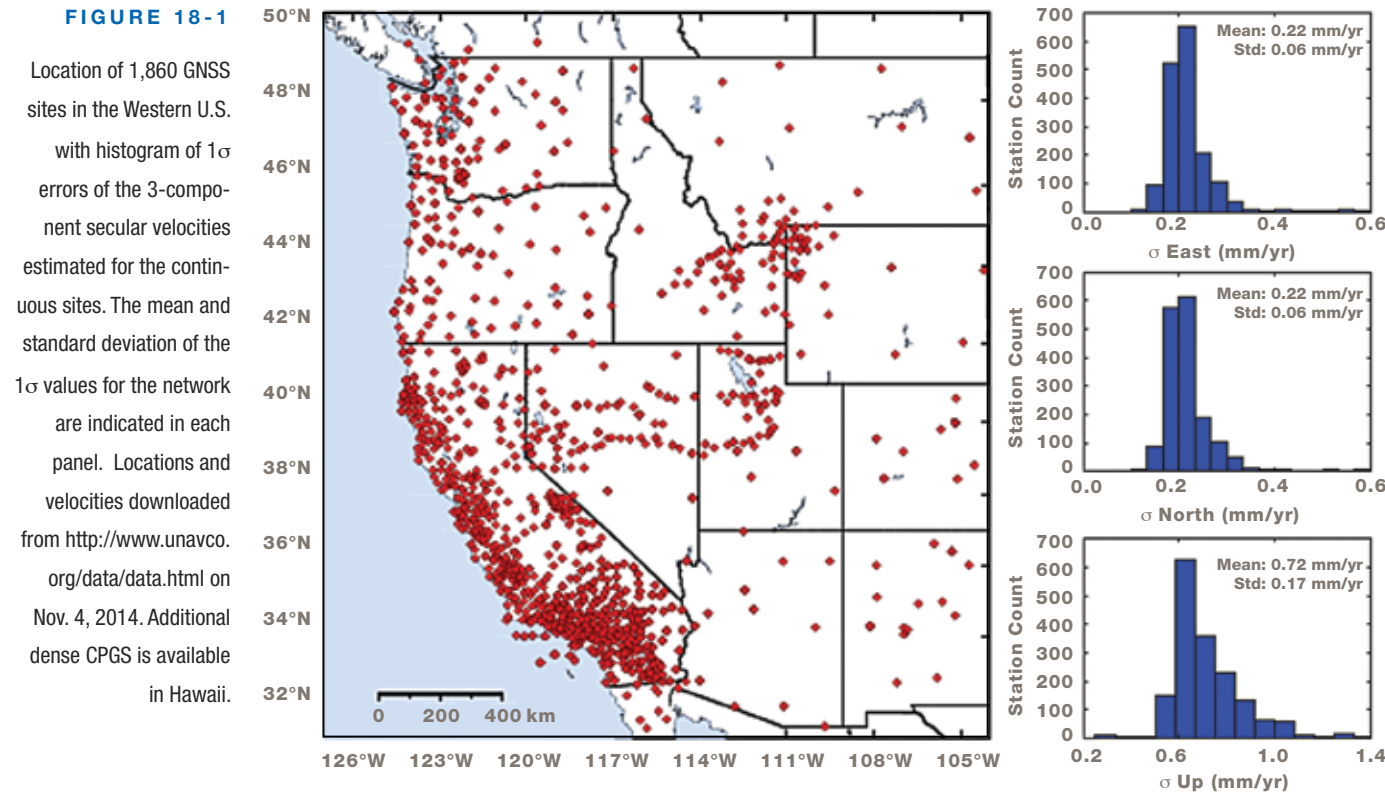
Comparisons of GNSS and InSAR observations will be done in regions where many (5+) GNSS observations are available within the footprint of individual InSAR data products (e.g., coseismic displacement map, velocity map, etc.). GNSS secular velocities are now routinely estimated at $1-\sigma$ levels of (0.2, 0.2, 0.6) mm/yr (east, north, up) – significantly better than NISAR's L2 requirements (Figure 18-1). Similarly, coseismic offsets can be estimated at $1-\sigma$ (0.8, 0.5, 1.3) mm (east, north, up) using 30-second position solutions (Liu et al., 2014), and significantly better using daily solutions. Generally, validation will occur in locations with stable, linear ground motion, i.e., with no events generating transient displacements, by comparing

background noise levels. Validating the ability to detect transients will be done by assessing agreement of contemporaneous GNSS and InSAR measurements of seasonal quasi-periodic displacements where these are known to occur (e.g., over shallow confined aquifers) (e.g., Lanari et al., 2004). Different length scales will be analyzed to validate performance over the length scales described in the L2 requirement.

This parameterization of ground deformation has a long heritage, both in the analysis of GNSS time series and more recently with InSAR data (e.g., Blewitt, 2007, Hetland et al., 2012, Agram et al., 2013). The project will have access to L2 position data for continuous GNSS stations in third-party networks such as NSF's Network of the Americas (NOTA), the HVO network for Hawaii, GEONET-Japan, and GEONET-New Zealand, which are located in target regions for NISAR solid Earth Cal/Val. Station data are post-processed by analysis centers that include NSF's GAGE Facility and the Nevada Geodetic Laboratory at the University of Nevada Reno (UNR), are freely available, and have latencies of several days to weeks. Current networks contain one or more areas of high-density station coverage (2~20 km nominal station spacing over 100 x 100 km or more), which will support validation of L2 NISAR requirements at a wide range of length scales. Future GNSS networks are likely to have even greater station density due to ongoing infrastructure investment at the federal and state levels.

SECULAR, COSEISMIC, AND TRANSIENT DEFORMATION CAL/VAL SITES

After assessing the current national infrastructure for GNSS processing and data availability, the NISAR Solid



Earth Science team decided to use the GNSS station displacement time series produced by the UNR Geodetic Laboratory for NISAR Cal/Val. The UNR dataset has global station coverage, uses the openly available GIPSY processing software written and maintained by JPL, and has been produced continuously for over a decade. UNR funds its operations via a mix of federal (NASA, NSF, USGS) and state (Nevada Bureau of Mines and Geology) support. Other processing centers in the U.S. (NSF's GAGE facility, JPL's MEaSURES program) currently process fewer stations globally and in North America, but they make their data openly available and would serve as a backup in the case of disruption to UNR funding or operations, mitigating the risk to the project of using a single processing center.

The GNSS displacement time series used for NISAR Cal/Val will be consistently processed across all Cal/Val sites. Additionally, the NISAR SES team will provide (either through its own work, or by linking to openly available data) corrections for offsets in GNSS time

series due to GNSS-specific instrument changes that would not appear in InSAR time series. GNSS and InSAR displacements also differ in their treatment of solid Earth and ocean tides, neither of which is currently included in NISAR's InSAR processing suite. In the case of solid Earth tides, UNR corrects GNSS displacements using IERS 2010 conventions, although it does not remove the permanent tide. Ocean tide load displacements are modeled and removed using the FES04 model, semiannual tidal loading is removed per IERS 2010 conventions using the hardisp.f program, and all load calculations are made relative to Earth's center of mass. The SES team will facilitate the development of the phase corrections needed to remove these tidal components in NISAR's interferometric products. These networks will contain one or more areas of high-density station coverage (2~20 km nominal station spacing over 100 x 100 km or more) to support validation of L2 NISAR requirements at a wide range of length scales.

The Cal/Val sites where the algorithms will be calibrated and the science requirements validated are listed in Table 18-1.

18.1.2 Permafrost Deformation

As InSAR is inherently a relative measurement, the calibration and validation of permafrost deformation measurements involves (1) the identification of suitable reference points (calibration) to tie NISAR measurements to an absolute datum, as well as (2) the provision of a suitable number of validation points that can be used to analyze the permafrost deformation accuracy that could be achieved by the NISAR system.

In the past, the community has used the following data types for calibration and validation of InSAR-based permafrost measurements:

- Dry floodplain areas as no-deformation sites (Liu et al., 2014; Liu et al., 2010).
- Dry margin of drained lake basins as no-deformation sites (Liu et al., 2013).
- Modeled seasonal subsidence at CALM grids based on active layer thickness and assumed soil water content (Schaefer et al., 2015).
- Bedrock outcrops as no-deformation sites.

TABLE 18-1. TABLE OF SOLID EARTH SCIENCE Cal/Val REGIONS (CHOSEN TO REPRESENT DIVERSITY OF TARGETS AND GPS COVERAGE). BHUJ, INDIA SITE IS TBD

Site Location	Köppen Classification*	Climate	Characteristics Relevant To Cal/Val
Desert, Scrub, Savanna			
Central Valley, CA	Csa	Temperate Dry/Hot	Agriculture, soil moisture, no relief
LA Basin/Mojave	Csa, Bsh	Temperate Dry/Hot, Arid/Steppe/Hot	Urban, range of relief and decorrelation sources, change in base elevation
Long Valley Caldera	Bwk	Arid/Steppe/Cold	Variable relief, snow, ground type
Bhuj, India	Bsh	Arid/Steppe/Hot	Climate, salt flats, seasonal flooding, agriculture
Mejillones, Chile	Bwk	Arid/Steppe/Cold	Hyper-arid, ionosphere, large relief, change in ground type
Mixed Forest			
SW of Portland, OR	Csb	Temperate Dry/Warm	Big trees, forestry, rain
North Island, NZ	Cfb	Temperate Wet/Warm	Southern latitude
Houston/Galveston	Cfa	Temperate Wet/Hot	Southern U.S. climate, swamps, urban, no relief
Oklahoma	Cfa	Temperate Wet/Hot	Agriculture, strong atmosphere, no relief
Nepal	Csa	Temperate Dry/Hot	Monsoon, relief, agriculture, atmosphere
Maritime Tropical			
Big Island, HI	Af, Aw, As	Tropical/Rainforest, Tropical/Savanna	Rain forest, relief, tropical climate, island, lava flows
Maritime High Latitude			
Unimak	Dfc	Cold/Wet	Arctic, ocean island, unstable atmosphere, relief, snow
Permafrost			
Dalton Highway, AK	ET	Polar/Tundra	Permafrost, northern climate, tundra, ionosphere

*Köppen climate classification codes can be found at https://en.wikipedia.org/wiki/Köppen_climate_classification

- e) Differential GNSS measurements (Iwahana et al., 2016).
- f) Thaw Tube measurements (Short et al., 2014).

Traditionally, data types (a) – (d) were predominantly used for algorithm calibration while (e) – (f) were used for measurement validation.

In addition to validating deformation measurements directly, Schaefer et al. (2015) used a more indirect approach and validated the InSAR-estimated active layer thickness (i.e., a higher level product) with the ALT measured from GPR and probing.

In this effort, we will use a combination of previously used methods for both algorithm calibration and requirement validation.

Validating surface deformation estimates in permafrost regions is difficult due to the extreme seasonality and often remote regions covered by this requirement and due to the fact that in-situ measurements of permafrost deformation are difficult to conduct without disturbing the soil and vegetation. Since the ground thermal regime is largely controlled by the surface mat of organic soils, peats, and/or vegetation any major disturbances to the land cover can lead to subsequent thaw and surface subsidence. To minimize disturbance, our strategy for validation will include two components. First, we will use ground-truth data at sparse locations with known surface deformation to assess the accuracy of NISAR-based permafrost deformation measurements. Second, we will perform statistical analyses of selected NISAR observations to arrive at robust estimates of the achieved precision of NISAR products.

For accuracy assessment, we will use the following types of ground-truth information:

1. We will adopt the common assumption that dry floodplain areas are free of seasonal surface deformation (Liu et al., 2014; Liu et al., 2010). To

a large extent, this assumption is based on the fact that low ice content sandy soils and coarse gravels present in floodplain deposits show very little potential for settlement or upheaval (Pullman et al., 2007). Additionally, the heat transfer from streamflow and spring flooding often causes the permafrost surface to be several or even tens of meters under the riverbed and reduces prevalence of ice-rich permafrost, further contributing to a reduction of long-term thaw settlement (Liu et al., 2010). Dry floodplain areas will be used both for calibration and validation.

2. Bedrock outcrops in the vicinity of target permafrost regions will be used as both calibration and validation points in similar ways.
3. In addition to these natural areas, regular field measurements at a small set of easy-to-maintain road-accessible locations should be taken.

Two general types of calibration and validation sites will be used for this effort, including sites designated as “passive” and “active,” depending on the efforts needed for their maintenance:

- Passive Cal/Val sites include gravelly flood plains (sites of type (1)) as well as rock outcrops (sites of type (2)). These sites do not need to be maintained long term. Pre-launch tests at passive Cal/Val sites should be conducted to verify their suitability for this effort.
- Additionally, “active” calibration sites should be maintained.

Sites should have historic records of repeated thaw-depth measurements at fixed locations (several repeated measurements per thaw season), soil moisture, and galvanic electrical resistivity tomography measurements. Repeated airborne lidar measurements are also desirable for all proposed sites, providing information on long-term surface elevations. Historic (5 years and counting) thermistor measurements are available at all sites.

Many potential passive calibration sites have been used in previous research studies either as reference location or as a means for validation (i.e., Bartsch et al., 2010; Liu et al., 2014; Liu et al., 2012).

For the active Cal/Val sites, historic records of repeated thaw-depth (several repeated measurements per thaw season), soil moisture, and galvanic electrical resistivity tomography measurements should have been collected in the past. Repeated airborne lidar measurements are desirable for all proposed sites, providing information on long-term surface lowering. Historic thermistor measurements should be available at all sites. Future field work will be required at some sites. Field work measurements will include:

- Thaw-depth measurements along the transects (every 4 m) following measurement protocols established by the NASA ABoVE team.
- Soil moisture measurements according to ABoVE protocols.
- Deformation measurements using differential GNSS equipment.
- Annual ground penetrating radar measurements at the beginning and end of the thaw season.
- Field work should be conducted twice per season, at the beginning (mid May) and the end (early October) of the thaw season.

Cal/Val sites for permafrost deformation fall into three categories:

- Dry floodplain areas.
- Bedrock outcrops in the vicinity of target permafrost.
- Easy-to-maintain road accessible locations where regular field measurements will be taken.

Two general types of Cal/Val sites will be used for this effort, “passive” and “active,” depending on the efforts needed for their maintenance:

- Passive Cal/Val sites include gravelly flood plains (sites of type (1)) as well as rock outcrops (sites of type (2)). These sites do not need to be maintained long term. Pre-launch tests at passive Cal/Val sites should be conducted to verify their suitability for this effort.
- Active calibration sites must be maintained (see Table 2.)

Active sites should have historic records of repeated thaw-depth measurements at fixed locations (several repeated measurements per thaw season), soil moisture, and galvanic electrical resistivity tomography measurements. Repeated airborne lidar measurements are also desirable for all proposed sites, providing information on long-term surface elevations. Historic (5 years and counting) thermistor measurements should be available at all active sites. Measurements should be acquired twice a year (at the beginning and the end of the thaw season) at these active sites, all currently maintained by the Cold Regions Research and Engineering Laboratory (CRREL) for many years. CRREL is a part of the U.S. Army Corps of Engineers Engineer Research and Development Center.

TABLE 18-2. ACTIVE PERMAFROST SITES IN ALASKA

Site Name	Center Coordinates	Site Owner
Permafrost Tunnel	64°57'3.61"N 147°36'51.48"W	CRREL
Farmers Loop West	64°52'33.83"N 147°40'47.83"W	CRREL
Farmers Loop East	64°52'32.24"N 147°40'23.14"W	CRREL
Creamers Field	64°52'3.53"N 147°44'17.72"W	CRREL
Goldstream	64°54'41.80"N 147°50'59.24"W	CRREL

18.2 CRYOSPHERE IN SITU MEASUREMENTS FOR CAL/VAL

Cal/Val for cryosphere requires comparing NISAR to known fast and slow ice velocity measurements. Horizontal and vertical velocities will be measured using GNSS and compared. Drift buoys will be used to validate sea ice velocities.

18.2.1 Fast/Slow Deformation of Ice Sheets and Glacier Velocity

The main validation approach for the ice sheet and glacier requirements will be to compare NISAR-derived velocity with points of known velocity. In particular, the science team and project personal will use stationary points (exposed bedrock) and velocities measured with GNSS on moving ice.

Residuals on rock will provide hundreds to thousands of zero-velocity validation points to allow monitoring of several sources of error, particularly the ionosphere. While these points are extremely useful, other data are needed to supplement exposed bedrock because:

- Bedrock data have zero motion and provide no information about slope correction errors
- Scattering characteristics are different for rock and firn surfaces, resulting in generally lower correlation over firn

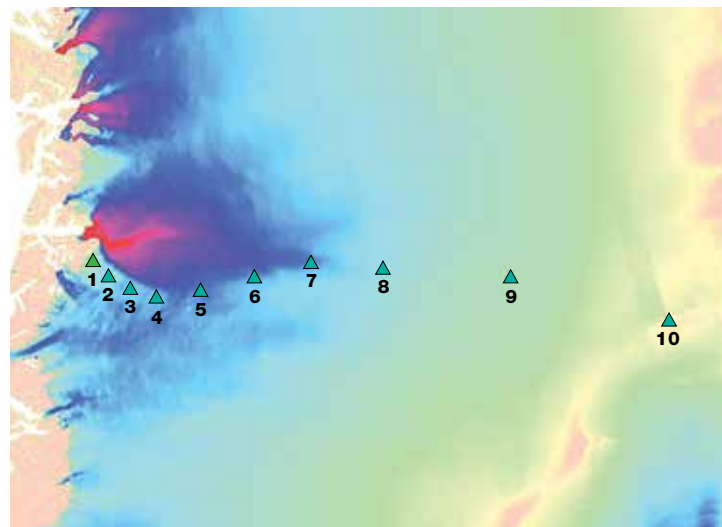
- Bedrock points don't provide information about other ice-related effects (e.g., vertical motion associated with firn compaction).
- As a result, GNSS data on moving ice will also be used to help validate ice-sheet velocities.

Greenland has the full range of snow facies, ranging from wet snow through percolation to dry snow. Hence, the mission will install 10 GNSS receivers along a divide-to-coast line to validate observations for all snow facies and melt states (Figure 18-2). The GNSS will operate throughout the 3-year mission and will collect data with at least daily frequency (e.g., daily 2-hour segments), foregoing continuous (e.g., 15-s) sampling at least during the winter when power is limited. Daily sampling will allow estimation of velocity for any 12-day interval, allowing validation of multiple overlapping tracks that cover the GNSS line (e.g., Figure 18-2).

These measurements will provide a consistent validation time series throughout the mission. These sites will be equipped with Iridium links to reduce data latency. Such methods are used routinely and no new technology development is required. Sites will be deployed near launch and maintained with annual service visits. With at least 60 observations per year per site, 10 stations will provide a robust statistical sample for validation (10 x 60 x 3=1800 individual image pair comparisons).

FIGURE 18-2

Preliminary locations of sites used for NISAR ice velocity validation. Final adjustment of points will occur just prior to deployment to take into account and avoid hazards such as crevasses. The locations of the points are designed to span a wide range of surface types and conditions, ranging from rapidly melting bare ice, to radar bright percolation zone where there is strong refreezing of summer melt, to the radar-dark interior of the ice sheet where accumulation rates are high.



While most of the GNSS receiver locations will be placed on slower moving ice (<100 m/year). To the extent that there are no safety issues, some GNSS devices will be placed on faster moving locations to validate the fast flow requirements.

18.2.2 Vertical Displacement and Fast Ice-Shelf Flow

GNSS receivers will also be placed on an ice shelf in Antarctica to validate the Vertical Differential Displacement Measurement requirement. These measurements also will contribute to validating the fast deformation rates (ice shelves have large areas of fast flow with few crevasses, making them well suited to GNSS deployment with little risk to the personnel installing them). Specifically, the project will deploy 4 GPS receivers at locations on an ice shelf near the grounding lines of major ice streams. To minimize logistics costs, this deployment likely can be carried out by UNAVCO personnel who staff McMurdo research station each Austral summer. These measurements will serve three

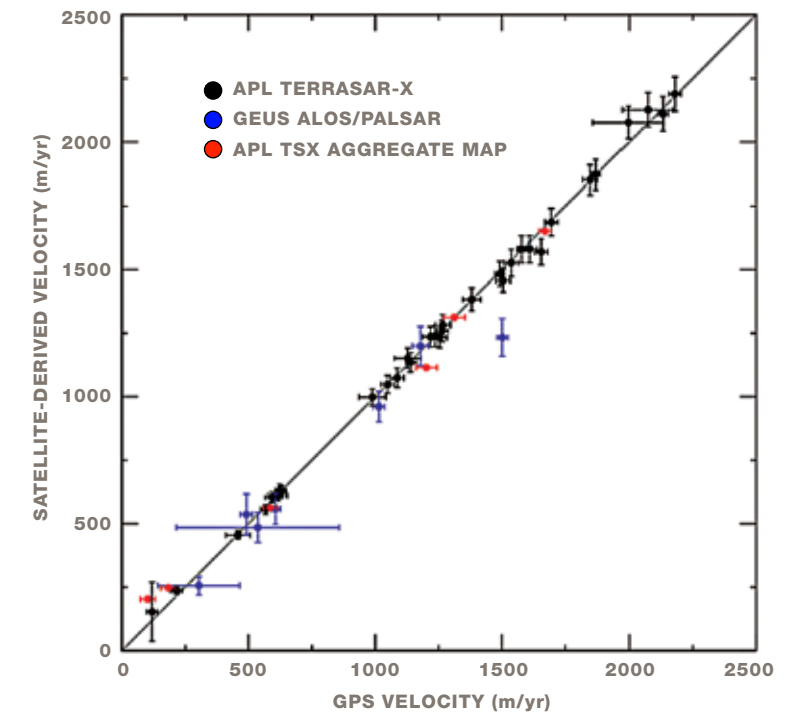
primary functions beyond those receivers deployed in Greenland. Specifically, they will:

- Provide data to validate the vertical differential displacement measurement requirement, as they measure vertical motion due to tidal displacement.
- Provide data to validate velocity requirements in regions that will rely on a tide model for correction.
- Provide information about the variability of the ionosphere in the southern hemisphere.

In addition, the mission also will piggyback on other independently funded logistics (i.e., ongoing field projects). In particular, these measurements are better suited to fast-flowing areas because the investigators are working in areas where they know the hazards and are doing only short term (a few weeks) deployments. In any given year, several independently funded investigators have GNSS stations on the ice in Greenland and Antarctica, although several years out from launch we have no firm knowledge with regard to from whom, when, and where the measurements will come. While such results will not provide the sampling consistency

FIGURE 18-3

Example of validation of SAR-derived glacier velocity data using GNSS (Ahlstrøm et al., 2013).



of project-supported sites, they will greatly expand the spatial coverage, particularly on fast moving ice.

An example of a validation using velocities derived from TerraSAR-X and ALOS is shown in Figure 18-3. In addition to validating results, the GNSS data will be useful for determining and analyzing the impact of the ionosphere's total electron content (TEC) on velocity measurements (Meyer, F. 2014).

Beyond GNSS, the mission will evaluate NISAR products against those derived from other spaceborne sensors (other SARs and optical) by science team and members of the larger community. This activity will help establish that there are no frequency, sweep-SAR or other sensor specific differences.

18.2.3 Sea Ice Velocity

For NISAR, sea ice velocity products will be validated using displacement comparisons with drift buoys. The deformation-related output products generated by the NISAR sea ice tracker (divergence, shear, rotation) will not be validated due to the significant expense of mounting an appropriate field campaign and because these quantities are not included in the Level 1 or Level 2 requirements. Errors in measurements of sea ice velocity trajectories, derived from image pairs, come from two primary error sources: errors in determining the location of ice in the second image that corresponds to the same ice in the initial image, and errors in the geolocation of either of the two images. The geolocation accuracy of NISAR is expected to be better than 10 m. Thus, the primary source of error is expected to come from the first source. Ambiguities in identification of the same ice in two images can arise from deformation and rotation of the ice field, SAR system noise, and variance in backscatter due to environmental conditions that results in reduced contrast of ice features such as ridges. One factor that can affect variations in ice ambiguities in SAR imagery is the repeat sampling interval of the image pairs. In general, previous studies show that 3-4 day intervals are suitable for tracking sea ice within the central pack. For sea ice within the marginal ice zones,

shorter repeat intervals of 1-2 days enhance tracking performance largely due to faster ice velocities often encountered in the outer ice zones where the ice is freer to move and less encumbered by surrounding ice. Another source of error will come from the in situ drift buoy data set used for SAR validation.

The most common approach to validate sea ice velocity (m/s) is by comparison of displacements derived from the SAR imagery with those from drift buoys, which is what will be done for NISAR. Sea ice drift buoy data are available from multiple sources, supported by other research programs. The International Arctic Buoy Program (IABP; <http://iabp.apl.washington.edu/>) began measuring sea ice motion using drift buoys in the Arctic Ocean in 1979 and continues this effort to the present day. This multi-country funded long-running program is expected to continue through the NISAR mission and well into the future. The position error for the older buoys reported by the IABP using the Advanced Research and Global Observation Satellite (ARGOS) positioning system was ~0.3 km (Thorndike and Colony, 1982; Rigor et al., 2002). Current buoys using GNSS have reduced this error to ~10 m or less and provide daily products at 1-hour intervals. Buoys are deployed in the fall or winter on thick sea ice intended to last through the summer, often remaining within the Arctic Ocean more than one season before exiting out of the Fram Strait. Often up to 15-20 buoys may be present at any one time (Figure 18-4). Additionally, drift buoys are being deployed that include ice and snow thickness measurements (<http://imb.crrel.usace.army.mil/buoyinst.htm>) as well as upper ocean properties (<http://www.whoi.edu/page.do?pid=20756>; <http://psc.apl.washington.edu/UpTempO/>), which can be added to the analysis pool. There is a parallel program for the Southern Ocean named International Programme for Antarctic Buoys (<http://www.ipab.aq/>), however the coverage is less dense due to deployment logistics and the typical shorter buoy lifespans of <1 year due to the seasonal nature of the ice cover in that region.

Cal/Val data for sea ice velocity will be provided by non-project supported sea ice drift buoys deployed every year in sea ice regions of the Arctic and Antarctic oceans. A representative array would consist of 10 or more GNSS buoys semi-randomly distributed across the Arctic which could be sampled over a period of time (between 15-30 days, for example) with consistent SAR-derived motion fields. The buoy positions reflect the continuous motion of the ice as well as provide indications of deformation events of the sea ice cover over time. The accuracy of the trajectories derived from both the drift buoys and the SAR will be compared during selected winter and melt periods and in both polar regions depending on buoy availability.

The two primary sources of error measuring ice motion with tracking of image pairs are the absolute geographic position of each image pixel and a tracking error, which is the uncertainty in identifying common features from one image to the next image. Ice drift buoys are fixed in the ice upon which they are deployed. Buoy position errors depend on the positioning systems utilized (e.g., GNSS), as discussed above. The comparison between SAR and buoy ice motion tracking then combines the errors in SAR geolocation, tracking, and buoy positioning. The buoy locations will be estimated for the SAR-derived positions and measurement times using the once hourly drift buoy data with linear interpolation.

The errors in motion that will be derived include 1) absolute geographic position error (provided by the project), 2) tracking errors between pairs of images, and 3) the mean magnitude and standard deviation of the displacement differences between SAR-derived and buoy-derived displacements.

The uncertainties in ice displacement, u , and spatial differences derived from SAR imagery are discussed by Holt et al. (1992) and Kwok and Cunningham (2002). The error in u has a zero mean and a variance of

$$s_u^2 = 2s_g^2 + s_f^2$$

where s_u and s_y are uncertainties in the geolocation of the image data and the tracking of sea ice features from

one image to the next, respectively. Locally, where the geolocation errors between two images are correlated when the points are close together, the calculation of spatial differences to determine velocity is no longer dependent on the geolocation error of the data and the error tends to s_f^2 (Kwok and Cunningham, 2002).

The SAR-derived trajectories are derived from sequential images obtained over a few days interval (approximately 3-5 days with NISAR) based on 5-km grids, with four known grid corner points, using the Eulerian technique. Using the 1-hourly buoy data, a buoy position is linearly interpolated to the time of SAR image A. Then the nearest grid point in Image A to the buoy position is determined. If the distance between the 2 points is less than 3 km, this pair of points is retained for analysis, Image A (x, y) and interpolated buoy (x, y). Then the buoy position is interpolated to the time of Image B to obtain buoy (x', y'), which is compared to the same grid point from Image A now in Image B (x', y'). The difference in displacement D between the SAR-image pair (s) and the interpolated buoy (b) is then derived for each comparison,

$$u_s = ((s_x' - s_x)^2 + (s_y' - s_y)^2)^{1/2}$$

$$u_b = ((b_x' - b_x)^2 + (b_y' - b_y)^2)^{1/2}$$

$$D = (u_s - u_b)$$

from which the mean, standard deviation and rms in m will be derived for multiple comparisons, by season and location.

The tracking error of the buoy/s is zero, since the buoy is stationary on the same piece of ice. The error will then be based on geolocation errors associated with the buoy location, the SAR grid point geolocation and the SAR grid point tracking error. Preliminary analysis of recent data from 12 buoys gives worst case errors of 32 m/day in each component of 3-day velocity estimates, which is of sufficient accuracy to validate the displacement requirement. Prelaunch, the displacement errors can be derived using image pairs from L-band (ALOS-1, ALOS-2, and potentially SAOCOM) along with C-band imagery from Sentinel-1 as a way to test the tracking algorithm. If there are significant differences

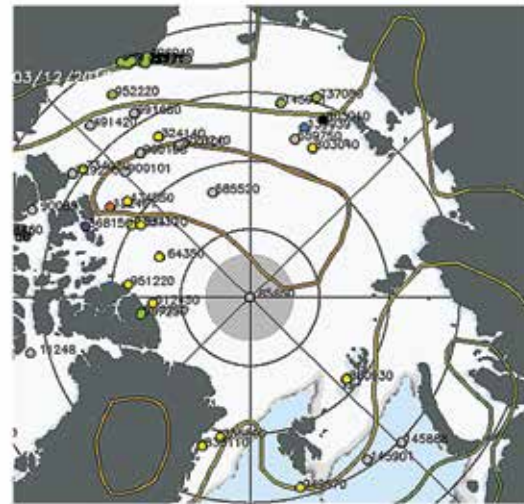
between the image pairs, this may be due to either sea ice deformation including shear and divergence relative to the SAR and buoy locations, and difference in backscatter due to environmental conditions including warming and presence of melt ponds.

As mentioned, previous evaluations of ice tracking errors using RADARSAT-1 using 3-day image pairs and IABP buoys (3-hour data, Argos tracking) have resulted in the following displacement errors: the squared correlation coefficient for RADARSAT-1 and buoy displacements was 0.996 and the median magnitude

of the displacement differences was 323 m (Lindsay and Stern, 2003). The tracking errors gave rise to error standard deviations of 0.5% /day in the divergence, shear, and vorticity. The uncertainty in the area change of a cell is 1.4% due to tracking errors and 3.2% due to resolving the cell boundary with only four points. It was also found that the displacement errors between buoys and SAR at the starting positions were significantly improved when the distance between a SAR image grid point and a buoy were <2 km (Figure 18-5a,b) compared to <5 km (Figure 18-5c, d), with the latter results indicating a greater likelihood of deformation occurring over time and leading to greater errors, which were not included in the error tracking.

FIGURE 18-4

Representative map of Arctic drift buoys (from IABP).



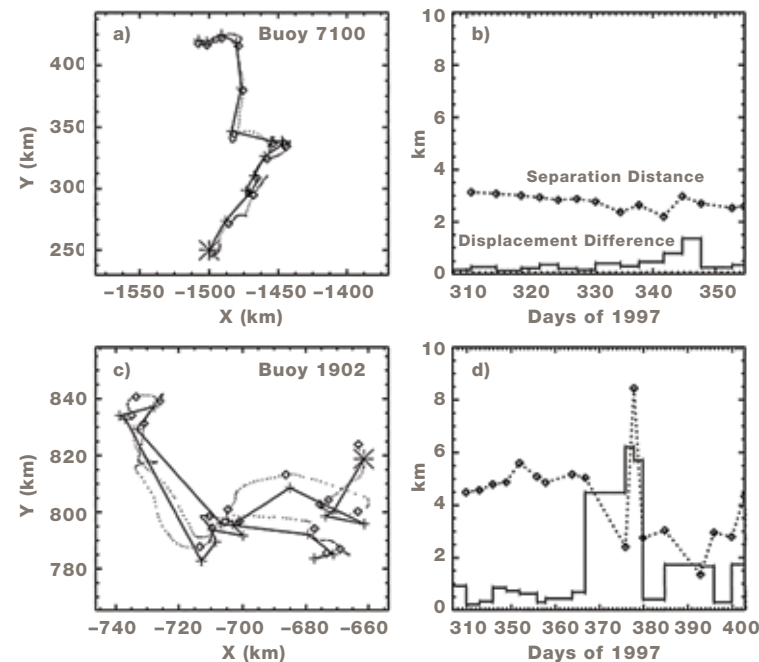
18.3 ECOSYSTEMS IN SITU MEASUREMENTS FOR CAL/VAL

Above ground biomass measurements will validate the NISAR measurements. Measurement of canopy reduction will be used for Cal/Val for forest disturbance. Inundation areas will be measured locally for calibrating and validating NISAR measurements. Cropland images from other measurements will be classified for matching with NISAR.

FIGURE 18-5

Examples of buoy (dots) and RADARSAT-1 (line) trajectories after Lindsay and Stern (2003).

Note the very similar displacement differences (<0.5 km) between buoys and SAR tracking over a 40-day period in (a,b), while a shearing event occurred in days 367-380, which resulted in large displacement differences in (c, d) that were not suitable for error tracking. Similar results to (a, b) will be generated with NISAR imagery.



18.3.1 Above Ground Biomass (AGB)

A multiscale approach based on in situ and lidar data is necessary for validation of the NISAR biomass measurement science requirement and to reduce uncertainty in AGB at the regional to continental scale. At the finest resolution, in situ field measurements of forest characteristics will be used to estimate AGB using allometric equations at the hectare or sub-hectare scale. These in situ estimates of AGB will then be upscaled with Airborne Laser Scanning (ALS) lidar forest canopy metrics to characterize the variations of AGB at the landscape scales (a minimum area of 100-1000 ha depending on the vegetation and topography). The landscape scale distribution of AGB in the form of a map will be used to calibrate algorithms and to validate the NISAR AGB product.

The NISAR biomass algorithm depends upon parameters that are a function of five global terrestrial biome types (broadleaf evergreen, broadleaf deciduous, needleleaf, mixed broadleaf/needleleaf, and dry forest and woodland savanna). Biomes are referred to regions with similar climate and dominant plant or vegetation types that may be sub-divided into continents to capture additional diversity in species and climate. The NISAR Cal/Val sites are required to represent these biomes and span across their structural and topographical diversity to insure the algorithms meet the requirements for global estimation vegetation AGB. For each biome a minimum of two sub-regions for independent training and validation that include AGB range 0-100 Mg/ha are recommended. However, a larger number of Cal/Val sites will be selected for data sufficiency and redundancy. The number and location of sites depend on three key requirements: 1) must represent the landscape variability of vegetation, topography and moisture conditions within each biome, 2) must be located in areas with existing data, infrastructure, or programs to guarantee quality control and future data augmentation, and 3) must include a combination of ground plots, Airborne Laser Scanning (ALS), and airborne or satellite L-band SAR imagery.

The main objective of pre-launch Cal/Val activities will be the development of algorithms and validation of algorithm performance to meet the science requirements using airborne and satellite L-band radar that simulates NISAR observations. Whereas, the post-launch Cal/Val activities are designed to potentially adjust and verify the performance of the algorithms when NISAR data are acquired.

The number of ground plots for each site must suffice to statistically develop the algorithmic model for achieving better than 20 percent uncertainty in AGB estimation (NISAR requirement). This number is expected to be 20-30 plots depending on vegetation heterogeneity. Ground measurements at each plot must include tree size (diameter, height), wood specific gravity (by identifying plants), GNSS measurements to characterize the plot shape and size (< 5 m accuracy), and other ancillary (optional) data such as soil moisture, soil properties, phenology, etc. Ground-estimated AGB must use established local or global allometric models and must include any uncertainties associated with the ground-estimated AGB. Ground plot data may include all field measurements or only AGB estimates with accurate location and size of plots if there are restrictions on disseminating the tree level measurements. For sites without the ALS data, the ground plot size must be >1 ha (100 m x 100 m) to allow direct calibration of the algorithmic model with radar imagery. For sites with ALS data, the plot size can vary from 0.1 ha to 1.0 ha (plot shape variable) depending on vegetation type and heterogeneity.

ALS data must cover the minimum site area (100-1000 ha) with point density necessary to have vegetation vertical structure and height, the digital terrain model (DTM) with less than 1 m vertical resolution and uncertainty at the plot size (2-4 points per m² depending on vegetation type). The ALS data may include the point density data (LAS files) or only the DTM and DSM (<1-3 m horizontal resolution depending on vegetation type) if there are restrictions on disseminating the point density data.

Ground plots will be used to derive lidar-AGB models to convert the ALS vegetation height metrics to develop maps over the Cal/Val sites and quantify the uncertainty at the 1 ha map grid cells. The AGB maps will be used for calibration and validation of the SAR algorithm and products including the propagation of uncertainty through all steps of algorithm development and implementation.

The pre-launch NISAR biomass Cal/Val activities will focus on developing the algorithmic model parameters with existing ground, ALS or SAR data. The calibration or validation will be performed by available time series SAR data (airborne or ALOS PALSAR) and simulations of soil moisture and vegetation phenology. Once algorithms are developed and tested on historical SAR data, they will be either directly applied to NISAR observations or adjusted for NISAR radiometric calibration and configurations during the post-launch Cal/Val activities. The validation of NISAR biomass products will be performed on selected test sites distributed across the terrestrial biomes.

The use of historical field measurements, ALS, and SAR data relies on international collaboration. Similarly, validation of the biomass is performed in collaboration with the Cal/Val programs of the NASA Global Ecosystem Dynamics Investigation Lidar (GEDI) and the ESA BIOMASS missions, as well as through partnerships with resource networks and field locations where biomass is measured and monitored.

BIOMASS CAL/VAL SITES

Biomass Cal/Val sites with contemporary field measurements and lidar data acquisitions will be selected from the following study sites with historical measurements (Table 18-3):

18.3.2 Forest Disturbance

The forest disturbance requirement is to detect a 50% area loss of canopy cover, taken over a 1-hectare region. This entails the detection of a ½ hectare reduction in canopy cover. While the establishment of the

calibration and validation of the accuracy requirement of the forest disturbance algorithm can take on a number of different forms, the primary one used by NISAR will be through the analysis of high-resolution (5 m or better) pairs of multi-spectral optical data, collected one year apart, in regions where disturbance is known to have occurred and where such data exist.

Several data sources are available to obtain Forest Fractional Canopy Cover (FFCC) estimates to support the generation of a calibration/validation data set. With the objective for consistency in the approach, the most suitable data sets are best chosen from globally acquired high-resolution optical imaging sensors for which NASA has data-buy agreements (e.g., as currently established for WorldView satellite data), or can be purchased in pairs in regions where disturbance is known to be occurring and where such data have been collected by satellite resources. Given the current availability of these data types, it is expected that they will continue to be available during the NISAR mission calibration and validation time frame.

Some flexibility exists in the combining of observation pairs from different sources, in particular, if a visual interpretation approach for reference data generation (Cohen et al., 1998) is employed. Using heterogeneous data should be avoided, but targets of opportunity for validation after a large natural disturbance event (e.g., fire, tornado) may have a good mix of viable reference data.

Alternatives to the optical classification and measurement of FFCC change are in the use of alternative sources of multi- or hyper-spectral optical, radar, and lidar data from space and airborne resources from which viable data sets may be used to determine FFCC. For optical observations (multi-spectral, hyper-spectral, and/or lidar) cloudy areas are masked from the data pairs. Field reference data collected by National Forest Services, research groups, or commercial timber management entities can serve as ancillary sources to provide geographically localized validation data. For a global comprehensive calibration and validation approach, algorithms that have been published

TABLE 18-3. BIOMASS CAL/VAL SITES WITH CONTEMPORARY FIELD MEASUREMENTS AND LIDAR DATA ACQUISITIONS.

Site Name	Country	Site Name	Country	Site Name	Country
Mondah	Gabon	Ordway - OSBS	USA (Florida)	Germany - Kljuntharandt	Germany
Mouila	Gabon	Tomé-Açu	Brazil	Germany - Traunstein	Germany
Lope	Gabon	Cantareira 1	Brazil	Italy - Trentino	Italy
Mai Ndombe	DRC	Cantareira 2	Brazil	Netherlands - Loobos	Netherlands
Lowveld, Kruger National Park	South Africa	Goiás	Brazil	Poland - Bialowieza	Poland
Amani Nature Reserve (ANR)	Tanzania	Bahía	Brazil	Spain - Soria_i	Spain
Miombo	Tanzania	Massaranduba	Brazil	Spain - Soria_ii	Spain
Bia Conservation Area and Dadieso Forest Reserve	Ghana	Rondonia	Brazil	Spain - Valsaincircle	Spain
West Africa (Gola Rainforest National Park)	Sierra Leone /Liberia	Tapajos	Brazil	Spain - Valsairect	Spain
Tumbarumba	Australia	Roraima	Brazil	Switzerland - Laegeren	Switzerland
Great Western Woodlands	Australia	Litchfield Savanna	Australia	Doi Inthanon	Thailand
Mulga	Australia	Harvard Forest - HARV	USA (Massachusetts)	Palangkaraya Peat Central Kalimantan	Indonesia
Karawatha	Australia	Smithsonian Environmental Research Center - SERC	USA (Maryland)	Sabah Forestry Research Center Area	Malaysia
Great Western Woodlands	Australia	Mai Ndombe	DRC	Sarawak	Malaysia
Litchfield Savanna	Australia	San Joachin SJER	USA (California)	Mudumalai	India
InJune	Australia	Laurentides Wildlife Reserve	Quebec, Canada	Xishuangbanna	China
Ft. Liard	NWT, Canada	Sycamore Creek - SYCA	USA (Arizona)	Changbaishan	China
Ft. Providence	NWT, Canada	Great Smoky Mountains National Park - GRSM	USA (Tennessee)	Gutianshan	China
Ft. Simpson	NWT, Canada	Niwot Ridge Mountain Research Station - NIWO	USA (Colorado)	Dinghushan	China
Bartlett Experimental Forest -BART	USA (New Hampshire)	Howland Forest	USA (Maine)	Donlingshan	China
Healy - HEAL	USA (Alaska)	Soaproot Saddle - SOAP	USA (California)	Heishiding	China
Delta Junction - DEJU	USA (Alaska)	SPER	USA (Colorado)	Hainan	China
Lower Teakettle - TEAK	USA (California)	England Newforest	United Kingdom	Badagongshan	China
Lenoir Landing - LENO	USA (Alabama)	Estonia - Rami	Estonia	Baotianman	China
				Daxinganling	China

in the literature can be used to determine FPCC and changes can be applied to image pairs, collected one year apart, from these potential data sources (Cho et al., 2012, Chubey et al., 2006, Clark et al., 2004, Falkowski et al., 2009, Immitzer et al., 2012, Ke et al., 2011; Lucas et al., 2008).

Algorithm calibration will be performed prior to the launch of NISAR, over the Cal/Val regions, using a pair of optical images, collected roughly one year apart. Ideally these image pairs will be obtained from the same sensor under similar acquisition conditions. During this calibration phase, manual interpretation of the high-resolution optical imagery will be coupled with supervised classification for determining percent of FFCC change derived from these optical resources for the NISAR disturbance Cal/Val sites. These data will be combined with available Sentinel-1 time series and/or ALOS-2 and SAOCOM data to create thresholds for the cumulative sum algorithm that is being used by NISAR for detecting disturbance.

To reduce errors in the FFCC change detection of the pairwise analysis of NISAR datasets, only exact repeat orbits and view angles are considered. Image pairs will be accurately co-registered, geocoded and geometrically matched to the NISAR time series data stacks. Because of modern orbital control and the availability of DEMs for geocoding, co-registration errors are negligible for the purpose of establishing 1 ha FFCC estimates. For a statistically viable validation approach, the reference image pairs need to be distributed in all observed biomes and image subsets of sufficient size need to be chosen to extract enough validation samples to detect all sources of error (see below). To obtain 1000 1 ha samples from a high-resolution image pair requires approximately 3.2 x 3.2 km image subsets. Given potential cloud cover pixel elimination, 4 x 4 km subsets will be obtained within which 1 ha samples can be placed. With respect to biome sampling, the stratification after the World Wildlife Federation (WWF) biomes classification will be used (Olson et al., 2001). Of the 14 global biomes, eight are critical for distur-

bance validation (Figure 18-6). Two validation sites will be chosen in each of the biomes with forest cover in each of the continents of North- and South America, Africa, Asia, Europe, Australia with forest cover (eliminating Antarctica and Tundra regions). This would bring the total number of validation sites to 6 continents x 8 biomes x 2 sites each = 96 validation sites.

With annual disturbance rates varying with disturbance type (fires likelihoods, infestations, legal and illegal logging operations), and with the fraction of annually disturbed areas tending to be relatively small, stratified sampling with sample sizes sufficiently large to cover most disturbance scenarios should be used. Forest management agencies will be consulted in advance to identify areas of disturbance to insure bracketing of disturbance events with optical data.

Disturbance will be validated on at least 1000 1 ha resolution cells for any given area, where each resolution cell is fully mapped FFCC change values. NISAR disturbance detection results will be evaluated against this full sample in order to capture errors of omission (false negative) and commission (false positive). This approach follows guidelines for sample designs, which have been established and discussed in the literature (Olofsson et al., 2014, Stehman 2005, van Oort, 2006, Woodcock et al., 2001). Two sites per continent/biome combination within the shown areas (Figure 18-6) are proposed, which results in a total of 96 validation sites.

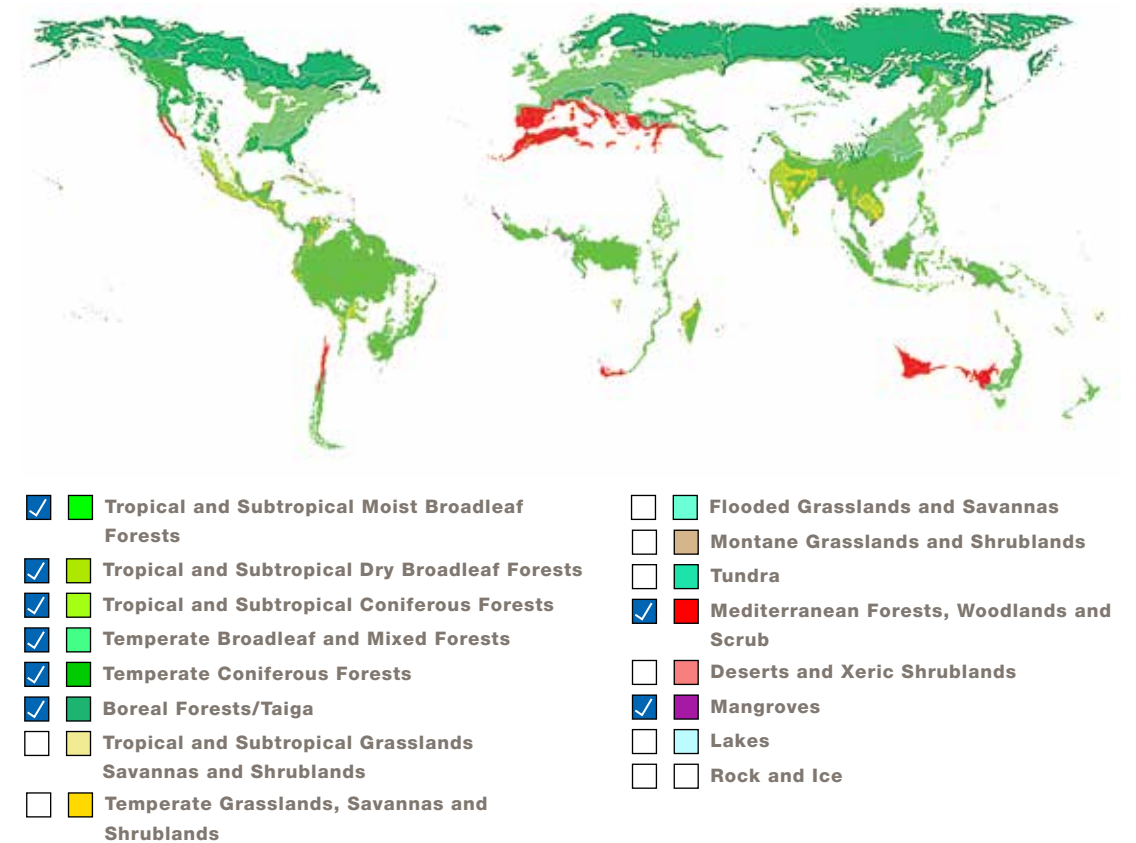
FOREST DISTURBANCE CAL/VAL SITES

Forest disturbance Cal/Val sites will be selected based the availability of alternative measurements of ongoing disturbance such as from cloud-free optical imagery bounding disturbance events or from information provided by forest management agencies. The sites will be distributed globally and in every forest biome.

Areas known to undergo regular forest disturbance are timber management sites. For example, large tracts in the Southeastern United States have forest regrowth

FIGURE 18-6

Target biomes for placement of forest disturbance validation sites. Map after Olson et al., (2001).



cycles of 20 years where a stand replacement rate of 5% per year for forest land under timber management. Forest management plans will be obtained for the year after NISAR launch from collaborators in the USDA Forest Service and timber industry sector to determine sites of forest disturbance a priori. International partnerships are established via collaboration in the GEO Global Forest Observing Initiative (GFOI) which operates a network of study regions of deforestation and forest degradation hotspots. Figure 18-7 illustrates where GFOI has established these study regions and constitutes a network of forest disturbance hotspots and thus a set of first order targets of opportunities for post-launch disturbance monitoring.

A resource to use for locating sites for fire based disturbance is the Fire Information for Resource Management System (FIRMS) (<https://earthdata.nasa.gov/earth-observation-data/near-real-time/firms>). FIRMS

distributes Near Real-Time (NRT) active fire data within 3 hours of satellite overpass from both the Moderate Resolution Imaging Spectroradiometer (MODIS) and the Visible Infrared Imaging Radiometer Suite (VIIRS). In the U.S., a resource for the estimation of burn severity is the Burn Area and Severity mapping service by the USGS (<https://www.usgs.gov/apps/landcarbon/categories/burn-area/download/>). This resource can be used to support the targeting of high-resolution optical image acquisition to estimate FFCC loss from fire disturbances.

18.3.3 Inundation Area

Inundation extent within wetland areas will be validated for two conditions: near-shore open water (within 100 m of a shoreline), and standing water with emergent vegetation. The requirement states that measurements should be validated at 1 ha resolution. If a 1 ha pixel is inundated, the predominate state will be

validated. Inundation extent will only be validated when the water and surrounding landscape are not frozen or snow covered.

The measurement of near-shore open water extent by NISAR can often be validated with data from optical sensors, limited only by cloud cover. Open water surfaces generally exhibit low radar backscatter similar to bare ground and beaches. In larger open water surfaces, wind induced roughening of the water increases radar brightness, especially at smaller incidence angles. Thus, the selection of thresholds to identify open water surfaces will depend on incidence angle and account for the size of the water bodies. However, these thresholds must remain biome independent. Inundation extent will not include snow-covered or frozen water. Desert areas will be excluded from analysis by the wetlands mask.

Error rates for this requirement will only be evaluated within a wetland mask. The initial wetland mask will be determined prior to launch from ancillary sources of information on wetland extent but may be modified after launch if additional information warrants updates.

It should encompass an area greater than that which typically experience inundation but will exclude all urban areas, deserts and permanent open water surfaces. The wetland mask will have a seasonal component such that inundation is not evaluated during frozen conditions or freeze/thaw transition periods. The wetland mask will indicate those areas that are agricultural.

All Cal/Val sites must be located within the wetland mask. The Cal/Val sites must represent the varying conditions present in different biomes, ranging from boreal to temperate to tropical biomes with distinct vegetation differences. The validation of open water is impacted by wind conditions, freeze/thaw state, and the "radar darkness" of the surrounding environment, while the validation of inundated vegetation is impacted by the structure and density of the emergent vegetation. The distribution of inundation Cal/Val sites should sample the cross-track NISAR imaging swath due to expected sensitivity to incidence angle and the noise properties of the SAR data.

The pre-launch and post-launch calibration of the algorithm thresholds, and the post-launch validation of the science requirement should be cost-effective. The planned launch of the NASA SWOT mission nearly coincides with NISAR's; thus coordination of Cal/Val activities is recommended for the mutual benefit of these projects.

The measurement of inundated vegetation by NISAR is enabled by the high-intensity backscatter observed in the Co-Pol (HH) channel, which results from double bounce reflections that occur when the radar-illuminated area contains vegetation that is vertically emergent from standing water. If the vegetation is small in stature and/or herbaceous, double bounce reflections may be reduced, leading to specular reflection over the open water (i.e., low backscatter). As inundated vegetation transitions to non-inundated vegetation, HH radar brightness reduces to the level of the imaged forest or marsh volume. L-band radar remote sensing is known to be a reliable tool for detection of inundated vegetation, and may overperform other remote sensing measurement available for validation. There are four potential methods that could be utilized for validation, some shown in Figure 18-8. The combination of these methodologies will be evaluated and selected prior to launch. The potential methods are:

1. Ground transects. This method is the most accurate and provides additional information such as inundation depth and vegetation characteristics. The disadvantages result from logistical considerations which will bias site selection and likely provide incomplete sampling of the wetland extent. Ground transects performed by research partners could facilitate the acquisition of validation ground transects. Time continuous measurement devices such as pressure transducers and soil moisture probes can be deployed along transects traversing wetlands. This method is best suited to areas where remote observations are expected to be less robust due to extensive canopy cover, such as tropical forests.

2. 3D inundation extent model. This method relies on the knowledge of water level through time, and accurate knowledge of the wetlands digital elevation model (DEM). The inundation extent is determined by numerically flooding the DEM given measurements recorded by an in situ water level gauge. This is the most efficient and reliable of all methods, but is limited by the sparse availability of DEMs. The latter can be obtained from ALS during dry periods (lidar returns will have no reflection where there is standing water, and therefore also has value during inundation periods) or in situ surveys with a Real Time Kinematic-GNSS (RTK). To capture inundation extent at the time of NISAR data acquisition, gauges (e.g., pressure transducer) must be recording water level continuously.

3. High-resolution optical data. This method utilizes spaceborne or airborne remote sensing instruments. For example, it was employed in 2012 using WorldView-2 multiband optical data. Malinowski et al., 2015 found overall accuracy greater than 80 percent. The advantage of this method is that it is possible to efficiently map large areas with good accuracy and low cost. The disadvantages are the reduced accuracy for detecting inundation in areas with dense vegetation cover (>80%), and the non-simultaneous timing of data acquisition with NISAR. The latter effect can be alleviated with the extremely high resolution (cm scale) imagery from UAS-type aircraft overflights coordinated with the NISAR acquisition times. Combined RGB plus IR cameras on UAS can be used to identify both vegetation extent (from RGB) and many cases of inundation (from IR) overlaid on a high resolution digital surface model (DSM) and digital terrain model (DTM) (though significant vegetation will diminish the IR signature of water). This method is best suited to boreal ecosystems where there is less obscuration by woody vegetation, and for open water areas where cloud free images can be obtained.

4. High resolution quad-pol SAR data. While the inundation extent algorithm for NISAR utilizes dual pol HH and HV data, validation could be done with enhanced quad-pol L-band or P-band SAR data (such as available

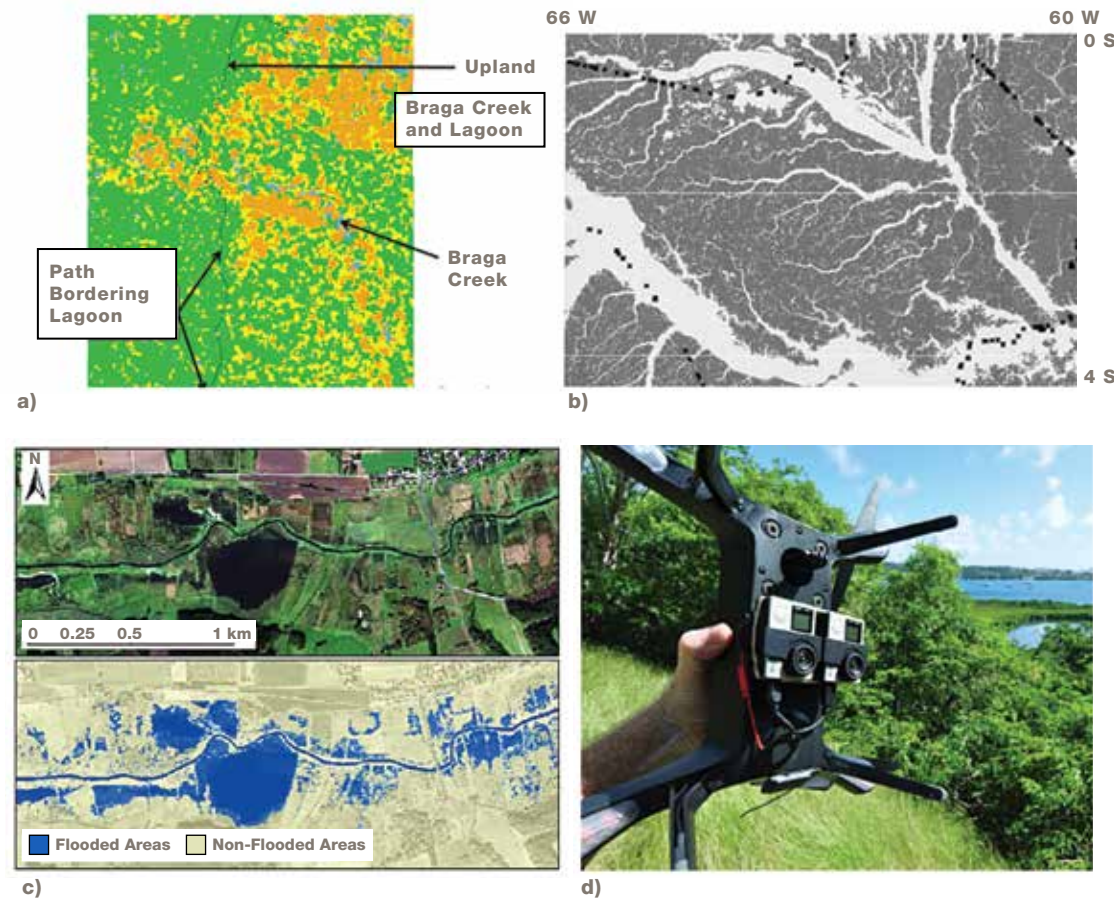
FIGURE 18-7

GFOI research and development study sites where a host of field and satellite data sets are being used to study forest disturbance (<http://www.gfoi.org/rd/study-sites/>).



FIGURE 18-8

Validation methods for inundation. a) measurements of inundation state along ground transect of Napo River floodplain with classification based on polarimetric decomposition (Chapman et al., 2014). b) video survey of JERS-1 SAR classification, validation points indicated (Hess et al., 2002). c) WorldView-2 classification of inundation extent (Malinowski et al, 2015). d) GoPro Cameras onboard Solo Quadcopter (Schill, S, Personal communication, 2016).



on the airborne NASA UAVSAR platform) by polarimetric decomposition. Polarimetric decomposition evaluates the contributions of the various scattering mechanisms and can therefore be used to isolate the double bounce effect that occurs in inundated areas. However, the methodology itself needs to be validated pre-launch. The advantage is that this approach provides wide area mapping and on-demand timing with NISAR acquisitions. Once validated, this spatially large product can be used to validate the large scale NISAR products.

INUNDATION AREA CAL/VAL SITES

Cal/Val sites for inundation extent will be selected from sites listed in Table 18-4. Methodology at each site will depend on vegetation and likely cloud cover.

18.3.4 Cropland Area

Similar to the disturbance Cal/Val effort described above, calibration and validation for NISAR's cropland area requirement will be principally based on high-resolution optically based image classification and informed through partners in the Group on Earth Observations' (GEO) Joint Experiment for Crop Assessment and Monitoring (JECAM, 2014) or similar collaborations that are formed in NISAR's pre-launch Cal/Val period.

The ground-based in situ observations will be employed in validation of active crop area. Airborne and spaceborne sensors will also be employed where possible to extend coverage from the plot level. Establishing and maintaining a robust and globally distributed set of consistent in situ land cover data

TABLE 18-4. WETLAND INUNDATION NOMINAL CAL/VAL SITES

Site	Vegetation Type	Logistics and Methodologies
Bonanza Creek/ Yukon Flats, Alaska	Boreal wetland (marshes, tussocks, some forested)	Ground transects, high resolution optical, and UAS data. (ABOVE site, possible SWOT site)
Scotty Creek and nearby sites, Canada	Boreal wetland	Ground transects, high resolution optical, and UAS data. (ABOVE site, Ducks Unlimited)
Florida Everglades	Freshwater marsh plus mangrove area (shrubs and trees)	Pressure transducers combined with DEM. (possible SWOT site)
Louisiana Delta	Fresh and brackish water, cyprus, willows, marshes	Pressure transducers combined with DEM. (Possible SWOT site)
Pacaya-Samiria, Peru	Tropical wetland (palms, etc.)	Pressure transducer and ground transects, lidar would be helpful
Pantanal, Brazil/ Paraguay/Bolivia	Mixture of moist tropical, semi-arid woodlands, and Cerrado and Chaco savannas	UAS imagery. Measure DEM with RTK in conjunction with pressure transducers
Ogooue River, Gabon	Freshwater marsh, tropical wetland palms, papyrus	UAS imagery
Bhitarkanika, India	Mangrove	ISRO monitoring site
Chilika, India	Lake near agriculture	ISRO monitoring site
Nalsarovar, India	Inland wetland	ISRO monitoring site
Sud, South Sudan	Marsh	In coordination with current studies
Carpinteria Salt Marsh Reserve	Marshes	Pressure transducer combined with RTK DEM
Magdalena River, Colombia	Mangroves	RTK plus pressure transducer
Mamirauá Sustainable Development Reserve	Tropical wetland	In coordination with local experts

will be essential to the success of the agricultural portion of the NISAR Cal/Val program. Recognizing the complexity of global agricultural systems, and the challenges involved in acquiring these data, the NISAR project will attempt to achieve its objective through partnerships with complementary operational and research programs around the globe. In addition to basic crop type measurements, additional information

on cropping practices are welcome, as this information can be useful in refining the algorithms in use and understanding NISAR's sensitivity to other agricultural measurements.

Another important consideration for implementation of the NISAR agricultural Cal/Val program (which will utilize data from a variety of organizations worldwide) is establishing global consistency in the correlative data.

While agriculture plays an important role on every continent outside Antarctica, field size, crop type, climactic conditions, and cropping practices can all vary greatly between locations. NISAR will provide products around the world; therefore, validation data should be representative of a wide range of agricultural variation, and will require cooperation from a range of groups both within the U.S. and internationally. To assist in establishing consistency between validation sites, a series of guidelines have been developed to set expectations for potential NISAR Cal/Val agricultural partners.

For consistency, the NISAR agricultural Cal/Val program is using the definition of annual cropland from a remote sensing perspective as defined by the Group on Earth Observations' (GEO) Joint Experiment for Crop Assessment and Monitoring (JECAM). The definition they use is as follows, and will be used throughout this document to define agricultural land:

The annual cropland from a remote sensing perspective is a piece of land of minimum 0.25 ha (min. width of 30 m) that is sowed/planted and harvestable at least once within the 12 months after the sowing/planting date. The annual cropland produces an herbaceous cover and is sometimes combined with some tree or woody vegetation.^o*

In order to categorize crop type consistently, this Cal/Val program will be using the general legend developed by the JECAM project to define crop type. It follows a hierarchical grouping and has been adapted from

* The herbaceous vegetation expressed as *fcover* (fraction of soil background covered by the living vegetation) is expected to reach at least 30% while the tree or woody (height >2m) cover should typically not exceed an *fcover* of 20%.

^o There are three known exceptions to this definition. The first concerns the sugarcane plantation and cassava crop which are included in the cropland class, although they have a longer vegetation cycle and are not planted yearly. Second, taken individually, small plots such as legumes do not meet the minimum size criteria of the cropland definition. However, when considered as a continuous heterogeneous field, they should be included in the cropland. The third case is the greenhouse crops that cannot be monitored by remote sensing and are thus excluded from the definition.

the Indicative Crop Classification (ICC) developed by the Food and Agriculture Organization of the United Nations (FAO) for use in agricultural censuses. This legend delineates only temporary crops falling under the aforementioned definition of agricultural land, with perennial crops listed at the end along with a few major nonagricultural land covers. See Section IIC of the JECAM Guidelines for Field Data Collection for the full legend (http://www.jecam.org/JECAM_Guidelines_for_Field_Data_Collection_v1_0.pdf). While the NISAR mission is most interested in data for the major crops barley, cassava, groundnut, maize, millet, potato, rapeseed, rice, rye, sorghum, soybean, sugarbeet, sugarcane, sunflower, and wheat, any type of annual crop type has value when making a crop/non-crop map. Minor crops should not be ignored or excluded from data collection, although they can be grouped into more general categories (i.e., vegetables, pulses, etc.). If fields are being actively managed off season, such as planted with a green manure crop, this should be reported as an additional season of data. Similarly, non-crop information is also vital to making an accurate crop/non-crop map, so it is requested that Cal/Val partners also provide information about the surrounding non-agricultural land covers.

Two types of in situ data will be acquired at NISAR agricultural Cal/Val sites. Tier I sites will provide a more comprehensive set of data about crop type, growing season, and cropping practices, whereas

Tier II sites will only provide crop type information. Tier I sites may receive priority over Tier II sites during Cal/Val activities by the NISAR project. The tier designations are used to formalize what is expected from each site in terms of data they will provide. A summary of expectations for each tier are as follows:

- Tier I
 - Crop type data at the most detailed level available (according to legend groupings)
 - Planting and harvesting information provided to within a week per field
 - Cropping practices reported per field (i.e., tillage, residues, irrigation, etc. – see legend)
 - Information reported once per season
- Tier II
 - Active crop type data at the most detailed level available (according to legend groupings) reported once per season

The in situ data collection should consist of a sample, large enough and spread out enough to adequately characterize the larger agricultural region. It is suggested that a “windshield survey” be conducted along the main roads from a motorized vehicle, allowing the data collector to easily and rapidly capture basic crop information of all visible fields, and capture long transects of data across the region under investigation. It is also recommended to complement the long transects with regular additional transects throughout the study area via secondary roads and tracks in order to reduce the spatial bias brought about by roadside sampling. Several long transects running in various directions ensure coverage of the entire area, while the secondary transects provide complementary data that reduces the bias in the Cal/Val data set.

At least 20 fields with the minimum size described below should be recorded for each of the primary crops in the region, whether or not they are one of the crops NISAR is most interested in. The fields should be spread

over an area of at least 100 km². A target sampling density would be about one observation/5 km², or within the range of one observation for every 1-10 km², depending on the complexity of the cropping systems and diversity of crop types. In addition to the crops, 20 samples of each of the major nonagricultural land covers should also be recorded, with each sample following the same minimum size restrictions as described above for crops. The locations of significant infrastructure, such as barns, processing facilities, parking lots, housing, and major power lines should also be noted.

Please note that exact survey methods are still being developed, and that further specifications will likely be added in order to ensure high-quality, consistent data between the different partners. Information beyond the location of the crop/non-crop areas such as planting and harvest times and cropping practices might be obtained through farm-to-farm surveys or through collaborations with agricultural collectives that might have knowledge of this type of information.

The in situ data would be provided once per growing season at planned intervals for at least two years before and after launch which, based on the current launch date, would be 2019-2023.

Two methods of data collection will be utilized, polygon-based or point-based, as described below.

POLYGON METHOD

The first of the two preferred methods of data collection is to mark field boundary polygons on high resolution multispectral cloud free imagery prior to gathering field data, and then once in the field confirm that there have been no major changes to field dimensions and record crop type and any other crop information (such as planting and harvest dates, and cropping practices) being collected as attributes to each field polygon. This can be done with a variety of mobile device apps and software, in order to mitigate potential error when

transferring paper notes to a GIS system. These data could be acquired during windshield survey described above.

POINT METHOD

The second of the two preferred methods of data collection is based on recording the GPS location of a specific in situ point and taking photos in each of the cardinal directions (N, E, S, W) as a way of consistently recording surrounding crops between different field locations. Photos should be annotated with the in situ

location, crop type information, and any other cropping practice information being collected (tillage, irrigation, etc.) for Tier I sites. These data could be acquired during windshield survey described above.

CROPLAND AREA CAL/VAL SITES

Cal/Val sites for validating active crop area will be selected from among the 50 current JECAM study sites shown in Figure 18-9.

FIGURE 18-9

JECAM sites (<http://www.jecam.org/?/interactive-map>).



19 APPENDIX G RADAR INSTRUMENT MODES

TABLE 19-1. OVERVIEW OF INSTRUMENT MODES BASED ON TARGET TYPES FOR NISAR L-SAR AND S-SAR INSTRUMENTS. (SP refers to single-polarization, DP is dual-polarization, QP is quad-polarization, and CP is compact-polarization)

Science			Performance				
PRIMARY SCIENCE TARGET	FREQ. BAND	POLARIZATION	BW	PRF	PW	SWATH	SWATH START LOOK ANGLE
			(MHZ)	(HZ)	(µSEC)	(KM)	(DEG)
Background Land	L	DP HH/HV	20+5	1650	25	242	30
Background Land Soil Moisture	L	QQ	20+5	1650	25	242	30
Background Land Soil Moisture High Power	L	QQ	20+5	1650	20	242	30
Land Ice	L	SP HH	80	1650	40	121	30
Land Ice Low Res	L	SP HH	40+5	1650	45	242	30
Low Data Rate Study Mode Single Pol	L	SP HH	20+5	1650	25	242	30
Sea Ice Dynamics	L	SP VV	5	1600	25	242	30
Open Ocean	L	QD HH/VV	5+5	1650	20	242	30
India Land Characterization	L	DP VV/VH	20+5	1650	25	242	30
Urban Areas, Himalayas	L	DP HH/HV	40+5	1650	45	242	30
Urban Areas, Himalayas SM	L	QQ	40+5	1650	45	242	30
Urban Areas, Himalayas SM High Power	L	QQ	40+5	1650	40	242	30
US Agriculture, India Agriculture	L	QP HH/HV/VH/VV	40+5	1600	45	242	30
US Agriculture, India Agriculture Low Res	L	QP HH/HV/VH/VV	20+5	1600	45	242	30
Experimental CP mode	L	CP RH/RV	20+20	1650	40	242	30
Experimental QQ mode	L	QQ	20+20	1650	20	242	30
Experimental SP mode	L	SP HH	80	1650	20	242	30
ISRO Ice/sea-ice	L	DP VV/VH	5	1650	25	242	30

Science			Performance				
PRIMARY SCIENCE TARGET	FREQ. BAND	POLARIZATION*	BW*	PRF	PW*	SWATH	SWATH START LOOK ANGLE
			(MHZ)	(HZ)	(µSEC)	(KM)	(DEG)
ISRO Ice/Sea-ice - Alternate	L	QD HH/VV	5	1650	25	242	30
Solid Earth/Ice/Veg/Coast/Bathymetry	S	Quasi-Quad	37.5	2200	10+10	244	30
Ecosystem/Coastal Ocean/Cryosphere	S	DP HH/HV	10	2200	25	244	30
Agriculture/Sea Ice	S	CP RH/RV	25	2200	25	244	30
Glacial Ice High Res	S	CP RH/RV	37.5	2200	25	244	30
New Mode	S	DP HH/HV	37.5	2200	25	244	30
Deformation	S	SP HH (or SP VV)	25	2200	25	244	30
Deformation Max Res	S	SP HH (or SP VV)	75	2200	25	244	30
Systematic Coverage	L+S	DP HH/HV	20+5	1910	25	242	30
		CP RH/RV	25		25	244	30
Systematic Coverage & Deformation	L+S	DP HH/HV	20+5	1910	25	242	30
		DP HH/HV	37.5		25	244	30
Coastal Mudbank (Wet Soil)	L+S	DP HH/HV	20+5	1910	25	242	30
		SP HH (or SP VV)	25		25	244	30
Ocean	L+S	SP VV	5	1910	25	242	30
		DP VV/VH	10		25	244	30
Sea Ice Type	L+S	L: DP VV/VH	20+5	1910	25	242	30
		S: CP RH/RV	25		25	244	30
Glacial Ice Himalayas	L+S	L: DP HH/HV	40+5	1910	45	242	30
		S: CP/RH/RV	37.5		25	244	30
High-Res Deformation (Disaster/Urgent Response)	L+S	L: DP HH/HV	40+5	1910	45	242	30
		S: SP HH (or SP VV)	75		25	244	30
India Agriculture	L+S	L: QP HH/HV/VH/VV	40+5	1550	45	242	30
		S: CP RH/RV	25	3100	10	244	30

Science			Performance				
PRIMARY SCIENCE TARGET	FREQ. BAND	POLARIZATION*	BW*	PRF	PW*	SWATH	SWATH START LOOK ANGLE
			(MHZ)	(HZ)	(µSEC)	(KM)	(DEG)
Coastal - Land	L+S	L: QP HH/HV/VH/VV	40+5	1550	45	242	30
		S: DP HH/HV	37.5	3100	10	244	30
ISRO Ice/Sea-Ice	L+S	DP VV/VH	5	1910	25	242	30
		CP RH/RV	25		25	244	30
ISRO Ice/Sea-Ice - Joint Alternate	L+S	DP VV/VH	5	1910	25	242	30
		DP VV/VH	10		25	244	30

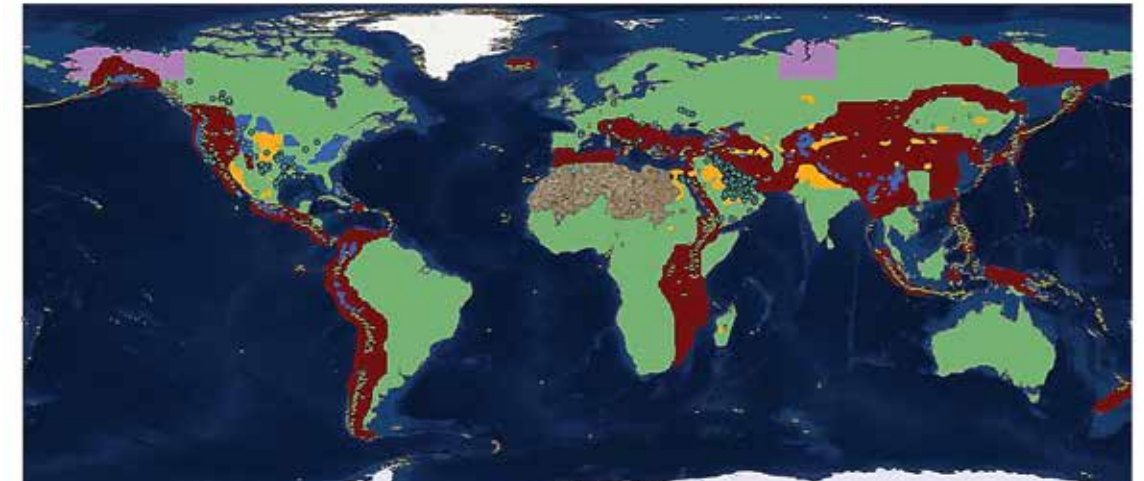
* May vary depending on target and operating conditions

20 APPENDIX H SCIENCE TARGET MAPS

Table 3-1 summarized the Level 1 requirements that NISAR must meet. The Level 1 requirements lead to Level 2 measurement accuracy, sampling and coverage requirements for each of the scientific disciplines. The coverage requirements are globally distributed, but the areas over which requirements must be met are discipline-specific and are codified by the project in a set of science target maps comprising geographical polygons.

For example, in the cryosphere the requirements specify coverage of ice sheets in Greenland and Antarctica, as well as polar sea ice, but do not specify all regions with mountain glaciers. Solid Earth deformation areas are specified in terms of fast-moving plate boundaries and selected areas with transient deformation. The figures below summarize the targets for each discipline.

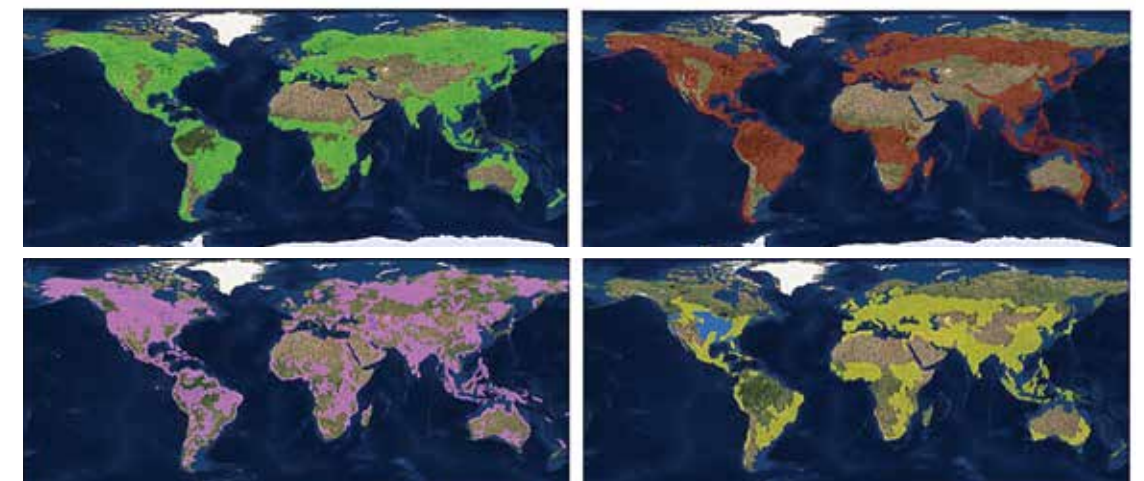
FIGURE 20-1
Solid Earth discipline
target map



SOLID EARTH TARGETS

- Background Land
- Landslides
- Aquifers
- Permafrost
- Secular Deformation
- Volcanoes
- Oil and Gas

FIGURE 20-2
Ecosystems discipline
target map



ECOSYSTEMS TARGETS

- Biomass
- Disturbance
- Wetlands
- Agriculture (World)
- Agriculture (USA)



FIGURE 20-3
Cryosphere discipline
target map

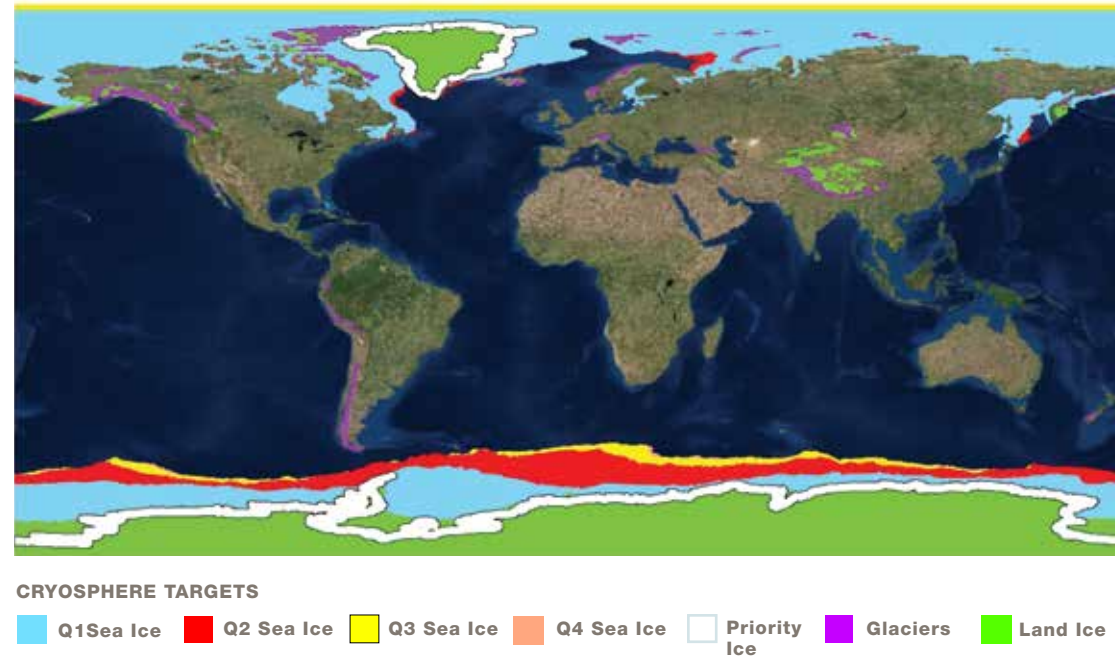
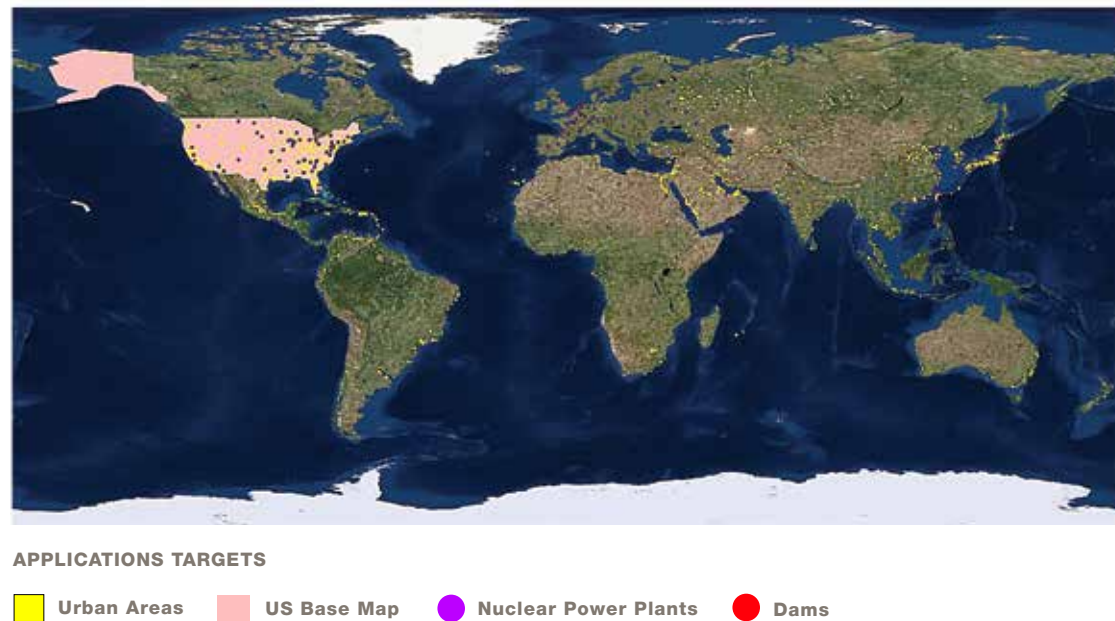


FIGURE 20-4
Applications discipline
target map



21 APPENDIX I DATA PRODUCT LAYERS

TABLE 21-1. L1 SLC DATA LAYER DESCRIPTION

Name	Number of Layers	Data Type	Spacing	Description
Primary Data Layers				
Complex back-scatter (primary mode)	Number of polarizations	CInt16	Full resolution	Focused SLC image. All channels are registered
Complex back-scatter (aux 5 MHz mode)	Number of polarizations	CInt16	Full resolution	Focused SLC image. All channels are registered
Data quality	1	Byte	Full resolution	Byte layer with flags for various channels
Secondary Layers				
Latitude	4	Float64	1 km	Latitude polynomial grid
Longitude	4	Float64	1 km	Longitude polynomial grid
Incidence angle	4	Float32	1 km	Incidence angle grid
Azimuth angle	4	Float32	1 km	Azimuth angle grid
Elevation angle	4	Float32	1 km	Elevation angle grid
σ^0	Number of polarizations	Float32	5 km az x 1 km rg	LUT to convert DN to σ^0 assuming constant ellipsoid height
γ^0	Number of polarizations	Float32	5 km az x 1 km rg	LUT to convert DN to γ^0 assuming constant ellipsoid height
Thermal noise	Number of polarizations	Float32	5 km az x 1 km rg	LUT for noise correction

TABLE 21-2. L1 MLD DATA LAYER DESCRIPTION

Name	Number of Layers	Data Type	Spacing	Description
Primary Data Layers				
Backscatter amplitude (primary mode only)	Number of polarizations	Int16	25 m	Focused SLC image. All channels are registered
Data quality	1	Byte	25 m	Byte layer with flags for various channels
Secondary Layers				
Latitude	4	Float64	1 km	Latitude polynomial grid
Longitude	4	Float64	1 km	Longitude polynomial grid
Ground range to slant range	1	Float64	1 km	Ground range to slant range grid
Incidence angle	4	Float32	1 km	Incidence angle grid
Azimuth angle	4	Float32	1 km	Azimuth angle grid
Elevation angle	4	Float32	1 km	Elevation angle grid
σ^0	Number of polarizations	Float32	5 km az x 1 km rg	LUT to convert DN to σ^0 assuming constant ellipsoid height
γ^0	Number of polarizations	Float32	5 km az x 1 km rg	LUT to convert DN to γ^0 assuming constant ellipsoid height
Thermal noise	Number of polarizations	Float32	5 km az x 1 km rg	LUT for noise correction

TABLE 21-3. IFG DATA LAYER DESCRIPTION

Name	Number of Layers	Data Type	Spacing	Description
Primary Data Layers				
Complex Interferogram (primary mode only)	Number of polarizations	CInt16	25 m	Focused SLC image. All channels are registered.
Mask	1	Byte	25 m	Byte layer with flags for various channels.
Amplitude	2*Number of co-polarizations	Int16	25 m	
Secondary Layers				
Latitude	4	Float64	1 km	Latitude polynomial grid
Longitude	4	Float64	1 km	Longitude polynomial grid
Incidence angle	4	Float32	1 km	Incidence angle grid
Azimuth angle	4	Float32	1 km	Azimuth angle grid
Elevation angle	4	Float32	1 km	Elevation angle grid
Baseline parallel component	4	Float32	1 km	Parallel baseline grid
Baseline perpendicular component	4	Float32	1 km	Perpendicular baseline grid
Range offsets	4	Float32	1 km	Range offset grid
Azimuth offsets	4	Float32	1 km	Azimuth offset grid
LUT	2*Number of co-polarizations	Float32	5 km az x 1 km rg	To translate amplitude DN layers to backscatter

TABLE 21-4. L1 UNW DATA LAYER DESCRIPTION

Name	Number of Layers	Data Type	Spacing	Description
Primary Data Layers				
Unwrapped phase (primary mode only)	Number of polarizations	CInt16	25 m	Unwrapped phase in radians
Coherence	Number of polarizations	Byte	25 m	Coherence range 0 – 1
Mask	1	Byte	25 m	Byte layer with flags for various channels
Connected components	1	Byte	25 m	Connected components flag for each pixel
Amplitude	2*Number of co-polarizations	Int16	1 km	This is needed for full covariance of interferograms
Secondary Layers				
Latitude	4	Float64	1 km	Latitude polynomial grid
Longitude	4	Float64	1 km	Longitude polynomial grid
Incidence angle	4	Float32	1 km	Incidence angle grid
Azimuth angle	4	Float32	1 km	Azimuth angle grid
Elevation angle	4	Float32	1 km	Elevation angle grid
Baseline parallel component	4	Float32	1 km	Parallel baseline grid
Baseline perpendicular component	4	Float32	1 km	Perpendicular baseline grid
Range offsets	4	Float32	1 km	Range offset grid
Azimuth offsets	4	Float32	1 km	Azimuth offset grid
Solid Earth tides	4	Float32	10 km	Solid Earth tide
Tropospheric dry delay	40	Float32	25 km	Dry delay estimated from ECMWF
Tropospheric wet delay	40	Float32	25 km	Wet delay estimated from ECMWF
Ionosphere phase screen	1	Float32	1 km	Ionosphere phase screen estimated from split spectrum method
LUT	2*Number of co-polarizations	Float32	5 km az x 1 km rg	To translate amplitude DN layers to backscatter

TABLE 21-5. L1 COV DATA LAYER DESCRIPTION

Name	Number of Layers	Data Type	Spacing	Description
Primary Data Layers				
Complex correlation	3 (Dual pol) 6 (Quad pol)	CInt16	25 m	Complex covariance matrix elements
Mask	1	Byte	25 m	Byte layer with flags for various channels (e.g., data quality and shadow-layover)
Secondary Layers				
Latitude	4	Float64	1 km	Latitude polynomial grid
Longitude	4	Float64	1 km	Longitude polynomial grid
Incidence angle	4	Float32	1 km	Incidence angle grid
Azimuth angle	4	Float32	1 km	Azimuth angle grid
Elevation angle	4	Float32	1 km	Elevation angle grid
LUT	3 (Dual pol) 6 (Quad pol)	Float32	5 km az x 1 km rg	LUT to convert Beta0 to σ^0 and γ^0 assuming constant ellipsoid height

TABLE 21-6. L2 GSLC DATA LAYER DESCRIPTION

Name	Number of Layers	Data Type	Spacing	Description
Primary Data Layers				
Complex backscatter (primary mode only)	Number of polarizations	CInt16	Full resolution	Focused SLC image. All channels are registered
Mask	1	Byte	Full resolution	Byte layer with flags for various channels
Secondary Layers				
Azimuth time	4	Float64	1 km	Azimuth time polynomial grid
Slant range	4	Float64	1 km	Slant range polynomial grid
Incidence angle	4	Float32	1 km	Incidence angle grid
Azimuth angle	4	Float32	1 km	Azimuth angle grid
Elevation angle	4	Float32	1 km	Elevation angle grid
σ^0	Number of polarizations	Float32	5 km az x 1 km rg	LUT to convert DN to σ^0 assuming constant ellipsoid height
γ^0	Number of polarizations	Float32	5 km az x 1 km rg	LUT to convert DN to γ^0 assuming constant ellipsoid height
Thermal noise	Number of polarizations	Float32	5 km az x 1 km rg	LUT for noise correction

TABLE 21-7. L2 GUNW DATA LAYER DESCRIPTION

Name	Number of Layers	Data Type	Spacing	Description
Primary Data Layers				
Unwrapped phase (primary mode only)	Number of polarizations	Float32	25 m	Unwrapped phase in radians
Coherence	Number of polarizations	Byte	25 m	Coherence range 0 – 1
Mask	1	Byte	25 m	Byte layer with flags for various channels (e.g., data quality and shadow-layover)
Connected components	1	Byte	25 m	Connected components flag for each pixel
Amplitude	2*Number of co-polarizations	Int16	25 m	This is needed for full covariance of interferograms
Secondary Layers				
Azimuth time	4	Float64	1 km	Azimuth time polynomial grid
Slant range	4	Float64	1 km	Slant range polynomial grid
Incidence angle	4	Float32	1 km	Incidence angle grid
Azimuth angle	4	Float32	1 km	Azimuth angle grid
Elevation angle	4	Float32	1 km	Elevation angle grid
Baseline parallel component	4	Float32	1 km	Parallel baseline grid
Baseline perpendicular component	4	Float32	1 km	Perpendicular baseline grid
Range offsets	4	Float32	1 km	Range offset grid
Azimuth offsets	4	Float32	1 km	Azimuth offset grid
Solid Earth tides	4	Float32	10 km	Solid Earth tide
Tropospheric dry delay	40	Float32	25 km	Dry delay estimated from ECMWF
Tropospheric wet delay	40	Float32	25 km	Wet delay estimated from ECMWF
Ionosphere phase screen	1	Float32	1 km	Ionosphere phase screen estimated using split spectrum method
LUT	2*Number of co-polarizations	Float32	5 km az x 1 km rg	To translate amplitude DN layers to backscatter

TABLE 21-8. L2 GCOV DATA LAYER DESCRIPTION

Name	Number of Layers	Data Type	Spacing	Description
Primary Data Layers				
Complex correlation	3 (Dual pol) 6 (Quad pol)	CInt16	25 m	Complex covariance matrix elements
Mask	1	Byte	25 m	Byte layer with flags for various channels (e.g., data quality and shadow-layover)
Projection angle		Float32	25 m	Projection angle grid
Secondary Layers				
Azimuth time	4	Float64	1 km	Azimuth time polynomial grid
Slant range	4	Float64	1 km	Slant range polynomial grid
Incidence angle	4	Float32	1 km	Incidence angle grid
Azimuth angle	4	Float32	1 km	Azimuth angle grid
Elevation angle	4	Float32	1 km	Elevation angle grid

National Aeronautics and Space Administration

Jet Propulsion Laboratory
California Institute of Technology
Pasadena, California

www.nasa.gov

CL# 18-1893

JPL 400-1707 08/19